SCIENCE ET TECHNIQUE DU FROID COMPTES RENDUS

CZECH AND GERMAN NATIONAL COMMITTEE FOR COOPERATION
WITH THE INTERNATIONAL INSTITUTE OF REFRIGERATION (IIR)

# The 12th
# CRYOGENICS 2012
## IIR International Conference

**Dresden, Germany**
**September 11 – 14, 2012**

INSTITUT INTERNATIONAL DU FROID
INTERNATIONAL INSTITUTE OF REFRIGERATION
Commissions A1, A2 and C1

# PROCEEDINGS

REFRIGERATION SCIENCE AND TECHNOLOGY

# Published by

**Icaris Ltd.**
Nám. Dr. Holého 8
180 00  Praha 8
Czech Republic

**Corresponding address:**
Malé náměstí 1
110 00 Praha 1
Czech Republic

**Contact:**
icaris@icaris.cz
www.icaris.cz

**www.icaris.cz/conf/Cryogenics2012**

ISBN: 978-2-913149-93-9
ISSN: 0151-1637
IIR code: 2012-4

# Content

# Committees

## The International Conference Committee

Alexey M. Arkharov, Russia
John Campbell, USA
Maciej Chorowski, Poland - Pres. Com. A2, IIR
Vaclav Chrz, Czech Republic
Didier Coulomb, France - Dir. IIR
Alexander Feher, Slovakia
Jacques Guilpart, France - Head Section C, IIR
Christoph Haberstroh, Germany
Ralf Herzog, Germany - Pres. Comm. A1, IIR
Zdenek Kaiser, Czech Republic
Mohammad Kalbassi, United Kingdom
Jürgen Klier, Germany
Philippe Lebrun, France - Head Section A, IIR
Stanislav Šafrata, Czech Republic
Ralph Scurlock, chairman, United Kingdom
Marija S. Todorović, Serbia - Pres. Com. C1, IIR

## The Organizing & Programme Conference Committee

Vaclav Chrz (chairman), Czech Republic
Christoph Haberstroh, Germany
Ralf Herzog (vice-chairman), Germany
Zdenek Kaiser, Czech Republic
Jürgen Klier, Germany
Tomáš Králík, Czech Republic
Radovan Kundera, Czech Republic
Martin Lánský, Czech Republic
Zdenek Machala, Czech Republic
Pavel Měřička, Czech Republic
Vera Musilová, Czech Republic
Stanislav Šafrata, vice-chairman, Czech Republic
Gabriele Spörl, Secretary, Germany
Pavel Schustr, Czech Republic
Pavel Urban, Czech Republic
Martin Vinš, Czech Republic

Dalibor Červinka, Icaris, Czech Republic
Ladislav Červinka, Icaris, Czech Republic
Romana Kočová, Icaris, Czech Republic

## Conference partners

CHART®

Innovation. Experience. Performance.™

ILK Dresden

A Member of
The Linde Group

KRYOTECHNIK

# Copyright and Disclaimer

International Institute of Refrigeration
Institut International du Froid
IIR/IIF

177 boulevard Malesherbes
75017 Paris
France
e-mail: iif-iir@iifiir.org

# CRYOGENICS IN PARTICLE PHYSICS

001

# Cryogenics for the Future Accelerator Complex NICA at JINR

**Agapov N.[*], Batin V.[*], Emelianov N.[*], Hisameev I.[**], Krakovsky B.[***], Mitrofanova Y.[*], Nikiforov D.[*], Popov O.[***], Trubnikov G.[*], Udut V.[***], Ziskin G.[**]**

[*] Joint Institute for Nuclear Research, Dubna, Russia;
[**] Joint-Stock Company "NIITURBOKOMPRESSOR", Kazan, Russia
[***] Joint-Stock Company "NPO GELIYMASH", Moscow, Russia

## ABSTRACT

NICA (Nuclotron-based Ion Collider fAcility), presently under construction at JINR [1], will be, upon its completion in 2016, among the most advanced research instruments of the physics community. The facility is aimed at providing collider experiments with heavy ions up to uranium (gold at the beginning stage) with a centre of mass energy up to 11 GeV/u and an average luminosity up to 1027 cm-2 s-1. The NICA cryogenics will be based on the modernized liquid helium plant that was built in the early 90's for the superconducting synchrotron known as the Nuclotron. The main goals of the modernization are: increasing of the total refrigerator capacity from 4000 W to 8000 W at 4.5 K, making a new distribution system of liquid helium, and ensuring the shortest possible cool down time. These goals will be achieved by means of an additional 1000 l/hour helium liquefier and "satellite" refrigerators located near the accelerator rings. This report describes the design choices of the NICA, demonstrates helium flow diagrams with major new components and briefly informs of the liquid nitrogen system that will be used for shield cooling at 77 K and at the first stage of cooling down of three accelerator rings with the total length of about 1 km and "cold" mass of 220 tons.

## 1. INTRODUCTION

Since 1992, the largest Russian liquid helium plant for the superconducting accelerator Nuclotron has been operating at the Joint Institute for Nuclear Research in Dubna near Moscow. The concept of its cryogenic system includes a large number of technical ideas and solutions never used before. The most significant of these solutions were the following: fast cycling superconducting magnets, cooling by the two-phase helium flow, an unusually short period of time for cool down till the operating temperature, parallel connection of about 150 cooling channels of the magnets, «wet» turbo expanders, screw compressors with a pressure rise of more than 25, and jet pumps for liquid helium. These technical solutions allowed one to construct an efficient and reliable cryogenic system.

The plans for further development of the basic installations at the JINR Laboratory of High Energy Physics are to build new accelerators: Booster and Collider, both using magnets with superconducting windings cooled to liquid helium temperatures. These two accelerators together with the existing Nuclotron will be united into the NICA complex.

The newly created accelerator complex will require additional refrigeration capacity at 4.5 K and 80 K. For the cryogenic system upgrading, we will use screw helium compressors with a new design, an additional 1000 l/hour helium liquefier, and a distribution system of cooling capacity based on the helium "satellite" refrigerators. Besides, a new 80 K refrigerating system will be made on the basis of nitrogen turbo compressors.

## 2. GENERAL VIEW OF NICA CRYOGENICS

A detailed description of the existing Nuclotron cryogenic system can be seen in [2-4]. New installations, which will appear while updating and building complex NICA, are shown in Figure 1. The main technical characteristics of the NICA helium cryogenic system are listed in Table 1.

The cryogenic systems of the future accelerators (Booster and Collider) will consist of the central helium liquefier and "satellite" refrigerators located near the accelerator rings. The "satellite" refrigerators operate using the liquid helium obtained from the central liquefier. It makes it possible to manage each of "satellite" refrigerators by using the minimum of the equipment. In this case this refrigerator, which consists only of heat exchangers, is highly reliable. Less reliable elements requiring more attention of the personnel will be located in one place – on the central liquefier. It is necessary to stress that this system needs minimum of cryogenic pipes but high thermodynamic efficiency is preserved.

Main installations of the existing cryogenic structure at the Nuclotron – two helium refrigerators KGU-1600/4.5 of capacity 2 kW at 4.5 K – were specifically designed by Joint-Stock Company “NPO GELIYMASH” for superconducting magnets of the JINR accelerators and have already been successfully operating for more than 25 years. Using this experience, the company has designed and now is manufacturing 1000 l/h helium liquefier OG-1000 (1), which represents the next generation of the Russian large-scale helium cryogenics. Its description will be given below.

We have got similar positive operation experience with helium screw compressors designed and manufactured by the Kazan Joint-Stock Company “NIITURBOKOMPRESSOR”. The first machine Kaskad-80/25 was purchased by JINR in 1990. This machine was made in a two-stage version with the outlet pressure of 2.5 MPa. Currently, the Nuclotron cryogenic system uses two of these compressors with helium flow rates of 5400 Nm$^3$/h each. To refrigerate new NICA accelerators, we have ordered two additional compressor units modified to increase the outlet pressure and capacity. This compressor modification named Kaskade-110/30 will be discussed in section 4 of the paper.

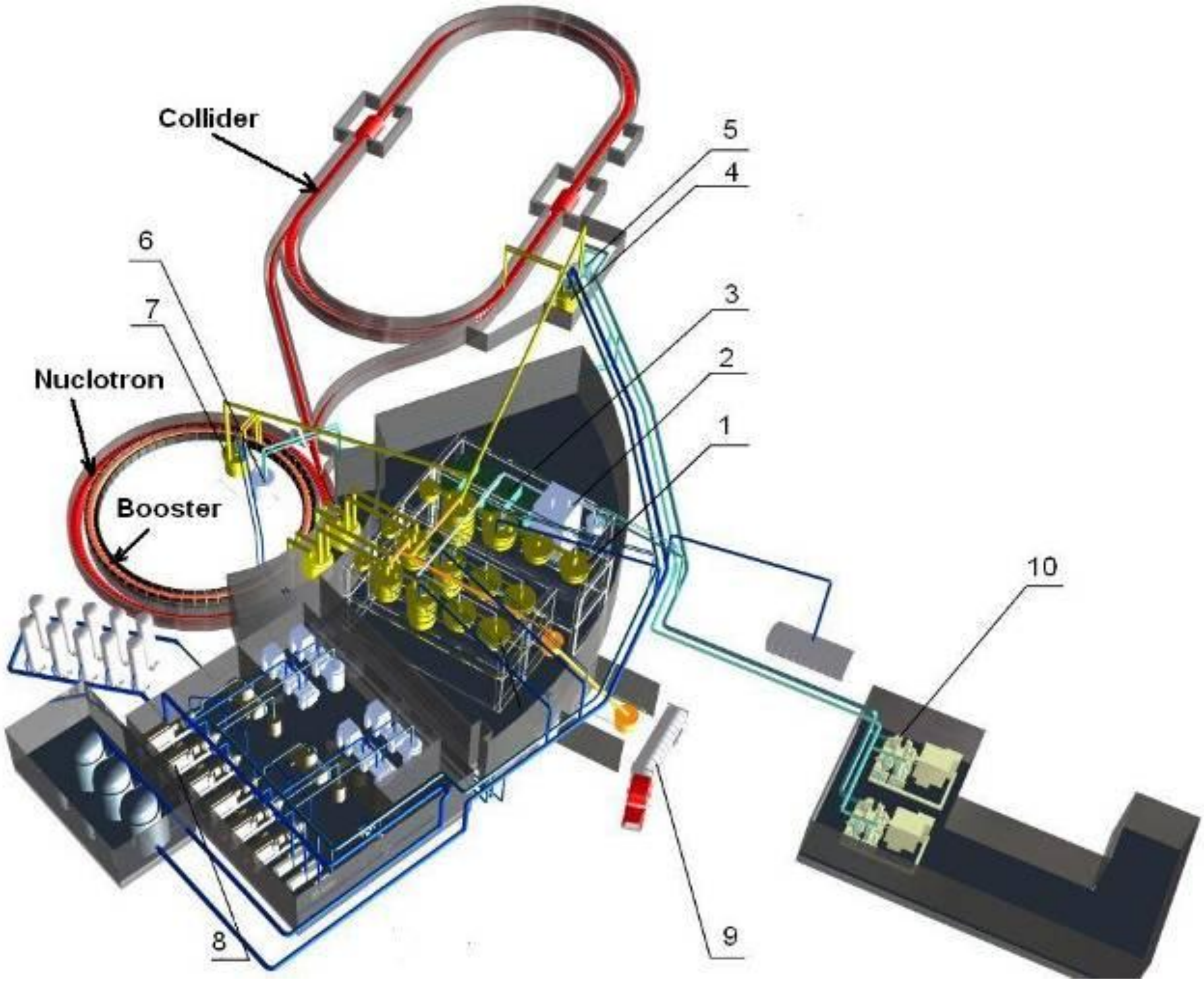

Figure 1. The general view of the cryogenic system for the NICA complex. New units for the NICA accelerators: 1- 1000 l/h helium liquefier OG-1000; 2 -1300 kg/h nitrogen liquefier OA-1,3; 3 – draining and oil-purification units; 4 – satellite refrigerator of the collider; 5 – 500 kg/h nitrogen re-condenser RA-0,5 of the collider; 6 - 500 kg/h nitrogen re-condenser RA-0,5 of the booster; 7 –satellite refrigerator of the booster; 8 – 6600 Nm$^3$/h screw compressors Kaskad-110/30; 9 -liquid helium tank; 10 - nitrogen turbo compressors.

Table 1. Basic parameters of the NICA helium cryogenics.

| | |
|---|---|
| Operating temperature (K) | 4.5 |
| Refrigerating capacity at 4.5 K (W) | 8000 |
| Total capacity of compressors (Nm3/h) | 31140 |
| Total power of electric motors (kW) | 7400 |
| Flow rate of cooling water ($m^3$/h) | 355 |
| Cold mass (tons) | 220 |
| Time for cool down to operating temperature (h) | 336 |

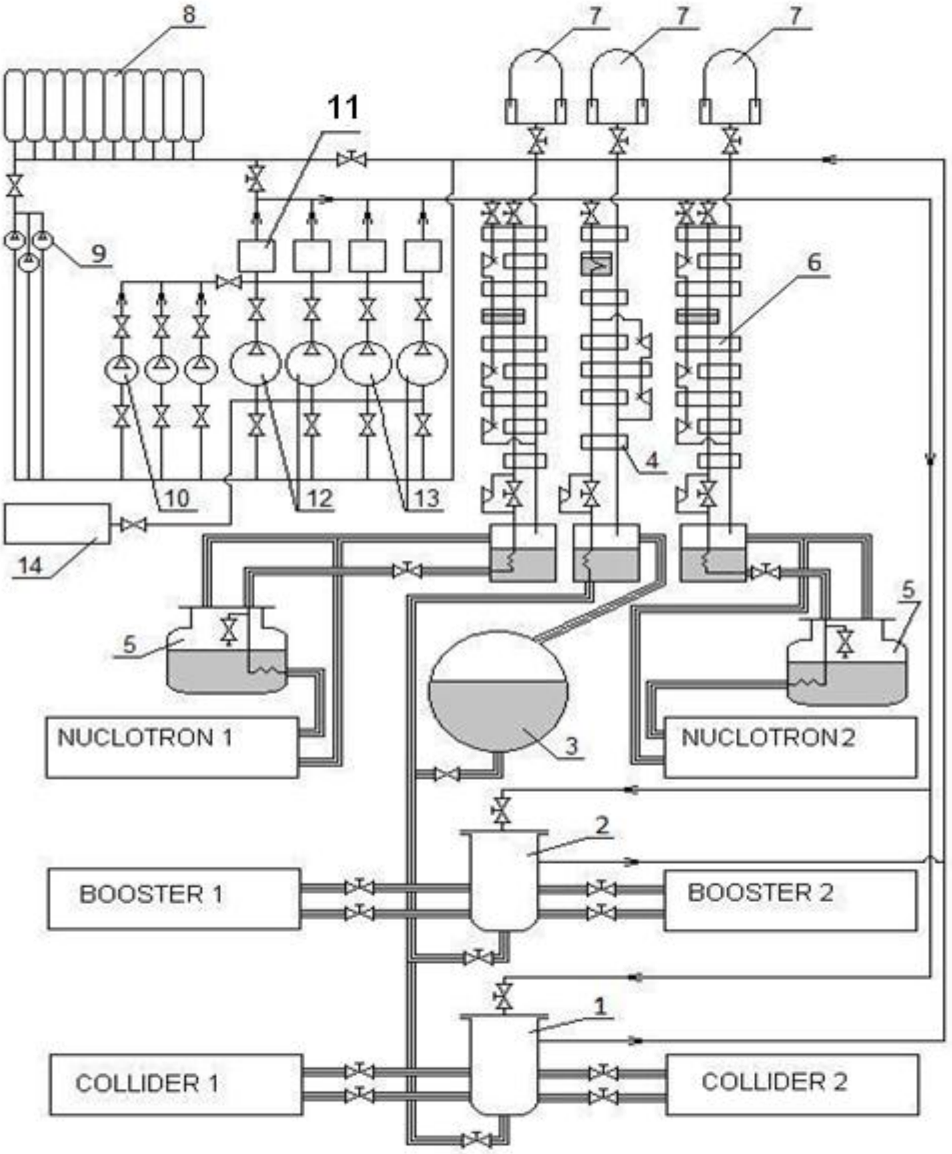

Figure 2. Schematic flow diagram of the cryogenic helium system for the NICA complex: 1- satellite refrigerator of the collider; 2 -satellite refrigerator of the booster; 3 – liquid helium tank; 4 –1000 l/h helium liquefier OG-1000; 5 – liquid helium separators; 6 – KGU-1600/4,5 helium refrigerators; 7 – gas-holders; 8 – compressed-helium reservoirs; 9 - 45 $Nm^3$/h piston compressors 1VUV – 45/150; 10 - 1200 $Nm^3$/h piston compressors 305NP-20/30; 11- draining and oil-purification units; 12- 6600 $Nm^3$/h screw compressors Kaskad-110/30; 13- 5400 $Nm^3$/h screw compressors Kaskad-80/25; 14 – 100 $m^3$ intake reservoir.

## 3. HELIUM LIQUIFIER OG-1000

In 2011, the helium liquefier OG-1000 was specially designed to meet the needs of the NICA complex by Joint-Stock Company “NPO GELIYMASH”. At present this company is manufacturing hardware. The flow diagram of the liquefier is shown in Figure 2 (point 4). Its thermodynamic cycle consists of two gas-expansion turbines, a vat of liquid nitrogen, two- and three-flow heat exchangers, and a «wet» expansion turbine. The liquefier is composed of six basic units (Figure 3), each enclosed in its own thermally insulated vacuum jacket and connected to the others by means of thermally insulated tubing. Impurities are removed from the helium at liquid-nitrogen temperatures in two switchable units 1 and 2 containing charcoal adsorbers. When one unit is operating, the other is being regenerated. This is done by heating with a hot gas followed by vacuum pumping. Besides, the picture shows two units 3 and 4 consisting of two- and three-flow twisted heat exchangers, an expansion turbine unit 5, and a liquefaction unit 6 with a liquid-helium collector of about 1000 l in volume. The expansion turbines are constructed following the design described in [5]. Basic parameters of the liquefier OG-1000 and technical characteristics of the turbo expanders are listed in Table 2 and 3.

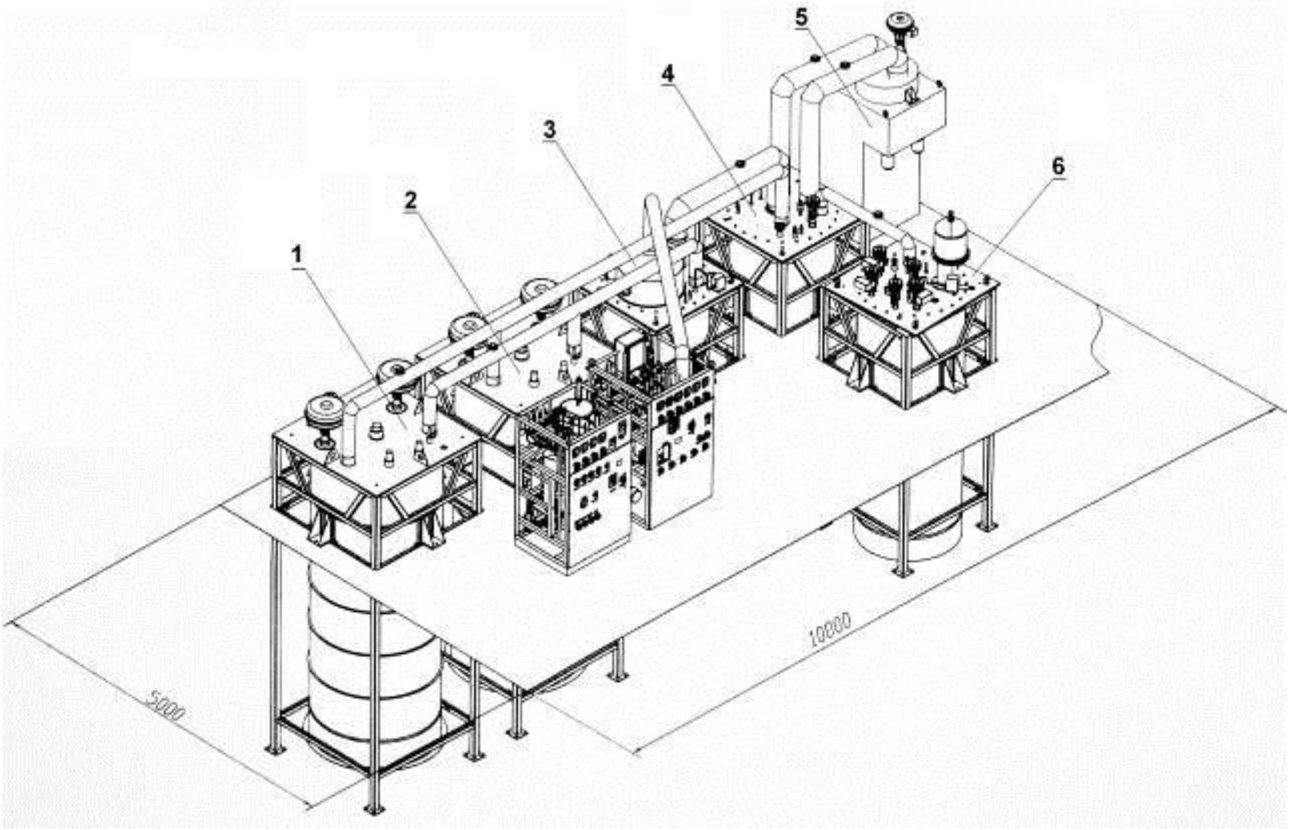

Figure 3. Helium liquefier OG-1000: 1, 2 - purification units; 3, 4 – heat exchangers units; 5 - expansion turbine unit; 6– liquefaction unit.

Table 2. Basic parameters of the liquefier OG-1000.

| | |
|---|---|
| Capacity (l/h) | 1100±100 |
| Liquid nitrogen consumption (kg/h) | ≤ 560 |
| Energy consumption (kW) | 1760 |
| Compressed helium pressure (MPa) | 2,5 |
| Compressed helium flow rate (Nm$^3$/h) | 6600 |
| Total mass (kg) | 14000 |
| External dimensions (m×m×m) | 5×5×10 |

Table 3. Technical characteristics of the expansion turbines.

| Parameters | Turbine 1 | Turbine 2 | «wet» turbine |
|---|---|---|---|
| Mass flow rate (kg/sec) | 0.2238 | 0.2226 | 0.1094 |
| Inlet pressure (MPa) | 2.29 | 1.16 | 2.21 |
| Outlet pressure (MPa) | 1.18 | 0.131 | 0.21 |
| Inlet temperature (K) | 54 | 22.3 | 7.98 |
| Expected isentropic efficiency | 0.72 | 0.75 | 0.65 |
| Output power (kW) | 10.9 | 10.9 | 1.25 |
| Speed (rpm) | 130 000 | 90 000 | 145 000 |
| Impeller diameter (mm) | 35 | 50 | 15 |

## 4. HELIUM COMPRESSORS OF NICA COMPLEX

The cryogenic system of the NICA will use compressors of various types and modifications. Technical characteristics of the machines are listed in Table 4. The main ones are four oil-lubricated screw compressor aggregates Kaskad-80/25 and Kaskad-110/30. For the stage-by-stage regulation of the flow rate and storage of compressed helium, smaller-capacity 305NP-20/30 and 2GM4-12/31 piston compressors are used. The evacuated helium is pumped into the reservoirs by small 1VUV-45/150 piston compressors, operating at higher outlet pressures.

At the present time, two Kaskad-80/25 have been installed in the cryogenic system of the Nuclotron, and there are plans to install two new compressors named Kaskad-110/30 by 2013. The total capacity of the helium compressors, located in the Nuclotron machine room, the installed power, and the flow rate of cooling water are 17940 Nm$^3$/h, 4.18 MW, and 200 m$^3$/h, respectively. After new machines are put into operation, these values will increase to 31140 Nm$^3$/h, 7.4 MW, and 355 m$^3$/h.

Table 4. Technical characteristics of the helium compressors in the NICA cryogenic system.

| | Kaskad-80/25 | Kaskad-110/30 | 305NP-20/30 | 2GM4-12/31 | 1VUV-45/150 |
|---|---|---|---|---|---|
| Number | 2 | 2 | 3 | 4 | 4 |
| Type | screw | screw | piston | piston | piston |
| Capacity (Nm$^3$/h) | 5400 | 6600 | 1200 | 840 | 45 |
| Outlet pressure (MPa) | 2,5 | 3.0 | 3.0 | 3.1 | 15 |
| Total power of electric motors (kW) | 1430 | 1600 | 200 | 160 | 22 |
| Voltage (V) | 6000 | 6000 | 380 | 380 | 380 |
| Number of compression stages | 2 | 2 | 3 | 3 | 3 |
| Speed (rpm) | 2970 | 2970 | 500 | 710 | 620 |
| Flow rate of cooling water, m$^3$/h | 60 | 78 | 15 | 7.2 | 1.5 |

The Kaskad-80/25 consists of three basic units: the first stage, the second stage, and the oil-cooling unit [4]. The first stage contains two compressors operating in parallel, driven by a single electric motor of power 0.63 MW with a voltage of 6 kV. The second stage consists of a single screw compressor. All aggregates have a single oil separator and an oil system common to the compressors of the first and second stages.

In comparison with Kaskad-80/25, the first step of the new machine (Figure 4) includes two compressors; each of them is placed on a separate frame and driven by its own motor of power 0.4 MW. The oil coolers for each compressor are located directly on the compressor unit. This solution together with using the slide valves allows one to adjust the compressor capacity from 100 to 20% of the nominal value.

The primary oil separation consists of a horizontally installed cylindrical vessel which also serves as the oil reservoir. The next stage is composed of a vertical oil separator and internal oil coalescing filter cartridges in parallel. The final oil separation is composed of three filters and one oil adsorber containing active charcoal.

## 5. LIQUID NITROGEN SYSTEM

The system of liquid nitrogen will be used for shield cooling at 77 K and at the first stage of cooling down of the accelerator rings. As it is shown in Figure 1, this system consists of one nitrogen liquefier (2) with capacity of 1300 kg/h, two 500 kg/h nitrogen re-condensers (5 and 6), and turbo compressors (10). The liquefier and re-condensers have identical thermodynamic cycles based on two gas-expansion turbines, where the compressed gas expands step-by-step from the pressure of 1.8 to 0.12 MPa.

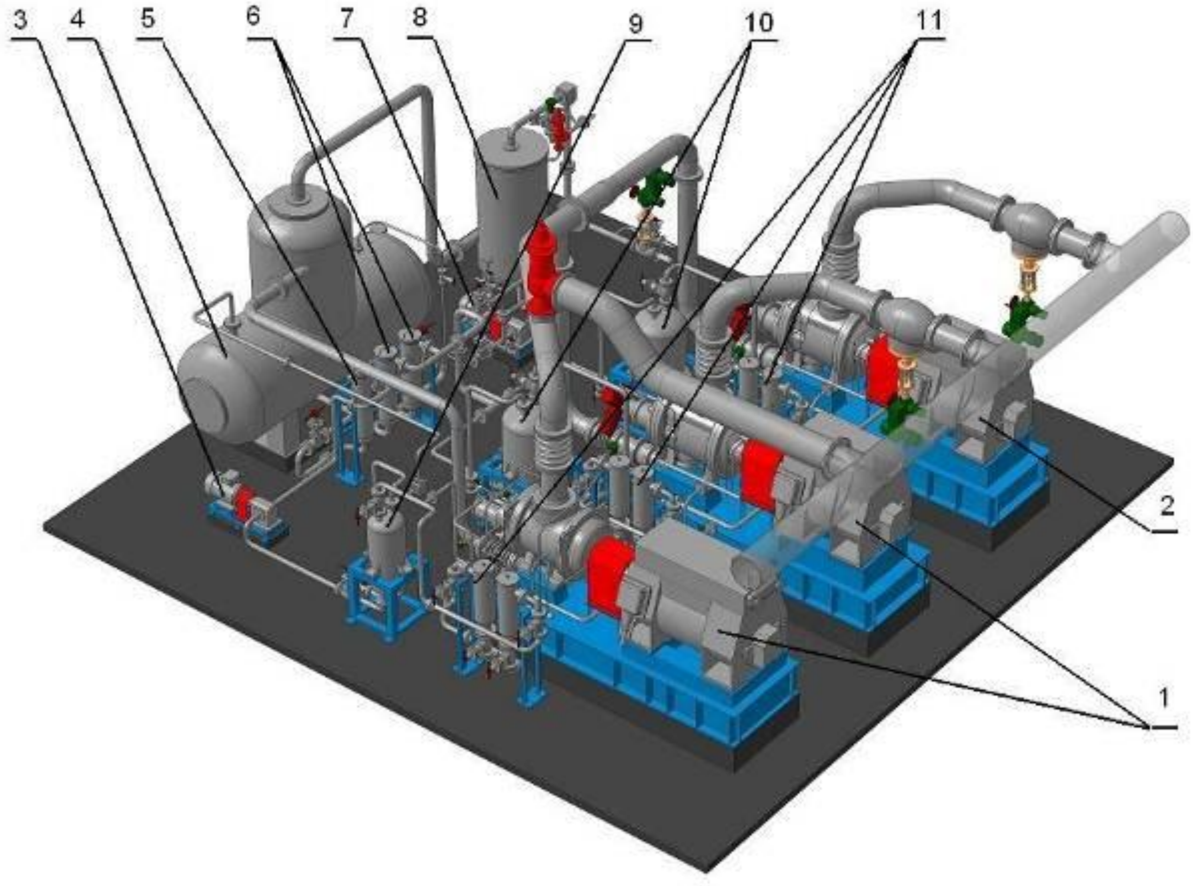

Figure 4. The general view of the helium screw compressor aggregate Kaskad-110/30: 1- two primary screw compressors; 2 – screw compressor of the second stage; 3 – oil pump; 4– oil reservoir; 5 - preliminary oil purification unit of the second stage; 6 – preliminary oil purification unit of the first stage; 7 – start-up oil pump of the primary screw compressors; 8 – oil separator; 9 – oil cooler of the second stage; 10 - two oil coolers of the first stage; 11 – fine purification oil filters.

## 6. REFERENCES

1. Trubnikov G, et al. 2008, Project of the Nuclotron-based Ion Collider Facility **(**NICA**)** at JINR. *Proc. of EPAC 08,* Genoa: 2581-2583.
2. Baldin A, et al. 1994, Cryogenic System of the Nuclotron – a New Superconducting Synchrotron, *Adv. Cryog. Eng.* 39: 501-508.
3. Agapov N, et al. 2004, Nuclotron Cryogenic System: Status and Recent Development, *Proc. of Eight* IIR *Conference,* Prague: 57-65.
4. Agapov N 1999, Cryogenic Technologies of the Nuclotron – Superconducting Accelerator of Relativistic Nuclei, *Physics of Elementary Particles and Atomic Nuclei*. 30(3): 760-804.
5. Agapov N, et al. 2001, More Effective «Wet» Turboexpander for the Nuclotron Helium Refrigerators, *Adv. Cryog. Eng.* 47: 280-287.

010

# Thermal Design of Cryogenic Permanent Magnet Undulator for SLS

**Anghel A.[*], Jakob B.[*], Bruegger M.[*], Schmidt T.[*], Tanaka T.[**], Kohda T.[***]**

[*]Paul Scherrer Institut, CH-5232 Villigen PSI, Switzerland;
[**]RIKEN/Spring-8, Koto 1-1-1, Mikazuki, Japan;
[***]Neomax Engineering Co., Ltd., 2-19-1 Minamisuta Suita-shi, Osaka, Japan

## ABSTRACT

The cryogenic permanent magnet undulator (CPMU) is an insertion device in which the permanent magnets are cooled down to cryogenic temperatures to improve the magnetic performance in terms of the remanent field and coercivity. As it was found recently, the peak field and coercivity of permanent magnet materials like NdFeB are increasing as the temperature is decreased and reached a maximum at around 130 K. This temperature is not directly attainable by boiling of standard cryogenic fluids like liquid nitrogen (77 K) or liquid helium (4.2 K). We present a practical and reliable cooling method based on the thermal shunt principle with either liquid nitrogen or a cryocooler as a cold source. Design criteria, cryogenic analysis and the layout of a CPMU based on this principle are presented. A new CPMU with a magnetic period of 14 mm and a magnetic length of 1.7 m, has been manufactured and is presently installed and in operation at the Swiss Light Source (SLS) as part of a collaboration between PSI (Paul Scherrer Institute), SPring-8 and Hitachi Metals, Ltd.

## 1. INTRODUCTION

In recent years, permanent magnet (PM), short-period undulators became more and more used in synchrotron radiation facilities. Short-period PM undulators increase the number of periods per unit length and generate therefore a brighter synchrotron radiation. Moreover, they enable the emission of high energy photons and allow the operation of an x-ray beam line in a medium size synchrotron like SLS [1]. A short period undulator is also useful for SASE-FEL facilities since it lowers the electron beam energy necessary for the FEL operation and makes it compact and economical [2]. At the Synchrotron Light Source (SLS) facility in Villigen we have designed and built a CPMU called U14 based on NdBFe, 50BH PMs. The length of the undulator is 1.7 m. Each array contains 120 magnets mounted in metallic keepers fixed by screws on the magnet support called I-beam. The I-beam is made of massive, good thermal conducting material aluminium alloy) having, besides the function of a mechanical support, also the function to flatten the temperature gradients along the undulator length. Hollow, thin-walled stainless-steel shafts (supports) hold the I-beams in position inside the vacuum chamber of the synchrotron and permit creating a variable gap between the two magnet arrays. The shafts are thermal insulators and are anchored mechanically and thermally on external, room-temperature movable iron-beams which are part of the machine frame. The electron beam ($I_b$=400 mA)

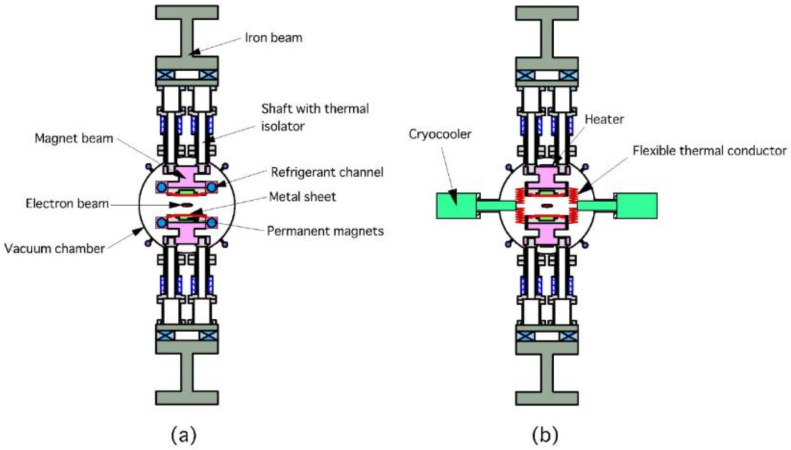

Figure 1. Two design examples of CPMU, a) with $LN_2$ cooling channels and b) with cryocoolers.

is placed symmetrical in the undulator gap. It produces image currents in the magnets which generate a large heat load. In order to protect the magnets from this heat, the magnets are covered with a thin copper foil, nickel-plated on one side. The 50 μm magnetic Ni sheet will be attracted by the magnets holding the foil in thermal contact to the magnets. The heat dissipated in the copper foil by the image currents of the electron beam is strongly reduced from 80 W/m to 5-8 W/m.

## 2. COOLING METHODS

In order to optimize its magnetic properties, the CPMU must be cooled down to a temperature in the range 130-140 K at which remanent field and coercivity is maximized [3]. There are two cooling methods which can be considered for CPMUs in this temperature range: liquid Nitrogen ($LN_2$) or a cryocooler. For $LN_2$ cooling, the CPMU is provided with cooling channels (pipes) where the refrigerant is circulated by means of a circulating pump. Because the cooling channel is at a temperature around 80 K and the desired temperature of the magnet array is 130-140 K, thermal shunts in form of thin metal foil are attached to the cooling pipes and the magnet support (I-beam). Temperature is regulated with an electrical heater mounted on the I-beam. The thermal resistivity of these shunts, the number of shunts and their distribution along the I-beam will decide the operating temperature and the temperature uniformity. In case of cryocooler cooling, the CPMU is provided with a metal plate of good thermal conducting material (copper) of the same length as the I-beam, placed parallel near the I-beam. The cryocooler cold head is attached mechanically and thermally to this temperature distribution plate. Between the plate and the I-beam, a number of thermal shunts, similar to those used in case of $LN_2$ cooling, are placed at position such to minimize the temperature gradient along the I-beam. A heater distributed over the length of the I-beam allows the temperature regulation. Each cooling method has qualities and drawbacks. LN2 cooling needs additional in-vacuum piping. The cryocooler needs a heavy thermal plate and produces vibrations. The acquisition and operational costs are also important. Only a detailed analysis can help in taking the decision for one or the other cooling method.

### 2.1. Cooling with sub-cooled $LN_2$

For our CPMU we chose cooling with $LN_2$ because our facility has already an installed $LN_2$ distribution. With $LN_2$ cooling there are in principle two possibilities: 1) to cool directly with $LN_2$ at normal pressure and 2) to cool using sub-cooled $LN_2$ at a pressure higher then the normal pressure. The first case is a typical two-phase flow cooling with large fluctuations in temperature and pressure inside the cooling channels. Therefore, although the cooling circuit becomes a little bit more complicated, we choose to work with sub-cooled $LN_2$. The cooling principle is illustrated in Fig.2 for a pressure of 6 bar. The boiling point of $LN_2$ is 77 K at 1 bar. At 6 bar, $LN_2$ would boil at ~95 K. We can cool-down equilibrium $LN_2$ at 6 bar in a heat-exchanger in a separate $LN_2$ bath boiling at normal pressure (1bar). We then obtain liquid at a pressure of 6

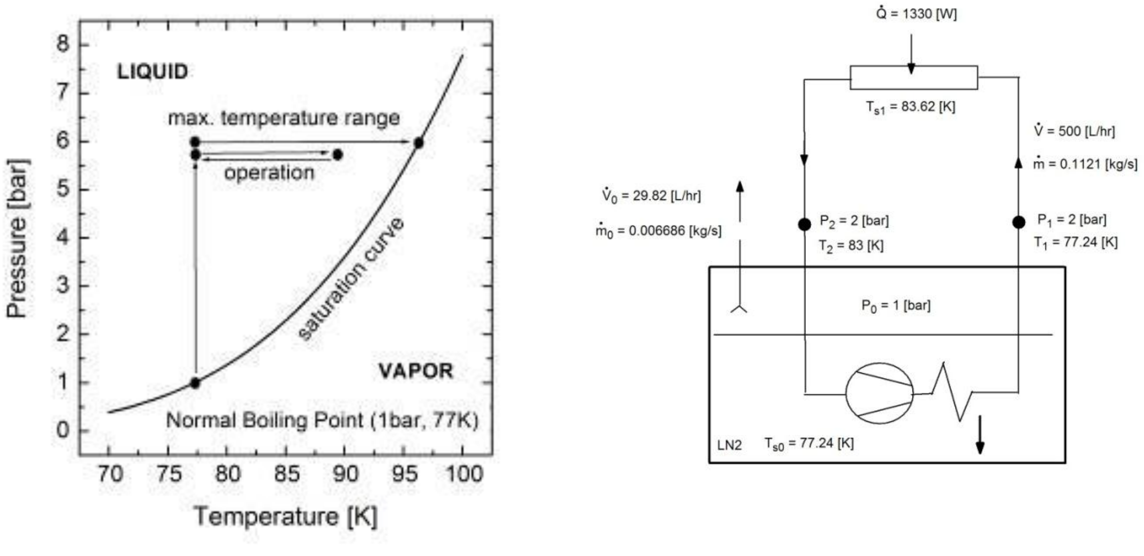

Figure 2. Phase diagram of $LN_2$, the saturation curve and the operation line for cooling with sub-cooled $LN_2$ at 6 bar. An example calculation for cooling with subcooled $LN_2$ at 6bar is shown in the right panel.

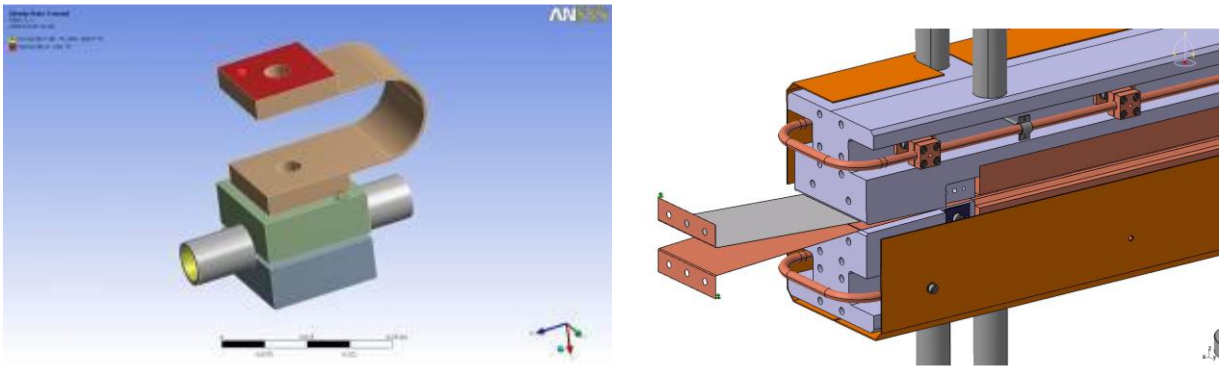

Figure 3. Design of the thermal shunt (a) and detailed view of cooling pipes, thermal shunts position, tapers and radiation shield.

bar but at a temperature very close to 77 K. This is the sub-cooled $LN_2$. This sub-cooled liquid can now be warmed-up 95-77=18 K above its initial temperature or allows a pressure drop of several bars before it starts to vaporize. At a lower operating pressure the temperature margin is lower, as can be seen from Fig.2. We chose to work at a pressure of 2 to 3 bars. In order to keep the magnets at a higher temperature (130-140 K) we use a number of thermal shunts ($N_s=2\times20$) as shown in Fig.3 clamped at fixed positions along the cooling tubes. The thickness of the flex foil is between 0.5 mm and 1.25 mm, depending on the desired minimum temperature without heating. The temperature is regulated with a heater mounted along the I-beam length.

## 3. UNDULATOR HEAT LOADS

The undulator heat loads are typical for a cryogenic environment: conduction, thermal radiation and residual gas to which one should add the heat generated by the beam in the Cu/Ni magnets cover-foil and the heat produced by the temperature control heaters mounted on the I-beams. Due to the good insulation vacuum in the beam line the residual gas conduction can be neglected. The heat by conduction between room temperature and undulator temperature (I-beam temperature), $Q_{sup}$ takes place in the $N_c=2\times12=24$ thin-walled, hollow tube stainless-steel shafts (supports)) on which the two I-beams are hanging/laying. These must have enough mechanical stability but conduct a minimum of heat into the system. On both ends of the undulator it is provides with tapers for a smooth transition from the aperture of the beam channel to the undulator aperture (variable gap). These tapers bridge a temperature difference from room temperature to the undulator operating temperature and conducts heat $Q_{tapers}$ into the system. The heat by conduction in the supports is calculated with the standard relation

$$\dot{Q}_{sup} = N_c k_{ss} A_s \frac{T_0 - T_2}{L_{sup}} \qquad (1)$$

where: $N_c$ is the number of columns, $k_{ss}$ -the thermal conductivity of the stainless-steel columns, $A_s$ -the cross-section area of one column, $T_0$ -the cryostat wall temperature (293 K) and $T_2$ –the I-beam temperature. A similar relation is used for calculating the heat load from the tapers $Q_{tapers}$. Finally, the thin Cu/Ni foil protecting the PMs from the eddy current produces by the e-beam travelling through the undulator generates the heat $Q_{beam}$ which must be included in the thermal balance. This can be calculated with the relation

$$\dot{Q}_{beam} = M I_b^2 \left(\frac{L_u}{\pi G}\right) \frac{\Gamma(3/4)}{\omega_0 \sigma_t^{3/2}} \sqrt{\frac{\mu_0 \rho}{2}} \qquad (2)$$

where: $I_b$=400 mA is the beam current, M=16 is the number of bunches in the beam, $\sigma_t$=30 ps, G=6 mm is the undulator gap, $\omega_0$=500 MHz the synchrotron frequency. For a stainless-steel foil ($\rho=8\cdot10^{-7}\ \Omega$m) the load would be 50 W/m and for a copper foil ($\rho=2\cdot10^{-8}\ \Omega$m) is only 7.5 W/m showing the importance of material choice. The thermal radiation has two components: the first, $Q_{shield}$ is from the room temperature parts to the 80 K shield (see Fig.3), the second one, $Q_{rad,e1}$ from the cold parts of the undulator at around 130-140 K to the 80 K shield. The corresponding equations are

$$\begin{aligned}
\dot{Q}_{shield} &= \sigma A_1 F_{\varepsilon}\left(T_0^4 - T_1^4\right)\\
\dot{Q}_{rad,e1} &= \sigma A_{e1} F_{\varepsilon}\left(T_2^4 - T_1^4\right)\\
\frac{1}{F_{\varepsilon}} &= \frac{1}{\varepsilon_1} + \frac{1-\varepsilon_2}{\varepsilon_2}\frac{U_{gird}}{U_{vac}}
\end{aligned} \tag{3}$$

with $\sigma=5.67\cdot 10^{-8}$ [W/m$^2$K$^4$], the Stefan-Boltzman constant, $\varepsilon_1$ and $\varepsilon_2$ the emissivities of the I-beam and shield material (Al and Cu) and $U_{gird}$ and $U_{vac}$ the perimeter of the I-beam and shield. Finally, there is a thermal load coming from heaters placed in contact with both I-beams, $Q_{cntrl}$. On each I-beam there are three heaters: left, middle and right. With the help of these heaters we can set the desired operation temperature, control the stability and adjust the temperature gradients along the undulator length.

## 4. THERMAL BALANCE

Due to the symmetry of the undulator one can model the thermal balance only for one half of it i.e. one I-beam. When the total heat load on the $LN_2$ bath is calculated this value is taken twice. We adopt a three node model with the following temperatures: $T_0$ –the ambient temperature (293 K), $T_1$ –the cooling temperature (also the shield temperatrure) and $T_2$ the temperature of the I-beam and magnets. The basic equations of the thermal balance for one I-beam are

$$\begin{aligned}
\dot{Q}_{\sup} + \dot{Q}_{beam} + \dot{Q}_{cntrl} + \dot{Q}_{tapers} &= \dot{Q}_{flex} + \dot{Q}_{rad,e1}\\
\dot{Q}_{flex} + \dot{Q}_{shield} &= \dot{m}C_p\left(T_{out} - T_{in}\right)
\end{aligned} \tag{4}$$

where $Q_{flex}$ is the heat flux in the thermal shunts, $T_{in}$ and $T_{out}$, the inlet and outlet temperatures of the subcooled $LN_2$, $\dot{m}$ –the mass flow of evaporated $LN_2$ and $C_p$ the specific heat of the subcooled $LN_2$, a function of pressure and temperature. The thermal balance for the $LN_2$ cooling loop is

$$\dot{Q}_{cryo} = 2\left(\dot{Q}_{flex} + \dot{Q}_{shield}\right) + \dot{Q}_{transf} = \dot{m}\lambda \tag{5}$$

where the factor 2 accounts for a complete undulator (2 I-beams) and $Q_{tranf}$ is the heat load on the transfer lines to and from the $LN_2$ subcooler-pump unit. This load is splitted in two halves, one half affecting the inlet line, the other one the outlet line. The temperatures at the inlet and outlet from undulator $T_{in}$ and $T_{out}$ are calculated using the equations

$$\begin{aligned}
h_{in}\left(T_{in}, p\right) &= h_{sat} + \frac{\dot{Q}_{transf}}{2\dot{m}_{sub}}\\
h_{out}\left(T_{out}, p\right) &= h_{in}\left(T, p\right) + \frac{2\left(\dot{Q}_{flex} + \dot{Q}_{shield}\right)}{\dot{m}_{sub}}\\
h_{back}\left(T_{back}, p\right) &= h_{out}\left(T, p\right) + \frac{\dot{Q}_{transf}}{2\dot{m}_{sub}}
\end{aligned} \tag{6}$$

where $h_{sat}$ is the enthalpy of saturated $LN_2$ and $m_{sub}$ the mass flow of subcooled $LN_2$ at the exit from the subcooler unit. The average temperature $T_1=(T_{in}+T_{out})/2$ is used to calculate all material properties. It is also the temperature of the shield and the clamped temperature of the thermal shunts. $T_{back}$ is the temperature of subcooled $LN_2$ at the return point of the subcooler-pump unit. The heat flux in the thermal shunts can be calculated with the formula

$$\begin{aligned}
\dot{Q}_{flex} &= N_s\frac{\left(T_2 - T_1\right)}{R_{flex}}\\
\frac{1}{R_{flex}} &= \frac{\dfrac{1}{hd_{in}} + \dfrac{1}{2k_{pipe}}\ln\left(\dfrac{d_{pipe}}{d_{in}}\right)}{\pi L_{contact}} + \frac{L_{flex}}{k_{Cu}A_{flex}}
\end{aligned} \tag{7}$$

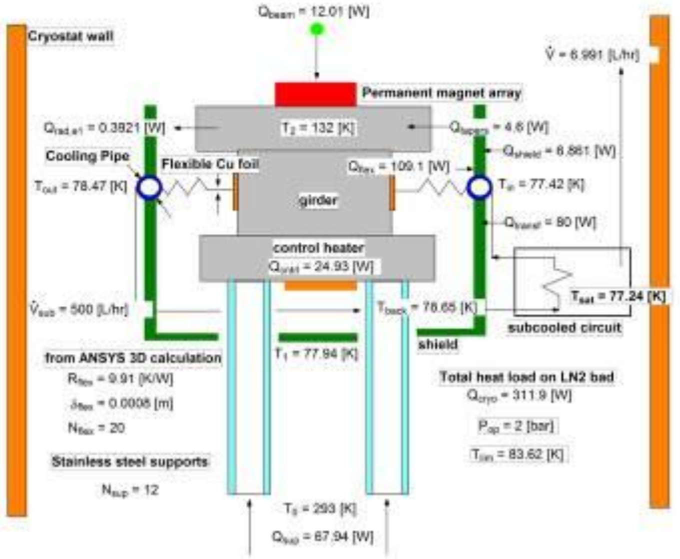

Figure 4. The EEE diagram window with the results of the thermal calculation.

where $R_{flex}$ is the equivalent thermal resistance of the thermal shunt, taking into account the heat exchange between $LN_2$ and cooling pipe, the heat conduction in the wall of the cooling pipe and finally the heat conduction in the flex band of length $L_{flex}$ and cross-section area $A_{flex}$. The heat exchange coefficient h for subcooled $LN_2$ is calculate with the Dittus- Boelter correlation $Nu = hk_{sub}/d_{in} = 0.023\,\mathrm{Re}^{0.8}\,\mathrm{Pr}^{0.4}$ where $k_{sub}$ is the thermal conductivity of subcooled $LN_2$ and $d_{in}$ the inner diameter of the cooling pipe of outer diameter $d_{pipe}$. $L_{contact}$ is the length of the contact clamp of the thermal shunt with the cooling pipe. An alternative procedure is to calculate the equivalent thermal resistance of the shunt with the help of a 3D finite element calculation. In both cases we ignored the thermal resistance at the contact between the surfaces.

This complex system of equation can be solved, if it is feed with appropriate material properties and design parameters. We chose to set the temperature of the magnets $T_2$ to a fixed value and find out the corresponding power of the control heater. Alternatively, in order to find the minimum attainable temperature we can set the power of the control heater to zero and find the temperature $T_2$. Each calculation gives out other important parameter like mass flow of $LN_2$ evaporated in the $LN_2$ subcooler, shield temperature $T_1$, inlet and outlet temperature of $LN_2$ from subcooler etc. The calculations have been performed with EEE [4]. An EEE script file with a graphical interface was prepared and a typical output is shown in Fig.4.

## 5. RESULTS

A summary of the calculated operating conditions is presented in Table 1. The following assumptions have been made: operating pressure, $P_{op}$=2 bar, total volumetric flow of subcooled $LN_2$, $V_{sub}$=500 L/hr, loss in transfer lines, $Q_{transf}$=80 W, the cooling circuit pipe is stainless-steel, I-beam is made of aluminium alloy and the thermal shunts are made of copper.

Table 1. Summary of undulator operating conditions. Minimum temperature and other two typical operating temperatures: 132 and 142 K for two different thermal shunts.

| Shunt thickness/thermal resistance | Minimum temperature $T_{min}$ | $LN_2$ consumption for $T_{min}$ | Operating temperature $T_{op}$ | Heater Power $Q_{cntrl}$ | Total $LN_2$ consumption at $T_{op}$ |
|---|---|---|---|---|---|
| [mm]/[K/W] | [K] | [Liter/hr] | [K] | [W] | [Liter/hr] |
| 0.8/9.91 | 121.8 | 6.073 | 132 | 24.93 | 6.991 |
|  |  |  | 142 | 49.30 | 7.888 |
| 0.7/11 | 125.6 | 5.997 | 132 | 14.21 | 6.511 |
|  |  |  | 142 | 36.62 | 7.319 |

## 6. COOLING CIRCUIT

The cooling circuit comprises a LN2 subcooler unit, a distribution manifold with valves and transfer lines. The subcooler unit is used to cool in parallel an optical monochromator. The most part of the transfer lines are flexible vacuum super-insulated lines with a loss of around 1 W/m. The rigid lines, have a loss of 0.45 W/m. For couplings we estimated the loss to be around 3W/coupler. The total load on the distribution system was estimated at 80 W. The schematic of the subcooler unit is shown in Fig.5.

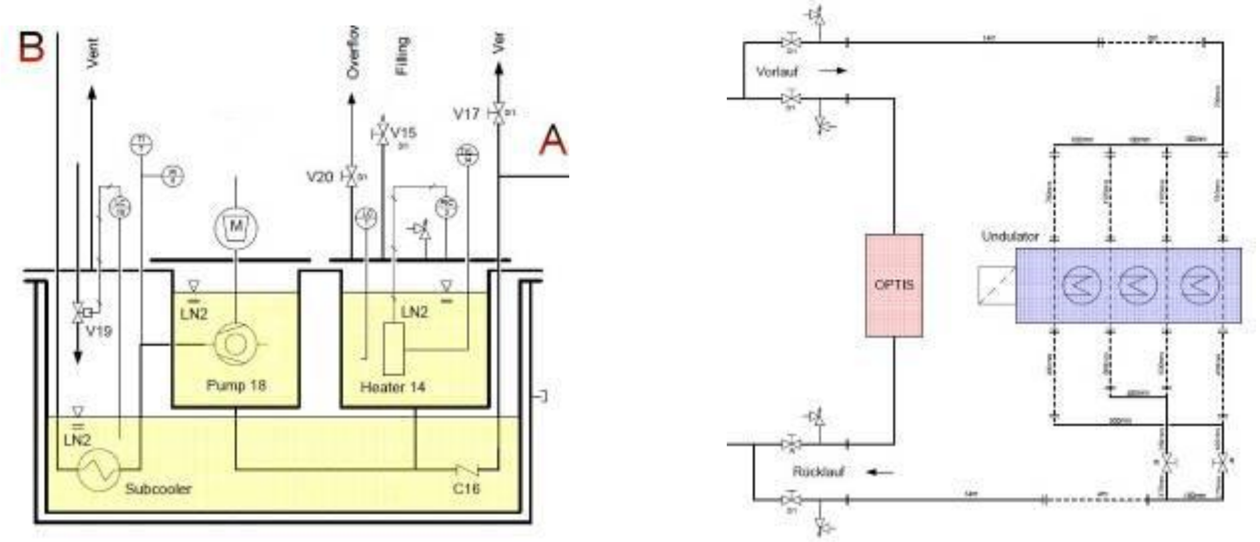

Figure 5. Left: Schematic of the subcooler unit used to prepare and circulate subcooled $LN_2$ in the cold undulator. Right: distribution manifold of undulator U14 and monochromator at the user beam-line OPTIS.

Warmer subcooled liquid coming from undulator enters the subcooler unit at point A. $LN_2$ flows over the non-return valve C16 and enters in two volumes. One is provided with a centrifugal pump 18, the second one contains a heater 14, a level indicator LC1 and a pressure controller PIC3. After being compressed in the pump 18, $LN_2$ is cooled-down in a subcooler heat exchanger in a third $LN_2$ bath at normal pressure. The temperature of $LN_2$ at the exit point B is around 77 K. With the help of the pressure regulator PIC3 the operating pressure of the subcooler and therefore the available temperature margin for the operation of the undulator can be set up. The subcooler unit is provided with valves for automatic refilling, valves for vent/overflow and a pressure relief valve.

## 7. CONCLUSIONS

Although very challenging, the design of the cold permanent magnet undulator could be managed with simple methods. The CPMU is now in operation over an almost 2 year period without problems. The temperature is very stable and the LN2 consumption is moderate, ~10 L/hr. The cooling was stopped once in December 2011 and then restarted end of January. According to our experience, the CPMU are as reliable as the room temperature permanent magnet undulators with the benefit of ~30% gain in performance.

## 8. REFERENCES

1. Schmidt T. et al., Insertion Devices at the Swiss Light Source, Nucl. Instr. and Methods Phys. Res. A **467-468**, 126 (2001)
2. Shintake T. et al., Startus of Spring-8 Compac SASE source FEL Project, Nucl. Instr. and Methods Phys. Res. A **507**, 382 (2003)
3. Hara T., Tanaka T. and Kitamura H., Cryogenic permanent magnet undulators, Phys Rev. ST **7**, 050702 (2004)
4. Engineering Equation Solver (EES) is a general equation solver that can solve coupled non-linear algebraic and differential equations.

036

# Analysis of the SIS100 Superconducting Magnet Cooling

**Bleile A.[*], Fischer E.[*], Khodzhibagiyan H.[**], Mierau A.[*]**

[*] GSI Helmholtzzentrum für Schwerionenforschung, Darmstadt, Germany
[**] Joint Institute for Nuclear Research, Dubna, Russia

## ABSTRACT

We present the cooling scheme of the superconducting SIS100 accelerator, which follows the Nuclotron design. This Nuclotron concept is based on forced two phase helium flow where the cooling channels of the individual magnets are connected in parallel to the helium supply lines. The cooling principle is described for both a single magnet and the magnet string and the analysis of the system parameters is given. It is shown, that for all requested operation modes, a uniform cooling of all magnets can be assured and will be stable. This stability will be achieved despite the fact that the SIS100 magnet size and losses are significantly larger than those of the Nuclotron magnets.

## 1. INTRODUCTION

The Facility of Proton and Ion Research (FAIR) will construct as a set of accelerators and storage rings at GSI. The aim of the project is to provide high intensity primary and secondary beams of ions and antiprotons for experiments in nuclear, atomic and plasma physics. The SIS100 synchrotron with rigidity of 100 Tm will accelerate ions and protons at a high repetition rate at about 1 Hz which requires fast-ramped superconducting magnets with high dynamic heat release. The starting point for the design of the magnets and of the cooling system for the SIS100 was the Nuclotron synchrotron at JINR in Dubna, which was constructed on the basis of the fast-cycling super-ferric magnets [1] and is successfully in operation since 1993 [2].

The accelerator will be used in different super cycles [3]. Each super-cycle consists of several pulses with different amplitude and repetition frequency of the magnetic field. While the ramp rate and the magnetic field at injection are fixed at 4 T/s and 0.23 T, respectively, the extraction field varies in the range from 0.5 T to 1.9 T. The repetition frequency varies from few tenths of hertz up to 1 Hz, depending on the maximal field and on the injection and extraction time. The big variety of different operation modes cause a wide range of dynamic heat load generated in the SIS100 magnets [4, 5]. The measured power losses in the dipole magnets varies from 7 W static losses up to 70 W in the continuous triangular cycle with short injection and extraction at maximal field of 1.9 T. The winding of the magnets is made from hollow superconducting cable of the Nuclotron type cooled by two-phase helium flow. The hydraulic and thermal calculations [6] show that only the cooling by two-phase helium allows to keep the maximum temperature in the coil constant over a wide range of the heat load. Thus for the SIS100 synchrotron the cooling scheme based on the Nuclotron concept was selected.

## 2. THE CONCEPT OF THE SIS100 MAGNET COOLING

The superferric dipoles (Figure 2) and quadrupoles for the SIS100 synchrotron consists of an iron yoke and a superconducting coil made from the inner-cooled superconducting cable. The cooling scheme of SIS100 magnets is shown on the Figure 2. All magnets are connected in parallel to the common supply and return headers. The helium from the supply header passes the magnet bus bars and the coil (Points 1 -2), the re-cooler attached to the supply header (2-2’), the yoke (2-3) and goes to the return header. Since the hydraulic resistances of the re-cooler and of the cooling channels in the yoke are low in comparison to the hydraulic resistance of the coil and of the bus bars, the pressure drop in the yoke can be neglected. One can assume that the pressure in the point 2 is equal to the pressure in the return header. The heat generated in the

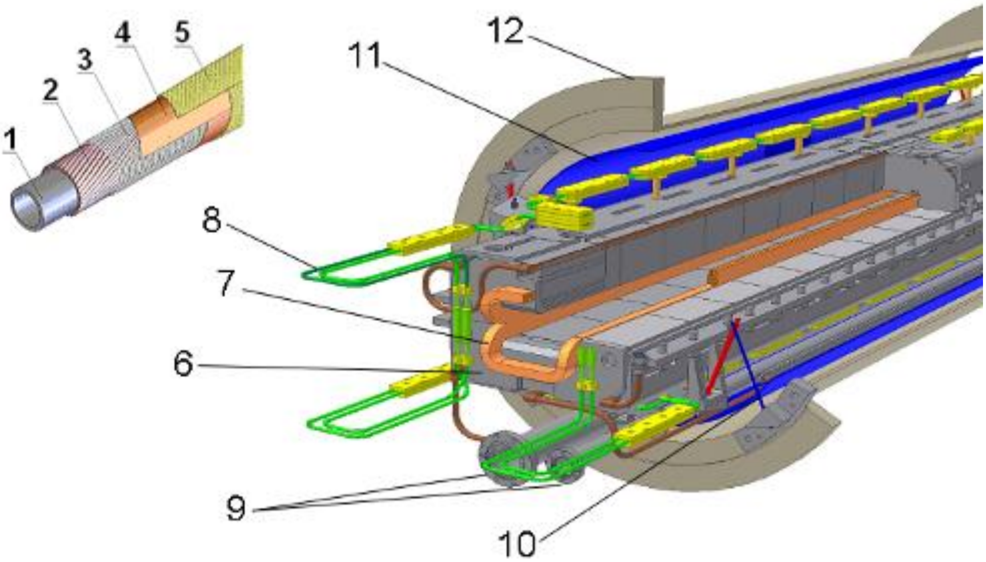

Figure 2 The structure of the Nuclotron cable and the SIS100 dipole magnet: 1 – cooling tube, 2 – superconducting wire, 3 - Nicrome wire, 4 – Kapton tape, 5 – adhesive Kapton tape, 6 – magnet joke, 7 – superconducting coil, 8 – bus bars, 9 – helium supply and return headers, 10 – support structure, 11 – radiation shield, 12 – vacuum vessel.

yoke is about 70% of the total power losses in the magnet. The helium in the supply header is a single-phase liquid, subcooled by 0.1 -0.2 K. In the magnet coil the liquid warms up until the saturation line is reached. Starting from this point the temperature of two-phase helium drops due to the pressure drop in the coil. The minimal temperature on the coil output is about 4.3 K and depends on the pressure in the return header. Afterwards the two-phase helium passes a re-cooler attached to the supply header (Points 2-2' on the Fig.2, right). The aim of the re-cooler is to keep the helium in the liquid state over the whole SIS100 sector and to avoid ingress of the helium vapour on the coil input. That way assures a reliable magnet cooling despite a big number of the parallel channels. The bypass valve on the end of the magnet string (Fig. 2, right) allows to control the flow rate on the end of a sector and to keep it above a certain limit, needed for the sufficient heat transfer in the last re-coolers. The SIS100 ring is divided into six sectors with about 50 parallel cooling channels in each sector [7].

This method of cooling requires an adjustment of the hydraulic resistances for all cooling channels. Dipole magnets with a total length of coil and bus bars of about 108 m define the upper limit of the hydraulic resistance. Two different scenarios for operation of dipole magnets are shown on the T-S diagrams (Fig. 3). The inner diameter of the cooling tube for all dipoles and quadrupoles is 4.7 mm. This value is optimized for a heat release in the dipole magnet of about 40 W, which corresponds to an operating cycle with a maximal field of 1.9 T, short extraction and an injection plateau of about 0.8 s. For the pressure difference between the helium headers of 0.5 bar the mass flow through the dipole magnet will be 2.4 g/s and the vapour quality on the yoke output about 0.9 (Fig. 3, left). For the most intensive triangular cycle with $B_{max}$ = 1.9 T the expected total heat release is about 70 W. With the same pressure difference between the helium headers of 0.5 bar the mass flow rate will drop to 2.1 g/s and the helium temperature at the yoke output will raise up to 6.4 K (Fig. 3, right), which is still sufficient for the reliable operation. The calculated operating parameters were experimentally verified on the two layer dipole prototypes [8]. First tests of the single layer dipole are expected in the beginning of 2013.

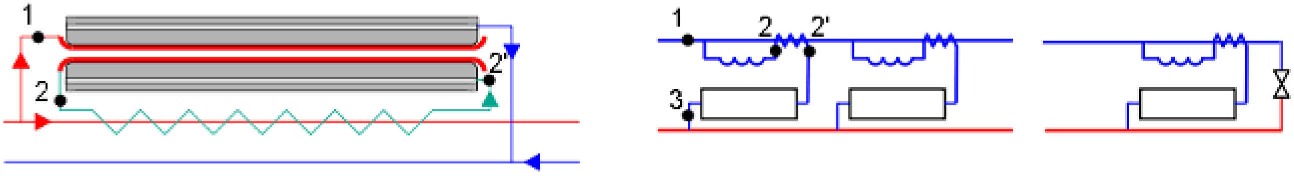

Figure 3 Cooling scheme of a single magnet (left) and of the SIS100 sector (right) 1 – coil input, 2 – coil output, 2'- re-cooler output, 3 – yoke output

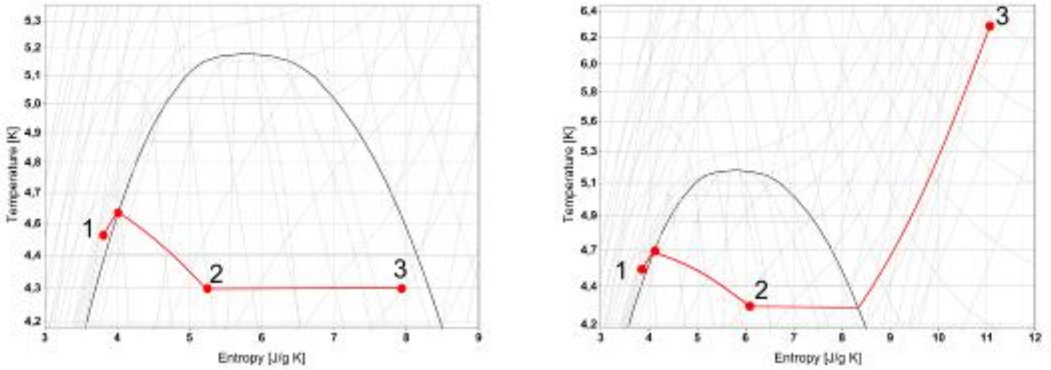

Figure 4 TS diagrams for the heat release in the dipole of 40 W (left) and 70 W (right)

Besides the 18 dipole magnets each SIS100 sector will contain 28 qaudrupole lenses combined in doublets. The length of one quadrupole coil with bus bars is 61 m; therefore the hydraulic resistance of the qadrupoles will be considerably smaller. Also the heat release in the quadrupoles is approximately two times smaller than in the dipoles. To assure a uniform distribution of the helium flow the adjustment of the hydraulic resistances of all parallel channels is required. This adjustment will be performed by combining of the quadrupole units with corrector magnets in series [7] and by introduction of additional impedances (flow restrictors) in the cooling circuits.

## 3. CONCLUSIONS

The cooling scheme of the SIS100 synchrotron is based on the Nuclotron concept. Because of the bigger number of the superconducting magnets in the SIS100 ring, it was divided into six independently cooled sectors instead of two sectors in the Nuclotron ring. That allows to reduce the number of parallel channels in one SIS100 sector by the factor of two in comparison to the Nuclotron sector. The reliability of the parallel cooling will be achieved by the adjustment of the hydraulic resistance for each channel, by usage of sub-cooled helium in the supply header and by the controlling of the helium flow in the last magnets in the sector by a bypass valve.

## 4. REFERENCES

[1] Baldin A.M. et al. 1995, Superconducting fast cycling magnets of the Nuclotron, *IEEE Trans.of Appl.Supercond.*, Vol.5, pp. 875-877

[2] Kovalenko A. 1994, Status of the Nuclotron, in *Proc. of the 4th European Particle Accelerator Conference*, London, vol. 1, pp. 161-164.

[3] Schuett P. 2003, Operation modes of the new accelerator complex for ions and antiprotons, *Report on EMAC II*

[4] Fischer E. et al. 2008, Full size model magnets for the FAIR SIS100 synchrotron, *IEEE Trans.of Appl.Supercond* , Vol.18, No. 2, pp. 260- 263.

[5] Fischer E. et al. 2009, Fast ramped superferric prototypes and conclusions for the final design of the SIS100 main magnets, *IEEE Trans.of Appl.Supercond* , Vol.19, No. 3, pp. 1087- 1091.

[6] Khodzhibagiyan H. et al. 2004, Some aspects of the cable design for fast cycling superconducting synchrotron magnets, *IEEE Trans.of Appl.Supercond.*, Vol.14, No. 2, pp. 1031-1034.

[7] Khodzhibagiyan H. et al. 2006, New design for the SIS100/SIS300 magnet cooling, *IEEE Trans.of Appl.Supercond.*, Vol.16, No. 2, pp. 411 – 414

[8] Fischer E. et al. 2010, Superconducting SIS100 prototype magnets: test results and final design issues, *IEEE Trans.of Appl.Supercond* , Vol.20, No. 3, pp. 164- 167.

# CRYOGENICS IN PARTICLE PHYSICS & FUSION

030

# Design, Manufacturing and Assembly of the Cryogenic Transfer Line for XFEL/AMTF

**Fydrych J.[*], Chorowski M.[*], Duda P.[*], Grzegory P.[**], Iluk A.[***], Malcher K.[***], Michalski G.[**], Rusinski E.[***], Strychalski G.[**]**

[*] Faculty of Mechanical and Power Engineering, Wroclaw University of Technology,
Wyb. Wyspianskiego 27, Wroclaw, 50-370, Poland
[**]KrioSystem Ltd, Muchoborska 18, Wroclaw, 54-424, Poland;
[***] Faculty of Mechanical Engineering, Wroclaw University of Technology,
Wyb. Wyspianskiego 27, Wroclaw, 50-370, Poland

## ABSTRACT

The cryogenic transfer line for XFEL/AMTF is dedicated for transferring cryogenic cooling power from helium refrigerators to a cryogenic test facility by means of the constant flows of supercritical and cold gaseous helium. The external envelope of this cryoline contains 4 cold process lines and a common radiation shield, as well as the system of supports and thermal contraction compensators. The line was designed and manufactured by Wroclaw University of Technology and KrioSystem Ltd, respectively, within the scope of Polish in-kind contribution to the XFEL project. Besides the minimisation of heat loads to transferred helium the design phase included the numerical analysis of the stresses and deformations on both the process lines and external envelope for a number of operational and failure modes. The paper describes the design of the cryogenic transfer line as well as the main phases of the manufacturing and assembly of its linear and elbow modules.

## 1. INTRODUCTION

European X-ray Free Electron Laser (XFEL) being under construction at DESY in Hamburg, Germany, will be composed of about 100 cryogenic modules, each holding eight superconducting cavities and one superconducting magnets assembly. Before their installation in the XFEL underground tunnel the cavities and cryogenic modules will be tested at their nominal operation conditions in the dedicated Accelerator Module Test Facility (AMTF). The cryogenic system of that facility will be supplied with cryogenic cooling capacity from helium refrigerators located of about 150 m from the AMTF hall. The cooling capacity, that is specified as the sum of 3 kW at 40 K, 0.5 kW at 4.5 K and 0.8 kW at 2.0 K, will be provided by means of two cold helium continuous streams: pressurised gaseous helium at 40 K and supercritical helium at 4.5 K. For that reason the AMTF hall will be connected with the helium refrigerators by multichannel cryogenic transfer line XATL1. The line will be located on a pipeline bridge, approximately 8 m in height, and will be exposed to weather conditions.

## 2. XATL1 PROJECT MANAGEMENT AND QUALITY ASSURANCE

The XATL1 project has been implemented by Wroclaw Technology Park (WTP) under Polish in-kind contribution to the European XFEL project. The requirements on the transfer line were provided to Polish party in the comprehensive specification prepared by DESY. The line was designed by Wroclaw University of Technology WUT according to the developed methodology presented in [1]. Then the design documentation of the line was provided to its final manufacturer, KrioSystem Ltd. The XATL1 project includes following phases:

1) Conceptual design (WUT),
2) Manufacturing design and technical documentation preparation (WUT),
3) Examination and acceptance of the technical documentation (DESY and notified body)
4) Procurement of materials (WTP),
5) Manufacturing of elements, components and subassemblies (WTP and subcontractors),
6) Assembly of the transfer line modules at assembly site (WTP and subcontractors)
7) Transportation of the modules to the construction site (WTP and subcontractors),

8) Module installation on the pipeline bridge at DESY (WTP and subcontractors),
9) Commissioning (WTP, WUT and DESY).

Since the specified high quality assurance requirements, both the design and manufacturing of the transfer line were performed according to the AD2000 code and the procedure described by Module G of the European Pressure Equipment Directive 97/23/EC. This module imposes, among other things, the necessity of applying a notified body for the verification of technical documentation, assessment of materials, approval of the welding procedures, as well as the verification of the qualifications of manufacturer's welders. Lastly the notified body approves the final pressure test and carries out the final inspection of all the pressure comprised in the vacuum jacket of the cryogenic transfer line, i.e. its internal process lines.

## 3. INTERNAL STRUCTURE OF THE CRYOGENIC TRANSFER LINE

The taken arrangement of process lines in the XATL1 cross section is presented in Figure 1. The cryoline consist of four process lines, which constitute two cryogenic circuits at 4.5 K and 40/80 K.

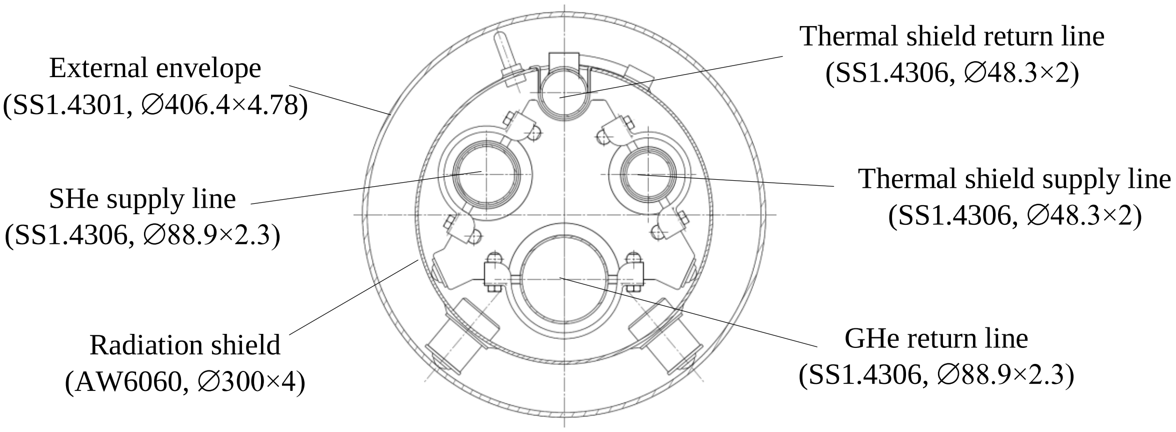

Figure 1. Cross section of the cryogenic transfer line XATL1

The 4.5 K circuit is composed of the SHe supply and GHe return lines, whilst the lines of thermal shield return and supply form the 40/80 K circuit. The thermal shield return line is connected with the radiation shield, thermalized at an average temperature of about 80 K, by a number of thermal bridges and it is used for gathering the radiation heat flux from the vacuum jacket, which temperature can vary from 260 K to 310 K due to external whether conditions.

## 4. ROUTING AND MODULARIZATION OF THE CRYOGENIC TRANSFER LINE

The routing of the cryogenic transfer line XATL1 is shown in Figure 2. The line runs from the Valve Box located at the helium refrigeration hall to the Subcooler Box located inside the AMTF hall. The line is located on the piping bridge 8 m above the ground level in order to do not collide with existing infrastructures (access roads, transforming station, cooling towers, and overhead crane in the AMTF hall).

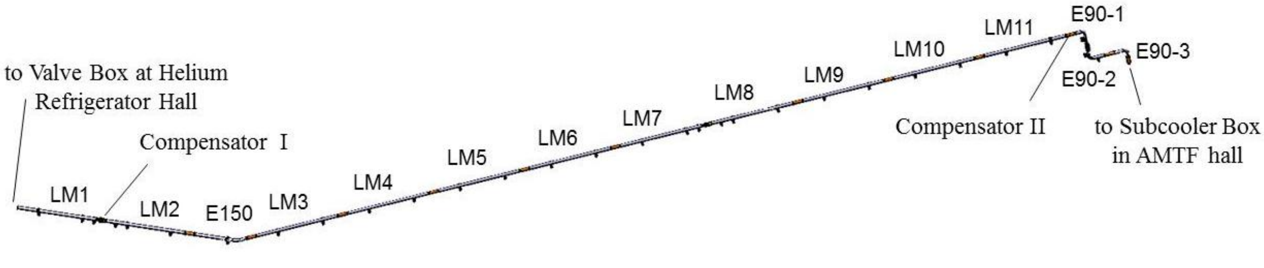

Figure 2. Routing of the XATL1 line with marked locations of the linear and elbow modules

The cryoline XATL1 has two long straight sections connected by a 150 deg elbow and it is ended with three short sections, two vertical and one horizontal, which include three 90 deg elbows. Its total length is equal to 167 m and exceeds the direct distance between the Valve Box and Subcooler Box by 11 m only.

The modularization of the cryogenic transfer line was done in respect to the necessity of the long-distance transportation to the XFEL/AMTF site and the facilitation of the final installation on the pipeline bridge as well. It took also into account some aspects of the minimisation of heat loads due to conduction through additional supporting structures. The size of each module could not exceed the dimensions of a standard lorry trailer. Thus the maximum length and width of the modules were specified as 13 m and 2.5 m, respectively. Finally, the whole line was divided into 11 linear modules LM1-LM11, and four elbow modules (E150, E90-1, E90-2 and E90-3). The proposed modularization resulted in 16 interconnections, which were designed as sleeve-shaped and dedicated to hold the elements of thermal compensation system.

## 5. DESIGN OF SUPPORTING AND THERMAL COMPENSATION SYSTEMS

The supporting and thermal compensation system of the external envelope is schematically presented in Figure 3a. Its supporting system consist of two fixed supports (VLA) which block all the possible movements (vertical, lateral and axial) in respect to the piping bridge, as well as it includes 21 sliding supports allowing for axial movements only (VL) and 2 sliding supports blocking the line movements only in vertical directions (V). The thermal expansion or shrinkage of the envelope is compensated by two axial and one lateral compensators. Both long straight sections are equipped with axial compensators as shown in Figures 2 and 3a, whilst the lateral compensator was built in the last interconnection, between module E90-3 and the Subcooler Box.

The external envelope will apply on the bridge not only its own pressure, thermal and weight loads but also the loads transferred from internal process lines. The supporting and thermal compensation system of each process line is shown in Figure 3b. It includes a set of one fixed (LA), four sliding supports (L) and one axial compensator (CA) per each linear module. The other modules have different supporting structure. Each process line in module E150 includes, apart from two sliding supports (L) and one axial compensator (CA), two fixed supports (LA) separated by a flexible hose (H). The section composed of three E90 modules contains two fixed supports (LA), two sliding support (L) and one metallic flexible hose.

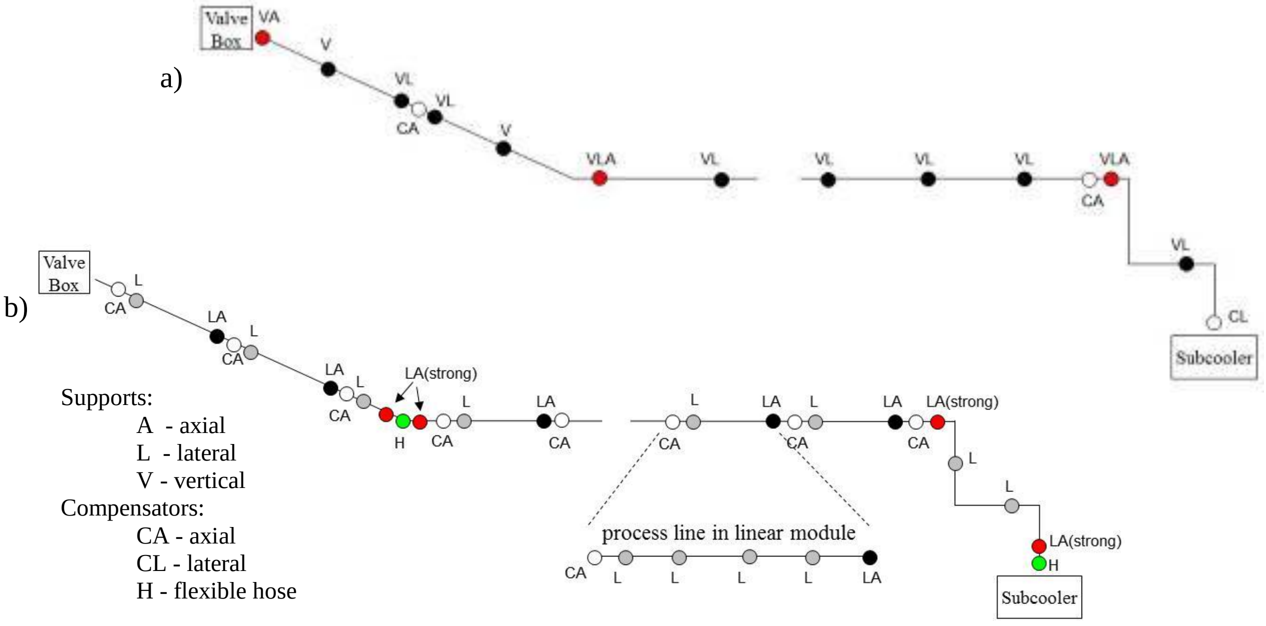

Figure 3. The schematic layout of the support and compensation system of external vacuum envelope (a) and process lines (b)

The proposed layout of supports and compensators was used as an input data to numerical thermo-mechanical analysis which allowed for checking the mechanical stability of the line exposed to all the possible operation conditions and failure modes. The analysis was also useful for the specification of the parameters of the crucial elements of supporting and thermal compensation systems. Due to exposure to outdoor whether condition the line as well as the pipeline bridge can shrink or elongate independently and strongly interact mechanically between themselves. Therefore the design of the line was strongly affected by the thermal performance of the pipeline bridge.

## 6. THERMO-MECHANICAL STRENGHT ANALYSIS

Stresses and displacements in the XATL1 process lines and vacuum jacket were checked numerically for various load cases. For that purpose a detailed numerical model of whole transfer line was developed and calculated with the use of Finite Element Method. The calculations were carried out for most dangerous load cases taking into account the thermal, pressure and weight loads acting on the XATL1. The developed model assumes that the pipeline bridge structure is much stiffer than the transfer line and the ambient operational temperature can vary from 260 K to 310 K. It takes also into account the thermal expansion of the bridge resulting from the ambient temperature variations. Additionally, because there is a safety exhaust on every module interconnection, which will open in case of helium leakage, the internal pressure in whole vacuum jacket during any failure modes increases to the 1,5 bara, whilst only two subsequent modules are cooled down by discharging cold helium. The thermo-mechanical strength analysis was carried out for design and pressure test conditions, as well as for three failure modes. The first mode (Helium leak I) analyses a helium leakage in LM2 and E150 modules, the second one (Helium leak II) considers leakage in LM10 and ML11 modules, whist the third mode (Helium leak III) covers the case of helium leakage in the section of all E90 modules.

The built FEM model uses shell elements for process lines, radiation shield and external envelope, beam elements for sliding supports and pipeline bridge construction elements, spring elements for all the compensators and finally membrane elements for elastic hoses. The model consist of 107 000 elements and includes all the kinematic joints of the external envelope, thermal shield and process line supports. A view of detail FEM model of a chosen section of XATL1 line is shown in Figure 4.

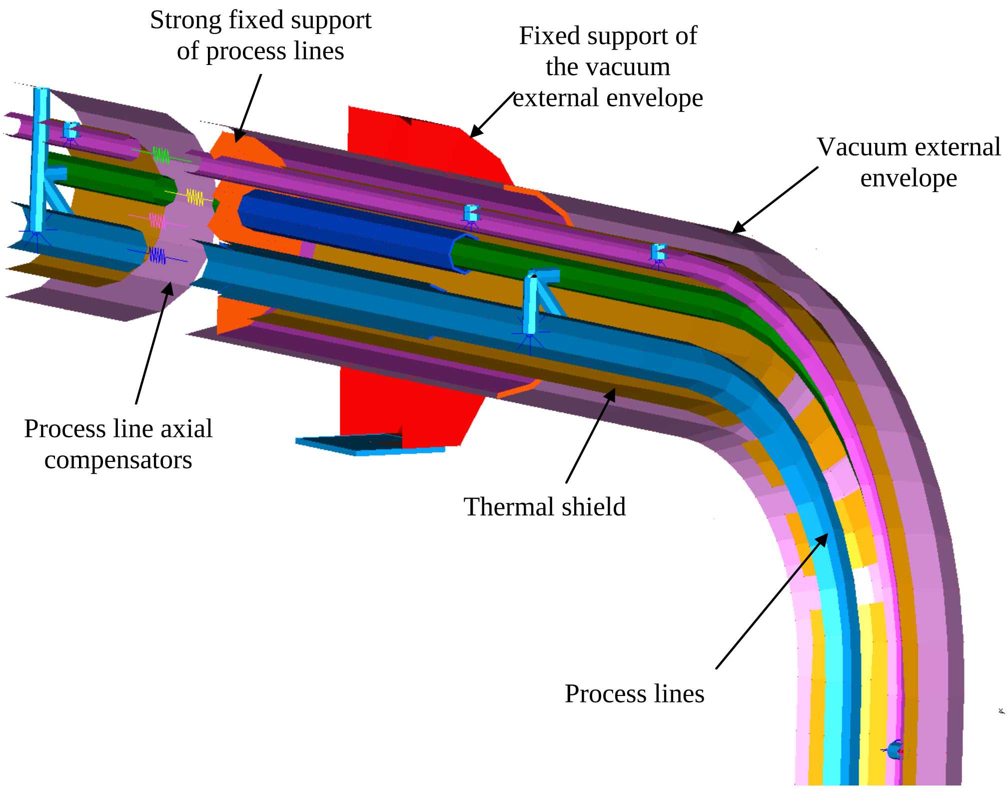

Figure 4. Schematic view of the FEM model of the E90-1 module

The numerical modeling resulted in the distributions of von Mises stresses and deformations as well as the forces acting on the supports. An example of the stress distribution is shown in Figure 5. The maximum stress values on the external envelope and process lines are 80.4 MPa and 87.2 MPa, respectively. The maximum allowable stresses, which take into account safety factors, are equal to 156.7 MPa for the external envelope and 146.9 MPa for the process lines. Thus, the maximum stresses do not exceed 75 % of the allowable stress values and therefore, according to [2], both the vacuum jacket and process lines are in stress category II. It means that the lowest temperatures of the external envelope and process lines can reach -273°C and -255°C, respectively.

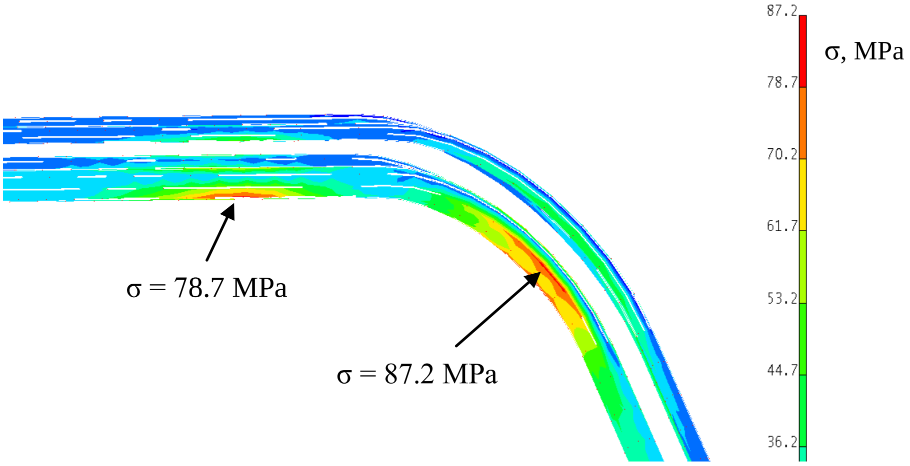

Figure 5. Location of maximal Von Mises stresses on process lines in the E90-1 module

The final design documentation of the cryogenic transfer line XATL1 included the functional specification, design calculation report, a set of 205 technical drawings, welding plan, test plan and hazard analysis. This documentation was verified and examined by TUV Nord Hamburg in agreement with the requirements of the guideline 97/23/EC and code AD2000 and the examination resulted in no objections.

## 7. MANUFACTURING AND ASSEMBLY OF THE XATL1 MODULES

The manufacturing and assembly of each module of cryogenic transfer line XATL1 contained the following set of technical operations:

1) Welding of process line sections and external envelope sections,
2) Test of the process line and external envelope sections,
3) Winding MLI on the 4.5 K and 40 K process lines,
4) Installation of the process line in their supports and radiation shield,
5) Fixation of thermal bridges to the thermal shield and thermal shield return line,
6) Winding MLI on the thermal shield,
7) Installation of the sliding supports to thermal shield,
8) Installation of the thermal shield in the external envelope,
9) Connection of the process line fixed supports to the external envelope,
10) Packing of the module and preparation for its transportation.

Some of listed above technical operations are shown in Figures 6-9. All used elements made of stainless steel, G10 and Teflon were brushed, cleaned and dried to remove all impurities as dust, oil, grease, welding cinder and other contaminants. All the operation done on cleaned elements as well as on MLI required handling with protective gloves (see Figure 6).

The tests of the process line sections included the radiographic examination of weld seams, pressure and helium-leak tightness tests as well as thermal shocking. The tightness tests and thermal shocking were carried out in a dedicated test rig, where a line section was closed in a 13 m long vacuum vessel connected to a helium leak detector (the smallest detectable helium leak rate $\leq 5\cdot10^{-12}$ $\text{mbar}\cdot\text{l}\cdot\text{s}^{-1}$). The tightness of each process line section was checked two times, separated by a cycle of three thermal shocking down to liquid nitrogen temperature level and rapid warming to the ambient temperature. All these performed tests did not reveal any defects of weld seams as well as any leaks exceeding and neither near to acceptable level ($10^{-8}$ $\text{mbar}\cdot\text{l}\cdot\text{s}^{-1}$).

Figures 6. Views of the installation of the process line sections in a doubled sliding support (courtesy Kriosystem)

Figures 7. View of the process line sections installed in their thermal shield with thermal bridges being installed (courtesy Kriosystem)

Figures 8. View of the thermal shield wound with 30 layers of MLI (courtesy Kriosystem)

Figures 9. View of the assembled linear module of XATL1 (courtesy Kriosystem)

## 8. CONCLUSIONS

The paper briefly describes the main issues of the design, manufacturing and assembly of the modules of the cryogenic transfer line for XFEL/AMTF. Both the design and assembly were performed according to the methodology and procedures developed at Wroclaw University of Technology and KrioSystem Ltd. The applied design methodology allowed for preparation of correct design documentation in respect to Directive 97/23/EC Module G and AD2000 code. This documentation was positively examined by TUV Nord Hamburg. Finally, the developed manufacturing and assembly procedure allowed for proper and efficient production of all the modules of cryogenic transfer line XATL1. Their production was completed within a very tight schedule.

## 9. ACKNOWLEDGMENTS

The work has been partly supported by the Polish Ministry of Science and Higher Education within the statutory activities of Wroclaw University of Technology. The authors would like to thank Detlef Sellmann for fruitful discussions and valuable pieces of advice on the cryogenic transfer line design.

## 10. REFERENCES

[1] Fydrych J. Chorowski M., Polinski J., Skrzypacz J. 2010. Design Methodology of Long Complex Helium Cryogenic Transfer Lines, *Trans. of Cryogenic Engineering Conference 2009*. Vol 55: 1103-1110.

[2] AD2000-Merkblatt W10, Materials for pressure vessels, Materials for low temperatures, Ferrous materials, ICS 23.020.30, November 2007 edition.

020

# Design Proposal For MITICA Cryogenic Plant

**Valente M.*, Fellin F.*, Haas H.**, Hanke S.**, Scannapiego M.**, Zaccaria P.***

* Consorzio RFX, Padua, Italy;
** Institute for Technical Physics (ITEP), Karlsruhe Institute of Technology, Karlsruhe, Germany.

## ABSTRACT

The MITICA Neutral Beam Injector, under construction in Padua at Consorzio RFX, will be equipped with a large cryosorption pump (composed by two halves). The cryopump, installed inside the MITICA Beam Line Vessel, will be supplied by a dedicated cryogenic plant with gaseous Helium (GHe) at 80 K and super critical Helium (ScHe) at 4.6 K. The design proposal for MITICA cryogenic plant is described in this paper. The cryogenic plant is divided in two main closed circuits: the 4.6 K circuit and the 80 K circuit. The first one is supplied by a Helium refrigerator via a LHe control cryostat acting as a thermal buffer due to the variable pulsed heat loads expected during MITICA operation. The second circuit is supplied by an 80 K facility where the refrigeration power is given by liquid nitrogen (LN2). Due to the expected large LN2 consumptions, a Nitrogen refrigerator is foreseen to recover and re-liquefy the evaporated LN2.

## 1. INTRODUCTION

In the framework of the ITER project, a new test facility called PRIMA (Padova Research on Iter Megavolt Accelerator) is under construction at Consorzio RFX (Padua, Italy). PRIMA will host two experiments: a full size plasma source with low voltage extraction called SPIDER (Source for Production of Ion of Deuterium Extracted from Rf plasma) and a full size neutral beam injector at full beam power called MITICA (Megavolt ITER Injector Concept Advancement). One of the MITICA internal components is a very large cryopump which must be supplied with ScHe at 4.6 K and GHe at 80 K from a dedicated cryogenic plant. This article describes in detail the actual status of the cryogenic plant design and configuration.

## 2. THE MITICA CRYOPUMP

The cryopump is divided in two halves located on the lateral sides of the MITICA Beam Line Vessel. Each half is 2.8 m high and 8 m long and it is divided in 8 modules (see Figure 5). It is constituted by two main circuits: the thermal shields circuit at 80 K and the cryopanels circuit at 4.6 K. The cryopanels are coated with an activated charcoal layer in order to adsorb gases during MITICA operation. The thermal shields have the aim of shielding the cryopanels from the heat loads (mainly radiation) coming from the hot surfaces of the other beam line components as well as from the 300 K vessel wall. The cryopump must be supplied with GHe at 80 K and 1.8 MPa, for the shielding system, and with ScHe at 4.6 K and 0.4 MPa, for the cryopanels system. The overall mass of thermal shields and cryopanels system are respectively 3960 kg and 1355 kg. The main materials are stainless steel and copper. The cryopump operation flow conditions are summarized in Table 1. These values refer to the stand-by and the pulse-on operation with $H_2$ and $D_2$ only.

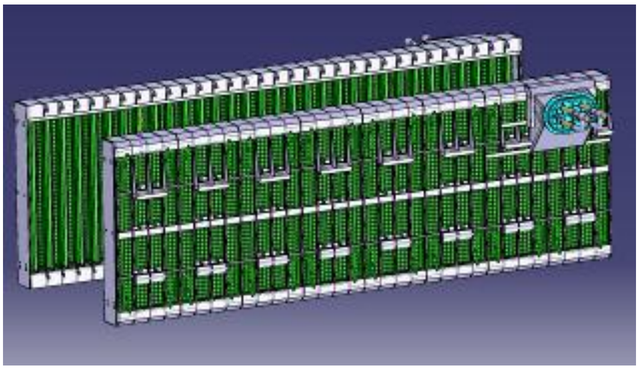

Figure 5 MITICA cryopump

Table 1. Cryopump operation flow conditions and requirements during steady state stand-by and pulse operations

| | Cryopanels system | | | | | | Thermal shields system | | | | | |
|---|---|---|---|---|---|---|---|---|---|---|---|---|
| | **Static heat load [W]** | **Mass flow rate [g/s]** | **Inlet T [K]** | **Outlet T [K]** | **Inlet P [MPa]** | **ΔP [kPa]** | **Static heat load [kW]** | **Mass flow rate [g/s]** | **Inlet T [K]** | **Outlet T [K]** | **Inlet P [MPa]** | **ΔP [kPa]** |
| **Stand-by (steady state)** | 400 | 25 | 4.6 | < 6.5 | 0.4 | 10 | 10 | 195 | 80 | 90 | 1.75 | 100 |
| **Pulse-on mode $H_2$ (steady state)** | 900 | 50 | | Max 6.5 | | | 16 | 310 | | ~ 90 | | |
| **Pulse-on mode $D_2$ (steady state)** | 800 | 45 | | | | | | | | | | |

Once the charcoal layer is saturated, the cryopump must be warmed up at 100 K and maintained at this temperature for a certain amount of time in order to perform the required charcoal regeneration. The cryogen flow conditions during the regeneration process for desorbing the trapped gases are summarized in Table 2.

Table 2. Cryopump operation flow conditions and requirements during transient 100 K regeneration

| | | Cryopanels system | | | | | | Thermal shields system | | | | | |
|---|---|---|---|---|---|---|---|---|---|---|---|---|---|
| | | **Heat load [W]** | **Mass flow rate [g/s]** | **Inlet T [K]** | **Outlet T [K]** | **Inlet P [MPa]** | **ΔP [kPa]** | **Heat load [kW]** | **Mass flow rate [g/s]** | **Inlet T [K]** | **Outlet T [K]** | **Inlet P [MPa]** | **ΔP [kPa]** |
| **Warm-up 20 min** | **Cold He release** | 400 | N/A | N/A | ~ 6.5 | N/A | Max 10 | Max 21 | 310 | 80 | Max 93.5 | 1.75 | 100 |
| | **Warm-up** | Max 500 | ~ 130 | ≥ 80<br>≤ 130 | ≥ 6.5<br>≤ 100 | 1.75 | Max 70 | | | | | | |
| **Exhaust (steady state)** | | | ~ 20 | > 100 | ≥ 100<br>≤ 110 | | 10 | | | | | | |
| **Cool-down 2 hours** | **Depressurization** | | N/A | N/A | ≥ 100<br>≤ 110 | N/A | Max 50 | ~ 10 | > 195 | | ~ 90 | | |
| | **Cool-down** | | ~ 9 | ~ 4.6 | ≤ 110<br>≥ 10 | 0.4 | Max 10 | | | | | | |
| | **Final cool-down** | | ~ 30 | 4.6 | ≤ 12<br>≥ 6.3 | | 10 | | | | | | |

*N/A: not available parameter*

# 3. MITICA CRYOGENIC PLANT DESIGN PROPOSAL

The current cryogenic plant design proposal is shown in Figure 8. The main plant components are:

1. Helium compression station with its own oil removal system and dryers
2. 900 W Helium refrigerator (equivalent power at 4.5 K)
3. LHe control cryostat (with two submerged heat exchangers and a ScHe cold circulator)
4. Valve box
5. Nitrogen compression station
6. 16 kW Nitrogen refrigerator
7. 80 K facility (with two submerged heat exchangers and a cold circulator)
8. Black box (for splitting circuits)
9. Medium pressure GHe storage tanks (2.0 MPa)
10. Helium atmospheric heaters
11. LN2 tank (for back-up purposes)

The cryogenic plant must be characterized by a high operational flexibility in order to fulfil the strongly variable cryopump requirements, especially during the transient 100 K regeneration process, which, according to current IO (ITER Organization) requirements, should be performed in maximum 3 hours (including the warm-up, exhaust and cool-down phase). This requirement has a strong impact on refrigerator size and on the overall plant configuration. For this reason, according to the current design, the refrigeration at 4.6 K is separate from the refrigeration at 80 K in order to guarantee the required plant flexibility.

## 3.1 Refrigeration at 4.6 K

The entire circuit for the refrigeration at 4.6 K is divided in two main closed loops (bolted blue lines in Figure 8): the supply loop between the Helium refrigerator and the LHe control cryostat and the cooling loop between the LHe control cryostat and the cryopump. During the stand-by mode the operational parameters inside the cryopump must be held constant in order to be ready for the next pulse operation. The refrigerator supplies cold Helium to the control cryostat. This cold Helium is partly used for the liquefaction as well as for the Joule-Thomson flow directly into the cooling circuit of the cryopump. The cooling loop must be pressure controlled. The backflow coming from the cryopump is partly released into the LHe bath of the control cryostat and also sent to the cryopump again via submerged heat exchangers. The fraction of the ScHe released into the control cryostat can be evaporated into the gaseous Helium volume or, depending on the operational parameters it can be liquefied in the LHe bath. In the supply loop the boiled off GHe is sent back to the refrigerator inside the heat exchangers column to cool down the GHe supply flow. In the cooling loop a cold circulator is used to increase or reduce the mass flow rate. In this way it is possible to adapt the flow rate to the actual heat loads at the cryopump. Inside the LHe bath in the control cryostat two heat exchangers are foreseen upstream and downstream the circulator. The main function of the LHe control cryostat is to separate the refrigerator itself from the cryopump acting as a thermal buffer. In this way a more stable operation of the refrigeration is guaranteed in spite of the pulsed heat loads during MITICA operation.

## 3.2 Cooling loop operation

The schematic layout foreseen for MITICA Cryogenic Plant is characterized by a closed loop in which 4.6 K ScHe flows during normal pulse-on and stand-by operation. This closed loop, named cooling loop in Figure 8, includes the LHe control cryostat, the valve box and the cryopanels circuit of the cryopump. A bypass valve is foreseen in the valve box in order to be able to open/close the loop. A simplified scheme of the ScHe loop is shown in Figure 6. During stand-by and pulse-on operation the ScHe flows from the control cryostat via the valve box to the cryopump. The return flow goes from the cryopanels outlet to the valve box again and then (bypass valve closed) to the control cryostat in which the heat load is removed into the LHe bath. During the 100 K regeneration the ScHe must be replaced with warm GHe at 100 K at higher pressure (1.8 MPa). The loop has to be interrupted. The bypass valve in the valve box must be opened and valves A and B must be closed allowing the 4.6 K ScHe to flow only from the control cryostat to the valve box and vice versa in order to keep the supply lines at operational temperature. At the very beginning of the regeneration phase the situation is the following: ~4.6 K and 0.4 MPa ScHe is flowing in the cryopanels circuit; this cold Helium must be replaced with warm Helium at ~100 K and 1.8 MPa. This temperature and pressure levels can be reached by mixing cold Helium with 300 K GHe from the storage tanks inside the valve box. All the cold Helium “lost” during this phase (the quantity of ScHe necessary to fill the internal volume of the cryopump, the cryojumpers, and the transfer lines between the black box and the valve box) must be liquefied again in order to be available at the beginning of the following cool down phase. After the exhausting phase (desorption of the cryopanels, about 30 minutes), the cool down phase starts. The warm high pressure GHe (~110 K) is discharged to other manifolds at lower pressure and the cryopanels system is depressurized. Once the pressure inside the system reaches 0.4 MPa the bypass valve in the valve box is closed, valves A and B are opened and 4.6 K ScHe supply flow into the loop starts. This cold Helium will be warmed up passing through the regenerated cryopanels. The Helium flow at the outlet of the cryopump is expected to have a temperature similar to the regeneration temperature (T >> 6 K). During the cool down phase the temperature will decrease until the target value of 4.6 K is reached. During this phase the warm outlet Helium (T >> 6 K) can’t be sent to the control cryostat due to excessively high temperature. The Helium will be discharged to other manifolds until the cryopump operation temperature of ~4.6 K is reached. At this point the discharge line is closed and the loop begins its normal operation again.

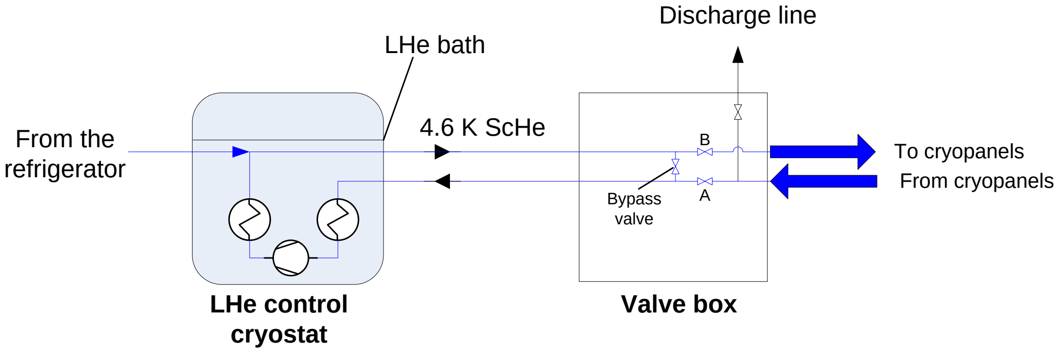

Figure 6. Simplified scheme of the cooling loop

### 3.3 Refrigeration at 80 K

The 80 K thermal shields circuit of the MITICA cryopump must be supplied with GHe at 80 K. In order to maintain the two circuits of the cryopump completely independent, a dedicated facility for the refrigeration at 80 K is foreseen. A dewar of suitable size filled with LN2 represents the so called 80 K facility. Two heat exchangers are immersed in the liquid nitrogen bath and a cold circulator is interposed in between. The circulator allows the adaptation of the mass flow rate according to the specific cryopump requirements. The GHe flows inside the circuit in a closed loop between the cryopump and the 80 K facility. The refrigeration power is given by the latent heat of the LN2. This configuration gives a high operational flexibility, which would not be possible with a single Helium refrigerator with two outputs at two temperature levels. A schematic view of the 80 K facility and the related closed loop is shown in Figure 7.

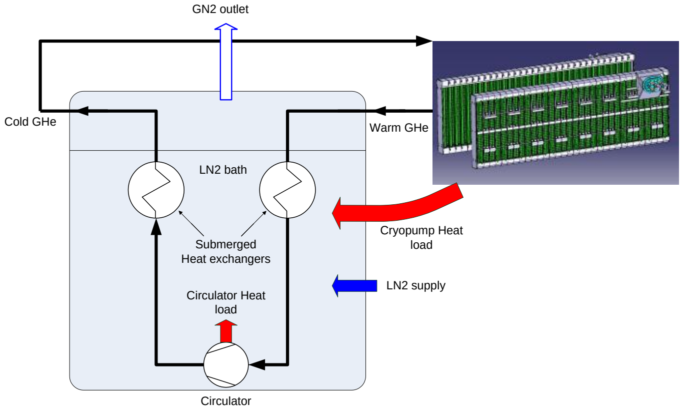

Figure 7. Closed loop and heat loads on the 80 K GHe flow

## 4. LN2 CONSUMPTION ESTIMATION

Considering the foreseen MITICA operational scenarios a large LN2 consumption is expected. In Figure 9 the LN2 consumptions during the foreseen experimental scenarios are shown. The contribution of the heat load introduced by the cold circulator during the different operating modes is also included. In Figure 10 the cumulative consumption during an entire operational day is shown. Depending on the operational scenario, consumptions between 9000 and 10000 litres per day have been estimated. Considering also the expected

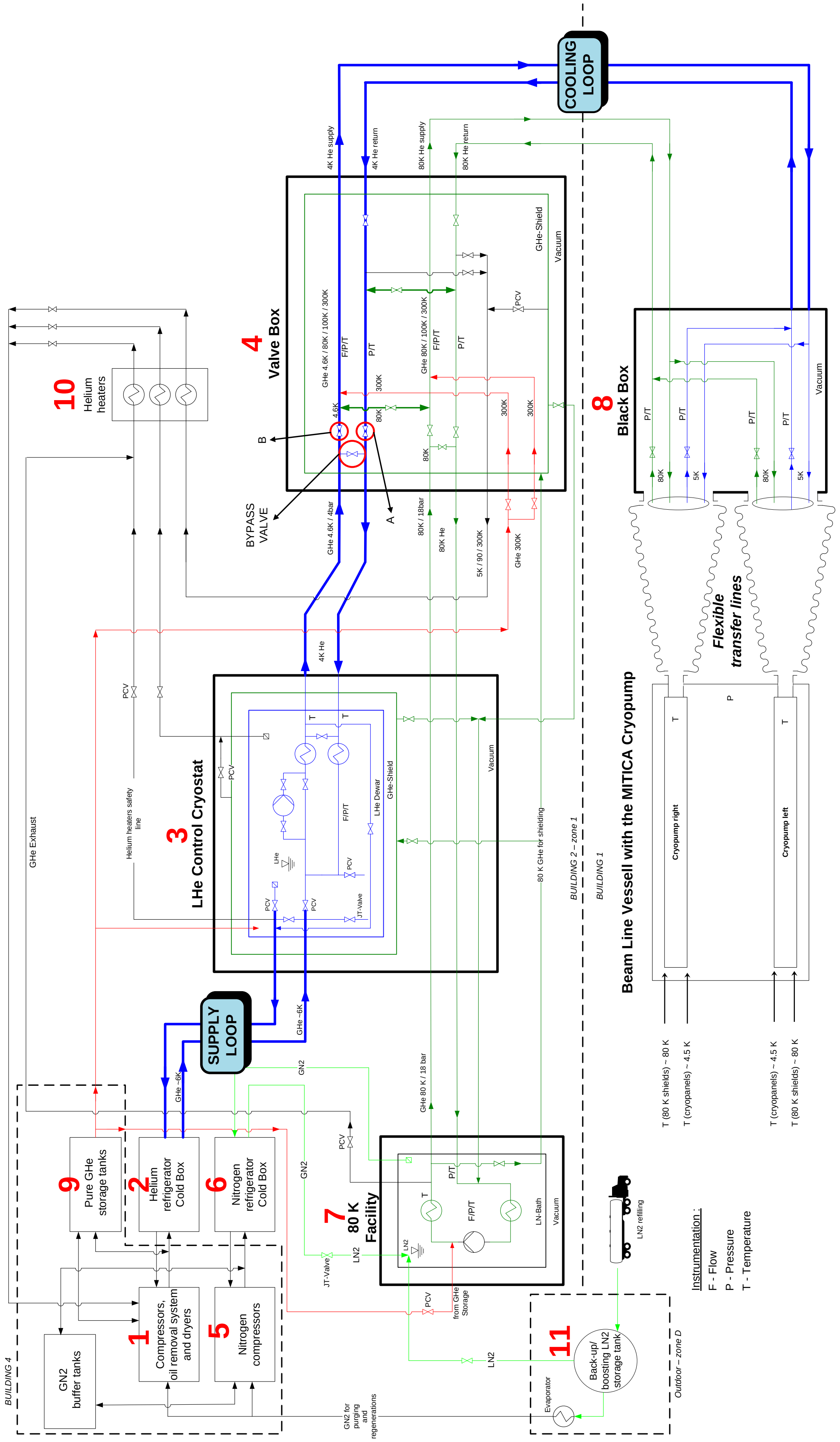

Figure 8. MITICA cryogenic plant design proposal

MITICA experiment life (20 years), from preliminary calculations and budget estimations seems that the installation of a N2 refrigerator is the most economical solution taking into account the operational costs. In this case the boiled-off GN2 in the 80 K facility returns to the N2 refrigerator to be re-liquefied and sent again to the dewar (as shown in Figure 8). The alternative solution is to install two 25000 litres LN2 tanks outside the buildings and to supply the LN2 for the refilling of the dewar from these tanks.

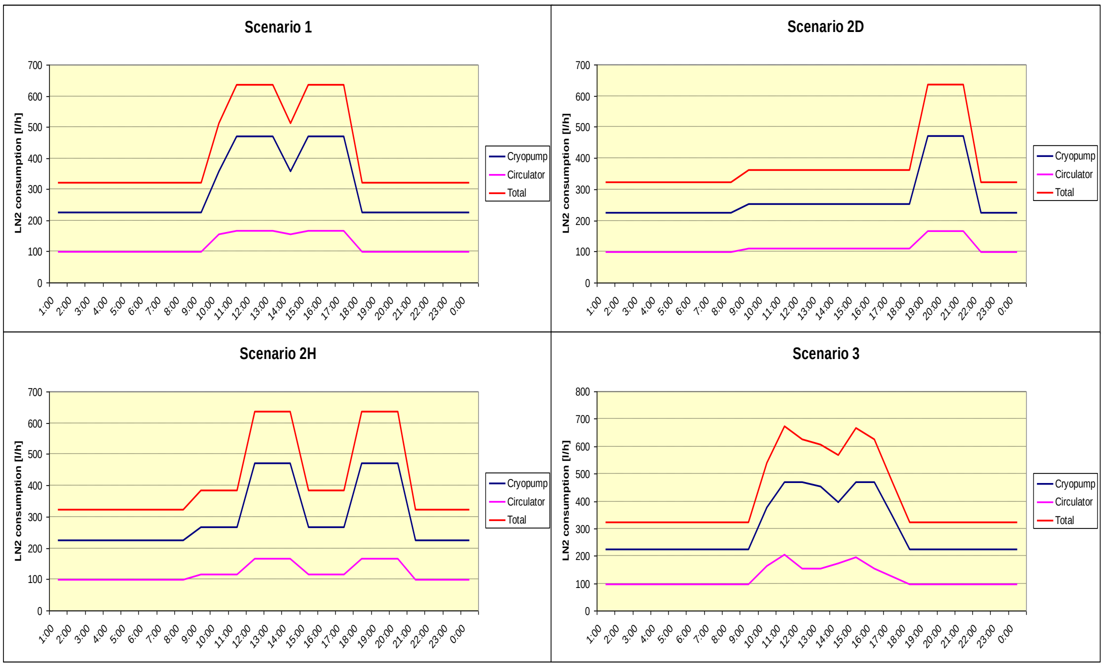

Figure 9. LN2 consumptions per hour during the entire experimental day in different operational scenarios

In this case the initial investment costs should be obviously lower but the operational costs during the overall experiment life would be much higher. A 10000 l LN2 tank is foreseen also in the case of N2 refrigerator solution for back-up purposes.

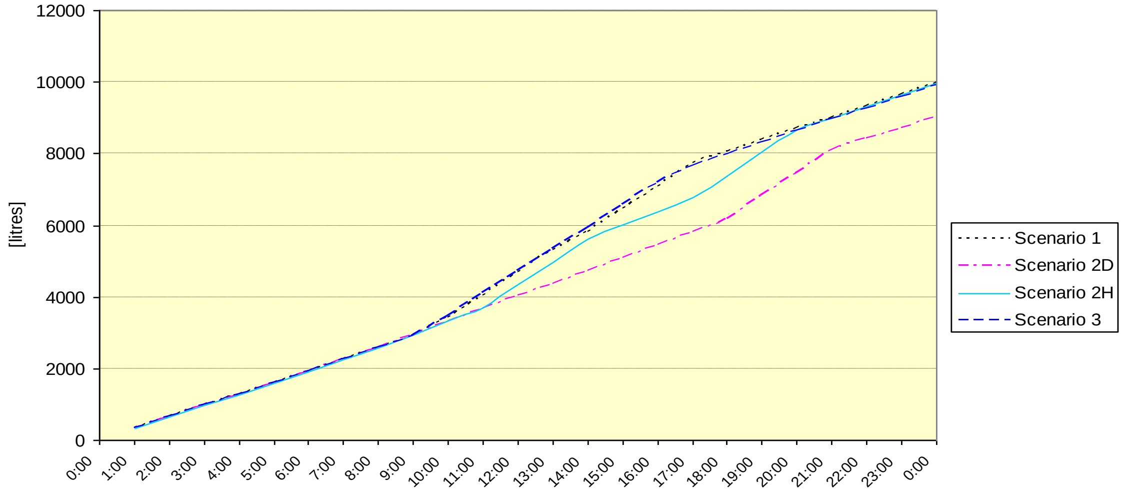

Figure 10 Cumulative LN2 consumptions during an entire day of operation in different operational scenarios

## 5. CONCLUSIONS AND FUTURE WORK

The MITICA cryogenic plant design proposal has been described in this article. Further steps are required in order to assess some important details regarding budget constraints and final requirements. Furthermore a technical dialogue with industry is planned in order to receive a feedback for the preparation of the final version of the technical specification. A critical analysis of the requirements must be carried out in order to fix an optimal design for the plant without exceeding the allocated budget.

This work has been carried out in collaboration and with financial support from Fusion for Energy (F4E).

018

# The MITICA Facility: A Possible Optimization of the Cryogenic Plant Cooling Capacity

**Fellin F.[*], Passardi G.[**], Valente M.[*], Zaccaria P.[*]**

[*] Consorzio RFX, Corso Stati Uniti 4, Padova, I-35127, Italy
[**] CERN, CH-1211, Geneve, Switzerland

## ABSTRACT

In MITICA experiment (Padova, Italy), a large sorption cryopump has to be installed in the Beam Line Vessel. A dedicated cryogenic plant has to be realized to supply the cryopanels with ScHe @ 4.6 K and GHe @ 80 K for radiation shields. Considering the various operation modes of MITICA cryopump, a possible way to decrease significantly the installed cryogenic power (referred to 4.6 K) is the use of a helium refrigerator sized on an average refrigeration power value instead of the peak heat load and constantly operating at full power. The additional refrigeration power requested during beam pulse operations would be supplied by LHe inside a Control Cryostat housing the heat exchangers that cool the cryopanels ScHe loop; the recovery of evaporated LHe can be carried out during the long regeneration time performed overnight. A test case of MITICA experiment in ITER conditions foresees fast cryopump regeneration, detailed in this paper.

## 1. INTRODUCTION

MITICA is an ITER facility in which the performance of a Neutral Beam Injector (named HNB, Heating Neutral Beams to be used in ITER) will be proofed and tested. The target of MITICA cryogenic plant is to allow the correct operations of the MITICA cryopump [1], an injector component placed into MITICA Beam Line Vessel. ITER cryogenic plant [2] has many cryogenic users (magnets, cryopumps, cryostat, etc.), while MITICA cryogenic plant shall be sized to supply a single user, the cryopump. This paper deals with expected experimental scenarios for MITICA experiment, involving cryopump and consequently the cryogenic plant, and a possible way to minimize cryogenic plant complexity and costs based on the effective requirements.

## 2. MITICA OPERATIONAL SCENARIOS DESCRIPTION

The MITICA test facility can use hydrogen or deuterium gas for performing the experiments [3]. The associated Cryogenic plant will be customized on the cryopump operating requirements. An exact definition of these requirements is essential in order to assure an optimized design of the plant avoiding extra costs due to excessive margins or over-estimation.

### 2.1. Preliminary experimental campaigns with hydrogen

The first period of MITICA experiment operations will be performed using hydrogen and not deuterium in order to avoid possible complications due to the activation of the materials. After having gained sufficient experience with the machine, it will be possible to switch from hydrogen to deuterium operations.

During this first period of operation, as well as in the future with deuterium, the limitation on the number of pulses per day (with hydrogen) or pulses duration is imposed by the gas saturation of the cryopump and not by the size of the refrigerator, which should be designed to cover all the foreseen operating scenarios.

### 2.2. Nominal reference scenario

The nominal reference scenario for MITICA cryogenic plant, named scenario 2D (Figure 1 and Table 1), consists of a series of identical pulses at full power beam (standard pulse), using deuterium; each pulse has a 300 s duration and a 900 s of stand-by (that is beam OFF) is foreseen between pulses. A maximum number of 21 pulses is foreseen during a nominal experimental day; after the operation a cryopump regeneration phase at 100 K of maximum 12 hours (during night) is foreseen.

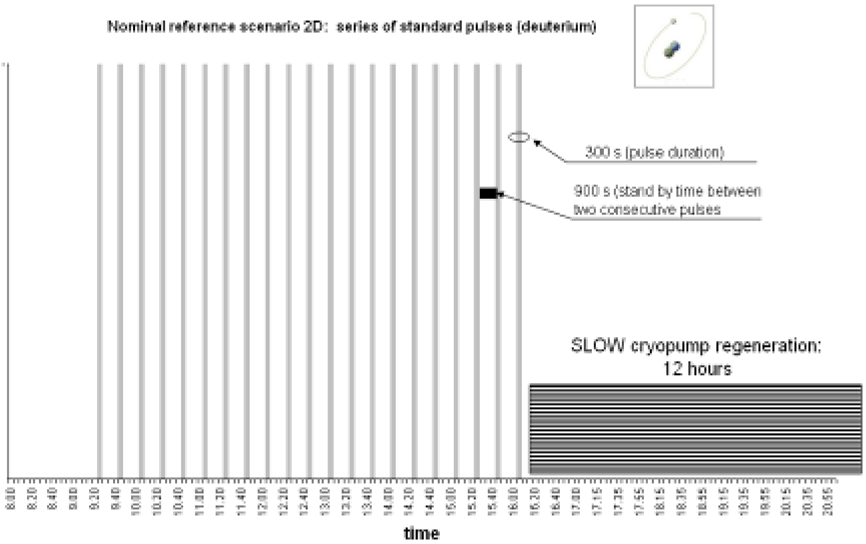

Figure 1 - Nominal reference scenario 2D: series of (maximum) 21 pulses in deuterium of 300 s duration with intervals of 900 s between pulses

### 2.3. Test cases

The main important test case is the demonstration of the reliability of Neutral Beam for long pulse, fulfilling the ITER contractual requirements:

- full power beam pulse, duration 3600 s;
- beam OFF for the three consecutive hours; during this time a regeneration process at 100 K is required;
- repetition of full power beam pulse, duration 3600 s (Figure 2 and Table 1).

It is still unclear whether the execution of a correspondent long pulse (test case 1H) using hydrogen instead of deuterium, is required or not; in any case, due to cryopump characteristics, pulse duration has to be limited, using hydrogen, to 3000 s duration. However, both test cases are planned to be executed only few times in the entire expected life of MITICA experiment (20 years), as a full performance test of Neutral Beam.

Based on these considerations, it is necessary to design the MITICA cryogenic plant to perform both nominal reference scenario and test cases. The execution of test cases will be possible also considering the purchase of temporary quantities of $LN_2$ and LHe as cryogenic plant boosters. The MITICA cryogenic plant will allow the processing of these quantities supplied by means of temporary trucks and/or tanks. This strategy would allow reducing the amount of installed cryogenic power, because the nominal reference scenario is less demanding than the test cases, and reaching the required power for test cases execution with temporary supply of cryogenic power on-demand. The proposed strategy would allow a reduction of capital costs with a slight increase of operational costs for test cases execution, as further explained.

Table 3 - Cryopump operation flow conditions in reference scenario and test cases

| | **Static heat load: pulse [W]** | **Cryopanels mass flow rate during pulse [g/s]** | **Pulse duration [s]** | **Regeneration type** |
|---|---|---|---|---|
| **Nominal reference scenario 2D** | 800 ($D_2$) | 45 | 300 s<br>(max. 21 pulses per day) | Slow, 12 hours |
| **Scenario 2H** | 900 ($H_2$) | 50 | 300 s<br>(max. 10 pulses per day) | Slow, 12 hours |
| **Test case 1D** | 800 ($D_2$) | 45 | 2 x 3600 s | Fast, 3 hours |

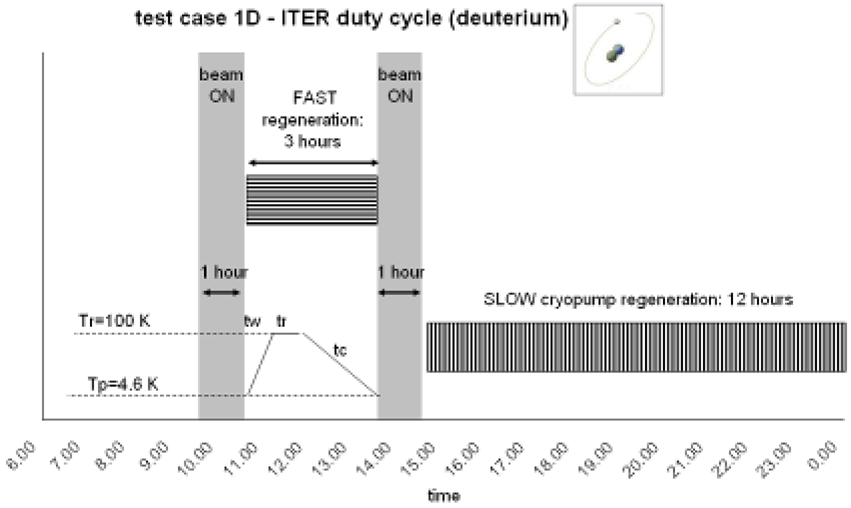

Figure 2 - Test case 1D: two long pulses in deuterium of 3600 s duration
with three hours for cryopump fast regeneration @ 100 K in between
(note to Figure 2: $t_w$ warm-up time, $t_r$ regeneration time (exhaust phase), $t_c$ cool-down time,
$T_p$ cryopanels temperature, $T_r$ regeneration temperature)

## 2.4. Considerations about MITICA experiment operations

Beside the nominal reference scenario 2D and the above mentioned test cases, a quite long intermediate phase should be considered in order to outline a more realistic view of MITICA experiment operations. The high demanding fast Pump Regeneration Sequence (3 hours), named fast PRS, will be not performed during this long phase because unnecessary. For this reason the fast cryopump regeneration, and in particular the fast cool down (see Table 2), should not be the reference for cryogenic plant size definition (see Table 2). The cryogenic plant will be sized on the nominal reference scenario 2D (Table 1 and Figure 1), where only slow Pump Regeneration Sequence is foreseen, without the use of additional quantities of LHe and $LN_2$. Also during the $H_2$ pulses (which will require an intermediate regeneration because hydrogen causes a more rapid saturation of the charcoal adsorbent layers), the regeneration should not be considered as a constraint for the cryogenic plant design. The real duration of the regeneration will depend on the effective capacity of the installed plant. Only when the test cases with long pulses will be scheduled, with the fast regeneration between two pulses, additional quantities of cryogens will be ordered by the gas supply Companies, in order to have the required refrigeration power. This solution has to be intended as extraordinary operation.

Furthermore, beside the operational scenarios there will be a series of general operating states involving all the experiment components and auxiliary systems for MITICA, including the cryopump and, consequently, the cryogenic plant. These operating states will not affect the cryogenic plant capacity, but should be carried out for a correct operation of the experiment.

Table 2 - Cryopump requirements during fast regeneration (performed @ $T_r$=100 K)

| | | **Heat load [W]** | **Cryopanels mass flow rate [g/s]** |
|---|---|---|---|
| **Warm-up ($t_w$=20 min)** | **Cold He release** | 400 | N/A |
| | **Warm-up** | Max 500 | ~130 |
| **Exhaust (steady state, $t_r$=30÷40 min)** | | | ~20 |
| **Cool-down* ($t_c$=2 hours)** | **Depressurization** | | N/A |
| | **Cool-down** | | ~9 |
| | **Final cool-down** | | ~30 |

* the cool-down is the most demanding phase for cryogenic plant, due to the necessity to cool down from 100 K to 4.6 K and further refilling with ScHe the cyopanels in a short time.
N/A means “not assessed value”

## 3. A POSSIBLE WAY TO REDUCE CRYOGENIC PLANT SIZE

Considering a long cryopump regeneration during night (slow PRS) and with reduced time constraints for the cool-down and warm-up phases the load on the refrigerator and the related size would be reduced. Also the control system performance requirements would be relaxed with consequent improvement in the operation easiness.

In Section 2.2 the nominal reference scenario 2D for cryoplant design is detailed. Based on this scenario the most demanding cryoplant operation phase (cryopump regeneration) is relaxed, since it is planned to be performed during night. Having long time available to liquefy the helium required during the cool-down after the warm-up phase, the load on the refrigerator is strongly reduced.

Dimensioning the helium refrigerator on the nominal reference scenario 2D, a cost saving would be possible. In order to perform also the test cases described in Section 2.3, a temporary boosting system based on hired LHe/$LN_2$ trucks/dewars shall be used. In this way it will be possible to reduce the size of the refrigerator without any functional penalization of the tests foreseen to verify the MITICA cryopump performance.

Nevertheless, right from the beginning the plant should be designed in order to be able to process the higher flows during the test cases with an easy integration of the external additional cooling facilities.

### 3.1. Cryogenic plant design scenario and test case execution

Considering the sizing of the cryogenic plant on the base of nominal reference scenario 2D mentioned in Section 2.2, the maximum heat load acting on the cryopump on which the plant could be sized is (currently) 900 W (maximum heat load during Hydrogen pulses, see Table 1). In this case the related refrigeration power required to remove this heat load from the cryopanels represents the driving factor for the sizing of the refrigerator, as detailed in [4].

In order to reduce the overall investment and operational cost of the plant, another possible alternative is here considered. Since the nominal reference scenario 2D (see Table 3) for plant sizing includes a long time available to perform slow PRS during night, a smaller refrigerator could be taken into account. An average power between the peak pulse heat load (900 W) and the stand-by heat load (400 W) could be chosen. Hence a refrigerator of 500÷600 W would be able to fulfil the requirements (in the remaining part of this document, to fix a size, a 500 W power will be considered; final size will be assessed in the future after the final design of cryopump). This refrigerator would work constantly at full power supplying the required refrigeration in stand-by mode~~)~~. Just before the pulse the cold circulator in the control cryostat begins to increase the ScHe mass flow rate in order to remove the higher heat load. The heat removed is transferred by ScHe loop in the LHe bath in the Control Cryostat; because of this increased heat load a larger quantity of LHe evaporates in the ullage space of the cryostat. The additional quantity of gas generated inside the cryostat cannot return to the refrigerator, which is sized to work out a gas quantity correspondent to stand-by operation only (or slightly higher). If this larger quantity of gas were sent to the low pressure side of the refrigerator a sub-cooling of the heat exchangers and the turbines with failures or interlock system intervention could be experienced. For these reasons the additional gas Helium generated inside the cryostat during pulses should bypass the refrigerator cold box, be warmed up and temporarily discharged into the buffer volumes before to be processed again.

During the entire experimental session there will be a continuous reduction of LHe level inside the bath. The LHe quantity required for the next day experimental session must be recovered during night. The refrigerator re-liquefies the necessary amount of Helium to refill the cryostat. At the same time the warm-up and the regeneration of the cryopanels is performed through the separate high temperature circuit. Once the refilling operation is completed the slow cool down of the cryopanels from 100 K to 4.6 K can start, in order to recover the operational conditions of the cryopump.

The so called test cases (see Table 4, where the more demanding test using Deuterium is shown) with fast PRS between two long pulses, can be performed using an additional external LHe quantity (around 600 l, as shown in the last row of Table 4) to be supplied directly inside the low temperature loop for the cool down of the cryopanels. If this quantity of liquid helium cannot be supplied in the given short time and subsequently reprocessed by cryogenic plant in parallel with the all the other duties because its capacity and overall design features are based on the nominal 2D scenario, it can be released into atmosphere after the performing of the fast cool-down phase.

Table 3 – Main parameters during execution of Scenario 2D

| | | |
|---|---|---|
| Refrigerator nominal power | 500 | W |
| Heat load (during pulses) | 800 | W |
| Number of pulses | 21 | |
| Duration | 300 | s |
| Maximum overnight time for slow PRS | 12 | h |
| Cryopanels cool down rate (overnight) | 1.5 | g/s |
| Evaporated LHe during pulses | 829 | l |
| Liquefaction rate during night | 3.8 | g/s |

Table 4 – Main parameters during execution of Test case 1D

| | | |
|---|---|---|
| Refrigerator nominal power | 500 | W |
| Heat load (during pulses) | 800 | W |
| Number of pulses | 2 | |
| Duration | 3600 | s |
| Maximum overnight time for slow PRS | 12 | h |
| Cryopanels cool down rate (overnight) | 1.5 | g/s |
| Evaporated LHe during pulses | 947 | l |
| Liquefaction rate during night | 4.1 | g/s |
| **Additional LHe required between the two pulses** | **540** | **l** |

### 3.2. Cryopump regeneration transient operation (@ 100 K)

During this operation, the cryopanels of the cryopump have to be regenerated at a temperature of 100 K. The 100 K regeneration operation is divided in three main phases: the warm-up, the exhaust, and the cool-down phases (Table 2). For the fast PRS, a maximum allocated time of 3 hours is imposed (12 hours for slow PRS).

1 - Warm-up of the cryopanel system

The cryopanels shall be first warmed up to a minimum temperature of 100 K. A part of the cold helium (supercritical helium between 4.6 K and 6.5 K) is previously removed from the cryopump. The envisaged way to remove the cold helium is to close the supply valves and open the return valves to a pressure lower than 0.4 MPa. This phase is time consuming and reduces the time allocated for the warm-up, leading to an increase of the average mass flow to warm up the cryopump.

Then the supply valves can be very slightly opened to progressively supply the cryopanels with warmer gas at 1.75 MPa, starting with a very small mass flow. Once the initial cold helium is totally removed, the mass flow can be increased. The cryopanels can be supplied from a mix of 80 K and 300 K gas helium in order to provide temperatures from 80 K up to 130 K. The warm-up phase is finished when a minimum temperature of 100 K is reached everywhere in the cryopanel system. The maximum allocated time for warming up the cryopanel system, including the preliminary cold helium release phase is 20 minutes.

2 - Exhaust phase

When a minimum temperature of 100 K is reached everywhere in the cryopanel system, this state must be maintained for a minimum duration (30-40 min) to ensure a complete release of the captured gases. Note that the captured gases start to be desorbed already during the warm-up phase.

3 - Cool-down of the cryopanel system

The cool-down first starts with the depressurization of the system from 1.75 MPa to a pressure below 0.4 MPa. The supply valves have to be closed and the return valves opened to a lower pressure. Then the supercritical helium at 4.6 K and 0.4 MPa can be supplied and the cool-down phase is finished when a temperature below 6.5 K is reached at the outlet of the cryopanel system. The maximum allocated time for cooling down the cryopanel system during a fast PRS, including the preliminary depressurization phase is two hours.

Estimations of the required mass flows to warm-up and cool-down the cryopanel system have been performed, taking into account only the internal cryopump components. As a consequence, the real required mass flows during the warm-up and cool-down phases could be increased. The two mass flow values for the warm-up and cool-down phases in the Table 2 (130 g/s and 9 g/s) should not be intended as requirements for the cryogenic plant but those evaluated assuming that the cryopump is directly connected to the supply of cooling power and that no other mass and volumes have been taken into account. Moreover, these estimations are based on preliminary calculations and no margin has been considered. The main results are reported in the Table 2.

Assumptions for the calculations:

- cryopanel system mass and volumes: capacity 105 litres, mass 1810 kg (referring to one half of cryopump, including welding materials, charcoal and glue);
- the static heat loads (solid conduction and thermal radiation) are taken into account. The variation of the radiation heat load with the variation of the cryopanels system temperature is also taken into account.

## 4. CONCLUSIONS

The reduced power refrigerator solution can represent a possible way for reducing the investment costs of the cryogenic plant with the associated external systems (electrical power supply and cooling water). Furthermore this solution presents three main advantages in terms of operational costs if compared with the 900 W refrigerator solution (as described in [4]).

1) The refrigerator must operate as far as possible in stable conditions; for this reason the load seen by the refrigerator should be maintained as constant as possible. In case of a 900 W refrigerator, electrical heaters must be used inside the LHe bath in order to compensate the reduced load during the stand-by phase between pulses. With a 500 W refrigerator the dissipative solution of the electrical heaters would not be required, because the refrigerator would work constantly at full power; a consistent amount of electrical energy costs will be saved, and this will be very important in a country, like Italy, with high electricity costs (around 130 €/MWh, VAT excluded, considering a wide quantity supplied at medium voltage level, 20 kV)
2) The refrigerator would work constantly in the range of the maximum efficiency for which the refrigerator itself is designed and realized;
3) A lower size motor allows saving the operative contractual costs for installed power supply since at least 300 kVA can be saved with a 500 W instead of 900 W refrigerator.

Acknowledgment: this work was set up in collaboration and financial support of Fusion for Energy (F4E).

## 5. REFERENCES

[1] Dremel M. et al. 2009, Cryopump design development for the ITER Neutral Beam Injectors, *Fusion Engineering and Design*, Volume 84, Issues 2–6, June 2009, pages 689–693.

[2] Kalinin V. 2006, ITER cryogenic system, *Fusion Engineering and Design*, Volume 81, Issues 23–24, November 2006, pages 2589–2595.

[3] Masiello A. et al. 2009, European programme towards the 1 MeV ITER NB injector, *Fusion Engineering and Design*, Volume 84, Issues 7–11, June 2009, Pages 1276–1280.

[4] Valente M. et al. 2012, Design proposal for MITICA cryogenic plant, *Acta of 12th Cryogenics 2012, IIR international Conference*, Dresden.

095

# Cryogenics for the European Spallation Source

**Wang X.L., Koettig T., Gallimore S., Hees W.**

European Spallation Source, P.O Box 176, Lund, SE-22100, Sweden

## ABSTRACT

The European Spallation Source (ESS) is an intergovernmental project building a multidisciplinary research laboratory based upon the world's most powerful neutron source. The main facility will be built in Lund, Sweden. The ESS linear accelerator (linac) will deliver protons with 5 MW of power to the target at 2.5 GeV, with a nominal current of 50 mA. Three fully independent refrigerators are foreseen to guarantee the necessary cooling capacity for the entire facility. The superconducting part of the linac consists of a total of 208 niobium cavities cooled with superfluid helium to 2 K. The cryogenic hydrogen moderators in the target will operate at around 20 K under supercritical conditions. The instruments and test stand cryoplant combines liquefaction for the instruments at 4.5 K and the occasional helium refrigeration for the two cryomodule (CM) test benches. This paper describes the baseline considerations, the conceptual design, the key cryogenic components and the preliminary heat load estimates for the cryogenic supply of ESS project.

## 1. INTRODUCTION

The ESS, a new international research infrastructure, is under pre-construction phase at Lund, Sweden [1], which will deliver first neutrons in 2019. At full specification, to be achieved in 2025, the ESS will deliver 2.86 millisecond, pulses (at 14 Hz) intense neutron beams at a power of 5 MW, to 22 independent experimental instruments. The general layout of the ESS is shown in Figure 1.

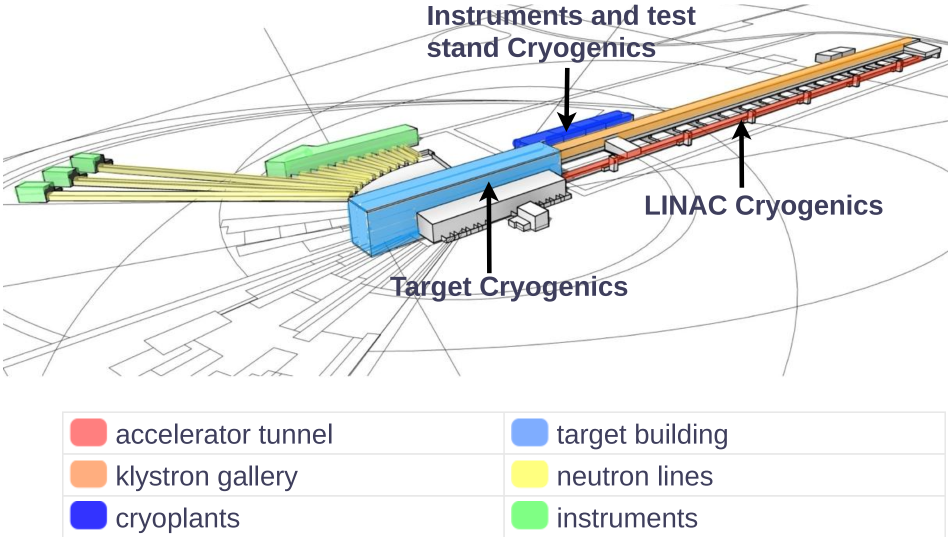

Figure 1. General layout of the ESS.

The high level parameters of the ESS, and its guiding scientific goals are recorded in Table 1.

Table 1. High level parameters of the ESS.

| Parameter | Unit | Value |
|---|---|---|
| Average beam power | MW | 5 |
| Number of target stations | | 1 |
| Number of instruments | | 23 |
| Number of moderators | | 2 |
| Proton kinetic energy | GeV | 2.5 |
| Average macro-pulse current | mA | 50 |
| Macro-pulse length | ms | 2.86 |
| Pulse repetition rate | Hz | 14 |
| Maximum acc. cavity surface field | MV/m | 40 |
| Maximum linac length | m | 502 |
| Upgrade length | m | 100 |
| Annual operating period | h | 5200 |
| Reliability | % | 95 |

ESS’ cryogenic system will serve three different parts of the machine, namely the linac, the target, and the instruments and test stand. The baseline concept of the cryogenic system foresees three fully separated cryoplants to cater for the liquid helium (LHe) needs. The linac cryoplant supplies 2 K LHe to the superconducting RF CMs of the accelerator. The target cryoplant provides the helium refrigeration power at around 16 K to the hydrogen moderators in the target. The instruments and test stand cryoplant feeds LHe in mobile dewars to experiments and instruments as well as supplying the the CM test stand, while collecting, purifying and reusing the warm return helium. The basic requirements, the reference cryoplant capacities, layout and the cryogenic components for the ESS will be presented in this paper.

## 2. LINAC CRYOGENICS

The ESS linac will deliver protons with 5 MW of power to the target at 2.5 GeV, with a nominal current of 50 mA. The general layout of the linac and its cryogenic infrastructure is shown in Figure 2. The superconducting section of the linac contains 14 spoke CMs with two double-spoke cavities in each which takes the beam to 191 MeV, 15 medium beta and 30 high beta elliptical CMs with four five-cell cavities in each which finally takes the beam to the full energy of 2.5 GeV. There are 59 CMs in total and the length of the cold linac is about 400 meters. All cavities will operate at 2 K helium bath temperature. As described by the BCS theory of the superconducting state, the surface resistance at radio frequencies and the dynamic losses decrease strongly with the temperature. At the same time, the efficiency of cryogenic plants decreases with decreasing the temperature. As a consequence, an optimum operation temperature needs to be defined.

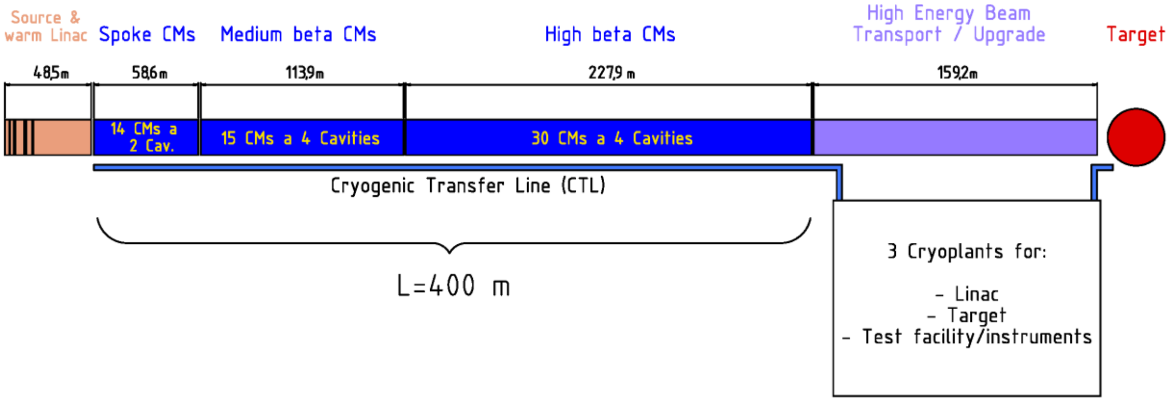

Figure 2. The general layout of the ESS linac and the cryogenic infrastructure.

The ESS linac cryogenic system will mainly consist of one central cryoplant, the distribution system, the cryogenic transfer lines with the length of 430 meters and the related warm piping system in order to supply the liquid helium to the CMs. To design the cryogenic system, the refined heat load estimates, the cavities and shield operation temperature optimization, safety aspects, redundancy concepts, machine component choice and the CM design need to be studied in details.

### 2.1. The Segmented CM Design

The CM design is crucially important to design and optimize the linac cryogenic system. The strategy of ESS CM design is to make use of the two existing designs for XFEL [2-5] and SNS [6-8], named respectively as the continuous module and the segmented module.

The XFEL continuous module design is based on the technology of TESLA Test Facility (TTF), which is driven strongly by the length of the cold linac and directly by the cost [9]. The TESLA linear collider project, like the ILC, would have a length of several km and consist of thousands of CMs. Compared with the segmented CM, the continuous CM design, got rid of the local distribution system including cryogenic valves, safety valves, low pressure heat exchangers, jumper connections etc. and used the 300 mm backbone tube as a process tube and support structure to the cavity string. It will cost much less for the individual CM, which reduces significantly the total cost of the project. For a short linac, like that of ESS, this cost issue has a minor effect so that there are no obvious advantages to use the continuous module design.

The other big concern about the CM design is the cryogenic heat load composed of the static and dynamic fractions. For the XFEL continuous CM, the static heat load of CM provides more than 50 % of the total heat load [10]. This kind of CM design could decrease as much as possible the CM static heat load and further reduce the size of the cryoplant and simplify the cryogenic system. For ESS CMs, the initial heat load estimates show that the total heat load is dominated by the dynamic fraction [11, 12]. It means that the additional static heat load from the cold-warm transition and the interface (Bayonet or VCR connections) between the main distribution system and the CM in terms of the segmented module design has a limited influence on the size and complexity of the cryogenic system. It results that the segmented module design is more suitable for the ESS case from the heat load fraction point of view.

Two key elements, the relative short linac and the heat load dominated by the dynamic fraction, determined the adoption of the segmented CM design for ESS. The segmented module design also provides additional advantages [13]. It allows replacing quickly one complete module without warming up the whole linac. A warm interlocked valve could isolate one module in case of beam pipe vacuum loss. The warm focusing magnets in between CMs are easy to access, align, maintain and update. Two ESS CM technology demonstrators are under development with extensive international collaboration including the mechanical and thermal design, required tooling design, preparation for the industry manufacture and development of infrastructure, like clean room, assembly hall and test area [14].

### 2.2. Proposed Flow Schematic

The schematic of the proposed distribution system of the linac with segmented modules is given in Figure 3 (see next page). There are three cooling circuits in the linac. The primary circuit (about 3 bar, 4.5 K) uses a heat exchanger to precool the forward flow, followed by a Joule-Thomson (J-T) valve to expand to saturation pressure at 2 K within the CM. The second circuit supplies a forced flow of about 4.5 K helium to cool the RF power couplers. The helium warms up from 4.5 K to ambient temperature towards the warm end of the power coupler and returns back to the cryoplant via a warm gas return line [15]. An on-going study will show if it’s necessary to use the second circuit as additional thermal intercept for the support posts, wires and cables as well as the cold-warm transition, in order to minimize the heat load into the CM. The third circuit provides helium at about 14 bar, 40-50 K to the thermal radiation shield. Each CM will be connected to the cryogenic transfer line via jumper connections in U-shape design. Cryogenic valves situated in a vacuum insulated valve box on the transfer line adjust the appropriate mass flow. A vacuum barrier in the jumper connection separates the vacuum of the transfer line from the individual insulation vacuum of the CM.

### 2.3. Requirements of the Cryoplant

For the time being, the overall cryogenic heat load of the ESS linac installation, including the distribution system, the main transfer line and the CMs, is estimated to in a range of 12-14 kW equivalent at 4.5 K under the full power operation of the ESS. The uncertainty factor of 1.8 [16] has been considered in this estimate related to the stage of the project. With reference to the experience with other large superconducting accelerator facilities like XFEL, LHC and SNS, it is expected that the cryogenic supply of the linac has to be maintained across a period in the order of several years without any major shut-down of the cryogenic plant. The availability and reliability should exceed 99 % in order to contribute to the overall goal of 95 % availability of ESS.

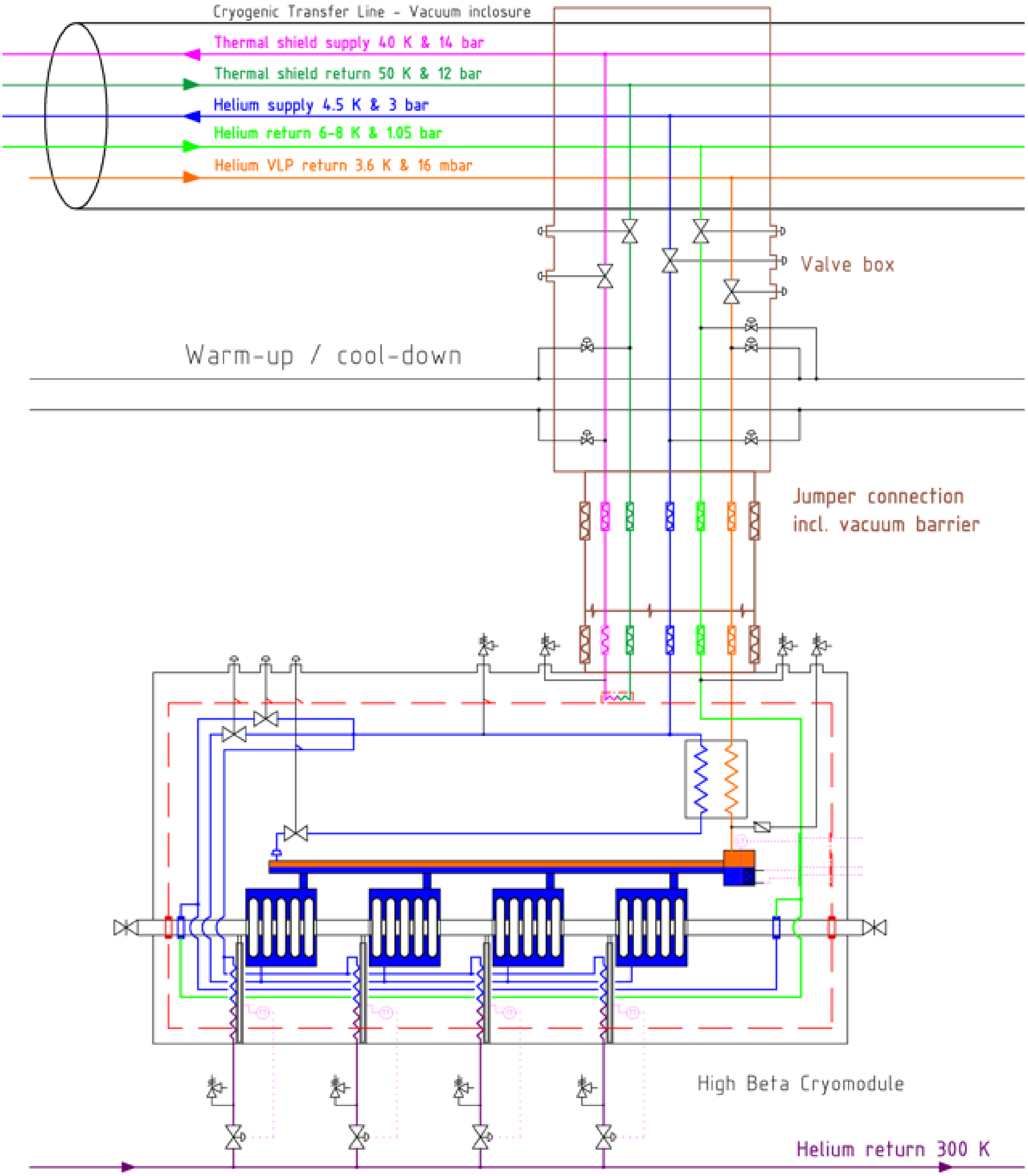

Figure 3. Schematic of the proposed helium distribution system of the linac with segmented modules.

## 3. TARGET CRYOGENICS

The ESS target station will have two cylindrical coupled liquid hydrogen cryogenic moderators each with wing-geometry water (at 300 K) thermal moderators - one above the target and one below. The target cryogenics in ESS has to continuously provide the moderator cooling system with cryogenic hydrogen. The cryogenic moderators share a common hydrogen loop and are connected in a parallel configuration. The hydrogen is maintained at a pressure exceeding 1.3 MPa and a temperature between 17-20 K under all operating conditions, thus ensuring that the hydrogen always remains in the supercritical state, which keeps the system free from all problems associated with two-phase flow.

The reference heat load at present for each cryogenic moderator is approximately 10 kW (0.4 kg/s at 17-20 K range) for a proton beam power of 5 MW, which will be significantly larger than the load of JSNS [17,18] and SNS [19]. The concept design of the target cryogenic system is approaching completion, and is similar to that of JSNS and SNS. The target cryogenic system will consist of:

- One helium refrigerator system to produce the refrigeration power of about 20 kW at around 16 K.
- The helium-hydrogen heat exchanger to transfer the cooling power to the hydrogen.
- The hydrogen circulation system to circulate the cryogenic hydrogen through the moderators and to absorb the heat of the moderators and the circulation system.
- Cryogenic hydrogen transfer lines to supply the cryogenic hydrogen to the moderators and to return the warm hydrogen.
- Other components such as a gas hydrogen supply unit, accumulator and heater system, an ortho-para hydrogen converter and a vacuum system.
- The hydrogen safety system to avoid the inflammation and explosion of the hydrogen and to guarantee the cryogenic system running safely and stably.

## 4. INSTRUMENTS AND TEST STAND CRYOGENICS

About 50 l/h of liquid helium are required for the instrument and experiment cooling. It is foreseen to use the liquefier that is supplying these quantities as well as refrigerator for the local CM test stand. During the construction of the ESS all 45 elliptical CMs have to be tested. The local test stand is in the proposal stage now and has recently passed the first preliminary approval. It will supply all cryogenic and RF stationary and transient operating conditions except the beam operation. The main purposes are:

- test the complete CM system at operation temperatures and at full RF load;
- qualify all CMs after the assembly;
- maintain and improve the superconducting linac and support power upgrade R&D;
- train the staff and accumulate CM operational experience as early and quickly as possible.

The preliminary cryogenic heat load estimate is about 0.5 kW equivalent at 4.5 K. The cryogenic supply for the instruments and the test stand will be integrated into one cryoplant which can supply the helium refrigeration and liquefaction at 4.5 K in parallel. The liquid helium supply will be buffered by a liquid helium storage vessel. Warm sub-atmospheric helium compressors will be used for the 2 K helium circuit of the test stand. In order to fit the elliptical CMs test plan, it needs to be operational by 2017.

## 5. CONCLUSIONS

The requirements for the cryogenic supply of the ESS project are preliminarily discussed. Three helium refrigerators will serve independently the three ESS cryogenic customers: the linac, the target as well as the instruments and test stand. The first and rough heat load estimates give an indication of cooling capacities, 12-14 kW equivalent at 4.5 K for the linac, 20 kW at 16 K for the target, and 50 l/h helium liquefaction for the instruments and 0.5 kW equivalent at 4.5 K for the test stand. It should be noted that these numbers still have a big uncertainty at this moment and that more reliable numbers will be given in further detailed studies. The baseline concept, cooling capacities and the key cryogenic components are described. The first cryoplant for the instruments and test stand will be commissioned and ready to run in 2017.

## 6. REFERENCES

1. Peggs S. 2012, *ESS Conceptual design Report*.
2. Petersen B. 2007, Some fundamentals of cryogenic and module engineering with regard to SRF technology, *SRF2007 Tutorial Program,*
3. Peterson T. 2005, What’s inside a TESLA Cryomodule, *Proton driver meeting.*
4. Pagani C, Pierini P. 2005, Cryomodule design, assembly and alignment, *SRF 2005*: 78-85.
5. Ohuchi N. 2009, Fundamentals of cryomodule, *SRF2009 Tutorial Program,* KEK, High Energy Accelerator Research Organization.
6. Schneider W.J., Campisi I.E. 2001, Design of the SNS cryomodule, *19th IEEE Particle Accelerator Conference*, Chicago: 1160-1163.

7. Whitlatch T., Curtis C. 2001, Shipping and alignment for the SNS cryomodule, *Proceedings of the 2001 Particle Accelerator conference*, Chicago: 1488-1490.
8. Hogan J., Daly E. 2003, SNS cryomodule production progress & key lessons learned, *11th workshop on RF superconductivity*, Lubeck, Germany.
9. Petersen B. 2003, High gradient CW modules for FEL/standard modules, SRF2003 workshop.
10. Petersen B. 2009, Layout, operation mode, incident scenarios and safety measures of XFEL cryogenic system, *XFEL status report*.
11. Bonomi R. 2012, SPL thermal studies, *Superconducting linacs for high power proton beams-SLHiPP2*, Catania, Italy.
12. Darve C. 2012, Cold linac heat load estimate: Hybrid vs. Segmented cryomodule design, *ESS AD Technical note*.
13. Parma V. 2010, Status of the SPL cryo-module development, *SPL seminar*, CERN.
14. Darve C. 2012, ESS cryomodules, *ESS light review*.
15. Capatina O., Renaglia T. 2010, SPL power coupler double walled tube thermo-mechanical studies, *Review of SPL RF power coupler*.
16. Claudet S., Lebrun Ph. 2008, Cryogenic heat load and refrigeration capacity management at the Large Hadron Collider (LHC), *LHC Project Report 1171*.
17. Aso T., Tatsumoto H. 2006, Design result of the cryogenic hydrogen circulation system for 1 MW pulse spallation neutron source (JSNS) in J-PARC, *Advance in Cryogenic Engineering*, Volume 823: 763-770.
18. Kato T., Aso T. 2003, Cryogenic system design for cryogenic hydrogen moderator of the spallation neutron source in J-PARC, *ICANS-XVI*, Dusseldorf+Neuss, Germany: 645-654.
19. *National spallation neutron source conceptual design report*, Volume 1, 1997, Oak Ridge National Laboratory.

# SUPERCONDUCTIVITY AND ITS APPLICATIONS

002

# Experimental Study of Superconducting Magnets for the NICA Accelerator Complex

**Khodzhibagiyan H., Bazanov A., Donyagin A., Galimov A., Karpinsky V., Kuznetsov G., Nikitaev P., Smirnov A., Trubnikov G.**

Laboratory of High Energy Physics, Joint Institute for Nuclear Research, Dubna, 141980, Russia

## ABSTRACT

NICA is a new accelerator complex being under design and construction at the Joint Institute for Nuclear Research (JINR) in Dubna. Full-size prototype dipole and quadrupole magnets have been designed, manufactured and tested for the booster synchrotron and the NICA collider. The magnets are based on a cold window frame iron yoke and a saddle-shaped superconducting winding made from a hollow NbTi composite superconducting cable cooled with a forced two-phase helium flow at T = 4.5 K. The maximal operating magnetic field in the aperture is 1.8 T. The magnetic field ramp rate of 1.2 T/s should be achievable. The quench history, AC losses as a function of the magnetic field ramp rate and pressure drop in the cooling channels of the magnets at different pulsed operation modes are presented.

## 1. INTRODUCTION

The NICA/MPD project [1] started at the Joint Institute for Nuclear Research (JINR) in Dubna in 2007. The goal of the project is to carry out experimental studies of the hot and dense strongly interacting quantum chromodynamics matter and light polarized ions. The NICA accelerator complex will consist of two injector chains, a new 600MeV/u superconducting booster synchrotron, the existing superconducting synchrotron – Nuclotron [2], and the new superconducting collider consisting of two rings each of about 503 m in circumference.

## 2. DESIGN AND MANUFACTURING OF THE PROTOTYPE MAGNETS

The Nuclotron-type design [3-5] based on a cold iron yoke and a saddle-shaped superconducting (SC) winding has been chosen for the booster and the collider magnet. The magnet includes a cold (4.5K) window frame iron yoke and a SC winding made of a hollow NbTi composite SC cable cooled with a two-phase helium flow. Lorentz forces in the winding are supported by the yoke. The view of the Nuclotron type SC cable is shown in Fig. 1. The main characteristics of the cable for the NICA magnets are given in Table 1.

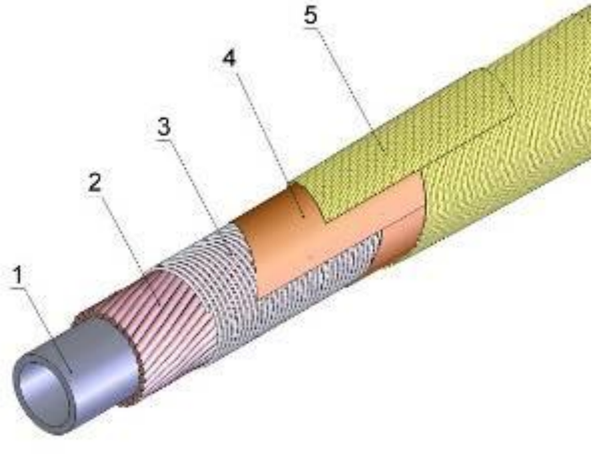

Figure 1. View of the Nuclotron cable: 1- copper-nickel tube, 2 - superconducting wire, 3 - nichrome strand, 5 - Kapton tape, 6 - glassfiber tape.

Table 1. Main characteristics of the cable for the NICA booster and collider magnets.

| Characteristic | Booster | Collider |
|---|---|---|
| Cooling channel diameter, mm | 3 | 3 |
| Number of strands | 18 | 16 |
| Transposition lay of strands, mm | 50 | 50 |
| SC strand diameter, mm | 0.78 | 0.9 |
| Superconductor | 50% Nb – 50% Ti | |
| Cu/SC ratio | 1.26 / 1 | 1.33 / 1 |
| Diameter of SC filaments, µm | 7 | 8 |
| Twist pitch of filaments, mm | 7 | 9 |
| Ni-Cr wire diameter, mm | 0.2 | 0.3 |
| Ni-Cr wire binding pitch, mm | 0.4 | 0.6 |
| Cable outer diameter with insulation, mm | 6.6 | 7.0 |
| Operating current at 1.8 T and 4.65 K, kA | 9.69 | 10.4 |
| Critical current at 2.5 T and 4.7 K, kA | 14.2 | 16.8 |

A cross-section view of the booster quadrupole and dipole magnets is shown in Figs. 2 and 3, correspondingly. The main characteristics of the NICA booster and collider magnets are summarized in Table 2.

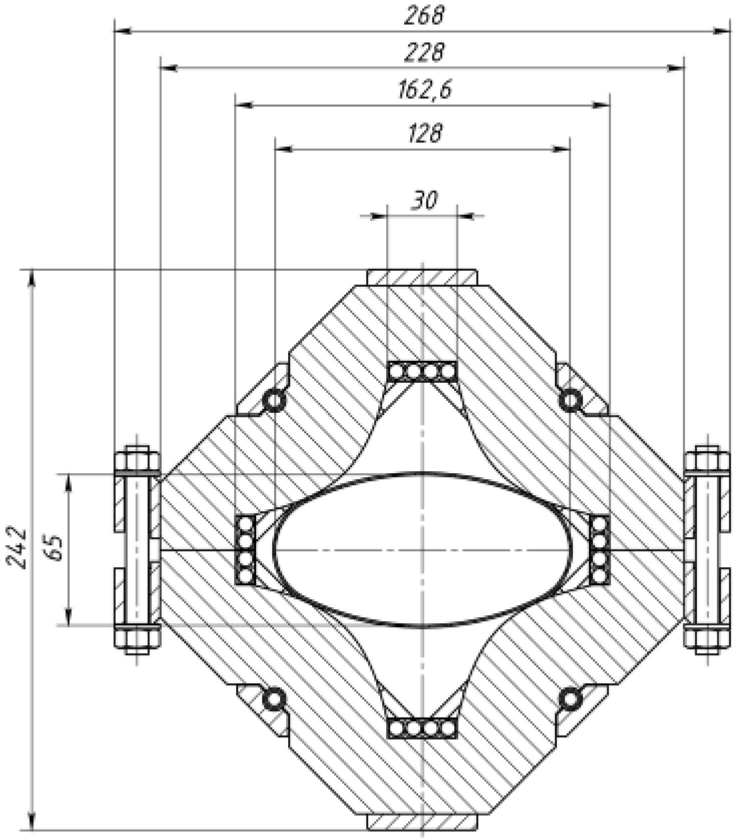

Figure 2. Cross-section view of the quadrupole magnet with hyperbolic poles for the NICA booster.

A full-scale curved model dipole magnet for the NICA booster was manufactured at the Laboratory of High Energy Physics (LHEP) JINR in April 2011. The use of the curved single-layer winding dipoles instead of the straight two-layer winding ones makes it possible to reduce the horizontal size of the magnet's useful aperture leading to less AC losses. The magnet is 2.2 m long and has a radius of the curvature of about 14 m.

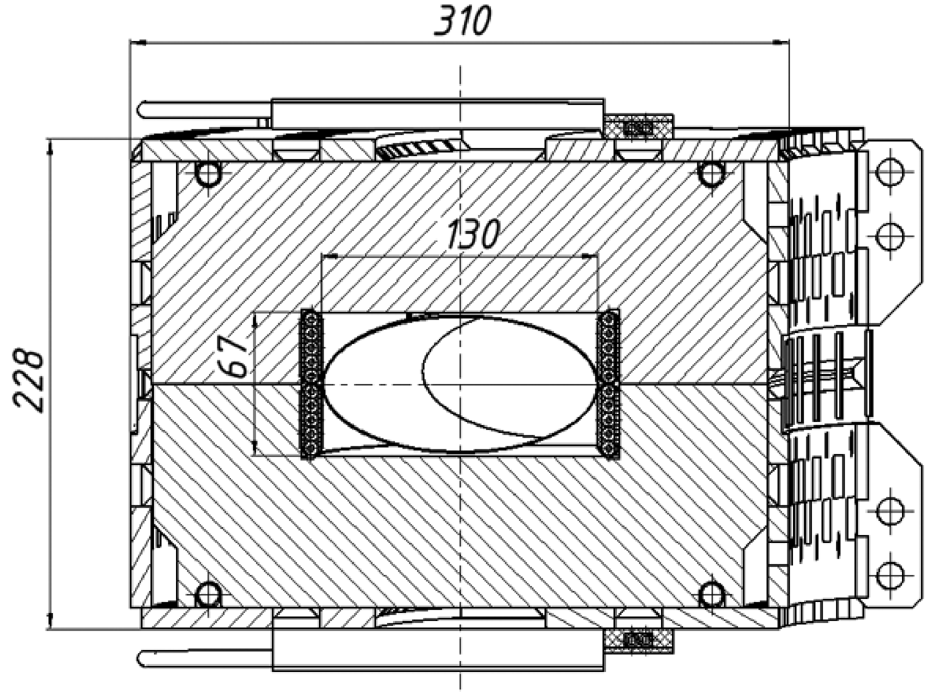

Figure 3. Cross-section view of the bent dipole magnet for the NICA booster.

Table 2. Main characteristics of the NICA booster and collider magnets.

| Characteristic | Booster | | Collider | |
|---|---|---|---|---|
| | Dipole | Lens | Dipole | Lens |
| Number of magnets in the ring | 40 | 48 | 80 | 86 (+12*) |
| Maximum magnetic induction, T<br>(field gradient), T/m | 1,8 | 20,2 | 1,8<br>- | -<br>23 |
| Minimum magnetic induction, T<br>(field gradient), T/m | 0,11 | 1,2 | 0,57<br>- | -<br>7,2 |
| Effective magnetic length, m | 2,2 | 0,55 | 1,94 | 0,46 |
| Ramp rate $^{dB}/_{dt}$, T/s<br>$^{dG}/_{dt}$, T/(m·s) | 1,2 | -<br>13,5 | $\leq 0,5$ | - |
| Field error $\Delta B/B$ ($\Delta G/G$) at R= 30 mm | $\leq 6\cdot10^{-4}$ | | $\leq 2\cdot10^{-4}$ | |
| Beam pipe aperture (horizontal/vertical), mm/mm | 128/64 | 130/64 | 120/70 | 120/70 |
| Pole radius, mm | - | 47,5 | - | 47,5 |
| Bending angle, deg | 9 | - | 4,5 | - |
| Radius of curvature, m | 14.01 | - | - | - |
| Yoke width, m | 0,31 | 0,226 | 0,304 | 0,258 |
| Yoke height, m | 0,228 | 0,226 | 0,554 | 0,548 |
| Distance between the beams, m | - | - | 0,32 | |
| Overall weight , kg | 850 | 110 | 1000 | 300 |
| Current at maximum field (field gradient), kA | 9,68 | | 10,4 | |
| Number of turns in the winding | 10 | 8 | 10 | 8 |
| Inductance , µH | 630 | 96 | 450 | 94 |
| Vacuum shell outer diameter , mm | 570 | | 812 | |
| Dynamic heat releases, W | 8,4 | 0,84 | - | - |
| Static heat leak, W | 4,4 | 4,0 | 8,0 | 5,0 |
| Helium pressure drop in the cooling channel, kPa | $\leq 27$ | | $\leq 27$ | |
| Maximal temperature of helium in the winding, K | 4,65 | | 4,65 | |

* - the final focus lens

The first NICA booster magnet in the cryostat is shown in Fig. 4 (left).

Figure 4. The NICA booster magnets: Installation of the cryostat with the dipole magnet on the bench for the cryogenic test (left) and quadrupole lens before mounting in the cryostat (right).

A full-scale model quadrupole magnet for the NICA booster was manufactured at the LHEP in December 2011. The first quadrupole magnet before installation in the cryostat is shown in Fig. 4 (right).
The Nuclotron-type design was chosen for the NICA collider. Two identical single-layer windings are located in the common straight iron yoke one over the other (see Fig. 5). Lorentz forces in the windings are supported by the yoke. The yoke consists of three parts made of laminated electrical steel. They are held together by longitudinal steel plates welded with laminations and frontal sheets. The magnets are cooled with a two-phase helium flow which in series passes from the supply header through the cooling channels of the bus bars, lower and upper windings, iron yoke and then enters the return header. Each twin bore dipole or quadrupole magnet is connected in parallel to the supply and return helium headers.

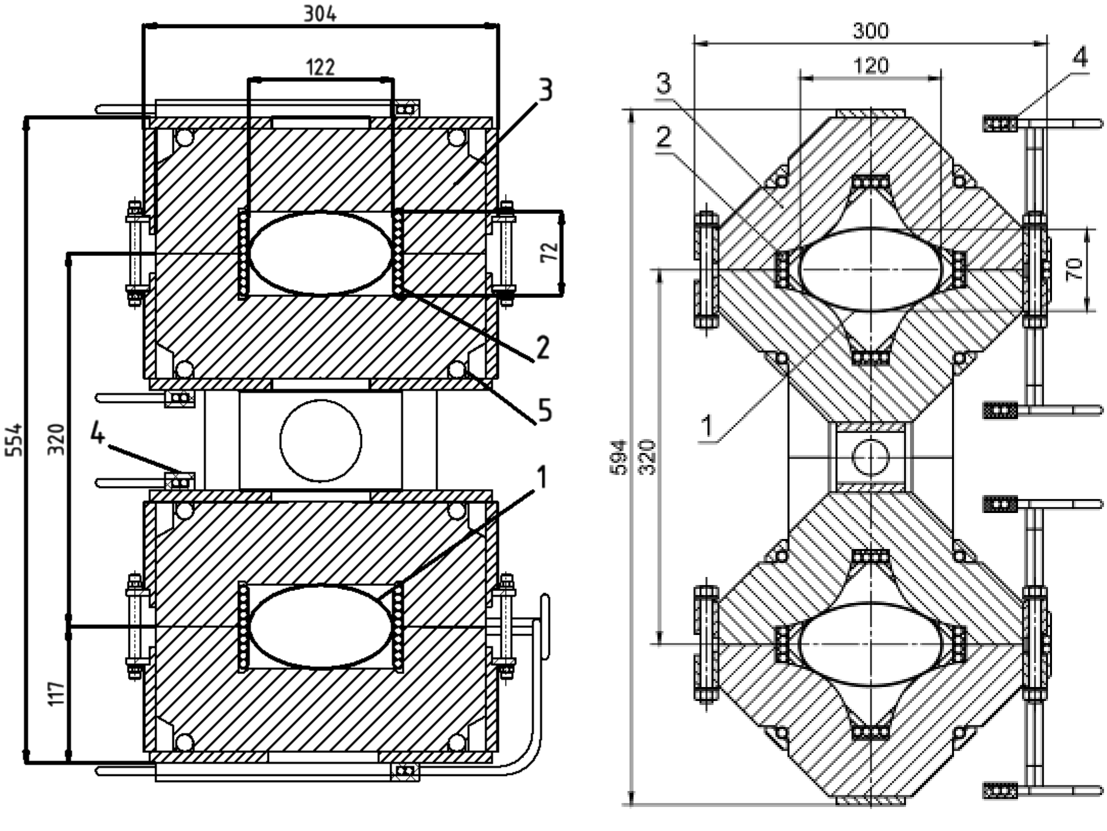

Figure 5. Cross-section view of the twin aperture dipole (left) and quadrupole (right) magnets for the NICA collider.

A twin aperture model dipole magnet for the NICA collider (see Fig. 6 left) was manufactured at LHEP JINR in August 2011. Completion of manufacturing of the model collider twin-bore quadrupole lens with hyperbolic poles is scheduled for May – June 2012. The iron yoke of the model quadrupole magnet for the NICA collider is shown in Fig. 6 (right).

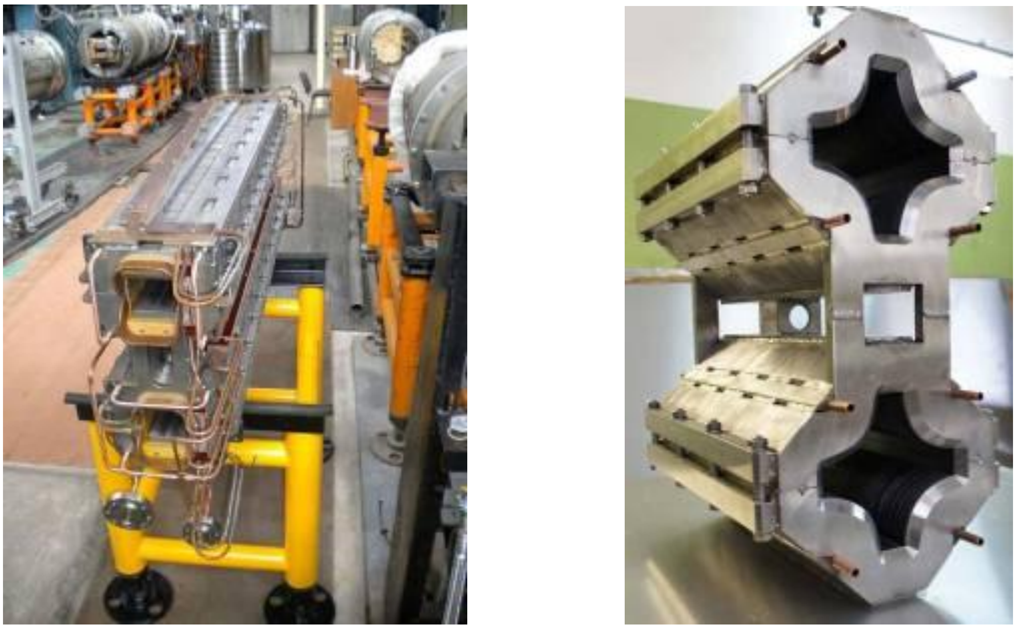

Figure 6. The first NICA collider twin-bore dipole magnet (left) and yoke of the quadrupole lens (right).

## 3. FIRST NICA MAGNETS TEST RESULTS

A cryogenic test of the first dipole magnet for the NICA booster synchrotron was carried out in May 2011. The first quench occurred at 7705 A (see Fig. 4). After the 13th quench the current reaches the nominal value of 9690 A. This corresponds to the magnetic field induction in the gap of 1.8 T. Further training was stopped because of the power supply limitation.

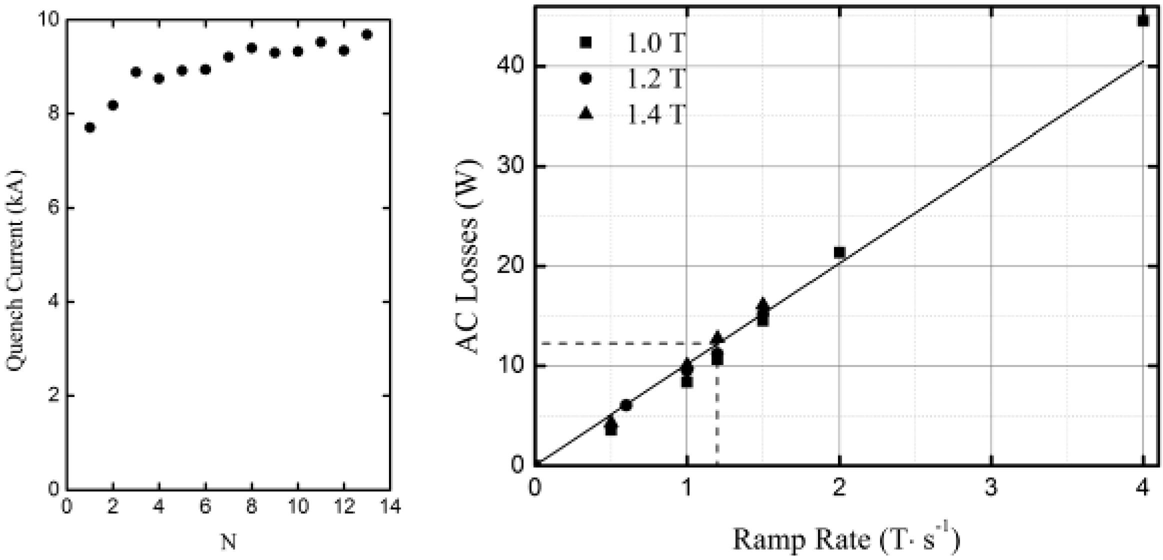

Figure 7. Quench history (left) and AC losses as a function of the magnetic field ramp rate in the aperture during the operation in the triangular cycle (right) for the NICA dipole magnet.

The measured static (at zero current) heat flow to the magnet was 5.8 W. AC losses of 12 W were measured by means of the calorimetric method while the magnet was operating in the triangular cycle with a magnetic field ramp rate of 1.2 T/s without a pause. This value agrees well with the calculation and confirms the correct choice of steel for the magnet yoke. AC losses as a function of the magnetic field ramp rate are shown in Fig. 7. The pressure drop of the helium flow in the cooling channel of the magnet was 47 kPa during the operation in the indicated mode. Hydraulic resistance of the cooling channel was 2 times higher than the calculated value due to the fact that the cooling channel of the cable has a diameter of 2.6 mm instead of the designed one equal to 3 mm. The new winding of the cable with a cooling channel of 3 mm in diameter was fabricated and installed in the yoke of the magnet in spring 2012. Cryogenic tests of the magnet with the new winding are scheduled for May 2012.

Experimental studies of the booster quadrupole magnet were carried out in spring 2012 after upgrading the power supply on the test bench. The current reached the nominal value of 9690 A after the 4th quench. The measured static (at zero current) heat flow to the quadrupole magnet was 3.3 W. AC losses of 4.4 W were measured by using the calorimetric method while the magnet was operating in the triangular cycle with the following parameters: amplitude of the magnetic field gradient of 20.3 T/m, and ramp rate of 20.3 T/(m•s) without a pause. The pressure drop of the two-phase helium flow in the cooling channel of the lense was 7 kPa during the operation in the indicated mode. AC losses as a function of the ramp rate of the magnetic field gradient are shown in Fig. 8.

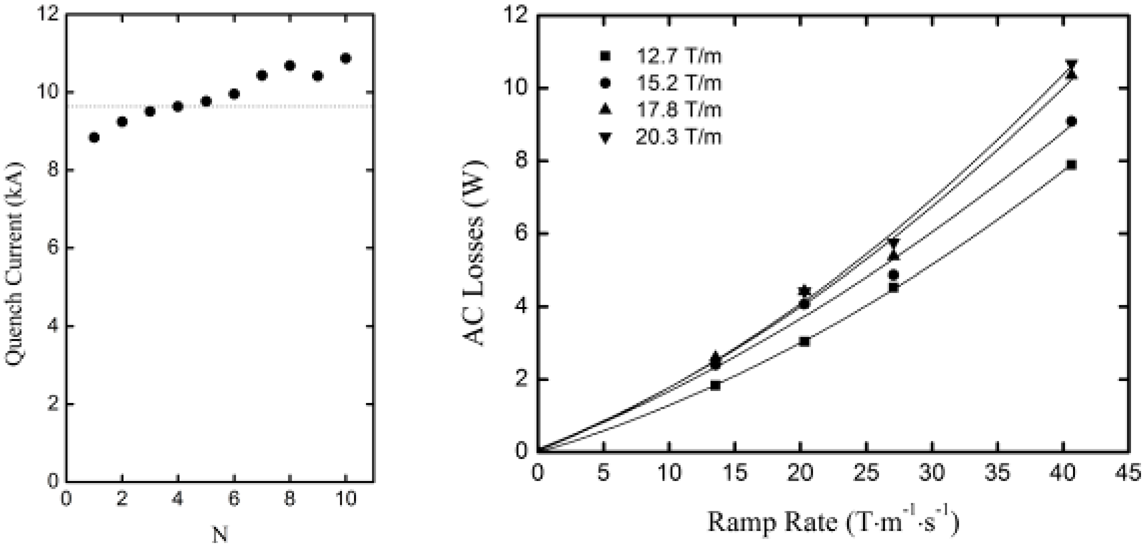

Fugure 8. Quench history (left) and AC losses as a function of the magnetic field gradient ramp rate in the aperture (right) for the NICA quadrupole magnet.

## 4. CONCLUSIONS

The full-scale Nuclotron–type superconducting model dipole and quadrupole magnets for the NICA booster and collider were manufactured at LHEP JINR. First dipole and quadrupole magnets for the NICA booster have successfully passed the cryogenic test on the bench . The nominal current of 9.7 kA was reached after short training. The magnets were successfully tested in the pulsed mode with a magnetic field ramp rate of up to 4 T/s. Further experimental studies of the booster magnet with new winding are scheduled for the end of May 2012. Tests of the model magnet and lense for the collider are scheduled for summer and autumn of this year.

## 5. REFERENCES

[1] Nuclotron -based ion collider facility. Available: http://nica.jinr.ru/

[2] Baldin AM et al. 1983, Nuclotron status report, IEEE Trans. Nucl. Sci.,4:3247-3249.

[3] Khodzhibagiyan HG, Smirnov AA. 1988, The concept of a superconducting magnet system for the Nuclotron, Proc. of the Twelfth Int. Cryogen. Eng. Conf., ICIC12, Southampton: 841-844.

[4] Khodzhibagiyan H, Akishin P, Bychkov A, K et al. 2011, Superconducting Magnets for the NICA Accelerator Complex in Dubna, IEEE Trans. Appl. Supercond., 3:1795-1798.

[5] Khodzhibagiyan H, Agapov N, Kovalenko A, Smirnov A, Starikov A. 2006, Development of fast-cycling superconducting magnets at JINR, Proc. of 21 Int. Cryogen. Eng. Conf., ICIC21, CRYOPrague, 1: 113-116.

037

# Measurement of Dynamic Heat Losses in the Fast Ramped Superconducting Magnets for the SIS100 Synchrotron

**Bleile A.*, Fischer E.*, Khodzhibagiyan H.**, Mierau A.* , Schnizer P.***

* GSI Helmholtzzentrum für Schwerionenforschung, Darmstadt, Germany
** Joint Institute for Nuclear Research, Dubna, Russia

## ABSTRACT

The dynamic losses in fast ramped super ferric magnets will create the main part of the expected heat losses in the superconducting synchrotron SIS100 – the primary accelerator in the Facility for Antiproton and Ion Research (FAIR). Two full size dipole models have been tested at the cryogenic magnet test facility at GSI and a third one at JINR Dubna. The heat losses were measured to verify the magnet design. Dynamic losses were measured for different operation cycles. VI and calorimetrical methods for loss measurements are presented next to the obtained results together with a parametric the model of the AC- losses.

## 1. INTRODUCTION

The SIS100 synchrotron, the core component of the international Facility for Antiproton and Ion Research, will provide proton and ion beams with high currents. The high repetition rate of the synchrotron of up to 1 Hz requires the rapidly-cycling dipole magnets with the ramp rates of 4 T/s. The ramp rate and the duty cycle of the synchrotron are mainly limited by the dynamic heat losses in the magnets: hysteresis and the eddy current losses in the iron yoke, superconducting coil and the beam vacuum chamber. The starting point of the magnet design was the magnets used in the Nuclotron ring in JINR in Dubna [1]. During an intensive R&D phase the AC losses were considerably reduced in comparison to the original Nuclotron magnets [2]. The losses were experimentally measured on short models in Dubna and in GSI. Finally three full-size models were built at BNG Würzburg, JINR Dubna and BINP Novosibirsk using different technologies and different electrical steel grades. Two of them – the straight dipole S2LD and the curved dipole C2LD were tested at the prototype test facility at GSI [3-8]. The main parameters of both tested dipoles are summarized in the Table **4**. This paper describes the applied methods for loss measurements – the V-I method and the calorimetric one. The obtained results for both dipoles are also presented besides the parametric model for the AC losses.

Table 4. Main parameters of the dipoles tested at the Prototype Test Facility at GSI.

| | S2LD | C2LD |
|---|---|---|
| Manufacturer | BNG/Würzburg | BINP/Novosibirsk |
| Maximal field, T | 2.1 | 1.9 |
| Effective length, m | 2.756 | 3.062 |
| Nominal current, kA | 7.5 | 6.4 |
| Ramp rate, T/s | 4 | 4 |
| Bending angle, ° | 3.33 | 3.33 |
| Bending radius | 47.368 | 52.632 |
| Steel grade | M700 | 3413 |

The third magnet was tested on the bench in Dubna. This magnet has the same design with the BNG magnet, but was assembled from Russian steel grade 3413 ET with sheets thickness of 0.5 mm instead German steel grade M700 with sheets thickness of 1 mm**.**

## 2. V-I METHOD

The AC losses in the magnet can be measured by integration of the instantaneous electrical power over the whole cycle. To obtain the instantaneous power the magnet current and the voltage drop on the magnet are simultaneously sampled by two high accuracy digital multimeters HP 3458A. The voltage is measured by two voltage tabs on the magnet coil, for the current measurements a Zero-Flux Current Transformer (DCCT) is used. Both DMM are synchronised – the output trigger signal of the first DMM is used to trigger the second one. The integration time of the both multimeters was set to one power line cycle (20 ms), with results a sampling rate of roughly 50 Hz. The energy loss in the magnet is calculated as:

$$E = \sum_{i=1}^{N} V_i I_i \Delta t$$

with the sum of the instantaneous power over the whole magnet cycle and $\Delta t$ the sampling interval.

## 3. CALORIMETRIC METHOD

The total losses in the magnet can be measured by calorimetric method. The super-ferric magnets for the SIS100 synchrotron are cooled by two phase helium flow. The helium in the supply header is a liquid at the temperature below the saturation line by 0.1-0.2 K. When the liquid flows through the magnet coil its temperature increases until the two-phase region is reached. Further heat load in the coil and in the yoke increases the vapour quality $x$, while the temperature drops with the pressure.

The heat losses can be calculated from the enthalpy difference of helium on the outlet and inlet of the magnet:

$$Q = \dot{m} \cdot (i_{out} - i_{in})$$

with $i$ the enthalpy of helium and $\dot{m}$ the mass flow. The measurements were done for the magnet cycles where the generated losses were high enough to reach the vapour quality $x = 1$ at the yoke output. In this case the helium enthalpy can be calculated as the function of two directly measured values - the temperature and the pressure. Since the helium passes the phase separator before it enters the magnet, we assume the pure liquid on the coil input and calculate the enthalpy $i_{in}$ from the saturation line for a measured pressure $p_{in}$ and the vapour quality $x = 0$. The mass flow rate has been measured by calorimetric sensor installed on the magnet outlet.

## 4. TEST RESULTS

Each of the both full-size dipole prototypes S2LD and C2LD were tested within several cold runs. The first runs were performed without beam vacuum chamber because of magnetic field measurements in the whole magnet aperture. The AC losses were measured by both methods - calorimetric and VI. The magnet was ramped with continuous triangular cycles with different ramp rates $\dot{B} = dB/dt$ as well as for different maximum fields $B_{\max}$. Since the cooling power for both dipoles is limited by the hydraulic resistance of the superconducting coil to about 35 W, delays was added to the cycles with high ramp rates and high maximal field to keep the generated losses below this limit. As an example the AC loss data for the C2LD dipole without beam vacuum chamber are shown on the Fig. 1. The data obtained by both methods are consistent within errors. On the Fig. 1 only the statistic errors of the VI data are shown, the systematic errors for these data are valued at about 10%, whereby the main error source is the accuracy of the DCCT transformer. The biggest error source of the calorimetric method was the slow deviations of the pressure and of the mass flow in the experimental set up. The errors of these measurements are valued about 5-10% of the measured power with a bigger error for the smaller power.

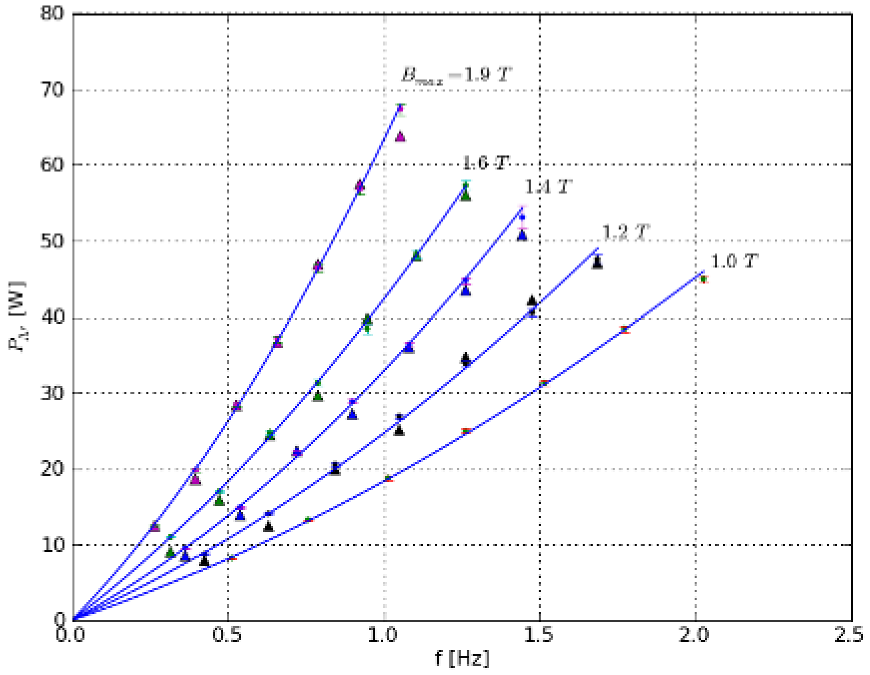

Figure 1. AC loss measurements on the C2LD dipole without beam vacuum chamber. Triangles denote the calorimetric data. Circles with error bars are the data obtained by the VI-method.

## 5. PARAMETRIC MODEL

The measured values for the energy losses per cycle $E$ respectively the averaged power $\overline{P} = E/t_{cyc}$ were used to calculate the equivalent power for the pure triangular cycle:

$$P_\Lambda = \overline{P}\,\frac{t_{cyc}}{t_\Lambda} \quad [\mathrm{W}] \tag{1}$$

$t_\Lambda$ is defined as $2B_{\max}/\dot{B}$ and is the length of a nominal triangular cycle without delays and with sharp edges. Since the edges in the real cycles are smoothed to assure the operation of the power converter unit, the measured cycle length $t_{cyc}$ is slightly higher than the sum of $t_\Lambda$ and the introduced delay $t_d$. The errors $\Delta\overline{P}$ were scaled by the same factor $t_{cyc}/t_\Lambda$. Then the power losses $P_\Lambda$ were fitted by function

$$P_\Lambda = q_h(B_{\max}) \cdot f + q_e(B_{\max}) \cdot f^2 \qquad (2)$$

with $f = 1/t_\Lambda$ the repetition rate of the triangular cycle. The fitting curves are also shown on Fig.2. The linear term in (2) can be interpreted as a hysteresis loss contribution of both the magnet coil and yoke. This term has the same value within errors for both dipoles (see Fig. 2). Also the beam vacuum chamber made of non-magnetic steel doesn't contribute to $q_h$, as expected. The function $q_h(B_{\max})$ can be described with sufficient accuracy with the function:

$$q_h = h \cdot B_{\max}^2 \qquad (3)$$

The second term in (2) can be evaluated for both dipoles and for their beam vacuum chambers. While the losses in both dipoles are similar (see Fig.3), the losses in the vacuum chambers differs clearly (Fig.4). The higher losses in the vacuum chamber of the S2LD dipole are caused by cooling tubes [9]. The quadratic term in (2) can be fitted with the function

$$q_e = e \cdot B_{\max}^{2.5} \qquad (4)$$

The fit curves are shown on Figs. 3-4 and the parameters $h$ and $e$ are summarised in the table 2.

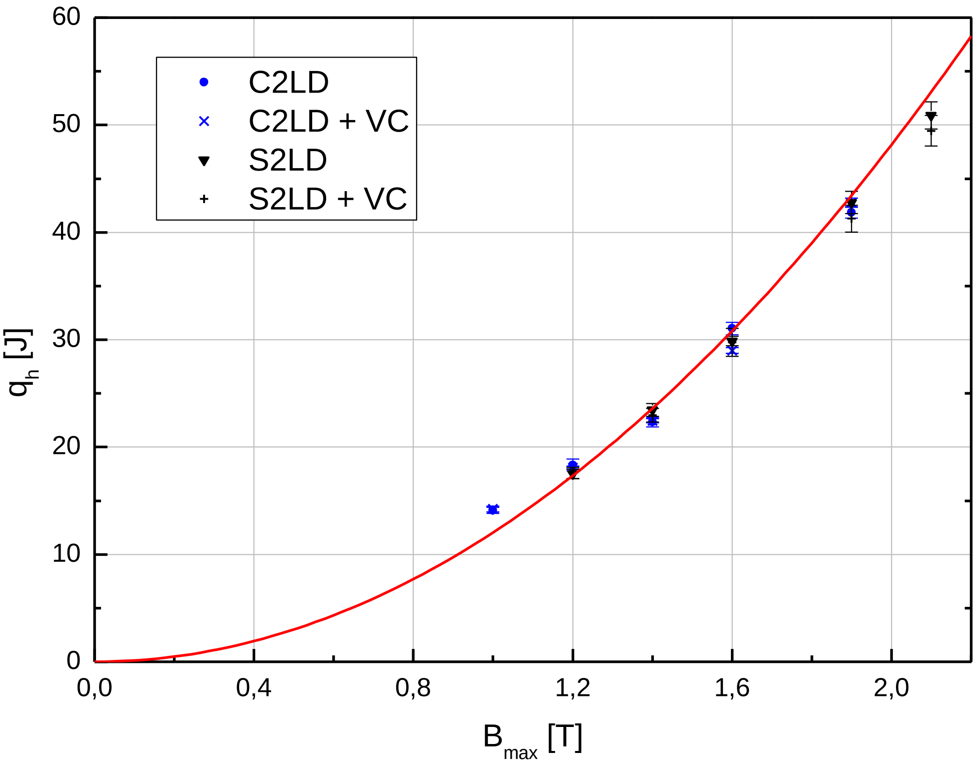

Figure 2 Linear term in the fit function (2) for both dipoles with and without beam vacuum chamber.

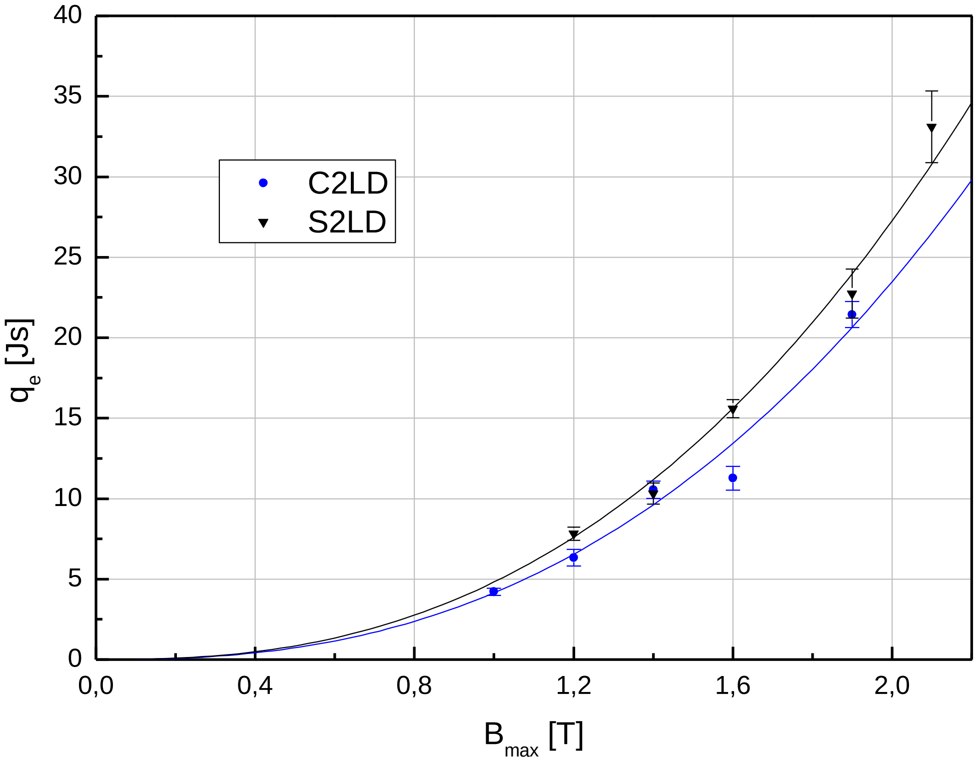

Figure 3 Quadratic term for both dipoles, runs without beam vacuum chamber

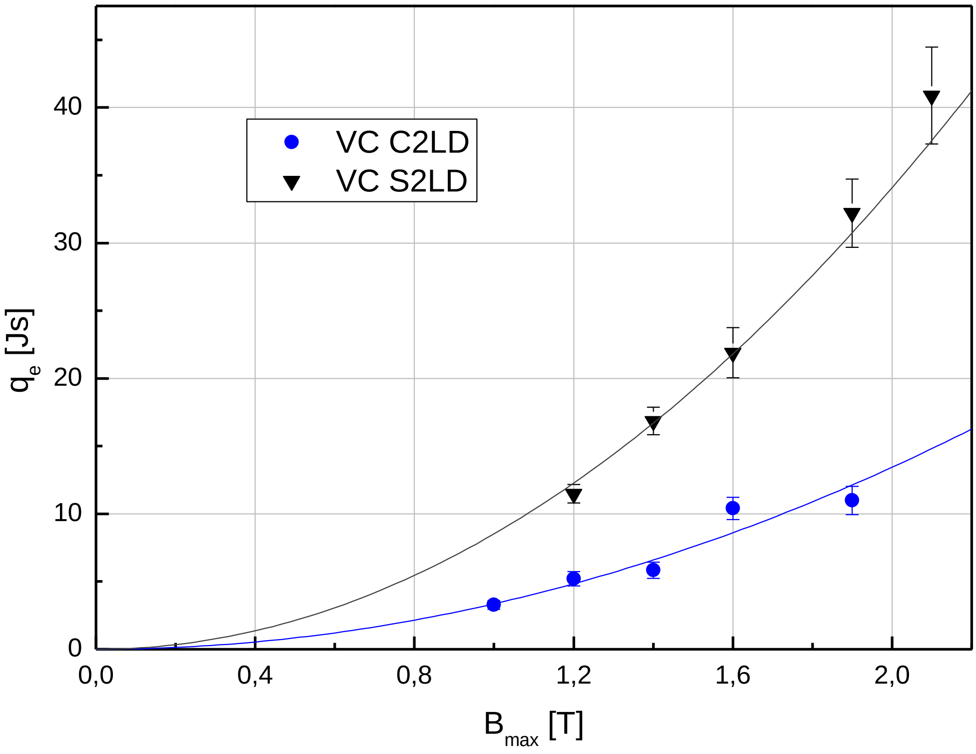

Figure 4 Quadratic term for vacuum chambers

Table 5 AC loss model coefficients

| | h | e |
|---|---|---|
| S2LD dipole | 12.0±0.4 | 4.8±0.3 |
| C2LD dipole | | 4.2±0.2 |
| S2LD Vacuum Chamber | 0 | 8.5±0.2 |
| C2LD Vacuum Chamber | | 3.4±0.2 |

The AC losses in the BNG magnet exceed the losses in the JINR magnet no more than 7% even for the most intense cycle of triangular shape with amplitude of 2 T, ramp rate 4 T/s and a frequency of 1 Hz. This result allows us the steel 3413 ET to replace on the steel M700 and reduce to approximately 2 times the cost of manufacturing the yoke of SIS100 magnets.

## 6. CONCLUSIONS

Two full-size magnets for SIS100 were tested on the Prototype Test Facility at GSI. The AC losses of the magnets as well as of their beam vacuum chambers were measured using two different methods – V-I and the calorimetric one. While the losses in the both magnets are comparable, the losses in the vacuum chambers differ clearly. As expected, the losses in the vacuum chamber of the C2LD dipoles are smaller due to electrically insulated cooling tubes. The losses in the triangular cycle could be parameterised by a model with two parameters and two variables – the maximal field $B_{\max}$ and the cycle repetition rate. It is shown experimentally that the AC losses in the yoke, made of steel grade M700 almost equal losses in the yoke, made from steel 3413 ET. This fact allows us to halve the number of laminations and the cost of the SIS100 magnet yoke.

## 7. REFERENCES

[1] Khodzhibagiyan H. and Smirnov A. 1988, The concept of superconducting magnet system for the Nuclotron, *Proc.of the 12th Int. Cryogen. Eng. Conf. ICEC12*, pp. 841-844.

[2] Kovalenko A. et al. 2006, New results on minimizing AC power loss in a fast cycling 2T superferric dipole with a cold yoke, *IEEE Trans. Appl. Supercond.*, vol. 16, no. 2, pp. 338-341.

[3] Staffiniak A. et al. 2008, Cold Testing of Rapidly-cycling Superconducting Model Magnets for SIS100 and SIS300 – Methods and Results, *Workshop on Accelerator Magnet, Superconductor, Design and Optimization*, CERN.

[4] Fischer E. et al. 2009, Fast ramped superferric prototype magnets of the FAIR project – first test results and design update, *IEEE Trans. Appl. Supercond.*, vol. 19, no. 3

[5] Fischer E. et al. 2010, Superconducting SIS100 Prototype Magnets - Test Results and Final Design Issues, *IEEE Trans. Appl. Supercond.*, vol. 20, no. 3, pp. 218-221.

[6] Fischer E. et al. 2010, Thermodynamic properties of fast ramped superconducting accelerator magnets for the FAIR project, *AIP Conference Proceedings*, vol. 1218, Issue 1, p. 989.

[7] Fischer E. et al. 2010, First test of a fast ramped superconducting curved dipole for FAIR, *Proc. of the Int. Cryog. Eng. Conf. ICEC23*, pp. 1071-1075.

[8] Fischer E. et al. 2011, Design and test status of the fast ramped superconducting SIS100 dipole magnet for FAIR, *IEEE Trans. Appl. Supercond.*, vol. 21, no. 3, pp. 1844-1848.

[9] Fischer E. et al. 2010, Impact of the beam pipe design on the operation parameters of the superconducting magnets for the SIS100 synchrotron of the FAIR project, *J. Phys.: Conf. Ser.*, Vol.234 Part 3.

026

# The Cryogenic System of the 43 T Hybrid Magnet of LNCMI Grenoble, France

**Ronayette L.*, Barbier R.*, Bredy Ph.**, Fazilleau Ph.**, Grandclément C.*,**
**Hervieu B.**, Juster FP.**, Pfister R.*, Pugnat P.***

* Laboratoire National des Champs Magnétiques Intenses (LNCMI), CNRS-UJF-INSA-UPS,
Grenoble, France.
** Commissariat à l'Energie Atomique et aux Energies Alternatives, Institut de Recherche sur les lois
Fondamentales de l'Univers, Saclay, Gif-sur-Yvette, France

## ABSTRACT

A CEA-CNRS French collaboration is currently developing a new hybrid magnet. This magnet combines a resistive insert, composed of Bitter and polyhelix coils, and a large bore superconducting coil (subsequently named "outsert" due to its outermost location), to create an overall continuous magnetic field of 43 T in a 34 mm warm bore aperture. The superconducting coil, based on the novel development of a Nb-Ti/Cu Rutherford Cable On Conduit Conductor (RCOCC) cooled down to 1.8 K by a bath of superfluid helium at atmospheric pressure, aims at producing a continuous magnetic field of 8.5 T in a 1.1 m cold bore diameter. The cryogenic requirements will be presented together with design principles and parameters.

## 1. INTRODUCTION

Hybrid magnets, *i.e.* the combination of a resistive inner coil with a superconducting outer one, allow generating the highest continuous magnetic field for a given electrical power. The present state-of-the-art hybrid magnet system was built by the NHMFL in Tallahassee, Florida, and has produced the highest DC magnetic field of 45.1 T in a 32 mm warm bore diameter [1]. Several hybrid magnets are under construction all over the world [2], [3]. The Grenoble project aims at reaching 43 T in a 34 mm warm bore diameter. A general overview of the Grenoble project can be found in [4], the final design of the large bore superconducting coil based on Nb-Ti and superfluid He technologies is reported in [5]. This article focuses on the cryogenic system of the project, the design and control aspects.

## 2. HYBRID MAGNET

The resistive insert is constituted of a set of 14 polyhelix coils surrounded by a set of two Bitter coils. Both magnets types have already been fully described in [6].

The 8.5 T superconducting outsert coil design of the new LNCMI hybrid magnet has been described in [4]-[5], and the most important choices that have been made can be summarized as follows:
- High current to reduce the inductance of the coil and therefore the voltage levels during quenches,
- Cu stabilized Nb-Ti Rutherford cable directly cooled by a static pressurized bath of superfluid He at 1.8 K,
- Modular coil made of 37 double pancakes, each of them being impregnated separately under vacuum

Table 1. Main parameters of the superconducting outsert coil

| **Parameters** | **Values** |
|---|---|
| Inner / outer diameter | 1150 / 1826 mm |
| Height | 1400 mm |
| Coil weight | 16.3 tons |
| Nominal current (@ 8.5 T) | 7100 A |
| Current density in the conductor | 30 A/mm$^2$ |
| Inductance | 3 H |
| Stored Energy | 76 MJ |
| Operating temperature | 1.8 K |

The existing infrastructure, coming from a previous project [7]-[8], has determined the maximum dimensions of the present superconducting coil. These dimensions are listed in Table 1 together with the main parameters of the superconducting magnet.

This new superconducting magnet is based on an innovative conductor development [4]. A Nb-Ti/Cu Rutherford cable of rectangular cross section, with a 15 µm stainless steel core, is soldered on a Cu-Ag stabilizer to form the so-called RCOCC: Rutherford Cable On Conduit Conductor (Figure 1). The studies and the developments of the RCOCC and its full technical specifications are reported in [9].

To ensure the internal cooling at 1.8 K of the fully impregnated coil winding, the stabilizer of each double pancake is equipped with a cooling channel of 6 mm diameter with both ends open to the static bath of pressurized superfluid He.

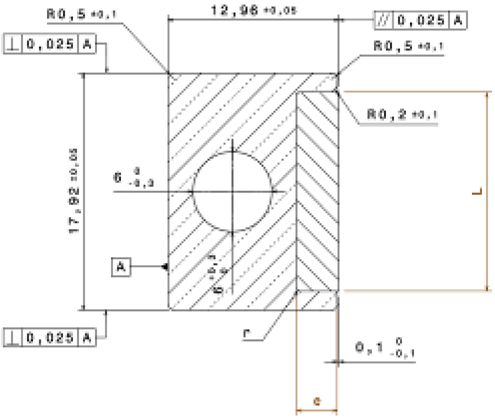

Figure 1. Cross-section of RCOCC, Rutherford Cable On Conduit Conductor (dimensions in mm).

## 3. CRYOGENIC SYSTEM

In order to safely drive the cryo-fluids in the magnet environment, all the valves have been transferred from the cryostat to a separate cryogenic satellite located in a limited magnetic stray field area. The cryostat only includes the burst disks as an ultimate security in case of vacuum failure. The main difficulties in the design of this cryostat are the cold mass weight (Table 2), and the very high magnetic forces applied to the cold elements in case of loss of a half resistive coil in the center (the forces are sufficient to cause an unexpected levitation of the 24 tons cold mass @ 1.8 K). The most critical part of the design of the cryostat concerns the support structure of the eddy-current shield. This part has corresponding costs in terms of energy. In the present state of studies, the eddy-current shield sustentation devices and the cryogenic line between the satellite and the cryostat are the last unknown features to solve.

The present estimation of thermal charges for the whole system (cryostat, cryogenic satellite, cryogenic line) at four levels of temperature (1.8 K, 4.2 K, 30 K and 80 K) gives an equivalent cooling power of 87 l/h LHe @ 4.5 K when the magnet is not energized and 115 l/h LHe @ 4.5 K when the magnet is energized at its nominal operating conditions (7100 A, 8.5 T). Since the eddy-current shield sustentations and the cryogenic line remain to be designed, this equivalent cooling power cannot be considered as final value. Nevertheless, at this step, one can assume that the operation of the magnet will require a dedicated helium liquefier of a production rate > 120 l/h LHe @ 4.5 K.

Based on a Claudet Bath principle [10], the cryogenic satellite is a standard model initially developed for SEHT coil at Saclay [11], also used for ISEULT [12], and adapted for the LNCMI Hybrid magnet.
The great difference with the original design from SEHT is that this satellite has an empty cold volume large enough to store all the helium contained in the magnet cryostat (and not only the channel volume), which eventually can be expelled in case of quench. This significantly reduces the pressure rise in case of quench.
Moreover, the resultant drying out (at least partial) of the coils enhances normal zone propagation velocities and, as a consequence, reduces the maximal and average temperatures of the magnet after a quench.

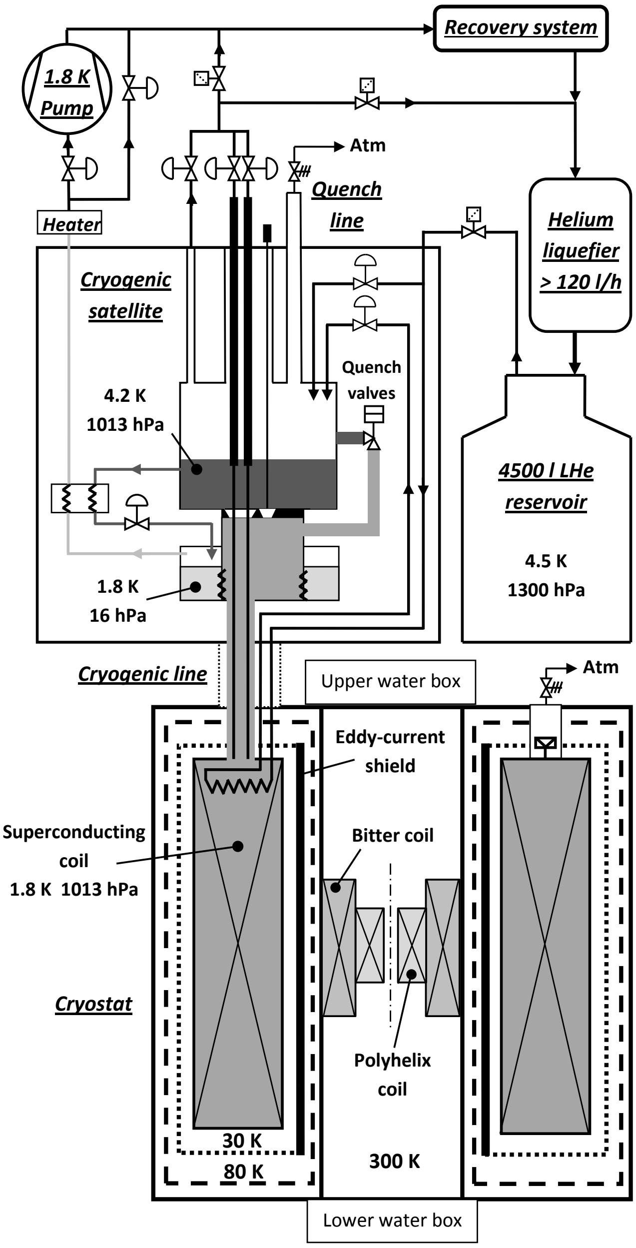

Figure 2. Simplified sketch of the Hybrid magnet and the associated cryogenic system

Table 2. Magnet components list and mass

| Description | Mass (kg) |
|---|---|
| **Total mass @ 1.8 K** | **24 060** |
| - Superconducting coil | 16 300 |
| - Helium vessel | 5 380 |
| - Mechanical structure | 2 380 |
| **Total mass @ 30 K** | **2 900** |
| - Eddy-current shield | 2 280 |
| - Thermal screens | 620 |
| **Total mass @ 80 K** | **710** |
| **-** Thermal screens | 710 |
| **Total mass @ 300 K** | **25 050** |
| - Outer vacuum chamber | 1 750 |
| - 14 polyhelix coils | 700 |
| - 2 Bitter coils | 2 600 |
| - Water boxes | 5 900 |
| - Mechanical structure | 14 100 |

The main difficulty of this strategy at 1.8 K is to use a fast quench valve between the 1.8 K pressurized bath and the expansion volume (for security reasons, 2 fast quench valves will be used). This principle has already been realized successfully in 2000 for the LHC SSS5 tests at the Saclay test facilities [13] and in 2005 for CLAS-DVCS [14].

The 1.8 K mass will be cooled by an external heat exchanger. This implies a longer time for the initial cool-down but avoids having big transient flows directly in contact with the coil. A $LN_2$/He exchanger will be used for the beginning of the cool down and, eventually, to maintain the cold mass at 80 K during long standbys.

The estimated time to cool down the 24 tons cold mass from ambient temperature to 1.8 K is 50 days with $LN_2$ and LHe (95 days with only LHe).

The satellite also contains the resistive current leads. The connections to the superconducting busbars are located in the 4.2 K normal boiling LHe bath before joining the pressurized 1.8 K bath through the lambda plate. The cryogenic line contains the superconducting busbars to power the magnet.

When the magnet is energized to its nominal conditions (7100 A, 8.5 T), an estimated power of 7.7 W is transmitted to the 1.8 K pressurized superfluid helium bath in contact with the superconducting coil. This power is transported from the cryostat to the cryogenic satellite via the pressurized superfluid helium bath of the cryogenic line. This heat transfer mechanism is driven by the Gorter-Mellink regime.

On the basis of a pre-designed 7 meter long (not a definitive value) cryogenic line, and using He properties from Hepak V3.4 [15], one can estimate a minimal inner diameter for a given transported power and a maximal thermal gradient between the cryostat and the satellite. For example: for 7.7 W and $\Delta T \leq 0.01$ K (1.81 K on the coil side, 1.80 K on the satellite side) the minimum equivalent hydraulic diameter of the cryogenic line is 62 mm. With the line length and the satellite bath temperature being fixed, there exists an upper flux limit or critical flux $q_c$ corresponding to a $T_\lambda = 2.17$ K (superfluid helium transition) given by eq (1).

$$q_c \times L^{.333} \approx 16000\ \mathrm{Wm^{-2}m^{.333}}\ \text{at}\ \mathrm{T_{bath}} = 1.8\,\mathrm{K}\ \text{and}\ \mathrm{P_{bath}} = 1\,\mathrm{bar} \qquad (1)$$

For an equivalent hydraulic diameter of 62 mm diameter, this leads to a maximal transported power of 25 W. Of course, increasing the diameter significantly improves the line transport properties and provides a comfortable margin against errors on evaluated thermal loads. For instance, for a 100 mm equivalent hydraulic diameter, 7 meter long cryogenic line, the maximal transported power increases to up to 65 W.

## 4. CRYOGENICS OPERATION: MCS (MAGNET CONTROL SYSTEM)

The aim of the Magnet Control System (MCS) is to control and monitor the cryogenics and the power supply of the superconducting magnet.

The safe operation of the superconducting magnet is controlled by a dedicated hardware named MSS (Magnet Safety System) [16]. The operation of the resistive coils is done via the LNCMI standard MCMS (Magnet Control and Monitoring System) [17].

The MCS (Figure 3) is made of standard industrial products for automation and is composed of a low level part for managing the process efficiently and a high level Human Machine Interface (HMI) for monitoring the parameters.

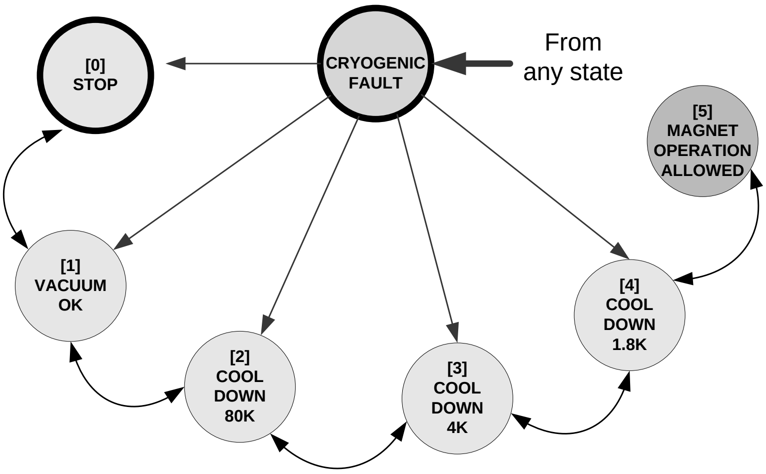

Figure 3. MCS simplified state diagram

The first task of the MCS is to realize the vacuum pumping for thermal insulation. There are two dedicated vacuum units: one for the cryostat and one for the satellite and the cryogenic line.

The second task of the MCS is to cool down the superconducting magnet. This operation is realized in 3 different steps: from ambient temperature to 80 K with the use of $LN_2$ from an external 17 000 litres tank, from 80 K to 4.2 K with LHe produced by the liquefier and stored in the 4500 litres Dewar and, finally, down to 1.8 K with the production of the superfluid pressurized helium bath with the help of the 1.8 K pump.

The third task is to maintain the temperature of the coil bath at 1.8 K during the operation of the magnet.

The MCS has to control 17 regulation loops and to check about 60 analog sensors.

Time constants of the regulation loops are quite slow (a few ten minutes can separate the reaction from the command). But, if a quench occurs, the helium is transferred to the inner cold volume of the satellite via the quench valves. In this case, the MCS has to deal with an emergency procedure.

On the hardware side (Figure 4), the automation of the cryogenic part is based on a Programmable Logic Controller (PLC) Siemens S7-400. This PLC is dispatched on several modules depending on the localization of the sensors and actuators.

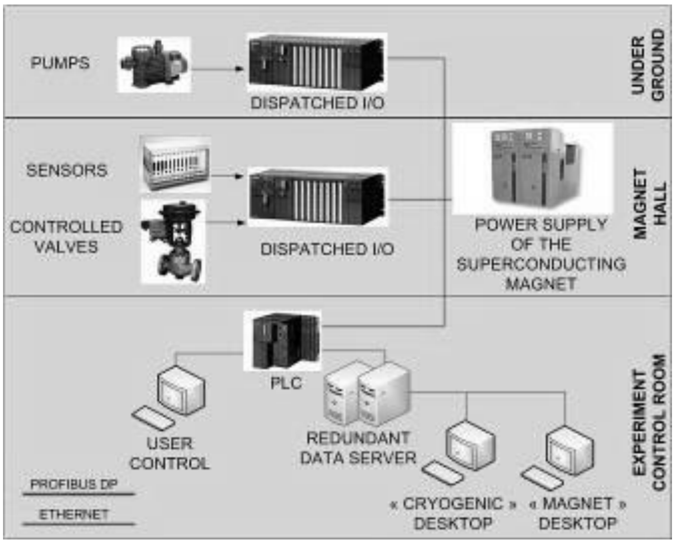

Figure 4. Hardware architecture of the MCS

This kind of architecture reduces wiring and offers a better efficiency of the analog measurement.

The program of the PLC is developed using Siemens S7Graph which allows the user to realize programs using sequential control graphic. The entire program is developed with this language to avoid problems due to a bad software specification.

For the temperature measurement, we use PT100 or Cernox™ sensors depending on the temperature range and the localization of the sensor. For the data acquisition of the Cernox™ sensors, we use Lakeshore Model 234 transmitter in rack format just before the PLC.

The HMI level is developed using a System Control and Data Acquisition (SCADA) software called Cimplicity from the company General Electric. This software allows the user to easily develop an informatics monitoring system using client/server architecture. It communicates with industrial devices using a standard OPC client layer and, it provides the possibility to use .NET script either at client or at server level. The SCADA software allows user to create component (Figure 5). For each sensor or actuator we develop a generic model describing all the parameters and all the actions needed.

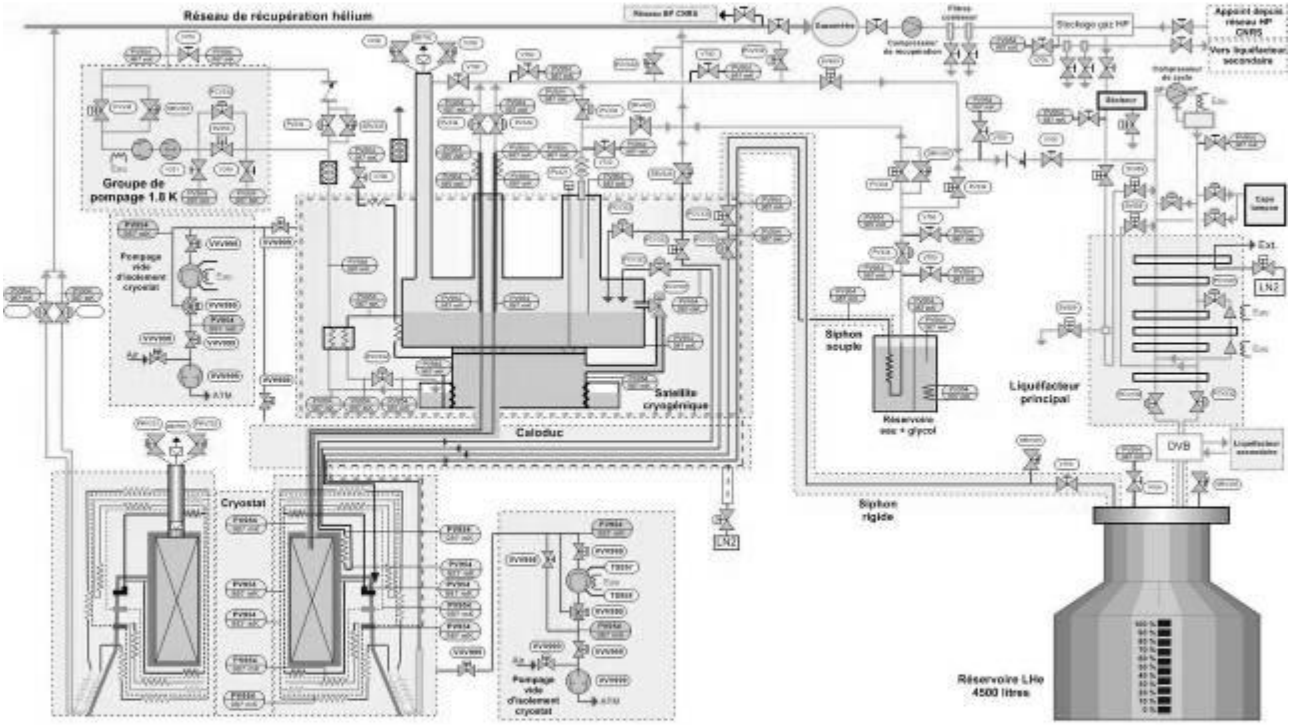

Figure 5. Screen shot of the HMI general view (prototype)

## 5. CONCLUSIONS

A CEA-CNRS French collaboration is developing a challenging Hybrid magnet, combining resistive and superconducting technologies, to produce a continuous magnetic field of 43 T in a 34 mm warm bore aperture.

The 24 tons cold mass will be cooled down to and maintained at 1.8 K by a static superfluid helium bath at atmospheric pressure. Due to the magnetic stray field and the limiting existing infrastructure, the superfluid LHe bath will be generated in a separated cryogenic satellite. The heat transfer between the helium vessel, containing the superconducting coil, and the cryogenic satellite will be made via the superfluid pressurized helium contained in the cryogenic line. The designs of the helium vessel and the cryogenic satellite are close to the final ones. The cryogenic line and the eddy-current shield sustentation devices remain to be defined.

The detailed studies should be finalized by the end of 2012, and the production of the different elements should start in mid-2013. A dedicated helium liquefier will also be purchased and installed in the LNCMI Hybrid experimental hall. The global assembly of the Hybrid magnet is scheduled to start in mid-2014. After cool down and validation tests, the delivery date of the Hybrid magnet to the users' community is planned at the earliest by the end of 2015.

## 6. Acknowledgements

This project is supported by the French Ministry of Higher Education and Research within the "Investissements pour l'avenir" LaSUP, the CNRS (Centre National pour la Recherche Scientifique) and the EU-FP7-Infrastructure-2008-1, Funding scheme Combination of Collaborative Project and Coordination and Support Action, EuroMagNET II, Grant agreement number 228043.

## 7. REFERENCES

[1] M.D. Bird et al. 2001, The 45 T hybrid insert: recent achievements, *Physica B: Condensed Matter, Volumes 294–295, p 639-642.*

[2] S.A.J. Wiegers et al. 2010, Conceptual Design of the 45 T Hybrid Magnet at the Nijmegen High Field Magnet Laboratory, *IEEE Transactions on Applied Superconductivity, vol 20, p 688-691.*

[3] G. Kuang et al. 2010, A 40 T Hybrid Magnet Under Construction in China, *IEEE Transactions on Applied Superconductivity, vol 20, p 680-683.*

[4] A. Bourquard et al. 2010, A New Design for the Superconducting Outsert for the GHMFL 42+ T Hybrid Magnet Project, *IEEE Transactions on Applied Superconductivity, vol 20, p 684-687.*

[5] Ph. Fazilleau et al. 2012, Final Design of the New Grenoble Hybrid Magnet, *to be published in IEEE Transactions on Applied Superconductivity, vol 22.*

[6] G. Aubert et al. 2004, Hybrid and Giga-NMR projects at the Grenoble High Magnetic Field Laboratory**,** *IEEE Transactions on Applied Superconductivity, vol 14, p 1280-1282.*

[7] A. Bonito Oliva et al. 2005, Preliminary Results of Final Test of the GHMFL 40 T Hybrid Magnet, *IEEE Transactions on Applied Superconductivity, vol 15, p 1311-1316.*

[8] A. Bonito Oliva et al. 2006, Investigation on ramp rate limitation on the superconducting magnet for the Grenoble 40 T Hybrid system, *IEEE Transactions on Applied Superconductivity, vol 16, p 940-944.*

[9] P. Pugnat et al. 2012, Study and Development of the Superconducting Conductor for the Grenoble Hybrid Magnet, *to be published in IEEE Transactions on Applied Superconductivity, vol 22.*

[10] G. Claudet et al. 1974, The design and operation of a refrigerator system using superfluid helium, *Proceedings of the 5th International Cryogenics. Engineering. Conference, p 265-267.*

[11] W. Abdel Maksoud et al. 2010 Quench experiments in a 8 T superconducting coil cooled by superfluid helium, *IEEE Transactions on Applied Superconductivity, vol 20, p 1989-1992.*

[12] Ph. Bredy et al. 2010, Cryogenics Around the 11.7 T MRI Iseult Magnet, *IEEE Transactions on Applied Superconductivity, vol 20, p 2066-2069.*

[13] F. Simon et al. 2002, Test results of the third LHC main quadrupole magnet prototype at CEA/Saclay, *IEEE Transactions on Applied Superconductivity, vol 12, p 266-269*

[14] J. Ball et al. 2006, Superconducting solenoid for the CLAS DVCS experiment, *Hadron structure - SPhN 2004-2006.*

[15] Hepak V3.4 1999, Computer program for calculating thermophysical properties of helium from fundamental state equations, *Cryodata Inc* http://www.cryodata.com .

[16] J-P. Charrier et al. 2012, In-line control in T2K proton beam line Magnet Safety System, *to be published in IEEE Transactions on Applied Superconductivity, vol 22.*

[17] R. Barbier et al. 2012, Magnet Control and Monitoring System, *to be published in IEEE Transactions on Applied Superconductivity, vol 22.*

054

# Cooling systems for superconducting power applications – Experiences gained from HTS cable and fault-current limiter projects

**Hobl A.**[*], **Bock J.**[*], **Allweins K.**[**]

[*] Nexans SuperConductors GmbH, Chemiepark Knapsack, 50351 Hürth, Germany
[**] Nexans Deutschland GmbH, Kabelkamp 20, 30179 Hannover, Germany

## ABSTRACT

The application of high temperature superconductors (HTS) in power engineering requires both efficient and reliable cooling. Several superconducting cables and fault-current limiters have been designed and installed by Nexans and were already thoroughly field tested. Dependent on the cooling power, temperature and pressure conditions, various solutions were realised and have resulted in different experiences during the field tests. Each system shows specific advantages and drawbacks, and in some cases improvements had been established even after commissioning or during the test period. The operating behaviour was not satisfying in all cases since high effort would be needed to ensure continuous operation and higher efficiency. A main reason is seen in the fact that the typical cooling demand is in a range of a few kW, a domain where large-series coolers are not available to date.

## 1. INTRODUCTION

HTS systems have been developed for various applications and have proven reliability in numerous test installations. Once tested and operational, the reliability is usually defined by the cooling system. Different field tests and pilot installations also for commercial applications have been realised for HTS cables and fault-current limiters (FCL). The cooling demand is usually between 300 W and 2 kW for FCL and between 2 kW and 20 kW for cables. In future, longer length cables might require more powerful cooling systems. For Nexans HTS cables and fault-current limiters, cooling systems have been designed as open or closed systems. Systems using cooling from bulk liquid supply are referred to as open systems. To reach operation temperatures below 77 K in such systems, vacuum pumps are needed to reduce the nitrogen gas pressure above the liquid bath.

## 2. REPRESENTATIVE SYSTEM DESIGN

A cooling system for HTS power applications consists of different components, see figure 1. Most of the systems require forced flow of the coolant, performed by a circulation pump. Electrical insulation requirements and height differences obviate 2-phase flow systems and sub-cooled cryogens are mostly used.

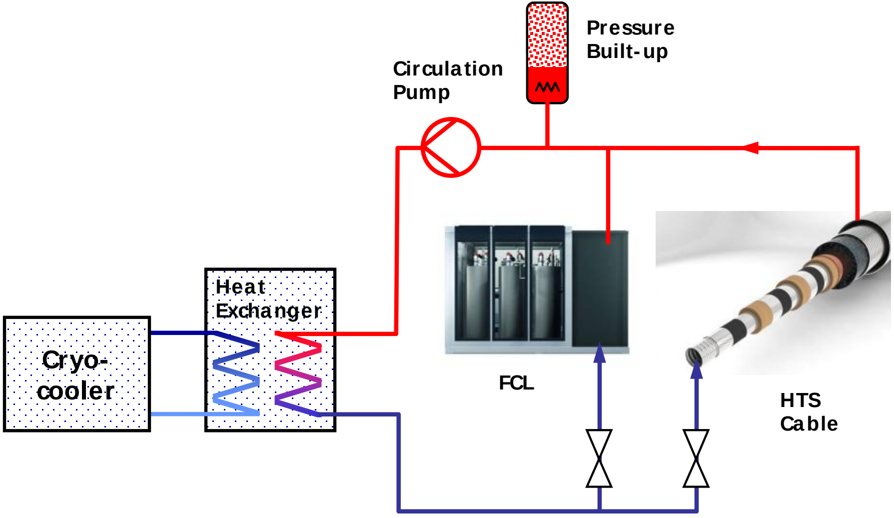

Figure 11: Sketch of cooling system for HTS power applications.

Therefore, a pressure regulation system inside the closed cooling circuit must be applied. The heat input to the circulation system is re-cooled in a heat exchanger. The primary side of the heat exchanger is either cooled by a cryocooler or from bulk liquid supply. Vacuum pumps may be applied on the liquid to reduce the operating temperature to below atmospheric pressure boiling point.

## 3. GENERAL REQUIREMENTS

The cooling demand of HTS systems is influenced by different factors like system size and intrinsic losses. In many cases, the current leads are a significant part of the overall losses, since for each current lead and kA of operating current about 45 to 50 W losses arise between room temperature and liquid nitrogen temperature. For a typical 40 MVA system at 10 kV, this is in total almost 700 W losses from the current leads only. There are heat losses due to radiation and conduction in the cryostats, cables and transfer lines. The HTS material has intrinsic heat input due to AC losses like hysteresis and eddy current losses. In case a cryogen circulation system is needed, this system causes friction and pressure rise losses. In total, the typical requirements for FCL and cable cooling systems are summarized in table 1. The cooling systems do not only have to enable normal operation, but also need to be safe and efficient in all operating modes like cool-down and warm-up as well as during any failure mode.

Table 1: Cooling system parameters for HTS FCL and cable systems.

| Parameter | FCL | Cable | |
|---|---|---|---|
| Cooling power | 0.5 ... 3 | 2 ... 30 | kW |
| Supply temperature | 65 ... 77 | 65 ... 70 | K |
| Mass flow | – | 0.3 ... 5 | kg/s |
| Supply pressure | 1 ... 20 | ~15 | bar |
| Pressure drop | – | 5 ... 10 | bar |
| Load conditions | 20 ... 100 | | % |
| Ambient temperature | -40 ... +50 | | °C |

In the range between a few W up to 600 W a larger variety of cryocoolers using pulse tube or GM cold heads are available. Such cryocoolers have been produced in large series for e.g. shield cooling applications in clinical magnetic resonance imaging systems. Cooling devices using efficient turbo expanders are mostly seen in large cooling or refrigeration systems like air separation and liquefaction systems having cooling powers well above 100 kW at 77 K. Smaller turbo-expander coolers have only been produced for niche applications at relatively high cost [1] due to their high complexity. In the range between 0.5 to 10 kW only a few cooling systems like Stirling machines are commercially available.

In FCL one intended operation condition is the limitation, where large energy amounts are deposited inside the FCL cryostat. This leads to an immediate pressure rise, and can either be handled by a relief valve and subsequent refill, or the pressure rise is accepted and the cryogen is re-cooled afterwards.

In addition to the purely technical requirements there are further needs:

- Availability: A planned up-time of 100% shall be possible. Therefore, a modular concept regarding reliability and maintenance operations has to be incorporated. Any control system used on the cooler should apply industry standard components.
- Low operational cost: The operational costs are influenced by the cost for electrical power, maintenance, and additional needs like cryogens and other media.

- High efficiency: A high coefficient of performance (COP = heat removed / work consumed in W/W) reduces both the electrical power consumption and the cost for re-cooling which is usually achieved by chillers with water-to-air heat exchangers.
- Low maintenance: Ideally maintenance should not disturb the operation of the cooling system. The maintenance intervals shall be large and the system design should reduce the maintenance effort.
- Low investment cost: Today, the investment costs for cooling systems in the 0.5 to 4 kW range are in the order of 50 to 100 k€/kW and therefore are a main cost driver for HTS systems. For a broader application of such systems, the cost should drop to 20 k€/kW or below.
- Modular design: A modular design is necessary to enable operation like it is standard in e.g. the power grid with (n-1)-criteria for redundancy.
- Long life time: Power system operators are used to life times of 40 and more years for their assets like transformers. Future cooling systems will have to be designed accordingly.

## 4. OPERATIONAL EXPERIENCE

### 4.1. HTS Fault Current Limiter

References are given in [2],[3]. The first resistive FCL which was field tested in the medium voltage distribution grid was developed in a funded project with the acronym Curl 10 [4], see figure 2. The cooling was realized using Stirling cryocoolers and the superconducting elements were operated at 65 K. Two Stirling coolers have been applied with some margin in the cooling power, which however did not provide full redundancy under all operating conditions. During the initial operation the coolers experienced nitrogen freezing at the heat exchanger, and the cooling power dropped dramatically. The problem was cured later on by temperature control and intermittent warming with heaters attached to the heat exchangers. The Stirling coolers provided 2×700 W @ 65 K cooling power. At 65 K the coolers have about 20%, at 77 K about 25% Carnot efficiency.

Nexans had produced a FCL for operation in a Vattenfall thermal power plant, see figure 3. The system operates at 65 K using bulk nitrogen supply plus vacuum pumps. Three vacuum pumps had been installed in parallel for redundancy, where two pumps only are sufficient for the heat input. The rotary claw vacuum pumps have a nominal pumping speed of 160 $m^3$/h, which reduces to 120 $m^3$/h @ 200 mbar and 60 $m^3$/h @ 100 mbar inlet pressure. The claw pumps showed not to be enduring longer durations of pumping at ultimate pressure, when the inlet valve on the vacuum side is closed and a bypass valve needs to be installed to ensure mass flow to permanently cool the claws.

Two FCL systems installed in UK used 1-stage GM cold heads for operation at around 70 K. The cryocoolers showed high reliability; however the cooling power is dependent on the cooling water inlet temperature. This type of coolers is produced in large series, is considered reliable, but is limited in cooling power and shows a lower efficiency. The Carnot efficiency is about 12% when operating at 80 K.

Figure 12: Curl 10 FCL.

Figure 13: Vattenfall FCL.

## 4.2. HTS Cable

References are given in [5],[6]. After different HTS cables produced at test lengths of up to a few ten meters, the largest cable to date is installed in the grid of LIPA (Long Island Power Authority, New York) with an ampacity of 2300 A and operating at 138 kV.

Figure 14 visualizes the LIPA installation on-site, showing the three phase HTS cable in the front and the corresponding outdoor terminations in the background. In Figure 15 the building including the cooling equipment is shown.

Figure 14: HTS cable installation in the grid of LIPA.

Figure 15: Building including the cooling equipment.

Figure 16 shows a sketch of the LIPA cooling system. The primary refrigeration system is a turbo expander cooler with a capacity of 5.65 kW @ 65 - 72 K, delivering a mass flow of 375 g/s of $LN_2$. With 5.1 kW cable cryostat / termination losses and 333 W refrigeration system losses there is a 5% margin of about 250 W. To ensure continuous cooling even during refrigerator failure there is a backup refrigeration system using bulk nitrogen supply at about 45 g/s providing a cooling power of about 6.8 kW. The system is supplied from a nitrogen tank with about 50 $m^3$ capacity.

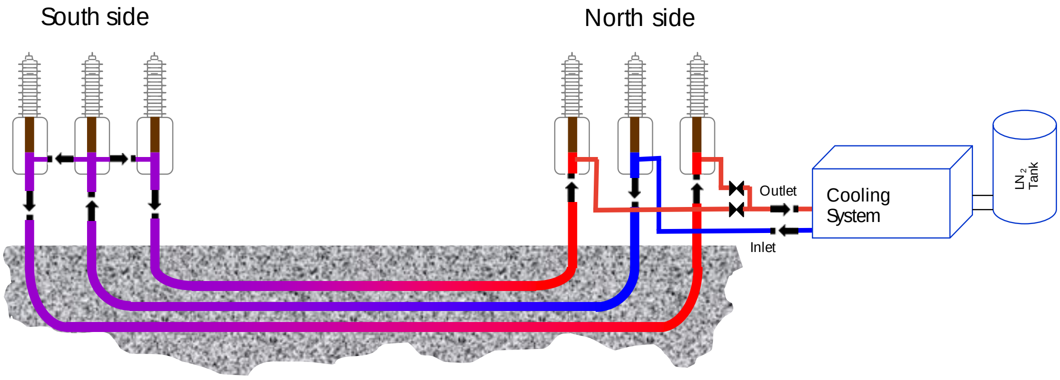

Figure 16: Sketch of the LIPA cooling system.

The system operation during about 2 years is shown in Figure 17. In October 2008 an internal transfer line had to be replaced. Each change of the grey dots between upper and lower end of the scale represents a switching from the primary cooling system to the backup system. Initially, there were temperature and pressure instabilities during such switching operations, which could be reduced after hardware and software changes.

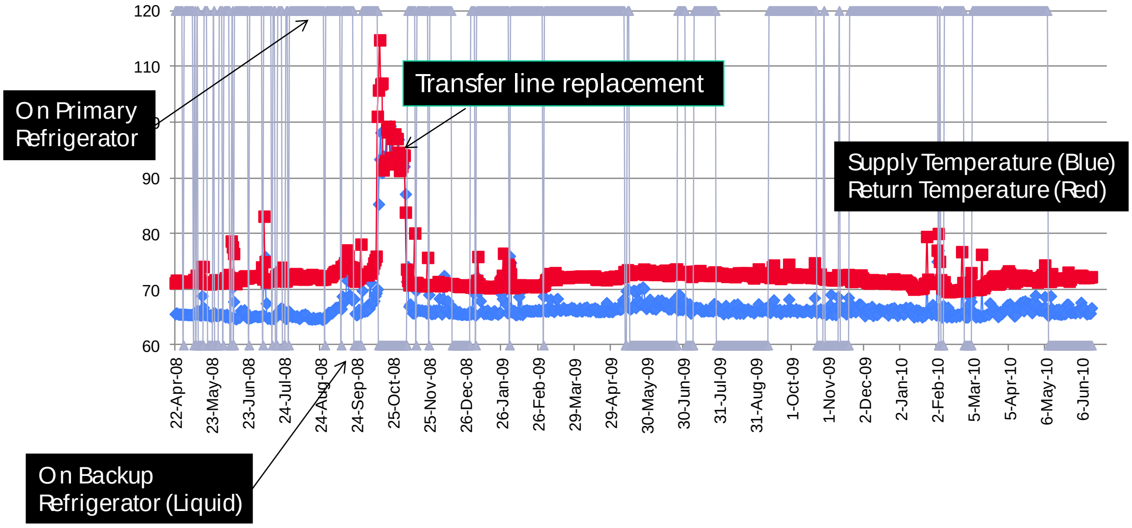

Figure 17: HTS cable cooling system performance.

Before design and installation of the HTS cable system an intensive search into relevant parameters and regulations relating to the cooling system had been performed. As soon as the proper cable design was available a more detailed investigation had been carried out. During the operating time analyses using Ishikawa diagrams (so-called fishbone diagrams) of the LIPA HTS cable trips out of service had been performed, including the typical categories like materials, methods, measurements, machinery (any equipment), environment (e.g. ambient conditions) and people involved. Such “cause-and-effect” lines showed dependencies of diverse parameters of the cooling system and resulted in a better understanding of processes of the whole cooling system and cable system. Despite of any efforts with the Ishikawa diagrams, the operating behaviour was not fully satisfying in the first month of the operating time, where e.g. the backup system did not start up for a short time or an over-temperature limit of the compressor was reached on a hot summer day. Nevertheless, a continuous optimization of the cooling system was possible by the analysis and structuring of the processes. As a result, since 2009 the cable has been running for several years without interruption. A comparison of the performance of the HTS cable during the years 2009 and 2010 is shown in table 2. Aside from a slight increase of the cable cryostat losses due to minor losses of vacuum quality of the cryostat, the cable system was operating like in the original conditions when it was supplied to the customer.

Table 2: Operating performance of the HTS cable.

| | | 2009 | | | 2010 | | |
|---|---|---|---|---|---|---|---|
| **Operating condition** | | **Case 1** | **Case 2** | **Case 3** | **Case 1** | **Case 2** | **Case 3** |
| Load | MVA | 0 | 16 | 82 | 0 | 17 | 87 |
| Current | A | 0 | 75 | 350 | 0 | 76 | 368 |
| Operational voltage | kV | 138 | 138 | 138 | 138 | 138 | 138 |
| Total losses | W | 3672 | 4301 | 4615 | 3958 | 4464 | 4922 |
| Cable cryostat losses | W/m | 1.3 | 1.3 | 1.3 | 1.35 | 1.35 | 1.35 |

## 5. CONCLUSIONS

Various cooling systems have been realized for HTS FCL and cable systems. The typical cooling demand is in the gap between cold heads on the one hand which are not powerful enough and show low efficiency and expensive refrigeration systems on the other hand which are built as complex systems using turbo expanders. After a HTS system has shown functionality, the availability and reliability of such a system is mostly dominated by the availability and reliability of the cooling system. Research and development as well as larger series production are needed to make cryocoolers of 0.5 to 30 kW cooling power more reliable and economically attractive.

## 6. REFERENCES

[1] R.W. Hill, J.K. Hilderbrand, M.V. Zagarola, 2011, An Advanced Compressor for Turbo-Brayton Cryocoolers, *International Cryocooler Conference, Inc. Bolder, CO*

[2] J. Bock, A. Hobl, S. Krämer, M. Bludau, J. Schramm, C. Jänke, S. Elschner, Nexans' Superconducting Fault Current Limiters for medium voltage applications – status and prospects, *21st International Conference on Electricity Distribution, 2011*

[3] J. Bock, M. Bludau, R. Dommerque, A. Hobl, S. Kraemer, M. O. Rikel, S. Elschner, HTS Fault Current Limiters – First Commercial Devices for Distribution Level Grids in Europe, *Applied Superconductivity Conference, Washington, D.C., 2010*

[4] J. Bock, F. Breuer, H. Walter, S. Elschner, M. Kleimaier, R. Kreutz, M. Noe, CURL 10: development and field-test of a 10 kV/10 MVA resistive current limiter based on bulk MCP-BSCCO 2212, *IEEE Transactions on Applied Superconductivity, 2005*

[5] J. F. Maguire, J. Yuan, F. Schmidt, R. Soika, S. Bratt, C. King, J. McNamara, T. E. Welsh, OPERATIONAL EXPERIENCE OF THE WORLD'S FIRST TRANSMISSION LEVEL VOLTAGE HTS POWER CABLE, *TRANSACTIONS OF THE CRYOGENIC ENGINEERING CONFERENCE—CEC: Advances in Cryogenic Engineering, 2009*

[6] J.F. Maguire, F. Schmidt, S. Bratt, T.E. Welsh, J. Yuan, Installation and Testing Results of Long Island Transmission Level HTS Cable, *IEEE Transactions on Applied Superconductivity, 2009*

051

# Components and Systems for HTS Applications

**Kade A., Kaiser G., Klupsch M., Schneider M., Herzog R., Klier J.**

Hauptbereich Kryotechnik und Tieftemperaturphysik, Institut fuer Luft- und Kaeltetechnik,
Dresden, Germany

## ABSTRACT

Individual cryostats have been developed for sensor (SQUID) and HTS-bulk material cooling, in particular for current-transformer cooling or inductive superconducting fault-current limiters (iSFCL). Apart from mechanical requirements, e.g. with respect to the pressure equipment directive, and vacuum lifetime, our developments are based on computational fluid dynamics (CFD) simulations. Furthermore, special components, e.g. for fluid handling, are presented. An innovative piston pump for cryogenic media, with a double-acting electro-dynamic linear motor of moving-magnet type, was manufactured to work from ambient temperature down to 4 K with a scalable volume flow in a pressure range up to 15 bar. Successful test results confirm the advantageous performance. Additionally, our current developments are supported by CFD simulations of complete cooling systems and by measurements of thermodynamic properties such as thermal conductivity and thermal expansion.

## 1. INTRODUCTION

In the framework of the global energy turnaround for sustainability and related changes in distribution of electricity, high-temperature-superconductor (HTS) applications are one of the most promising future components. In recent years individual components like fault current limiters and power transmission cables with corresponding peripheral components have been developed.

With reference to these components, specific HTS materials and related applications need reliable, powerful and affordable cooling systems like cryocoolers, cryostats, or pumps for liquid cryogens. Several developments require non-metallic materials or parts for minimization of eddy currents (electromagnetic interaction) in the final construction.

Within a 10 kV/15 MVA inductive superconducting fault-current limiter project, which is currently being developed by Bruker EST, a special non-metallic ring-cryostat with a warm bore hole is required for an arrangement of coils and HTSL tapes [1].

Because fiberglass is a lightweight material with outstanding material properties, the usage of GFRP (glass-fiber reinforced plastic) materials for example in HVDC (high voltage direct current) electric power transmission systems as insulators or the application in low-noise magnetic field cryostats is well proved.

As one part of this paper, calculations of mechanical strength for special fiber reinforced plastic (FRP) pressure-vessel cryostats for energy deposition will be presented. Furthermore, the leakage rate after final pressure-test procedure is given.

For energetically optimized filling processes of such complex systems, the amount of flash gas (decompression) has to be minimized. Therefore a piston pump with an electrodynamic linear motor for liquid cryogens should be a good candidate. Such a device has been developed and tested successfully at the ILK.

## 2. CONCEPT CONSIDERATIONS AND NUMERICAL ANALYSYS

### 2.1. Cryostats – mechanical requirements

Using the electrical properties of HTS material, the iSFCL system should almost instantaneously protect power grids against short circuits. The cooling is to be carried out in a customized $LN_2$ cryostat. The rapid annihilation of the superconducting state caused by large field changes due to fault currents results in a massive energy deposition into the $LN_2$ reservoir. The corresponding amount of evaporated nitrogen enhances the system pressure, which corresponds to an increase of boiling temperature. The dynamics of such systems is governed by the energy per time deposited in the $LN_2$, which is why designing of cryostats has to be done according to pressure vessel rules. In particular, the German pressure vessel association published a regulation conforming to the Pressure Equipment Directive 97/23/EC also called AD 2000 [2].

Apart from the difficult dimensioning of the wall thicknesses of pressure vessels made of filament winding material like GRP, we favored a sealing concept based on modified PTFE (polytetrafluoroethylene) with openings for the screws. In the warm state a helium leakage rate smaller than $1 \times 10^{-12}$ mbar/l s was measured.

In contrast to standard pressure vessels without a warm bore in the middle, cryostats for iSFCL need a lead-through for the central iron core (see $r_i$ in Fig. 1). Unlike common cryostats, the so-called ring-cryostat shows a much better force distribution behavior during pressure enhancement in the $LN_2$ volume. The number of screws in the dimension M10 (according to AD 2000) has to be calculated for specific several bolt circle diameters. For optimal tightness of gasket, a smaller distance of screws has to be taken into account. By this, typically about 25 N/mm² of contact pressure per unit area on a 2 mm thick seal can be reached.

Due to the possibility of reversible opening of the $LN_2$ volume for mounting of HTS material and space-saving architecture, a special fixing module for the inner screws (without flange) was created (see Fig. 1). Characteristic forces on a 0.5 m² cover configuration during quench can reach up to 15.000 kg.

The key of success of FRP cryostat manufacturing are, on the one hand, harmonized handling of semi-finished products, constantly well proved bonding surfaces and choosing of proper adhesives, and, on the other hand, the joining technology.

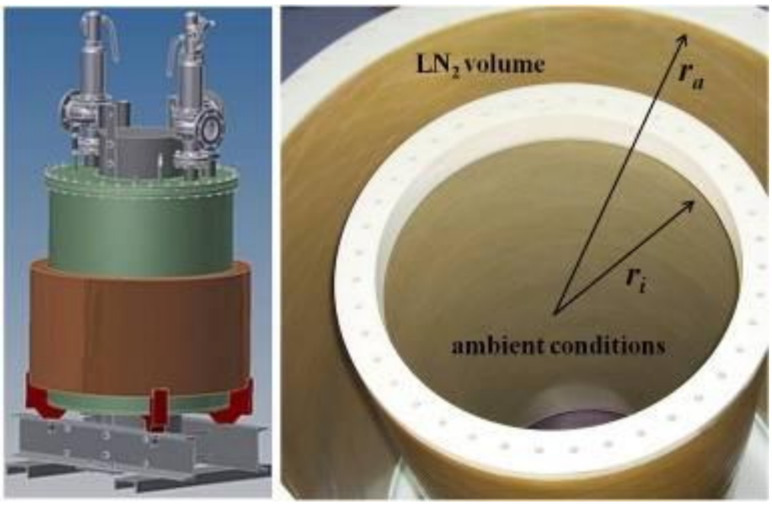

Figure 18. (left) Schematic draw of an iSFCL (By courtesy of Bruker ASC). GRP cryostat warm bore in the middle and modules for pressure-sealable cover plate fixing (right). ($r_a$ and $r_i$ - radius of the outer and inner FRP tubes, respectively)

## 2.2. Cryostats – general considerations

For minimizing the electromagnetic interaction, we support the vacuum room of these cryostats with non-conductive multilayer insulation (MLI) from RUAG Space GmbH. This special MLI from a separate research project with squared 1 cm demetallization and an emissivity factor of 0.02 is connected to the $LN_2$ vessel through a plurality of special FRP bolts (see Fig. 2).

Figure 19. Non-conductive MLI mounted via bolts to the $LN_2$ vessel

The measured noise spectral densities (SQUID - Superconducting QUantum Interference Device measurements) of 20 Layers with 10 × 10 cm² in size are shown in Table 6. [3].

Table 6. Noise spectral densities of non conductive MLI (20 Layers, 10 × 10 cm²) [2]

| Frequency [Hz] | Noise spectral density [fT/√Hz] |
|---|---|
| 10 | 4.20 |
| 40 | 2.60 |
| 100 | 2.00 |
| 500 | 1.70 |
| 1000 | 1.64 |
| 10000 | 1.57 |

The considered MLI shows an extremely low noise and therefore a non-conductive behavior.

Apart from the careful choice of MLI sensitive GRP cryostats need mechanical supports for the $LN_2$ vessel, which are mounted in the vacuum part of the cryostat. Figure 20 shows the static temperature distribution calculated with computational fluid-dynamic calculations (CFD) for a special support structure made of Hgw 2372 FRP laminate.

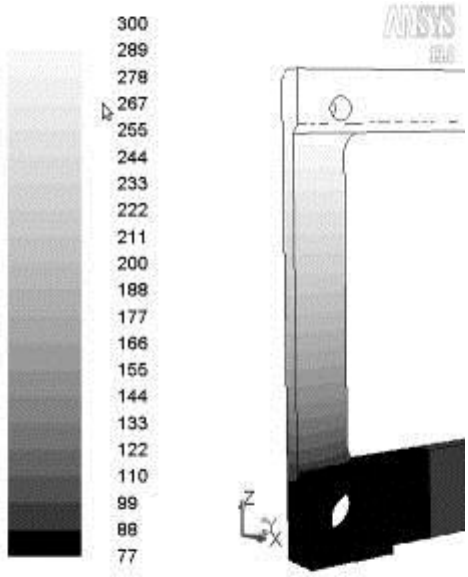

Figure 20. Contours of static temperature [K] of a GRP support used in cryostats

This last consideration is necessary with respect to the resulting dew-point at the outer surface of a cryostat wall because the condensation of air within electric power systems has to be avoided under all circumstances.

## 2.3. Cryogenic liquid pump – overall concept

The general concept of the cryogenic liquid pump is based on a combination of two piston pumps connected by an electro-dynamic linear motor. This conceptual design is shown in Figure 4. A detailed description was given in [4]. The pump principle and its technical solution is patented technology [5]. The “cold pump” is designed to provide a volume flow of 360 l/h against a pressure head of 1.5 MPa.

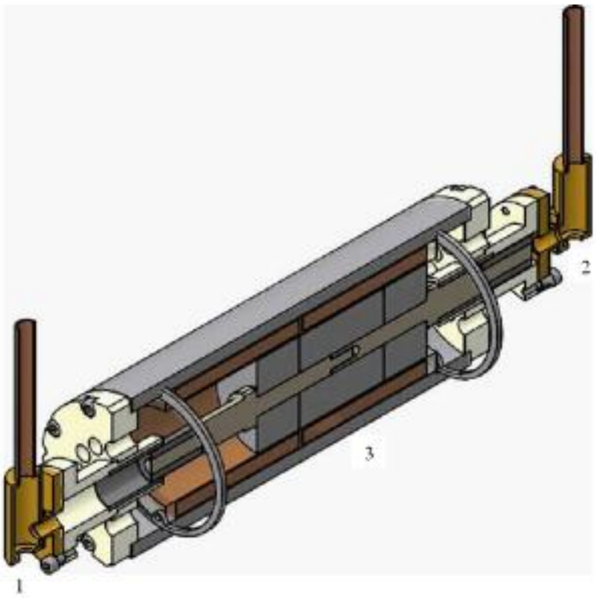

Figure 4. Conceptual design (cross-sectional view) of the cryogenic liquid pump
(1) and (2) – valve units, both including inlet and outlet; (3) – motor and pistons

### 2.4. Cryogenic liquid pump – design details

A cryogenic electrodynamic linear motor based on the moving-magnet principle forms the driving subsystem of the pump. Its composition is shown in Figure 5.

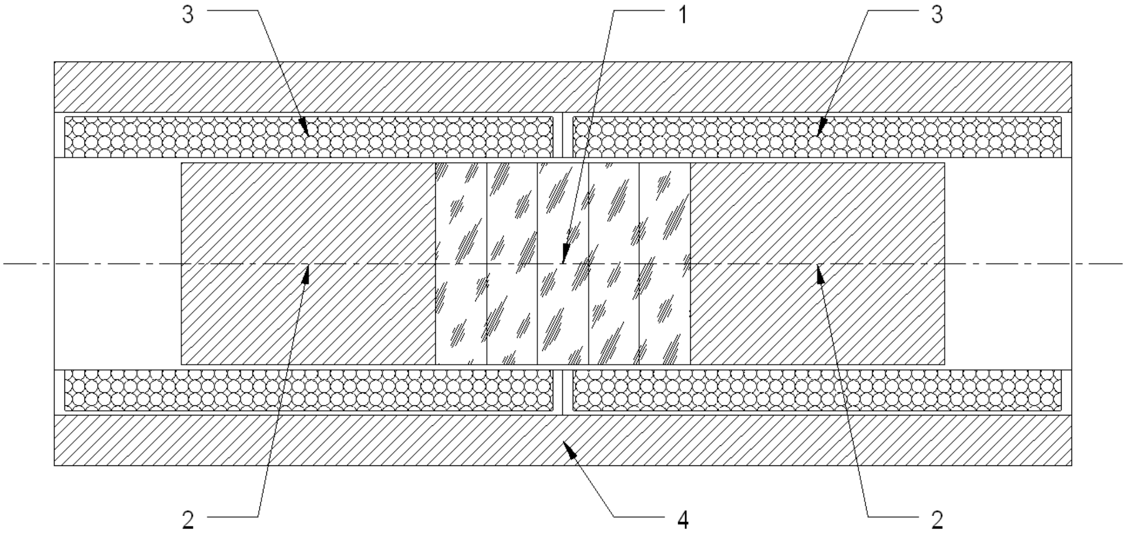

Figure 5. Design of the cryogenic electrodynamic linear motor
(1) NdFeB permanent magnet; (2) pole cylinders; (3) driving coils; (4) hollow cylindrical magnetic yoke

The stator comprises the hollow cylindrical magnetic yoke, also forming the motor housing, which contains a pair of driving coils. The armature consists of the central cylindrical axially-magnetized NdFeB permanent magnet and the pole cylinders at both sides. NdFeB has been favoured despite its spin-reorientation transition at 135 K, since SmCo and AlNiCo materials had been tested as less suited for this application due to their brittleness and their unfavourable magnetization direction in the commercially available form.
The motor is designed to have no reluctance force which could determine a spring constant. This design leads to the capability of operating the motor at variable speed and frequency.

The pump consists of a cylinder housing made of polycarbonate carrying the Invar (nickel-iron alloy FeNi36) bushing of the cylinder. The pump piston consists of an Invar carrier with a Vespel SP-22 (registered trademark of Du Pont ) liner.

The valve consists of a brass housing containing the valve seats and valve balls. The valve balls were made of Vespel SP-1 (registered trademark of Du Pont ) in order to reduce weight and to avoid freezing at the valve seats. The functional sketch and the completed valve are shown in Figure 6. The valve principle and its technical solution is patented technology [6].

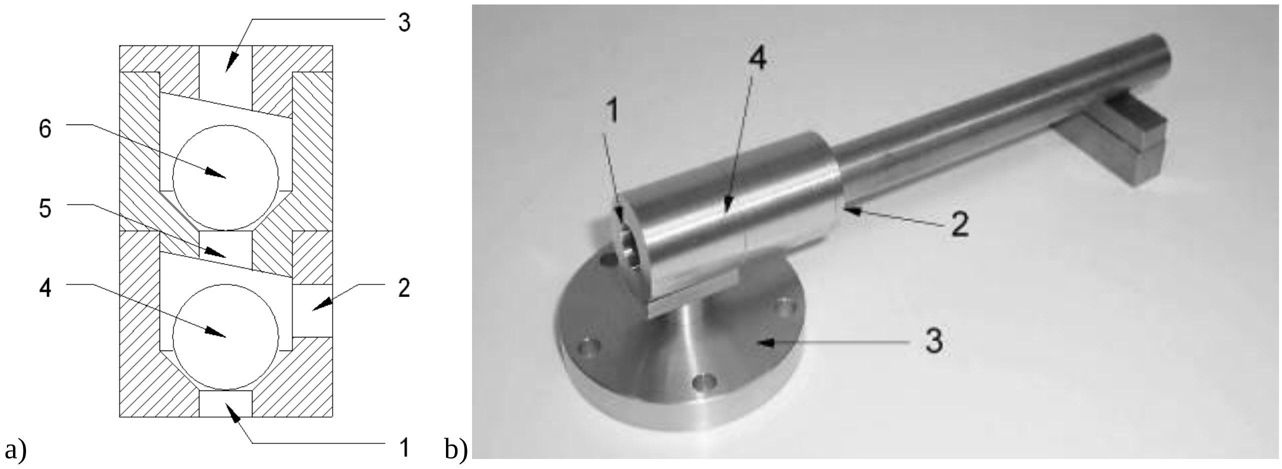

Figure 6. a) functional sketch: (1) inlet; (2) pumping cylinder overflow; (3) outlet; (4) inlet valve ball; (5) inner valve overflow; (6) outlet valve ball;
b) completed valve: (1) inlet side; (2) outlet side; (3) flange joint to polycarbonate cylinder housing; (4) brass housing containing the valve seats and valve balls

## 3. RESULTS AND DISCUSSION

### 3.1. Cryostats - tests and results

During the pressure test of the cryostat with 200 liters $LN_2$ within, the force on the top cover was approximately 15 tons (3 bar) for 40 minutes.

After this extensive pressure test a helium leakage rate of $9 \times 10^{-10}$ mbar l/s for the complete FRP cryostat was found.

The virtual leak rate as a result of measurements of pressure rise can be given as $4.1 \times 10^{-10}$ mbar l/s cm².

The ability of such cryostats under long term usage in power applications for example in iSFCL systems has to be proofed by further investigation (in progress).

### 3.2. Cryogenic liquid pump – tests and results

Most performance tests of the pump have been arranged using liquid nitrogen due to its uncomplicated handling and relatively large latent heat enabling precise measurements (see Figure 7). During cooling down, neither does the large temperature difference harm the hardware of the pump nor its operating behaviour. Furthermore, tests with the pump immersed in liquid argon have been performed successfully. In the case of argon the Bernoulli effect might lead to evaporation and, possibly, cool down the liquid below its triple point, hence blocking the piston or the valves. Such phenomena, however, have not been observed.

For an autonomous control of the pump depending on the input voltage an electronic circuit has been tested, which automatically reverses the polarity of the coil. By approaching the mechanical stop, the piston causes an increase in the current that is evaluated by a comparator. The output signal switches the relays, which reverse the polarity of the coil and make the piston move into the other direction.

It should be emphasized that, for given working conditions (kind of liquid and back-pressure), the optimum working parameters of voltage and frequency can be chosen. Hence, in a final application no control will be required anymore. Results for controlled voltage operation (at constant frequency) are shown in Figure 8. The tests have been performed under atmospheric back-pressure. For higher back-pressures, the acceleration force on the valve bodies will increase, thus resulting in higher volume flows. Already in the unfavourable case of atmospheric back-pressure, a volume flow of more than 100 l/h for liquid nitrogen has been obtained. Higher back-pressures will lead to increased forces acting on the inertia of the valve balls, which will increase the maximum operating frequency of pump.

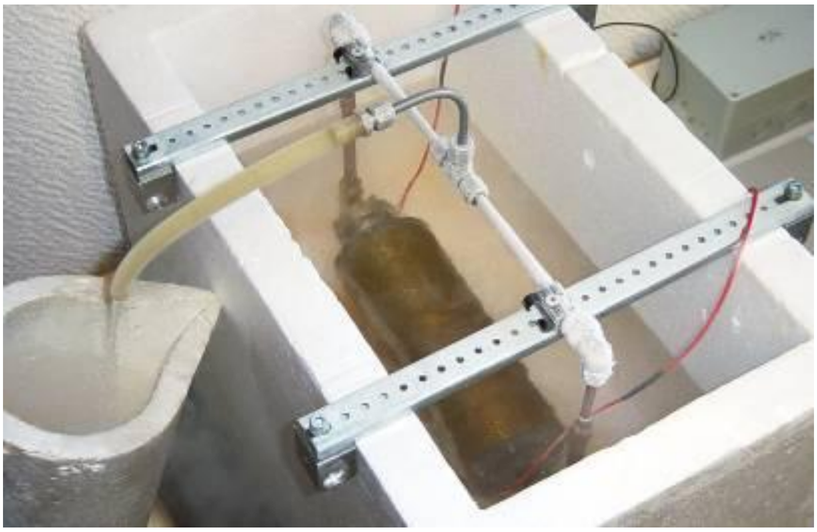

Figure 7. Pump delivering liquid nitrogen

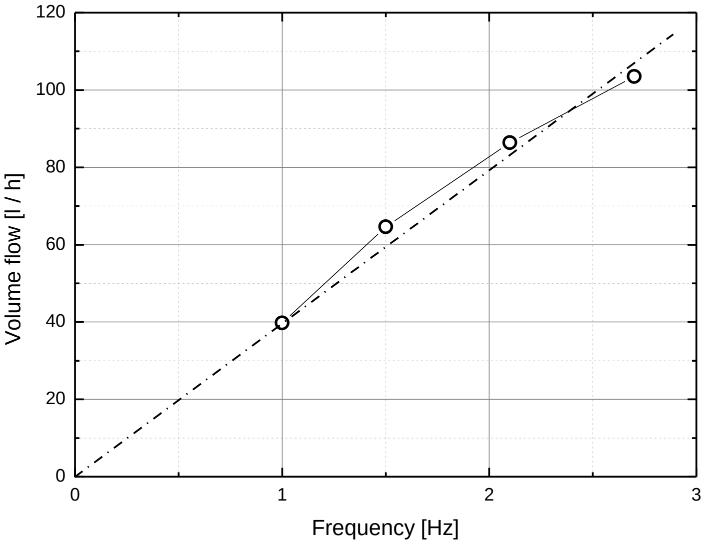

Figure 8. Volume flow as a function of frequency obtained at varying values of driving voltage. The voltage is alternated by control using the current signal, measurements are performed under atmospheric back-pressure. The dash-dotted line is just a guidance to the eye.

## 4. ACKNOWLEDGEMENT

This work has been supported by the German Federal Ministry of Economics and Technology (contracts nos. EURONORM MF 100087, EURONORM IW 080056).

## 5. REFERENCES

[1] http://www.bruker-est.com/isfcl.html (2012-06-14)

[2] AD 2000 rules, https://www.vdtuev.de/publikationen/ad2000/

[3] RUAG Space GmbH, PTB Berlin

[4] Kaiser G., et al. 2011, “Cold Pump” for Cryogenic Liquids, 23rd IIR, Prague

[5] ILK Dresden patent: DE 102008011456 A1

[6] ILK Dresden patent: DE 10039214 A1

# SUPERCONDUCTIVITY
# & VERY LOW TEMPERATURES

015

# Superconducting Current Feeders System for SST-1

**Gupta N.C., Garg A., Sonara D., Panchal R., Shah P., Nimavat H.,**
**Sharma A.N., Prasad U.,Tanna V.L., Pradhan S.**

Institute for Plasma Research, Gandhinagar, 382 428, India

## ABSTRACT

The superconducting (SC) current feeders system (CFS) for Steady State superconducting Tokamak (SST-1) consists of (+/-) ten pairs of 10,000 Ampere (A) leads, Cu-SC joints, cryo compatible SC feeders ducts operating at high voltage with extensive cryo as well as room temperature hydraulic network. Appropriate design drivers have been considered to provide the safe design of the CFS. A horizontal cryostat in cylindrical configuration with active liquid nitrogen ($LN_2$) cooled 80 K shield provides ease of installation and maintenance of all the critical components. The required thermo-structural and thermo-hydraulic analyses for cryostat and SC feeders have been carried out. The planned fluid flow scheme of the CFS provides the better temperature margin available for SCMS operation. The required instrumentation and control system is being upgraded and validated through tests. The paper describes the design, analysis, flow scheme with instrumentation and control and engineering commissioning experience of the current feeders system.

## 1. INTRODUCTION

The CFS is essentially an optimized bridge between the power supply at room temperature and superconducting magnet system (SCMS) of the SST-1 machine at 4.5 K. The system consists of (+/-) ten pairs of 10,000 Ampere (A) rating helium vapour cooled conventional current leads (VCCL), forty numbers of Cu-SC joints, three numbers of cryo compatible SC feeders ducts, current leads assembly chamber along with the hydraulic network and three numbers of joint boxes operated at different current rating are required to charge Toroidal Field (TF) and Poloidal Field (PF) magnets separately. Nine pairs of VCCL are required to energize the PF magnets at different operating currents in the range of 1 kA - 9 kA with various current ramp up/down as defined in the SST-1 plasma reference scenario [1] and plasma shaping requirements. One pair of VCCL is required to charge TF coils at 10,000 A. It is essential to have safe, stable and reliable design of the CFS because the whole stored magnetic energy of the SCMS during the quench is being dumped though the CFS path [2]. The hydraulic network of the CFS consists of liquid helium (at 1.2 bar / 4.4 K), pressurized helium (at 4 bar / 4.5 K), $LN_2$ (2 bar / 80 K) and room temperature helium gas hydraulic networks. The architecture of the CFS also includes extensive instrumentation, diagnostics, data acquisition and control system.

## 2. DESCRIPTION OF THE CURRENT FEEDER SYSTEM

### 2.1. Current Leads

Looking at the numbers of current leads requirement, operating current range and SST-1 operation duty cycle, the conventional helium vapor cooled current leads (VCCLs) concept has been adopted. Basically, the concept uses an optimally designed metallic heat exchanger from the room temperature down to 4.5 K. The heat exchanger design is simple with rod in thin tubes. Indigenously, we designed the current leads rated for 10,000A and the first (+/-) pair was in-house manufactured in 2006 [3] and then upgraded in 2009 [4] with stringent follow-ups of QA/QC at each stages of manufacturing. The developed VCCL had been tested at operating conditions in a specially designed cryostat. The purpose was after successful performance test demonstration; the series production of next nine pairs should be done with follow-ups of similar QA/QC procedures. The test results of the first pair of such current leads have been reported in [4]. Afterwards, all other current leads were developed by maintaining stringent QA/QC. Figure 1(a) shows the VCCL developed at IPR. A typical 3 kA/s ramp rate results of the VCCL is shown in Figure 1 (b).

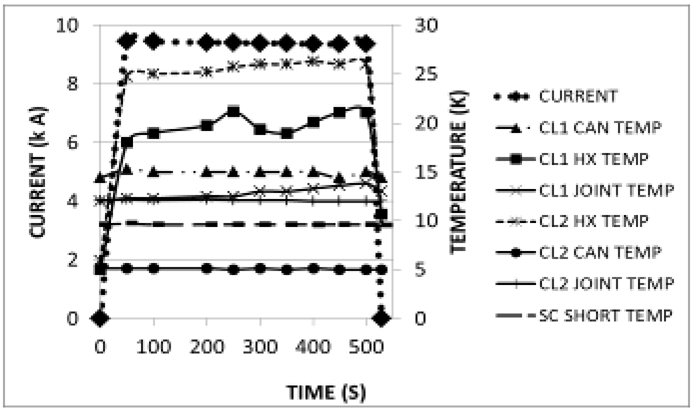

Figure 1(a) Series production of VCCLs Figure 1(b) Typical test result with 3kA/s ramp rate

## 2.2. Current Leads Assembly Chamber (CLAC)

As stated earlier, all the SC magnets will also be charged in their representative start-up scenarios. This necessitates a dedicated CLAC equipped with suitable in-out cryogenic network, liquid helium baths for the current leads and isolators for maintaining electrical isolations between the source helium lines connected to the plant and gas return lines. The CLAC in horizontal configuration with one open able dish end has been installed at 10 m away from the SST-1 machine. The CLAC has vacuum of $10^{-6}$ mbar, 80 K thermal shield cooled by liquid nitrogen ($LN_2$). A FE analysis for this chamber was carried out under different load case scenarios. Figure 3 and 4 show the typical load case and Von-Mises stress distribution of the chamber respectively. A Figure 5 shows the CLAC during the manufacturing. Figure 6 shows the cool down and temperature profile of the 80 K shields of chamber.

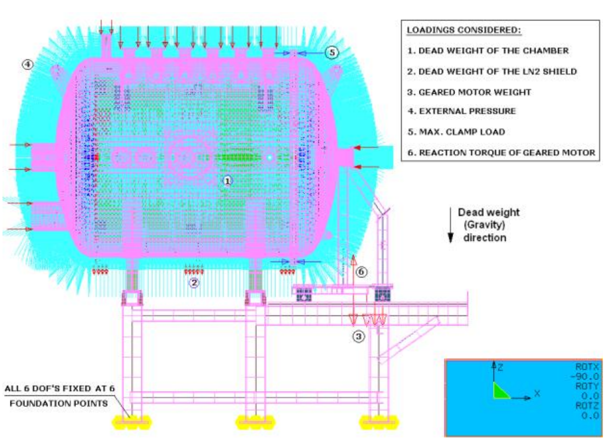

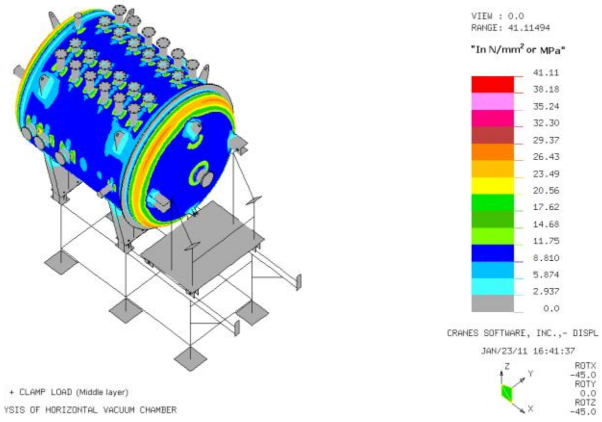

Figure 3 Typical Load Case of CLAC Figure 4 Von Mises stress distribution (Max. 41 MPa)

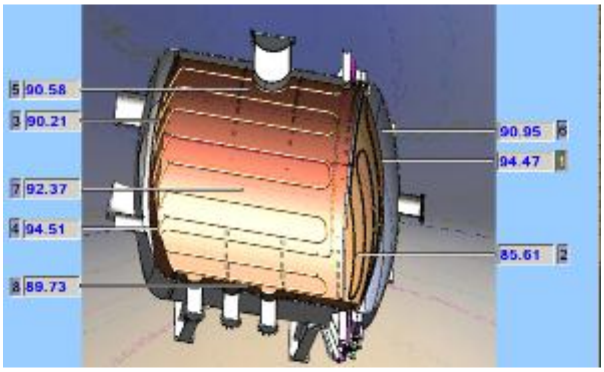

Figure 5 CLAC photo during manufacturing Figure 6 Temperature distribution of $LN_2$ shield in CLAC

### 2.3. Superconducting Feeders for TF and PF magnets

The NbTi/Cu based cable-in-conduit-conductor (CICC) is used as SC feeders. They are connected at the bottom of the current leads with sub-divided joints configurations and terminated inside the joint boxes. In order to avoid the transient electro-magnetic effects of the PF feeders on the TF feeders, three different ducts have been planned. One duct is dedicated for the TF feeders whereas other two are for the PF feeders. The bus ducts design and layout have been chosen as per the leads configuration of the TF and PF coils inside the SCMS. The SC feeders are supported with low thermal conductivity spacers made of G-10 CR to minimize heat load and electromagnetic forces. The required electrical isolation (~ 60 GOhm at 2kV) in bus bar is achieved by wrapping Kapton and E-glass fibre tapes with epoxy resin. The outer vacuum duct and 80 K shield have been designed and fabricated in segments to suit the assembly requirement and flexibility in maintenance. Figures 7 and 8 show the model of hydraulic network within the CLAC and actual assembly respectively,

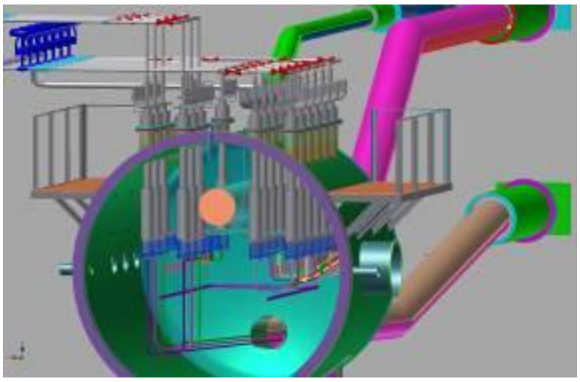

Figure 7 Model including hydraulic network

Figure 8 Insight of actual assembly in CLAC

### 2.4. Copper -Superconducting Joints

Figure 9 Vacuum barrier installed at the TF duct

Total forty numbers of Cu-SC joints are required to interface VCCL and SC feeders with SST-1. In CLAC, sub divided joint had been adopted, whereas twenty shake hand type Cu-SC joints are installed in all the three joint boxes. Special design of ceramic based vacuum barrier offers vacuum and electrical isolation of 60 G-ohm to the SST-1 cryostat and the CLAC. Figure 9 shows the typical vacuum barrier installed at TF feeders ducts.

## 3. DIFFERENT HYDRAULICS NETWORKS AND FLOW DISTRIBUTION

Three different cryogens are used to maintain the CFS at operating conditions. All the SC feeders are cooled with pressurised helium whereas LHe is used to cool all the VCCLs. The 80 K thermal shield is cooled by $LN_2$. Vapor return line for each pair of VCCL and LHe header has one flow control valve and one Venturi meter. An optimised flow distribution network for pressurised helium has been installed for the CFS. Coolant exit from all the PF magnets at SST-1 is fed to their respective feeders thus makes the flow direction from SCMS to VCCL. The flow direction for TF feeders is from the bottom of current lead inside the CLAC towards the SCMS. Pressurised helium exit from individual VCCL is collected in common header via electrical isolators which provides electrical break in between VCCL and collecting header. Similarly, LHe from a common header is fed to individual VCCL via electrical isolators. Detailed flexibility analyses for the loops and inter-connecting feed lines have been carried out using ANSYS [5].

## 4. INSTRUMENTATIONS AND DIAGNOSTICS

To control and monitor the different parameters of the CFS a PLC and SCADA based system is implemented. The CFS is equipped with large number of calibrated instruments at different strategic locations to monitor the behaviour of the current leads and SC feeders. The details of these sensors and diagnostics are as follows as mentioned in Table 1.

Table 1 Sensors and Diagnostics details used in the CLAC

| Sr. No. | Type of measurements | Instrumentation Make | Nos. of sensors |
|---|---|---|---|
| 1 | Temperature at 4.5 K | TVO | 62 |
| 2 | Temperature at 80 K | PT-100 | 04 |
| 3 | Temperature at 300 K | PT-100 | 20 |
| 4 | Pressure at 4.5 K | Piezo-resistive type | 02 |
| 5 | Liquid Level at 4.2 K | SC filament type | 21 |
| 6 | Flow meter (at room temperature) | Venturi Type | 11 |
| 7 | Flow meter (at 4K) | Venturi Type | 2 |
| 8 | Voltage Taps | Isolated Transmitter type | 60 |

All temperature sensors were connected with indigenously developed cryogenic grade temperature transmitter modules [6]. This module provides input isolation of 2.5 kV and output isolation of 1.5 kV. The output of transmitter is linear 4-20 mA for temperature range of 4 K to 325 K, which is fed to analog input of the PLC. Thermal anchoring of sensor wire was provided on $LN_2$ tube to minimize the error due to heat conduction through lead wire to sensor element.

## 5. QUALITY ASSURANCE AND QUALITY CONTROL

A stringent and well established quality assurance plan was established during the development of the CFS as per ASME section V. As a part of QAP, starting from raw material inspection (chemical, mechanical test etc.), stage wise helium leak test, thermal shocks test, high voltage breakdown test, flow test and the testing of the final assembly at different stages were carried out during the installation of CFS. A special attention was given on the safety aspects.

## 6. CONCLUSION

The SST-1 CFS, along with the in-house developed (+/-) ten pairs of 10 kA rated conventional current leads have been designed, manufactured, tested and finally installed with extensive hydraulic network and diagnostics. The performance test results on the VCCLs are found to be satisfactory. The expeirmental results of different components, tested separately were found to be consistent with the design and analyses. The pre-commissioning test results of the of the integrated CFS have shown the safe, stable and relaible design as a whole.

## 7. REFERENCES

1. S. Pradhan et al, SST-1 Status and Plans, *IEEE Transactions on Plasma Science, March 2012, Volume 40, number 3, P 614.*
2. V.L. Tanna et al, Superconducting current feeder system with associated test results for SST-1 Tokamak, *IEEE Transactions on Applied Superconductivity, June 2004, Issue 2, pp. 1711-1714.*
3. B. Sarkar et al, Design, fabrication and performance test of 10 kA current leads for SST1, *21st International Cryogenic Engineering Conference (ICEC21), July 2006*

4. N.C. Gupta et al, Characterization and testing of 10 kA vapor cooled conventional current leads under long pulse operation , *IIR Cryogenic conference at Slovakia Conference Proceedings pp. 64-71, April 26-29, 2010*

5. ANSYS® Academic Research, Release 10.0

6. P. Panchal et al, Advances in Cryogenic Engineering, Vol 53, July 2007, pp. 981-988.

042

# Study of Refrigeration Characteristics of Slush Nitrogen in Flow System

**Nakamura N., Komagome T., Lee Y., Boone J.**

MAYEKAWA MFG. CO., LTD, 2000 Tatsuzawa, Moriya City, Ibaraki Pref, 302-0118, Japan

## ABSTRACT

Slush Nitrogen (SN2), mixture of liquid nitrogen (LN2) and solid nitrogen particles with the characteristic temperature of 63.1 K allows more heat load and larger temperature rise in HTS cable system than LN2. We have confirmed the advantages of SN2 by calculation, showing that SN2 effectively suppress temperature rise in HTS cable. To examine these favourable properties of SN2 at laboratory level we have developed an SN2 generator and set up a small scale SN2 cooling system, with which we succeeded in flowing the refrigerant at about 63 K. We are going to measure the density of SN2 (the amount of flowing solid nitrogen) and quantitatively study the refrigeration characteristics of SN2. In this paper, we discuss our SN2 cooling system and the calculational and experimental results for refrigeration characteristics.

## 1. INTRODUCTION

For HTS cables, sub-cooled liquid nitrogen (LN2) below 77 K is usually used in consideration of critical current and dielectric performances of the HTS cables. Many different types of LN2 refrigeration systems for HTS cables have been studied, in most of which LN2 is circulated through cable using pumps and constantly sub-cooled by refrigerators to be kept from vaporization (1). In these cases, however, the flow rate, pressure and temperature of nitrogen need to be controlled to meet the requirements of HTS cables such as cooling power, while maintaining the sub-cooled state of LN2 between melting and saturating curves. Although lowering the temperature of refrigerant has some merits for HTS cables such as the improvement in the current transmission and the extension of the distance between cooling stations, there is a limit to lowering the temperature of LN2 due to its solidification which should be avoided for continuous circulation. Slush nitrogen (SN2), mixture of LN2 and particles of solid nitrogen, remains at 63.1 K that is the solidifying temperature of nitrogen until solid nitrogen is consumed by latent heat of fusion. Thus by using SN2 as refrigerant, the inlet of the HTS cable system can be cooled at lower temperature than by using conventional sub-cooed liquid nitrogen, which makes it possible to lengthen the HTS cable by allowing more temperature increase in the system.

To handle the difficulty with LN2, a refrigeration system for the HTS cable making use of SN2 has been studied as a Japanese national project since 2000. In that project, the refrigeration characteristics of SN2 for HTS cables travelling a long distance was studied, and the flow characteristics and heat transfer characteristics of SN2 were also reported {(2,3)}. In those works, however, the measurements were taken only for a few minutes. In this study, the refrigeration characteristics of flowing SN2 and LN2 are measured for over ten minutes using a circulation system as well as a linear one-way flow system. In sections 2 and 3, the results obtained using both flow systems are discussed, comparing the refrigeration characteristics of flowing SN2 and LN2, and our circulation system is described in detail in section 4. We then summarize our work in section5.

## 2. RELATION BETWEEN THE TRAVELLING DISTANCE AND TEMPERATURE OF REFRIGERANTS

We calculated the relation between the travelling distance and the temperature and pressure of refrigerants (Figure 1). In these calculations the flow rate was set to 40 L/min (1), and the total loss per cable length and the ice packing factor were assumed 2.85 W/m and 20 % respectively. As the inlet temperature of LN2 66 K, the lowest possible temperature for the actual facility (1) was used, while 63.1 K was used for SN2. The density and specific heat of SN2 were calculated from the ice packing factor, and the viscosity of SN2 was evaluated by the Mori-Ototake equation. Throughout the calculations, the temperature of SN2 was assumed to remain constant as long as solid particles existed in the fluid. The values of the constants used in the calculations are summarized in Table 1.

It is found that the SN2 cooling system has improved the performance of the HTS cable, as the temperature of SN2 remains about 4.9 K lower than that of LN2 until 5 km from the cooling station. It is also observed that the distance at which the temperature reaches 75 K is longer for SN2, which indicates that the distance between cooling stations can be extended by using SN2. The pressure at the cable inlet, or the pressure at the pump outlet is shown to be larger for SN2 than for LN2, and so is the pressure drop due to the viscosity of SN2. It should however be noted that the pressure drop can be reduced by increasing cable diameter and/or decreasing flow rate.

To simulate an SN2 station, we have set up a small scale SN2 cooling system and investigated the effect of the latent heat of fusion on cooling as well as the movement of SN2 in cable.

Table 1. Values of parameters used in the calculations

| | |
|---|---|
| AC loss | 0.3 W |
| dielectric loss | 0.5 W |
| Flow rate | 40 L/min |
| Fluid volume per meter | 2.18 L/m |
| Heat loss | 2 W |
| Hydraulic diameter | 10 m |
| Pressure at the cable outlet | 0.3 MPa |
| Pressure drop | 100 Pa/m |
| Specific heat of SN2 | 2018 J/kg・K |

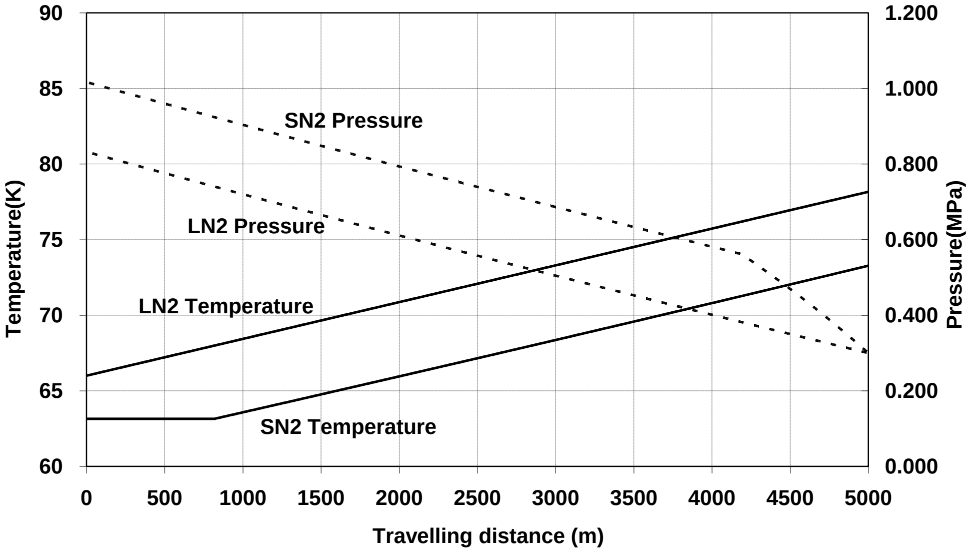

Figure 1. Temperature/pressure of refrigerant versus travelling distance (calculations)

## 3. ONE-WAY FLOW SYSTEM

To study the effect of latent heat of melting SN2 we made an SN2 flow system consisting of an LN2 tank, an SN2 generator and a 4 meter long transfer tube and a pump (Figure 2). Since it is important to constantly provide solid nitrogen particles to SN2 cooling system, we have designed a generator to continuously produce solid nitrogen particles using Auger method. In our experiment the generation rate of solid nitrogen particles was set to 5 g/s with the average particle diameter 119 µm (4) The inner diameter of the transfer tube is 14 mm, and four heaters are set on the tube at one meter intervals as shown in Figure 2. To measure the temperatures of refrigerants five thermometers are set in the middle of the transfer tube at one meter intervals (Figures 2 and 3). To prevent the thermometers from contacting the tube wall support rings are fitted in the tube as shown in Figure 3.

In this one-way flow system LN2 flows from the LN2 tank to the generator, in which LN2 mixes with solid nitrogen particles and then flows into the transfer tube. The solid nitrogen particles then flow into the transfer tube specially designed to measure the fluid temperature to study the effect of latent heat of melting SN2.
In the case of SN2 cooling, the pressure in the LN2 tank decreases, as the temperature of LN2 is kept below 64 K. We therefore increased the pressure in the tank to 11 kPaG by injecting helium gas into it and forced LN2 and thus SN2 to flow into the transfer tube. We then measured the flow rate immediately after the fluid flowed out of the transfer tube.

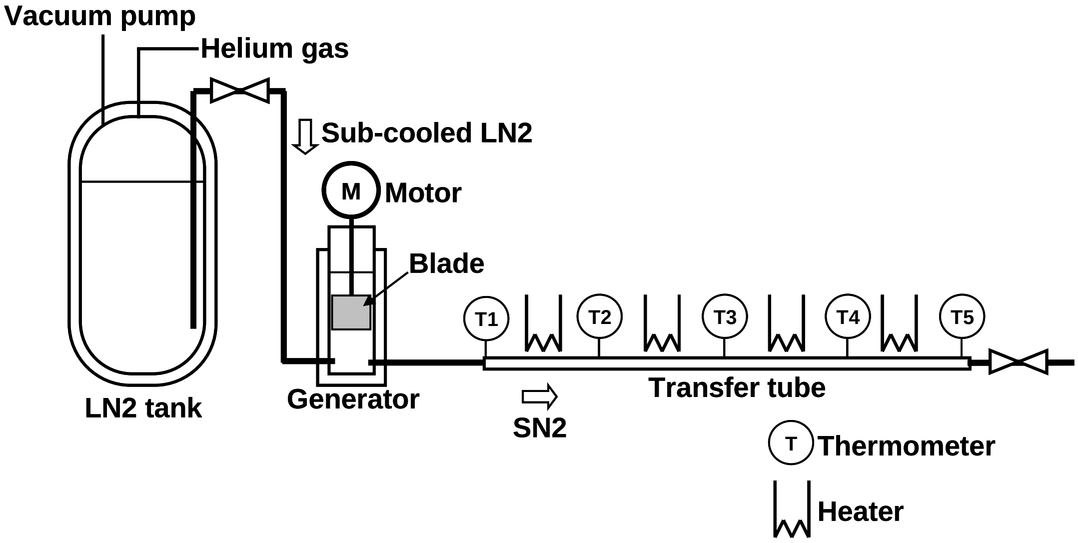

Figure 2. A diagram of one-way flow system

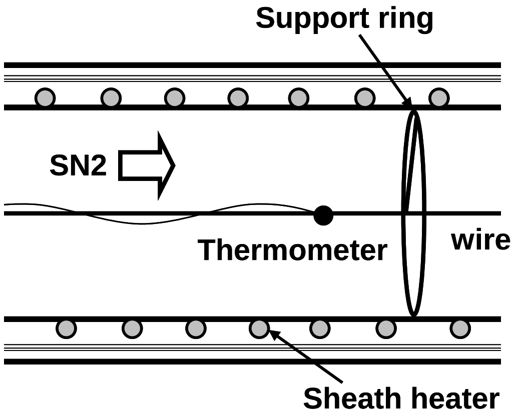

Figure 3. A schematic of the transfer tube

Figure 4 shows the temperatures measured at several places of transfer tube. In these measurements, the flow rate and ice packing factor were 4 L/min and 2.8 % respectively, and the total heater power was varied from 0 to 110 W. We first flowed the fluid through the system more than 30 minutes and then started measurement after the fluid temperature was stabilized.
In this work, we did not measure the relative amount of solid nitrogen. Instead, we inferred the presence of SN2 from the temperature distribution along the transfer tube. As shown in Figure 4, the temperature of refrigerant for a heat load of 50 W remains near 63 K up to 1m from the inlet of transfer tube, from which we conclude that SN2 has flowed 1m along the tube.

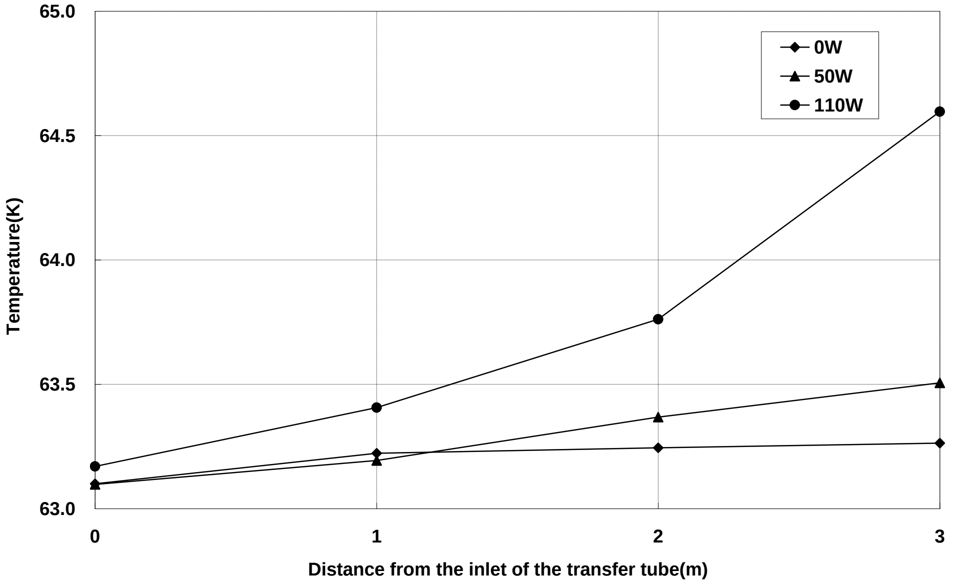

Figure 4. Temperature of SN2 versus travelling distance (one-way flow system))

## 4. CIRCULATION SYSTEM FOR SLUSH NITROGEN

The structure of the circulation system is shown in Figures 5 and 6. This equipment includes a pre-cooling cryostat (PCC) with an LN2 pump and a GM-refrigerator, a transfer tube and a mass flow meter as well as the SN2 generator used in the one-way flow system. The specifications of the circulation system are summarized in Table 2. In this circulation system, LN2 is sent by the pump to the heat exchanger of refrigerator the temperature of which is kept between 63.1 and 64 K. Subsequently LN2 goes into the generator where it mixes with solid nitrogen particles and then flows into the transfer tube. Unlike the one-way flow system, the inlet for the generator is located near the top of the generator in an attempt to improve the mixing of LN2 with solid nitrogen particles (Figure 5).

Before measuring the fluid temperature, we ran the circulation system for 6 hours, continuously generating and circulating SN2 until the fluid temperature became stable. Figure 7 shows the temperatures of SN2 measured at one meter intervals along the transfer tube. In this measurement the flow rate is 4.0 L/min, and the total heater power is 0 W. As shown in Figure 7, we succeeded in flowing the refrigerant through the circulation system at about 63 K, although SN2 (solid particles) did not flow well from the generator to the transfer tube. We guess that the poor transfer of SN2 may be related to the way LN2 enters the SN2 generator. As stated above, we let LN2 enter the generator from above to facilitate the mixing of LN2 and solid nitrogen particles. It however seems as though LN2 was slightly warmed up in the upper part of the generator which is a little away from the cold head, resulting in the reduction of SN2.

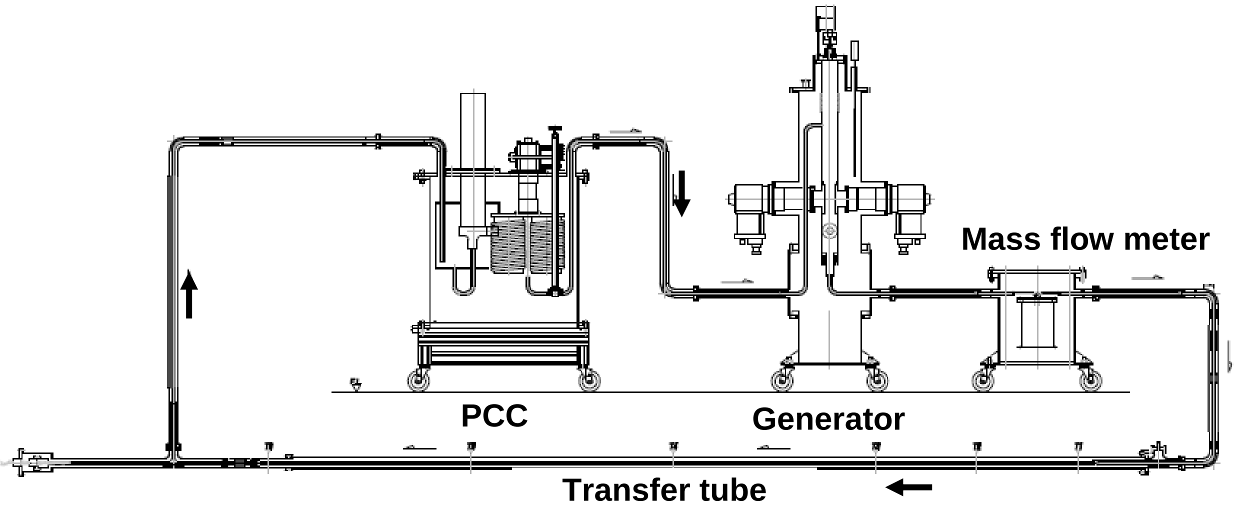

Figure 5. A schematic of the circulation system

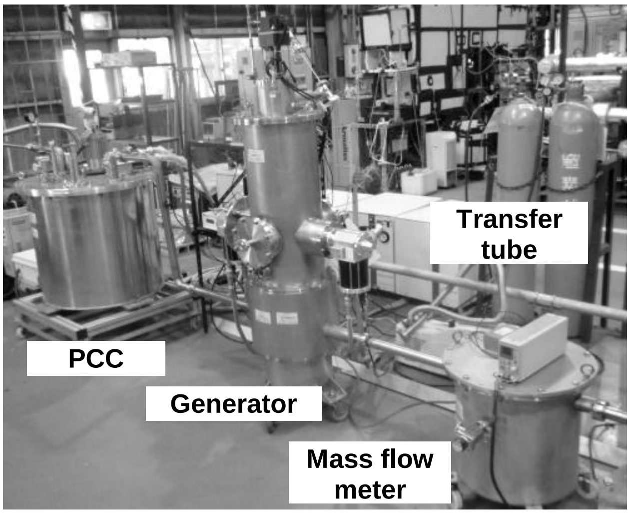

Figure 6. Photograph of the circulation system

Table 2. Specifications of the circulation system

| | |
|---|---|
| Refrigerators | GM-Type<br>92 W@63K (2 units) Generator<br>120 W@63K PCC |
| Pump | Flow rate 7-12 L/min<br>Pump head 0.07 MPa |
| Generator | Rotational speed 17 rpm<br>Motor power below 50 W |
| Transfer tube | Length 4 m<br>Inside diameter 14.9 mm |

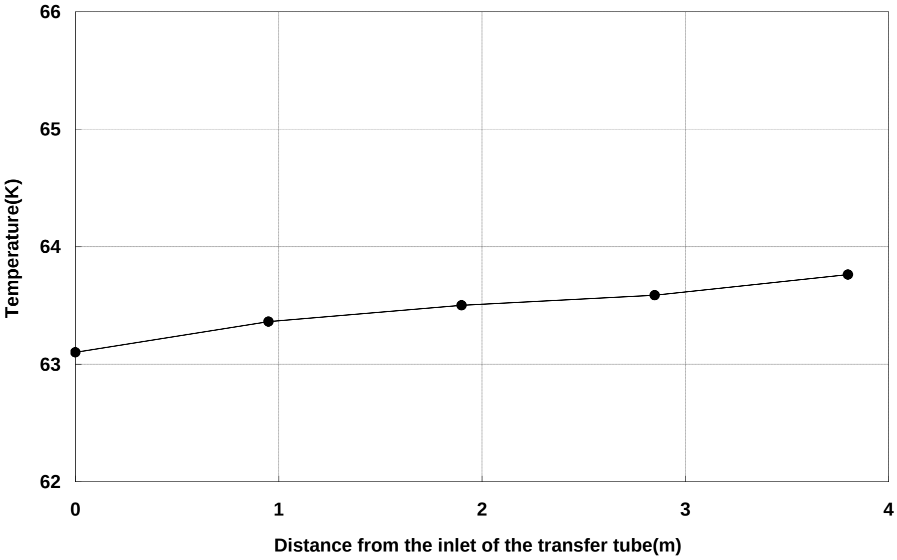

Figure 7. Temperature of SN2 versus travelling distance (circulation system)

## 5. SUMMARY

We have introduced a new refrigerant SN2 and calculated its refrigeration characteristics, evaluating its merit. We have developed an SN2 generator and set up a small scale SN2 cooling system. In our one-way flow tests, SN2 was confirmed to flow 1 m along the tube with a heat load of 50 W. We have also succeeded in flowing SN2 through our circulation system more than 6 hours, keeping the fluid temperature around 63 K. As a next step, we are going to measure the density of SN2 so that we can quantitatively study the refrigeration characteristics of SN2.

## 6. ACKNOWLEDGEMENTS

This work was supported by Ministry of Economy, Trade and Industry, through New Energy and Industrial Technology Development Organization, subsidy to research and development of Technological Development of Yttrium-based Superconducting.

# 7. REFERENCES

1. M.Watanabe et. al, 2010, “Liquid nitrogen cooling system (LINCS) for Yokohama HTS cable project”, Proceedings of the ICEC23 and ICMC2010, pp1049-1055

2. K. Matsuo, et al, "Fundamental study of the pipe flow characteristics of slush nitrogen”, J Cryo Soc Jpn, 39 (2004) 475-482

3. M. Ikeuch, et al, “Fundamental Study of Heat Transfer Characteristics of Flowing Slush Nitrogen”, J Cryo Soc Jpn, 42 (2007) 96-101

4. N.Nakamura et. al, 2010, “Refrigeration characteristics of slush nitrogen for High Temperature Superconducting Cable”, Proceedings of the ICEC23 and ICMC2010, pp1023-1028

053

# Compact Dilution Refrigerator for Sensor Cooling

**Schneider M., Arndt J., Giesel J., Zerweck-Trogisch U., Klier J., Herzog R.**

Institut fuer Luft- und Kaeltetechnik, Hauptbereich Kryotechnik und Tieftemperaturphysik,
Dresden, Germany

## ABSTRACT

A special dilution refrigerator with pulse-tube pre-cooling has been designed, constructed and tested with the purpose of cooling (terahertz) radiation sensors or cryogenic electronics to very low temperatures. The whole setup features tilt independence, angles of up to 45° from its upright position are possible without significant loss of cooling power due to specially designed key components as for example the mixing chamber. Two independent but thermally coupled $^3$He circulations permit a high level of temperature stability. The experimental optimisation includes for example an improved design of the radiation shields. Furthermore, different types of heat switches have been investigated in order to find the best refrigerator performance.
This work has been supported by the German Federal Ministry of Economics and Technology (contract numbers ZIM KF2067102AB8, ZIM KF2067112PR9, and EN MF 110057).

## 1. INTRODUCTION

During past years, cryogenic-free pre-cooling for applications at very low temperatures has become more and more available. Besides sorption cooling and, for single-shot applications, adiabatic demagnetisation, $^3$He-$^4$He dilution refrigerators are the most employed cooling technologies for the temperature range below 1 K. For a stable and low-noise operation of radiation sensors however, additional features are required often.

For example, a tiltable dilution refrigerator is very advantageous for many astronomic applications. The installation of such a device is intended at the University of Trento [1]. In principle, dilution refrigerators may operate even gravity-free but such developments are open-cycled or they feature significant complexity [2]. The current development is characterised by a tilt independence of the complete system with angles of up to 45° from its upright position, no need of external pumps, and a continuous and stable operation.

Some details of this dilution refrigerator will be presented in this paper. Additionally, systematic investigations of gas-gap and superconducting heat switches have been performed in order to gain reliable performance characteristics over a wide range of temperature.

## 2. DETAILS OF DESIGN

The two-stage pulse-tube pre-cooler for the dilution refrigerator has been developed by TransMIT Giessen, especially adapted to the demands described in this paper including high tilt independence. Its base temperature is about 2 K.

For operating the complete system, an electronic control has been developed by Supracon and IPHT Jena. Thus, a very user-friendly design could be realised.

The design of the dilution refrigerator is based on a development at IAP Berlin, which is marked by two independent but thermally coupled $^3$He cycles. This provides the possibility to regenerate the sorption pump of one of the cycles without significant heat flux into the $^3$He-$^4$He cycle. Additionally, a $^4$He cycle has been included due to required thermal stability. All components have been dimensioned based on thermal and fluidic calculations. Figure 1 shows a part of the construction drawings.

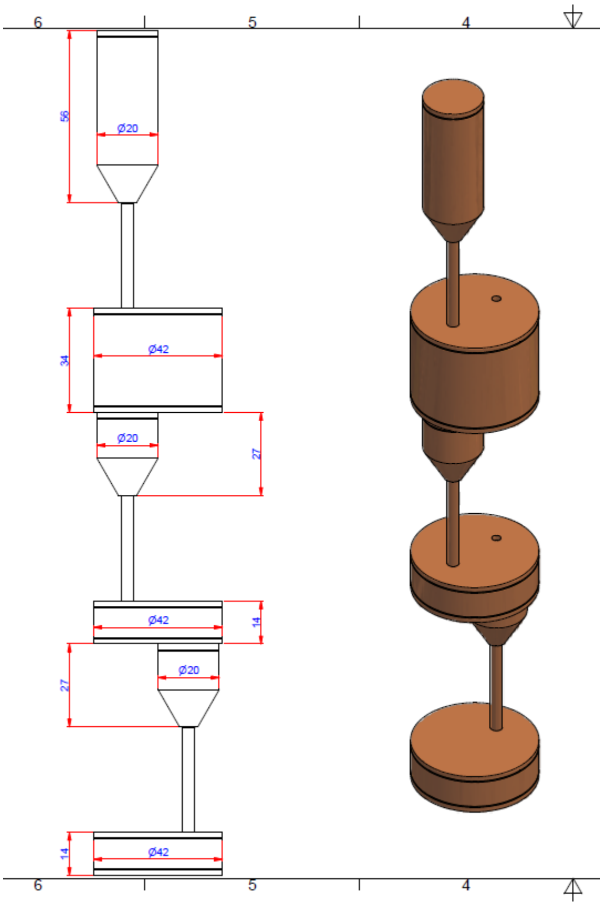

Figure 1. Drawing of the $^3$He and $^4$He cycles of the dilution refrigerator. The sorption pumps are not shown.

The design of the radiation shields has a very subtle influence on the performance of the cooling system. Besides the required mechanical stability, the cool-down time and, in particular, the minimisation of heat losses have to be considered. Best results have been achieved using a standard copper shield with multi-layer insulation (MLI) at the first stage of the pulse-tube refrigerator whereas, at its second stage, a copper-free MLI shield with a supporting structure made of fibre-reinforced plastics is fixed.

The design of the mixing chamber [3] enables tilted operation of the dilution refrigerator with angles of up to 45° from its upright position. The challenge of charging and discharging into/from the correct phase might also be solved by a bottle-shaped chamber. Such design however, would suffer from a reduced area of the phase boundary resulting in a decreasing cooling power. The configuration shown in figure 2 with a special arrangement of capillaries as filling material avoids such disadvantages. Furthermore, a usual outside shape of the chamber can be realised.

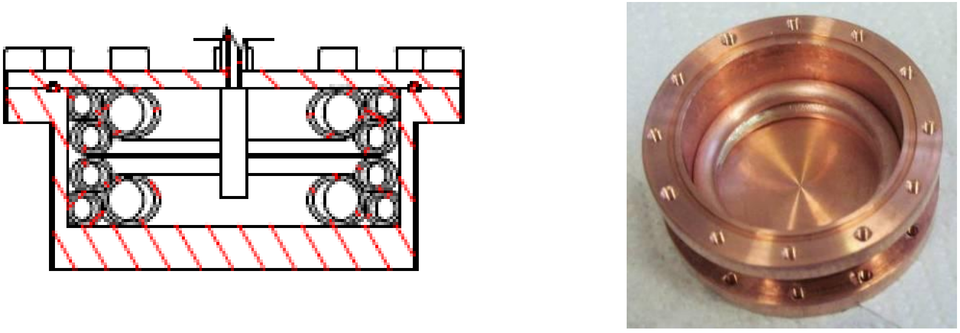

Figure 2. Mixing chamber for tilted operation as drawing (left part) and during manufacturing (right part). Due to further investigations on the prototype cooler, an indium seal is used.

## 3. EXPERIMENTS

For precise investigations of the complete cooling system, a special apparatus is available which provides the possibilities of tilting and rotating (see figure 3). An active damping (air legs) strongly reduces the influence of external mechanical noise.

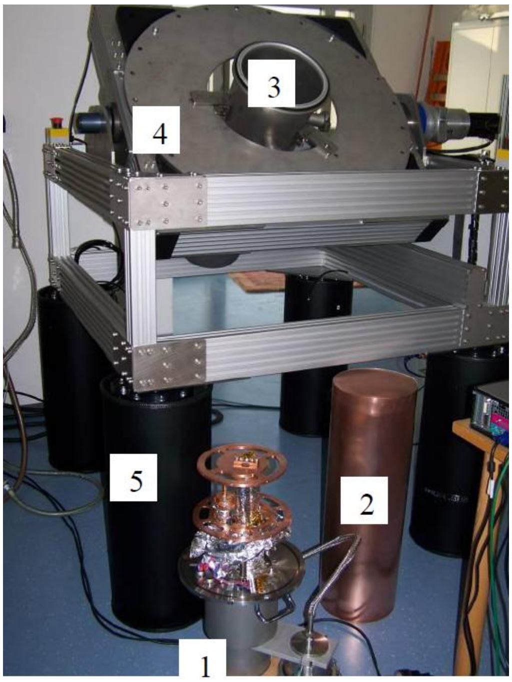

Figure 3. Apparatus for tilting and rotating the cooling system with puse-tube cooler (1; TransMIT Giessen), outer radiation shield (2), vacuum flask (3), feeder plate (4) and air legs (5).

Despite of minimised mechanical vibrations of the pulse-tube cooler as developed by TransMIT Giessen, further mechanical decoupling from the mixing chamber is necessary. An optimised combination of rigid connections with capillaries supported by mounting elements results in significantly reduced noise at the mixing chamber (see figure 4). Noteworthy, the operating frequency of the pre-cooler of 1.4 Hz is clearly to be seen at its second stage (bottom) but can not be resolved at the mixing chamber.

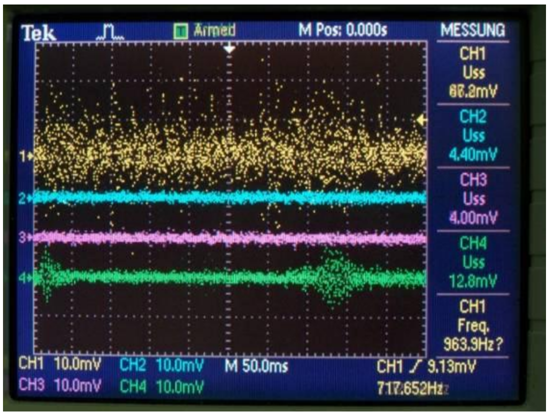

Figure 4. Time-resolved acceleration values measured at different positions: (from top to bottom) neighbourhood signal for comparison, mixing chamber (radial direction), mixing chamber (axial direction), pulse-tube cooler (second stage, axial). In good approximation, the values are proportional to the measured voltage (right scale, please note the varying voltage ranges).

The main principle of the thermally coupled helium cycles has been confirmed, also using a modified design for $^4$He. Typical values for the regeneration of the sorption pumps are a heating power of 3 W, a heating time of 15 minutes, and a cycle time of 5 h. A stable operation of these cycles has shown to be realised. Further investigations are progressing.

Superconducting and gas-gap heat switches are the only configurations which are known to work reliably at very low temperatures. For superconducting heat switches, materials with relatively low critical field have to be chosen. Thus, pure elements like lead, niobium or indium are considered. Figure 5 shows a set-up used for tests on different kinds of superconducting heat switches.

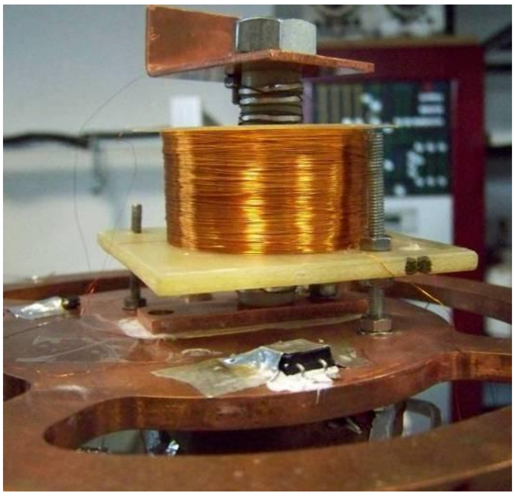

Figure 5. Set-up for investigations on superconducting heat switches.

A set-up for investigations on gas-gap heat switches is shown in figure 6. Most important parameter for the operation characteristics is the amount of filled helium. As a reference value, a helium pressure of about 100 mbar at room temperature can be given. The variation of the resulting performance with different designs of the heat switch or with the base temperature is relatively weak. Larger helium pressures provide minor improved thermal coupling but demand significantly longer cool-down.

Figure 6. Set-up for investigations on gas-gap heat switches.

## 4. CONCLUSIONS

The currently developed dilution refrigerator is characterised by a tilt independence of the complete system with tilting angles of up to 45°, no need of external pumps, and a continuous and stable operation. One of its key components is the mixing chamber with a special arrangement of capillaries as filling material. The main principle of the thermally coupled helium cycles has been confirmed, further investigations are progressing. Systematic investigations on superconducting an on gas-gap heat switches also provide a basis for the further development of cooling systems for very low temperatures.

## 5. REFERENCES

[1] http://www.janis.com/Products/productsoverview/DilutionRefrigerators/JDryCryogenFreeDilutionRefrigerators/JDry-100-ASTRA_CryogenFreeDilutionRefrigerator.aspx#

[2] Martin F et al., 2010, A closed cycle $^3$He–$^4$He dilution refrigerator insensitive to gravity. *Cryogenics*, doi:10.1016/j.cryogenics.2010.02.014

[3] ILK´s Patent DE 10 2009 025 544

073

# The AEGIS´Low Temperature System

**Eisel T., Bremer J., Burghart G., Doser M., Dudarev A.**

CERN, 1211 Geneva 23, Switzerland

## ABSTRACT

The antimatter experiment AEGIS is being constructed at CERN. Its scientific goal is to measure the gravitational interaction between antimatter and ordinary matter. Therefore neutral antihydrogen is subjected to the earth's gravitational field. In order to perform precise measurements, the antihydrogen needs to be produced at very low temperatures. This is achieved by cooling the combining antiprotons to temperatures of about 100 mK.

The antiprotons are trapped and cooled in a Penning trap. The required electrical fields are generated by a series of electrodes, which are charged independently with peak voltages of up to 1 kV. The electrodes are formed by thin gold layers sputtered onto polished sapphire. Sapphire provides reliable electrical insulation and very high thermal conductivity. The bottom of the sapphire is gold sputtered too and is pressed against the mixing chamber of a dilution refrigerator. An indium foil sandwiched between the sapphire and the mixing chamber is used to reduce the thermal boundary resistance.

## 1. INTRODUCTION

Still there is a question mark in the standard model of particle physics concerning the gravitational force. In order to study its nature AEGIS (Antimatter Experiment: Gravitation, Interferometry, Spectroscopy) is currently under construction. It is located at CERN's (European Organization for Nuclear Research) Antiproton Decelerator. The primary scientific goal of AEGIS is the direct, high precision measurement of the Earth's local gravitational acceleration on antihydrogen [1]. The antihydrogen is formed by antiprotons and positroniums. In order to perform precise measurements the antihydrogen needs to be produced at very low temperatures, which is achieved by cooling first the antiprotons to temperatures of about 100 mK [2].

The antihydrogen is created in a Penning trap, which is also used to trap and to cool the antiprotons during about 120 s. The Penning trap consists of several high voltage electrodes charged with time-dependent voltages of up to 1 kV. The trap is thermalized at the mixing chamber, the coldest part of a $^3$He-$^4$He dilution refrigerator. In this temperature range only a dilution refrigerator is capable to provide the required continuous cooling power.

## 2. INVESTIGATIONS REGARDING THE THERMAL LINK

Since the electrodes of the Penning trap are charged independently, they need to be individually electrically insulated. However, the electrical insulation implies at this low temperature generally a poor thermal contact, depending on the thermal conductivity of the bulk materials and on the usually dominant thermal boundary resistances. The boundary resistance significantly increases towards low temperatures depending on the available heat carriers, being either phonons or electrons [3].

Different designs of the thermal link between the electrodes and the cold source have been investigated in a previous work [4]. The designs differ in the dominant heat carriers. The so called Rod design uses electrons and phonons whereas the Sandwich design uses phonons only for transferring the heat. Due to the advantageous electrical insulation a Sandwich design is chosen to be applied in AEGIS.

The Sandwich design consists of an electrically insulating material, which thermally connects the electrodes with the mixing chamber. A sapphire (mono-crystalline $Al_2O_3$) is used as dielectric. It provides only very little lattice imperfections, on which phonons are scattered. The phonon mean free path in a pure sapphire is considered to be rather large. It can be estimated to about 1 mm at the related temperatures using the equation for the lattice thermal conductivity [5]. A similar value was measured with propagating heat pulses at 2 K [6]. Lowest thermal resistances in the bulk material can thus be achieved.

Sapphire shows another beneficial property for the presented application, which is its thermal diffusivity. The thermal diffusivity is a measure of the propagation speed, with which a temperature disturbance at one point in a bulk material travels to another point. It is therefore a vital material property for transferring dynamic heat loads. The thermal diffusivity is calculated by dividing the thermal conductivity of the bulk material by its volumetric heat capacity. Using the thermal conductivity [7, 8] and the specific heat [9] the thermal diffusivity of a typical sapphire in the relevant temperature range can be calculated to 2 $m^2/s$. This value is even slightly higher compared to very pure copper or aluminium [10].

As already discussed the phonons are little scattered in the bulk of the sapphire, but they are strongly scattered and reflected at its surface, which causes a very high thermal boundary resistance. This resistance, also known as Kapitza Resistance [11] strongly depends on the temperature, the phonon velocity and the acoustic impedance. The thermal boundary resistance is described by the acoustic mismatch theory [12]. However, the acoustic mismatch theory considers a perfect mechanical connection of the materials involved. To get the solid material as perfectly as possible connected to the sapphire is the real challenge.

When connecting two solids the actual contact area is often extremely small because of microscopic irregularities or the roughness in the larger scale. For pressed metal-metal joints contact areas of only $10^{-6}$ of the nominal area have been observed [13]. If the pressure for such contacts is increased, the touching material peaks undergo plastic deformation and larger contact surfaces develop until the pressure is just below the yield strength of the material.

It can be found in literature that the thermal boundary resistance of metal-sapphire pressure joints can be reduced by placing a thin foil of indium as intermediate layer [14]. Indium is still pliable at low temperatures and creeps at fairly low pressures. However, it could be proved by several researchers [10, 15] that a further reduction of the thermal boundary resistance can be achieved by vapour depositing the sapphire surface with the metal. Measurements with a test setup depicted in Figure 1 show thermal boundary resistances, for a sandwich made of an indium vapour deposited and optically polished sapphire, agreeing very well at low temperatures with the acoustic mismatch theory [4].

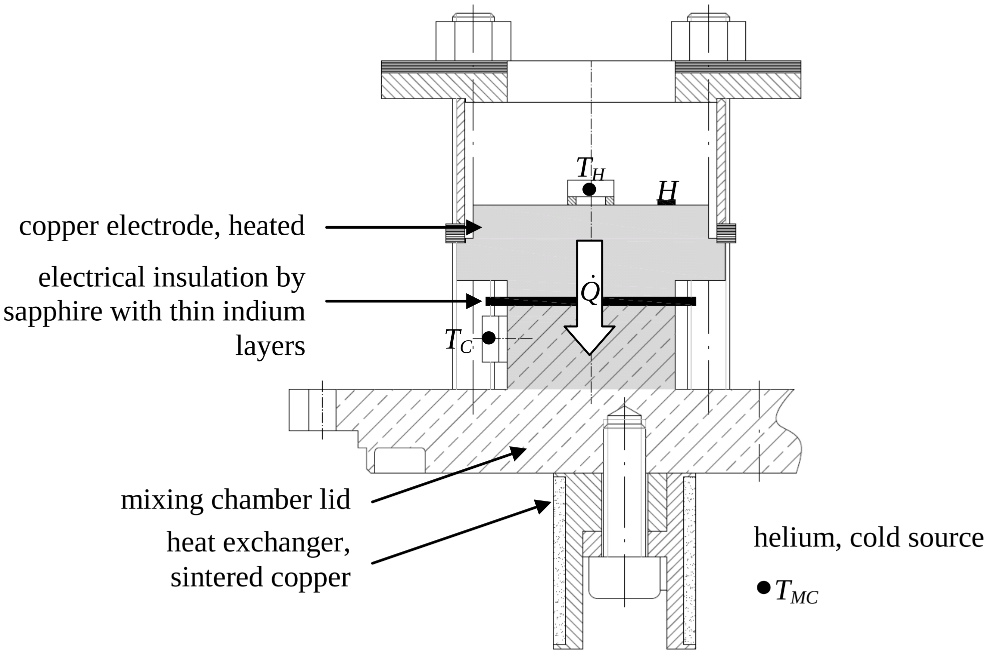

Figure 1: Sandwich design with the position of the heater ($H$) and the temperature sensors [4]. The temperatures of the heated ($T_H$) and the cold side ($T_C$) of the sandwich as well as of the helium in the mixing chamber ($T_{MC}$) were measured.

## 3. THE AEGIS' THERMAL LINK DESIGN

The Penning trap of AEGIS is a stack consisting of 10 cylindrical electrodes, of which 5 are split into 4 sectors. All sectors and electrodes must be electrically insulated and cooled. The heat load can be split into time constant heat loads, mainly thermal radiation and thermal conduction via cables, as well as time depending heat loads due to the pulsed creation of antimatter. The latter is mainly caused by the annihilation of the positroniums in the electrode material.

The deposited heat increases with the thickness of the electrodes, which shall thus be as thin as possible. Therefore the electrodes are made of only some micrometre thin gold layers sputtered onto the polished sapphire substrate. All the gold layers are sputtered in one process, in which the insulating gaps are masked. The gold sputtered electrodes have further advantages, e.g.

- the low thermal bulk resistance,
- the short way the heat carriers have to over bridge between the warm and cold surface of the electrode providing short thermal time constants,
- only one thermal boundary resistance to the sapphire,
- a small volume to be charged, which reduces charging times and Joule heating and
- a low electrical resistance.

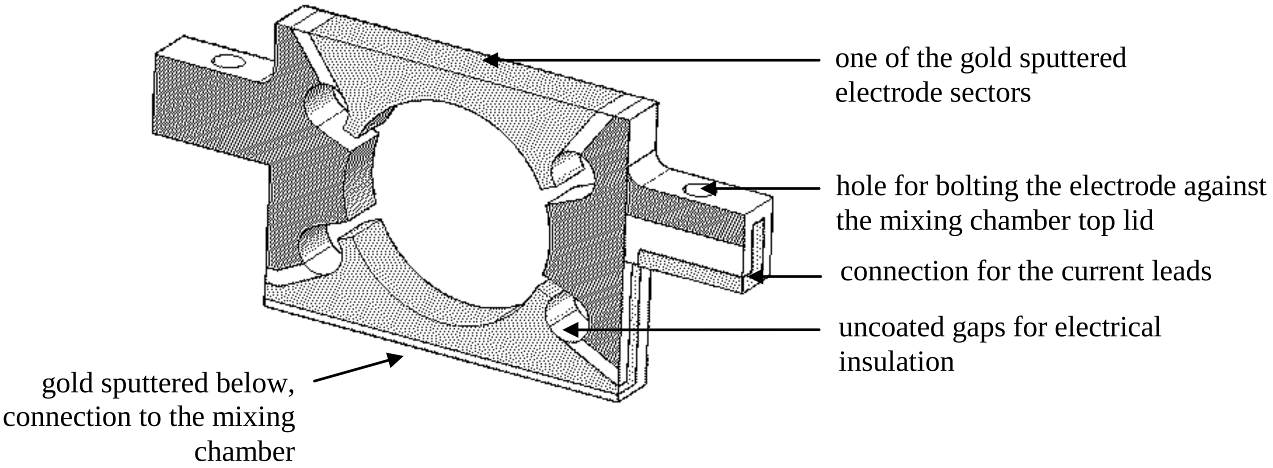

Figure 2: Electrode of the Penning trap with 4 electrically insulated sectors. Two sectors are shown in light grey, the other two in dark grey and the blank sapphire substrate in white.

The sapphire surface in contact with the mixing chamber lid is gold sputtered too. A thin indium foil is used to improve the thermal contact between the sapphire block and the mixing chamber lid made of copper. The square blocks of sapphire with the sputtered electrodes and the round beam hole are pressed directly onto the top plate of the mixing chamber using copper bolts. The differential thermal dilatation will increase the pressing force when cooling down.

## 4. CONCLUSIONS

High voltage electrodes of a Penning trap need to be cooled down to about 100 mK. Thermal measurements regarding the thermal link between the electrodes and the mixing chamber of a dilution refrigerator are performed. They show an excellent compliance of the thermal boundary resistance with the theoretical values of the acoustic mismatch theory when using a metal deposition, e.g. vapour deposition or sputtering onto polished sapphire and a ductile sandwiched layer like indium foil. With this information the thermal link for AEGIS is designed. The design consists of a sapphire block on which the electrode is directly gold sputtered. The sapphire block in turn having a gold sputtered surface is pressed against the mixing chamber lid made of copper. A thin indium foil is sandwiched in between in order to improve the surface in contact.

Currently measurements are performed in order to verify the thermal performance of the AEGIS' thermal link design.

## 5. ACKNOWLEDGEMENT

Parts of this work were carried out in the framework of a Doctoral Student Program at CERN, funded by the German Federal Ministry of Education and Research (BMBF). Many thanks to the CERN's Cryolab team, in particular to D. Crochet, L. Dufay-Chanat and S. Prunet.

## 6. REFERENCES

[1] http://aegis.web.cern.ch/aegis/home.html.

[2] M. Doser. AEGIS: an experiment to measure the gravitational interaction between matter and antimatter. *Journal of Physics: conference series*, 199:1-7, 2010.

[3] G. Frossati. Experimental techniques: Methods for cooling below 300 mK. *Journal of Low Temperature Physics*, 87:595-632, 1992.

[4] T. Eisel, J. Bremer, G. Burghart, S. Feigl, F. Haug, T. Koettig. Cooling of electrically insulated high voltage electrodes down to 30 mK. *Proceedings of the twenty third cryogenic engineering conference, Wroclaw Poland*, 2010

[5] C. Enss and S. Hunklinger. *Low-Temperature Physics*. Springer, 2005.

[6] W. Kieninger, W. Metzger and R.P. Huebner. Propagation of heat pulses in single-crystalline sapphire. Appl. Phys., A 41:179_183, 1986.

[7] J.K.N. Sharma. Heat conductivities below 1 °K. I. *Cryogenics*, 7(1-4):141-156, 1967.

[8] R. Berman, J.M. Ziman, and E.L. Foster. Thermal conduction in artificial sapphire crystals at low temperatures. I. Nearly perfect crystals. *Proceedings of the Royal Society of London. Series A, Mathematical and Physical Sciences*, 231:130-144, 1955.

[9] W.A. Phillips, editor. *Amorphous Solids Low-Temperature Properties*. Springer, 1981.

[10] T. Eisel. *Cooling of electrically insulated high voltage electrodes down to 30 mK*. PhD thesis, Technical University Dresden, 2011.

[11] P.L. Kapitza. The study of heat transfer in helium II. *J. Phys. (U.S.S.R.),* 4:181, 1941.

[12] I. Khalatnikov. *Zh. Eksp. i Teor Fiz.*, 22:687-704, 1952.

[13] F. Pobell. *Matter and Methods at Low Temperatures*. Springer, 2002.

[14] L.J. Salerno and P. Kittel. *Thermal Contact Conductance*. NASA Ames Research Center, 1997.

[15] C. Schmidt and E. Umlauf. Thermal boundary resistance at interfaces between sapphire and indium. *Journal of Low Temperature Physics*, 22(5):597-611, 1976.

# CRYOCOOLERS, LIQUID HELIUM

039

# A 3-Dimensional Numerical Study a Co-Axial type Acoustic Stirling Cryocooler

**Farouk B.*, Spoor P.**, Corey J.**, Antao D.S.***

*Department of Mechanical Engineering and Mechanics, Drexel University, Philadelphia, PA, USA
**Chart Industries, Troy, NY, USA

## ABSTRACT

A 3-dimensional numerical study is reported here for the investigation of the performance of a co-axial single stage acoustic Stirling cryocooler. The cryocooler is driven by a cyclically moving piston with helium as the working fluid. The buffer tube section is concentric with the annular regenerator. The porous media heat-exchangers at each end of the buffer tube act as flow straightners and prevent mixing of the flow. The regenerator and the heat-exchangers are modeled as ‘porous media heat exchangers’ and a non-equilibrium heat transfer model (between solid and gas) is applied in these regions. The management of flow patterns from the regenerator sections to the buffer tube is of significant importance in the performance of the proposed co-axial cryocoolers. Three types of flow distribution systems in the cold head region are studied via detailed simulations of the 3-D flow and temperature fields. The first system consists of slots that evenly distribute the turning gas flowing from the regenerator to the buffer tube region. In the second system the slots are replaced by an open cold head region. Finally, in the third system the open cold head is filled with copper mesh screen. The three systems are compared for cryocooler performance.

## 1. INTRODUCTION

The acoustic stirling cryocooler is a developing technology that emerged largely in the early 1980's with a series of innovations in the broader field of thermoacoustics. In contrast with other cryocoolers (e.g. Stirling cryocooler and Gifford-McMahon cooler) this type of cryocooler can be made without moving parts in the low temperature part of the device, making the cooler suitable for a wide variety of applications (industrial applications such as semiconductor fabrication and in military applications such as for the cooling of infrared sensors) [1]. Acoustic stirling cryocoolers will be particularly useful in space-based telescopes where it is not possible to replenish the liquid cryogens as they are depleted. With the added benefits of extended lifetimes and low vibrations at the cold head, these cryocoolers have found their niche application where stable operation is desired. It has also been suggested that acoustic stirling cryocoolers (refered to as pulse tube cryocoolers (PTRs) can be used to liquefy oxygen on Mars [2].

Acoustic stirling cryocoolers come in three basic configurations [1, 3]. These configurations are the In-line, the U-tube and the Co-axial type. The co-axial type is the most compact of the configurations and offers the best geometry for direct contact with the cold region (due to the presence of a cold head). Recently, there has been a push to build PTRs that work efficiently at higher frequencies [4, 5]. The use of high frequency oscillations allows the system to be comparatively small in size- for applications in the space industry or high temperature superconductivity (HTS) where localized medium – low power (1 – 10 W) cooling systems with extremely fast cool-down times are required.

A 3-dimensional numerical study is reported here for the investigation of the performance of a co-axial single stage acoustic Stirling cryocooler. Three types of flow distribution systems (from regenerator to the buffer tube) in the cold head region are studied. The first system consists of slots that evenly distribute the turning gas flowing from the regenerator to the buffer tube region. In the second system the slots are replaced by an open cold head region. Finally, in the third system the open cold head is filled with a porous media substance.

## 2. PROBLEM GEOMETRY

Figure 1 below shows a 2-D slice of the 3-D geometry studied (i.e. a co-axial cryocooler). The components of the co-axial cryocooler include a compression chamber with a moving piston, an aftercooler (component B), an annular regenerator with coarse stainless steel mesh (component D), a second set of regenerator mesh (fine stainless steel mesh, component E), a buffer tube (component J) with a flow straightner at each end (components I and K), a hot heat-exchanger (component L), a diffuser cone to connect warm heat-exchanger to the inertance tube, an inertance tube and a compliance volume. The aftercooler and hot heat-exchanger were simulated as porous media zones with properties (porosity and permeability) of a shell and tube heat-exchanger and the flow straightners (porous media) had properties of diffusion bonded phosphor bronze mesh.

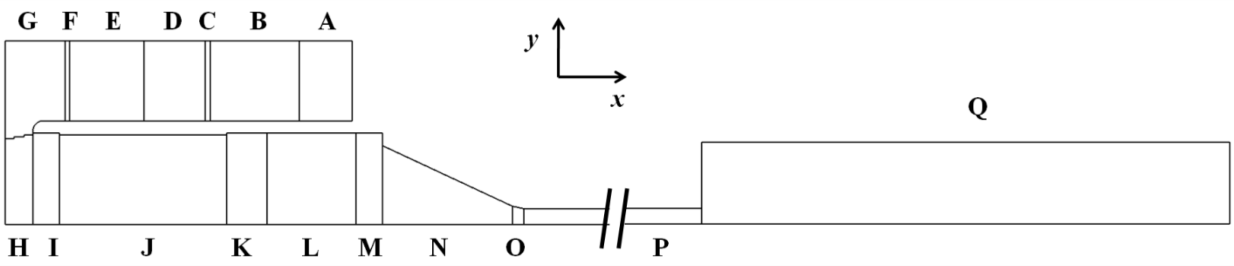

Figure 21. Schematic of co-axial type acoustic stirling cryocooler simulated

In this study three different cold head configurations were studied (Table 1- cases simulated). In case 1, the cold head comprised of a set of slots ($0.4^{o}$ each or 0.6 mm thick) at the end of the regenerator (component G, see figure 2a), in case 2, the cold head is a void region (component G, see figure 2b) and in case 3, the void cold head is packed with wire mesh (component G, see figure 2b). The porous media properties for this region are the same as those for components C and F.

Table 1. List of cases studied

| Case No. | Cold Head Geometry (G) | Simulation domain |
|---|---|---|
| 1 | 0.6 mm thick slot | Gas (Helium) |
| 2 | Void zone | Gas (Helium) |
| 3 | Wire mesh | Porous media (Copper) |

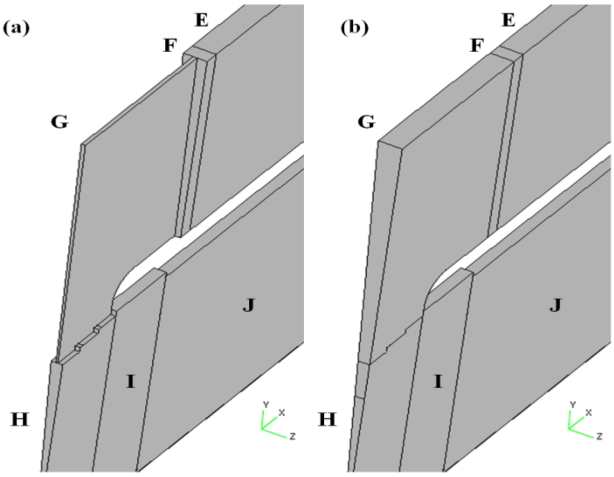

Figure 22. Schematic of different cold head configurations studied (a) slot and (b) void or porous

# 3. MATHEMATICAL MODEL

## 3.1. Governing Equations:

The flow and heat transfer simulation model incorporates the fluid dynamic equations of conservation of mass (continuity equation), momentum (Navier-Stokes equation) and energy in the fluid domain. The various heat exchangers, flow straightners and the regenerator are modelled as porous media with the relevant solid properties (Table 2). The mass, momentum and energy conservation equations for the porous media (solid) regions are solved simultaneously with the gas phase equations for the cryocooler. Further details of the governing equations are given in Antao and Farouk [6, 7].

## 3.2. Porous Media Conditions:

3.2.1. In the porous media regions, the three heat exchangers (components B, C, F and L in figure 1) have properties of copper with density 8950 kg/m$^3$, constant specific heat 380 J/kg-K and temperature dependent thermal conductivity. The regenerator (components D and E) has properties of 316 stainless steel, with density 7810 kg/m$^3$, constant specific heat 460 J/kg-K and temperature dependent thermal conductivity. The flow straightners 'FS' (components I, K and M) have properties of phosphor bronze, with density 8800 kg/m$^3$, constant specific heat 360 J/kg-K and temperature dependent thermal conductivity. Table 2 below lists the porous media parameters used in the governing equations of the porous media.

Table 2. Porous Media parameters used in the simulation

| **Component** | **Name** | **Porous Media Material** | **Porosity '$\varepsilon$'** | **Permeability (m$^2$) '$\kappa$'** | **Drag Factor '$C_F$'** |
|---|---|---|---|---|---|
| B | Aftercooler HX | Copper | 0.13 | $4.5\times10^{-10}$ | 0.2 |
| C, F | Copper Regenerator | Copper | 0.774 | $4.08\times10^{-08}$ | 0.187 |
| D | Regenerator Top | Stainless Steel | 0.719 | $9.7\times10^{-11}$ | 0.242 |
| E | Regenerator Bottom | Stainless Steel | 0.717 | $5.92\times10^{-11}$ | 0.236 |
| I | Cold FS | Phosphor-Bronze | 0.702 | $5.8\times10^{-10}$ | 0.278 |
| K, M | Warm FS | Phosphor-Bronze | 0.702 | $4.9\times10^{-11}$ | 0.278 |
| L | Warm HX | Copper | 0.13 | $4.5\times10^{-10}$ | 0.2 |

## 3.3. Initial and Boundary Conditions:

### 3.3.1. Initial Conditions

3.3.2. The initial pressure in the system is set to 2.8 MPa for all the cases. Two temperature initial conditions were simulated to study the system. For the first temperature initial condition, a constant temperature of 300 K was assumed in all the components to simulate the cooldown characteristics of the cryocooler. In order to predict the system's performance near quasi-equilibrium, a second initial condition was prescribed that represents an expected quasi-steady temperature distribution (cold head at 77 K, the aftercooler and warm heat-exchangers at 300 K and a linear gradient across the regenerator and buffer tube regions).

### 3.3.3. Boundary Conditions

3.3.4. The walls of the aftercooler heat-exchanger and the warm heat-exchanger were maintained at 300 K and the other components were maintained adiabatic. The piston is modelled as a reciprocating wall having an oscillatory velocity. The velocity of the piston is defined by the function, $u = A_0\omega Cos\ (\omega t)$, where $A_0$ is the maximum displacement of the piston (1.8 cm) and $\omega$ is the angular frequency ($\omega = 2\pi f$) and $f$ is the frequency of operation. For the current simulations (all cases), the frequency is set at 50 Hz.

### 3.4. Numerical Scheme:

The numerical scheme for solving the governing equations is based on the finite volume approach. The continuity, momentum and energy equations are solved for the fluid as well as the porous media using a 2nd order upwind scheme. The motion of the piston is captured by a moving grid scheme near the piston wall (the Transfinite Interpolation scheme [8]).

A 2nd order Crank-Nicholson scheme (with a blending factor of 0.7) is used for the time derivatives in the continuity, momentum and energy equations. The time-step size was determined by allowing 50 time-steps/cycle, which was sufficient to accurately simulate the problem ($\Delta t = 4 \times 10^{-4}$). An overall convergence criterion was set for all the variables at $10^{-4}$ in the iterative implicit numerical solver.

A 2.4° pie slice of the problem geometry was simulated to save on computation time. A hybrid (structured-unstructured) grid system is used in the simulations. Structured grid (non-uniform orthogonal mesh) was used in most of the components except the cold head (components G and H) and the diffuser cones (components N and O) near the inertance tube. A total of 55000 - 62000 grid points were used in the simulations (depending on the geometry, i.e. cases 1, 2 or 3). The governing equations and the boundary conditions were solved using CFD-ACE+ [8].

## 4. RESULTS AND DISCUSSION

In the following section, results for spatio-temporal evolution of the flow and temperature fields in the co-axial acoustic stirling cryocooler (figure 1) are presented and the effects of the cold head geometry on the performance of the system are discussed.

### 4.1. Temporal temperature and pressure evolution

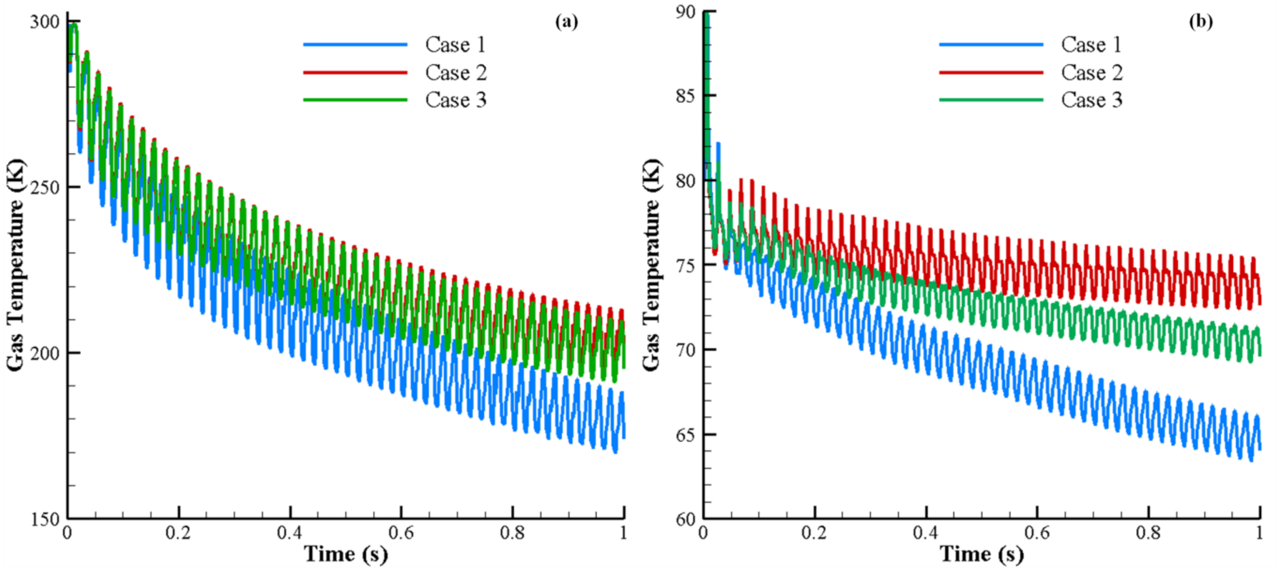

Figure 23. Transient variation of the gas temperature at the exit of the cold flow straightner (component I) for the three cases studied (a) cooldown from room temperature (300 K cold head) and (b) cooldown from near quasi-steady state temperature initial condition (77 K cold head)

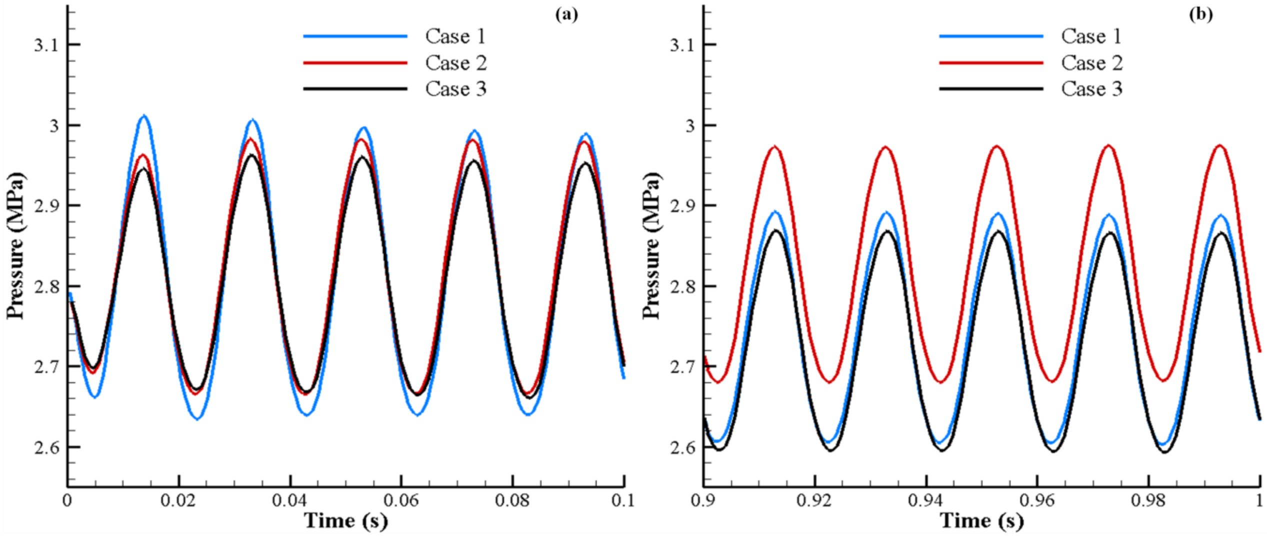

Figure 24. Transient variation of the pressure at the entrance of the buffer tube (component J) for the three cases studied (a) early time and (b) 1.0 second of simulation time near quasi-steady state

Figure 3a shows the cooldown curves of the gas temperature at the exit of the cold flow straightner and inlet to the buffer tube section (i.e. $x$ = 2.59 cm, $y$ = 4.5 cm, $z$ = 0.095 cm) for the cases studied using the room temperature initial condition. The corresponding temporal evolution of the gas temperature from the near quasi-steady state initial condition is shown in figure 3b. The cyclic temperature profiles are not sinusoidal in nature and the non-sinusoidal behaviour is due to secondary streaming flow (the pressure exhibits sinusoidal behaviour at the same location). The slot geometry (figure 2a) simulated in case 1 performs the best due (quasi-steady cycle-average temperature is about 58 – 60 K) to the high pressure amplitudes. Comparing the temporal pressure profiles at the same location (figure 4a and 4b) shows that the pressure amplitude in case 1 is the highest (~ 0.16 MPa). The pressure amplitude in case 3 is the lowest and this can be explained by the increased pressure drop in the porous cold head region (case 1 and 2 have void cold head regions). The lowest performance of the three cases is case 2 due to the increased void space in the cold head which leads to adiabatic heating of the oscillating gas in that region. The addition of slots provides the benefit of decreasing the void space in the cold head without compromising the pressure amplitude (addition of mesh or porous media will increase the pressure drop as seen in case 3).

## 4.2. Spatio-temporal transport processes

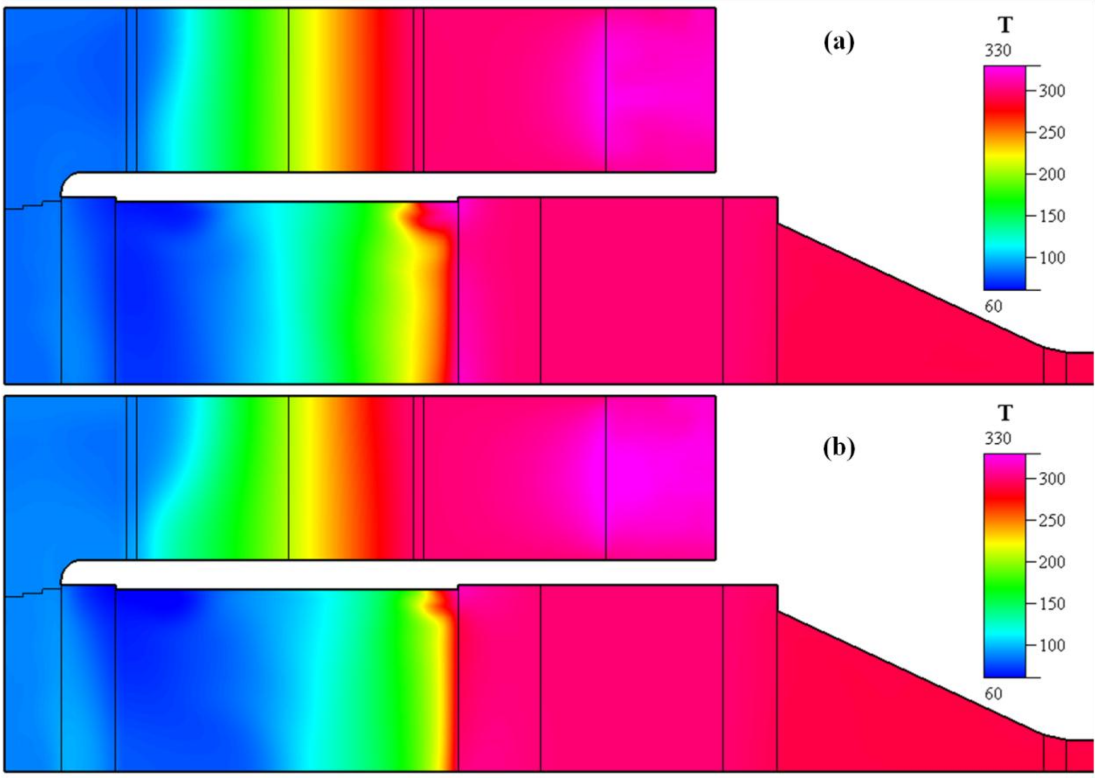

Figure 25. Gas temperature contours in the cold head region of the cryocooler (components A – P) for case 1 simulated using the near quasi-steady state initial condition at (a) 1.0 sec and (b) 4.0 sec

In figure 5a and 5b, the instantaneous temperature contours in the cold head (components A – P) are plotted for a 2-D slice of the geometry ($\theta$ = 1.2$^{o}$) simulated in case 1 at 1.0 sec and 4.0 sec of simulation time respectively. The temperature fields clearly show a two-dimensional structure in the regenerator and the buffer tube. A comparison of the two figures shows a distinct variation in the temperature fields in the bottom regenerator (component E). This variation is possibly due to the flow fields in the slot (component G) and the void cold head region (component H). A plot of the instantaneous velocity vectors for the same 2-D slice of the geometry (figure 6) shows velocity vectors with large magnitudes and large vortical structures in these components. Additionally, large velocity magnitudes are visible in the compression chamber, the aftercooler, the warm heat exchanger and the diffuser cone, with non-uniform flow in the latter two components. However, the flow in the buffer tube is fairly uniform (except near the walls) and laminar due to the flow straighteners at its ends.

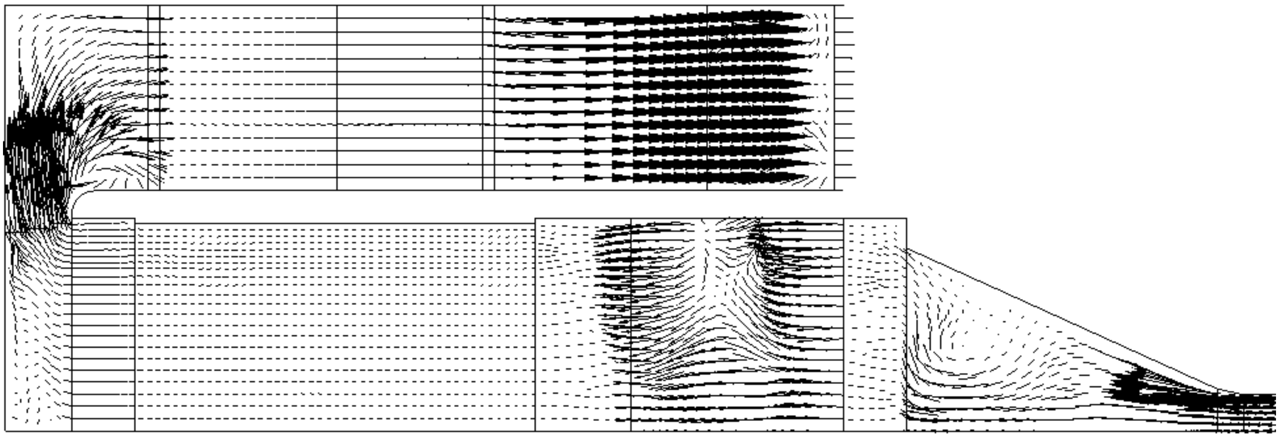

Figure 26. Velocity vectors in the cold head region of the cryocooler (components A – P) for case 1 simulated using the near quasi-steady state initial condition at (a) 1.0 sec and (2) 4.0 sec

## 5. CONCLUSIONS

A 3-dimensional numerical study is reported here for the investigation of the performance of a co-axial (buffer tube section is concentric with an annular regenerator) acoustic Stirling cryocooler. The porous media heat-exchangers at each end of the buffer tube act as flow straightners and prevent mixing of the flow. Three types of flow distribution systems in the cold head region are studied via detailed simulations of the 3-D flow and temperature fields. The first system consists of slots, in the second system the slots are replaced by an open cold head region and in the third system the open cold head is filled with a porous media substance (copper mesh screen). The simulations predict the best performance for the first case studied (i.e., slots) where the cooldown from room temperature and the quasi-steady state temperature attained is the lowest. The reduced performance for case 2 is due to the addition of void space which leads to high temperature oscillations in the region. When the open cold head was filled with porous media (wire mesh) to reduce the void space, the performance improved, however the addition of porous media added to the pressure drop in that region and ultimately reduced the pressure amplitude in the buffer tube. It can be concluded that the addition of slots provides the benefit of decreasing the void space in the cold head without compromising the pressure drop in that region.

## 6. ACKNOWLEDGEMENTS

BF and DA acknowledge support from the US National Science Foundation under grant CBET-0853959 and CFIC-Qdrive, Troy NY (via DOE Contract #DE-FOA-0000397)

## 7. REFERENCES

1. Radebaugh, R. Pulse tube cryocoolers for cooling infrared sensors. 2000. San Diego, CA, USA: Society of Photo-Optical Instrumentation Engineers.
2. Marquardt, E.D. and R. Radebaugh, Pulse Tube Oxygen Liquefier. Adv. Cryo. Eng., 2000. 45: p. 457-464.
3. Radebaugh, R., Cryocoolers: the state of the art and recent developments. Journal of Physics: Condensed Matter, 2009. 21(16): p. 164219 (9 pp.).
4. Radebaugh, R., I. Garaway, and A.M. Veprik. Development of miniature, high frequency pulse tube cryocoolers. in Infrared Technology and Applications XXXVI, 5-9 April 2010. 2010. USA: SPIE - The International Society for Optical Engineering.
5. Vanapalli, S., et al., 120 Hz pulse tube cryocooler for fast cooldown to 50 K. Applied Physics Letters, 2007. 90(Compendex).
6. Antao, D. and B. Farouk, Computational Fluid Dynamics Simulations of an Orifice type Pulse Tube Refrigerator: Effects of Operating Frequency. Cryogenics, 2011. 51(4): p. 192-201.
7. Antao, D.S. and B. Farouk, Numerical simulations of transport processes in a pulse tube cryocooler: Effects of taper angle. International Journal of Heat and Mass Transfer, 2011. 54(21-22): p. 4611-4620.
8. ESI-CFD-Inc., *CFD-ACE+ v2009.4 User Manual*. 2009, Huntsville, AL: ESI Group.

038

# Effects of the Inertance Tube Length and Diameter on Pulse Tube Refrigerator Performance

**Farouk B., Antao D.S.**

Department of Mechanical Engineering and Mechanics, Drexel University, Philadelphia, PA, USA

## ABSTRACT

A numerical study is reported here for the investigation of the effects of the inertance tube length and diameter on the performance of a single stage inertance pulse tube refrigerator (IPTR). A detailed time-dependent axisymmetric computational fluid dynamic (CFD) model of an IPTR is used to predict its performance. In the CFD model, the continuity, momentum and energy equations are solved for both the refrigerant gas (helium) and the porous media regions (the regenerator and the three heat-exchangers). The resultant flow fields (pressure, velocity and temperature) are used to study the phase relationships between the pressure and the mass flow in the regenerator, pulse tube and inertance tube regions and the performance of the system. The effects of the length and diameter of the inertance tube on these phase relationships and the effect of the inertance on the system performance are also investigated. The predictions compare well with previously published theory and results. The CFD model offers an accurate and economical alternative to design of efficient pulse tube refrigeration systems.

## 1. INTRODUCTION

The Pulse Tube Refrigerator (PTR) is a type of regenerative thermoacoustic gas-cycle refrigerator that runs on gases like helium, argon, nitrogen or air. The PTR runs on the reverse Stirling cycle and is capable of achieving cryogenic temperatures. The small number of moving parts required to build a PTR makes it a simple and hence potentially reliable cryocooler. Being a regenerative cryocooler, it operates with oscillating pressures and mass flows in the cold head.

In the pulse tube cryocooler, the displacer piston (as found in the Stirling and GM regenerative systems) is eliminated [1]. This displacer piston is replaced by a hollow tube (called the pulse tube). The proper phase shift (the function of the displacer piston in a Stirling or GM cryocooler) in a PTR is maintained by using an orifice, a double-inlet pulse tube or an inertance tube. The inertance tube can be used instead of an orifice or in addition to one. Marquardt and Radebaugh reported the highest efficiency for the pulse tube refrigerator when using a combination of the orifice and the inertance tube [2].

In this study we investigate the effects of the inertance tube length and diameter on the performance of an IPTR. A detailed time-dependent axisymmetric CFD model of an IPTR is used to predict its performance. In the CFD model, the continuity, momentum and energy equations are solved for the refrigerant gas (helium) and the regenerator and three heat-exchangers which are modelled as porous media. The effects of the length and diameter of the inertance tube on the phase relationships (between the pressure and velocity) and the effect of the inertance on the system performance are investigated.

## 2. PROBLEM GEOMETRY

Figure 1 below shows the geometry studied (i.e. an inline IPTR system). Only half the geometry shown in figure 1 was simulated (the axisymmetric assumption) due to the cylindrical nature of an actual system and to save on computation time. The IPTR simulated has the same components and dimensions (see Table 1) as the experimental system studied by Antao and Farouk [3] (no orifice valve is used in the current study). These include a compression chamber with a moving piston, a transfer tube, an aftercooler (the first red hatched region), a regenerator (blue cross-hatched region), a pulse tube with a heat exchanger at each end (the other two red hatched regions), a diffuser cone to connect hot heat-exchanger to the inertance tube, an inertance tube and a compliance volume.

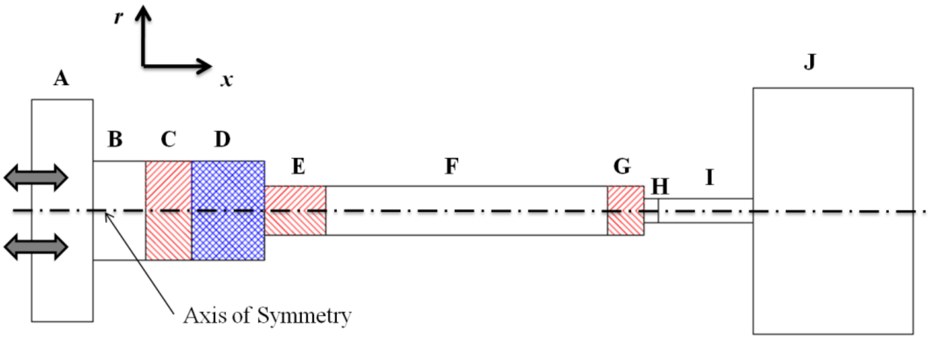

Figure 27.  Schematic of IPTR simulated

Table 1. Dimensions of the IPTR system simulated and time invariant thermal boundary conditions

| **No.** | **Component** | **Radius (cm)** | **Length (cm)** | **Boundary condition along the outer wall** |
|---|---|---|---|---|
| A | Compression Chamber | 3.0 | 1.1 | Adiabatic |
| B | Transfer Tube | 0.85 | 4.0 | $h_c$ **= 20 W/m²-K** |
| C | Aftercooler | 0.85 | 3.0 | $T_w$ **= 293 K** |
| D | Regenerator | 0.85 | 6.0 | Adiabatic |
| E | Cold Heat-Exchanger | 0.47 | 5.0 | Adiabatic |
| F | Pulse Tube | 0.47 | 23.0 | Adiabatic |
| G | Hot Heat-Exchanger | 0.47 | 3.0 | $T_w$ **= 293 K** |
| H | Diffuser Cone | $r_1 = 0.193$<br>$r_2 = r_{IT}$[a] | 0.4 | Adiabatic |
| I | Inertance Tube | -[a] | -[a] | Adiabatic |
| J | Compliance Volume | 2.6 | 14.9 | Adiabatic |

[a] See Table 2

Table 2. Cases of the various conditions (length and diameter of the inertance tube) simulated

| **Case No.** | **Length (cm)** | **Radius '$r_{IT}$' (cm)** | **Inertance '$M$' (Pa-s²/m³)** |
|---|---|---|---|
| 1 | 150.00 | 0.1930 | 442227.62 |
| 2 | 93.50 | 0.1524 | 442090.21 |
| 3 | 217.60 | 0.2324 | 442360.18 |
| 4 | 46.75 | 0.1524 | 221045.11 |
| 5 | 187.00 | 0.1524 | 884180.42 |

Tale 2 lists the various inertance tube geometries studied.  The value of inertance '*M*' is given by the formula [4]:

$$M = \frac{m}{\left(\pi r_{IT}^2\right)^2} = \frac{\rho_0 l}{\pi r_{IT}^2} \qquad (8)$$

where, $r_{IT}$ is the radius of the inertance tube, $m$ is the mass of the gas in the inertance tube, $\rho_0$ is the mean density and $l$ is the length of the inertance tube. The purpose of the study is to identify the best operating conditions of the IPTR and to investigate the role of the inertance tube in achieving the optimum operating conditions.  Five cases are studied in this paper.  The first case represents the dimensions of an experimental PTR system studied [3].  Cases 1, 2 and 3 are for similar values of inertance, but different combinations of length and diameter. The values of inertance tube radius are chosen based on commercially available copper tubing. The final two cases (i.e., cases 4 and 5) are for the same radius of the inertance tube as case 2; however the lengths have been changed from case 2 in order to study the effects of changing the value of inertance on the performance of the system- half the value of inertance in case 2 (case 4) and double the value of inertance used in case 2 (case 5).

## 3. MATHEMATICAL MODEL

### 3.1. Governing Equations:

The flow and heat transfer simulation model incorporates the fluid dynamic equations of conservation of mass (continuity equation), momentum (Navier-Stokes equation) and energy in the fluid domain. The various heat exchangers and the regenerator are modelled as porous media with the relevant solid properties of the regenerator and the heat exchanger materials (Stainless Steel and Copper respectively). The mass, momentum and energy conservation equations for the porous media (solid) regions are solved simultaneously with the gas phase equations for the OPTR. Further details of the governing equations are given in Antao and Farouk [5, 6].

### 3.2. Porous Media Conditions:

In the porous media regions, the three heat exchangers (components C, E and G in figure 1) have properties of copper with density 8950 kg/m$^3$, constant specific heat 380 J/kg-K and a thermal conductivity of 470 W/m-K. The regenerator (component D in figure 1) has properties of 316 stainless steel, with density 7810 kg/m$^3$, constant specific heat 460 J/kg-K and a thermal conductivity of 10 W/m-K.

Table 3 lists the porous media parameters used in the governing equations of the porous media. The values for porosity, permeability and drag factor are the same as those used in a previous study [3].

Table 3. Porous Media parameters used in the simulation

| Component | Material | Porosity | Permeability (m$^2$) | Drag Factor |
|---|---|---|---|---|
| Heat-Exchangers | Copper | 0.774 | $4.08 \times 10^{-8}$ | 0.2 |
| Regenerator | Stainless Steel | 0.72 | $9.70 \times 10^{-11}$ | 0.3 |

### 3.3. Initial and Boundary Conditions:

3.3.1. Initial Conditions

The initial pressure in the system is set to 2.2 MPa for all the cases. In order to predict the system's performance near quasi-equilibrium, the computational model was run with a prescribed initial condition that represents an expected quasi-steady temperature distribution (cold heat-exchanger at 100 K, the aftercooler and warm heat-exchangers at 300 K and a linear gradient across the regenerator and pulse tube). With this initial condition, the simulations were run for until a quasi-stead state was achieved.

3.3.2. Boundary Conditions

Table 1 (given earlier) specifies the heat transfer boundary conditions used at the surface boundaries of the various components. The piston is modelled as a reciprocating wall having an oscillatory velocity. The velocity of the piston is defined by the function, $u = A_0 \omega Cos\ (\omega t)$, where $A_0$ is the maximum displacement of the piston (1.75 mm) and $\omega$ is the angular frequency ($\omega = 2\pi f$) and $f$ is the frequency of operation. For the current simulations (all cases), the frequency is set at 65 Hz. This value of frequency was chosen based on an study performed by the authors where the effect of the frequency on the performance of the system was tested experimentally [3].

### 3.4. Numerical Scheme:

The numerical scheme for solving the governing equations is based on the finite volume approach. The continuity, momentum and energy equations are solved for the fluid as well as the porous media using a 2nd order upwind scheme. The motion of the piston is captured by a moving grid scheme near the piston wall in the compression space (component 'A' in figure 1) and the re-meshing scheme used is the Transfinite Interpolation scheme [7].

A 2nd order Crank-Nicholson scheme (with a blending factor of 0.7) is used for the time derivatives in the continuity, momentum and energy equations. The time-step size was determined by allowing 80 time-steps/cycle, which was sufficient to accurately simulate the problem ($\Delta t$ = 1.923077 × $10^{-4}$). An overall convergence criterion was set for all the variables at $10^{-4}$ in the iterative implicit numerical solver. Mass and energy conservation were verified in the simulations.

A hybrid (structured-unstructured) grid system is used to discretize the computational domains. A total of 4000 – 4600 grid points were used in the simulations. The number of grid points chosen was dependent on the length of the inertance tube. The governing equations and the boundary conditions were solved using CFD-ACE+ [7].

## 4. RESULTS AND DISCUSSION

In the following sub-sections, results for temporal evolution of the flow and temperature fields in the IPTR (figure 1) are presented and the effects of the inertance tube's geometric parameters on the performance of the system are discussed.

### 4.1. Transient processes in the IPTR

The transient behaviour of an IPTR is very important to its operation. Figure 2a shows this temporal variation of the gas temperature at the exit of the cold heat exchanger and inlet to the pulse tube section (i.e. $x$ = 19.1 cm, $r$ = 0.4699 cm) for the cases studied. The banded profiles are cyclic variation of the gas temperature in the system. The cyclic temperature profiles are not sinusoidal in nature (figure 2b) and the amplitude of temperature oscillation varies between 2 K and 5 K. The amplitudes of oscillation are dependent on the pressure amplitude at that location (ideal gas assumption) and non-sinusoidal oscillations are due to secondary streaming flow (since the pressure exhibits sinusoidal behaviour). For a constant value of inertance (changing the length and diameter of the inertance tube), the change in performance of the IPTR was fairly small (~ 2 – 4 K difference between cases 1, 2 and 3). When the value of the inertance was varied (keeping the diameter of the inertance tube constant and changing the length), a larger variation in the performance of the IPTR was observed. The IPTR with the inertance tube used in case 5 ($M$ = 884180.42 Pa-$s^2/m^3$) demonstrates the best performance with the quasi-steady state temperature ~ 42 K.

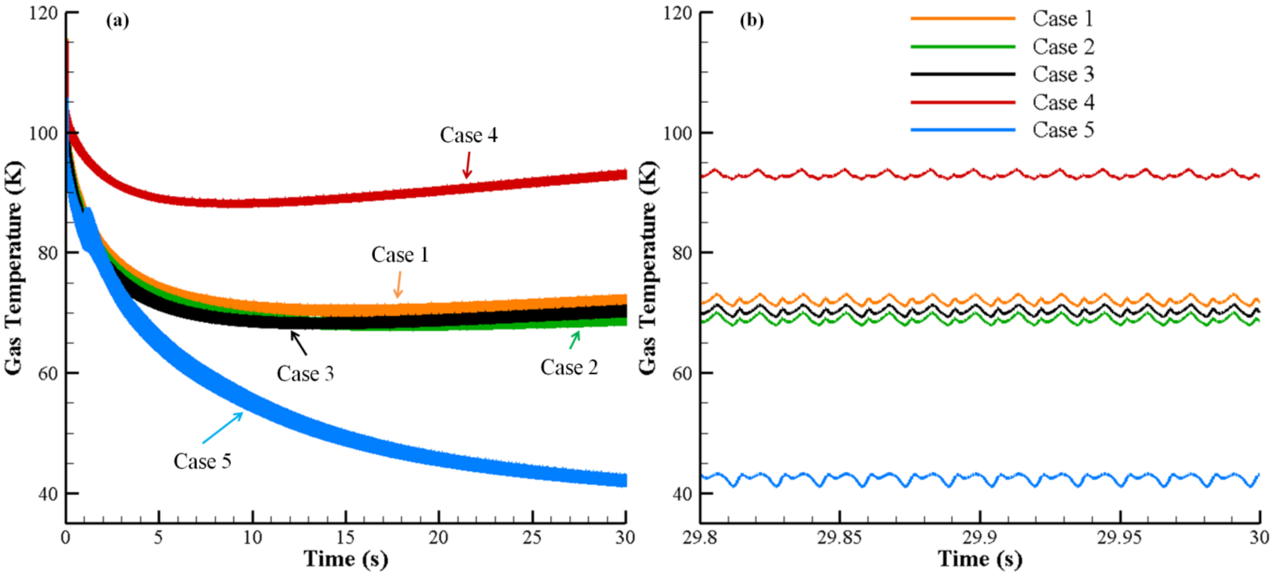

Figure 28. Temporal evolution of the gas temperature at the exit of the cold heat-exchanger from the initial condition (100 K)

The inertance tube helps maintain the proper phase relationships in an IPTR system. The main phase relationship in a PTR is the phase angle difference between the pressure and the flow rate (or velocity) in the regenerator and at the entrance of the inertance tube. For a constant inlet acoustic power (constant piston amplitude), the efficiency of the regenerator is maximised when the pressure and velocity (or mass flow rate) are in phase at the center of the regenerator [8]. In figure 3, the axial velocity and pressure are plotted for three cycles near quasi-steady state at the center of the regenerator (figure 3a) and at the inlet of the inertance tube (figure 3b) for case 5 (best performance). In figure 3a, the phase difference between the pressure and the velocity at the center of the regenerator is fairly small (~ $5^{o}$ – $6^{o}$) with the velocity leading the pressure. At the inlet to the inertance tube, the phase difference is ~ $81^{o}$ with the pressure leading the velocity. In the following sub-section, we discuss the effect of the variation in the phase angle on the performance of the system.

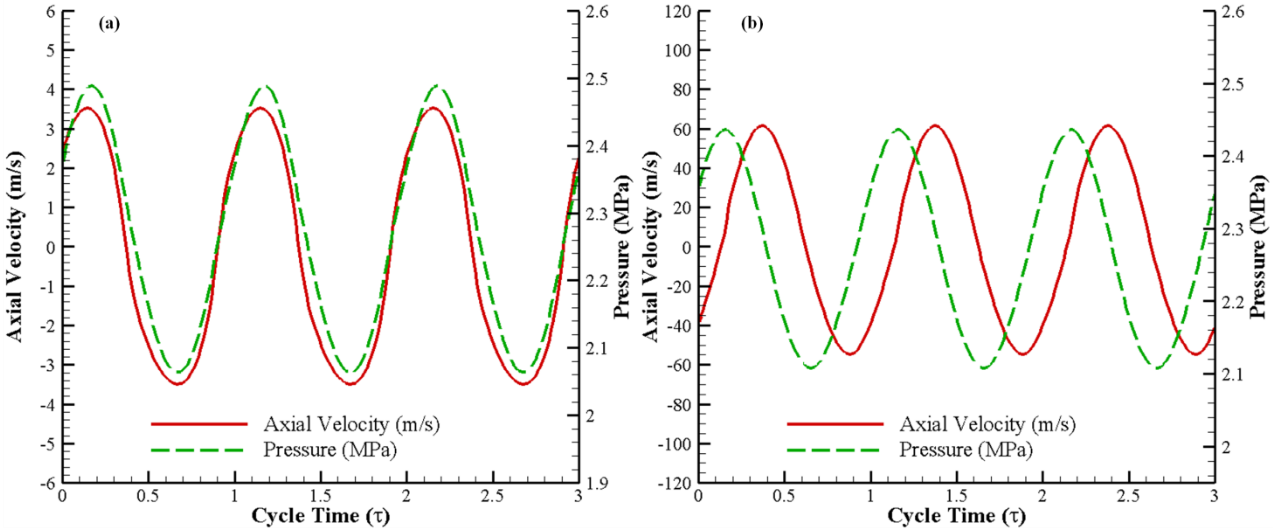

Figure 29. Temporal evolution of the pressure and velocity near quasi-steady state for case 5 at (a) center of the regenerator and (b) entrance to the inertance tube

### 4.2. Variation of the phase angle between pressure and velocity

In the previous sub-section, changing the value of inertance (varying the length of the inertance tube and keeping the diameter constant) was shown to affect the performance of the cryocooler. In figure 4a, the quasi-steady state (at 30 seconds) gas temperature at the exit of the cold heat-exchanger is plotted as a function of the inertance. As the inertance is increased, the temperature in the system decreases. This improvement in the performance is possible due to the increase in the pressure amplitude in the system (note: the piston amplitude is not changed) from 0.14 MPa to 0.21 MPa (see figure 4b).

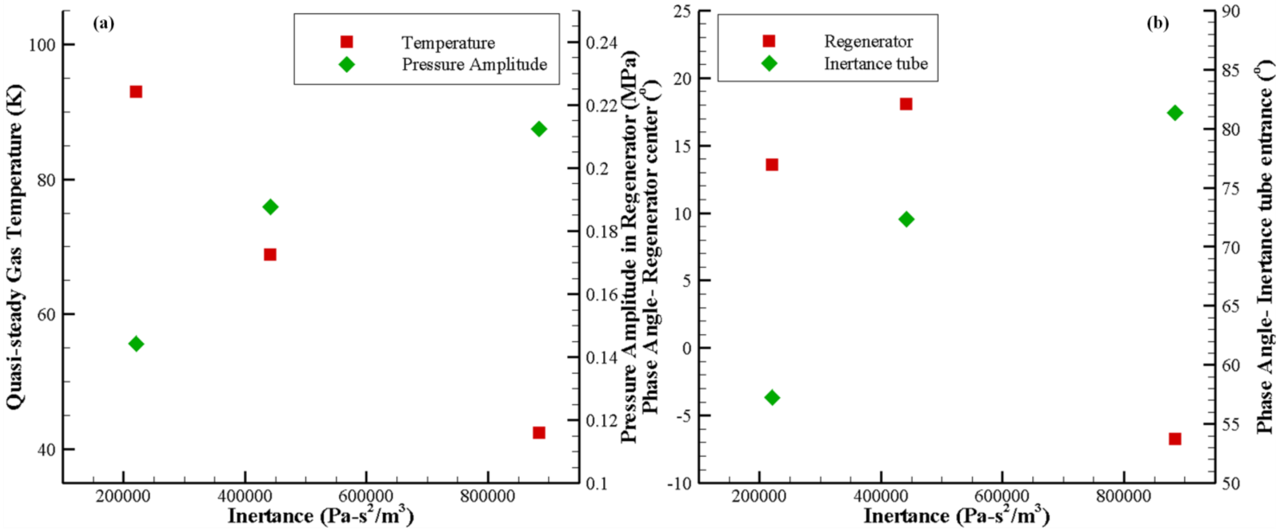

Figure 30. (a) Quasi-steady gas temperature and pressure amplitude in the center of the regenerator and (b) phase angle between pressure and velocity at different locations as a function of the Inertance '$M$'

The phase angle difference between the pressure and the velocity in the regenerator and at the entrance to the inertance tube is important to the performance of a pulse tube cryocooler. For a given input acoustic power (PV power, i.e. for a constant piston amplitude), the pressure and velocity (or mass flow rate) at the center of the regenerator must be in phase [1]. This reduces the magnitude of the velocity in the regenerator and hence reduces the losses that occur in the regenerator (which are dependent on the velocity/mass flow rate) [1]. In figure 4b, the phase angle difference between the pressure and the velocity is plotted as a function of the inertance. As seen in figure 4a, an increase in the inertance increased the pressure amplitude and hence improved the performance. However, at the highest value of inertance investigated here, the phase angle difference is at a minimum and this consequently reduces the losses in the regenerator. In keeping with previously published theory [1], the magnitude of the velocity decreases in the regenerator when the phase difference decreases. For case 5 (phase angle $\varphi$ = -6°), the magnitude of the velocity in the regenerator center is 3.52 m/s compared to case 2 where the magnitude of the velocity is 4.92 m/s ($\varphi$ = 18°).

## 5. CONCLUSIONS

The numerical study reported here investigates the effects of the length and diameter of the inertance tube on the performance of an IPTR. In the CFD model, the continuity, momentum and energy equations are solved for both the refrigerant gas (helium) and the porous media regions (the regenerator and the three heat-exchangers). The effects of different diameter of the inertance tubes and different values of inertance on the performance of the system are investigated. The value of inertance is maintained constant by changing both the diameter and the length of the inertance tube (the inertance is proportional to the ratio of the two). Maintaining this value constant does not significantly affect the performance of the system (2 – 5 K difference in the three cases studied). When the value of inertance is changed (keeping the diameter constant and varying the length of the inertance tube), larger variations in the performance are observed (~ 50 K). In the current study, increasing the inertance increased the pressure amplitude in the regenerator and hence an improvement in the performance was observed. However, it is important to note that at the highest value of inertance studied ($M$ = 884180.42 Pa-s$^2$/m$^3$), the phase angle difference between the pressure and the velocity at the center of the regenerator was minimum. This is another possible reason for the improvement in the performance observed. By minimising this phase difference, the velocity magnitude in the regenerator was decreased and hence the regenerator losses were decreased (losses are dependent on the velocity). Further investigation is required to find the inertance value (and the corresponding phase difference at the entrance to the inertance tube) at which the phase difference between pressure and velocity at the center of the regenerator is close to zero (optimum performance), however the present results compare well with established theory.

## 6. ACKNOWLEDGEMENT

The work reported is supported by the US National Science Foundation under grant CBET-0853959.

## 7. REFERENCES

1. Radebaugh, R. *Pulse tube cryocoolers for cooling infrared sensors*. 2000. San Diego, CA, USA: Society of Photo-Optical Instrumentation Engineers.
2. Marquardt, E.D. and R. Radebaugh, *Pulse Tube Oxygen Liquefier.* Adv. Cryo. Eng., 2000. **45**: p. 457-464.
3. Antao, D.S. and B. Farouk, *Experimental and numerical investigations of an orifice type cryogenic pulse tube refrigerator.* Applied Thermal Engineering, 2012.
4. Kinsler, L.E., et al., *Fundamentals of Acoustics*. Third ed. 1982, New York: John Wiley & Sons, Inc.
5. Antao, D. and B. Farouk, *Computational Fluid Dynamics Simulations of an Orifice type Pulse Tube Refrigerator: Effects of Operating Frequency.* Cryogenics, 2011. **51**(4): p. 192-201.
6. Antao, D.S. and B. Farouk, *Numerical simulations of transport processes in a pulse tube cryocooler: Effects of taper angle.* International Journal of Heat and Mass Transfer, 2011. **54**(21-22): p. 4611-4620.
7. ESI-CFD-Inc., *CFD-ACE+ v2009.4 User Manual*. 2009, Huntsville, AL: ESI Group.
8. Radebaugh, R., et al., *Inertance Tube Optimization for Pulse Tube Refrigerators.* AIP Conference Proceedings, 2006. **823**(1): p. 59-67.

052

# 3-Cycle Pulse Tube Cooler for Cryogenic High-Power Applications

**Kuhn M., Kaiser G., Schildbach T., Schroeder G., Klier J., Herzog R.**

Hauptbereich Kryotechnik und Tieftemperaturphysik, Institut fuer Luft- und Kaeltetechnik
Dresden, Germany

## ABSTRACT

A new type of high-power pulse tube cryocooler (3C-PTC), composed of three connected single PTCs with a prospected cooling capacity of 1 kW at 80 K has been developed and is currently under investigation. With this arrangement the orifice or inertance tube at the warm end of the pulse tube of common PTC is replaced by an expansion piston. This principle enables a coefficient of performance (COP) which is comparable to that of Stirling cryocoolers. Furthermore, this arrangement allows the exact adjustment of the phase shift between pressure wave and volume flow. In the 3C-PTC the expansion piston of the previous cycle supports the compression piston of the following cycle, being combined to form a single moving part driven by a high-force synchronous oscillating motor. So a crank shaft can be avoided what ensures low vibration and low-noise operation. The 3C-PTC is suitable to supply cooling power for high-power applications like high-temperature superconducting fault-current limiters, motors and generators. The target COP of about 12% is significantly higher than that of commercial systems. The 3C-PTC is already manufactured and first experimental results will be presented.

This work has been supported by the German Federal Ministry of Economics and Technology (contract no. EN MF 090051)

## 1. INTRODUCTION

The market of high-temperature superconducting (HTS) power applications is growing intensively. The first prototypes of HTS-cables, motors and fault current limiters are already running, all requiring a cooling capacity between 50 W up to some kW between 65 and 80 K. Some detailed information is summarized in Table 7 [Gouge]. Most of these devices are designated to guarantee our energy supply in the near future. Reliability, low or free maintenance and low costs are therefore the main prerequisites for a cryocooler for such systems which are not available on the market at present. The intention of the authors was to develop an energy-efficient cryocooler with high cooling capacity which meets these demands of the HTS applications.

Table 7: Typical or anticipated heat loads at Top for HTS components [Gouge]

| **HTS Component** | **BSCOO Heat Load, $T_{op}$** | **YBCO Heat load, $T_{op}$** |
|---|---:|---:|
| Cable (per phase) | 3-5 kW/km at 65-80K | 3-5 kW/km at 65-80 K |
| Transformer (5-100 MVA) | 50-100’s W at 25-45 or 65-80 K | 50-100’s W at 60-80 K |
| Motors (750-7500 kW) | 50-200 W at 25-40 K | 50-200 W at 50-65 K |
| Generators (10-500+ MWe) | 100-500 W at 25-40 K | 100-500 W at 50-40 K |
| FCLs | 30 W at 30 K, 750 W at 80 K | ~ kW at 50-80 K |
| SMES, magnetic separation, MRI, etc. | 10’s of watts at 20-30 K | 10-100 W at 50-65 K |

# 2. CRYOCOOLER CONCEPT

## 2.1. Phase Shifter Concept

One of the main drawbacks of ordinary pulse tube coolers is the exergy loss due to irreversible thermodynamic processes in the passive phase shifter, like inertance tube or orifice. The expansion piston with its active-reservoir of the 3C-PTC obviates this exergy loss. The heat gained (e.g. the cooling capacity) at the cold heat exchanger, is generated by volume work and transferred via the pulse tube as in any pulse tube cooler. As distinguished from ordinary pulse tubes a high percentage of heat at the warm end of the pulse tube is transferred to the expander for the transformation into mechanical work. The hot heat exchanger at the end of the pulse tube is therefore obsolete. It should be noted that also other pulse developments offer solutions to avoid these drawbacks. Examples are for instance the development of Matsubara [Matsubara] with active buffers at the hot end of the pulse tube, the four valve pulse tube refrigerator of Thürk and Kaiser [Thürk], or a pulse tube cooler with a phase shifter of Kaiser [Kaiser] et al. presented at the ICEC 23 in July 2010.

## 2.2. How it works

The working principle of the 3C-PTC is based on the development of an active reservoir pulse tube cooler (AR-PTC) which is shown in Figure 31.

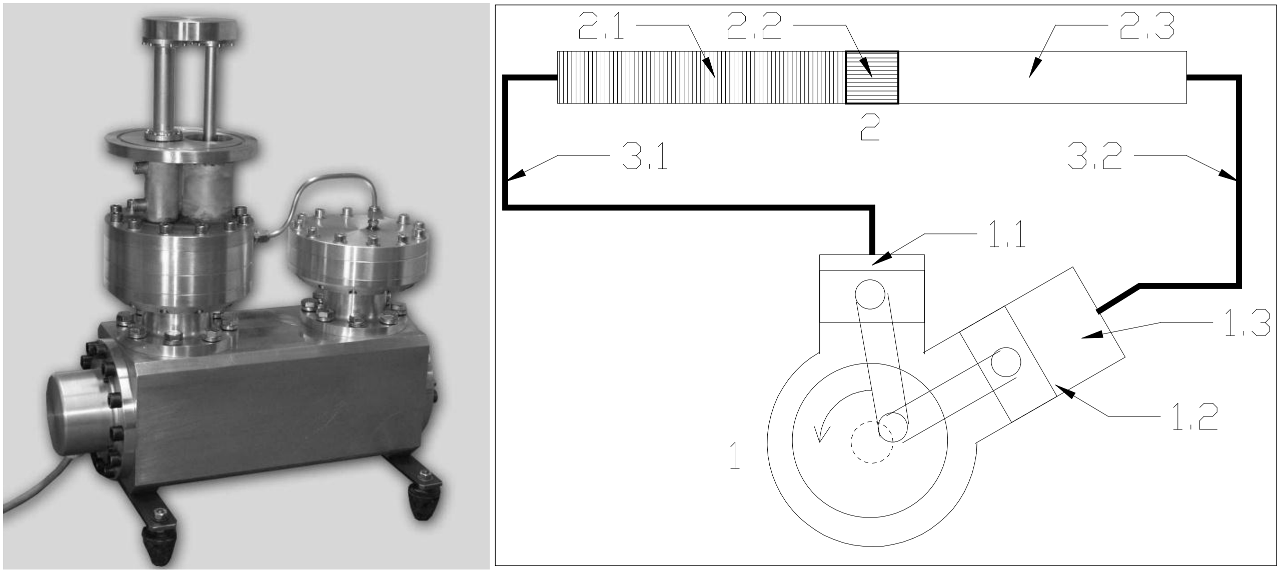

Figure 31: Activ-Reservoir-Pulse-Tube-Cooler (1 drive, 2 thermal head, 1.1 compression piston, 1.2 expansion piston, 1.3 expansion space, 2.1 regenerator, 2.2 cold finger, 2.3 pulse tube, 3.1/3.2 pressure lines)

The working principle can be described in four phases.

First, in the compression phase the working gas is moved via hot heat exchanger, regenerator and cold heat exchanger to the pulse tube by the ascending compression piston. Compression heat is removed in the hot heat exchanger mainly; a lower part is absorbed in the regenerator so that the gas enters the cold heat exchanger with almost the same temperature. Due to the adiabatic pressure rise, the temperature increases at the warm end of the pulse tube.

In a second phase, by further ascending compression piston and descending expansion piston the superheated gas is transferred to the expansion space isobaric. The temperature rise of the first phase is removed in the expansion pipe partly.

In the following expansion phase the pressure is relieved by further descending pistons. In this way the gas cools down. The temperature rise at the warm end of the pulse tube is removed completely. At the cold end of the pulse tube and in the cold heat exchanger the gas is already sub-cooled. The gained mechanical work supports the compression piston.

In the last phase with a descending compression piston and an ascending expansion piston, the sub-cooled gas it transferred via cold heat exchanger, regenerator and hot heat exchanger to the compression space isobaric. Heat is removed in the cold heat exchanger and the regenerator is re-cooled. From this point the cycle starts again.

The AR-PTC is able to deliver a cooling capacity of 12 W at 80 K. The design, mainly the crank shaft, leads to some drawbacks like frictions losses, high vibrations and noise emissions, which will be avoid in the novel 3-cycle arrangement.

### 2.3. 3-cycle arrangement

The arrangement is shown in Figure 32. In the case of the 3C-PTC this mechanical work is directly used to support the compression. Consequently the compression piston of the previous cycle is combined with the expansions piston of the following cycle to a single oscillating compressor-expander unit. The driving force is generated by linear motors powered by a 3-phase frequency converter; hence the phase shifting is exact 120 degree. The three cold parts are composed of a hot heat exchanger, a regenerator, a cold heat exchanger and pulse tube in series.

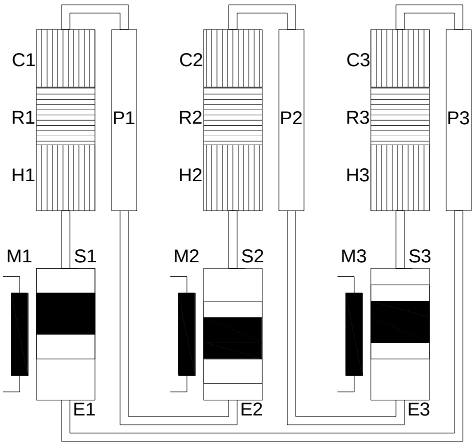

| | | | |
|---|---|---|---|
| 1-3 – index of cycle | E – expansion space | M – linear motor | S – compression space |
| C – cold heat exchanger | H – hot heat exchanger | P – pulse tube | R – regenerator |

Figure 32: Arrangement of the three cycles

A fixed phase shift between volume flow and pressure wave of 120° is inherent by this arrangement which also leads to a low-noise and low-vibration operation. A patent for this arrangement is already published [EP].

## 3. CALCULATION

### 3.1. Calculation of the thermodynamic cycle

The 3C-PTC was designed and modelled by the use of the commercial software package SAGE (Gedeon Assoc.). The calculation was performed with the parameters shown in Table 1.

Table 8: Parameters 3C-PTC

| **Parameter** | **Value** |
|---|---:|
| cold head temperature | 80 K |
| cooling capacity | 1000 W |
| input power | 8.5 kW |
| re-cooling temperature | 323 K |
| operating frequency | 25 Hz |
| working gas | Helium |
| average pressure | 25 bar |

Figure 33 shows the calculated performance chart of the 3C-PTC. At the nominal cold-head temperature of 80 K the coefficient of performance (COP) is 12%, which is 33% of the Carnot efficiency. However, even at a cold head temperature of 65 K the cooling power is 650 W.

### 3.2. Calculation of the linear motors

For the dimensioning and calculation of the linear motors a spreadsheet tool was developed. The calculated data of the motor performance is shown in **Table 9**.

Table 9: Parameter Linear Motor

| **Parameter** | **Value** |
|---|---|
| magnetic induction | 294 mT |
| DC resistance | 2.6 Ω |
| force coefficient | 180 N/A |
| mechanical power | 8.5 kW |
| efficiency | 82% |

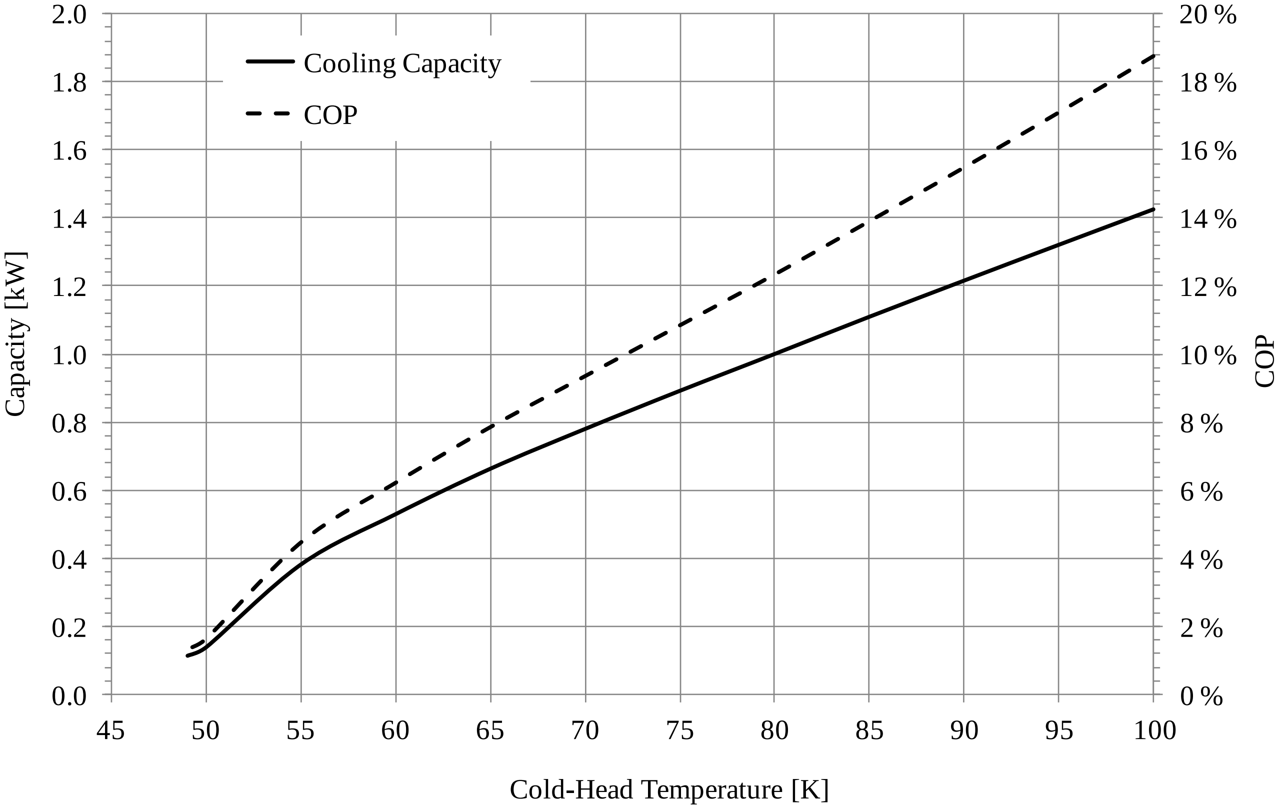

Figure 33: Calculated Performance Chart 3C-PTC

## 4. CONSTRUCTION DETAILS

### 4.1. Drive

The pressure wave generators are equipped with linear motors of the moving-magnet type. Sealing and guiding are realized with piston rings made of PTFE-carbon (see Figure 34 a), with the advantage that no lubricant is needed. Oil deposits in the regenerator matrix which is made of finest metal wire mesh (mesh #320) are therefore avoided.

### 4.2. Heat exchangers

Hot and cold heat exchangers are slot heat exchanger of the same design with different slot lengths. Wire erosion was used to manufacture the slots which are 0.45 mm high, leading to large areas for the heat transfer by small flow cross section. Figure 34b) shows one of the three hot heat exchangers with the water jacket. The hot heat exchangers are 180 mm long with a diameter of about 100 mm. The cold heat exchangers are 70 mm long; in the experimental model an electrical heater is attached to each cold heat exchanger to simulate a heat load.

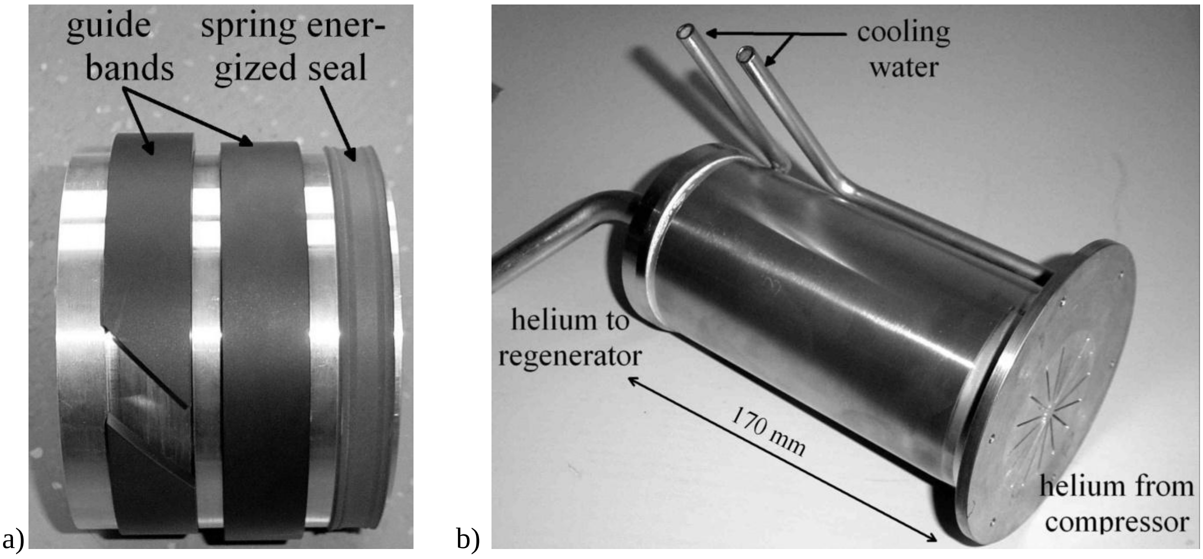

Figure 34: Construction details, a) piston with piston rings, b) hot heat exchanger

## 5. FIRST EXPERIMENTAL RESULTS

The assembling of the 3C-PTC was completed in springtime 2012. A 3-phase grid simulator is used for the fine adjustment of frequency, current and voltage to evaluate the best performance of the linear motors and the overall efficiency. Later a commercial 3-phase frequency converter is sufficient to operate the 3C-PTC. The first measurements were related to the testing of the sealing and guiding of the pistons to achieve an optimum between friction and leakage, resulting in a maximum pressure wave. In a next step performance tests will be carried out to determine the minimal cold head temperature and to record a performance chart of the whole system.

## 6. CONCLUSION

The intention was to design a self-sustaining cryocooler which is not only suitable for HTS-applications in matters of cooling capacity at a certain cold head temperature, but also meets the demands regarding low-maintenance, energy efficient and costs. The 3C-PTC was designed under the aspect to minimize the material and manufacturing costs in accordance with a compact design. As shown in Figure 35 the required footprint is less than 1 m² with a height smaller than 1 m.

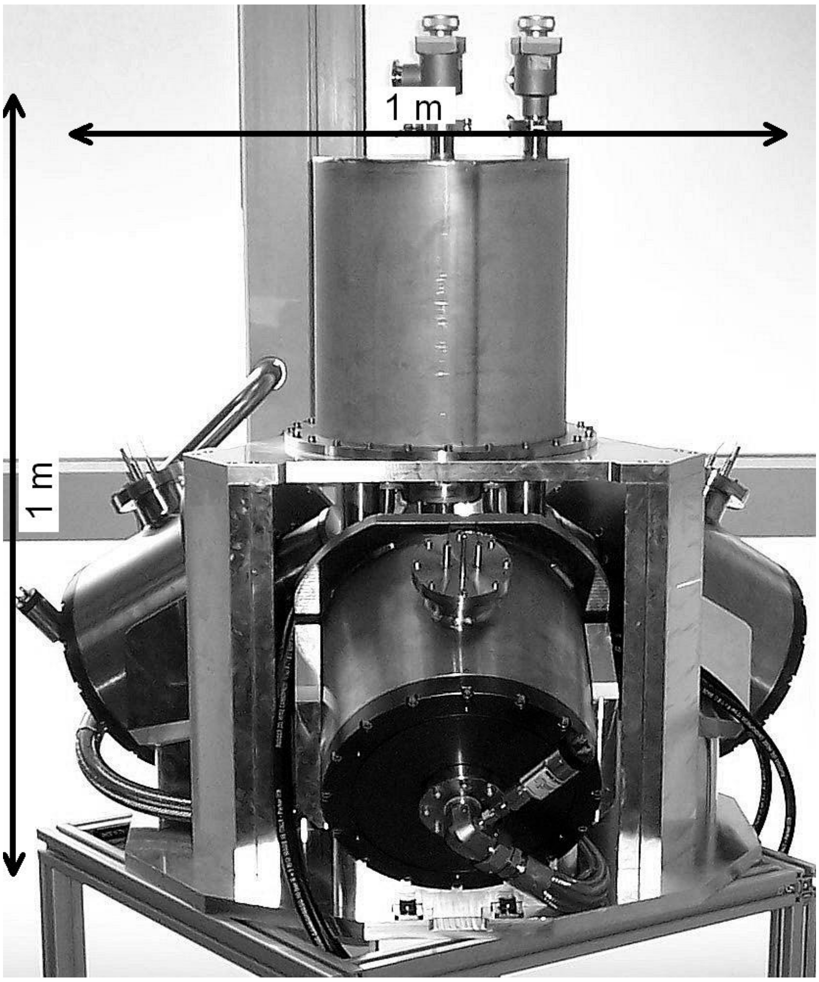

Figure 35: 3C-PTC

## 7. REFERENCES

Gouge M. J., et al., Cryogenics Assessment Report of *Oak Ridge National Laboratory*, May 2002, http://www.ornl.gov/sci/htsc/documents/pdf/CryoAssessRpt.pdf

Matsubara Y., et al., Investigation of active-buffer pulse tube refrigerator, *Cryogenics* Volume 37, Issue 8, August 1997, Pages 461–471

Thürk M., Kaiser G., Thermodynamic analysis of an ideal four-valve pulse tube refrigerator, *Cryogenics* Volume 36, Issue 7, 1997, Pages 527–533

Kuhn M., Kaiser G., Hadlich J., Bauer R., Klier J., About a new type of pulse tube cooler with linear motor drive and phase shifter, *Proceedings of the ICEC 23- ICMC 2010*, Wroclaw, Poland, July 2010, Pages 211–215

Kaiser G., Klier J., Kuhn M., EP2312239 (A2), Compound pulse tube cooler, European patent application

008

# Low Temperature Phase Equilibria of Refrigerant Mixtures

**Winkelmann D., Oellrich L.R.**

Karlsruhe Institute for Technology KIT Campus South, Institute for Technical Thermodynamics and Refrigeration (ITTK), Engler-Bunte-Ring 21, Karlsruhe, 76131, Germany

## ABSTRACT

There is a growing potential for possible areas of application for mixed refrigerant cycles (MRC), i.e. in bio-freezing, in cryo-medicine, in ht-superconductivity or for the liquefaction of gases. The attractiveness of MRCs lies in the possibility to employ commercially available standard refrigerant components also for cryogenic applications. The key to an efficient MRC design is the correct choice of the mixture's composition. Generally, wide-boiling mixtures are applied with some exhibiting strong non-ideal-behaviour like liquid-liquid-separation (VLLE). This requires exact knowledge of the phase behaviour of the applied refrigerants in the temperature range of interest. In case of a prerequisite of non-flammability currently the only choice to reach temperatures down to 100 K or below is the combination of fully and partially fluorinated HC with Argon, Nitrogen and/or Neon.

At ITTK, a test rig has been built to perform phase equilibrium measurements of binary mixtures in a temperature range from ambient to 100 K and pressures from near 0 to 35 bars. Two measurement principles were applied: A static equilibrium cell to measure boiling points and a cell with vapour circulation (dynamic method) allowing sampling of both, liquid and vapour phase. Thus, the complete set of phase equilibrium data (p-T-x-y-data) is obtained. The setup modifications are described and experimental data as well as models for adequate description of the phase equilibrium data are presented.

Key words: Low temperature phase equilibria, VLE, VLLE, MRC, refrigerant mixtures

## 1. INTRODUCTION

A steadily rising demand for refrigeration availability in the temperature range of 100 to 200 K can be satisfied efficiently by employing mixed refrigerant cycles (MRC). Constructed like an ordinary Joule – Thomson – Cycle, it is operated with a refrigerant mixture usually composed of up to 5 components. For the prerequisite of non-flammability possible refrigerant candidates include HFCs, FCs as well as Argon and Nitrogen. Due to the use of the mixture's heat of vaporization in the internal heat exchanger, the working pressures can be kept low and standard off – the – shelf components can be employed. By choice of a suitable mixture composition, the temperature glide of the evaporating refrigerant fluid can be extended from near ambient to the low target temperature (i.e. 100 K). As there are no moving parts at the cold end a MRC is also suitable for vibration – sensitive application in electronics cooling as well as for ht – superconductivity. By application of non-flammable refrigerant components, the fields of cryo – surgery and cryo – conservation of biological samples are also accessible. Once the refrigerant mixture displays a liquid – liquid – equilibrium at low temperatures, part of the evaporation takes place at near constant p,T which also permits the efficient (re-) liquefaction of pure gases on a small scale.

The key to an efficient use of this technology is the determination of the correct refrigerant mixture's composition. While mixture phase behaviour in most cases can be described adequately by use of thermodynamic models (EOS, $G^E$-approach) these models require experimental binary phase equilibrium information in the temperature range of interest to adjust the model's parameter. By looking at the open literature, reliable data for the envisaged non – flammable mixtures is scarce.

Therefore, the aim of this project is to provide experimental vapour – liquid – equilibrium – data (VLE) of binary mixtures of potential refrigerant candidates. A general setup equipped with 2 different cells was constructed. For near – boiling mixtures at low pressures a boiling point cell was constructed. It permits the measurement of boiling point data (p-T-x-data) for binary mixtures. In order to accomplish low temperatures in MRCs, however, some mixture's components must be wide boiling. Thus a second cell was constructed for measuring data of mixtures containing Argon and Nitrogen. This cell features a vapour circulation and permits the simultaneous determination of p-T-x-y-data.

# 2. EXPERIMENTAL SETUP

## 2.1. The Gas Cryostat

The main component of the setup to achieve the low temperatures is the gas cryostat (Figure 36). It denotes a volume, insulated against ambient by a double - walled vacuum shell and insulation material. The gas cryostat is filled with $GN_2$ as heat transferring agent. The centre area provides the space for an equilibrium cell which is suspended from a top flange. The equilibrium cell is surrounded by a vertical cylinder, referred to as the “guiding vane”. Together with the ventilator at the bottom it forces the $GN_2$ on a toroidal track. On its way, the $GN_2$ passes a copper heat exchanger inside which liquid nitrogen ($LN_2$) evaporates. Hence, heat is withdrawn from the system and cooling provided. On its way along the outer side of the guiding cylinder, the flux of $GN_2$ passes an electric heater to fine – tune the temperature. The $GN_2$ then is sucked in by the bottom ventilator and pushed upwards in the centre part along the equilibrium cell. For the vapour circulation cell, the gas cryostat is equipped with observation windows on opposite sites. On one side, a light source is located. It illuminates the cell, enabling observations of the refrigerant mixtures physical phase condition inside the cell.

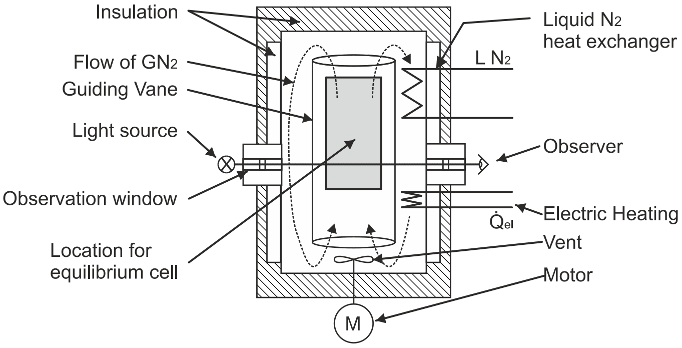

Figure 36: Schematic of the gas cryostat

With this setup, temperatures of about 90 K are experimentally accessible. At this level, the temperature can be kept constant to a value better than ±50mK inside the both equilibrium cells, see Figure 37(a) and (b). For higher temperatures, the fluctuation decrease significantly to about ±15mK (@ 173 K).

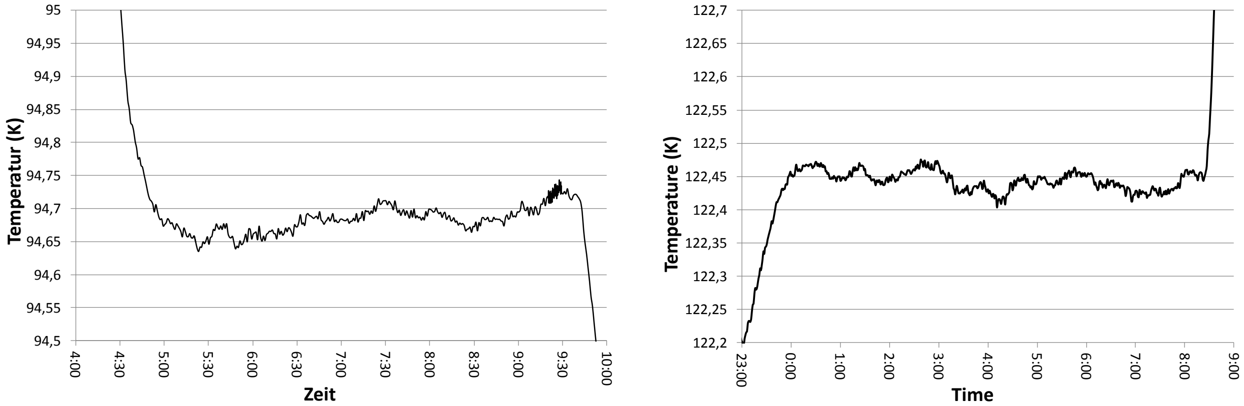

Figure 37: Course of temperatures in the boiling point cell (a) and the vapour circulation cell (b)

## 2.2. The Boiling Point Cell

For close boiling binary mixtures at pressures below 5 bars, the boiling point cell was built to measure boiling point data (p-T-x-data). The measurement principle demands for the cell to be almost completely liquid full. If the remaining vapour volume is negligible and if the equilibrium pressures are moderate, the liquid composition does not differ noticeably from the total composition which was gravimetrically filled in. Thus, the liquid equilibrium composition is determined from the total composition and the equilibrium is not disturbed by sampling.

A flow scheme is given in Figure 38(a). The equilibrium cell is placed inside the gas cryostat in the designated space. Once the cell is evacuated and cooled to low temperature, filling can take place. After evacuating and flushing the piping several times, refrigerant from a reservoir bottle is first condensed into a weighing bottle, placed on a high precision balance (Mettler Toledo Comparator PR2003). A capillary connection ensures gravimetric separation of the bottle’s weight from the piping. By differential weight measurement, the cell is then filled from the weighing bottle with the first component. Next, conducting a pure substance vapour pressure measurement ensures the purity of the refrigerant used. The pressure measurement is performed alike for pure substances and mixtures using the following steps. On the “secondary” side of the dead weight gauge, pressurized nitrogen is used to establish a slightly higher pressure than in the equilibrium cell. To achieve this, the “primary” equilibrium cell side and the “secondary” pressure side are connected by a high sensitivity differential pressure transducer (Rosemount 3051CD) with a range of 0..36 mbar. Once the differential pressure transducer senses the slight overpressure on the “secondary” nitrogen side, the exact value of the “secondary” side’s pressure is determined with the dead weight gauge (Pressurements T3500) and a barometric pressure transducer (Hg-Barometer). During these measurements, the cell’s temperature is continuously monitored by a Pt100 sensor. The obtained set of simultaneously taken p – T – data is then compared to the Refprop database [1] taken as the standard. Deviations of the pure substance vapour pressure were below 1% compared to the reference data (purity of substances at least 3.0 grade). By changing the first component upon every other binary mixture’ composition, the purity of both components could be monitored during the course of the experiments.

Once the purity was assured, the second component was condensed into the cell after thoroughly flushing the refrigerant supply side from the first component. With experimental skill, the challenge was met to fill the cell almost completely liquid full such that the remaining vapour volume did not alter the liquid composition from the total composition within an admissible value set as 1 mol%.

Due to the low temperatures, complete mixing takes a long period of time. To accelerate this process, a driver on the outside moved a magnetically coupled agitator vertically on the inside of the cell. During this process at constant temperature, the pressure signal was monitored. Usually after 8..10 h no change was detected anymore and thus, complete mixing and thus equilibrium was assumed and a pressure measurement of the mixture conducted as described above.

The range of application for this setup reaches from ambient to about 90 K as lowest temperature and from almost 0 to 35 bars, limited in pressure only by the dead weight gauge in use. The single values of the p – T – x – dataset could be determined with the following precision: for pressures above 184 mbar the relative deviation was less than 1 %, in temperature it was less than ±50 mK for the entire range and in composition it was chosen such that the relative deviation ranged below 1 mol% (i.e. mixture composition between 10 and 90 mol%).

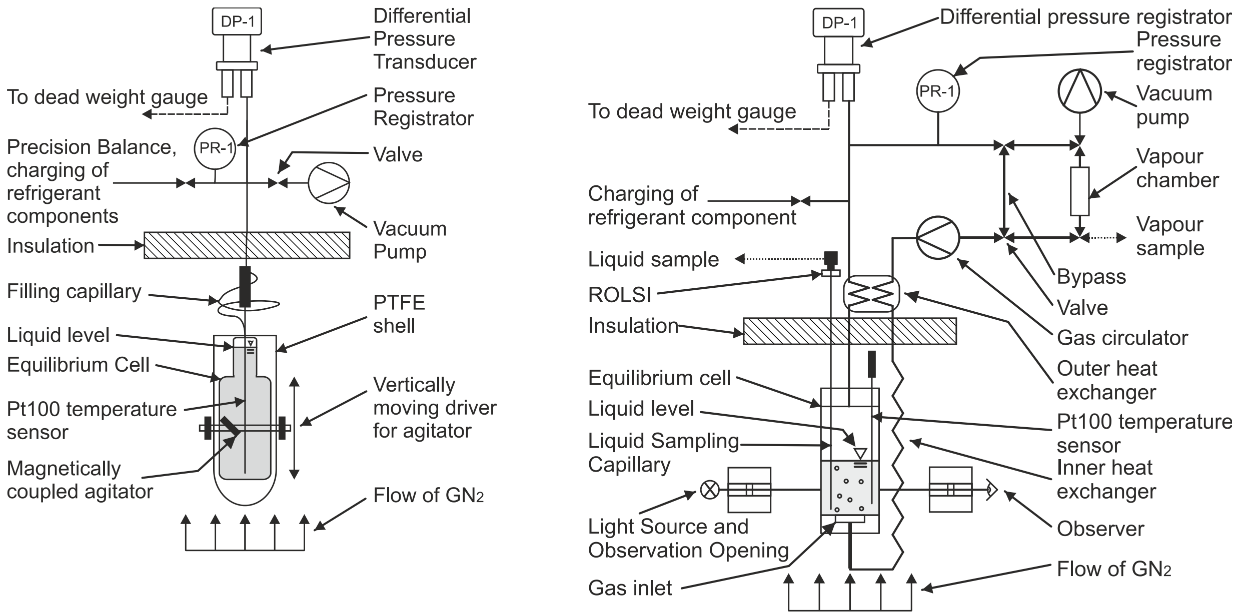

Figure 38: Scheme of the boiling point cell (a) and scheme of the vapour circulation cell (b)

## 2.3. The Vapour Circulation Cell

As the MRC process is based mainly on the use of wide – boiling multi – component refrigerant mixtures, there was the necessity to determine phase equilibria of wide – boiling binary mixtures such as partially fluorinated ethanes mixed with Argon or Nitrogen. From different cell types reported in literature [2], the setup given in Figure 38(b) was constructed with the following features. To cope with the wide – boiling mixtures, the cell was designed for high pressures of up to 70 bars. The vapour circulation accelerates the process to establish equilibrium conditions in the cell. Also, vapour phase samples can easily be drawn at ambient conditions. Together with a liquid sample the complete set of VLE – information is available (p – T – x – y - data). Moreover, an observation window offers the possibility to detect physical phenomena such as liquid – liquid – equilibria (LLE).

The cell is placed in the same gas cryostat described above in Figure 36. Filling of the cell is done directly from the refrigerant reservoir into the already evacuated and cooled equilibrium cell. Pure substance vapour pressure measurements ensured the purity of the substances used. Only if the relative deviations of vapour pressure to the reference database of Refprop [3] did not exceed 1%, the second substance was added.

To accomplish equilibrium conditions rapidly, the vapour phase was continuously circulated. It was withdrawn from the vapour space of the cell, led outside the cryostat through an outer heat exchanger to limit the heat input to the system and passed the differential pressure transducer (Rosemount 3051CD). By either sending the vapour through the vapour sampling chamber or via bypass, a representative volume of vapour could be isolated and analysed chromatographically (Agilent GC6890, GS-GasPro 60mx0.32mm column, TCD). The vapour circulation itself was driven by a gas circulator (Thomas Pumps GK-M12). Returning into the gas cryostat, the vapour is pre-cooled in the outer heat exchanger and then brought back to the equilibrium cell’s temperature in a second inner heat exchanger. Eventually, the vapour phase enters the cell through the bottom and mixes intensively with the liquid phase.

By observation of the pressure under isothermal conditions, equilibrium was achieved after 4..6 h and a binary phase equilibrium measurement could be performed. Immediately after the pressure was recorded, a total of 5 liquid phase samples were taken via the liquid sampling valve (Transvalor ROLSI). This commercially available magnetic valve was connected with the equilibrium cell with a 600x0,1 mm capillary. To avoid a vapour phase that may have formed inside the upper part of the capillary thus possibly falsifying the true liquid composition, the first volume after opening the valve was purged to the vacuum pump before switching to fill a sample cylinder. The quantity of the sample had to be sufficient for chromatographic analysis on the one side (considering strong asymmetric compositions of the wide – boiling mixtures) but small enough to not disturb the equilibrium itself. Finally, by diverting the vapour flux to the bypass, a vapour sample was taken, which could be sent directly to the GC for analysis.

With this setup, temperatures around 100 K were experimentally accessible. Again, the accessible pressure ranged from almost 0..35 bars. The temperature stability inside the cell was about ±15 mK.

As for the single sets of p - T – x – y – data, each quantity is afflicted with an uncertainty. These are for the temperature ±50 mK for the entire range, for the pressure generally below 1% and in concentration ±0,25 mol%.

## 3. EXPERIMENTAL RESULTS

### 3.1. The binary mixture of $N_2$ / Ar

To validate the proper working of the boiling point cell at the lowest temperature the system $N_2$ / Ar was examined.

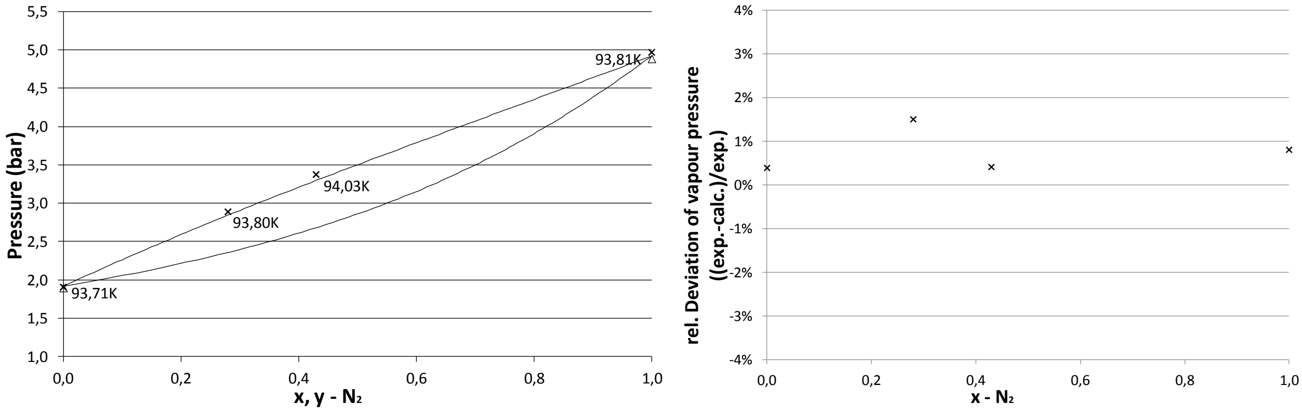

Figure 39: p-x-y-Diagram of the binary mixture $N_2$ / Ar at 93,8 K [5] (a) and relative deviation of vapour pressure of ITTK experimental data compared to GERG-2008 (b)

The experimentally determined boiling points are given in Figure 39(a). As a reference, the GERG - 2008 [4] method incorporated in Refprop [3] was available and the phase envelope for 93,8 K is also given in Figure 39(a). In [4] experimental literature data were examined and evaluated before fitting the GERG - parameters only to approved datasets. The approved datasets in the temperature range of interest show a deviation in vapour pressure below 1 % [6]. This value is not exceeded by our own results which display an average deviation in vapour pressure of 0,78 %. The deviations of the individual ITTK data points to the GERG – 2008 model are given in Figure 39(b).

### 3.2. The binary mixture of $CH_4$ / $C_2H_6$

As a proof of function for the vapour circulation cell, the binary mixture of $CH_4$ / $C_2H_6$ was chosen as reliable literature data are available. The experimentally determined boiling- and dew – points are given in Figure 40(a) for an average temperature of 174,5 K (note the slightly higher temperature for the 2 highest concentrations). The envelope given in Figure 40(a) was calculated by Refprop [3] again with the GERG – 2008 - model. Also for this binary, the examined and approved GERG data sets were taken as a benchmark. The approved data sets in the temperature range of interest [7] possess a largest average vapour pressure deviation of 2,13 %. This exceeds by far the average deviation of vapour pressure of our own ITTK data points to the GERG reference (0,87%), see Figure 40(b).

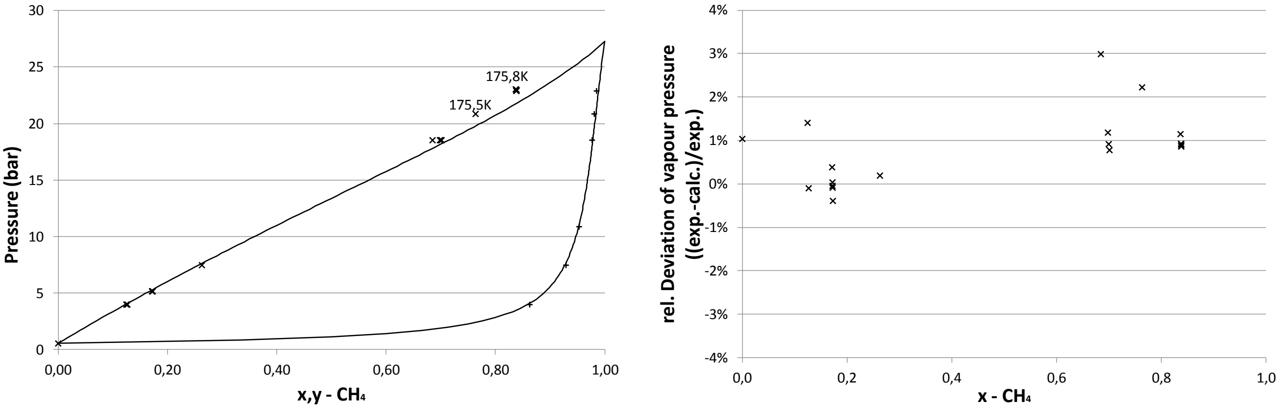

Figure 40: p-x-y-Diagram of the binary mixture $CH_4$ / $C_2H_6$ at 174,5 K (a) and relative deviation of vapour pressure of the ITTK experimental data compared to GERG-2008 from [3] (b)

### 3.3. The binary mixtures of Ar / R14 and Ar / R23

In order to expand the range of available phase equilibrium data for the synthesis of proper refrigerant working mixtures, among others the wide – boiling mixture of Argon and R14 was examined. The experimental data are given in Figure 41 for a temperature of about 142,8 K. Due to the chemical structure of the both components with each being (approximately) spherical and of non - polar character, the molecules fit together quite well. Accordingly, the mixture behaves near to an ideal mixture.

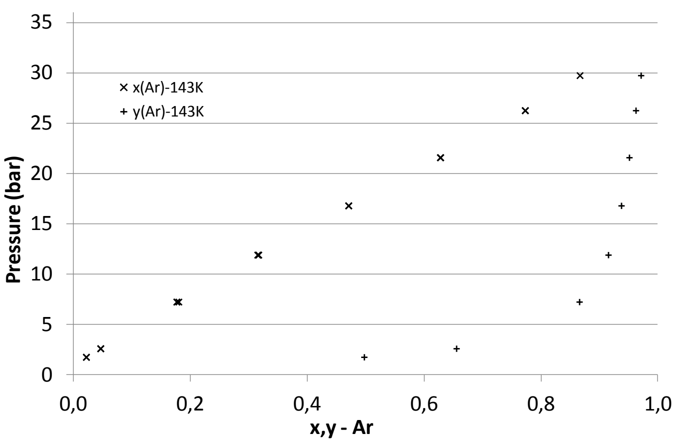

Figure 41: p-x-y-Diagram of the binary mixture Ar / R14 at 142,8 K

Phase equilibrium data of Argon and R23 (with R23 being the next relative to R14 in a homologous sequence from R14 to methane) is quite different. The experimental results for 2 isotherms at 142,9 K and 123,4 K are given in Figure 42. The difference in normal boiling points of the pure substances shifts from roughly 63 K (Ar / R14) to 94 K for Ar / R23. At 142,94 K / 34,51 bars and 123,24 K / 14,32 bars the continuous liquid phase separates into a light Argon –rich and heavy R23 – rich phase. The phase separation could be observed through the cell windows. Despite this behavior of the AR / R23 mixture, simple EOS like the Peng – Robinson – EOS (PR - EOS) [8] are capable of describing the physical behavior correctly. As can be seen from Figure 42, the PR – EOS depicts the loci of the LLE after their binary parameters were fitted to the ITTK data (please note the change of scale of the abscissa in Figure 42).

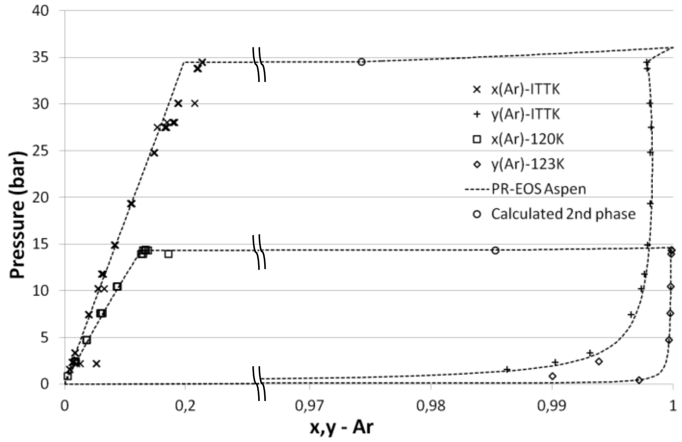

Figure 42 p-x-y-Diagram of the binary mixture Ar / R23 at 142,9 and 123,4 K with calculated phase envelopes at respective temperatures (PR-EOS)

## 4. SUMMARY

The present paper introduces 2 different types of equilibrium cells for the experimental determination of VLE data at low temperatures. The first, a static cell is designed for close boiling mixtures at moderate pressures. By applying this method one only receives boiling point data. Thus, the vapour phase composition has to be determined analytically. For wide boiling mixtures a second cell with vapour circulation was built. The vapour circulation accelerates the establishment of equilibrium conditions and allows easy sampling of the vapour phase. Due to the installed liquid sampling valve, the complete set of p – T – x – y – data is available. Together with the visual information about the physical condition of the mixture specific phase behaviour (liquid – liquid - separation) can be described correctly. Experimental data for validation as well as for binary mixtures of Argon with R14 and R23 is presented. Moreover it is shown that the physical behaviour (liquid – liquid - split) of some of these mixtures can be adequately described using simple cubic EOS.

## 5. ACKNOWLEDGEMENT

The authors would like to thank the Deutsche Forschungsgemeinschaft DFG for supporting this project.

## 6. REFERENCES

[1] Lemmon E.W. Huber M.L. McLinden M.O. 2007, NIST Standard Reference Database 23, Version 8.0, Boulder CO USA

[2] Muehlbauer A. Raal J-.D. 1998, *Phase Equilibria – Measurement and Computation*, Taylor and Francis, Washington USA

[3] Lemmon E.W. Huber M.L. McLinden M.O. 2010, NIST Standard Reference Database 23, Version 9.0, Boulder CO USA

[4] Kunz O. Klimeck R. Wagner W. Jaeschke M. 2006, The GERG-2004 Wide-Range Reference Equation of State for Natural Gases and Other Mixtures. To be published as GERG Technical Monograph. Fortschr.-Ber. VDI, VDI-Verlag, Düsseldorf Germany

[5] Winkelmann D. Oellrich L.R. 2009, Aufbau und Inbetriebnahme einer Tieftemperaturgleichgeswichtsanlage, *Proc. DKV Annual Meeting Berlin*, I.03

[6] Wilson G. M. Silverberg P. M. Zellner M. G. 1965, Advances in Cryo Eng. 10, 192

[7] Price A. R. Kobayashi R. 1959, Low Temperature Vapor-Liquid-Equilibrium in light Hydrocarbon Mixtures: Methane-Ethane-Propane System, J. Chem. Eng. Data Vol. 4 No. 1: 40-52

[8] Peng D.-Y. Robinson D.B. 1976, A new two-constant Equation of State, Ind. Eng. Chem. Fundam. Vol. 15 No. 1: 59-64

088

# Studies of Adsorption Characteristics of Activated Carbons down to 4.5K for the Development of Cryosorption Pumps

**Kasthurirengan S.[*], Behera U.[*], Gangradey R.[**], Krishnamoorthy V.[***], Udgata S.S.[***], Tripathi V.S.[****]**

[*]Centre for Cryogenic Technology, IISc, Bangalore 560012, India.
[**]Cryopump Group, Institute of Plasma Research, Gandhinagar, Gujarat 382428, India
[***]I-Design Engineering Solutions Ltd., Ubale Nagar, Wagholi, Pune 412207, India
[****]HEG R&D Centre, Mandideep, Raisen Dt. 462 046, India.

## ABSTRACT

Pumps based on cryosorption are the only solution to pump helium, hydrogen in the high magnetic field and high temperature environment of a tokamak. Activated carbons are the most suitable adsorbents for the above. For this development, the knowledge of their adsorption characteristics of activated carbons in the range from 4.5 K to 77 K is needed, but is scarce in the literature. Towards this, an experimental setup is developed for studies of adsorbents down to 4.5 K, which uses a commercial micropore analyzer operating at 77K along with a two stage GM Cryocooler for cooling the sample down to 4.5 K. This work presents the adsorption isotherms of several activated carbons from 4.5 K to 10 K for helium adsorbate along with their pore size distributions and surface areas. The effect of adhesives (used in bonding the activated carbons to panel) on the adsorption characteristics are also discussed. These results are useful in the development of cryosorption pumps.

## 1. INTRODUCTION

The pumping of helium, hydrogen and its isotopes in tokamaks is possible only by cryosorption pumps, since they offer high pumping speeds and can operate in the environment of radiation, high temperature and high magnetic field. Normally, the cryo-condensation pumps operating at 4.2 K, condenses all the gases whose boiling points are well above 4.2 K. This excludes helium and to some extent hydrogen also. To condense these gases, the cryosorption pumps are needed in which a porous sorbent is coated on the cryopanels. Of the various sorbent materials, activated carbon provides the large surface areas and hence high pumping speeds [1]. Also, activated carbons require moderate regeneration temperature (~ 400K). They are suitable for use to pump large volume flow rates of gases encountered in industrial processes [2-3]. To have the sorbent adhered to the cryosurface, it needs to be bonded by an adhesive. Thus the fabrication of the cryosorption panel involves the selection of the right sorbent (with high adsorption and long term performance) and the adhesive (with high thermal conductivity and withstanding temperature cycling).

To develop cryosorption pumps with high pumping speeds, the knowledge of the adsorption characteristics of activated carbons is necessary. Part of the adsorption surface areas of the activated carbons used is lost because some of their pores are blocked by adhesive. So there is a need to choose the activated carbon with the maximum possible surface area and high sticking coefficient for helium. However, such data is not available in the literature especially below 77K [1].

Hence an experimental setup has been built which uses a commercial micropore analyzer which operates at 77 K along with the two stage GM Cryocooler which enables the maintain the sample temperature from 4.5 K to 77 K. The sample port mounted on the Cryocooler is connected to the micropore analyzer by a thin walled stainless steel tubing and adsorption characteristics of the sample is studied by the micropore analyzer by the standard routines. Using the above, the adsorption isotherms of several activated carbons have been studied from 4.5K to 10K with helium gas as adsorbate. From this data, their pore size distributions and surface areas have also been evaluated. Some of the above works are discussed here.

## 2. EXPERIMENTAL SETUP

Figure 1. Experimental setup to measure adsorption characteristic at 4.5K

The photograph of the experimental setup built for adsorption studies is shown in Figure 1. A commercial micropore analyzer (Autosorb IQ, Quantachrome Instruments, USA), has been procured and this instrument can measure the adsorption characteristics of porous materials at 77 K with the sample is mounted in a glass sample chamber. This instrument initially degasses the sample by simultaneous heating and pumping. After degassing, the sample under study is moved analyzer port, wherein the measurements are performed. The sample in the glass port is maintained at 77 K by surrounding with the help of a liquid nitrogen bath. The warm and cold zone volumes are measured automatically and used in the measurements.

For measurements down to 4.5 K, the sample needs to be cooled to this low temperature. This is done by using a Cryocooler (Model SRDK-415 from Janis Research Systems Inc. USA). This two stage GM Cryocooler provides a refrigeration power of ~ 1.5W at 4.2 K at its second stage and ~ 35 W at 50 K in its first stage respectively. The sample under study is now mounted on the second stage cold head of the Cryocooler replacing the standard LN2 dewar. The thermal load to the second stage is minimized using the cooling power of the first stage as the thermal radiation shield.

Several layers of superinsulation are wrapped around first and second stage cold head to reduce radiation losses. Turbo molecular pumping system is used to evacuate the inter-space of the vacuum jacket. Silicon diode sensors (DT670 and SI410, from M/s SI, USA) are used to monitor the temperatures of second stage cold head. The cold head temperature can also be increased above 4.2 K with the help of two cartridge heaters (each of 50 ohms). The sample temperature can be maintained at any specific temperature in the range from 4.5 K to 77 K using a temperature controller (Model 332 from M/s Lakeshore).

For 4.5 K measurements, a stainless steel sample chamber with copper bottom is fabricated and mounted on the 2nd stage cold head of the Cryocooler and replaces the standard glass sample chamber used normally for 77 K measurements. Also, for experiments at temperatures other than that of the cold head, the sample temperature needs to be raised without affecting the Cryocooler performance. For this purpose, a gas heat switch is interposed between the sample chamber and the cold head. This consists of two interpenetrating copper parts welded into a thin walled stainless steel cylinder such that they are separated by a narrow gap. Normally, the upper and lower copper blocks do not touch each other. Hence, when this gap is evacuated, the switch is open. The upper part can be maintained at a temperature different from that of the lower part. However, when helium is filled in the gap, the heat switch is closed and both upper and lower parts will be at the same temperature, i.e. that of the cold head. This helps to raise the sample temperature from 4.5 K to 77 K without affecting the performance of the Cryocooler.

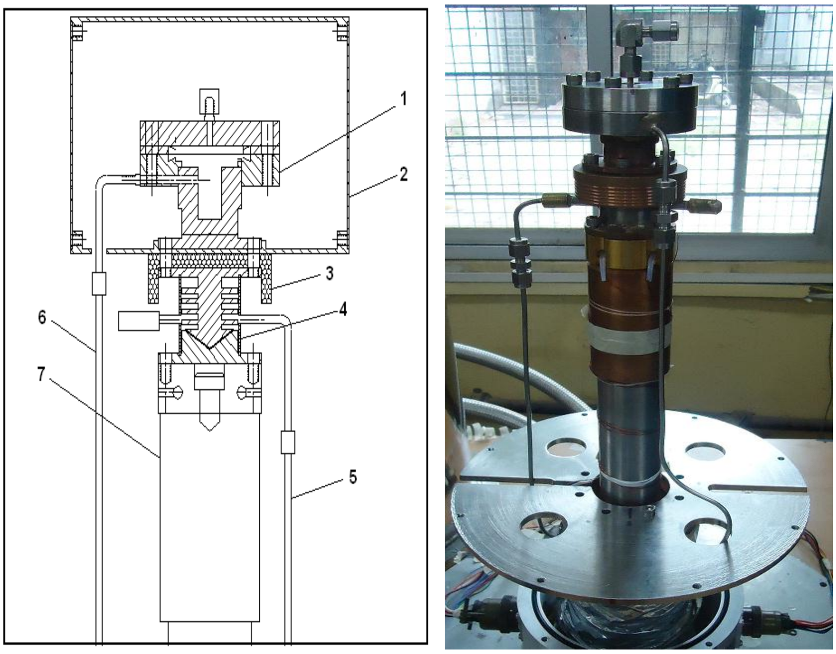

(a) (b)

Figure 2. (a) Drawing of sample chamber mounting on the cold head. 1. Sample chamber, 2. Radiation shield, 3. Heater, 4. Heat Switch, 5. Gas line for Heat Switch 6. Gas line for adsorption, 7. Second stage cold head. Figure 2(b) Photograph of the sample mount on the cold heat exchanger of the GM cryocooler.

The sample port has a volume of ~ 1 $cm^3$ and is connected to the adsorption analyzer with the help of 3.17 mm id stainless steel tube with appropriate end coupling. This smaller cross section pipe is used to reduce the void volume. Also similar pipe connections are used for gas entry into or evacuation of the heat switch. The sample under study is degassed outside since the cold head of GM Cryocooler cannot be overheated. After GM Cryocooler reaches the set cold end temperature, the adsorption measurements are carried out by the analyzer by a dosing routine run by a predefined program

## 3 EXPERIMENTAL RESULTS

The adsorption isotherms of several types of activated carbons have been studied at 77 K and in the temperature range 4.5 K to 10 K. The preliminary experiments were carried out with nitrogen gas as adsorbate at 77 K and later the same samples were studied between 4.5 K to 10 K using helium gas. The adsorption surface areas and the pore size distributions were determined from the measured adsorption isotherms using standard software.

### 3.1 Experimental studies at 77K using nitrogen gas

The adsorption isotherms plot the specific volume of gas adsorbed by the sample as a function of the relative pressure (ratio of actual pressure to saturated vapor pressure) at a constant temperature. Figure 3(a) shows the adsorption isotherms for different activated carbon samples. The samples studied are ACS-3 (Activated Carbon Speares-3), ACF- NW3 (Activated carbon fibers- Non woven), ACF-FK2 (Activated carbon fibers-Flate Knitted). Also included in this figure is the adsorption isotherm for standard alumina sample (SARM-2005) for comparison, which has a surface area of ~ 105 $m^2$ per gram. It is seen that activated carbon has higher volumes of adsorption when compared with the standard. Most of the carbon samples exhibit IUPAC classification type-I isotherms with an almost vertical rise at lower relative pressure range above 0.1. The alumina sample exhibits type-V isotherm.

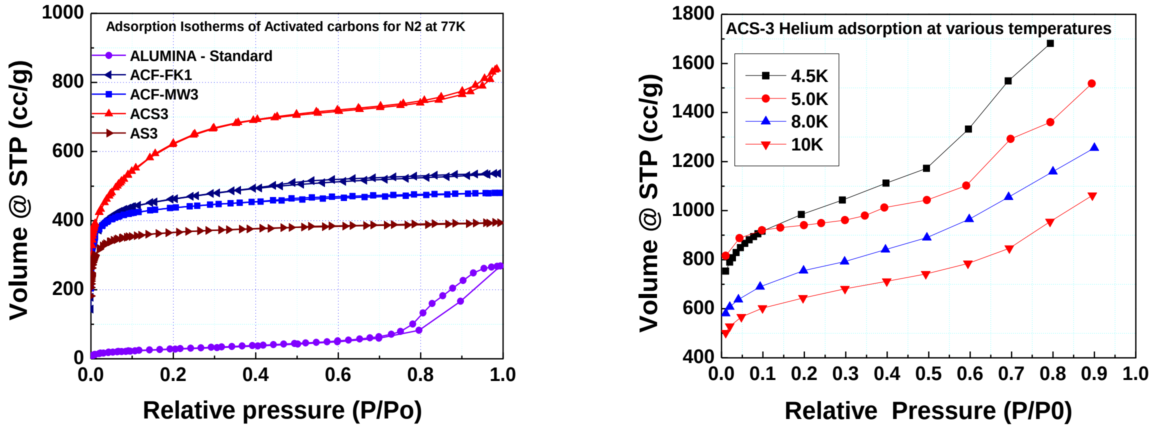

(a) (b)

Figure 3 (a) Adsorption isotherms of Standard Alumina sample and the activated carbon samples for nitrogen gas adsorption at 77 K. (b) Adsorption isotherms of ACS-3 activated carbon samples with helium between 4.5 and 10K

### 3.2 Experimental studies at 4.5 to 10 K using helium gas

The experimental procedure of measurements at 4.5 K is different when compared to 77 K measurement. At 77K, the dead volume measurement is done using helium gas because adsorption of sample at 77K with helium is nearly zero. However, at 4.5 K, helium gas itself is chosen as the adsorbate. Hence, the blank (adsorption of the sample chamber without the sample) measurements at these temperatures are carried out separately. This data is used for the measurements with the sample mounted in the sample chamber. The typical adsorption isotherms of a typical activated carbon globule sample namely ACS 3 is shown in Figure 3(b). It is observed that the adsorbed volume gradually increases with lowering of temperature. The adsorption volumes are also higher at lower temperatures for helium as adsorbate.

## 4. SURFACE AREAS AND PORE SIZE DISTRIBUTION

The adsorption surface areas of the samples can be determined by assuming that multilayer adsorption occurs over the sample surface starting from the initial monolayer. Thus, the standard BET technique is used in calculation of the surface areas of the activated carbons starting from the adsorption isotherms. The software provided along with the Autosorb IQ is used for the above calculations. The pore sizes are arrived at using the Density Functional Theory (DFT) method, using the experimentally measured isotherm data. The Autosorb IQ software enables the calculation of the pore size distributions.

Table 1 shows the surface areas of different activated carbon samples as determined by BET method with nitrogen as adsorbate at 77 K and helium as adsorbate in the temperature range from 4.5 K to 10 K. We note that the surface areas are in general larger at lower temperature and the surface area with nitrogen at 77 K nearly matches with that of helium in the temperature range 5 to 8 K.

Pore size distribution is one of the important characteristic of a porous material. The volume adsorbed by the sample depends on the pore size and pore type. The overall pore sizes for the activated carbon is in the range from 10 to 50 Ǻ. The pore sizes above 20 Ǻ contribute less to the adsorption. Activated carbon samples ACS-3, ACF- NW3, ACF-FK2 have pore sizes below 20 Ǻ and they are highly microporous [4]. On the other hand, SARM - Alumina sample has pore diameter of ~ 25 Ǻ and it is mesoporous.

To understand the influence of the pore size distribution on adsorption, we chosen activated carbon globules ACS-3 for the analysis. Figure 4 shows the pore size distributions of activated carbon ACS3 at 77K and at 4.5 K.

Table 1 Total surface area of the activated carbon samples by BET method at different temperatures.

| SAMPLES | SURFACE AREA MEASUREMENT –($m^2$/g) | | | | |
|---|---|---|---|---|---|
| | 77K (Nitrogen as adsorbate) | 4.5K (Helium as adsorbate) | 5K (Helium as adsorbate) | 8K (Helium as adsorbate) | 10K (Helium as adsorbate) |
| Blank | 0.00 | 0.12 | 0.00 | 0.00 | 0.00 |
| Carbon pellets | 1003.1 | 1465.1 | 1031.5 | 894 | 887.2 |
| ACS-3 | 2038.2 | 2700.3 | 2639.45 | 1963.4 | 1736.8 |
| ACFNW3 | 1773.2 | 1951.01 | 1924.1 | 1589.3 | 1335.2 |
| Srilanka Charcoal Granules | 1364.5 | 1801.2 | 1797.6 | 1188.5 | 1069.2 |
| ACF- FK3 | 2230 | 2920.2 | 2697.2 | 2582.6 | 2014.9 |
| Charcoal granule Coarse | 1126.74 | 1668.84 | 1576.49 | 1374.52 | 1235.61 |

From figure 4, it is seen that at 77K, the pore sizes have a distribution over the range from 10 Å to 35 Å. On the other hand, the 4.5K studies show that the major pore sizes are concentrated at about 15 Å. The pore size distributions at temperatures 5 to 10 K indicate a similar behaviour except that the peak around 15 Å gradually decreases with increasing temperatures

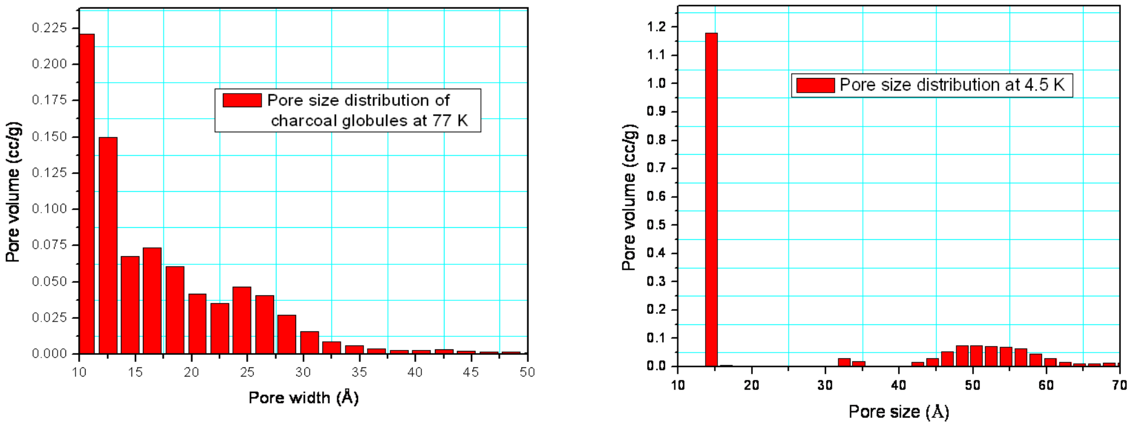

(a) (b)

Figure 4. (a) Pore size distribution of ACS-3 at 77K using nitrogen gas as adsorbate. (b) Pore size distribution of ACS-3 at 4.5 K

## 5. STUDIES ON ACTIVATED CARBON COATED ON ADHESIVE PANEL

To understand the actual performance of cryopanels, experiments are conducted on small size cryopanels wherein the activated carbons are mounted using an epoxy based adhesive. ACS-3 charcoal is chosen for this purpose. The base stainless steel cryopanel needs an adhesive coating onto which ACS-3 sample is adhered. It is observed that the epoxy based adhesive performs better than other types and hence this is chosen. The adsorption characteristics of the cryopanels coated with activated carbon ACS-3 samples were studied as follows. Initially the plain ACS-3 samples were characterized. Next, a stainless steel sheet of size 20 mm x 10 mm x 1 mm is finely coated with adhesive on its surface and experimented for its adsorption characteristics. Subsequently, the same size stainless steel plate coated with the adhesive and filled with activated carbon ACS-3 is studied for its adsorption characteristics. The performance characteristics of the various samples are shown in Table 2.

The results indicate that there is a reduction in the surface area of the ACS-3 coated onto the cryopanel and this value is ~ 10 % of that of the bare activated carbon ACS-3. This is easily understood since some of the pores are closed by the adhesive. Also, the average pore size of ACS-3 coated on the panel is found to be greater than that of the bare ACS-3. This is perhaps due to the interference of adhesives into the porous structure of the sample. Even though there is a decrease in the surface area and rearrangement of pore distribution, ACS-3 still exhibits micropore structure.

Table 2. Comparison of surface areas and average pore sizes of ACS-3 under different conditions.

| S.No. | Sample under study | Surface area in 77K with $N_2$ ($m^2/g$) | Average pore size in 77K with $N_2$ (Å) | Surface area in4.5K with He gas ($m^2/g$) | Average pore size in 4.5K with He gas (Å) |
|---|---|---|---|---|---|
| 1 | Activated carbon ACS-3 | 2031.6 | 7.60 | 2700.1 | 6.21 |
| 2 | Stainless steel sheet | 0.00 | 0.00 | 0.00 | 0.00 |
| 3 | Stainless steel coated with Adhesive | 0.00 | 0.00 | 0.00 | 0.00 |
| 4 | Stainless steel coated with Adhesive and ACS-3 | 1978.00 | 12.3 | 2600.7 | 11.81 |

## 6. CONCLUSION

An experimental setup has been designed and developed to measure adsorption characteristics of activated carbons down to 4.5 K. For this purpose, a commercial micropore analyzer operating down to 77K is coupled to a two-stage GM cryocooler, to enable cooling the sample temperature down to 4.5 K. A heat switch is mounted in between the second stage cold head and the sample chamber helps to vary the sample temperature from 4.5 K to 77K without affecting the performance of the cryocooler. The experimental results of adsorption of different types of activated carbons at 77K with nitrogen as adsorbate and in the temperature range 4.5K to 10 K with helium as adsorbate are presented. These results are evaluated in terms of surface area, pore sizes and their distributions. Also the performance of the small size cryopanels wherein the activated carbon ACS-3 is adhesively bonded is studied. It is observed that ACS-3 activated carbon is one of the best samples that can used for the development of cryopanels

## 7. ACKNOWLEDGEMENTS

The authors wish to acknowledge the financial support given by NFP, IPR, Ahmedabad, which enabled setting up of this experimental setup. They also acknowledge the valuable support given by M/s I-Design Pvt. Ltd., Pune and CCT staff towards the fabrication of this experimental setup.

## 8. REFERENCES

[1] Hauer.V, and Chr. Day., 2002, “Cryosorbent characterization of activated charcoal in the Coolsorb Facility”, Wissenschaftlische Bericht, FZKA 6745, Forschungszentrum Karlsruhe.

[2] Autosorb-1 Gas sorption analyzer system manual, 2009, Quantachrome Corporation, Boynton Beach, Florida. P/N 05098.

[3] Blacher.S, B. Sahouli.B, Heinrichs, P. Lodewyckx. R. Pirard Smith, H. L. and Jones, 2000, Micro pore size distributions of activated carbon, Langmuir 16, 6754-6756.

[4] Chr. Day, 2001, Use of active carbons as cryosorbents, Colloids and Surfaces, A: Physicochemical and Engineering Aspects 187–188, 187–206.

[5] Chr. Day, 2001, Use of porous materials for cryopumping, Hand book of surface and interference of materials, Academic press, 5, 265-278.

# CRYOTHERAPY, CRYOBIOLOGY

006

# Cryotherapy State-of-art and Challenges in Poland

**Chorowski M.*, Piotrowska A.*, Adamowicz B.**, Haladyn E.****

* Faculty of Mechanical and Power Engineering, Wrocław University of Technology, Wroclaw, Poland
** Kriosystem, Wroclaw Technology Park, Wroclaw, Poland

## ABSTRACT

Cryomedicine, especially cryotherapy aimed at tissue non-destructive treatment has been widely recognized as an appreciated method of pain relief, health improvement and biological regeneration. During a local treatment only a part of the body, like a joint or a muscle, is affected by low temperature. Local cryotherapy is realized with apparatuses consisting of a dewar vessel equipped with a vaporizer and a flexible hose. Whole body therapy can be carried out in cryochambers, which are supplied with liquid nitrogen, liquid air, or can be cooled with a cascade vapor compression cycle. The number of cryotherapy portable devices and whole body cryochambres is increasing. The paper gives an overview of the low-temperature medicine therapeutic methods and the current state-of-art in the cryotherapy and cryosurgery equipment. The construction of the cryochamber should provide a required temperature profile, lack of oxygen deficiency hazard and low liquid nitrogen consumption. Exploitation issues like mist formation and temperature variation are discussed.

## 1. INTRODUCTION

Poland is a country where cryomedicine is clinically approved, very well developed and widely used method of medical treatment. Figure 1 presents the classification of cryomedical methods together with cooling medium used in a dedicated apparatus.

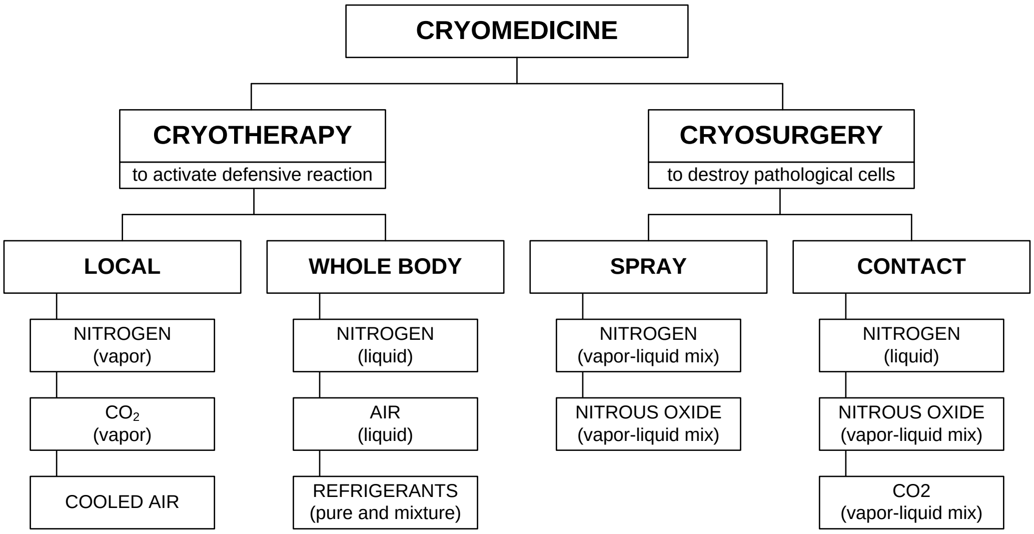

Figure 1. The classification of cryomedical methods

Considering the effect of low temperature influence, cryomedicine can be divided into cryotherapy and cryosurgery. Cryotherapy is a stimulating therapy, when a patient body is subjected to an effect of low temperature (as a rule below 150 K) within less than 3-4 minutes, in order to activate defensive reactions. These reactions are therapeutically beneficial and very effective in restoring the natural balance of the organism by raising of pain level threshold, muscle’s tension decrease and mobility increase, as well as shortening of convalescence time after contusions.

Cryosurgery is aimed at tissue necrosis (the destruction of pathological cells) following freezing of the water cellular. The decrease of tissue temperature can be obtained by two methods: either spray (direct evaporation of cryogens on the tissue surface) or contact (there is no direct contact between cryogen and tissue, liquid cryogen flows inside closed tip).

The following media are used as a working fluids in cryomedical equipment: nitrogen (both cryotherapy and cryosurgery), nitrous oxide (cryosurgery only), carbon dioxide (both cryotherapy and cryosurgery) and synthetic air (cryotherapy only).

## 2. CRYOTHERAPY

There are two main ways of cryotherapy specified in medical nomenclature: local cryotherapy and whole body cryotherapy.

### 2.1. Local cryotherapy

Removal of heat from a part of body like joint, or muscle (local cryotherapy) can be provided by either venting the cold gas over it or using cold cover. Four main methods to produce needed cooling power are commonly used: phase change, Joule-Thomson effect, heat transfer or thermoelectric effect. Figure 2 shows the structure of the local cryotherapy, whereas Figure 3 presents the exemplary functional schemes of equipment.

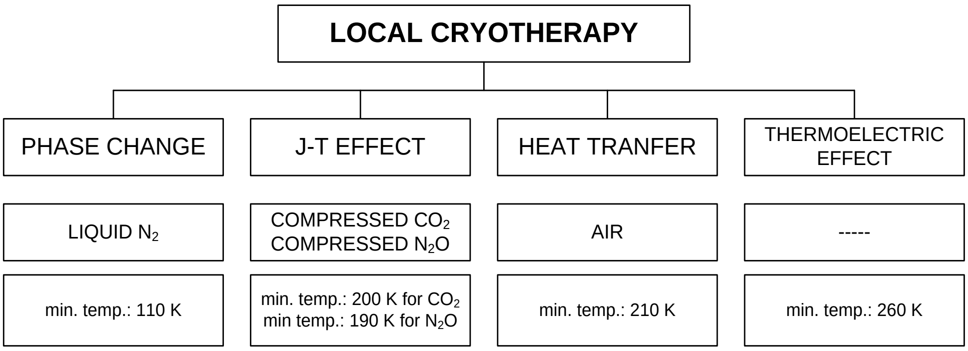

Figure 2. Local cryotherapy classification.

Figure 3a presents the apparatus where phase change is caused by heater installed inside dewar vessel filled with liquid nitrogen. Other option is that compressed nitrous oxide or carbon dioxide flowing through throttling valve, expands to the atmospheric pressure simultaneously decreasing its temperature (apparatus in Figure 3b). Different solutions are demonstrated in Figure 3c and 3d, where cooling system of the air flow is based on classic refrigeration unit, whereas low temperature can be also produced by Peltier effect.

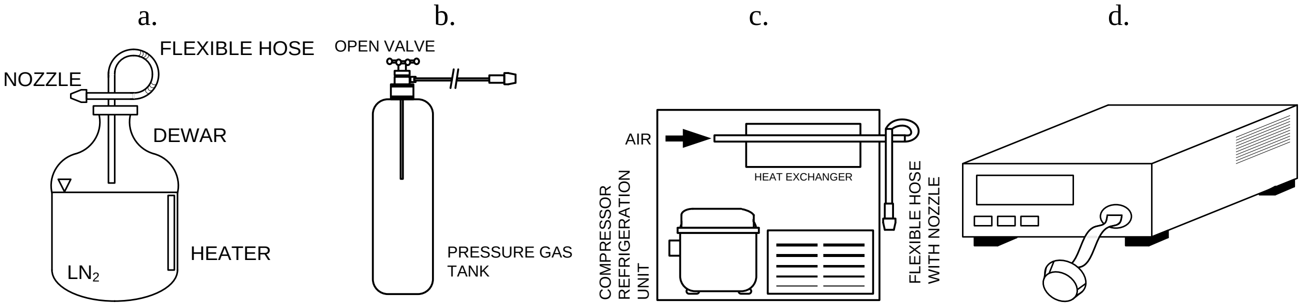

Figure 3. Cryotherapy equipment a. supplied with liquid nitrogen, b. supplied with compressed $N_2O$ or $CO_2$, c. using compressor refrigeration unit, d. using thermoelectric (Peltier) effect

### 2.2. Whole body cryotherapy

Whole-body cryotherapy is based on exposing whole body of a patient to the cryogenic temperatures influence. It is performed in so called cryochambers. A cryochamber is a large, closed, stationary and computerized medical device, supplied with a liquid nitrogen, synthetic air or compressor unit to provide cryogenic temperature inside. There are 3 construction concepts of cryochamber, room-type, cooling-retention type and cryo-barrel (called also cryo-sauna). The categorization of cryochambers together with appropriate working fluid is presented in Figure 4.

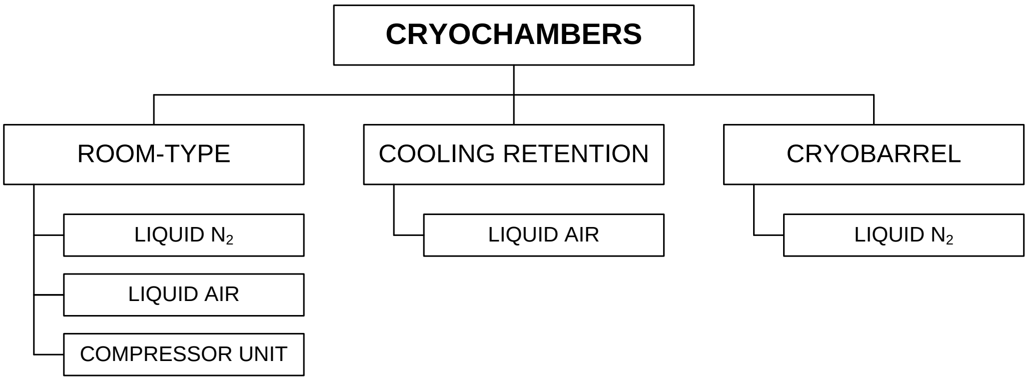

Figure 4. The classification of the cryochambers.

Figure 5 shows the overview of cryochamber design features. Room-type cryochamber is the most popular model, designed for clinics offering treatments for up to 300 patients per day (50-60 patient per hour).

A cryochamber consists of two rooms, pre-chamber (vestibule) and main cabin (Figure 5a). The vestibule is a transitional room with temperature level of about 210 K (- 60ºC), where the patients can get used to much more extreme thermal conditions. After about 30 seconds spent in the vestibule, the patients proceed into the main cabin. In the main cabin the temperature is maintained with thermal gradient from 150 K (-120ºC) to 110 K (-160ºC) at the level of knees to 240 K (-30 ºC) at the height of head. A typical cubature of the cabin and the vestibule is of about 15 $m^3$. One session of the whole body cryotherapy can last no more than 3 minutes.

The heat exchangers in cryochambers can be supplied either with liquid nitrogen, synthetic air or refrigerant fluid (circulating in compressor-based unit). In the $LN_2$ and refrigerant cooled cryochamber, the air vented into both cabins has to be purified, dried and cooled down, while the cryogenic installation of a cryochamber supplied with synthetic air is much simpler, the vaporized air does not need any additional purification and can be directly used for breathing.

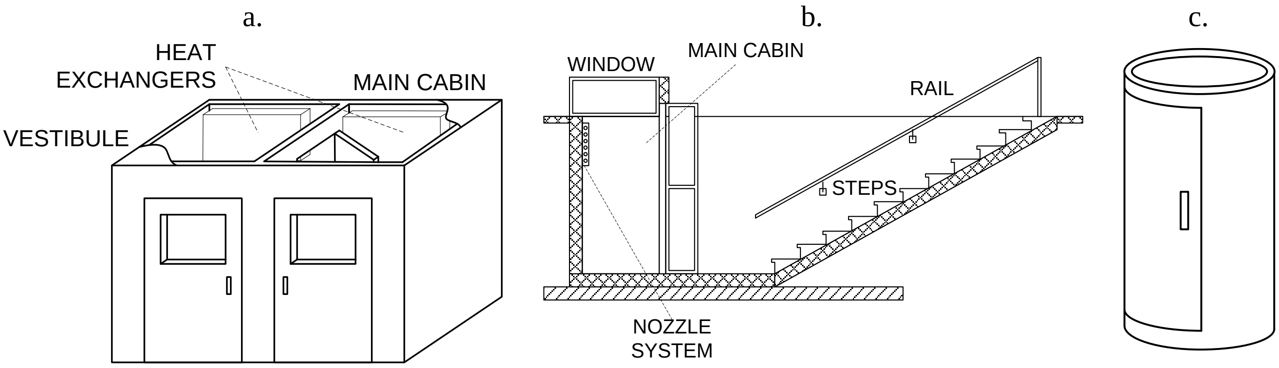

Figure 5. Cryochambers a. room-type b. cooling-retention type, c. cryo-barrel (cryo-sauna)

The cooling-retention type cryochamber is shown schematically in Figure 5b. The construction is based on phenomenon of keeping coldness close to the ground. The main cabin is located below the level of the operative floor, the staircase leading downstairs functions as the pre-chamber (vestibule). The system of the nozzles injects synthetic liquid air into cryochamber. It gives the possibility of enriching the atmosphere in the cabin with oxygen, up to 24-26%.

In each case an online monitoring of oxygen content in the chamber is necessary. The chamber door must be heater protected against freezing. Cryochamber under operation requires 10 minutes break each hour to decrease fog effect.

Cryo-barrel is a single-person cryochamber using the cold vapor of nitrogen to achieve a required temperature from 130 K (-140 ºC) to 110 K (-160 ºC). This kind of cryochamber provides no gradient temperature inside. The chamber is equipped with an elevated floor, so the patient inside is submerged in cold gas up to the shoulders only. The head is held above the low temperature “bath”, therefore the user breathes with warm environmental atmospheric air.

Since 1989, when the first cryochamber was designed, constructed and commissioned in Poland, the number of working chambers increases each year (see Figure 6). Dotted line presents perspective development of the market in next years.

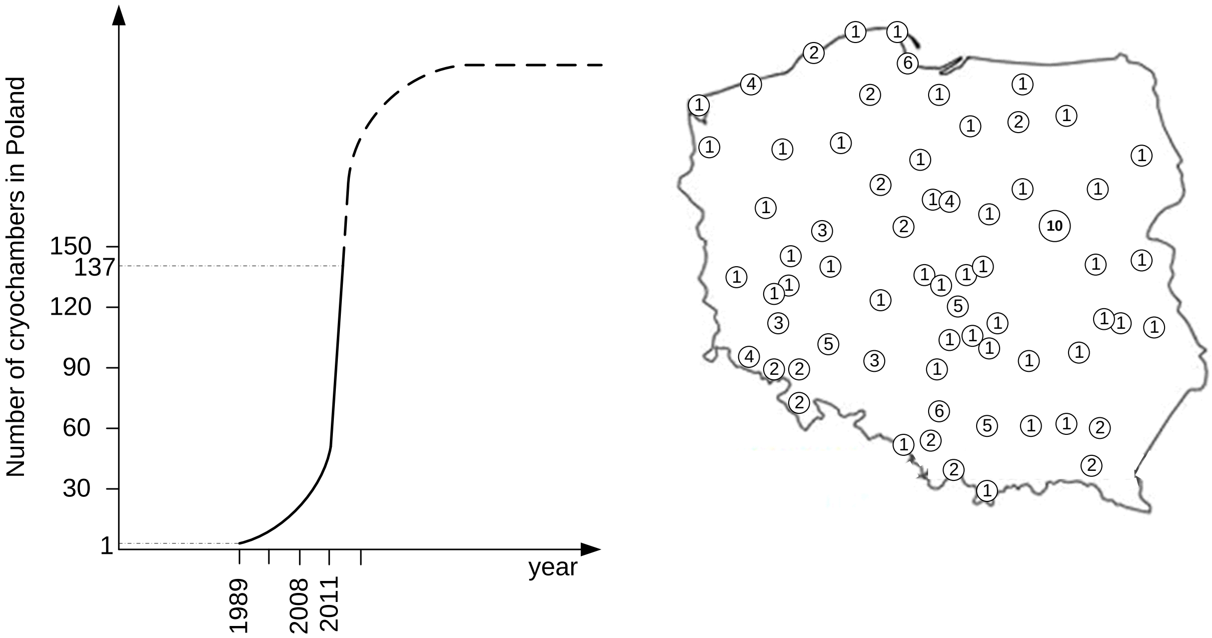

Figure 6. Market development for cryochambers in Poland, a. number of cryochambers installed and perspective development (dotted line), b. locations of the cryochambers in Poland

## 3. CRYOSURGERY

The main goal of cryosurgery is to destroy pathological cells. To complete the phase transition of cellular water, the temperature tissue has to be decreased to min. 250 K (less than -20°C). To provide required cooling power, either direct evaporation of liquid nitrogen or Joule-Thomson effect of $N_2O/CO_2$ expansion is used in cryosurgical apparatus. Figure 7 presents the categorization of cryosurgery methods together with working fluid and minimum temperature.

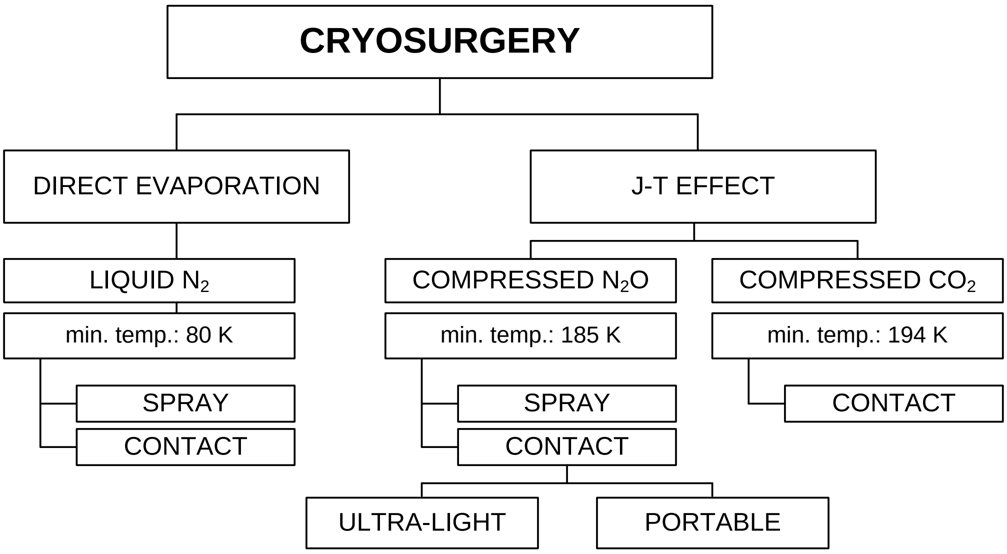

Figure 7. The categorization of cryosurgical methods.

Figure 8 shows the examples of cryosurgical equipment.

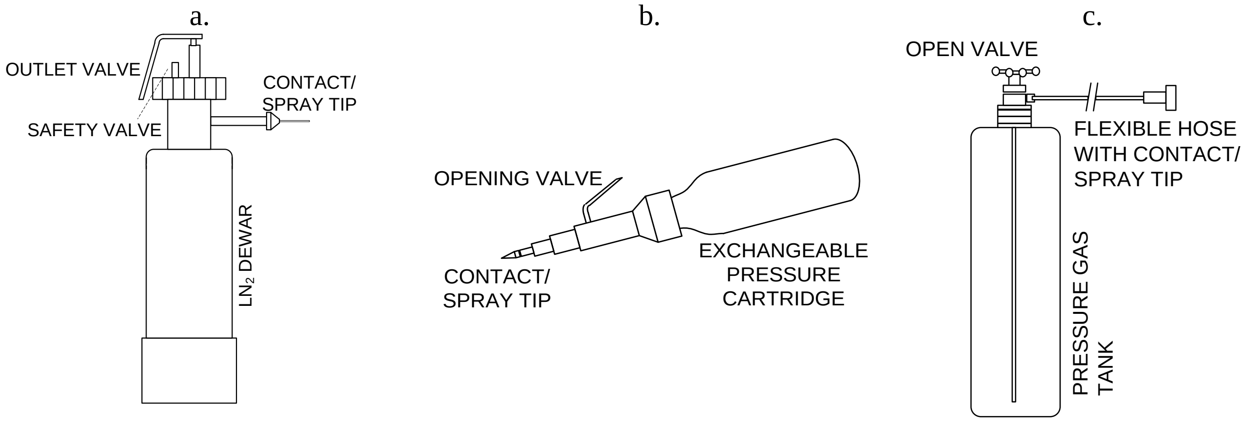

Figure 8. Cryosurgical equipment, a. supplied with liquid nitrogen, b. ultra-light device supplied with $N_2O$, c. portable apparatus supplied with $N_2O$

Figure 8a presents cryosurgical apparatus using direct evaporation of liquid cryogen at the tissue surface. Dewar is filled with liquid nitrogen and it is equipped with head including outlet and safety valves, contact or spray tip. Due to heat transfer through vessel wall, part of the liquid evaporates causing the increase of pressure. To start the flow the outlet valve has to be open.

Novel concept of ultra-light apparatus is presented in Figure 8b. The technical solution is similar to the portable apparatus (see Figure 8c), both devices are using J-T positive effect of nitrous oxide expansion, nevertheless ultra-light type is equipped with replaceable cartridge of 8 to maximum 25 g $N_2O$ (max. 70 treatment sessions per cartridge with highest volume).

## 4. CONCLUSIONS

Cryomedicine has been am emerging branch of medicine for more than 30 years. Poland is a country with the highest number of cryochambers installed worldwide. The market of cryotherapeutical apparatus in Poland is constantly increasing offering wide range of different devices and stimulating the technology development. Crymedical devices, especially cryochambers create a significant consumption sector for liquid nitrogen.

## 5. REFERENCES

Chorowski M., Liquid Gases in Cryo-Therapeutical Applications, Present Status and Perspective Development, *Proceedings of the CryoPrague 2006,* Praha, ICARIS, 2007

Chorowski M., Piotrowska A., Comparative analysis of the cryogens used in cryomedical applications, *Proc. XX International Cryogenic Engineering Conference,* Beijing China 2004, Elsevier 2006

Gabryś M. S., Popiel A., *Krioterapia w medycynie*, Urban & Partner Editor, Wrocław, 2003

Chorowski M., Piotrowska A., Polinski J., Nitrogen separation and liquefaction apparatus for medical applications and its thermodynamic optimization, *Adv. In Cryog. Eng.,* AIP, vol.51A, 2006

077

# Study of Contact Methods to Cool Biological Tissue in Local Surgery

**Kondratenko R.**[*], **Butorina A.**[**], **Nesterov S.**[*]

[*] Vekshinski State Research Institute of Vacuum Technology, Nagorny passage 7, Moscow, 117105, Russia
[**]Russian State Medical University, Ostrovityanova St. 1, Moscow, 117997, Russia

## ABSTRACT

The method to cool a biological tissue with capillary – porous coverage is studied for application in local cryotherapy and to cure consequences of acute injuries (contusions and sprains). The isotherm dynamics T(τ) by the depth Z of the cooled tissue (gel 4% gelatin solution, the tissue analogue in vitro) is investigated. The obtained data on isotherm dynamics T(τ) have been compared with calculation results. A flexible capillary-porous coverage is chosen, which is convenient for local cryotherapy practice. It is quickly (during 5 seconds) soaked with a cooling agent, is pressed to the tissue, is fixed and cools the biological tissue for 3 minutes and longer. The basic diagram was obtained for the cooling power of a tissue by use of an ice package. The two cooling methods are compared.

## 1. INTRODUCTION

Cooling of biological tissues is an urgent issue in orthopaedics, emergency surgery, sports medicine in order to achieve rapidly the anesthetization effect, to eliminate hyperthermia, to improve blood microcirculation, to reduce bacterial activity, to stimulate regeneration processes in cooled and surrounding tissues [1,2,3]. The paper presents the results of the temperature field study of biological tissues by contact cooling method – for example by an ice package or by capillary-porous covering (gauze of many layers or cotton wool) soaked in a cooling agent. Nowadays there exists a method to create basic graphs according to the isotherm dynamics to express the cooling power of the applied cold source in contact with the tissue [4,5]. For cryotherapy purposes they are curves *T(τ)* which reflect isotherm dynamics in biotissue for various convection cooling conditions created, for example, by various cryoapplicator usage, a system of gas jets, cold water, cryosauna, etc. The aim of this study is to experimentally check the existing methods which would be convenient in cryotherapy and cryosurgery practice to establish the cooling power of a cold source of any design in contact with the tissue. The lack of the above-mentioned graphs in scientific literature and the lack of practical guidance for doctors prevent standardization and wide application of cryomethods. In particular this makes it difficult to compare results and to find in the market or to create a new effective design of a cryoapparatus convenient for working conditions. Further the *T(τ)* isotherm dynamics is studied by the depth *Z* of a cooled tissue (gel 4% gelatin solution, tissue analogue in vitro) using the precision infrared thermograph.

## 2. KEY PART. RESEARCH

The experimental stand scheme is presented in Fig.1. A cooling agent in saturation state is injected into the container (1). During the experiment the mixture is sprayed on various capillary-porous coverings (3) placed on the cooled surface. A precision infrared thermograph "IRTIS-2000 C" is used to study the temperature field in the cooled medium section (7). A thin polyethylene film (5) transparent for infrared range is used to determine the temperature field. This film makes it possible to obtain the flat section. The Fresnel lens (6) is also transparent in the infrared range and is used to magnify the picture obtained by the thermograph. Variable values during the experiment are presented in Table 1.

As a result the data are obtained on the *T(τ)* isotherm dynamics at the depth *Z* = 0, 2, 6 mm in the gelatin solution by the melting ice cooling at the temperature $T_0 = 0\ ^0$C. They are given together with the experimentally obtained data in Fig.3.

Fig.4 shows calculation and experimental data for comparison on the *T(τ)* isotherm dynamics in the gelatin solution by cooling with the propane-butane mixture/R123 at $T_0 = -15\ ^0$C with the use of capillary-porous covering (gauze, 18 layers, 50x40x5 mm).

Table 1. Variable values during the experiment to study the $T(\tau)$ isotherm dynamics in the cooled medium at various depths from the cooled surface

| | |
|---|---|
| Cooling agent | Propane/butane mixture [40/60% mol]; $T_O$ = -35,5 $^0$C;<br>Propane/butane/R123 [28/42/30% mol], $T_O$ = -25 $^0$C;<br>Propane/butane/R123 [12/18/70% mol], $T_O$ = -15 $^0$C;<br>Melting ice in a polyethylene bag. |
| Capillary-porous covering | Cotton wool (40x35x5mm) compressed from 5 to 3 mm to obtain good contact;<br>Cotton wool (40x35x5mm) compressed from 5 to 3 mm to obtain good contact, perforation (d= 2 mm, L = 6 mm)<br>Gauze 18 layers (50x40x5mm), compressed from 5 to 3 mm to obtain good contact |

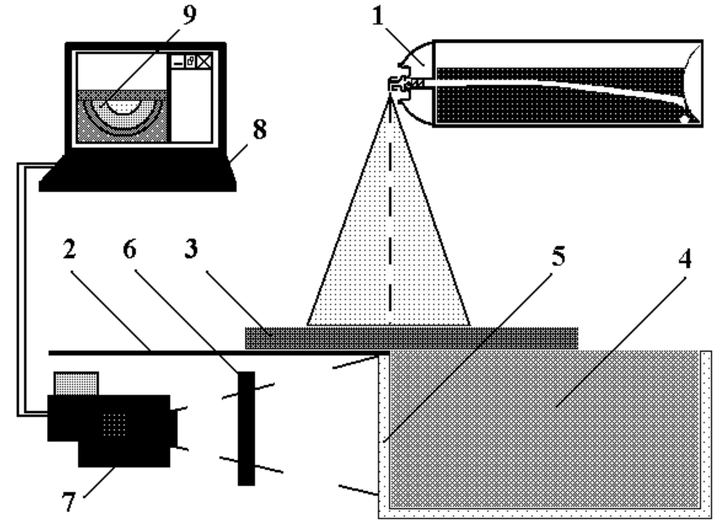

Figure 1. The scheme of the experimental stand to study the T(τ) isotherm dynamics at the depth Z of the cooled tissue by the precision infrared thermograph. 1 – container with the cooling mixture; 2 – protective film; 3 – capillary-porous covering; 4 – experimental medium (4% gelatin solution, the tissue analogue in vitro); 5 – a thin polyethylene film transparent for the infrared range; 6 – lens; 7 – thermograph; 8 – computer; 9 – temperature field of the cooled object obtained by the thermograph use

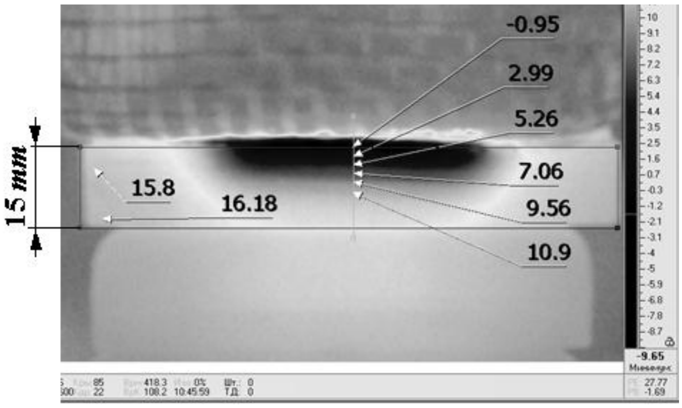

Figure 2. Thermogram in the infrared gel range (4% gelatin solution, tissue analogue in vitro) at the depth by the local cooling of its surface by the capillary-porous covering (gauze 18 layers 50x40x5mm) soaked in cooling agent with the temperature $T_0$ = -15$^0$C during 7 minutes. The picture was taken with the precision infrared thermograph “IRTIS – 2000 C”. The temperature in the picture is given in $^0$C

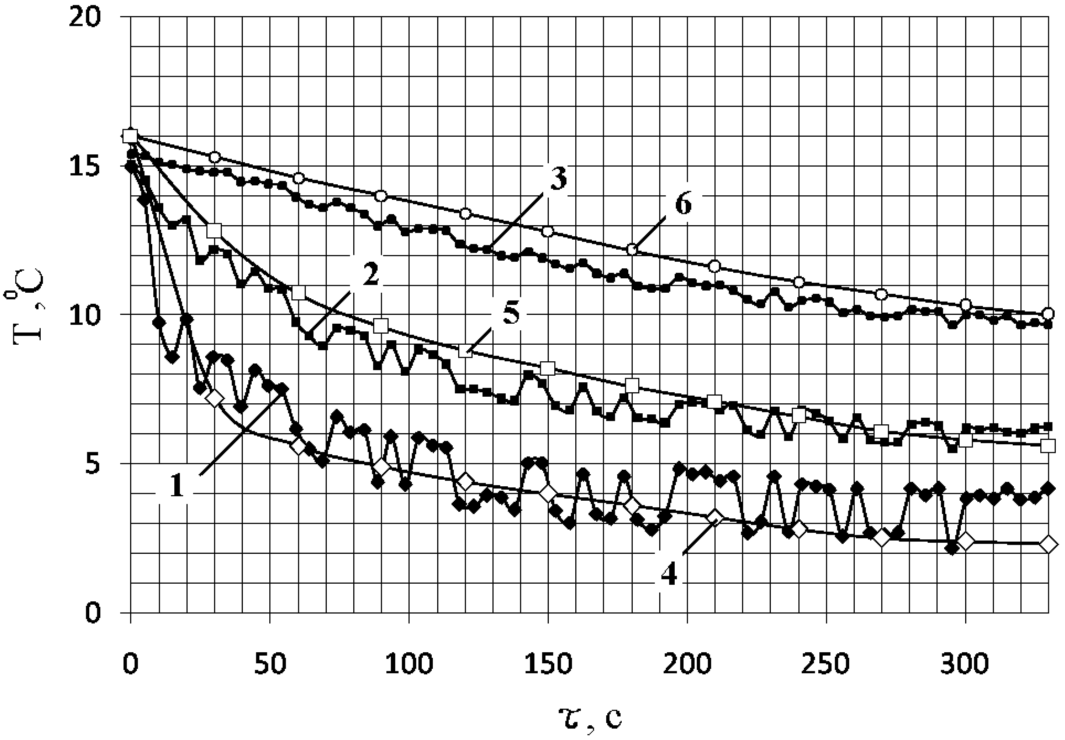

Figure 3. *3* – experiment, Z = 6 mm; 4 – calculation, Z = 0 mm; 5 – calculation, Z = 2 mm, 6 – calculation, Z = 6 mm. Calculation and experimental data on the T(τ) isotherm dynamics at the depth Z = 0,2,6 mm in a gelatin solution at cooling of its surface by the melting ice bag $T_0$ = 0 $^0$C. Divergence of the experimental data from the calculated data is ± 2 $^0$C. 1 – experiment, Z = 0 mm; 2 – experiment, Z = 2 mm;

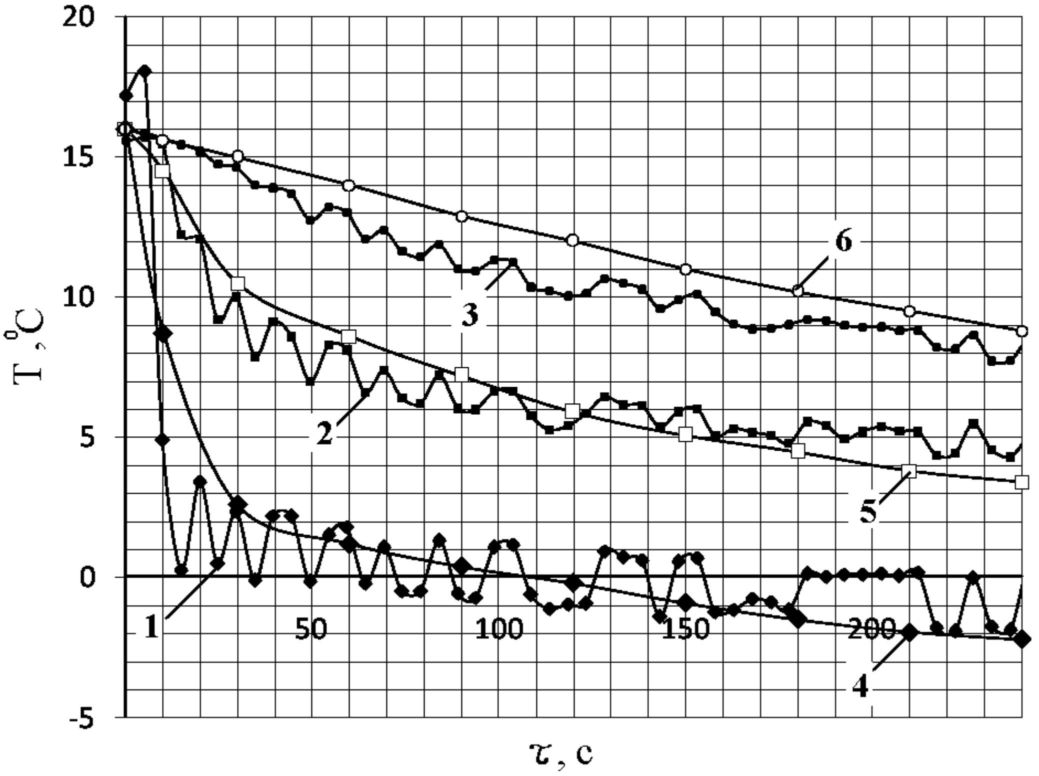

Figure 4. Calculation and experimentally obtained data on the T(τ) isotherm dynamics in a gelatin solution by cooling with the propane/butane mixture/R123 at $T_0$ = -15 $^0$C and by the use of capillary-porous covering (gauze 18 layers (50x40x5 mm). Divergence of the experimental data from the calculated data is ± 2 $^0$C. 1 – experiment, Z = 0; 2 – experiment, Z = 2 mm; 3 – experiment, Z = 6 mm; 4 – calculation, Z = 0 mm; 5 – calculation, Z = 2 mm; 6 – calculation, Z = 6 mm.

The existence of basic graphs $T(\tau)$ for convective conditions of cooling makes it possible:

1. to compare the method of biological tissue cooling by the capillary-porous covering soaked in the cooling agent to other methods of local cryosurgery: to the method of local cryosurgery with the use of various cryoapplicators, bags with cryogel, ice, to the method of jet cooling and also by general cryosurgery with cold water or cryosauna use;
2. to observe the dynamics of temperature change at the tissue depth with time by its cooling;
3. to compare the obtained data on the $T(\tau)$ isotherm dynamics to the calculated data in order to confirm the precision of the calculating methods;
4. to choose effective cooling conditions for the given part of biological tissue to achieve temperature $T_T = 12\ ^0C$ at the depth $Z = 3$ mm (achievement of the anesthetization effect);
5. to determine operating time of the cooling agent evaporation from capillary-porous covering by cooling.

## 3. CONCLUSIONS

Relatively precise measurements have been made (which satisfactory accordance to the calculation results) on the isotherm dynamics at the tissue depth in vitro or for a transparent gel (water + gelatin 2-4%) by cooling of its surface with various cold sources using precision infrared thermograph.

It is established that: it is advisable to use the jet of the propane/butane mixture (40/60% mol) by local cryosurgery, especially in sports, alongside with capillary-porous covering 0.5-2.5 cm thick and 6.5 - 12 cm in diameter, which is practical and available in the market. The covering is rapidly (during 10 seconds) soaked with the mixture, then it is fixed on the given surface. This provides a rational cooling period for biotissue in cryotherapy - 3-6 minutes - and a quicker cooling in comparison to the melting ice bag.

## 4. REFERENCES

Chernigolovki V, Kurbatova I. 1941, On the temperatures of appearance and taking down of the cold stasis. In the book: *Neurohumoral regulations in the organs and tissues*, Leningrad, pp.164-178.

Mikheev M, Mikheeva I. 1977, *The basis of heat transfer*, “Energy” edition, Moscow, 344 p.

Butorina A.V., Kondratenko R.O., Arkharov A.M. 2011, New cryogenic technologies in fitness and sports // Cryogenic Technologies and Equipment. The Prospects. *Proc. of the Moscow Conference*. Moscow: 73-75

Boodrik V.V. 2007, *Physical foundations of cryomethods in medicine*, Lika, Moscow, 136 p.

Schneider P.D. 1977, *Engineering issues of heat conductivity*, Mir, Moscow , 478 p.

Kondratenko R.O., Nesterov S.B., Butorina A.V. 2010, *Cooling of the biological tissue in local cryosurgery*, NOVELLA, Moscow, 50 p.

Kondratenko R.O., Garskov R.V., Nesterov S.B., Shcherbakov M.I. 2012, Study of contact cooling methods of biological tissue in local cryosurgery // Vacuum Equipment, Materials and Technologies. *Proc. The 7th International Scientific Conference*, Moscow: 264-268

004

# Application of the Very Low Temperatures for the Preservation of Rare Plants´Seeds of Ukraine

**Arapetyan E.**[*]**, Usatenko Yu.**[**]

[*]Botanical Garden, [**]Center of Low Temperature, National University by I.Franko,
University str.1, Lviv, 79000, Ukraine

## ABSTRACT

Alpine aster is included in the Red Data Book of Ukraine and spread in the Ukrainian Carpathian Mountains. Survival of seeds Alpine aster in liquid nitrogen was studied. The seeds were immersed into Dewar vessel filled with liquid nitrogen (-196$^0$C). Cryoprotectants were not used. After a month of cryopreservation the seeds did not lose their viability. In investigated species no significant difference in the final germination percentages between experiment and control variants was found. The storage in liquid nitrogen within a month period did not affect the further growth and normal development of the cryopreserved object. Plantlets, which were formed as a result of germination tests were planted in the living collections of the Botanical Garden. Growth and development of these plants were in the normal range within three years. Flowering began on the third year.

Keywords: Aster alpinus, rare species, Carpathian Mountains, preservation, liquid nitrogen, seed germination, survival

## 1. INTRODUCTION

The world of plants is an important element providing life for mankind. The plant resources of each country are now considered not only as the national wealth, but as international genetic resource too. The current degree of destruction of natural vegetation cover forces us to protect environment. International documents give extra attention to the active protection of flora genefond and specifically of the local native flora. The conservation of wild plant diversity is based on *ex situ* conditions. The XVIIth International Botanical Gardens Congress gave the specific attention to the role of botanical gardens as the centers of phytodiversity preservation (Gibbs, Wyse Jackson, 2005). “The International Agenda for Botanical Gardens in Conservation” was published in 2000 (Wyse Jackson, Sutherland, 2000). Nowadays Botanical gardens play the leading role in the preservation of wild plant species (Wyse Jackson PS., Dulloo E. 2005). Conservation of rare and endangered plants in Botanical Gardens is performed mainly the living collections. However, in the current stage it is not enough to conduct the floristic diversity preservation only on the open soils. Such approach has several weaknesses, including the following: i) Botanical Gardens areas are non sufficient to conserve growing number of plants that are included in the Red Book and are under the threat of disappearance; ii) according to the requirements on preservation of genetic variability of the species, the collections should include the amount of 500 samples that reproduce across one territory to ensure preservation for several generations that is physically impossible to execute in the single Botanical Garden; iii) living collections are constantly under the negative influence of the climate changes. During the last years, the botanical world community has been paying great attention to the problem of climate change (Schulman, Lehvavirta, 2011). The Fifth European Botanical Gardens Congress, EuroGardV was held in Helsinki in 2009 under the highlight of the role of Botanical Gardens in the age of climate change. Living collections do not meet the requirements of long-term storage of phytogenefond. In response to these challenges preservation of the seeds that are the main form of the genetic biodiversity preservation is incorporated as the main solution to the problem of genetic diversity preservation. They are the main element of preservation of genetic information. According to scientific researches, seeds keep all the information of the genotype, that was formed during the all the period of the evolution of the species. The fact that seed plants have gained stronger positions in the Earth flora segment proves that seeds are more efficient approach to the preservation plant kingdom (Bonner, 1968).

The workshop “Encouraging and enabling seed conservation in botanical gardens” wrote in their abstract that “seed collections in seed banks provide insurance against loss of valuable plants in the wild and in botanical gardens" (http://www.luomus.fi/eurogardv/abstracts.html). Botanical gardens all around the world being the reservations of plants *ex situ*, conduct organized gathering of the plant seeds that were grown up in the collections and plant seeds from the natural places of growth. Seed banks is needed primarily for presentation of biological characteristics of given plants, as well as of the material for seeds exchange between gardens through Index Semina, which is believed to have started in the late 16th century when Jacobs Bobart for the first time completed a list of seed collection of the Oxford University Botanical Garden. Basically, the seeds were kept in the laboratory at room temperature under $25^0$C that leaded to quick destruction of seed viability and their mutation. The main factors of the negative influence on the seeds germination are temperature, moisture and oxygen. So the period of the seed viability and germination has its limits. As a possible answer to the given challenges The Millennium Seed Bank prepared the project "European Native Seed Conservation Network" (ENSCONET). The main aim of the project was to coordinate of botanical garden activities in the *ex situ* conservation of native plants through long-term seed storage (Puchalski, 2004).

It is important to develop conservation technology that enables long time conservation of plant material without genetic information destruction and with reservation of its germination and morphogenetic potential. Preservation of the ability of seeds to germinate is the main aim of this research. The modern method of phytogenefond diversity preservation with conservation of its integrity is plant preservation under ultralow temperature of liquid nitrogen ($-196^0$C). Conservation of plant material using liquid nitrogen is consistent with the requirements of durable preservation of plant genetic information without negative changes of their biological characteristics. Cryopreservation technique is considered today to be the most promising alternative to traditional conservation (Benito, 1997). This technique has strong advantages over the traditional approaches. Cryopreservation gives the opportunity to protect gene pool from the influence of the abiotic and biotic factors in comparison to the traditional approach flora conservation in the form of plant collections on the open soil that are influenced by negative factors (temperature, fungus etc.). Recently, this method has become more important (Wyse Jackson, 2002). Cryopreservation protocols have been established for a large range of plant species (Gomes-Campo, 2007). The possibility of long-term preservation of plant material under ultralow temperature with retaining of its viability and genetic integrity has become the main method of wild plant conservation *ex situ.* Cryopreservation method has been successfully applied for preservation of seeds of several species. As written by Pritchard "Storage of seeds is arguably the most effective and efficient method for the *ex situ conservation* of plant genetic resource. Low storage costs, combined with ease of seed distribution and regeneration of whole plants from genetically diverse material, offer distinct advantages for the storage for preservation of seeds compared with other types of plant tissues, such as meristems and pollen" (Pritchard, 1995). It is known that development of a protocol for cryopreservation is very species-specific. The main practical side of seed cryopreservation research is regime selection of conservation and reconservation of plant material which depends on the species.

Our work is aimed at *ex situ* conservation of seeds of rare and endemic plants using modern method. The aim of this study was the development of cryogenic protocol for the seed preservation of such species as Alpine aster (*Aster alpinus* L. from family *Asteraceae*).

## 2. MATERIALS AND METHODS

### 2.1. PLANT MATERIAL

The object of our investigation is mountain species that represent the Carpathian Mountains flora, that is one of the floristic richest regions' of Ukraine. The territory of the Carpathian Mountains is divided between six European countries. The Carpathians are one of the 200 selected ecoregions. The native mountain flora of the Ukrainian Carpathian was found to consist of 2020 species, of which more than 20% are endemic and relict (Tasenkevich, 2002). *A. alpinus* is included into the Red Data Book of Ukraine and its status properly according to it is defined as rare (Red Data Book of Ukraine, 2009). The reason for decrease in their numbers is urban or other kind of human activities. *A. alpinus* is a relict arcto-alpine species with fragmented distribution. The area of its distribution covers mountain and forest regions of Europe and Asia and rarely in the mountains of Middle Europe. There are about 10 populations of the given species in the Carpathian Mountains. The species grows within 1200-2000 m above sea level at alpine and subalpine zones. It is protected in the Carpathian Biospheric reserve. Alpine aster is herbaceous perennial. It grows up to 30 cm in height. Flowering usually starts in July - August with blue flowers. Seeds ripen in August. The population is maintained by means of seed and vegetative reproductions (Red Data Book, 2009). The seeds don`t have the rest period. Alpine aster is an ornamental plant. Mature seeds of *A. alpinus* were collected from plants growing in the botanical garden. Collected seeds are stored in tightly packed paper bags in a laboratory at ambient temperature for 3 months.

### 2.2. CRYOPRESERVATION

For cryopreservation seeds without any pretreatment were transferred to Eppendorf tubes and directly plunged into liquid nitrogen. Following one month storage, the tubes were removed and than warmed using slow warming. The tubes were warmed at room temperature (22 ± 2°C) for few days. Uncryopreserved seeds remained at room temperature.

### 2.3. GERMINATION TEST

Germination viability was tested. Seeds were tested for germination in soil condition. Three replications with 50 seeds were sown in peat-leaves mix. The test was monitored every day and germinated seeds were counted. Testing was continued until it was obvious that no further germination could occur. The germination percentages were calculated. The time of initial germination was determined and final germination percentage (mean values ± SE) was calculated. To analyze the significance of differences between mean values, analysis of variance was applied as was the Student test at a significance level of $P < 0.05$. The development of seedlings was analyzed too. Seedling evaluation of the germinated seeds follows the "Rules” by Vellington (Vellington, 1972).

## 3. RESULTS

Cryopreservation of *A. alpinus* seeds was successful. No damage was observed after cryogenic storage of seeds. Tested species showed positive response to the 30-day exposure to liquid nitrogen when compared with controls. The seeds began to germinate after exposure in liquid nitrogen (Table 1).

Table 1. Average soil germination of *A. alpinus* seeds.

| Day of germination | Average Control germ | | Average Lquid Nitrogen germ | |
|---|---|---|---|---|
| | Quantity of germinating seeds | Germination percentage | Quantity of germinating seeds | Germination percentage |
| 4--th | 5.3 ± 2.3 | 10.0 ± 4.6 | 8,0 ± 1.8 | 16.0 ± 3.6 |
| 8--th | 9.5 ± 3.0 | 19.0 ± 6,2 | 12.8 ± 0.8 | 25.5 ± 1.7 |
| 10--th | 11,0 ± 3.9 | 22.0 ± 7.9 | 14.5 ± 0.6 | 27.5 ± 0.9 |

Seed germination of Alpine aster after cryostorage was 27,5%. The final percentage of viable seeds in frozen variant (27.5 ± 0.9) was higher than in controls (22.0 ± 7.9). The difference in percentage of seed germination between germination after liquid nitrogen treatment and unfrozen controls was not significant and statistically not reliable. It demonstrates that germinating ability of frozen seeds did not change in comparison with unfrozen seeds. Similar results were reported for another species (Arapetyan et al., 2004).

Seeds of both variants started germinating on the 4-th day after the saw. Cryopreserved seeds presented the same development as the uncryopreserved ones. The growth of seedlings from treated seeds was initiated on the 10-th day as the unfrozen controlled seeds. Radicle, hypocotyls and cotyledons were present. Cotyledons leaves opened on the 14-th day from the time of germination in controlled and cryopreserved variants. The first leaves appeared earlier from seedlings of cultivated seeds (on the 14-th day) than from seedlings of unfrozen seeds (on the 20-th day). But later there was no significant difference in size and quantity of leaves between the plantlets derived from cryopreserved and control seeds.

Seedling development of cryopreserved variant was faster than that in controls, but no morphological variation was detected between seedlings from uncryopreserved (control) and cryopreserved seeds. The root systems were developed in both variants, but the root length of the seedlings from cryopreserved seeds was bigger than that of the seedlings of the controls. Plantlets, produced as a result of germination tests were planted into living collections of Botanical Garden. Growth and development of these plants were normal during three years. Flowering began on the third year.

# 4. CONCLUSIONS

Influence on seeds germination after exposure to ultralow temperature of liquid nitrogen was investigated for rare species included into the Red Data Book of Ukraine. Experiments with *Aster alpinus* L. seeds were conducted. The obtained results have demonstrated that seeds of the studied species can be fast frozen at -196°C without the loss of their viability. Cryoprotective substances were not used.. The stimulatory effects of liquid nitrogen exposure on seed germination were revealed on the early stages of germination. The final germination capacity of cryopreserved seeds was not significantly different from that of the studied non-preserved species. This indicates normal development of seedlings derived from the seeds treated by liquid nitrogen into the normal plantlets and plants. Only slight increase of leaves development was found in the seedlings from non-frozen seeds.

The *A. alpinus* seed storage technology does not require special preparations for the experiment or special equipment for input and output from the cooling. Containers for storage of seeds in liquid nitrogen are easy to use. Seeds of the studied species do not require a gradual cooling. Fast freezing can be used for the *A. alpinus* seeds. The schedule of seed warming is one-step. Preservation of seeds viability is assessed by conventional standard methods. Seed contamination does not affect its germination. The cryotechnique is environmentally safe and does not require large expenditures. Thus, taking into account the tolerance to liquid nitrogen, cryogenic storage would be a suitable method for a long-term preservation of Alpine aster seeds.

# 5. REFERENCES

Benito ME. Gonzalez 1997, Cryopreservation as a tool for preserving genetic variability: its use with Spanish wild species with possible landscaping value, *International Conference*, Torino, Italy: 11-12.

Bonner J., Varner JE. 1965, *Plant biochemistry,* Academic press, New York – London, 624 p.

Gibbs D, Wyse Jackson P. 2005, The past, present and future of botanic gardens, *XYII International Botanical Congress,* Vienna, Austria: 207.

Gomes-Campo C. 2007, *A guide to efficient long term seed preservation,* Univ. Politecnica de Madrid 170: 1-17.

Puchalski J. 2004, International programmes for seed preservation of European native plants, *Bulletin of Botanical gardens* 13: 11-18.

Pritchard HW. 1995, Cryopreservation of seeds. *Methods in molecular biology. In book: Cryopreservation and Freeze-Drying Protocols*, 38: 33-144.

*Red Data Book of Ukraine. Plant World* 2009, Diduch JaP. (ed.), Globalkonsulting, Kyiv, 912 p.

Schulman L., Lehvavirta S. 2011, Botanic gardens in the Age of Climate Change, *Diversity and Conservation* 20(2): 217-220.

Tasenkevich L. 2002, *Red List of Vascular Plants of the Carpathian Mountains*, Carpathian Ecoregion Initative, Lviv, 28 p.

Wyse Jackson PS., Sutherland L. 2000, *International Agenda for Botanic Gardens in Conservation*, Botanic Gardens Conservation International Descanso House, U.K., 52 p.

Wyse Jackson PS. 2002, The Global Strategy for Plant Conservation, *An International Conference for Botanic Gardens "Science for Plant Conservation"*, Dublin, Ireland: 2.

Wyse Jackson PS., Dulloo E. 2005, The 2010 challenge in *ex situ* conservation and threatened species recovery for botanic gardens and genetic resources communities, *XYII International Botanical Congress*, Vienna, Austria: 141.

Wellington PS. 1972, *Handbook for seedling evaluation*, Kolos, Moscow, 174 p.

Arapetyan E., Bondar V., Tsaryk Y., Tymchyshyn G., Panasiuk M. 2004, Influence of Ultralow Temperature on Seed Germination, *Acta Physiologiae Plantarum* 26(3): 286.

094

# A Preliminary Method for Ultra-Rapid Freezing of the Nicotiana Tabacum BY-2 Cell Line by Encapsulation / Vitrification

**Schumacher H.M., Bitter E., Heine-Dobbernack E.**

DSMZ-Deutsche Sammlung von Mikroorgansimen und Zellkulturen GmbH
Inhoffenstraße 7B, D-38124 Braunschweig

## ABSTRACT

Plant cells are especially difficult to cryopreserve. The reason can be seen in the high water content and the sub-cellular structure of these cells containing vacuoles filled with water. Nevertheless different technical approaches exist today to achieve a mild dehydration of plant cells avoiding intracellular ice crystal formation or achieving vitrification of the protoplast during exposure to ultra low temperatures. For most dedifferentiated cell cultures still “slow freezing” is applied. One of the cell cultures used most often for applications in fundamental research is the BY-2 cell line. This cell culture has been initiated from the Nicotiana tabacum variety “Bright Yellow 2”. The cell line has also been preserved by “slow freezing” approaches. Recently we developed another approach based on vitrification/encapsulation and combined it with ultra-rapid freezing. Although the method yielded positive results, there is still no professional equipment to guarantee a reproducible and safe application of the method.

## 1. INTRODUCTION

The preservation of plant genetic resources considering plant material from the temperate zones can easily be achieved by the storage of dried seed material for many years. In contrast many crop plants from the tropics do not form seeds which can be dried or stored, other plants do not form viable seeds at all and are propagated vegetatively and finally, also for cell cultures and germplasm generated by biotechnological methods alternative long term preservation methods are needed. The only possible method in this case is cryopreservation. Damage of cells during cryopreservation is usually caused by the formation of intracellular ice crystals. This can be avoided by deyhydration of cells. Alternatively, methods can be applied leading to the vitrification of the protoplast as a glass at ultra low temperatures, also involving dehydration of cells. Dehydration of plant cells is difficult to achieve without cell damage because of the specific sub-cellular structure of these cells. They normally contain vacuoles filled with water which requires the removal of more water and in addition through different membrane systems, the cell membrane separating the cell from the outer space and the tonoplast separating protoplast and vacuole.

Different approaches have been worked out to achieve survival of plant cells and tissues at liquid nitrogen temperature. The most simple approach is “ultra-rapid droplet freezing” (Schäfer-Menuhr et al. 1997). Here very fast freezing rates and the use of very small volumes lead to avoidance and/or minimization of intracellular ice crystals. Using methods termed “vitrification” the cells are first loaded with a cryoprotectant and then dehydration is achieved by the application of vitrifying solutions (Sakai et al. 1997). The consequence is that the protoplast solidifies as a glass at ultra low temperatures. The “Encapsulation/dehydration” method is performed in three steps. First cells or small regenerative tissues like meristems are immobilized in alginate beads. Then they are loaded with sugar and afterwards dehydrated in air (Fabre and Derreudre 1990). The first method that has been successfully applied for the cryopreservation of plant cells has been “slow freezing” (Withers and King 1990). Cells or tissues are first osmotically dehydrated in a preculture phase over several days. Afterwards cells are loaded with a cryoprotectant, in most cases DMSO, or a mixture containing DMSO. Finally they are frozen by a slow cooling rate (–0.1°C to –1°C) to app. –40°C and then plunged into liquid nitrogen.

The “slow freezing” method is still the method of choice in the case of dedifferentiated plant cell cultures. This type of plant cell cultures is used for the production of secondary metabolites for pharmacy and the cosmetics industry, even more for screening applications and mainly to replace plants for certain experiments in fundamental research. For all applications a safe long term preservation method would be desirable. At DSMZ safe long term preservation is also needed to conduct the deposition of patent strains under the Budapest treaty.

One of the most prominent plant cell lines is the so called “BY-2” cell line. The cell line has been initiated from a plant of the tobacco cultivar “Bright Yellow 2” in Japan. This tobacco cell line has been applied worldwide for various research purposes (Nagata et al. 1992) as well as for biotechnological applications, like the production of recombinant proteins (Schmale et al. 2006). Two different methods have been developed for the cryopreservation of this specific cell line. One method is based on classical controlled rate freezing or slow freezing (Schmale et al. 2006). Another very simple and efficient approach, published by Kobayashi et al. (2005), is based on a combination of encapsulation and slow freezing.

More recently for the cryopreservation of meristems ultra-rapid droplet freezing in combination with vitrification turned out to be a powerful approach. Also vitrification methods have been combined with encapsulation. We therefore tested whether a combination of encapsulation and vitrification according to Hirai and Sakai (2003) could be combined with ultra rapid cooling to cryopreserve BY-2 cells.

## 2. MATERIAL AND METHODS

100 ml MSBY-2 medium was inoculated with 5 ml of a 7 days old BY-2 suspension culture, cultivated for another 7 days in a 300 ml Erlenmeyer flask under shaking (100 rpm) and supplemented with 25 ml fresh medium. After three more cultivation days, cells were immobilized in 3 % alginic acid according to the method of Fabre and Derreudre (1990). Alginic acid beads were cultivated for 6 days either in normal or preculture medium (normal medium+ 0.25 M or + 0.5 M sucrose) before freezing.

Vitrification freezing consisted of a loading, vitrification and unloading step. After preculture, cells were incubated directly in PVS2 solution or first in loading solution (normal medium + 0.8 M or + 1.2 M sucrose) and then in PVS2 solution (30% glycerol, 15% ethylene glycol, 15% dimethyl sulfoxide in medium containing 0.4 M sucrose). Incubation was carried out in 50 ml Falcon tubes. After PVS2 incubation freezing was carried out in a laminar flow bench by plunging the beads containing the cells directly in a mortar filled with liquid nitrogen. With a forceps or a spoon frozen beads were transferred into pre-cooled cryovials. Cryovials for storage were filled with liquid nitrogen and cooled in a styrofoam box filled also with liquid nitrogen (see Figure 1). Thawing was performed by plunging 10 beads contained in one cryovial directly into 11 ml unloading solution (culture medium with 1.2 M sucrose) in a Petri dish. After an incubation time of 20 minutes beads were put on normal growth medium solidified with 0.8 % agar. Cryopreservation success was assessed by TTC test and regrowth test of thawed samples. For TTC test 3 almost equal amounts of bead material were transferred into 2 ml Eppendorf vials and 300 µl TTC reagent ( 2% TTC in 50 mM Tris buffer, pH 7.5) and 1.2 ml Tris buffer were added. After incubation over night, the dye was extracted with ethanol and measured at 500 nm. Regrowth was indicated by cells growing out of the beads and was measured 4 weeks after thawing.

## 3. RESULTS

To achieve an ultra rapid cooling rate liquid nitrogen was poured into a precooled mortar and the beads directly plunged into the liquid nitrogen using a metal spoon (Figure 1). When almost all nitrogen had evaporated the beads were filled into precooled cryovials. These vials were placed in a Styrofoam box filled with liquid nitrogen. The nitrogen in the box cooled the vials from below so that liquid nitrogen could be poured into the vials cooling prevented the nitrogen from evaporating out of the vials (Figure 1). Vials were closed with screw caps and stored in a liquid nitrogen container over night.

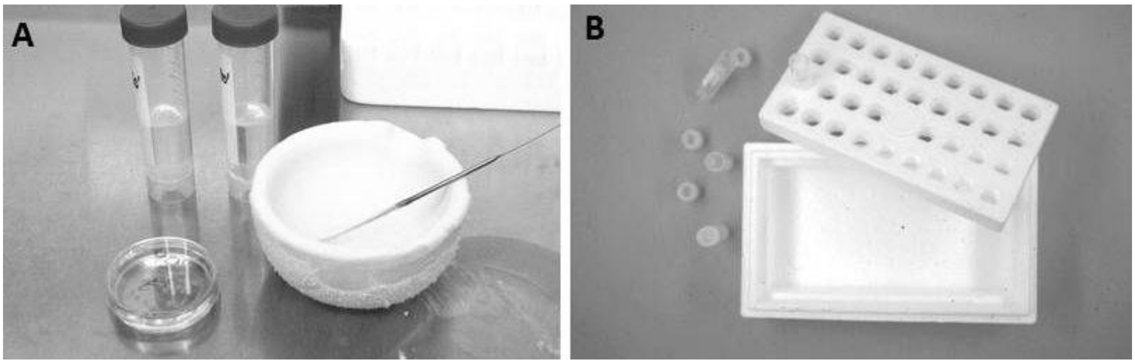

Figure 1 **A.** Mortar filled with liquid nitrogen. For freezing beads were plunged in the liquid nitrogen in the mortar. **B.** Styrofoam box filled with liquid nitrogen. 2 ml cryovials were inserted in the holes of the lid and cooled from underneath. When liquid nitrogen had almost evaporated from the mortar beads were transferred into these vials.

In an first approach BY-2 cells were precultured in medium containg either 0.25 M sucrose or 0.5 M sucrose and without loading step subsequently incubated in PVS2 solution for various times and afterwards frozen. Already here regrowth of samples could be achieved (Figure 2)

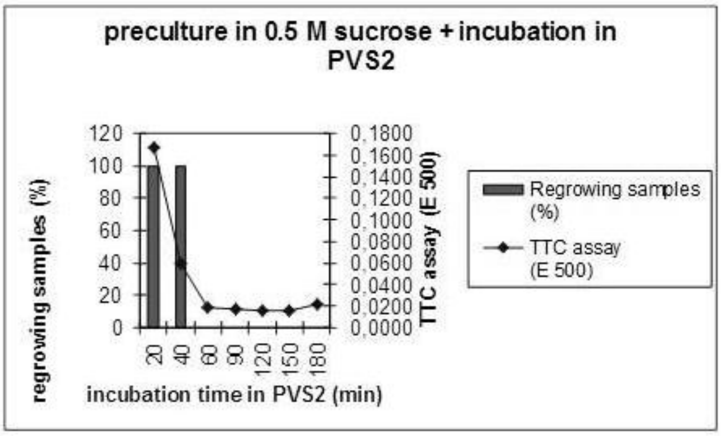

Figure 2. Regrowth of samples could be achieved after 20 and 40 minutes of incubation in PVS2 solution after preculture of samples in medium supplemented with 0.5 M sucrose.

Application of a loading step with loading solutions containing different sucrose concentrations (0.8M or 1.2M) led to even better regrowth of the samples (data not shown). Regrowth could now be achieved also after longer incubation periods in PVS2 which shows that preculture and loading improved the osmotic tolerance of the cells. Best regrowth results were achieved by a combination of preculture in medium containing 0.5 M sucrose, a loading step in medium containing 1.2 M sucrose and a PVS2 incubation time of 20 or 40 minutes (Figure 3).

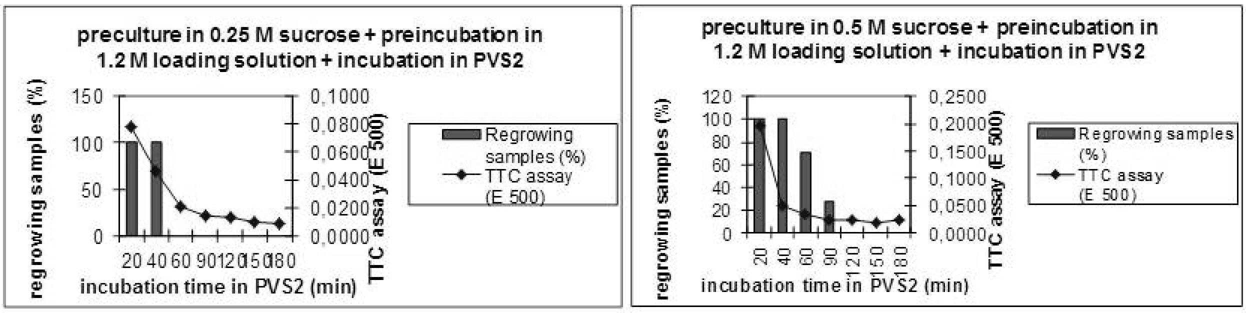

Figure 3. Regrowth of samples after preculture in medium supplemented with 0.25 M or 0.5 M sucrose, loading in 1.2 M sucrose anf finally incubation in PVS2 for various times.

Incubation time in PVS2, necessary to achieve regrowth, was investigated after thawing and unloading in 1.2M sucrose for 20 minutes. After two month of recultivation all samples incubated for 20, 40 and 60 minutes showed good regrowth. The samples incubated for 90 minutes in PVS2 showing some regrowth after 4 weeks could not recover and ceased growth later (Figure 4). Using even longer incubation times in PVS2 no regrowth could be observed.

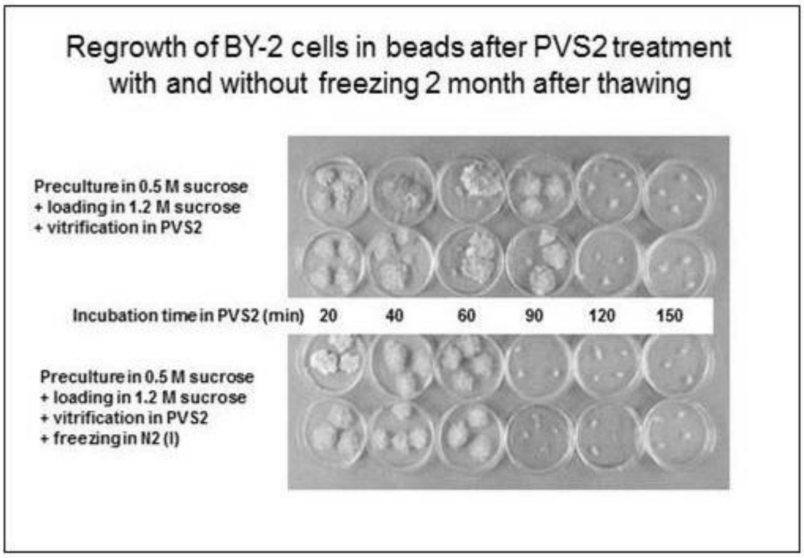

Figure 4. BY-2 cells regrowing from alginate beads 8 weeks after thawing from cryostorage and unloading.

## 4. DISCUSSION

Even today the first method that has been developed for the cryopreservation of dedifferentiated plant cell cultures is still the method of choice for this type of cells. The big advantage of slow freezing for preservation of dedifferentiated cell suspensions is the easy handling and the possibility to preserve a high number of samples from the same batch of culture. On the other hand a drawback is the need to optimize a lot of different parameter to achieve survival, like kind and concentration of the preculture osmotic, duration of preculture treatment, kind, concentration and residence time of the cryoprotectant and finally the freezing rate. At DSMZ we developed a mini test approach to overcome these disadvantages (Heine-Dobbernack et al. 2008). The benefit of this system is that optimization of these parameter can be carried out very fast and with a minimum amount of cell material. Anyway the need for optimization persists. The method presented here is easy to carry out and the encapsulation technique allows to handle large amounts of cells easily. However the system has different pitfalls. In our viability test using TTC longer incubation phases lead to decoloration of the samples so that the application of this test is critical for quantitative measurements. Another disadvantage is that during ultra-rapid cooling the beads disintegrated. This complicates the transfer of the bead material into the cryovials and especially to transfer equal or at least comparable amounts of bead material also complicating quantitative measurements by detecting the regown fresh or dry weight after a certain time. A more severe drawback is that samples have to be kept sterile performing cryopreservation. This is difficult to guarantee during the transfer of bead material into the cryovials while liquid nitrogen is still boiling from the mortar disturbing the laminar flow of the clean bench. Furthermore the bead material is exposed to large quantities of liquid nitrogen during the cooling phase. Recently J. Keller and his group at IPK Gatersleben isolated bacteria from liquid nitrogen containers (personal comm.) which are currently identified at DSMZ. Although the method provides an interesting alternative to slow freezing and may open up the avenue for better application of virtification techniques for the cryopreservation of dedifferentiated plant cell cultures, the technical approach and the equipment for routine and safe application of this method still has to be optimized.

## 5. REFERENCES

Fabre J, and Dereuddre J, 1990, Encapsulation-dehydration: a new approach to cryopreservation of Solanum shoot tips. *Cryo-Letters* 11: 413-426.

Heine-Dobbernack E, Kiesecker H and Schumacher HM, 2008, Cryopreservation of dedifferentiated cell cultures, in: Reed B. *Plant Cryopreservation – A Practical Guide*, Springer, New York, 141-176.

Nagata.T., Nemoto Y, Hasezawa S, 1992, Tobacco BY-2 cell line as the "HeLa" cell in the cell biology of higher plants. *Int. Rev. Cytol.* 131: 1-30.

Hirai D, Sakai A, 2003, Simplified cryopreservation of sweet potato (Ipomoea batatas (L.) Lam.) by optimizing concentrations for osmoprotection. *Plant Cell Rep.* 21: 961.

Kobayashi T, Niino T, Kobayashi M, 2005, Simple cryopreservation protocol with an encapsulation technique for tobacco BY-2 suspension cell cultures. *Plant Biotechnology* 22: 105-112.

Sakai A, Kobayashi S, Ojima I. 1990, Cryopreservation of of nucellar cells of navel oragne (*Citrus sinensis* Osb. var. *brasiliensis* Tanaka) by vitrification. *Plant Cell Rep.* 9: 30-33.

Schäfer-Menuhr A, Schumacher HM and Mix-Wagner G, 1997, Cryopreservation of potato cultivars – design of a method for routine application in genebanks. *Acta Horticultura* 417: 477-481.

Schmale K, Rademacher T, Fischer R, Hellwig S, 2006, Towards industrial usefulness - cryo-cell-banking of transgenic BY-2 cell cultures. *J. Biotechnol.* 124(1): 302-311.

Withers LA and King PJ, 1980, A simple freezing unit and routine cryopreservation method for plant cell cultures. *Cryo-Letters* 1: 213-220.

074

# Standardization of the Cryopreservation Process for Parathyroid Glands

**von Walcke-Wulffen V.[*], Mohrbacher J.[*], Gepp M.[**], Schmidt T.[**]**

[*] BioKryo GmbH, Industriestraße 5, Sulzbach/Saar, 66280, Germany
[**] Fraunhofer IBMT, Ensheimer Straße 48, St. Ingbert, 66386, Germany

## ABSTRACT

The treatment of secondary Hyperparathyroidism may require cryopreservation of parathyroid glands to allow autotransplant. So far, cryopreservation and cryostorage has been done by the clinicians themselves. In some cases, investment in necessary equipment was not effective due to the small number of cases.

In this paper, we evaluate a new combination of cryopreservation and transportation processes. The intention was to facilitate cryopreservation in the hospital and to store the tissue in a facility conforming to GMP. The tissue is stored in the gas phase of liquid nitrogen (LIN) in a cryostorage vessel. Tissue viability and function can be kept high to optimise the overall results. The high cryopreservation standards and the necessary equipment allows hospitals to use Good Storing Practice (GSP) and to reduce process costs. At the central facility, a new standard of storing tissue has been introduced, which enables a closed cooling chain and automated data collection as well as the storage of the tissue.

## 1. INTRODUCTION

Secondary hyperparathyroidism (SHPT) may occur in patients with renal failure leading to abnormally high serum phosphate. Also, SHPT is a side effect in patients with decreased calcium uptake caused by diseases such as Morbus Crohn, celiac disease or cirrhosis of the liver. Continuously high phosphate levels induce overproduction of parathormone (PTH) in the parathyroid glands and its secretion[1]. This leads to strongly reduced serum calcium levels which are then compensated by resorption of calcium out of bone matter. Persistent PTH production therefore leads to bone diseases like different kinds of osteodystrophy. The abnormal calcium and phosphate levels may also cause cardiovascular diseases in patients with SHPT leading to increased mortality[2].

Treatments includes improving calcium uptake with calcium, vitamin D, calcitriol or calcimimetic agents and decreasing phosphate levels with calciumcarbonate, calciumacetate or aluminiumhydroxide. Reduction of parathormone levels can be achieved by cinacalcet treatment [3,4,5].

Permanent synthesis of parathormone causes, in almost all cases, hyperplasia of all parathyroid glands. Therefore, surgical excision of the parathyroid glands often improves the health of the patient very quickly[6]. In some cases, patients develop a permanent hypoparathyroidism[7]. Cryopreservation and -storage of parathyroid tissue immediately after removal is recommended for all patients with SHPT to allow autotransplantation (Deutsche Gesellschaft f. Chirurgie). Cryopreservation of parathyroid glands has been performed in a variety of ways. The German guideline for surgical treatment of SHPT suggests a freezing rate of about -1°C / min and the use of a cell culture medium combined with DMSO (dimethyl sulphoxide) and autologous serum as cryopreservation medium[8].

Often, hospitals have no cryostorage facilities or staff trained in such techniques. The combination of an easy-to-use protocol; materials for cryopreservation and external storage facilities might be a potential alternative for these hospitals.

Our aim was, therefore, to find a method for successful alcohol-free cryopreservation of tissue and a transportation process using dry ice.

## 2. METHODS AND RESULTS

A freezing rate of about -1° C/ min can be achieved without a programmable liquid nitrogen freezing device. An alcohol-based device like Mr. Frosty (Nalgene, Thermo Fisher Scientific) works well for the freezing of cells[9]. Transportation, however, is critical. 2-propanol, which is used as the heat transfer agent, is volatile. Contact of this alcohol with the cryovials during transportation cannot be avoided. Furthermore, biological specimens must be packed in accord with official instructions, UN3373 Cat B, which include the use of an absorbing material sufficient for the complete liquid content. In the case of the Mr. Frosty device, this means about 450 ml of isopropanol plus the volume of the specimen. Since 2-propanol is highly flammable, transport is only allowed in completely leak proof packaging, a condition not fulfilled by the alcohol-based freezing device.

We tested an alcohol-free freezing device. As recommended by the manufacturer, the device was not pre-cooled. 10 cryovials each with a volume of 2 ml and filled with 1 ml cell culture medium were placed inside the device. Two additional cryovials were each fitted with two type T thermocouples, which were connected to a multichannel temperature control unit. (Agilent, USA). Temperature measurement started at the moment the freezing device was placed within a secondary packaging with absorbent (BioPouch, Bio-packaging Ltd, Great Britain) in a transportation box with dry ice as used for shipments (ThermoGBOX650 S, Alex Breuer GmbH, Germany) (fig.1 A).

Temperature was measured for about 250 minutes. The mean temperature values are shown in fig. 1B. We observed a freezing rate of 0.86 K/min in the temperature range from 0°C to -60°C. The temperature approximated then asymptotically from -60°C to -80°C.

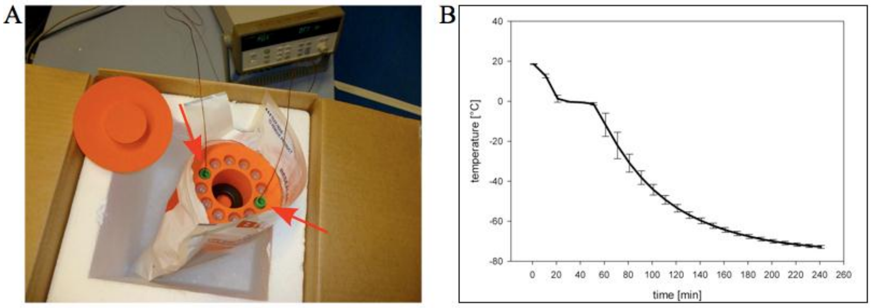

Figure 1: Freezing rate determination of an alcohol-free freezing device; A: experimental set-up, thermocouples in 2 ml cryovials were placed in the freezing-device in secondary packaging in a dry ice box. B: freezing rate of 2 ml cryovials within alcohol-free freezing device. Error bars indicate standard deviation.

To test cell viability in different freezing devices, human mesenchymal stem cells (hMSC-UC, Human MSCs from umbilical cord matrix, PromoCell GmbH, Germany) were chosen because of their reliability in growth and sensitivity to external factors[10]. Cells were grown to 80% confluence, then harvested using trypsin and aliquoted at a concentration of 500000/ml with cryopreservation medium in 2 ml cryovials. Cells were then frozen: in the non-alcohol freezing device; in an alcohol-containing freezing device (both in a -80°C freezer) or in a programmable liquid nitrogen-based device at – 1°C / min (Sy-Lab, Austria).

The viability of fresh, non-frozen cells served as a positive control and the influence of the cryopreservation medium was tested as well.

After thawing, the cryopreservation medium was removed and replaced by regular growth medium and cells were plated and incubated in a 96-well plate for 24 hours. Viability was then tested using the alamar blue assay (Invitrogen, USA) with fluorescence measurement in a plate reader (Tecan, Switzerland).

Best viability of MSCs was achieved with the programmable device (fig. 2). Cells survived the non-alcohol device slightly better (although not significantly) than the alcohol-containing device. The comparison of cells results from the alcohol-containing device with those from the programmable device shows a highly significant reduction of cell viability, whereas we could not observe a significant difference between the cell viability preserved with the non-alcohol device compared to the viability of cells using the programmable LIN-device.

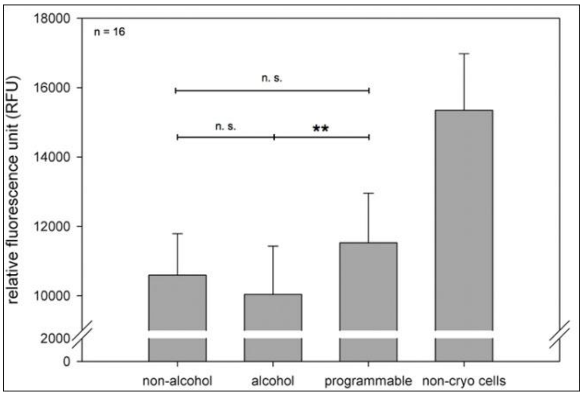

Figure 2: Cell viability of human mesenchymal stem cells after cryopreservation in different types of freezing device measured with alamar blue fluorescence. non-alcohol: Alcohol-free freezing device; alcohol: alcohol-containing freezing device, programmable: programmable LIN-based freezing device, rate -1°C/min; non-cryo cells: cells were not cryopreserved and used as a control Error bars indicate standard deviation.

MSC cells were also used for testing the transportation process during the cryopreservation time. Cells were again grown under standard conditions until 80% confluence. After harvesting with trypsin, the cells were aliquoted at a concentration of 500000/ml with cryopreservation medium in 2 ml cryovials. The aliquots were then placed into the non-alcohol freezing device. This was then packed in a secondary packaging with absorbing material and placed in a transportation box filled with 5 kg dry ice. This box was then closed according to the manufacturers instructions and transported by car for about 30 km and left overnight in the car. On the next day, the aliquots were stored in the gas phase of LIN in a cryostorage vessel at a temperature of about -150°C. After about one week of storage, the cells were thawed, plated in a 96-well plate, grown overnight and an alamar blue viability assay was performed.

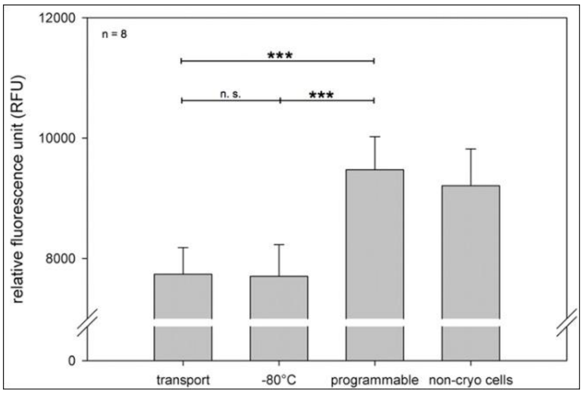

Figure 3: Cell viability of human mesenchymal stem cells after cryopreservation with different cryopreservation methods measured with alamar blue fluorescence assay. transport: Cryopreserved in alcohol-free freezing device packed in dry ice and transported; -80°C: cryopreserved in alcohol-free freezing device in -80°C freezer, programmable: cryopreserved in programmable LIN-dependent freezing device, rate -1°C/min; non-cryo cells: cells were not cryopreserved and used as a control. Error bars indicate standard deviation.

Transportation during the cryopreservation process had no negative effect on the viability of the hMSCs when compared to the cryopreservation in a -80°C freezer, both with the alcohol-free device. Cell viability was similar in both situations (fig. 3). In this test, the difference between the cryopreservation with the alcohol-free device and the programmable device was slightly higher than in the test before (fig. 2), so the difference between these methods could here be shown as extremely statistically significant (fig. 3).

## 3. DISCUSSION

Cryopreservation of cells or tissue in a non-programmable freezing device is a widely used method in the laboratory. Simultaneous cryopreservation and transportation has not been shown before.

For the surgical treatment of secondary hyperparathyroidism SHPT, hospitals need highly expensive cryostorage capacities and trained staff. The combination of effective and easy cryopreservation with the external storage of the transplant tissue would be a cost effective method for more hospitals to offer the surgical removal of the parathyroid glands and their cryopreservation.

Our tests show that the use of a non-alcohol freezing device is a suitable method for freezing highly sensitive biological material when no programmable LIN-based freezing device is available (as is the case in most hospitals). The freezing rate and the temperature curve given by the manufacturer was verified in our experiments[11].

Compared to the programmable method of freezing, cryopreservation in the alcohol-free device reduced cell viability by less then 20 %. For parathyroid glands this is acceptable.

Transportation in packaging conforming to UN3373 Cat. B in dry ice during freezing does not at all impair the viability of the highly sensitive cells when compared to freezing in an expensive -80°C freezer.

Simultaneous non-alcohol freezing and transportation to the storage facility is a cheap, easy and reproducible method for the cryopreservation of transplant tissues. Transportation shortly after excision lowers the risk of the specimen getting lost or forgotten within the hospital.

Further experiments will be performed to test the influence of this whole clinical process on the structure of parathyroid glands as well as on the viability and functionality of parathyroid cell culture.

## 4. REFERENCES

[1] Almaden Y, Hernandez A, Torregrosa V, Canalejo A, Sabate L, Fernandez Cruz L, Campistol JM, Torres A, Rodriguez M, 1998, High phosphate level directly stimulates parathyroid hormone secretion and synthesis by human parathyroid tissue in vitro, J. Am. Soc. Nephrol., 9: 1845-1852

[2] Block G, Port FK, Calcium phosphate metabolism and cardiovascular disease in patients with chronic kidney disease, Semin Dial, 16: 140-147

[3] Teruel JL, Tenorio MT, Rodriguez JR, Marc n R, Orofino L, Rivera M, Ortuño J, 1999, Treatment of secondary hyperparathyroidism in hemodialyzed patients with high-dose calcium carbonate without vitamin D3 supplements. Am. J. Nephrol.. , 19: 428-432

[4] Locatelli F, Cannata-Andia JB, Drueke TB, Hörl WH, Fouque D, Heimburger O, Ritz, E, 2002, Management of disturbances of calcium and phosphate metabolism in chronic renal insufficiency, with emphasis on the control of hyperphosphataemia, Nephrol. Dial. Transplant, 17: 723-731

[5] Block GA, Martin KJ, de Franciso ALM et al, 2004, Cinacalcet for Secondary Hyperparathyroidism in Patients Receiving Hemodialysis, N. Engl. J. Med., 350,15:1516-1525

[6] Leapman SB, Filo RS, Thomalla JV, King D, 1989, Am Surg, 55:359-365

[7] Shoback D, 2008, Clinical practice. Hypoparathyroidism, N. Engl. J. Med., 359: 391-403

[8] Dt. Ges. f. Chirurgie 1999, Grundlagen der Chirurgie G 86, Mitteilungen der dt. Ges. f. Chirurgie, 28. Jg., Nr. 4

[9] Venkataraman M, 1992, Effects of cryopreservation on immune responses: VI. An inexpensive method for freezing human peripheral blood mononuclear cells, J. Clin. Lab. Immunol., 37: 133-143

[10] Uccelli A, Moretta L, Pistoia V, 2008, Mesenchymal stem cells in health and disease, Nat. Rev. Immunol., 8: 726-736

[11] BioCision, 2012, Cool Cell Overview

# AIR SEPARATION AND PRODUCT STORAGE, $CO_2$ SEQUESTRATION

058

# Air Separation Unit Installation and Qualification at the French Guiana Space Centre

**Burdaszewski P.**

Ground Facilities Development Sub-Directorate, CNES-Launchers Directorate, Toulouse, France.

## ABSTRACT

Launchers equipped with cryogenics stages use important volumes of liquid oxygen as combustive and also need wide quantities of liquid nitrogen for conditioning and sub-cooling functions. The implementation of Soyuz at the French Guiana Space Centre in 2011 and the Ariane V cadence increase, generate higher needs for production and storage capacity. In that way, a new Air Separation Unit (that only delivers liquid products) and additional cryogenic storages were installed close to the launch pads. The objective was to double the current LOx production and to double the existing LIN&LOx storage capacity.

Besides standard constraints linked to such a project, the Kourou SILPA (Standard Integrated Liquid Plant Air liquide) project was characterized by specific aspects: high purity of LOx, very low particles pollution requirements, equatorial environment with extreme corrosive conditions, Guiana high voltage network limitations, atypical storage sizes (four 500m$^3$ horizontal cryogenic storages that are among the biggest in the world) , launch campaign constraints and qualification mode.

This paper reminds the main inputs for plant and tanks design, gives details on installation (range of LIN/LOx ratio, new energy consumption per liter, …), the way to manage constraints and finally outlines the gain for the Soyuz&ArianeV launches preparation.

## 1. INTRODUCTION

The European spaceport – also known as the **Guiana Space Centre** (**CSG**) – is a strategically-located facility that provides optimum operating conditions for Ariane launchers family. Qualified in 2005, the lastest version of Ariane V (Ariane V ECA), basically consists of a main cryogenic stage, two boosters, a vehicle equipment bay and a type A cryogenic upper stage (ESC-A). The main cryogenic stage is filled with roughly 130 tons of **liquid oxygen (LOx)** that ensure enough combustive for the 600s of propulsion duration. At an other scale, the upper cryogenic stage contains 12 tons of LOx at lift-off. As regards cryogenic propellant, Ariane V loading is operated on a **launch pad** (**ZL3**) during final chronology from **semi-mobile cryogenic tanks** (**RSM**). The LOx ones, 160 m$^3$-water-capacity each, come from the Air Liquid plant located at 4 km distance where they were previously totally filled, then forwarded up to a dedicated zone near the launch pad for the J0 transfer (lift-off day). In fact, the real LOx quantities needed for a launch are much higher than the strict loaded mass in the stages (130 + 12 tons). Several losses as flash phenomenon, vaporization during the waiting phase in ZL3 for thermal stabilization or huge volumes needed for transfer pipes and on-board equipment freezing, hamper the general balance. Moreover, due to temperature stratification in storage tanks and strict thermal requirements for loading, it’s not allowed to load “hot” LOx into cryogenic stages and, as a result, the liquid under 23% level in RSM is no longer usable for chronology operations. Considering all these constraints and reasonable margins, significant amounts of available LOx are necessary and four RSM (~800,000 litres of LOx) are transported to ZL3 ten days prior to each launch.

On the other hand, an other cryogenic product **- liquid nitrogen (LIN) -** is involved in the final chronology and more generally during all the Ariane campaign. The compressed gaseous nitrogen generates the most important consumption of LIN. Liquid is stored in fix horizontal vacuum insulated storages (150m$^3$ of water each), pressurized and vaporized at Air Liquide plant in order to be delivered at 250barg through a general distribution network of several kilometres. Compressed nitrogen is used in a very wide range in all the buildings of Spaceport. It’s particularly used for conditioning, ventilations, inerting, flushing or simply as facilities. A singular use of LIN in its “liquid form” is the sub-cooling function of LOx and high pressure Helium (Ariane V requirements) through impressive cryogenic exchangers. Thus, set apart the Spaceport standard consumption, a refill of the 6 LIN storages (about 800,000 litres) is required before each Ariane chronology in order to sustain the most degraded configuration (aborted launch for instance).

Situated in French Guiana, the Spaceport's location close to the equator at 5.3 deg. North latitude makes it ideally-situated for missions into geostationary orbit. Launching near the equator reduces the energy required for orbit plane change manoeuvres. This saves fuel, enabling an increased operational lifetime for satellite payloads. For several years, the main activity had been linked to the exploitation of Ariane V but, because of assets offered by the space centre, new launchers (and their own launch pad) appeared in the Guyanese landscape: **SOYUZ** with its fuel-LOx based propulsion and **VEGA**, the lastest of the Ariane family.

With a view to facing Ariane V cadence increase and new needs triggered by Soyuz, a deep change had to be undertaken: the storage system configuration (for LIN&LOx) generated too many constraints for the exploitation and the former air separation plant was no longer adapted to the LOx consumption. Therefore, it was decided to enhance LIN/LOx production capacity with the installation of a new Separation Plant and to increase LIN/LOx storage capacities with the implementation of new horizontal cryogenic tanks in addition to the current ones.

## 2. NEW AIR SEPARATION UNIT AND STORAGE REQUIREMENTS

### 2.1. Air Separation Unit (ASU)

French Guiana is an optimized site for spatial activity due in particular to the low Guyanese population density. The low industrial network doesn’t require any heavy industrial infrastructure in hundreds of kilometres in the neighbourhood and, therefore, European Spaceport concentrates a wide part of industrial production and consumers. At the time, the only ASU of the 80,000 km² of Guiana was located in CSG, without any alternative solution in the nearby countries. The design of such a plant was necessarily focused on proper Spaceport needs. For instance, as launchers do not use Argon, it wasn’t required to add an Argon column in the design. In addition, as oxygen is only used in its liquid form and the existing compressed nitrogen installation is based on liquid nitrogen source, the design of distillation column had to be adapted to a 100% liquid production mode.

As regards purity, cryogenic propulsion requires pure combustion $H_2$-$O_2$ and thus, delivered LOx can’t accept more than 0.2% of total impurities ($O_2 \geq 99.8\%$). Unlike standard ASU whose purity levels is generally close to 99.6%, the ratio Air flowrate entrance/LOx production or Energy consumption/LOx production is expected to be higher than usual. An other impact of such a purity level is the oversizing of first desiccation stages and the re-enforced safety monitoring of methane content in the LOx condenser. On the other hand, there is no specific constraint associated with the LIN specifications.

As for the production capacity, in addition to the Ariane V current consumption, the future ASU design must take into account new needs, beginning by the Soyuz ones: as regards the LOx quantities, a Soyuz launch campaign is more or less equivalent to an Ariane V campaign, that is to say around 300 000 litres per launch to which it’s necessary to add losses due to product transportation from AL plant to Soyuz launch pad (12km with standard 20m$^3$ semi-trailers), freezing operation of general Soyuz fix tanks (3x200m$^3$) at beginning of each campaign, vaporization rate of new storage tanks without forgetting medical LOx contribution for Guiana hospitals. On the same way, LIN production sizing includes Soyuz&Ariane V - liquid and gas - consumption per campaign, losses due to product transportation to Soyuz pad, freezing operation of general Soyuz fix tanks, vaporization rate of new storage tanks, efficiency of 250bar pumping station, quantities involved in the Liquid Helium boil-off condenser and in the pre-cooling stage of Liquid Hydrogen production, without forgetting LIN contribution for Guiana industry. Based on a target cadence of launches per year, it appears that the future ASU shall be able to deliver, with standard settings, more than 21,000 LOx litres per day and more than 41,000 LIN litres per day (while the former ASU was able, in maximum LOx configuration, to deliver 12,000 LOx litres per day and 34,000 LIN litres per day).

Finally, the non linearity of spatial activity in CSG (between 6 and 10 launches not uniformly distributed in a year + large amounts of cryogenic liquids used during single day chronology operations) demands a wide flexibility in the production mode. So, it’s requested to switch quickly and easily from a standard production to a maximum LOx or LIN mode in a wide range, specially for LOx production.

Considering all those requirements, the **SILPA 70** (**Standard Industrial Liquid Plant Air liquide 70tons**) model were chosen and installed in Guiana.

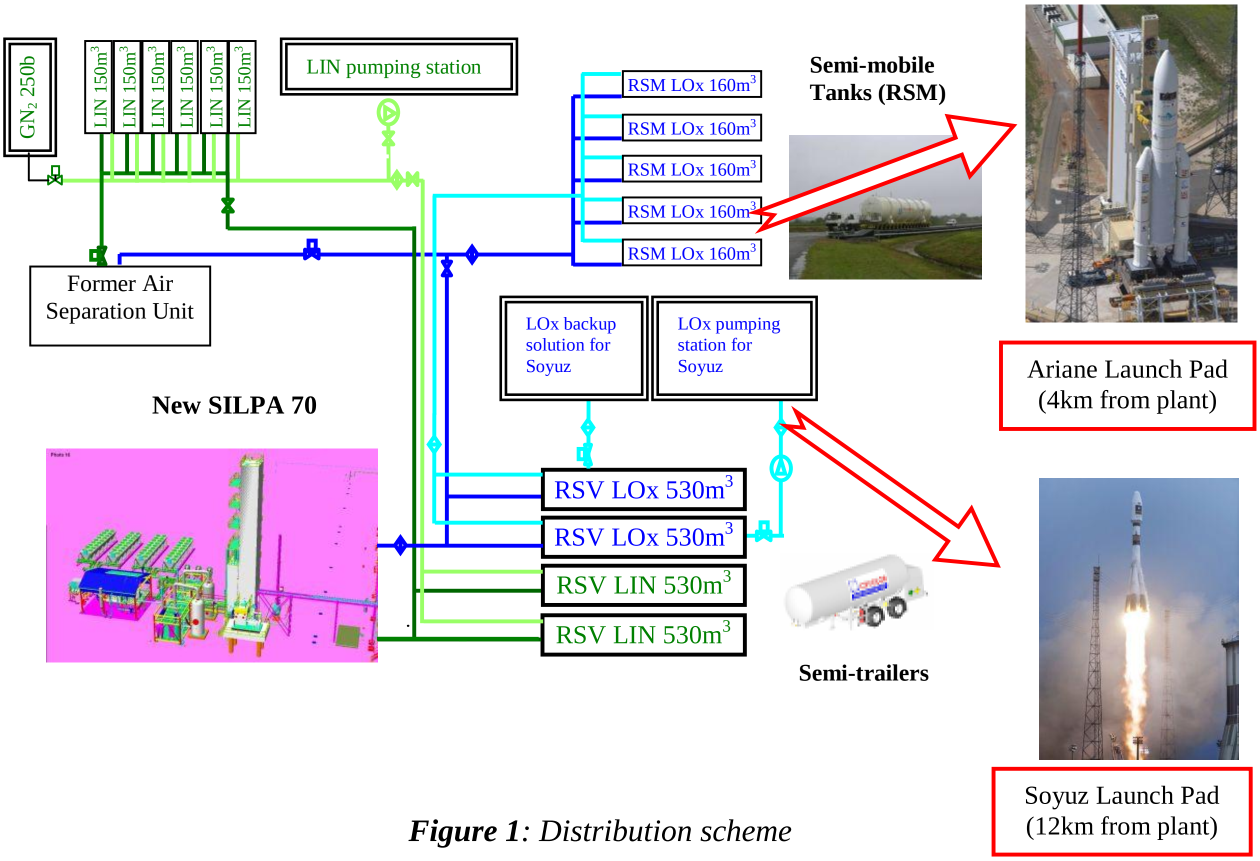

***Figure 1**: Distribution scheme*

## 2.2. New cryogenic storage tanks

As mentioned before, the current storage tanks consist of around 800 000 litres of LIN and 800 000 litres of LOx whose characteristic is to be **semi-mobile tanks** (**RSM LOx**). It implies that from the moment the RSMs leave the cryogenic plant location to be conveyed to the Ariane V launch pad, there is only one tank left to receive LOx production and the ASU is likely to stop till the RSMs return. Moreover, the degraded case of multiple launch attempts consuming large oxygen and nitrogen quantities that makes necessary to refill cryogenic storages as quickly as possible before the next campaign, was compliant with the ~ 3 weeks incompressible duration between two Ariane V chronologies (due mainly to buildings limitations and fluids stocks reconstitution). The introduction of the Soyuz system with independent ground segment facilities and separated campaign teams in regard with Ariane V organization, now makes it possible to operate two dimensioning launches with a short time span. The current storage capacities fail to fulfil this flexibility requirement, even if production performances are enhanced. Thus, it was decided to complement the current storages with 2 x 1 million litres storage capacity per product.

Technology and production tools in vacuum insulated double wall cryogenic tanks being limited with respect to the size of such equipments, it has been proposed to manufacture two 530m$^3$ water volume horizontal cryogenic fix tanks per product in order to reach the target. Due to the heavy density and the induced strong loads, the 2 cryogenic oxygen tanks (**RSV** LOx) were considered in 2009 as the world's biggest or among the biggest LOx horizontal tanks (manufactured in Czech Republic by Chart Ferox).

So as to reduce losses from storages boil-off, a vaporization rate threshold of 0.15% max capacity/day was introduced and tested during qualification tests.

Eventually, due to the distance between the Soyuz launch pad and the Air Liquide plant location, and because of the RSM exclusivity for Ariane V systems, semi-trailers have to commute between the two sites in order to refill fix cryogenic Soyuz tanks few days before the launch. Thus, a new LOx loading station (the LIN one already exists) was introduced in the general specifications.

## 3. MANAGEMENT OF SPECIFIC CONSTRAINTS

Although Spaceport offers many advantages, we mustn't overlook the environment drawbacks. Local climate is hot and damp, with more than 3 metres of accumulated rainfalls per year. As a consequence, civil works can't be managed outside the dry season (July to November), all the electronic devices must be equipped with a heating resistance in order to enhance lifetime, electrical box located outside are continuously flushed with compressed dry air to maintain an acceptable hygrometry content, all metallic equipment are to be provided in stainless steel, heat-galvanized, or coated with a three layers off-shore-type protection. The local fauna is also to be taken into account with, in particular, special grids installation at the cryogenic vent pipes output in order to prevent any animal from getting in and blocking it.

As indicated before, the Guiana infrastructures are adapted to their own needs. With a population of 230,000 people (January 2009 estimate), only two electric sources deliver electric power in the country: the Cayenne thermal power station and the Petit-Saut hydroelectric power station. Therefore, the resultant high voltage short-circuit power is so low (110MVA) that SILPA main compressor risks to cause a general network shutdown at the starting of the engine (need a minimum 140MVA short-circuit power). Thus, an adapted 6,600 Volts frequency converter was introduced in the unit electric architecture in the sole purpose of starting smoothly the 2.5 MW main engine and preserve the Guiana network stability. It's a real concern because the new main compressor power consumption represents the major power consumer of Guiana (2% of full Guiana and 17% of Spaceport consumption).

From a logistic point of view, transportation of RSVs (35m long, 5m diameter, 135 tons empty) or cold box, generated many constraints due mainly to the loads limitation (90 tons) of the Cayenne river's principal bridge. Generally used for the Ariane V stages sea transport, the special flat-bottomed boat "Toucan" had to be chartered in order to convey the 4 new storage tanks from Bremen harbour directly to Kourou harbour, avoiding any bridge crossing. Facing to the lack of heavy lifting systems in Guiana, the 300 tons crane and the four mobile lifting devices for tanks moving came from Europe on the same ship.

***Picture 1**: flat-bottomed boat "TOUCAN"*

Given the strict reliability objectives of such a system, it was decided during the development phase to install a "hot" redundant device in order to fulfil the LOx semi-trailers loading function in case of pump failure, anomaly on installation, liquid product pollution or empty cryogenic tank. Reliability rules recommend the use of a different technology and separated lines for redundant systems. In that way, a suction port by gravity was implemented on the second LOx RSV leading to an optimized tanks setting with respect to the maximum height induced by the SILPA outlet and to a minimum height induced by the first RSV NPSH pump (Net Positive Suction Head).

***Picture 2**: the 4 RSV installed on their supports*

On the other hand, it's important to highlight that, as regards liquid oxygen utilization, Guiana Space Centre activity really differs from the other industrial activity, using it directly under its liquid form, particularly for propulsion engines. Four days before lift-off, RSMs are transported to a dedicated zone near the launch pad and, during the chronology day, LOx is pressurized and delivered to the launcher interfaces for stages loading through hundreds of metres of 4" vacuum insulated double wall lines, full equipped with many valves, filters and instrumentation. The chronology is similar to a music partition: everything is perfectly defined, each operation is expected to respect its own duration, every milestone must be reached on due time with the risk to exceed the allowed launch window and generate an expensive launch report. Knowing that, we can easily imagine that a slight deviation of LOx flow conditions could have a deep impact on launch success. In that way, everything is done to eliminate particles and traces of contaminants as hygrometry or carbon dioxide. Indeed, particles whose diameter is over 10 microns, ice flakes and dry ice constitute the main cause of filters clogging on ground segment side and the main cause of launch failure on on-board side (propulsion engine is very sensitive to obstruction concern in injection plates). So, strict protocols are respected on every new work on cryogenic equipments on such systems. High level of cleanliness is obtained by degreasing, chemical oxidizing, rinsing, flushing and using control methods adapted to each line configuration. Beside the nitrogen gas flushing operated before and after cryogenic pipes integration (with particles and hygrometry checks), the LOx lines are then flushed with liquid nitrogen or oxygen in order to eliminate heavy particles that have not been drained with gas flushing. Considering the liquid sampling not really adapted to a particle count, successful criteria adopted by the launch operator Arianespace is based on a empiric method consisting in delivering fix LOx flow through a monitored 10µm filter and checking the pressure drop evolution. If the maximum threshold is not reached during an inter-storage liquid transfer and if, after the dismounting operation, there is no damage identified in the filter media, the cleanliness of the upstream system is considered acceptable. Obviously, this heavy procedure requires a lot of time and wide volumes of cryogenic product but years of experience in risk analysis in the “spatial sphere” have confirmed the deployment of such precautions.

Finally, it’s important to point out that the 2.5 years of on-site works had to adapt its proper planning to the Spaceport operation constraints. About ten days before a launch, all the systems involved in the chronology are “frozen”. All the operation not directly linked to the on-going campaign are forbidden. Moreover, in the first weeks after a lift-off, liquid plant is totally focused on the cryogenic store reconstitution for the next launch. With an average rhythm of 6 Ariane V launches per year, it results in an important reduction of allowed window for work.

## 4. QUALIFICATION AND RESULTS

### 4.1. SILPA performances

Qualification tests of the new cryogenic plant consisted in checking the specifications compatibility for flowrates, purity, pollution content, outlet pressure and power consumption. These parameters were also checked for the limit modes, maximum LOx production and maximum LIN production. Final results can be found in *table 1*.

Minimum LIN&LOx outlet flows are easily obtained with successful product purity results. The max LOx & max LIN modes results show a wide range of tuning with a possibility to make the 100% LOx production grow or increase the LIN production by an additional 50%.

Monitored by an oxygen traces analyzer, the LIN purity values confirm large margins as regards the CSG needs (0.02 ppm $O_2$ for $\leq$ 50 ppm required) even during Max LOx mode (up to 0.7 ppm $O_2$) while LIN draw off is at minimum to focus on LOx production. As for LOx purity, the recurrent 100% obtained are understandable by the limited oxygen analyzer accuracy that is not able to detect $10^{-5}$ pollution content.

The very low and stable contents of hygrometry and carbon dioxide are obtained thanks to a right purification design and an adapted alternative management. On the other hand, the variability of methane content is due to the lack of specific treatment system for hydrocarbon components and therefore, the value is mainly linked to the production mode: the higher the LOx draw off is (Max LOx mode), the lower the $CH_4$ concentration is in the LOx vaporizer; conversely, the lower the LOx draw off is (Max LIN mode), the higher the $CH_4$ concentration is.

As concerns the specific power consumption, mainly due to the general centrifuge compressor, it appears that even in limit mode, the requirement of 2.77 MW/h is fulfilled.

***Table 1**: results of SILPA performance tests*

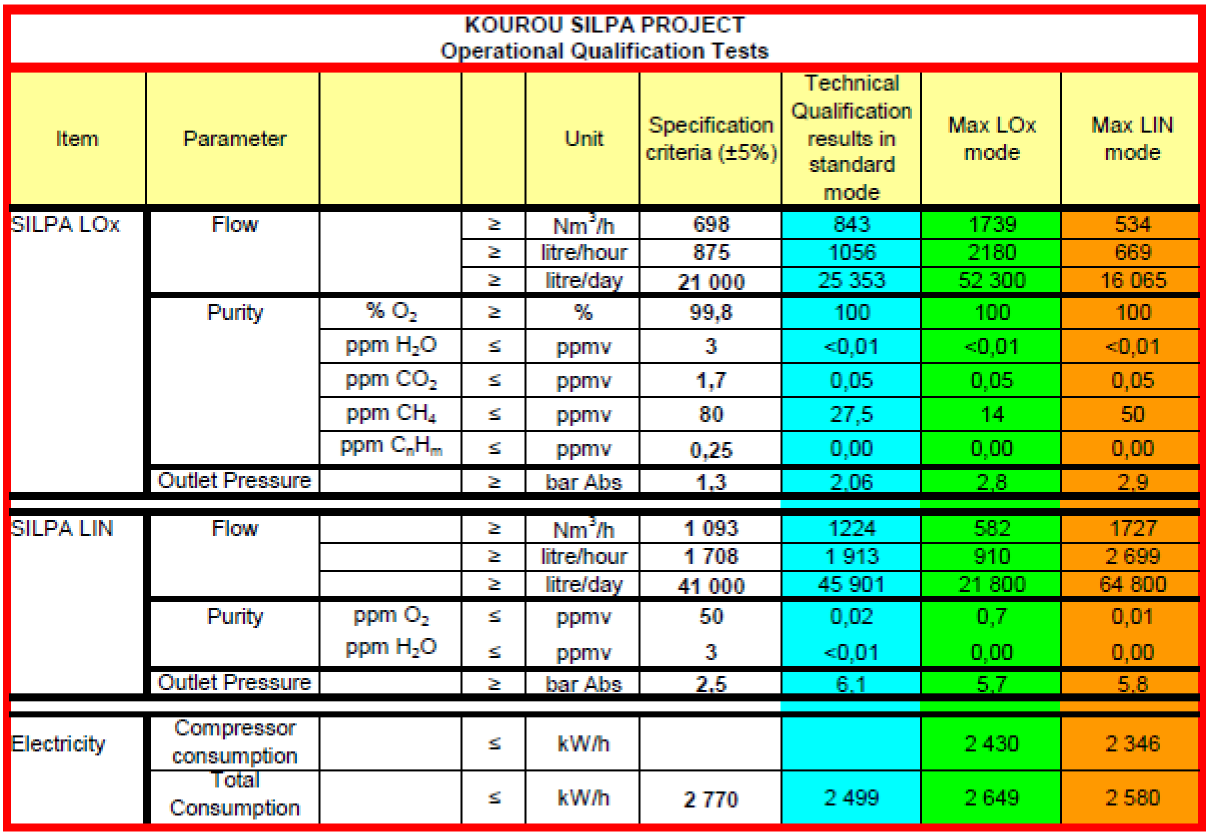

KOUROU SILPA PROJECT
Operational Qualification Tests

| Item | Parameter | | | Unit | Specification criteria (±5%) | Technical Qualification results in standard mode | Max LOx mode | Max LIN mode |
|---|---|---|---|---|---|---|---|---|
| SILPA LOx | Flow | | ≥ | $Nm^3/h$ | 698 | 843 | 1739 | 534 |
| | | | ≥ | litre/hour | 875 | 1056 | 2180 | 669 |
| | | | ≥ | litre/day | 21 000 | 25 353 | 52 300 | 16 065 |
| | Purity | % $O_2$ | ≥ | % | 99,8 | 100 | 100 | 100 |
| | | ppm $H_2O$ | ≤ | ppmv | 3 | <0,01 | <0,01 | <0,01 |
| | | ppm $CO_2$ | ≤ | ppmv | 1,7 | 0,05 | 0,05 | 0,05 |
| | | ppm $CH_4$ | ≤ | ppmv | 80 | 27,5 | 14 | 50 |
| | | ppm $C_nH_m$ | ≤ | ppmv | 0,25 | 0,00 | 0,00 | 0,00 |
| | Outlet Pressure | | ≥ | bar Abs | 1,3 | 2,06 | 2,8 | 2,9 |
| SILPA LIN | Flow | | ≥ | $Nm^3/h$ | 1 093 | 1224 | 582 | 1727 |
| | | | ≥ | litre/hour | 1 708 | 1 913 | 910 | 2 699 |
| | | | ≥ | litre/day | 41 000 | 45 901 | 21 800 | 64 800 |
| | Purity | ppm $O_2$ | ≤ | ppmv | 50 | 0,02 | 0,7 | 0,01 |
| | | ppm $H_2O$ | ≤ | ppmv | 3 | <0,01 | 0,00 | 0,00 |
| | Outlet Pressure | | ≥ | bar Abs | 2,5 | 6,1 | 5,7 | 5,8 |
| Electricity | Compressor consumption | | ≤ | kW/h | | | 2 430 | 2 346 |
| | Total Consumption | | ≤ | kW/h | 2 770 | 2 499 | 2 649 | 2 580 |

## 4.2. Particle check

In spite of taking all the necessary precautions, first transfer of LOx from RSV n°2 to a RSM failed, due to an in-line filter clogging. After dismounting, the identified pollution was established by metallic pieces and dross. To face this inescapable initial pollution, a new filter was fitted in the LIN transfer lines between RSV and fix storages, and the conic filter on LOx transfer line was substituted by another 10µm absolute filter type (with cartridge) which offers a larger filtration surface. The second step consisted in cleaning the more or less filled tanks: the most filled LOx RSV used its dedicated pump and filter operating a closed filtration loop, the second LOx RSV downloaded by gravity the cryogenic product in several semi-trailers (20m$^3$ each) through an adapted filtration device while LIN RSV had been totally drained.

After this drastic cleaning operation, new transfer tests were carried out with the objective not to exceed the threshold of 65 mbar pressure drop through the 10µm absolute filter (3µm nominal filtration) and with a 6000 litres/hour flow. *Figure 2* shows the final results with the LOx RSV n°2.

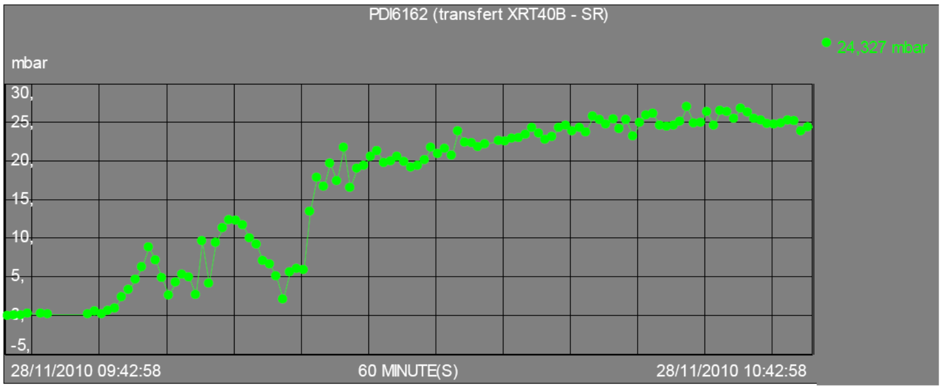

***Figure 2**: pressure drop evolution in a 10µm absolute filter with 6000l/h LOx flow*

The noted pressure drop stabilizes close to 30mbar for the two LOx RSV and confirms the acceptable cleanliness of the two systems (RSV + pipes). No anomaly was identified either during the LIN transfer.

## 4.3. Tanks boil-off

While former LIN fix storage tanks waste around 0.45% per day of maximum capacity by boil-off, the new ones (RSV) are expected to limit natural vaporization up to 0.15% per day. Due to the operation constraints, the priority given to the launch campaign and the consequent RSV volumes, the boil-off qualification took time. Finally, tests were implemented (see *table 2*) on the two LOx RSV and the two LIN RSV with different configurations. On LOx side, whatever the initial level or the test duration, a maximum of 400 litres lost per day by boil-off allocate a boil-off performance better than 0.09%. As for LIN side, the average value of liquid lost is 750 litres per day which corresponds to the 0.15% boil-off requirement.

***Table 2****: results of tanks boil-off tests*

| **LOx RSV n°1** | Duration (days) | RSV initial&final levels (litres) | Volume of vaporized liquid (litres) | Boil-off (litres per day) |
|---|---|---|---|---|
| Test n°1 | 30 | 76 174<br>64 274 | 11 900 | **390** |
| Test n°2 | 14 | 244 295<br>239 103 | 5 192 | **370** |

| **LIN RSV n°1** | Duration (days) | RSV initial&final levels (litres) | Volume of vaporized liquid (litres) | Boil-off (litres per day) |
|---|---|---|---|---|
| Test n°1 | 21 | 137 318<br>123 550 | 13 768 | **655** |
| Test n°2 | 12 | 510 552<br>501 522 | 9 030 | **752** |

| **LOx RSV n°2** | Duration (days) | RSV initial&final levels (litres) | Volume of vaporized liquid (litres) | Boil-off (litres per day) |
|---|---|---|---|---|
| Test n°1 | 92 | 96 356<br>59 626 | 36 730 | **400** |

| **LIN RSV n°2** | Duration (days) | RSV initial&final levels (litres) | Volume of vaporized liquid (litres) | Boil-off (litres per day) |
|---|---|---|---|---|
| Test n°1 | 28 | 421 216<br>400 970 | 20 246 | **723** |
| Test n°2 | 31 | 504 416<br>480 618 | 23 798 | **767** |

## 4.4. Liquid transfer flowrate and LOx pump performance

In order to enhance Arianespace flexibility as launch operator, it's necessary to use the full potential of the new storage capacity, particularly for liquid oxygen, allowing quick transfer to the complete set of LOx RSM that have been used for a chronology. The faster the RSM will be re-filled, the better the Space Centre availability will be for another launch. In that way, the general requirement is to allow a complete re-fill of 4 RSM and a 20m$^3$ semi-trailer in 5 days maximum. Taking into account the operation time for manually switching RSMs when loaded, this constraint leads to a 6000 litres per hour objective. Confronted with the operational constraints developed above (chapter 2), it was unconceivable to carry out a real and complete qualification test putting Ariane campaign to one side for several days. Thus, a representative test minimizing the number of involved RSMs consisted in filling completely a RSM, switching to another and starting a new transfer for a few hours. The interest of this procedure was to confirm RSV pressurization and interconnection pipes freezing durations, measure the transfer flow during a significant duration, check the flow evolution all along the transfer (influence of head of water due to bottom filling mode) and characterize the real time needed to operate manually the RSM switch at the end of first loading. Results are shown in *table 3*.

***Table 3****: results of liquid transfer tests*

| Operation | Time | Duration | LOx RSV n°1 Pressure (barg) | LOx RSV n°1 Level (litres) | LOx RSV n°1 Volume drop (litres) | LOx RSM n°E then n°A Level (litres) | LOx RSM Volume drop (litres) |
|---|---|---|---|---|---|---|---|
| **Pressurization start** | 16h21 | 49 min | 0,30 | 346 730 | 930 | | |
| **Pressurization end** | 17h10 | | 0,80 | 345 800 | | | |
| **Freezing start** | 18h00 | 1h35 | 0,80 | 345 500 | 1 750 | | |
| **Freezing end** | 19h35 | | 1,45 | 343 742 | | | |
| **Transfer start** | 19h40 | 14h | 1,45 | 343 742 | 89 771<br>**Average flow: 6400 l/h** | 63 218 | 87 881 |
| **Transfer stop** | 9h40 | | 1,45 | 253 971 | | 151 099 | |
| **Transfer re-start** | 9h50 | 1h50 | 1,45 | 253 971 | 12 118<br>**Average flow: 6600 l/h** | 128 218 | 12 014 |
| **Transfer stop** | 11h40 | | 1,45 | 241 793 | | 140 232 | |
| **Depressurization start** | 11h43 | 50 min | 1,45 | 241 793 | 0 | | |
| **Depressurization end** | 12h33 | | 0,30 | 241 793 | | | |

Provided an anticipation of the RSV pressurization and the pipe network freezing, the system design fulfil perfectly the purpose in view. From a organization point of view, it seems obvious that the operators will have to schedule RSV-RSM transfers by batches and not separately in order to minimize liquid lost.

As regards the LOx pump and its redundant system performances, transfer tests from RSV to semi-trailers showed a full compliance of the pumping equipment (flow > 30 $m^3/h$; 30 min of pump freezing) while backup solution delivered up to 10 $m^3/h$ without any anomaly.

## 5. CONCLUSION

On-site works started in October 2008, SILPA technical qualification was done in December 2010 and operational qualification ended in May 2011. The first launcher loaded with new LOx production was the 199th flight of an Ariane launch vehicle (VA199) which was successfully performed on the 20th of December, 2010. The historic inaugural launch of Soyuz in Guiana (VS01 on the 21th of October, 2011) confirmed the perfect adaptation of the new LIN&LOx production and storage installations to the new context in the CSG.

LIN production increased and LOx production doubled with a possibility to double again in maximum LOx mode, ensuring the product availability as regards the new needs.

The LIN and LOx storage capacities were increased by 1 million litres each, offering wide margins for production and flexibility for launches cadence.

Quick transfers from new storages (RSV) to LOx semi-mobile tanks (RSM) exit the cryogenic production limitations from the critical path between two Ariane V flights.

At last, the new LOx semi-trailers loading system offers a dedicated and redundant solution to the Soyuz campaign preparation and LOx transportation to the Soyuz launch pad.

Under Arianespace financing, **CNES**, as Spaceport Ground Segment designer, realized the specifications and managed the totality of the project, till the final qualification. The plant was then given in operation to **Arianespace** and **Air Liquide** teams.

**Picture 3**: panoramic view of new air separation unit in Guiana Space Centre

032

# Advanced Cryogenic Processes for low Purity Oxygen Production

**Kirchner L., Lochner S., Dowy S.**

Linde AG, Engineering Division, Dr.-Carl-von-Linde-Str. 6-14, 82049 Pullach, Germany

## ABSTRACT

The use of low purity oxygen is attractive for the latest technology available for the production of non-ferrous metals. In these applications it allows improvements in productivity, fuel efficiency and helps to protect the environment, as the total throughput of gas in the plants can be reduced.

The penalty for use of oxygen is the additional capital expenditure (CAPEX) for the oxygen plant plus the additional energy consumption (OPEX) for operating the plant. The presentation will show how the topology and the parameters of the process can be chosen so that both CAPEX and OPEX can be minimised.

The presentation summarises the state of the art technology for cryogenic oxygen recovery processes and then introduces an advanced approach to provide low purity oxygen for smelter applications. The physical background and mechanisms of the process cycle definition under the given boundary conditions is described, as well as the technical parameters for selection of machinery and equipment.

## 1. INTRODUCTION

Innovation of oxygen production technologies leading to the reduction of production cost has opened up new applications for oxygen use ever since oxygen plants became available. The development of techniques for the low cost oxygen plants to produce oxygen in sufficient quantities at a low enough cost for metallurgical use, competing with low cost fuels, represented an important phase of metallurgical development. The first commercial uses of tonnage oxygen in metallurgy were in the iron and steel industry. The use of oxygen to enhance carbon elimination from pig iron was recognised by Bessemer but actual application was not possible until processes were developed for the manufacture of low cost, tonnage oxygen. [1]

The rising cost of energy combined with higher environmental requirements for smelters and converters make the use of oxygen in the non-ferrous metal production more attractive. With innovative oxygen recovery processes for lower purities the overall cost for the production of metal can be minimised. This paper presents a highly efficient process for the production of impure oxygen for metallurgical use. The development of process cycles in air separation technology needs methods to compare the efficiency of different cycles. This paper also presents an exergy evaluation of air separation processes based on the example of the discussed process.

## 2. PRINCIPLES OF AIR SEPARATION

In all production processes with high throughput, air is separated by rectification. Many different process cycles are now available. The principles are described for an example of a Linde patent for low purity oxygen production, which is shown in figure 1.

The air is compressed in a main air compressor (MAC) and fed to a pre-purification system to remove water, carbon dioxide and other contaminants. The MAC discharge pressure depends on the required purity for the oxygen product. The lower the purity requirement is, the lower the MAC pressure can be. A portion of the air is cooled in a main heat exchanger to the dew point. It is then introduced into the high pressure column of a double rectification column. The trays in the high pressure column rectify the air into a nitrogen product taken from the top of the column and an oxygen rich liquid taken from the sump. The required refrigeration duty for the top condenser of the high pressure column is provided by boiling the bottom liquid of the low pressure column and by that creating ascending vapour for the low pressure column. The liquid generated in the top condenser of the high pressure column is used in two ways: one part serves as reflux for the pressure column while the remaining part is used as top reflux for the low pressure column. Two other liquid streams are taken out of the high pressure column: the bottom liquid, which contains app 33% to 37% of oxygen and a liquid air stream taken from the lower part of the high pressure column. Before these are reduced in pressure and fed into the low pressure column as refluxes, they are subcooled against the nitrogen fraction coming from the low pressure column in a separate heat exchanger. This subcooling operation reduces the flash portion when the liquids are throttled in the expansion valves to the low pressure column and thus increases the efficiency of the rectification in the low pressure column.

To create the refrigeration duty for the process, which means to recover heat transfer losses, insulation losses and produce liquid products, an expansion turbine is used. In the example, a second portion of the air stream from the MAC is partially cooled in the main heat exchanger and taken to a generator loaded turbine. The turbine expands the air to the low pressure column pressure and the cold gas is now fed into the low pressure column, where approximately air composition is achieved.

The oxygen product is taken from the bottom of the low pressure column, pumped to the required product pressure and fed into an auxiliary condenser, which vaporises the liquid oxygen against high pressure air. The heating air for the auxiliary condenser is provided by a booster air compressor (BAC). The liquefied air coming from the auxiliary condenser is then fed into the high pressure column to take part in the rectification.

In the 1990s, Linde patented this process for producing oxygen in the wide range of 50% oxygen purity up to 96% oxygen purity. This process will be used as reference for the improved process.

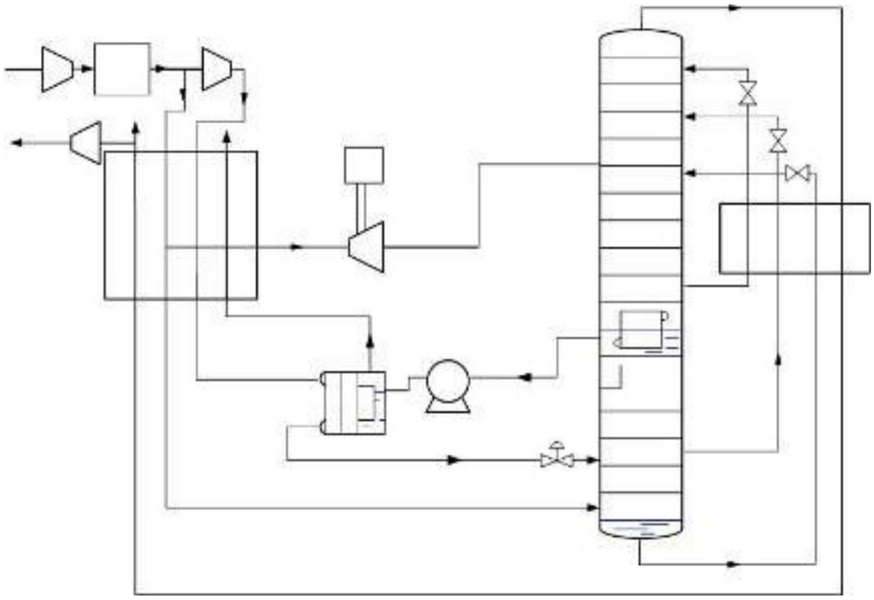

Figure 1. Reference process with HP and LP column and auxiliary condenser

To systematically improve the process further, the method of exergy evaluation can be applied. This method is described below.

## 3. PRINCIPLES OF EXERGY EVALUATION

Exergy is defined as the energy, which can be transformed into any kind of usable energy under given ambient conditions. Or, in other words, exergy is the part of any kind of energy, which can be transformed into physical work under given ambient conditions.

Using the exergy evaluation of processes does not require the comparison to an ideal thermodynamic process (e.g. Carnot cycle). It is only looked at the balance of the exergies fed into a system and the exergies leaving the system plus the loss of exergy in the process [2]:

$$\sum_{in}\dot{\mathrm{E}}_\mathrm{i} = \sum_{out}\dot{\mathrm{E}}_\mathrm{i} + \dot{\mathrm{E}}_\mathrm{l} \ \ with\, \dot{\mathrm{E}}_\mathrm{l} \geq 0 \tag{1}$$

where

$\dot{\mathrm{E}}_\mathrm{l}$ $Exergy\ loss\ in\ the\ process$
$\dot{\mathrm{E}}_\mathrm{i}$ $Exergy\ of\ the\ component\ i$

For a continuous process the exergy efficiency is defined as the ratio of the exergy fed into the system minus the exergy losses divided by the exergy fed into the system [3]:

$$\eta_\mathrm{ex} = 1 - \sum\left(\dot{\mathrm{E}}_\mathrm{l,\,i}\right)/\dot{\mathrm{E}}_\mathrm{in} \tag{2}$$

In general for an ideal gas the exergy is the sum of the exergy of the enthalpy and the work for the reversible separation of the components. The reversible separation work is identical to the mixing entropy. So for the calculation of the exergy of the separation process, only the mixing entropy is used. The resulting exergy equations applying these simplifications can be separated in one term for compression power, one for liquefaction power and one for the separation power:

1. The minimum theoretical compression power for all products including waste gas is calculated as isothermal compression work of the pure component from ambient conditions to the product discharge pressure according to the following equation:

$$\Delta\dot{\mathrm{E}}_\mathrm{comp} = \mathrm{R} * \mathrm{T} * \dot{\mathrm{m}} * \frac{\ln\left(\frac{p_{out}}{p_{in}}\right)}{1000} \tag{3}$$

2. The liquefaction power for all liquids is calculated as the difference of the enthalpy exergy of the pure component at ambient conditions and at liquid state:

$$\Delta\dot{\mathrm{E}}_{liq} = \Delta h * \dot{\mathrm{M}} \tag{4}$$

3. The separation exergy streams for all products including the waste gas and the process air is calculated as

$$\dot{\mathrm{E}}_{sep} = -R * T * \dot{\mathrm{m}} * \left(x_{N_2} * ln\left(x_{N_2}\right) + x_{A_r} * ln\left(x_{A_r}\right) + x_{O_2} * ln\left(x_{O_2}\right)\right) \tag{5}$$

where

$$R = 8.31441\frac{kJ}{kmol * K}(ideal\ gas\ constant)$$

$$T = ambient\ temperature\ [K]$$

$$x_i = mol\ fraction\ of\ component\ i$$

$$\dot{\mathrm{M}} = mass\ flow\ [\frac{Nm^3}{h}]$$

$$\dot{m} = mass\ flow\ [\frac{mol}{s}]$$

$$\Delta h_{O_2} = 292\frac{W}{Nm^3}, \Delta h_{N_2} = 266\frac{W}{Nm^3}, \Delta h_{Ar} = 371\frac{W}{Nm^3}$$

## 4. APPLICATION OF THE EXERGY METHOD TO THE REFERENCE PROCESS

With the method described above, the overall process cycle can be evaluated regarding efficiency and processes can be compared. The result is independent from the machinery efficiency. The exergy efficiency is defined as the ratio of the exergy balance and the total power needed for compressors and pumps, minus the produced generator power:

$$\eta_{\mathrm{ex}} = \frac{(\dot{\mathrm{E}}_{sep,in} - \dot{\mathrm{E}}_{sep,out} + \Delta\dot{\mathrm{E}}_{liq,out} + \Delta\dot{\mathrm{E}}_{\mathrm{comp,out}})}{\mathrm{P}_{\mathrm{comp}}} \qquad (6)$$

With the empirical formula for compressor power consumption:

$$P = 0.1 * \dot{\mathrm{M}} * \log(\frac{p_{out}}{p_{in}})$$

Equation (6) can now be applied to the reference process described before. As an assumption, the process is fed with 100,000 Nm³/h net. process air. The other prerequisites are that the ambient pressure is 1.001 bara and the ambient temperature is 293.1 K. With this the following results are achieved:

Table 1. Apply the exergy balance to the reference process

| **Products** | Flow<br>$Nm^3\ h^{-1}$ | FLOW<br>$mol\ s^{-1}$ | PRES<br>bar | $O_2$<br>% | Separation Power<br>kW | Compression Power<br>kW | Liquefaction Power<br>kW |
|---|---|---|---|---|---|---|---|
| GOX | 20858 | 258.5 | 1.45 | 98.00% | 262 | 233 | |
| GOX IC | 0 | 0.0 | 7.2 | 98.00% | 0 | 0 | |
| LOX | 193 | 2.4 | 1 | 98.00% | 2 | 0 | 117 |
| GAN | 3877 | 48.0 | 5.1 | 0.4000% | 57 | 191 | |
| LIN | 58 | 0.7 | 1 | 0.40% | 1 | 0 | 32 |
| Waste | 75014 | 929.7 | 1.00 | 0.40% | 1104 | 0 | |
| Process Air | 100000 | 2564.1 | 5.6 | 20.95% | | | |
| | | | | | Sum of min. theoretical power kW | | 1999 |

Table 2. Estimated power consumption for the reference process

| **Machine** | Flow<br>$Nm^3\ h^{-1}$ | Pin<br>bar | Pout<br>bar | estimated Power<br>kW |
|---|---|---|---|---|
| MAC | 100822 | 1.0 | 5.6 | 7539 |
| BAC 1 | 0 | 5.4 | 8.6 | 0 |
| GAN EXT | 3977 | 1.2 | 5.1 | 250 |
| Turbine 1 | | | | 0 |
| Pump 1 | | | | 80 |
| Pump 2 | | | | 0 |
| TOTAL | | | | 7869 |

The final step is to apply equation (6) and divide 1999 kW by 7869 kW. This gives the result for the exergy efficiency for the reference process of 25.4%

## 5. IMPROVED PROCESS FOR IMPURE OXYGEN PRODUCTION

The process is a modification of the so called dual reboiler process. The rectification consists of one low pressure (LP) column and two high (HP) pressure columns each one having its own condenser. The two high pressure columns run on different pressure levels. The oxygen product is vaporised in a conventional auxiliary reboiler/condenser against condensing air. The low pressure column 12 is divided into two sections by the main condenser 26. The top section works similar to the conventional LP column but the condenser 26 receives instead of product purity oxygen a liquid with app. 70% oxygen content. Consequently the condensing liquid nitrogen from the first HP column only needs a pressure of 3.5 bara. The section below the condenser has a much lower load and provides the remaining separation capacity to produce the required oxygen purity. It receives it vapour from the condenser 27.

The condenser 28 is the auxiliary condenser for vaporising the oxygen product at the elevated pressure. It condenses the BAC air at elevated pressure to evaporate the oxygen with specified product purity. The BAC also feeds the second HP column.

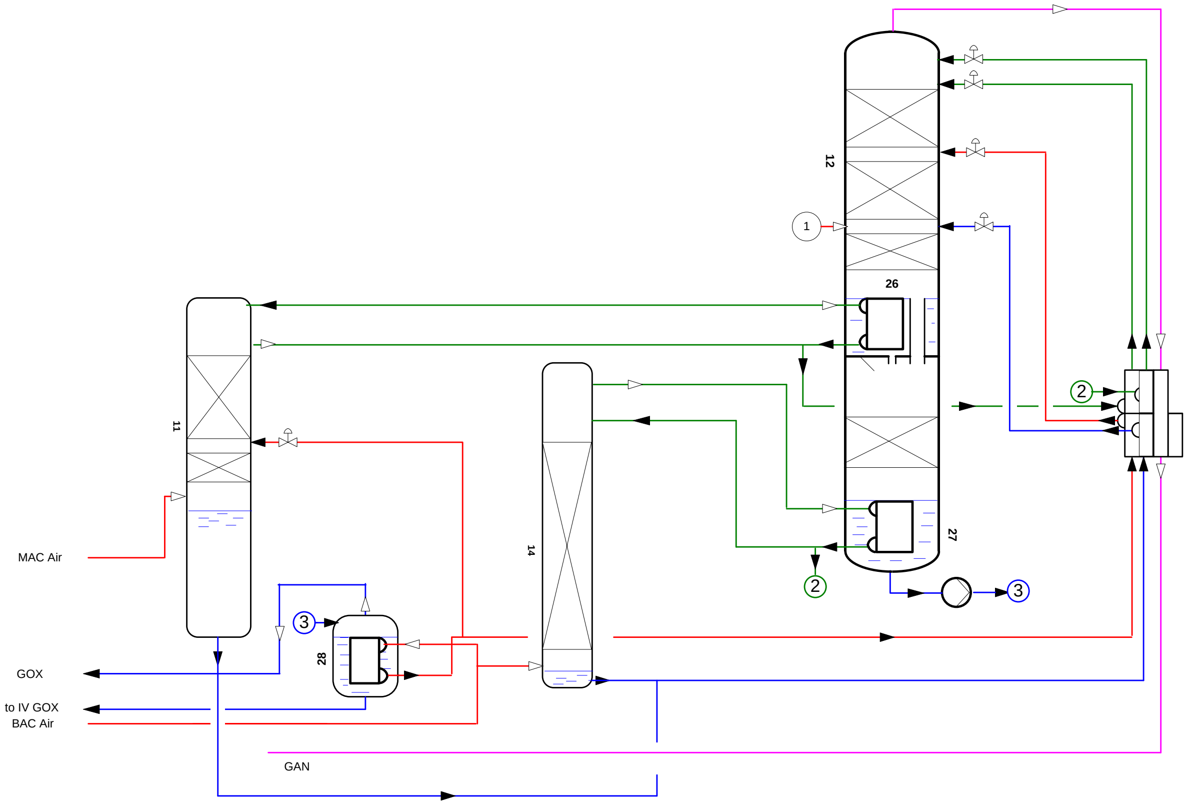

Figure 2. Improved process with two HP columns

The process has two main advantages against the conventional process:

a) For the main part of the process air a lower pressure is sufficient. This saves compression energy.

b) Conventional dual reboiler systems condense a big portion of process air to produce the vapour in the top section of the LP column. Here nitrogen is condensed instead of air. This enhances the separation efficiency in the LP column, because reflux ratios in the top section can be improved.

## 6. APPLICATION OF THE EXERGY METHOD TO THE IMPROVED PROCESS

Using the same procedure as for the evaluation of the reference process, the following results are achieved for the improved process:

Table 3. Apply the exergy balance to the improved process exergy

| **Products** | Flow | FLOW | PRES | $O_2$ | Separation Power | Compression Power | Liquefaction Power |
|---|---|---|---|---|---|---|---|
| | $Nm^3 h^{-1}$ | $mol s^{-1}$ | bar | % | kW | kW | kW |
| GOX | 18792 | 232.9 | 1.45 | 93.00% | 147 | 210.4 | |
| GOX IC | 2821 | 35.0 | 7.2 | 96.00% | 29 | 168.1 | |
| LOX | 0 | 0.0 | 1 | 96.00% | 0 | 0,0 | 0 |
| GAN | 3877 | 48.0 | 5,1 | 0.5000% | 56 | 190.7 | |
| LIN | 0 | 0.0 | 1 | 0.50% | 0 | 0.0 | 0 |
| Waste | 74510 | 923.4 | 1,00 | 1.10% | 1019 | 0.0 | |
| Process Air | 100000 | 2416.7 | 3.8 | 20.95% | | | |
| | | | | | Sum of min. theoretical power kW | | 1821 |

Table 4. Estimated power consumption for the improved process

| **Machine** | Flow | Pin | Pout | estimated Power |
|---|---|---|---|---|
| | $Nm^3 h^{-1}$ | bar | bar | kW |
| MAC | 100908 | 1,0 | 3.8 | 5869 |
| BAC 1 | 44231 | 3,6 | 5.4 | 756 |
| GAN EXT | 3977 | 3,2 | 5.1 | 79 |
| Turbine 1 | | - | - | -393 |
| Pump 1 | | | | 3 |
| Pump 2 | | | | 12 |
| TOTAL | | | | 6326 |

Apply equation (6) and divide 1821 kW by 6326 kW. This gives the result for the exergy efficiency for the reference process of 28.8%

## 7. CONCLUSION

The method allows to compare processes with different product specifications according e.g. pressures and purities, as the ratio of min theoretical power and an estimation of the real power is used. The example for the exergy evaluation of different processes shows, that efficiencies can be quantified with this method. The comparison shows that especially in the area of impure oxygen production new process cycles offer new opportunities. The increased efficiency of the improved (dual reboiler) process is based on the reduction of the air flow requiring the high pressure of the normal high pressure column. This can be achieved by using an additional reboiler and a second pressure column, which operates at a lower pressure. The increase of efficiency is significant and it makes the application of oxygen in non-ferrous metal production more attractive.

## 8. REFERENCES

[1] Mackey P.J. 1987,Oxygen in the Non-Ferrous Metallurgical Processes Past, Present and Future, 26th *Conference of Metallurgists - 1987*
[2] Baehr H.D., Kabelac S.2009, Thermodynamik, *Springer-Verlag Berlin Heidelberg 14. Auflage*
[3] Franke U. 1998, Prozeßbewertung ohne Exergie

085

# Oxygen Supply for CO2 Capture by Oxyfuel Coal Combustion

**Higginbotham P., Kalbassi M., Gibson S.**

Air Products PLC, Hersham Place, Molesey Road, Walton-on-Thames, Surrey, KT12 4RZ, UK

## ABSTRACT

The air separation unit (ASU) is one of the key parts of an oxycombustion power plant with CO2 capture and it is important that its design is optimised to give the right balance between power consumption, capital cost, flexibility and operability. To achieve the maximum benefit, this design optimisation should include not only the ASU, but also integration with the rest of the plant. In previous papers, Air Products has given details of the factors that need to be considered in the specification and design of an ASU, and how these influence the final design. In this paper, we will summarise the results of these earlier studies and then go on to describe in more detail how the overall oxycombustion system can be optimised by integration of the ASU process with the rest of the system, and by designing the ASU with operating flexibility.

## 1. INTRODUCTION

The air separation unit (ASU) is a major element of an oxycombustion power plant with CO2 capture. It must supply all the combustion oxygen as and when required, it consumes a significant percentage of the total generated power and it accounts for a sizeable proportion of the additional capital cost associated with CO2 capture. Because of this, it is important that its design is optimised to give the right balance between power consumption, capital cost, flexibility and operability.

To achieve the maximum benefit, this design optimisation should not include the ASU alone, but should also investigate opportunities for integration with the rest of the plant. However, such integration leads to additional complexity, and the operation and flexibility of the integrated system under a variety of conditions also need to be considered to ensure that it remains close to optimal

In previous papers, Air Products has given details of the factors that need to be considered in the specification and design of an ASU, and how these influence the final design. We have also listed the unique combination of these factors in the case of oxyfuel coal combustion and indicated how the low pressure and low purity (~95%) required provides a particular opportunity for reducing the power consumption of the ASU. Most recently, we have explained how the quoted power consumption of an oxygen plant can differ according to the basis used and provided examples to demonstrate this and assist in putting comparisons on a common basis. In addition we have presented a comparison of several different air separation process cycles and described the cycle and equipment chosen for Air Products' scalable reference ASU for oxyfuel coal combustion applications.

In this paper, we will summarise the results of these studies and then describe in more detail how the overall oxycombustion system can be optimised in two ways; firstly by integration of the ASU process with the rest of the system, and secondly by designing the ASU with operating flexibility to efficiently decouple its oxygen production rate from the required oxygen supply rate and so transfer power consumption from peak to off-peak periods. Air Products' has experience in the integration of ASUs with other processes and we will examine the thermodynamic benefits and practical constraints of heat integration between the power plant and the ASU and CO2 purification plant including integration of heat of compression; preheating of oxygen, condensate and boiler feed water; and heating of waste nitrogen for ASU adsorber regeneration and potential power recovery. Air Products has designed air separation plants for other applications so as to minimise operating costs in the face of variable oxygen demands and variable power tariffs and we will illustrate how such a scheme could be suitable for an oxyfuel coal combustion power plant.

## 2. FACTORS INFLUENCING ASU DESIGN

When designing an ASU, it is important to know certain key pieces of information about the products needed, the utilities available, the site location and the economics of the project. Firstly, and most importantly, the process conditions (temperature, pressure, flow, composition) of the feed air and desired products should be specified. It is also essential to identify the required operating range and demand profile of each product and whether it needs a back-up supply, as well as the availability and conditions of utilities such as power, cooling water and steam. The scope for integration with other processes should also be considered, for example whether heat of compression or waste nitrogen from the ASU could be used in an associated process. In addition, it is important to know certain details relating to the project execution, such as schedule, site conditions and limitations on the transport of large items of equipment to the site. Finally, to allow appropriate optimisation of the process, it is essential to understand the economic drivers, in particular the value of the utilities, normally expressed as the capital expenditure worthwhile to save one unit of utility (for example $/kW for power).

## 3. COMPARISON OF QUOTED POWERS

The power consumption of an ASU for producing a given set of products from a given set of feeds under particular ambient conditions is made up of three components – compression, separation and refrigeration. When comparing powers, it important to understand, and if necessary correct for, any differences in ambient and cooling water conditions or additional products or product conditions. It is also important to determine what the power includes, for example it could be quoted at the electrical incomer, including all electrical losses and auxiliaries, or as just the shaft power of the main machines excluding auxiliaries and electrical losses. It might also be quoted as “separation power”, and therefore also exclude the power of a hypothetical compressor from atmospheric pressure to the required product pressure. In a similar way, benefits from integration of exported heat may or may not be included in the quoted ASU power. Project-specific factors such as required operating range and level of integration could also affect the design point efficiency of the compressors, and hence the ASU power.

## 4. ASU CYCLE COMPARISON AND NITROGEN INTEGRATION

Five different process cycles to produce low purity (95%), low pressure (1.2 bara) oxygen were compared (Higginbotham et al. 2011); a conventional double column cycle, a three-column cycle operating at normal and elevated pressure and a dual reboiler cycle at normal and elevated pressure.

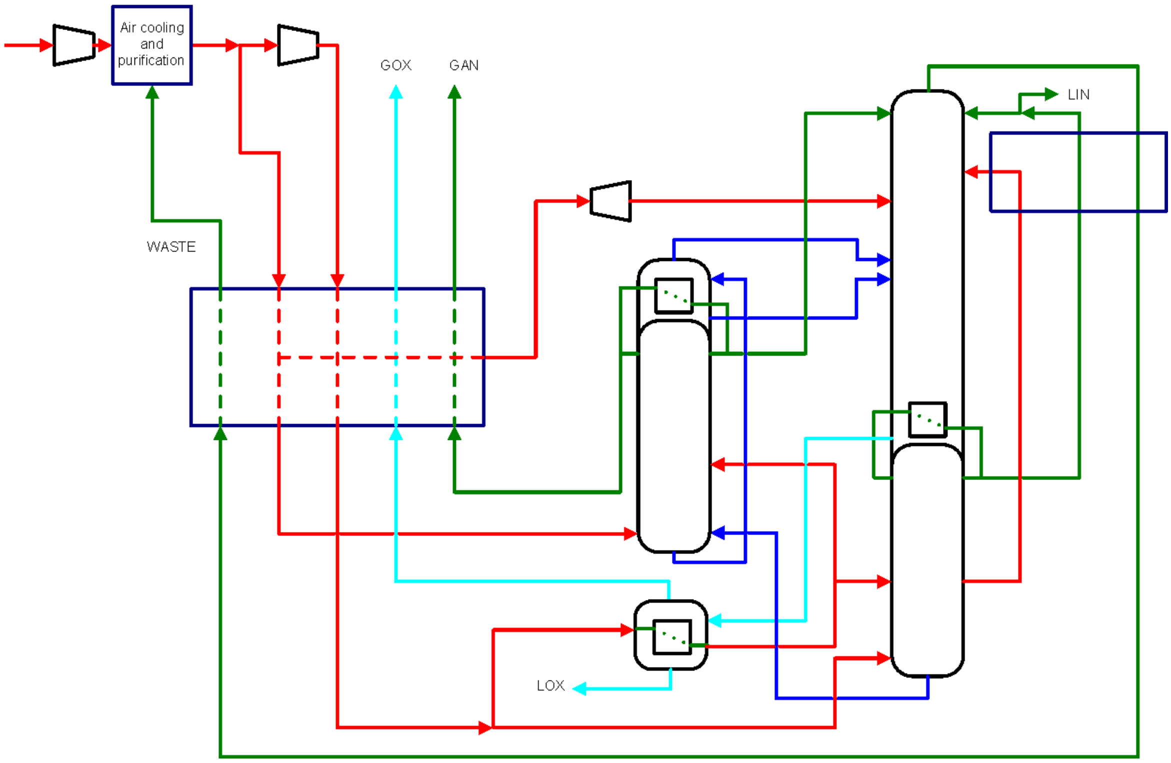

Figure 1 – Three-column cycle

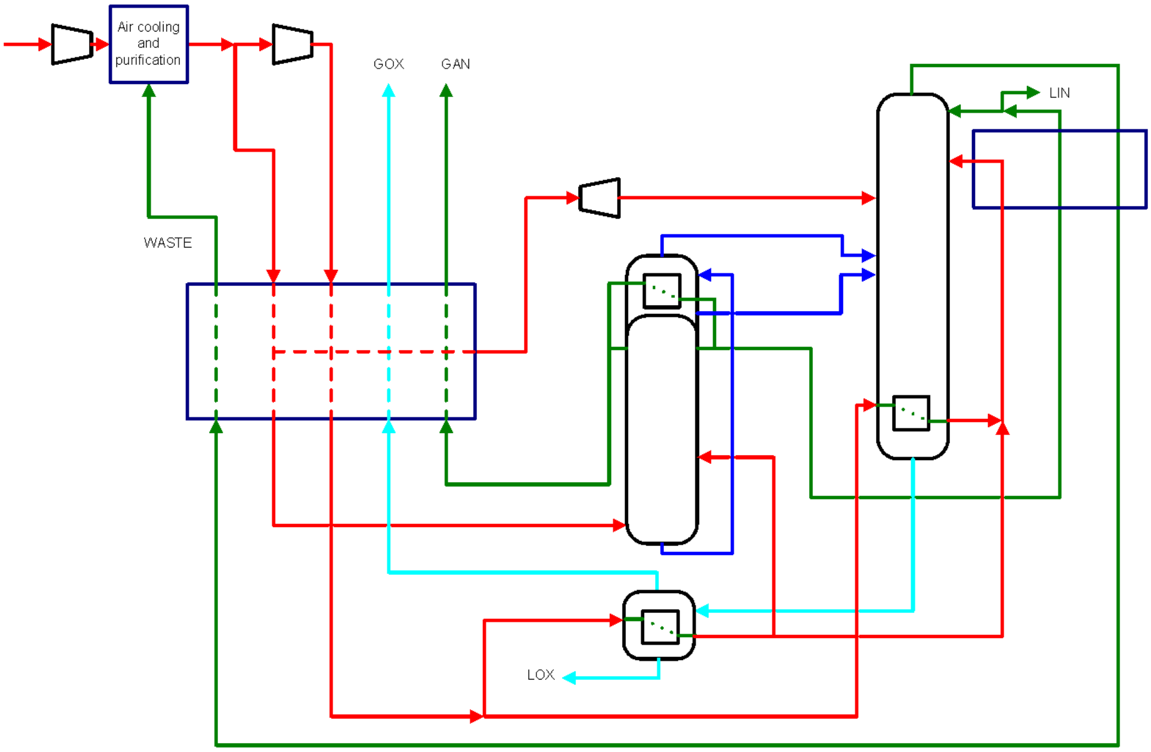

Figure 2 – Dual reboiler cycle

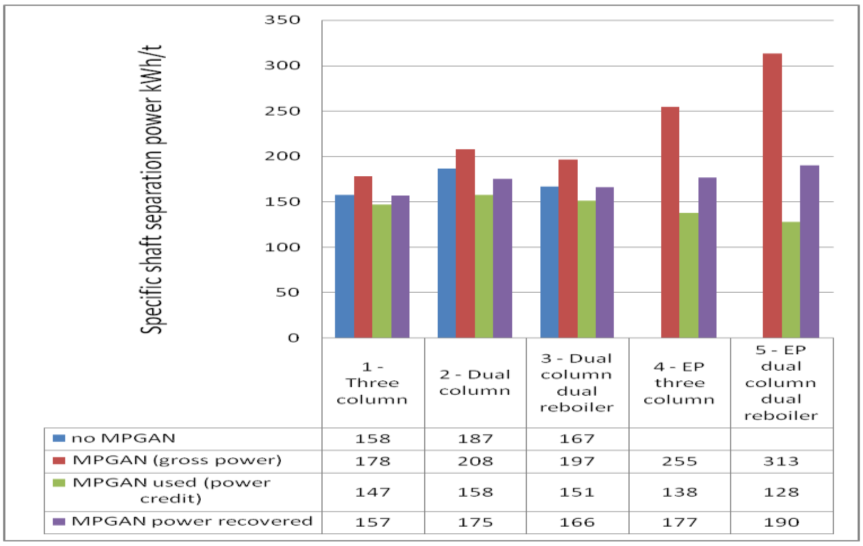

| | 1 - Three column | 2 - Dual column | 3 - Dual column dual reboiler | 4 - EP three column | 5 - EP dual column dual reboiler |
|---|---|---|---|---|---|
| 🟦 no MPGAN | 158 | 187 | 167 | | |
| 🟥 MPGAN (gross power) | 178 | 208 | 197 | 255 | 313 |
| 🟩 MPGAN used (power credit) | 147 | 158 | 151 | 138 | 128 |
| 🟪 MPGAN power recovered | 157 | 175 | 166 | 177 | 190 |

Figure 3 – ASU cycle comparison

The oxygen separation power at ISO conditions (Darde et al. 2009) was calculated for each cycle.

The three-column cycle is illustrated in Fig. 1 and differs from the conventional dual column cycle by the addition of a column operating at a pressure between that of the high and low pressure columns and condensed by boiling part of the crude liquid oxygen feed to the low pressure column. The low pressure column is therefore boiled up at the bottom and at a second intermediate location. Liquid oxygen from the low pressure column is boiled by condensing air in an oxygen vaporizer in the same way as the conventional cycle. A pressurized GAN product can be taken from the intermediate pressure column.

The dual reboiler cycle (Fig. 2) is similar to the three-column cycle, but the high pressure column is not present, and the LP column bottom reboiler condenses feed air directly instead of nitrogen from the high pressure column. Like the other cycles, this cycle also has an oxygen vaporizer.

When the columns operate at normal pressure, the waste nitrogen is produced at atmospheric pressure, but when they operate at elevated pressure the pressures of all the columns are increased so that the feed pressure is higher and the waste nitrogen pressure is higher than atmospheric. The plant consumes more power, but more power is contained in the pressurized nitrogen product. Elevating the operating pressure of an ASU increases its efficiency because of the reduced effect of pressure drops and temperature differences at the higher operating pressures and temperatures, however the pressure energy in the waste nitrogen must be used to realize the efficiency benefit. This may be the case if, for example, the nitrogen is used for dilution in a gas turbine. In such cases, the compression energy for the nitrogen can be credited against the air feed compression to reduce the oxygen separation power.

The three-column cycle was found to have the lowest power at normal pressure (15% better than a conventional cycle with no nitrogen).

Taking nitrogen at pressure (GAN) from any of the cycles was found to reduce the oxygen separation power so long as a credit equal to the power to compress the nitrogen from atmospheric pressure could be applied to the total power. However, this is only possible if there is a use for the nitrogen.

If there is no nitrogen requirement and power has to be recovered from the nitrogen by heating and expanding it, the benefit is reduced significantly unless the thermal efficiency of this Brayton power generation cycle exceeds that of the Rankine steam cycle. This is only true at temperatures in excess of 600°C, and to realise such a process novel machinery and boiler designs would be required.

## 5. HEAT INTEGRATION

In an oxyfuel coal power plant, the net fluegas flow from the boiler is significantly reduced compared to an air fired system, and the water concentration and dewpoint temperature in the fluegas are increased. Thus there is a substantial excess of low grade heat available from the fluegas condenser just below its dew point. So, if this heat can be recovered, there is no value in capturing heat from the ASU or CPU below this temperature. However, recovered heat above this temperature can be used instead of steam for preheating water in the steam cycle. This releases the steam for additional power generation. Intercooled compression of the air feed to the ASU can provide some useful heat, but partially-cooled or adiabatic compression can provide more heat, but at the cost of increased power consumption. Our results show a net benefit for heat integration up to a certain temperature, but above this the power penalty balances the benefit of the increased temperature; it is worth the modest power increase to convert the heat from waste to a useful temperature level, but not the additional penalty to upgrade it further. However, adiabatic compression allows the heating of only part of the condensate and leaves scope for heating the rest with another heat source (for example in the CPU). So, in an optimal design, heating of oxygen, nitrogen or condensate should use heat from the fluegas condenser at low temperature, and heat from the ASU and CPU compressors above this temperature.

The start-up of an integrated scheme and its operation in different modes need careful attention. For example, relative changes in heat supply and heat demand must be considered, especially during start-up and at turndown when the heat supply from compressors on recycle may be more than the heat demand from the turned-down power generation process. Additional equipment such as coolers and heaters may be needed for these eventualities.

## 6. ELECTRICAL LOAD MANAGEMENT

Along with other industrial gas companies, Air Products has designed ASUs whose oxygen supply rate can change independently of their oxygen production rate by incorporating gaseous and/or liquid buffer storage. For example in steelmaking, where instantaneous oxygen rates are very high and there are short intervals where no oxygen is required, the variable demand can be satisfied by the ASU whilst its oxygen production rate is kept constant. Air Products has also designed ASUs to take advantage of variable power tariffs. In this case, the oxygen supply rate is constant but the oxygen production rate is adjusted to reduce the electrical load during peak periods and increase it during off-peak periods. In oxyfuel combustion applications, it is possible to turn up the ASU at times of reduced power output (and therefore reduced oxygen demand), and to turn it down at times of increased power output, so that the ASU can effectively store energy and swap it from one time period to another.

In the ASU cycles considered, liquid oxygen is produced from the distillation column system and evaporated against condensing air. So the supply of oxygen and the operation of the distillation columns can be decoupled by storing liquid oxygen and liquid air. The oxygen production can be supplemented when required from storage and the resultant liquid air sent to storage with no net refrigeration requirement or disturbance to the column system. All that is needed is an increase in air flow from the compression system to provide the extra air to be liquefied. If on the other hand the ASU is producing more oxygen than required, liquid air can be injected to provide refrigeration to produce liquid oxygen that can be stored rather than evaporated. In this case, less air has to be provided by the compression system, as part of the feed is provided as liquid air. Alternatively, the oxygen supply rate can be maintained whilst the ASU is turned down to reduce its power consumption during peak power demand periods and turned up during off-peak periods. The effective cost of the power provided to the ASU can therefore be reduced.

To design such a system, it is important to understand the likely operating profile of the plant so that the ASU and storage can be sized appropriately. For example, it may be worthwhile oversizing the ASU to allow load swapping at full oxygen output, or the system may be designed only to take advantage of reduced average production rates.

## 7. CONCLUSION

- Oxygen supply requirements for oxyfuel coal combustion are unique and enable the use of process cycles with particularly low power consumption. Even lower power consumption is possible by integration of the ASU and power plant, but operability of the integrated scheme must be ensured.
- Care is needed when comparing specific power consumption figures to ensure they are comparable and attainable considering project-specific factors such as required operating range and level of integration.
- Several processes were evaluated as part of the Air Products reference plant development, and it was found that the triple column process proposed by Air Products had the lowest power in most cases.
- To realise a lower power consumption than Air Products selected process would require significant machinery development and modification of well-proven boiler equipment to enable high temperature expansion of pressurised waste nitrogen.
- Heat integration of the ASU with the boiler system can significantly lower the effective energy consumption of the oxygen plant, however the usefulness of the heat from the ASU depends on its temperature level and the configuration of the power generation cycle.
- It is possible to configure the ASU to store energy by swapping electrical load from one time period to another. To design the system appropriately the expected average loading of the ASU and power plant must be considered and the benefits of increased stored energy weighed against additional ASU costs.
- Air Products has developed a state-of-the-art scalable ASU concept that uses an efficient and cost-effective three column cycle optimised to provide a low specific power for oxyfuel coal combustion applications whether or not it is integrated with the power generation cycle.

## 8. REFERENCES

Allam, R.A. and Spilsbury, C. G., 1992. A study of the extraction of $CO_2$ from the flue gas of a 500MW pulverised coal fired boiler. Energy Convers. Mgmt. Vol. 33, No. 5-8, pp. 373-378.

Allam, R.A., Higginbotham, P., White, V. 2003. The use of oxygen in $CO_2$ efficient power generation. International Congress of Refrigeration.

Beysel, G. 2009. Enhanced cryogenic air separation – a proven process applied to oxyfuel. 1st Oxyfuel Combustion Conference, Cottbus Sep 8th.

Darde, A., Prabhakar, R., Tranier, J.-P., Perrin, N. 2009. Air separation and flue gas purification units for oxy-coal combustion systems. Energy Procedia 1 527-534.

Dillon, D.J., White V., Allam, R. J., Wall, R. A. and Gibbins, J. 2005. Oxy combustion processes for $CO_2$ capture from power plant. IEA GHG report 2005/9.

Higginbotham, P., White, V., Fogash, K. and Guvelioglu, G. 2011. Oxygen supply for oxyfuel $CO_2$ capture. International Journal of Greenhouse Gas Control. Vol. 4, No. 5, pp. 194-203.

Tranier, J.-P., Dubettier, R., Perrin, N. 2009. Air separation unit for oxy-coal combustion systems. 1st Oxyfuel Combustion Conference, Cottbus Sep 8th.

White, V., Armstrong, P., Fogash, K. 2009. Oxygen supply for oxyfuel $CO_2$ capture. 1st Oxyfuel Combustion Conference, Cottbus Sep 8th.

078

# Feasibility Study of "CO2-Free Hydrogen Energy Supply Chain" Utilizing Australian Brown Coal Linked with CCS

**Inoue K., Yoshino Y., Kamiya S., Harada E.**

Kawasaki Heavy Industries, Ltd., 1-1 Kawasaki-cho Akashi, 673-8666 Japan

## ABSTRACT

Efforts to reduce CO2 emissions have been accelerated all over the world in an attempt to move toward a low-carbon society. We have investigated feasible measures to reduce CO2 emissions and have concluded that introduction of new fuels with near-zero CO2 emissions is required to achieve Japan's commitment of 80% CO2 reduction by 2050. Although it was originally thought that nuclear power is promising in this regard, it is difficult to increase nuclear power at the moment, especially in Japan. Although much attention has been paid to renewable energies like solar or wind power, these problems concerning the stability and mass supply still exist. Therefore, we have moved forward with focus on hydrogen. The use of hydrogen will not produce CO2 emissions, and the production of hydrogen produces limited CO2 emissions. In this context, we aim to realize a CO2-free hydrogen chain utilizing Australian brown coal linked with CCS (carbon capture and storage). Australia has abundant resources of unused brown coal and the Federal Government of Australia and the State Government of Victoria actively encourage effective use of brown coal. Simultaneously, they energetically promote plans for a CO2 storage hub (Carbon Net), led mainly by Victoria. This enables stable, economic production of CO2-free hydrogen. In a CO2-free hydrogen chain, hydrogen is produced from brown coal in Australia and then the hydrogen is liquefied and transported to Japan by a liquid hydrogen carrier. It is the world's first attempt to transport massive amounts of liquid hydrogen across the ocean. We have conducted a feasibility study on the CO2-free hydrogen chain at a commercial scale and the results show that this chain concept is technically and economically feasible.

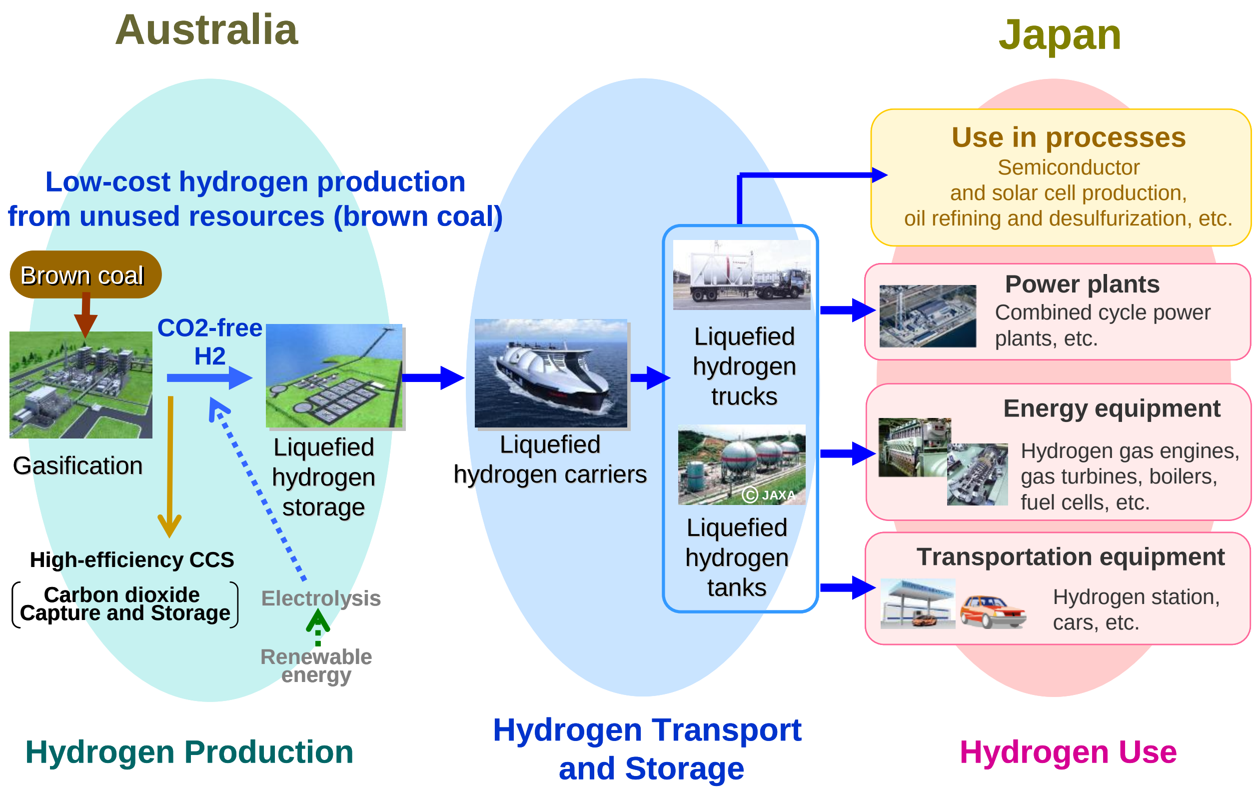

Fig. 1 $CO_2$-Free Hydrogen Energy Supply Chain

# 1. INTRODUCTION

Reserves of coal are larger than those of other fossil fuels. Coal is superior in terms of stability of supply and economy and therefore is widely used. However, issues including the recent increase in energy demands of newly developing countries and a price hike related to the price of crude oil have emerged. From the viewpoint of global warming preventative measures, it is now critical to soon establish a technology to separate, capture, and store $CO_2$ (CCS) at coal thermal power plants. Japan is developing a superior basic technology for separating and capturing $CO_2$, whereas various other are continuing demonstration tests. Before practical application and dissemination of CCS technology, the problem of storage must be addressed. In an age where it is very hard to increase nuclear power by a large margin, more attention is being paid to renewable energies. However, there are many problems in the aspects of stability and mass supply. We have focused on the large reserves of Australian low-rank coal (brown coal), which has been used only locally (mine-mouth power generation) because it has a high water content. We propose a hydrogen energy supply chain to import hydrogen as a carbon-free and clean fuel and use such hydrogen domestically with high efficiencies by first producing hydrogen from brown coal and then locally separating, capturing, and storing $CO_2$ in the process of production, with the eventual aim of applying such a hydrogen chain model to practical use.

Fig. 1 shows the overall concept of a $CO_2$-free hydrogen energy supply chain model. In this figure we designated Australia as the country with resources and Japan as the country using hydrogen. In Australia, first, brown coal is gasified to produce synthesis gas. Second, the synthesis gas is refined to produce hydrogen. Next, $CO_2$ is separated, captured, and stored, and finally, the refined hydrogen is liquefied, stored and transported to Japan by a liquefied hydrogen transport ship from a loading base. The imported hydrogen is stored at the unloading station and is delivered to several facilities for use as a fuel, e.g., in gas turbine combined cycle power plants, in energy equipment such as gas engines or fuel cells, and in hydrogen fuel cell vehicles (FCV).

# 2. METHODOLOGY

We have focused on the large reserves of Australian brown coal, which have been used only locally (mine-mouth power generation) due to its high water content and self-ignitability. We propose production of hydrogen from brown coal through a gasification process and establish a hydrogen energy supply chain for user countries. The imported and highly efficient hydrogen is then utilized as a carbon-free and clean fuel. Simultaneously, the $CO_2$, which is a by-product of the gasification process, will be captured and sequestered at the world-class $CO_2$ storage site located near the coalmine. To realize this hydrogen chain, optimization of the whole system and development of the facilities and components are of significant importance. In this paper, it is assumed that the resource country is Australia and the user country is Japan. The feasibility of the total supply chain system is examined for a commercial phase of the hydrogen energy supply chain.

To set a target for the commercialization of this model in the year 2030, when a large demand for hydrogen is expected, hydrogen cost and the price of this model at that time are calculated and analyzed as prerequisites for economic evaluation.

In this paper, hydrogen cost refers to costs arising from the processes from purchase of brown coal to transportation of hydrogen to Japan.

## 2.1. Hydrogen Chain Model

In the hydrogen chain model, various process schemes are possible that are based on applied technologies and site conditions. Therefore, it is necessary to select the optimum process by considering the best technology for each component and facility in the process system. In the present study, four processes using oxygen-blown gasification are examined as options in terms of hydrogen cost (Fig. 2).

(a) Gas transportation by pipeline: a comparison is made between the methods of transportation of the hydrogen from the production plant at the mine to the loading base at the port. In this case, the hydrogen liquefaction plant is located at the port.

(b) Truck transportation of liquefied hydrogen: liquid hydrogen is transported by truck. Thus, the liquefaction plant is located at the mine.

(c) Gasification at the waterfront: to eliminate the transportation of hydrogen in Australia, a hydrogen production plant located at the port is considered. However, it is necessary to transport brown coal via trucks from the mine.

(d) Electrolysis hydrogen production: the possibility is examined to compare results with those of the gasification process.

For cases (a) through (d), mass balances were calculated. In addition, the amount of brown coal processed, the consumption of oxidants (oxygen/air), the amount of CCS processing, the amount of $CO_2$ released, and the required utility amounts were calculated to reveal the characteristics of each case.

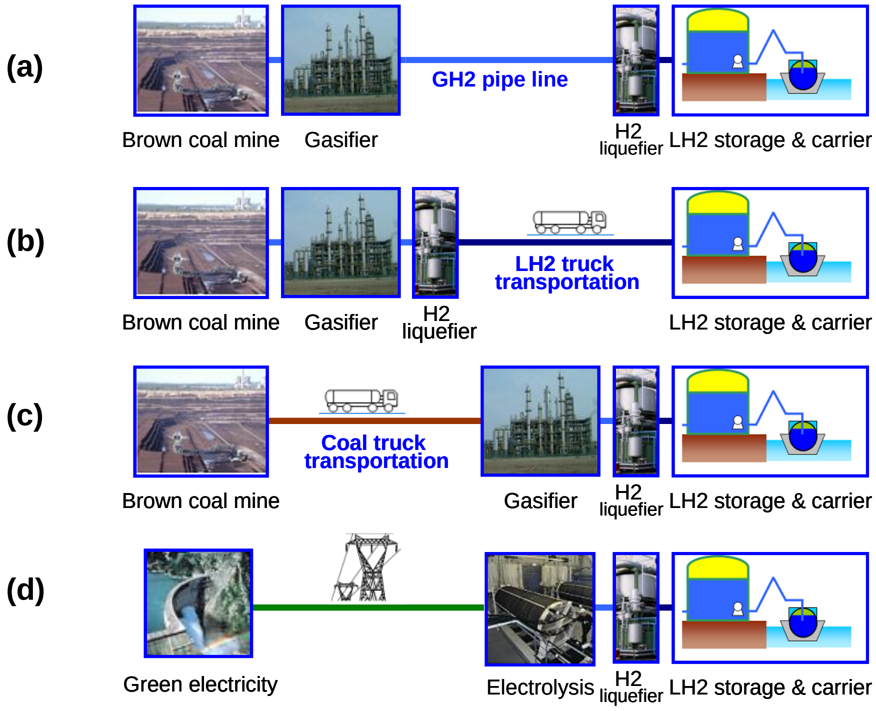

Fig. 2 Process schemes for hydrogen energy supply chain

For all four processes, costs were investigated roughly by clarifying characteristics to calculate initial facility cost and annual operation/maintenance costs. The objective in this project is to meet the specifications of the project and to be able to produce hydrogen in the most economical way possible.

Table. 1 Comparison of process schemes

| Case | a | b | c | d |
|---|---|---|---|---|
| Brown coal consumption (million tons/year) | 4.8 | 4.8 | 4.8 | 0 |
| Power consumption (GWh/year) | 4,859 | 4,758 | 4,758 | 11,000 |
| CO2 emission (ton) /hydrogen production (ton) | 0.25 | 0.30 | 0.35 | 0 |
| Hydrogen production cost (%) | 100 | 105 | 110 | 139 |

Table 1 shows the results of comparing the characteristics of the four process schemes with the roughly calculated hydrogen production cost. The relative hydrogen productions costs are calculated relative to case (a). All cases are technically possible. Economically speaking, the transportation of hydrogen or brown coal by lorries or trucks over the distance of 80 km between the hydrogen production site and the export port site is not realistic when the number of required units is considered. Pipeline transportation of hydrogen gas was found to be advantageous in terms of cost. Electrolysis of water using green electricity will become feasible when the cost of CCS becomes high or the unit price of green electricity becomes low. As a result of summarizing the above information, case (a) was selected as the most feasible process.

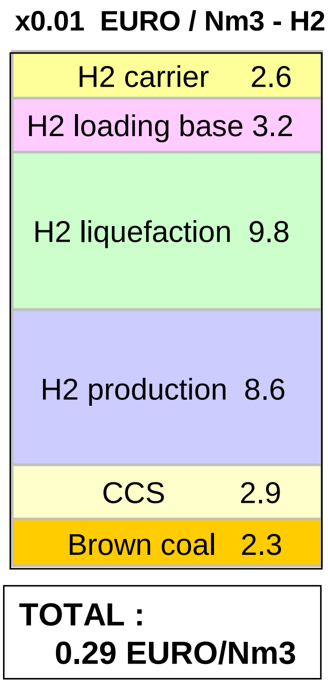

Fig. 3 Breakdown of hydrogen cost

## 2.2. Hydrogen Cost

(a) Calculation of hydrogen cost

Hydrogen cost is calculated from facility cost and operating cost and is defined, as shown below, along with the average cost in the project period.

$$\text{Hydrogen Cost} = \frac{\{\text{CAPEX} + \sum(\text{Interest} + \text{Tax})\} / \text{Project Years} + \text{OPEX}}{\text{H2 Annual Production}}$$

CAPEX : Capital Cost, OPEX : Operation cost, 100 YEN/EURO

The result of the calculation is not disclosed in this paper, but the breakdown of hydrogen cost is shown in Fig. 3. Large portions of the cost consist of the cost of the hydrogen production plant, including the gasifier and hydrogen liquefaction. Because the cost of electricity dominates such cost, it is critical for the improvement of the facility's efficiency to reduce electricity consumption in order to reduce the cost of the facility.

(b) Cost sensitivity analysis

The result of a sensitivity analysis of hydrogen cost in terms of the main parameters is shown in Fig. 3 and it shows that hydrogen cost is affected heavily by the exchange rate between Japanese YEN and Australian dollars, CAPEX (Capital Cost), and unit price of electricity. On the other hand, it is hardly affected by CCS cost and brown coal price.

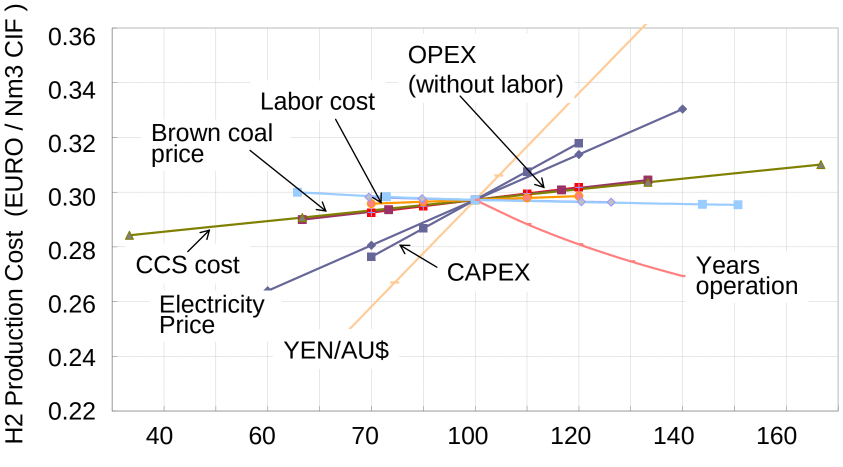

Fig. 4 Hydrogen cost sensitivity analysis in term of the main parameters

## 3. RESULTS & DISCUSSION

The business feasibility of this model is verified through the economic evaluation of the use of hydrogen produced in the model for FCVs and power generation.

### 3.1. Utilization for FCVs

Fig. 5 compares fuel costs by considering the differences in fuel consumption among FCVs, hybrid cars, and traditional gasoline cars. The present gasoline price in Japan is approximately 1.40 EURO/Liter and this is equivalent to the hydrogen station prices of 0.80 EURO/Nm$^3$ for hybrid cars and 1.37 EURO/Nm$^3$ for traditional gasoline cars. Based on the results of the calculations in the previous section, $H_2$ CIF (Cost, Insurance and Freight price: It indicates the hydrogen price at a Japanese port.) cost is approximately 0.30 EURO/m$^3$-$H_2$, along with delivery cost, and hydrogen station prices are approximately 0.60 EURO/Nm$^3$. These prices are competitive with those of gasoline, and thus this should provide a sufficient margin to develop the market for hydrogen fuelled FCVs.

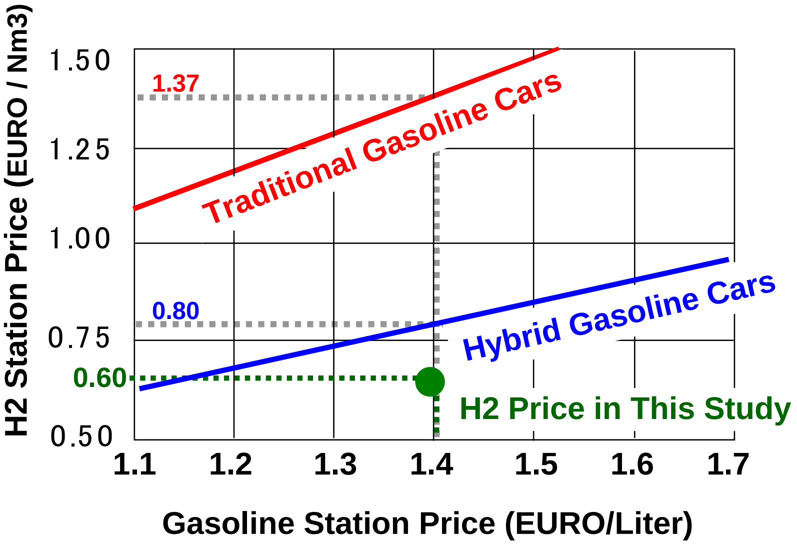

Fig. 5 Comparison of fuel costs among FCVs, hybrid cars and traditional gasoline cars cost

### 3.2. Utilization for Power Generation

Fig. 6 compares the costs for power generation by nuclear power, LNG, coal, oil, wind, and solar with those for hydrogen from brown coal in 2030, when the hydrogen chain model will be introduced*1). Compared with renewable energies such as wind power and solar power, the cost of hydrogen power generation is the lowest.

Note that the cost of hydrogen from brown coal power generation is calculated by substituting the cost of brown coal with the cost of fuel for LNG power generation and an equal rate of return is considered for each case.

## 4. CONCLUSION

From the results of the evaluation, our future energy system model for a $CO_2$-free hydrogen energy supply chain has been confirmed to be highly realizable and economical. We will demonstrate our technologies and their safety by introducing a pilot chain that is planned to start operations in 2017, and lead the new hydrogen energy system through to commercialization of the model in the year 2030.

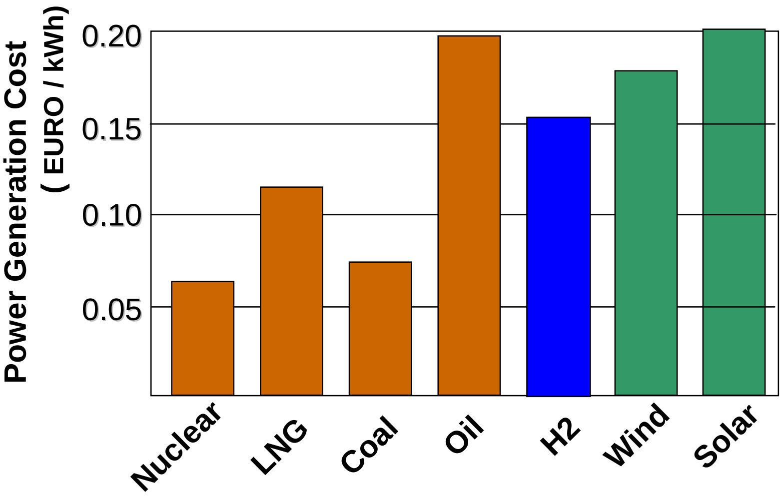

**Fig. 6 Comparison of power generation costs (2030)**

## 5. REFERENCE

1) Research Institute of Innovation Technology for the Earth (RITE), Keigo Akimoto “Alternative Pathways toward Sustainable development and climate stabilization (ALPS),” 2012.

# MISCELLANEOUS

076

# Thermosiphon Tanks for Reliable Pump Operation

**Hnizdil T., Chrz V., Kotek M., Lánský M.**

Chart Ferox, a.s., Ustecka 30, Decin 5, 405 30, Czech Rep.

## ABSTRACT

Cryogenic tanks for application with cryogenic reciprocating high-pressure pumps have been equipped with thermosiphon, which ensures sufficient hydrostatic pressure head at the pump inlet. However, what the pump requires is sufficient NPSH, which is further influenced with hydrodynamic pressure losses and heat leak during the liquid flow through the pumps. On requests of the industrial gas companies, Chart Ferox, a.s., designed high thermosiphons with well sized inlet and outlet pipes. The paper is dedicated to analysis of the design of the outer piping with respect to its sizing and insulation. The main aim is ensuring the full function of the pump for complete emptying of the tank without any need of controlled increase of pressure in the tank. Recommendations on the design of the outer piping and its insulation are specified. Operation experience validates suitability of the design to the application.

## 1. INTRODUCTION

Thermosiphon tanks have been used with reciprocating high-pressure pumps, which compress a cryogenic liquid typically to pressures of 20 to 30 MPa for its further vaporization in high-pressure ambient vaporizers and filling high-pressure cylinders at filling centers for distribution of air gases (oxygen, nitrogen and argon) or special gases. Another application is compression of liquefied natural gas at compressed-natural-gas (CNG) vehicle fueling stations. Basic arrangement of the thermosiphon tank see in the Fig. 1.

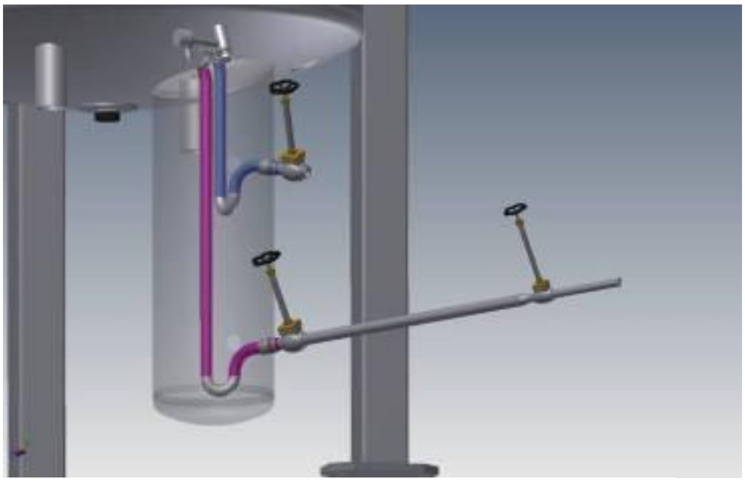

Figure 1. Assembly of the thermosiphon

Filling of high-pressure cylinders can be done also with conventional cryogenic tanks, but operation in this way brings a lot of disadvantages. The suction line to the pump is withdrawn from the bottom of the tank while the return line is leading to gas phase of the tank. Pump return leading to gas phase results in faster pressure rise in the tank and consequently, especially in case of frequent periodical start-ups, to product loss from venting. Venting of the pump outlet is required to subcool the pump inlet for start-up, which again represents product loss. It is difficult to cool the pump sufficiently and the pump is tending to cavitation. To sum up this incorrect not integrated system consisting of tank, pump and piping is increasing pump wear, maintenance and down time and result in lower efficiency and throughput.

Thermosiphon tank is designed specifically for cylinder filling systems with suction and return line feeding back to liquid phase. Such design is the best solution to reduce operating costs in relation to product losses and pump maintenance. This design is fully utilizing thermo – siphon effect. It is thermo-dynamic circulation of liquid from tank to pump inlet and sheeting and back to the bottom of the tank. The warmed liquid with possible bubbles returning from the pump is directed to the liquid phase, where it is cooling down thus minimizing pressure rise in the tank. A well designed pump station with reasonable liquid consumption can operate with zero gas losses.

## 2. REQUIREMENTS

The important requirements on the system are as follows:

a) Easy start-up of the pump after subcooling with the thermosiphon natural flow on the first trial depends on sufficient subcooling of the liquid at the inlet nozzle of the pump, which is achieved by fast subcooling of the inlet line from original ambient temperature to a temperature, which is close to the temperature of the liquid in the tank. The hydrostatic pressure head, reduced by pressure drop of the line results in the required subcooling. When the liquid height in the tank is high or medium, it mostly doesn't make any problem. However, at low liquid level, especially at small tanks, problems of insufficient subcooling may be encountered.

b) Smooth operation, similarly, depends on maintaining the sufficient subcooling during the pumping process up to relatively warm liquid, when the tank is close to empty. High hydrostatic column height and well sized pipe dimension guarantee reliable operation at a low liquid level.

c) Tanks are staying on extended legs, which allow withdrawing of all the content fully without consideration of any residual amount. Every tank is operated with certain reserve of liquid before filling, but the reserve has its function only if it can be exploited if fully in the case of need.

d) Piping system is operating according to thermosiphon principle and larger dimensions of the pump feed and suction lines help prevention of cavitation.

e) Minimum heat leak into the suction line of the pump guarantees the lowest temperature of the liquid. Insulation of the return line from the pump to the tank maintains the minimum heat leak into the tank. Chart thermosiphon tanks have the larger part of the lines insulated by the thermosiphon shell with relatively thick perlite insulation under the same vacuum, which is in the annular space of the storage tank. No visible frosting can be seen on the shell even during long-time operation. Pressure increase in the tank is minimized.

f) The tank, pump and interconnecting piping are engineered as one integrated pump station. It is designed to keep suction and return lines as short as possible and with a constant slope in order to guarantee optimal performance of the thermosiphon principle.

NPSH (Net Positive Suction Head):
For prevention of boiling liquid at the pump and creation of vapor bubbles in the pump cylinder the temperature has to be under the boiling point at the pressure inside the cylinder. Because the inlet valve(s) of the pump and the inlet nozzle have no-negligible pressure drop, the inlet pressure has to be higher than the saturated vapor pressure, which is function of the actual temperature of the liquid.
*NPSH* is defined as the difference between gauge (manometric) pressure *(Pg)* and actual saturated vapour pressure *(Psat)* required at the pump inlet nozzle to allow the liquid to remain completely (or almost completely – see chapter 3.1.) free from bubbles of vapor at the most critical point inside the pump cylinder. NPSH expresses the pressure difference in the units of hydrostatic height. Thus:

$$NPSH = (P_g - P_{sat})/(\rho . g) \quad [\mathrm{m}] \qquad (1)$$

where is:
$P_g$ gauge (manometric) pressure at the pump inlet [Pa]
$Psat$ saturation pressure at the pump inlet [Pa]
$\rho$ density of liquid at the temperature and the pressure at the pump inlet nozzle.
$g$ gravity acceleration [m/s$^2$]

The basic condition of the proper function of the pump can be expressed then:

$$NPSHa > NPSHr \qquad (2)$$

where is:

*NPSHa* *NPSH* available at the pump inlet nozzle
*NPSHr* *NPSH* required at the pump inlet nozzle

Although general requirements on the tank-pump system were set long time ago by companies Cryostar, (2000), Cryomech (2003) and others, the authors feel the need of a more detail analysis of the function of the system and specification more focused requirements.

## 3. ANALYSIS

### 3.1. Hydraulic losses:

Components of pipelines within the thermosiphon are DN40 – 1,5m (48,3 x 2,77) , three elbows 90° with ration of r/d = 3. Another significant part of this part is globe valve DN40 with Kv 22,4 m3/h. Inner pipelines connect to outer pipelines which is 1m length with reducers and globe valve DN25 with Kv 10,4m3/h. The last parts of the considered system are filling line into pump, strainer and pump. Diameter of filling line is DN20 (26,7 x 2,11) – 0,3m

The operation parameters of the pump were taken, as an example, from the Cryostar (2003) document:
NPSHr for minimum flow 4,1 liter/min is 0,3m, for maximum flow 25,3 liter/min it is 1 m.
Quadratic function was approximated between these two points for to achieve data for each flowrate.

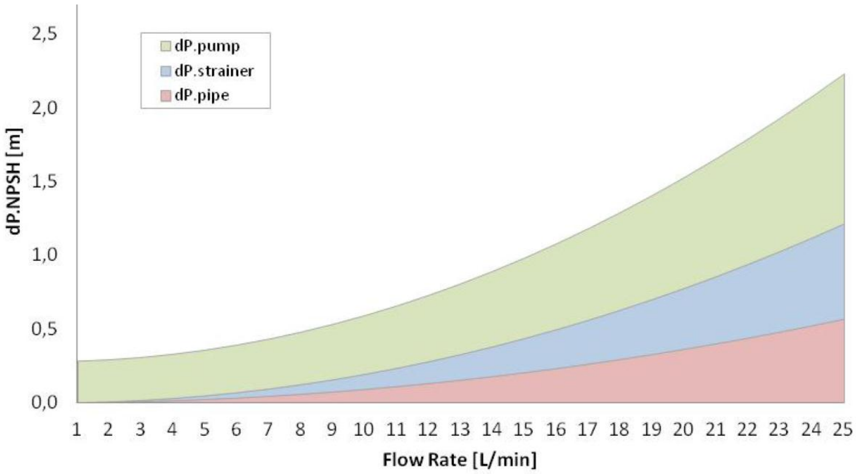

Figure 2: Components of the pipeline pressure drop.

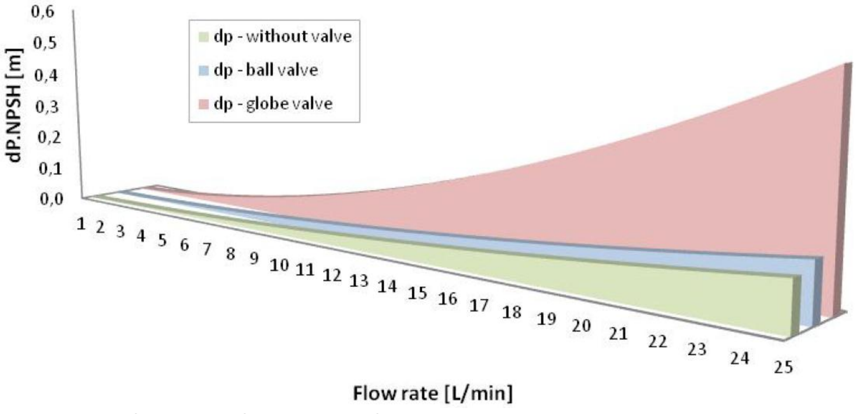

Figure 3: Influence of the type of the pump inlet valve on the pressure drop.

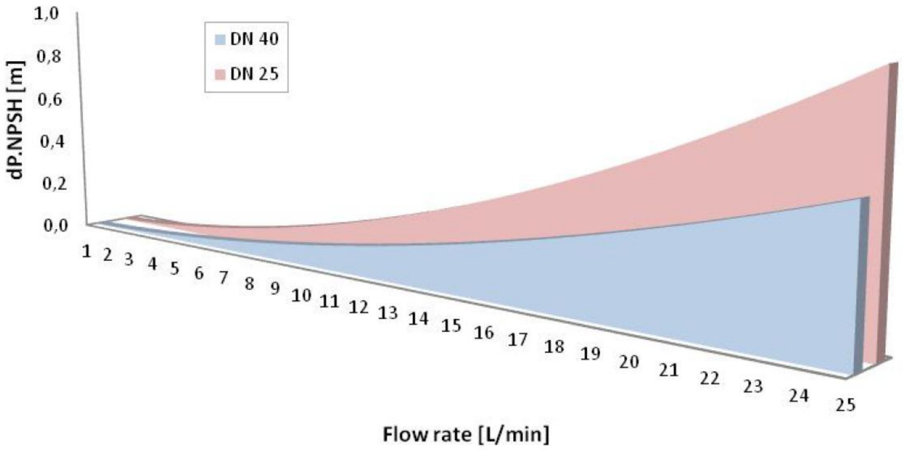

Figure 4. Effect of the size of the inner pipeline of the thermosiphon including the outlet valve.

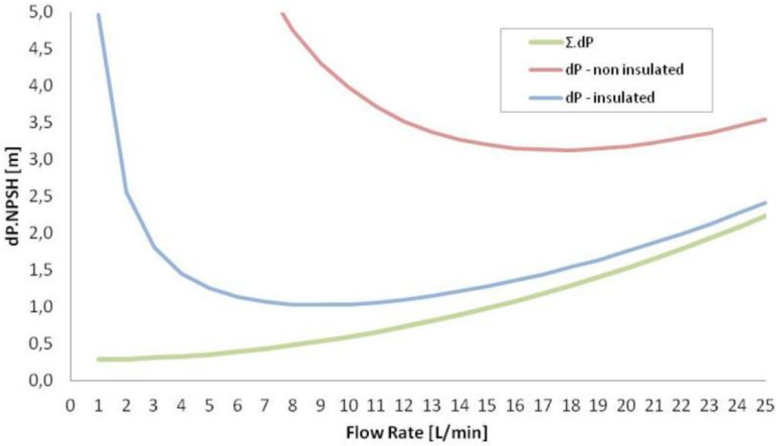

Figure 5. Influence of the insulation on NPSHr.
Green line: Hydrodynamic pressure losses.
Blue line: Increasing of NPSHr due to warming of the liquid at foam insulated outer pipeline. (Insulation: Armaflex, thermal conductivity= 0,035W/(m.K), thickness = 20 mm).
Red line: Non-insulated outer pipelines.

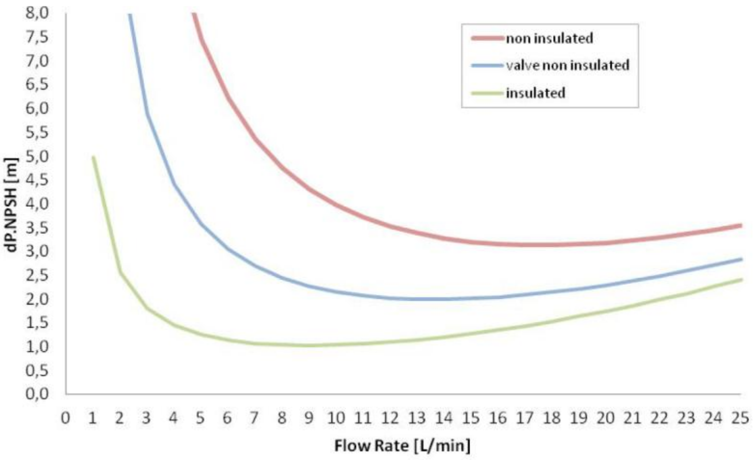

Figure 6. Influence of partial insulation.
Red line: Neither the pipe nor valves insulated
Green line: Both the pipe and valves insulated
Blue line: Only the pipe is insulated

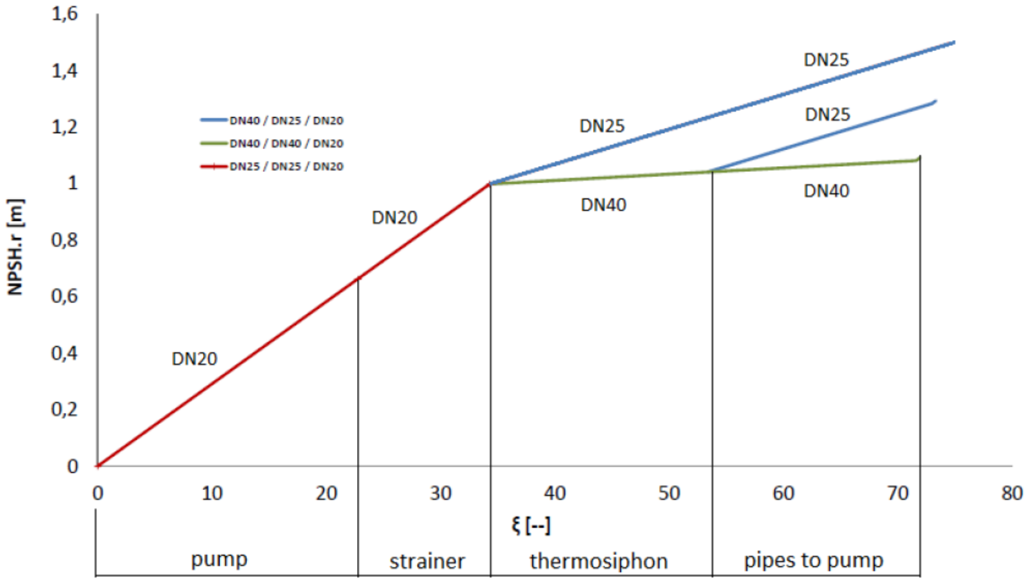

Figure 7. NPSHr as a function of pressure resistance coefficients $\zeta$ for constant flow 18 liters/min

$\zeta=2\times\Delta p/(\rho\times w^2)$

*where*

$\Delta p$............pressure loss of the respective part of the system [Pa]

w.............liquid velocity [m/s]

## 4. COMBINED CASES

### 4.1. Average flow

Analysis was done for the whole line from the inner vessel to the pump strainer inlet. It was done for the lowest practically achievable pressure in the tank 200 kPa abs. However, the results are applicable to any higher pressure. They would be only marginally influenced by lower density of liquid. Following combinations were analyzed:

- The thermosiphon height 1400 mm, DN40
- The length of the line between the theromsiphon outlet and the pump 1000 mm.
- The elevation of the pump inlet above the theromsiphon outlet 88 mm (5° slope angle).
- Outer piping variants DN25 and DN40
- Outer pipeline
    - Vacuum insulated
    - PU foam insulated including valves
    - Non-insulated
- Flowrate 18 liter/min
- The gauge pressure in the tank is 200 kPa abs.
- The liquid in the tank is at equilibrium to the pressure
- The height of the liquid in the tank is zero. Special conclusions for higher height of liquid were done for particular cases.

Results are shown in the diagram in the Fig. 7

The diagram shows the (blue) vapor-liquid equilibrium line in co-ordinates T-p (p-sat).

Vapor phase is below the line, liquid phase is above. The red and green lines show the additional pressures required for the pump inlet and strainer inlet respectively for the given flowrate. The outlet of the liquid from the inner vessel is represented with the blue circle. The bottom of the thermosiphon including its outlet valve is at the pressure, increased by hydrostatic pressure to 210 kPa approx. and only negligibly reduced by the hydrodynamic pressure losses. Six points for particular flow cases overlap at this point. From here, the lines for particular cases are branching downwards as the pressure is decreasing towards the pump inlet due to hydrostatic height and hydrodynamic losses depending on the outer piping size and as the temperature of the liquid gets warmer due to heat leak for various insulation or non-insulation cases.

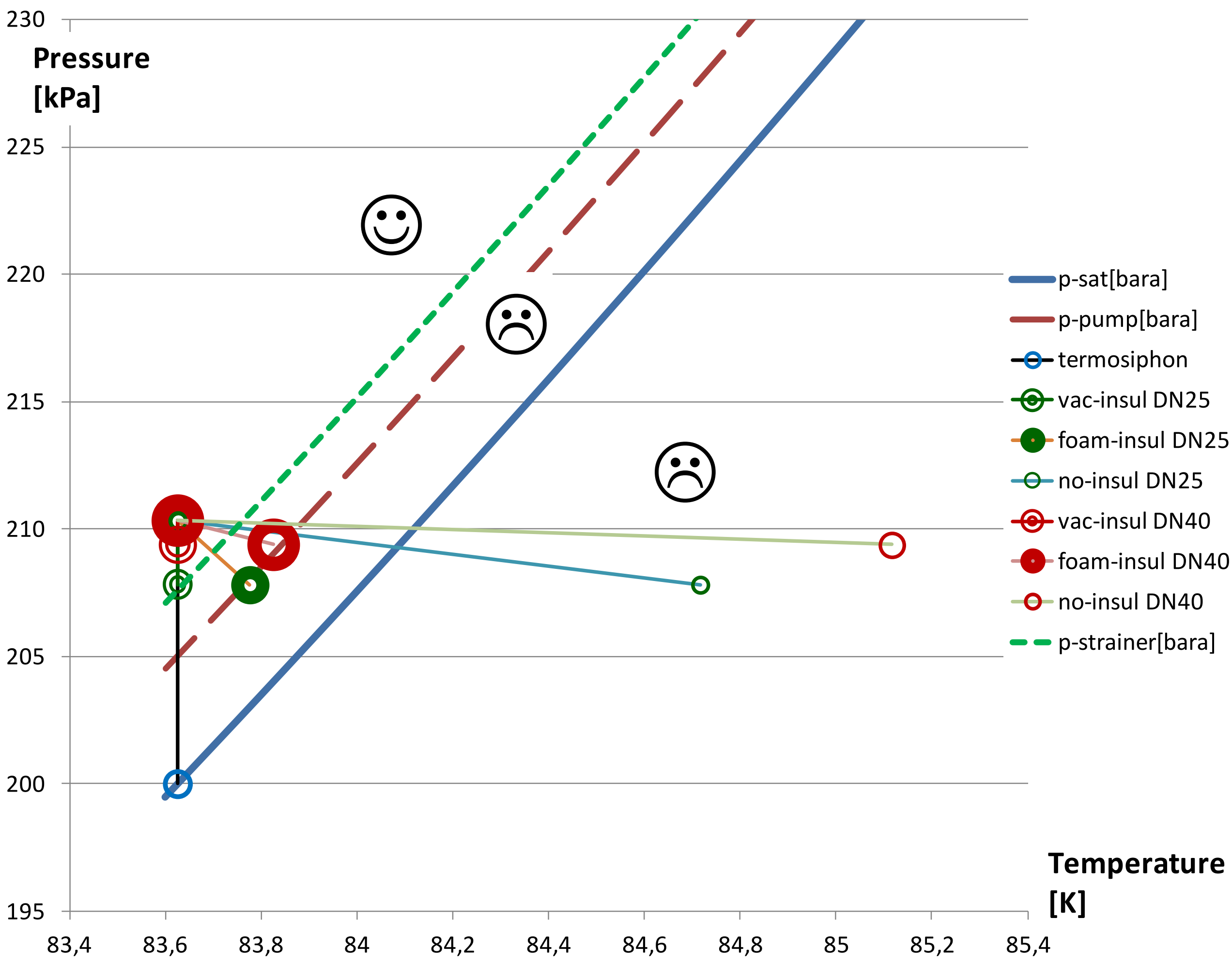

Figure 7. Development of pressure and temperature from the inner vessel to the pump strainer inlet for various pipe sizes and types of insulation. (Regular average flow)

Warming of the liquid is negligible and cannot be shown in the diagram for vacuum insulation of the thermosiphon and for the variants of vacuum insulated outer piping including vacuum insulated valves. Vacuum insulated outer piping is represented with double circles. Foam insulation (polyurethane foam for valves and Armaflex platic foam for the pipes) is represented with bold circles. No-insulation cases are shown with simple circles.
Different sizes of the piping are distinguished with colors: Green for DN 25, red for DN 40.

For reliable operation of the pump the pressure and temperature at the strainer inlet have to be above the green line of pressure, required for the inlet of the strainer. When there is zero height of the liquid in the tank (total emptying of the tank), only vacuum insulated pipes can ensure reliable function of the pump. All the other less effective insulations would require some rest fo liquid in the tank. 1 m height of the liquid in the tank makes 7,6 kPa pressure. The entire constellation of the points in the diagram can be moved up with adding this hydrostatic pressure. Approximate required rest height in the tank is shown in the Table 1. The table shows clearly that non-insulated piping is not acceptable, although, in practice, certain insulation effect is randomly provided by variable frost.

Table 1. Required rest height of the liquid in the tank in meters for various pipe sizes and type of insulation.

| | vacuum insulated | foam insulated | non-insulated | foam ins. pipes, non-ins. valves |
|---|---|---|---|---|
| DN25 | 0 | 0,4 | 3 | (1,5) |
| DN40 | 0 | 0,3 | 4 | (2) |

The calculation showed that even the frequently applied case (Fig. 8) with foam insulated pipes and non-insulated valves is not any good (compare the Fig. 6). The valves cause half of the thermal losses, so the required rest of the liquid would be, as approximated in the last column.

Figure 8. Insufficient partial foam insulation of the outer piping to the pump.

## 4.2. Special aspects of reciprocating pumps:

All the above analysis was done on the presumption of the average flow, which is a basic parameter of the reciprocating pump. However, the actual flow of a reciprocating pump is oscillating (Fig. 9). No suction flow takes place during the discharge half-period. During the suction half-period, the movement of the piston is sinusoidal. Its velocity is zero at both the top and bottom centers, while it reaches maximum in the middle of the piston stroke.

The maximum flow, corresponding to the maximum velocity, is 3,14× of the average flow. The pressure losses in the pipelines and in the local resistance points are proportional to the second power of the velocity. This means that the pressure losses and, consequently, the NPSHr, are $3{,}14^2\times = 9{,}87\times$ than those calculated for the average flow. This would require NPSHr in the order of 10 to 15 m of hydrostatic height, which, according to experience, is not needed.

With lack of specific experimental data, the explanation of the fact that the system works anyway is based on two speculative hypotheses:

***Hypothesis 1:***

Duration of the maximum velocity is very short, 0,1 to 0,15 s. As known from various examples in thermodynamics, building of the two phase mixture needs certain time. Existence of oversaturated liquid is possible in very short periods of time.

***Hypothesis 2:***

This hypothesis was advised by Poživil (2012). Here is our speculative description of the process. As result of the pressure drop, the pressure is decreased below the saturation pressure in some parts of the flow. This causes generation of a small amount of vapor in a form of micro-bubbles. Building of vapor takes away heat from the liquid. Liquid enthalpy is decreased, which stops further vaporization. (Throttling of saturated liquid into the two-phase region.) The closer is the location to the pump piston, the lower the pressure; the bigger is population of the bubbles. This means that the occurrence of bubbles is most present inside the pump cylinder and parts of pipeline close to the pump suction nozzle. The bubbles don’t have enough time for cumulating and building larger bubbles, which might cause cavitation, because the reverse process of slowing the flow down, increasing pressure and collapsing the bubbles by condensation takes place instantly. Under such conditions the pump can work but occurrence of bubbles can reduce the volumetric efficiency of the pump compared to the flow calculated from geometry of the cylinder-piston. Further, the bubbles increase the volume of the two phase flow and they further increase the pressure drop.

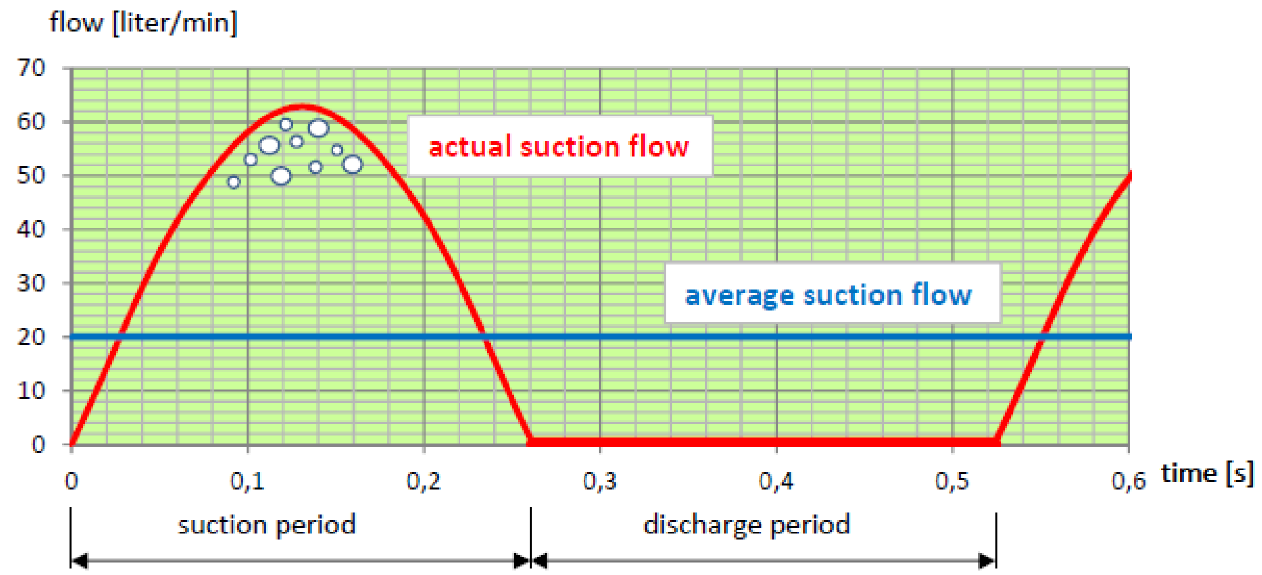

Figure 9. Oscillation of the suction flow of a reciprocating pump during one period (360° rotation of the flywheel).

The larger is the average suction pressure (and this has nothing with the subjects of saturation or NPSH), the smaller are the bubbles for the same vaporization and, consequently, for the same temporary subcooling of the liquid.

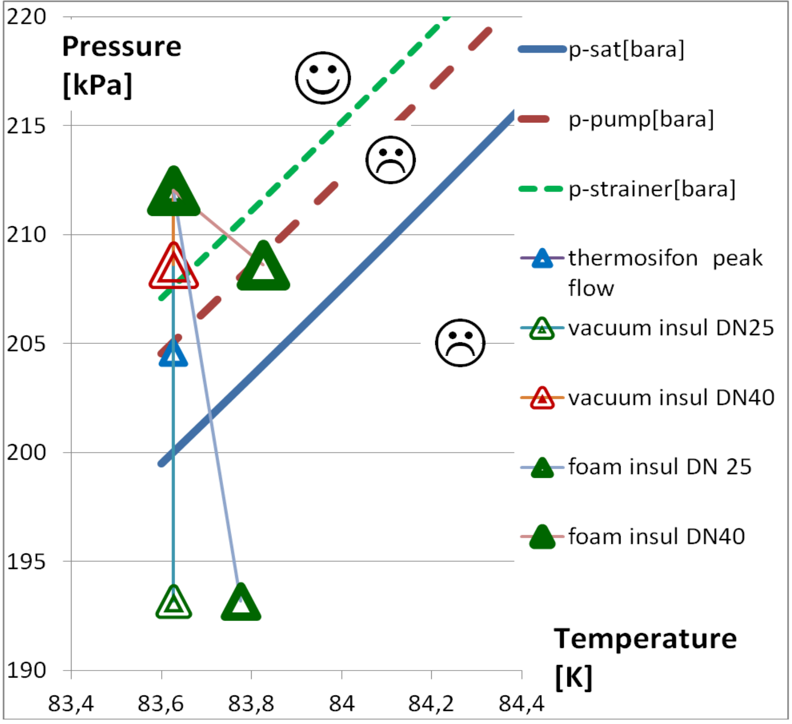

Figure 10. Development of pressure and temperature from the inner vessel to the pump strainer inlet for various pipe sizes and types of insulation. (Peak flow of the reciprocating pump – the case of rest liquid height in the tank 0,6 m.)

It is also implicitly coded in some data of the Cryostar (2003) literature, which specifies that the pump characteristics is valid for suction pressures larger than 0,7 barg pressures.

Being conscious of all the unknown aspects of the effects of irregular flow of the reciprocating pump, we nevertheless did calculation for vacuum insulation and foam insulation also for the peak flow. The required pressures at the strainer and pump inlets remained the same, which also is under questionmark. The results are shown in the Fig. 10.
The calculation was done for the liquid height in the tank 0,6 m for the maximum flowrate 18 × 3,14 = 56,5 liter/min. The blue triangle shows the saturation pressure 200 kPa increased with the hydrostatic pressure of the liquid in the tank. The high thermosiphon moves the pressure to the “safe” area and the high hydrodynamic pressure losses of the peak flow pull the

strainer inlets to very low positions. Only the vacuum insulated DN40 can deliver satisfactory conditions to the strainer inlet. Other variants would require much higher liquid rest height in the tank. It would be 3 m for the foam insulated DN25, but only 1,1 m for the foam insulated DN40. Advantage of the outer pipes DN40 for irregular flow of the reciprocating pump is obvious from this diagram. These results are not verified and can be challenged in the light of hypotheses 1 and 2 explained above.

## 5. RECOMMENDATIONS

As proved in this paper, hydrodynamic pressure loss and warming of liquid between the inner vessel and the inlet of the pump assembly have an important impact on the function of the pump and ability of withdrawing of all the liquid of the tank or on the height of remaining liquid, which cannot be withdrawn. The remaining liquid is useless ballast, which has to be kept in the tank, reduces the useful tank capacity and increases the heat leak to the tank and as such it should be minimized, for which, following recommendations might be considered when designing the thermosiphon tanks and the piping to the pump. The calculations were done for nitrogen. However, the results are applicable to any other cryogenic liquid, because both the hydrostatic pressure and the pressure loss are proportional to the density of liquid.

Recommendations for the design and installation of thermosiphon tanks with reciprocating pumps:

a) The thermosiphon shall have sufficient size of pumps and sufficient height. DN40 and 1400 mm was verified as well improving the conditions of the whole pump-tanks system.

b) The outer piping to the pump should be as short as possible. The position of the pump should be as low, as required by the 5° slope requirement, not higher.

c) The outer piping to the pump shall be of sufficient size. With respect to the irregular flow of the reciprocating pump DN 40 is justifiable. When selecting the valves, those with higher flow capacity (Kv) should be preferred.

d) The outer piping to the pump shall be well insulated. Non-insulated pipe or valves increase saturation pressure at the pump inlet importantly and would require impractically high rest height of the liquid in the tank. Partial foam insulation is still not any good solution. The best solution are vacuum insulated pipes and valves. This, however, requires high CAPEX. Foam insulation of pipes and valves is acceptable, however with the penalty of the rest height 0,6 m (or higher with respect to irregularity of flow), which blocks a useless ballast volume in the tank.

e) In case of low NPSHa, in case of variable pump drive, it is possible to reduce the pump speed which would reduce the NPSHr proportionally to the square of the pump speed ratio.

## 6. FEEDBACK FROM INDUSTRIAL APPLICATION

Chart Ferox, a.s., as the cryogenic tank manufacturer and also vendor of complete pump-tank installations has wide feedback from operation. However, in case of delivery of the tank only, Chart has no influence on customer plant designs. While the thermosiphon was well sized according to gas industrial companies requirements, outer piping is often designed by local installation providers. Although the company didn’t face any complaints on the tank function, the authors feel the need of issuing the above recommendations on the tank design, because they believe, that frequently not sufficient care is paid to proper piping layout and insulation, which results in higher ballast volumes required for additional hydrostatic pressure for achieving the required NPSH.

Chart USA and their customers experienced good results with implementation of the vacuum insulated pump inlet line while the return line is partially insulated for ensuring heat leak need for warming the liquid for achieving difference of liquid density for circulation. The heat leak shall not be too large for maintaining heat management of the tank. It depends on frequency of the pump operation. The experience showed that continuous circulation through the thermosiphon return during the pump working and stops periods is the best for the pump operability.

Reliable operation of the thermosiphon allowed starting the pump in a short fixed period of several minutes after opening the inlet line.

The pump starts well independently on the level in the tank and with initial pressures after the pumps up to 100 bar.

Pump lifetime to major repair was prolonged from 1600 to 3200 hours thanks to the thermosiphon design.

The thermosiphon works well also with low density liquids like liquefied natural gas or liquid hydrogen.

## 7. CONCLUSIONS

When designing piping of the tank – reciprocating pump system, sufficient pipe sizing and good thermal insulation is unavoidable for achieving possibility of maximum liquid withdrawal from the tank, for which concrete recommendations are proposed in the paper. Irregularity of reciprocating pump flow may have an important effect on the Net Positive Suction Head required, for which contingency in pipe sizing is desirable.

## 8. REFERENCES

Pozivil, J., (Cryostar), 2012, personal communication
Cryostar, 2003, Performance diagram MRP 40/55, 700130745-01, company literature
Cryostar, 1988, Kwickstart with thermosiphon tank, 705 106 518, company literature
Cryomech, 2003, pump catalogue

045

# Numerical Simulation of Mixed Convection Heat Transfer to Forced Flow Supercritical Helium

**Rebelo N., Ghosh P.**

Cryogenic Engineering Centre, Indian Institute of Technology Kharagpur, Kharagpur, 721302, India

## ABSTRACT

Supercritical helium has found its application as a coolant for superconducting magnets in accelerators and fusion devices. However, due to wide variation in thermodynamic and transport properties like specific heat, density and thermal conductivity in the vicinity of the transposed critical line, accurate prediction of heat flux using heat transfer correlations becomes difficult. Existing correlations have been compared with data obtained from CFD analysis for cases where experimental data are not available. Finally, effect of natural convection on forced convection heat transfer has been explored to gain in-sight into the underlying physical mechanism. CFD analysis has been performed using commercial software Ansys® Fluent. From the analysis, it has been found that fluent can predict experimental trends accurately over the wide range of heat fluxes. The observations have been used to arrive at conclusions regarding the causes of difficult phenomena and their impacts on the design of equipment involving supercritical helium.

## 1. INTRODUCTION

Supercritical helium is a fluid at a pressure above its critical pressure, $P_c$ (0.227 MPa). Due to its single phase and comparable thermal and transport properties, supercritical helium is seen as beneficial substitute for liquid helium where boiling can lead to two phase flows, leading to thermodynamic instabilities and higher pressure drops. Apart from high heat transfer rates, a wider range of operating temperatures can be obtained and the large pressure drops encountered in pool boiling of helium are avoided. However, there are a few difficulties in designing, analysis and operation of systems involving supercritical fluid [1-2]. Due to wide variations in thermophysical and transport properties like specific heat ($c_p$), density (*Rho*), viscosity, thermal conductivity etc., accurate prediction of properties in this region becomes difficult. Also as the density drops drastically when the fluid crosses the pseudocritical line, a large volume expansion of the fluid occurs. The above issues lead to complex heat transfer and pressure drop behaviour in such systems [3]. Available data are limited in scope and contradictory in this region.

In literature, experimental studies on heat transfer to supercritical helium in vertical tubes at turbulent flow have been performed. It is understood that due to the effect of buoyancy forces, the heat transfer becomes complex to be analyzed. One of the early works by Giarratano et al. [4] predicted an enhancement in heat transfer as the bulk temperature ($T_b$) approached the pseudocritical temperature and also suggested a modification of the Dittus-Bolter correlation for pure convection to account for property variations. Later Giarratano et al. [5] found that at a lower operating pressure, $P$=0.25 MPa, under certain conditions a degradation in heat transfer takes place. Under conditions of high heat flux ($q_w$), the heat transfer could not be well predicted by the correlation given by them. Brassington et al. [6] performed experiments on larger diameter tubes and proposed separate correlations of forced convection type for the prediction of heat transfer during upflow and downflow respectively. They obtained less deviation by replacing the bulk Prandtl number ($Pr_b$) by a harmonically averaged one between the wall and the bulk. Bogachev et al. [7] performed experiments for upward and downward flows and proposed a correlation taking into account the effects of buoyancy forces on heat transfer. Cornelissen et al. [8] studied numerically heat transfer to turbulent flow supercritical helium using finite difference based technique. They compared two different models of turbulence namely the mixing length and $k$-$\varepsilon$, of which it was claimed that the mixing length model was more suitable. They observed a severe deterioration from the widely used correlation by Giarratano et al. [4] for cases near the pseudocritical point but obtained better results using the correlation by Yaskin [9]. Most recently experiments on heat transfer from an inner surface of a horizontal cylinder to forced flow of supercritical helium were performed by Shiotsu et al. [10]. For a flow velocity of 0.8 m/s, they found the heat transfer coefficient almost doubles for bulk Reynolds number values of $1\times10^5<Re_b<2.8\times10^5$. The table 1 below gives the range of these experiments and the standard deviations (*SD*) of the predictions. It may be observed that there are wide variations in important parameters when computed using existing correlations.

Table 1: Results of heat transfer experiments and simulations of supercritical helium in heated pipes obtained from literature

| **Author** | **Flow direction** | ***P* (MPa)** | ***T* (K)** | **Reynolds no (*Re*)** | **$q_w$ (W/m$^2$)** | **Mass flow** | **%-*SD*** |
|---|---|---|---|---|---|---|---|
| Giarratano [4] | Down | 0.3-2.0 | 4.4 – 30.0 | $10^4$– $3.8\times10^5$ | | | ±8.5 |
| Giarratano [5] | Down | 0.25 | 4.05,5.04 | | 80-7130 | 7,12,22 (g/s-cm$^{2)}$ | > ±20 |
| Brassington [6] | Up & down | 0.22-1.4 | 4.4-15 | $5\times10^4$-$10^6$ | Upto 2500 | | ±12<br>(20 at $Re=10^5$) |
| Bogachev [7] | Up & down | 0.23-0.3 | 4.21-4.24 | $(3.6 – 9)\times10^4$ | | 0.19-0.25 (g/s) | ±25 |
| Cornelissen [8] | Down | 0.25 | 4.056-5.043 | | 80-1730 | | ±10-55 |

## 2. OBJECTIVE

In the present work, accuracy of correlations available in the literature has been studied for supercritical helium flow, where little experimental data are available. For this purpose, a commercial CFD tool, Ansys® Fluent v12.0.16 has been validated with the experimental data available in literature. Using the above CFD tool, effect of mixed convection in forced flow of supercritical helium has been studied. Data generated and conclusions of this study will be useful for designers of equipment involving supercritical helium.

## 3. METHODOLOGY

The cross-section of the tube is circular. The simulations have been done to replicate the experimental results by Bogachev et al. [7]. Supercritical helium flow in a vertical tube of diameter $d$=0.0018 m, thickness $t$= 0.0001 m is simulated under different heat flux conditions. The tube length is $L$=0.510 m, the heated section is $L_h$=0.400 m and a hydrodynamic developing section of length $L_d$=0.078 m is added before heating section.

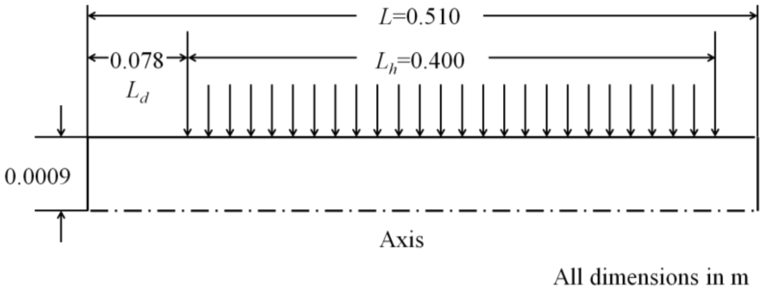

Fig.1: 2D representation of the heated stainless steel tube

The geometry and mesh were built using Gambit® v2.1.6. The flow is assumed to be steady, two dimensional and axisymmetric as shown in Fig.1, due to negligible variations of flow parameters along the circumferential direction. Also 2D simulations resulted in a considerable computational time saving. The conservation equations for mass, momentum and energy for compressible flow considering the variation with transport properties like thermal conductivity and viscosity with state properties along with turbulence are solved using the SIMPLE algorithm. The two equation realizable $k$-$\varepsilon$ model of turbulence is employed as it has been found more accurate. The properties of helium were obtained from the NIST real gas models provided by Fluent. A grid independence study was performed and a quadrilateral mesh having 6000 nodes in the axial direction and 30 nodes in the radial direction was considered to be accurate enough. In the present work, heat transfer for upflow and downflow conditions have been analysed for validation of the software.

## 4. VALIDATION OF FLUENT CODE FOR ANALYSIS OF SUPERCRITICAL HELIUM SYSTEMS

### 4.1) Upward flow

The operating conditions for the simulation are inlet pressure, $P_{in}$=0.25 MPa, inlet temperature, $T_{in}$=4.2 K, Reynolds number at inlet, $Re_{in}$=20000 and the acceleration due to gravity $g_x$=9.81 m/s$^2$ is against the flow. While at inlet condition of $P_{in}$=0.25 MPa and $T_{in}$=4.2 K the fluid remains at compressed fluid, when the temperature exceeds 5.7 K due to heating effect, it enters the region of a supercritical region. The mass flow rate at the inlet $\dot{m}$ = 0.10 g/s. The boundary conditions are given below (*u* is velocity; *x* and *r* represent axial and radial components, respectively).

At, $x = x_0, u_x = u_0,\ x = x_i, \dfrac{\partial u_x}{\partial r} = \dfrac{\partial T}{\partial r} = 0;\ \ r = r_0, u_r = u_{\max},\ r = r_w, u_r = 0, q_w = const.$

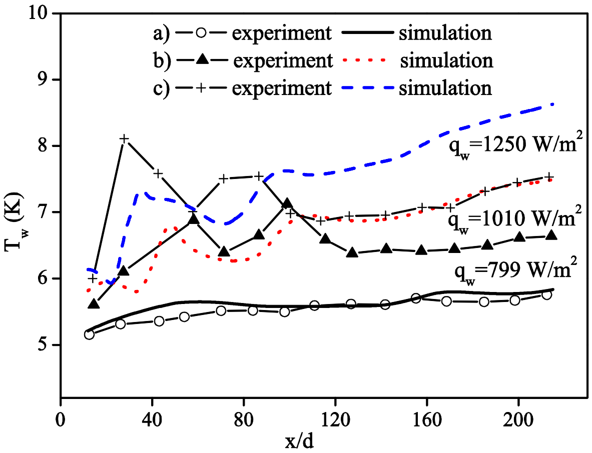

Fig. 2: Wall Temperature variation for different heat fluxes

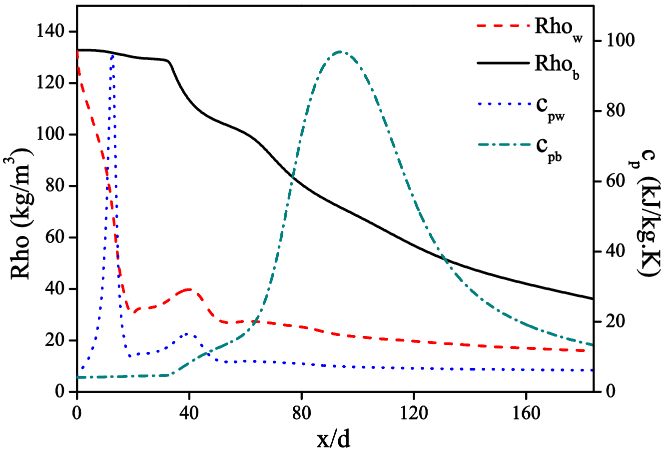

Fig. 3: Variation of density (*Rho*) and specific heat along the tube section for $q_w$=1250 W/m$^2$

The temperature profiles for all three cases are oscillatory in nature (Fig.2). Two distinct jumps in the temperature profile can be seen at higher heat fluxes for curves (b) and (c) which match with experimental results. These jumps occur earlier along the section as the heat flux increases. For curve (a) though, a distinct peak in wall temperature is not observed as seen in experimental results. In this case, the wall fluid density $Rho_w$ variation across the pseudocritical line is ~70 kg-m$^{-3}$ indicating a lesser acceleration of fluid. Also the bulk fluid reaches the pseudocritical point at the end of the section.

The explanation of the two peaks has been analyzed to understand the reason behind it. As supercritical helium flows upwards in the tube, it gets heated along the section by the constant heat flux applied at the wall. At a particular section for a given heat flux, if the wall fluid temperature reaches the pseudocritical temperature, this results in a drastic drop in the density (Fig.3). As a consequence of this the buoyancy effect increases and the fluid is accelerated upwards. This will cause high density fluid from the bulk to rush towards the wall thereby increasing the temperature of the wall fluid. This explains the first peak in wall temperature. As the bulk fluid approaches the pseudocritical temperature, its density changes abruptly causing the fluid to be accelerated thereby creating a drop in pressure. As a result, some wall fluid moves into the bulk thus causing cooler high density fluid to replace it at the wall causing a second peak.

### 4.2) Downward flow

The operating conditions are same as that specified for the upward flow case except the acceleration due to gravity, $g_x$=9.81 m/s$^2$ acts along the flow direction. The mesh quality as well the solver settings were kept the same.

For supercritical helium flowing in the downward direction, we can see that the wall temperature profiles match except in the small region for the case (c) (Fig.4). In this region the wall fluid crosses the pseudocritical line, thereby causing a sharp decrease in density and a peak in $c_p$ (Fig.5).

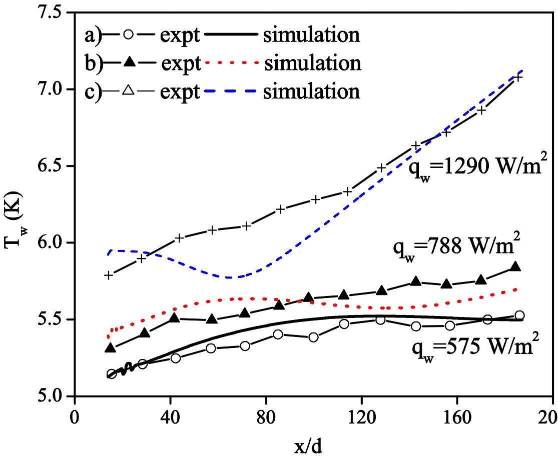

Fig. 4: Wall temperature variation for different heat fluxes

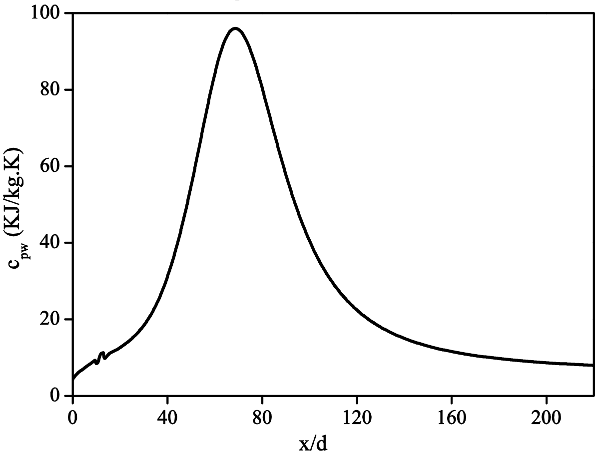

Fig.5: Wall specific heat variation along tube length

Table 2: Shows root mean square deviation (RMSD) of wall temperature (K) for various simulation cases.

| Type of Flow | Cases | RMSD (K) |
|---|---|---|
| **Vertically upward** | a)$T_{in}$=4.2K,$q_w$=799W/m$^2$, $\dot{m}$ =0.1 g/s<br>b)$T_{in}$=4.2K,$q_w$=1010W/m$^2$, $\dot{m}$ =0.1 g/s<br>c)$T_{in}$=4.2K,$q_w$=1250W/m$^2$, $\dot{m}$ =0.1 g/s | ± 0.116<br>± 0.535<br>± 0.795 |
| **Vertically downward** | a) $T_{in}$=4.2K,$q_w$=575W/m$^2$, $\dot{m}$ =0.1 g/s<br>b) $T_{in}$=4.2K,$q_w$=788W/m$^2$, $\dot{m}$ =0.1 g/s<br>c) $T_{in}$=4.2K,$q_w$=1290 W/m$^2$, $\dot{m}$ =0.1 g/s | ± 0.060<br>± 0.097<br>± 0.171 |

## 5. COMPARISON OF HEAT TRANSFER CORRELATIONS WITH FLUENT DATA

After observing that Fluent simulation may be a reasonable substitute for experimental data an attempt has been made to fit the Nusselt number (*Nu*) obtained from the simulation results against some of the correlations stated in the literature mentioned in table 3 where there is a dearth of experimental data. This has been done for two cases (case A and case B), at low and high mass flow rates as shown in Fig.6 and Fig.7, respectively. In each case a low and a high heat flux are considered. All the cases considered are for upward flow in the tube. The inlet conditions are maintained the same for both cases. However the diameter of the tube has been changed, to study the effect of mass flow rate.

Table 3: Various correlations for Nusselt number (Suffixes *w* and *b* denote wall and bulk, respectively)

| **Sr. No.** | **Correlation** | **Author** |
|---|---|---|
| **1.** | $Nu=C_1Re^{0.8}Pr_{avg}^{0.4}$;$C_1$=0.0201 (constant); $Pr_{avg}$ is average Prandtl no | Brassington et al. [6] |
| **2.** | $Nu=0.023Re^{0.8}Pr^{0.4}(T_w/T_b)^{C}{}_4$; $C_4$=-0.716 (constant) | Giarrantano et al. [4] |
| **3.** | $Nu=0.023Re_b^{0.8}\,Pr_{min}^{0.8}(Rho_w/Rho_b)^{0.3}$; $Pr_{min}$ is minimum Prandtl no | Shitsman [11] |
| **4.** | $Nu=0.023Re_b^{0.8}\ Pr_b^{0.4}(2/(0.84+0.2)^{0.5}+1)^2F$, where $F=(c_{pmean}/c_{pb})^{0.28}$ , when $c_{pmean}>c_{pb}$, $F$=1, when $c_{pmean}<c_{pb}$ | Yaskin et al. [9] |

It has been observed, for low mass flow conditions (case A), all the correlations except correlation (4) match our simulation data accurately within a confidence level of ±15% (Fig.6a). However it is also observed at $q_w$=1250 W/m$^2$ (Fig.6b), only correlation (4) yields results within ±50%. For case B all these correlations break down for both cases of heat flux with deviations of over ±100% (Fig.7). Therefore, it can be concluded that at a higher mass flow rate the existing correlations are less accurate.

## Case A: Lower mass flow rate

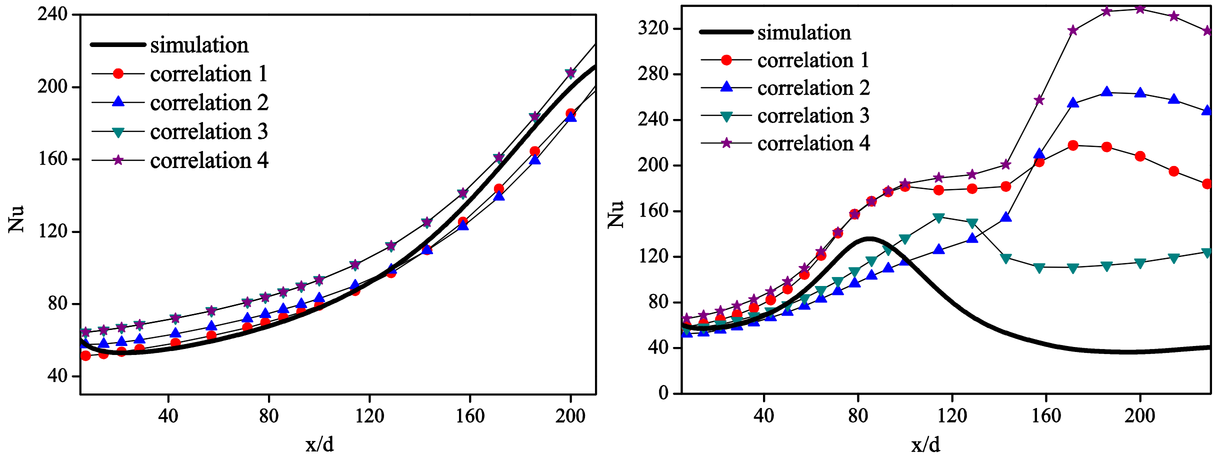

(a) (b)

Fig. 6: Comparison of Nusselt no. correlations along the tube under conditions $d$=0.0014 m, $\dot{m}$ =0.078 g/s, $T_{in}$=4.2 K, $P_{in}$=0.25 MPa, $Re_{in}$=2.10$^4$ for a) $q_w$=608 W/m$^2$ and b) $q_w$=1250 W/m$^2$

## Case B: Higher mass flow rate

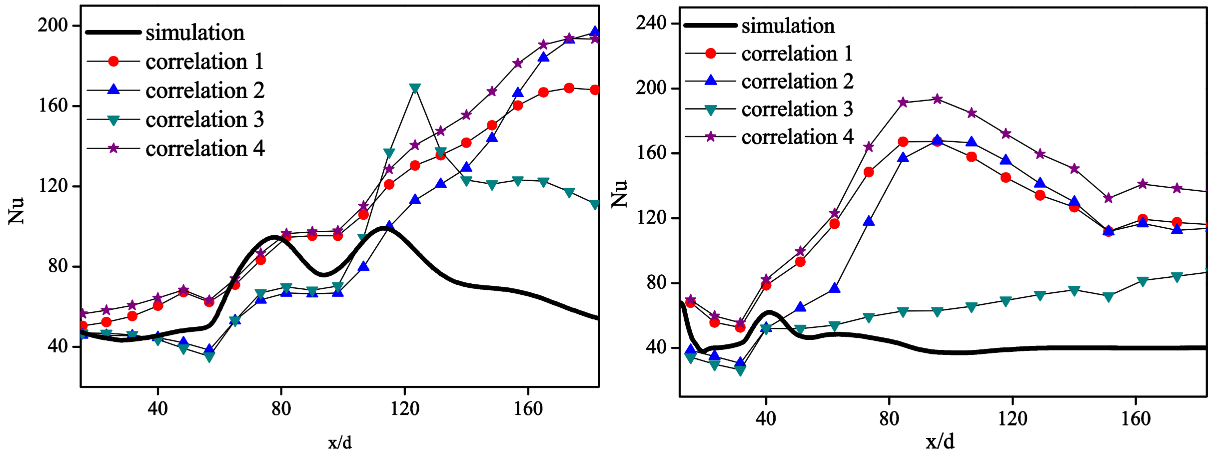

(b) (b)

Fig. 7: Comparison of Nusselt no. correlations along the tube under conditions $d$=0.0018 m, $\dot{m}$ =0.10 g/s, $T_{in}$=4.2 K, $P_{in}$=0.25 MPa, $Re_{in}$=2×10$^4$ for 1) $q_w$=608 W/m$^2$ and 2) $q_w$=1250 W/m$^2$

## 6. MIXED CONVECTION HEAT TRANSFER IN VERTICAL FLOW OF SUPERCRITICAL HELIUM

In order to study the effect of natural convection on forced flow of supercritical helium, heat transfer is simulated for three different values of mass flow rate $\dot{m}$, with varying values of heat flux at each of these. The flow geometry and operating conditions have been considered same as described above. The values of heat flux for upward and downward studies range between 575-2000 W/m$^2$.

The parameter as proposed by Jackson et al. [12], $\left(Gr/\mathrm{Re}^{2.7}\right) < 10^{-5}$, $Gr$ being the Grashof number, is the condition under which influence of buoyancy forces on forced convection can be neglected. For $\dot{m}$ = 0.05 g/s and $\dot{m}$ = 0.1 g/s, for upward flow (Fig. 8) and downward flow (Fig.9), the values of ratio $\left(Nu/Nu_F\right)$ are found to be less than one indicating that free convection effects impede forced convection heat transfer when compared to the Nusselt number for pure forced convection $\left(Nu_F\right)$ calculated from Dittus-Boelter correlation. At $\dot{m}$ =0.5 g/s, heat transfer in terms of $\left(Nu/Nu_F\right)$ has improved two times under both flow conditions. However, effects of buoyancy on heat transfer are negligible in this region.

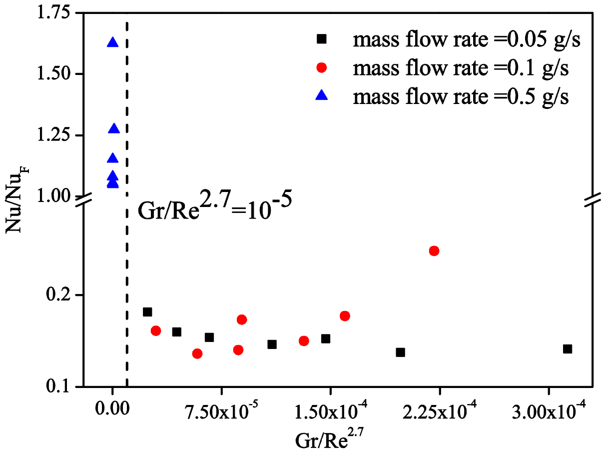

Fig.8: Effect of free convection on Nusselt number in upward flow

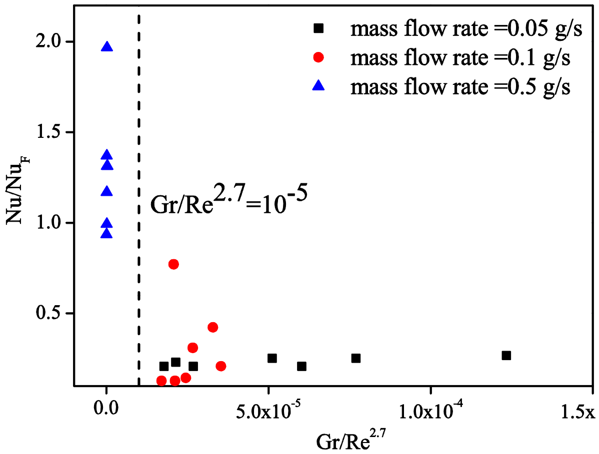

Fig.9: Effect of free convection on Nusselt number in downward flow

## 7. CONCLUSIONS

Commercial software ANSYS® Fluent provides good tool for simulating complex heat transfer phenomena associated with supercritical helium. The results provide good agreement with those of experiment. Heat transfer to supercritical helium deteriorated at certain sections along the wall evident from the peaks in wall temperature. These sections have been observed at places where the wall fluid and the bulk fluid reached pseudocriticality. Plots of Nusselt number shows that heat transfer to supercritical helium shows a peak followed by deterioration at high heat fluxes. All the correlations break down at as the mass flow rate is increased. A study on mixed convection in vertical tubes showed that buoyancy forces impede heat transfer for both conditions of flow at lower flow rates. Therefore, experimental data based on certain mass and heat fluxes may not be used for designing equipment with higher or lower values.

## 8. REFERENCES

[1] R.C. Hendricks, R.J. Simoneau, R.V. Smith, 1970, Survey of heat transfer to near-critical fluids, Lewis Research Centre, Cleveland, NASA Technical Note TN-D-5886, Washington, DC.

[2] I.L Pioro, H.F. Khartabil, R.B. Duffey, 2004,Heat transfer to supercritical fluids flowing in channels-empirical correlations (survey), Nuclear Engineering and Design, 230(1-3), 69-91.

[3] G. P. Malyshev and V. G. Pron'ko, 1972, Characteristics of heat transfer during turbulent flow of supercritical helium, Translated from Inzhenerno-Fizicheskii Zhurnal, Vol. 23, No. 5, pp. 814-819.

[4] P.J. Giarratano, V.D. Arp, R.V. Smith, 1973, Forced Convective heat transfer to supercritical helium, Cryogenics, 11(5):385-393.

[5] P.J. Giarratano, M.C. Jones, 1974, Deterioration of heat transfer to supercritical helium at 2.5 atmospheres, International J. of Heat and Mass Transfer, 18: 649-653.

[6] D.J. Brassigton, D.N.H. Cairns, 1977, Measurements of forced convective heat transfer to supercritical helium, International Journal of Heat and Mass Transfer, 20:207-214.

[7] V.A. Bogachev, V.M. Yeroshenko, O.F. Snyitina, L.A. Yaskin, 1985, Measurements of heat transfer to supercritical helium in vertical tubes under forced and mixed convection conditions, Cryogenics, 25:198-201.

[8] M.C.M. Cornelissen, C.J. Hoogendorn, 1985, Forced convection heat transfer to supercritical helium, Applied Scientific Research, 42:161-183.

[9] V.M. Yeroshenko, L.A. Yaskin, 1981, Applicability of various correlations for the prediction of turbulent heat transfer of supercritical helium, Cryogenics, 21(2): 94-96.

[10] M. Shiotsu, Y. Shirai , K. Hama, 2010, Forced convection heat transfer of He I in a horizontal cylinder under supercritical conditions, Int. Cryogenic Eng. Conference-23, Poland .

[11]M.W. Shitsman, 1974, Heat transfer to supercritical helium, carbon dioxide, and water: Analysis of thermodynamic and transport properties and experimental data, Cryogenics, pp. 77-83.

[12] J.D. Jackson, M.A. Cotton, B.P. Axcell, 1989, Studies of mixed convection in vertical tubes, Int. J. Heat and Fluid Flow, 10(1):2-15.

055

# Presentation of the German Working Committee NA 016-00-07 AA: Safety Devices for Helium Cryostats

**Blum L.[*], Grohmann S.[**], Haberstroh Ch.[***], Lau M.[****], Otte W.[*****], Reinhardt M.[******], Schröder C.H.[*******], Süßer M.[********]**

[*]Linde Kryotechnik AG, Pfungen, Switzerland
[**] Institute for Technical Thermodynamics and Refrigeration (ITTK), Institute for Technical Physics (ITEP), Karlsruhe Institute of Technology KIT, Karlsruhe, Germany
[***] Technische Universitaet Dresden, Bitzer Chair of Refrigeration, Cryo and Compressor Technology, Dresden, Germany
[****] DIN Deutsches Institut für Normung e.V., Normenausschuss Druckgasanlagen, Berlin, Germany
[*****] Air Liquide Deutschland GmbH, Krefeld, Germany
[******] Herose GmbH, Bad Oldeslohe, Germany
[*******] Gesellschaft für Schwerionenforschung GSI, Darmstadt, Germany
[********] Institute for Technical Physics (ITEP), Karlsruhe Institute of Technology KIT, Karlsruhe, Germany

## ABSTRACT

The European Pressure Equipment Directive 97/23/EC (PED) is the guideline for the design, manufacture and conformity of pressure equipment and assemblies with the 'maximum allowable pressure P·S' greater than 0.5 bar. According to the PED the momentary pressure surge must be kept to 10 % of the maximum allowable pressure. Maximum allowable pressure PS stands for the maximum pressure for which the equipment is designed, as specified by the manufacturer.

In Europe two standards are applied, namely DIN EN ISO 4126 (Safety devices for protection against excessive pressure) and in particular for cryogenic applications EN 13648 (Cryogenic vessels – Safety devices for protection against excessive pressure). But these standards ignore serious details very important for helium applications.

Recently a national committee had been established in Germany to work on a proposition for a new standard regarding pressure protection of helium pressure equipment (DIN SPEC 4683). The members of the working group consist of experimental scientists and engineers from research facilities, safety equipment manufacturers and administrative institutions.

The presentation will introduce the working group and its task. The final directive currently being edited will include guidance for hazard analysis, operational safety assessment, damage prevention and damage control for helium pressure equipment.

## 1. INTRODUCTION

A national advisory committee was established to work on a proposition for a standard for pressure protection of helium pressure equipment (DIN SPEC 4683), because the existing standards have some loopholes and ignore serious details very important for helium applications.

A starting point of this work may be seen in the existing directives and regulations:

### Directive 97/23/EC of the European Parliament and of the Council of 29 May 1997 on the approximation of the laws of the Member States concerning pressure equipment

> Article 1
>
> 1. Scope and definitions
>
> This Directive applies to the design, manufacture and conformity assessment of pressure equipment and assemblies with a maximum allowable pressure PS greater than 0.5 bar.

2. For the purposes of this Directive:

2.1. ‘Pressure equipment’ means vessels, piping, safety accessories and pressure accessories. Where applicable, pressure equipment includes elements attached to pressurized parts, such as flanges, nozzles, couplings, supports, lifting lugs, etc.

2.1.1. ‘Vessel’ means a housing designed and built to contain fluids under pressure including its direct attachments up to the coupling point connecting it to other equipment. A vessel may be composed of more than one chamber.

2.11. Safety accessories

2.11.1. Safety accessories must be so designed and constructed as to be reliable and suitable for their intended duty and take into account the maintenance and testing requirements of the devices, where applicable, be independent of other functions, unless their safety function cannot be affected by such other functions, comply with appropriate design principles in order to obtain suitable and reliable protection. These principles include, in particular, fail-safe modes, redundancy, diversity and self-diagnosis.

2.11.2. Pressure limiting devices

These devices must be so designed that the pressure will not permanently exceed the maximum allowable pressure PS; however a short duration pressure surge in keeping with the specifications laid down in 7.3 is allowable, where appropriate.

7.3. Pressure limiting devices, particularly for pressure vessels
The momentary pressure surge referred to in 2.11.2 must be kept to 10 % of the maximum allowable pressure.

## 2. STANDARDS

According to today’s regulations, the following standards harmonized within the European Community are to be applied:

- DIN EN ISO 4126 -1 to 4146 -7 Safety devices for protection against excessive pressure

- EN 13648 Cryogenic vessels-Safety devices for protection against excessive pressure
  - Part 1: Safety valves for cryogenic service
  - Part 2: Bursting disc safety devices for cryogenic service

- EN 13458 Cryogenic vessels - Static vacuum insulated vessels
  - Part 1: Fundamental principles
  - Part 2: Design, fabrication, inspection and testing
  - Part 3: Operational requirements

Presumption of conformity:

- AD 2000 Pressure vessel
- AD 2000-Merkblatt A1 Sicherheitseinrichtungen gegen Drucküberschreitung – Berstsicherungen
- AD 2000-Merkblatt A2 Sicherheitseinrichtungen gegen Drucküberschreitung – Sicherheitsventile
- AD 2000-Merkblatt W10 Werkstoffe für tiefe Temperaturen Eisenwerkstoffe

- ASME Code

## 3. MISSING HINTS IN THE STANDARDS FOR HELIUM APPLICATION

EN 13648 is specified for storage containers, not for experimental equipment with inserts like e.g. superconducting magnets. Applying this for helium cryostats or other cryogenic helium applications, a number of deficiencies become obvious:

- No hints about the pressure drop inlet piping beyond the 3 % - rule
- No hints about staggered pressure levels on cryogenic pressure vessel
- No hints about ullage
- No hints about thermoacustic oscillations
- No hints about thermocatastrophic loss of vacuum
- No hints about large stored energy in case of a superconducting magnet.

## 4. PRESSURE LOSS OF THE SAFETY VALVE INLET PIPING

In the EN 13648-3 for cryogenic vessels safety devices for protection against excessive pressure are addressed. There is indication on the allowable pressure drop for a safety valve pipework given in detail, than high pressure loss in the inlet pipe work could be the reason for chattering.

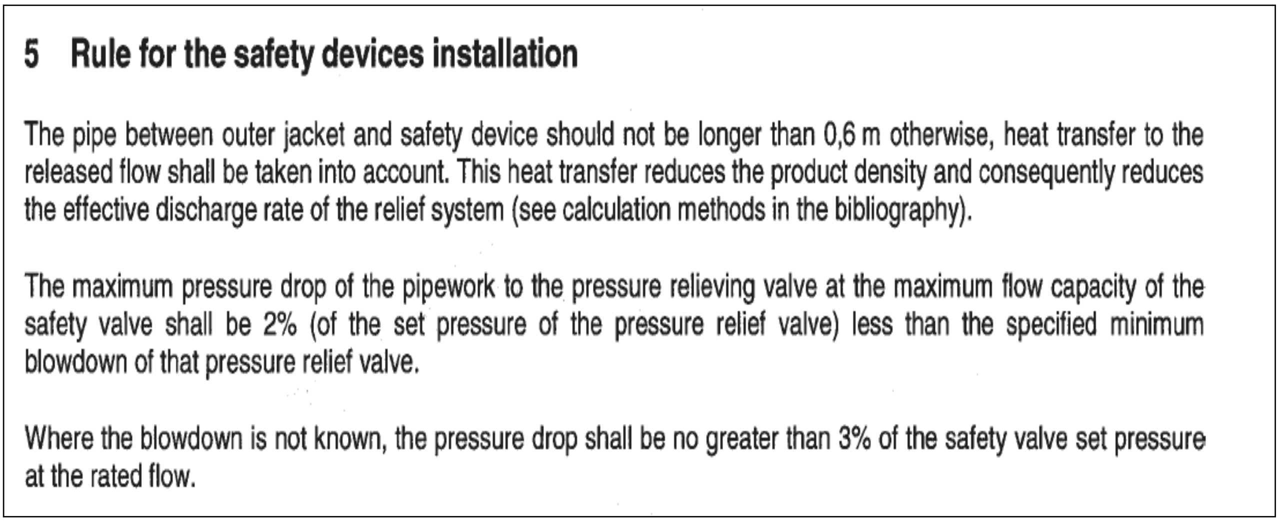

### 5 Rule for the safety devices installation

The pipe between outer jacket and safety device should not be longer than 0,6 m otherwise, heat transfer to the released flow shall be taken into account. This heat transfer reduces the product density and consequently reduces the effective discharge rate of the relief system (see calculation methods in the bibliography).

The maximum pressure drop of the pipework to the pressure relieving valve at the maximum flow capacity of the safety valve shall be 2% (of the set pressure of the pressure relief valve) less than the specified minimum blowdown of that pressure relief valve.

Where the blowdown is not known, the pressure drop shall be no greater than 3% of the safety valve set pressure at the rated flow.

## 5. SAFETY VALVE CHATTERING

Chattering of a safety valve is defined as an abnormal, rapid reciprocating motion of the moveable parts of the safety valve. Shock waves due to the rapid opening or closing of the valve may appear. The chattering frequency typically is found at approx. 10 - 100 Hz. Such pressure oscillation in the inlet piping usually has a number of detrimental consequences:

- Reduction of relieving capacity
- Risks of pressure increase above the maximum accumulation pressure
- Risk of firing the rupture disc in a staggered configuration
- Risk of misalignment, valve seat damage, mechanical failure of valve internals and associated piping.

For examples, an impressive arrangement for a safety valve inlet line is shown here. The medium is air at room temperature and the pressure drop is about 9 % of the set pressure. As shown in the figure, during the chattering the pressure in the vessel increases and there are large pressure amplitudes in the inlet piping. Such behavior must be prevented in any case, because such pressure amplitudes may be the reasons for unexpected response or injury of the staggered rupture disc [1, 2].

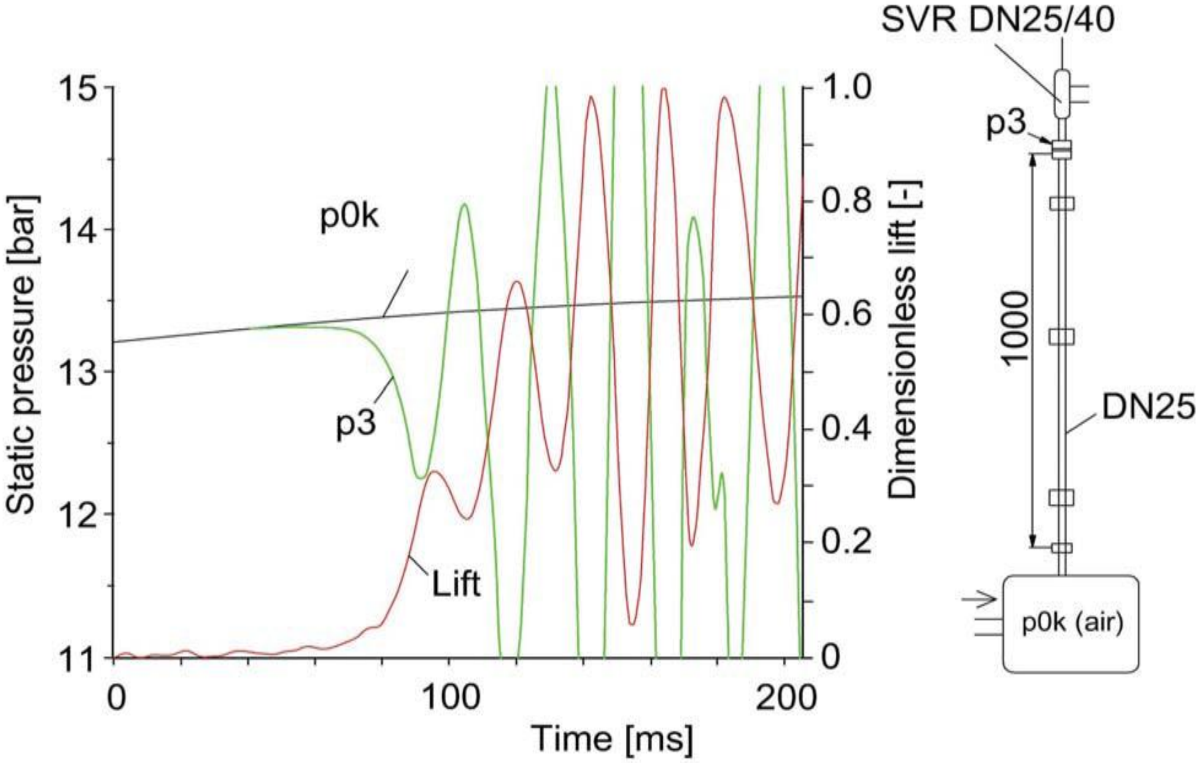

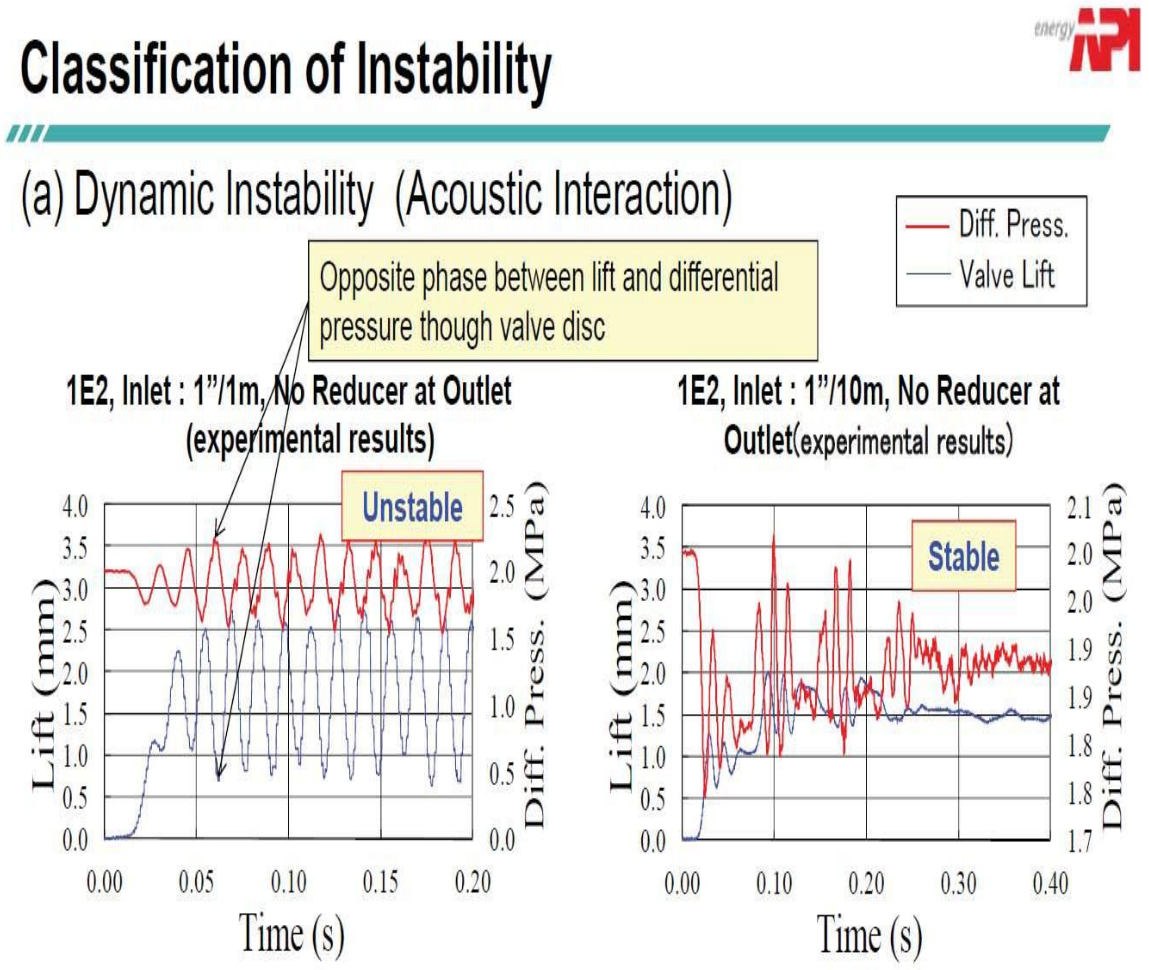

## Classification of Instability

(a) Dynamic Instability (Acoustic Interaction)

Opposite phase between lift and differential pressure though valve disc

Diff. Press.
Valve Lift

**1E2, Inlet : 1"/1m, No Reducer at Outlet (experimental results)**

**Unstable**

**1E2, Inlet : 1"/10m, No Reducer at Outlet(experimental results)**

**Stable**

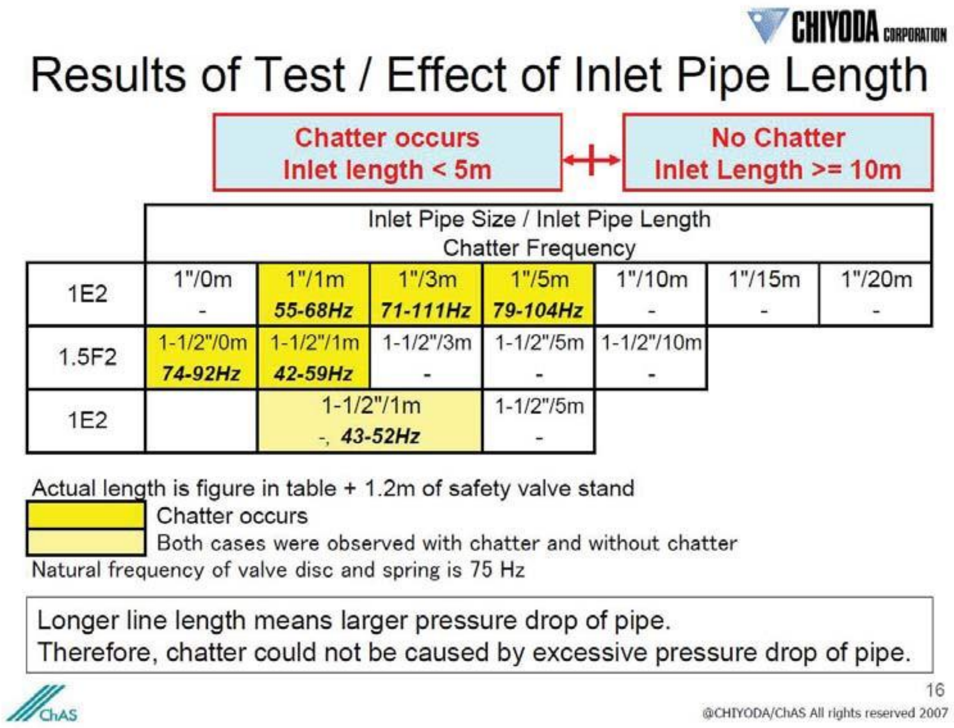

CHIYODA CORPORATION

Results of Test / Effect of Inlet Pipe Length

Chatter occurs Inlet length < 5m ↔ No Chatter Inlet Length >= 10m

| | Inlet Pipe Size / Inlet Pipe Length<br>Chatter Frequency | | | | | | |
|---|---|---|---|---|---|---|---|
| 1E2 | 1"/0m<br>- | 1"/1m<br>*55-68Hz* | 1"/3m<br>*71-111Hz* | 1"/5m<br>*79-104Hz* | 1"/10m<br>- | 1"/15m<br>- | 1"/20m<br>- |
| 1.5F2 | 1-1/2"/0m<br>*74-92Hz* | 1-1/2"/1m<br>*42-59Hz* | 1-1/2"/3m<br>- | 1-1/2"/5m<br>- | 1-1/2"/10m<br>- | | |
| 1E2 | | 1-1/2"/1m<br>-, *43-52Hz* | | 1-1/2"/5m<br>- | | | |

Actual length is figure in table + 1.2m of safety valve stand

🟨 Chatter occurs

▨ Both cases were observed with chatter and without chatter

Natural frequency of valve disc and spring is 75 Hz

Longer line length means larger pressure drop of pipe.
Therefore, chatter could not be caused by excessive pressure drop of pipe.

ChAS

16

@CHIYODA/ChAS All rights reserved 2007

## 6. STAGGERED PRESSURE LEVELS ON CRYOGENIC PRESSURE VESSEL

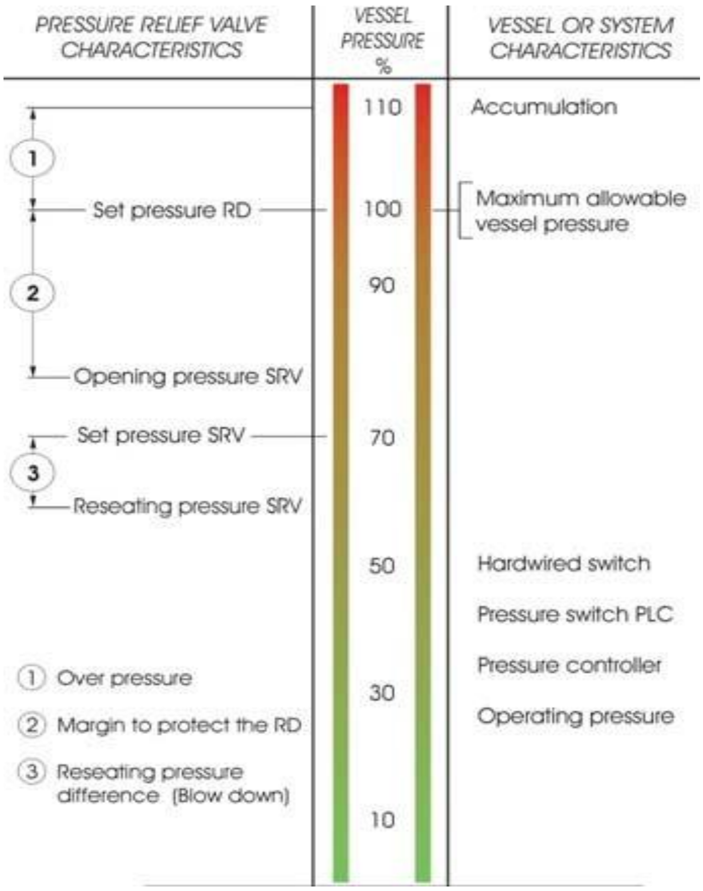

There are no hints in the standards about staggered pressure levels. In the following scheme a favourable setting of the respective pressure levels is shown:

Rupture disc (RD) for maximum mass flow. For example: vacuum loss and afterwards quench of sc magnet. The safety valve (SRV) selected for more likely lower mass flow. For example: quench of sc magnet.

2 = Gap of respective size necessary here; otherwise in case of operation of the safety valve a firing of the rupture disc will occur.

## 7. ULLAGE

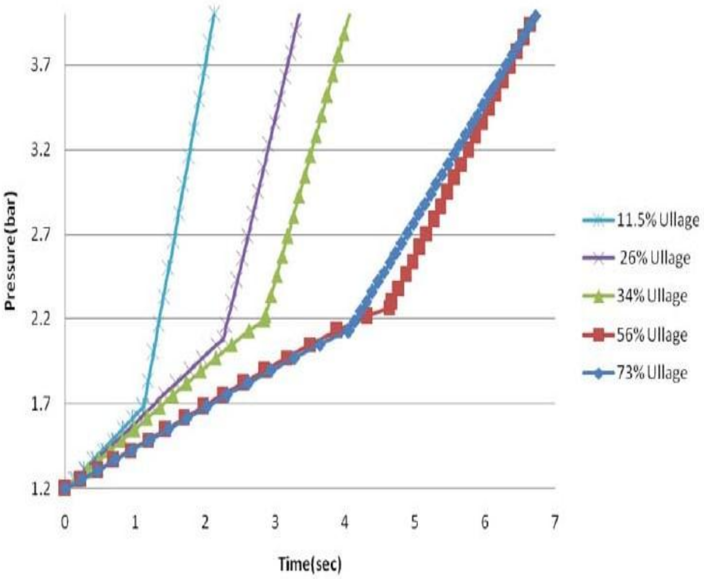

A very important operation parameter is the ullage of the vessel, because there is a different pressure rise in case of non-venting cryostat for different ullage [3]. The thermal expansion coefficient of helium at saturation pressure of 1 bar is very large compared to other cryogenic fluids:

LHe: 0.2 [1/K]

$LN_2$: 0.006 [1/K].

For the minimum ullage lower than 20 % risk of overfilling with the consequences of thermoacoustic oscillations in the vent line and fast pressure rise in case of energy input must be taken into account.

## 8. THERMOACOUSTIC OSCILLATIONS

There are some potential influences on the ruptured disc in case of thermoacustic oscillations in the inlet pipe. This could be a formation of an ice plug in case of a disc equipped with a knife or increasing of the rupture pressure in case of cooling down of the disc [4].

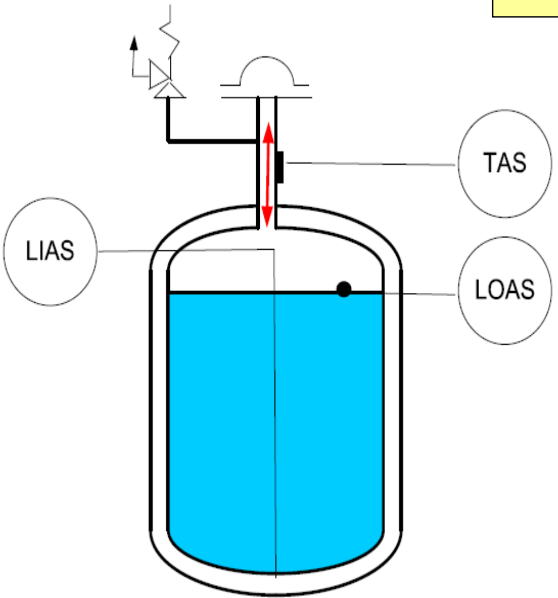

Ice plug on the knife

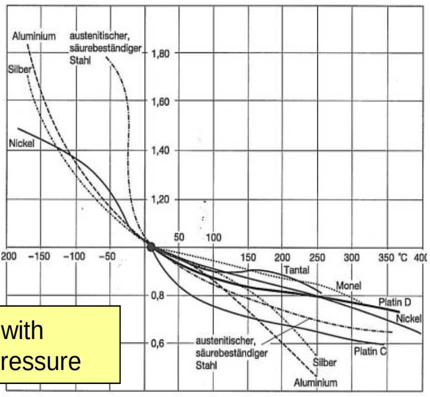

Cool down of rupture disc with increasing of the rupture pressure

## 9. RISK ANALYSIS
## CRYOSTAT WITH SUPERCONDUCTING MAGNETS

All aspect of possible sources of errors must be taken in consideration.

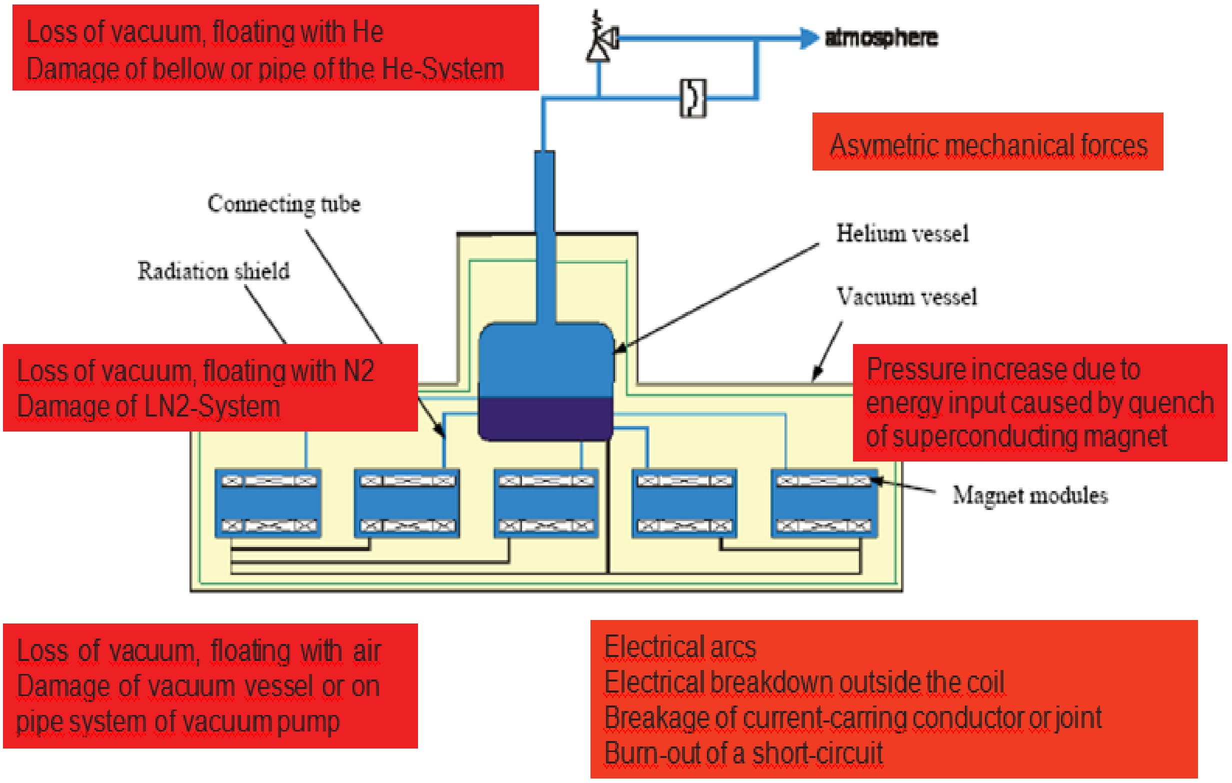

Loss of vacuum, floating with He
Damage of bellow or pipe of the He-System

Asymetric mechanical forces

Loss of vacuum, floating with N2
Damage of LN2-System

Pressure increase due to energy input caused by quench of superconducting magnet

Loss of vacuum, floating with air
Damage of vacuum vessel or on pipe system of vacuum pump

Electrical arcs
Electrical breakdown outside the coil
Breakage of current-carring conductor or joint
Burn-out of a short-circuit

## 10. ENERGY INPUT DUE TO CATASTROPHIC LOSS OF VACUUM

Particular attention must be given to the loss of insulation vacuum as a source of pressure [4, 5].

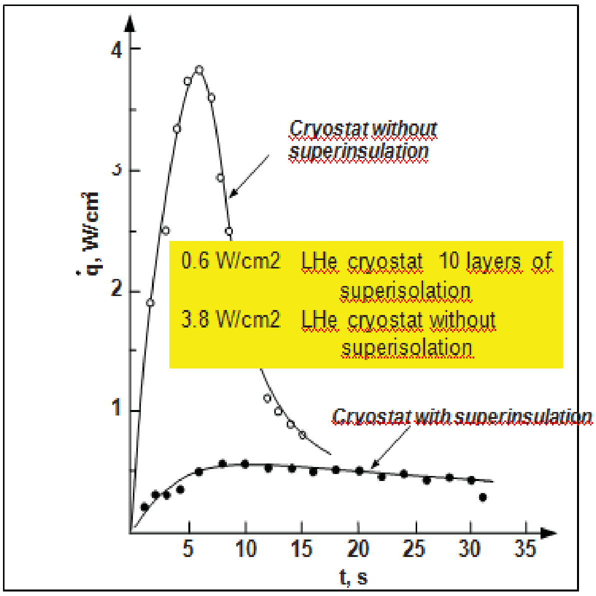

0.6 W/cm2 LHe cryostat 10 layers of superisolation
3.8 W/cm2 LHe cryostat without superisolation

0.4 W/cm2 LHe cryostat with superisolation
3.1 W/cm2 LHe cryostat without superisolation

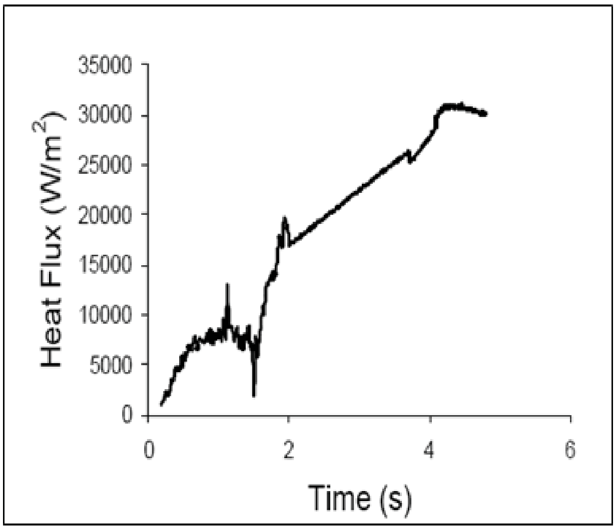

## 11. OBJECTIVE OF THE WORKING COMMITTEE NA 016-00-07 AA

The tasks of the established working committee can be defined as follows:

- Systematic compilation of specific conditions for cryogenic helium pressure vessels and protection against overpressure.
- Compilation of a supplement for existing standards.
- Support for the cryogenic community for all kinds of safety issues on helium pressure vessels.

## 12. REFERENCES

[1] Frommann O, Friedel L. 1998, Analysis of safety relief valve chatter induced by pressure waves in gas flow, Journal of Loss Prevention in the Process Industries 11.

[2] Izuchi H. 2008: Chatter of safety valve, API Meeting.

[3] Bhattacharyya P, et al. 2010, Experiment and Analysis: Partial loss of insulation vacuum in K-500 superconducting cyclotron cryostat, Proc. of Cyclotrons, Lanzhou.

[4] Boyle R.F, Whitehouse P.L 2001, Dewar safety: Risks and corrective actions, Adv. Cry. Eng. Vol. 51

[5] Lehmann W, Zahn G. 1978, Safety aspects for LHe cryostats and LHe transport containers, ICEC Vol.7.

[6] Harrison S. M. 2002, Loss of vacuum experiments on a superfluid Helium vessel, IEEE Transactions on Applied Superconductivity, Vol12, NO1.

# LIQUEFIED NATURAL GAS (LNG)

031

# Conceptual Design of an Efficient Small LNG Production Facility

**Quack H.**

Bitzer-Stiftungsprofessur für Kaelte-, Kryo- und Kompressorentechnik
Technische Universitaet Dresden, D-01062 Dresden, Germany

## ABSTRACT

For environmental reasons more and more cars, trucks and buses are using compressed natural gas (CNG) as fuel. This trend could be enlarged, if there were more CNG gas stations. Presently such stations can only be built near the distribution grid of natural gas. To build a station away from the grid, it would be necessary to transport the natural gas there in form of liquefied natural gas (LNG). Sometimes it is economical to transport the LNG from far away locations, but it would be beneficial, if gas companies could produce LNG within their own grid.

An optimum location for such a small LNG production facility would be a place in the grid, where high pressure gas from the pipeline with a pressure higher than 40 bar is throttled to a medium pressure distribution grid with a pressure below 6 bar. Here one can efficiently liquefy a small part stream. The main stream is used to supply precooling due to the Joule-Thomson effect. It can act as heat sink for the heat given off by the liquefaction process and it also can absorb those components of the natural gas, which are separated upstream or during the liquefaction process like $H_2O$, $CO_2$, higher hydrocarbons and $N_2$.

The liquefaction process is a Joule-Thomson process supported by precooling of a cascade with e.g. $CO_2$ and ethylene as refrigerants. To improve the quality of the CNG for the use in internal combustion engines it is advisable to reduce the content in ethane below about 3 %. For this purpose one can include a small rectification column in the process, which can work at a pressure level between 10 and 40 bar.

The concept is usable for plant sizes between 5 and 50 T/d. The power consumption is in the order of 0.2 to 0.22 kWh/kg, which is lower than the specific power needed in large bulk LNG facilities.

## 1. INTRODUCTION

The ideal location for a small LNG production facility at a place in the pipeline network, where high pressure gas is throttled to the medium pressure network. At these locations the following installation exists (Fig. 1).

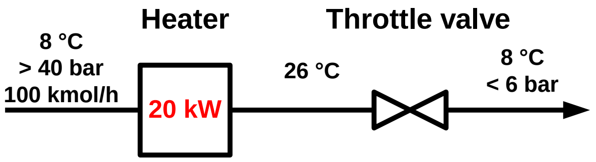

Figure 1. Present installation

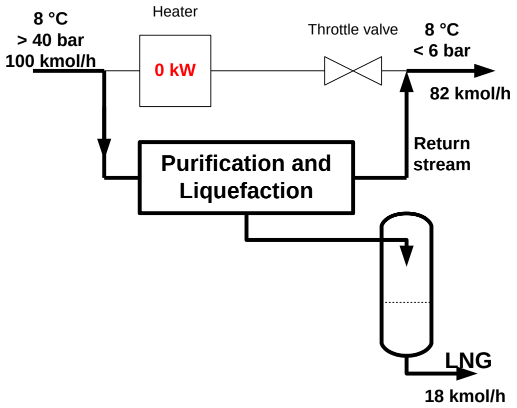

Figure 2. Intended installation

Upstream of the throttle valve the high pressure gas is heated to about 26 °C so that downstream of the throttle valve the temperature of the gas is about 8 °C. For a flow rate of 100 kmol/h (2240 $Nm^3/h$) one needs a heating power of about 20 kW, which is produced by burning a part of the natural gas.

Figure 2 shows the intended installation. The gas for the liquefaction plant will be taken from the high pressure line upstream of the heater. The gas is purified and partially liquefied. The liquefied portion will be stored in a storage vessel, from where it can be distributed by truck. The not liquefied portion will be returned to the medium pressure line.

The return stream fulfils the following three tasks:

1. Through its Joule-Thomson cooling capacity it provides precooling for the liquefaction process.
2. It can absorb those components of the natural gas, which are not wanted in the liquefaction process or the LNG.
3. It provides a heat sink for the heat given off from the refrigeration process.

## 2. FEED AND DESIRED PRODUCT

Table 1 and 2 show the quantity and composition of the available natural gas ("feed") and the desired capacity and composition of the LNG.

Table1. Specification of feed and product

| | Feed | Product LNG |
|---|---|---|
| Flow rate | 100 kmol/h is available | 18 kmol/h |
| Pressure | > 40 bar | 2 bar (abs.) in storage vessel |
| Temperature | 8 °C (281 K) | 118.5 K |

Table 2. Composition

| | Range of composition of natural gas in mol % | Specification of LNG composition in mol % |
|---|---|---|
| Methane | 88 – 90.6 | > 97 |
| Ethane | 4.2 – 5.3 | < 2.5 |
| C3 + C4 | 1.1 – 1.6 | < 0.1 |
| C5+ | < 0.1 | < 0.001 |
| $CO_2$ | 1.2 – 1.8 | < 0.01 |
| $N_2$ | 1.7 – 3.2 | < 1.0 |

$CO_2$ and C5+ have to be removed, because they could freeze out in the liquefaction process. Ethane does not present any problem during liquefaction. But in the intended application only a low content of ethane in the LNG is desired. Most of the LNG will later be used as compressed natural gas (CNG) to be burnt in internal combustion engines. A content of ethane in CNG above 5 percent can cause problems with some engines. In the handling of LNG downstream of the liquefaction facility the content of ethane may rise because of the preferential boiling of methane. Therefore it has been specified, that the content of ethane in the LNG storage vessel of this facility should be below 2.5 %. If the content of ethane is being reduced, the content in propane and butane is reduced even more. The content of nitrogen should be reduced, because it is more difficult to liquefy than the methane.

## 3. BLOCK DIAGRAM OF PROPOSED SYSTEM

Small capacity plants should have a simple process, should need only few components, should be reliable, but should nevertheless have only a moderate specific power consumption. Figure 3 shows a proposal, which fulfils these requirements.

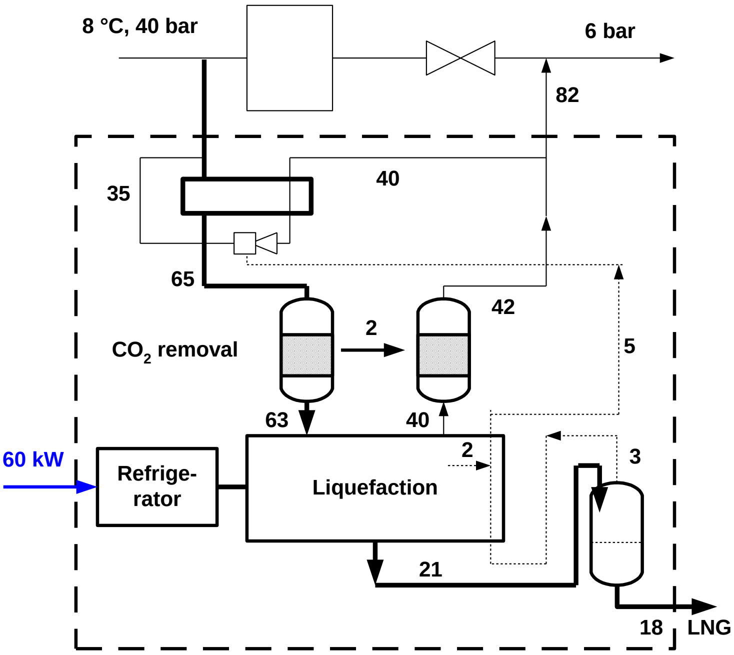

Figure 3. Block diagram with flow rates in kmol/h.
The numbers in the diagram show the approximate flow rate in kmol/h.

The natural gas arrives with a pressure of 40 bar and 8 °C. 65 kmol/h are used for the liquefaction process. If additional natural gas is available (in Figure 3 a quantity of 35 kmol/h are assumed), this can be used for the pre-cooling of the feed.
The first stage of the purification is the removal of $CO_2$ in a dual bed adsorption process. It is proposed to use a mixture of pressure and temperature swing adsorption. The $CO_2$ is adsorbed at 40 bar total pressure and a temperature between -1 °C and 8 °C. And it is desorbed by a return stream from the coldbox at 6 bar total pressure and a temperature between 70 and 60 °C.
A flow rate of 63 kmol/h enters the liquefaction plant at a temperature of 272 K (– 1 °C). In this plant additional components like most of the ethane, the higher hydrocarbons and nitrogen are removed. The 6 bar return stream is used to regenerate the adsorber. The LNG, which is first produced at 6 bar, is then throttled to 2 bar in the storage vessel. The flash gas from the storage vessel is warmed in the liquefier and then compressed by an ejector by the precooling stream to the network pressure of 6 bar.
The refrigeration needed for the liquefaction is produced by the Joule-Thomson effect of the return gas and additionally by a mechanical refrigerator, which needs an electric input power of about 60 kW.

## 4. CASCADE REFRIGERATOR

Due to the available excess natural gas flow rate, the cooling from about 190 K downward can be totally produced by Joule-Thomson cooling. So the external refrigerator has to cool the natural gas only to about this temperature. For this cooling one can use several different refrigeration cycles. The traditional one is a cascade refrigerator. Such a system is shown in Figure 4.

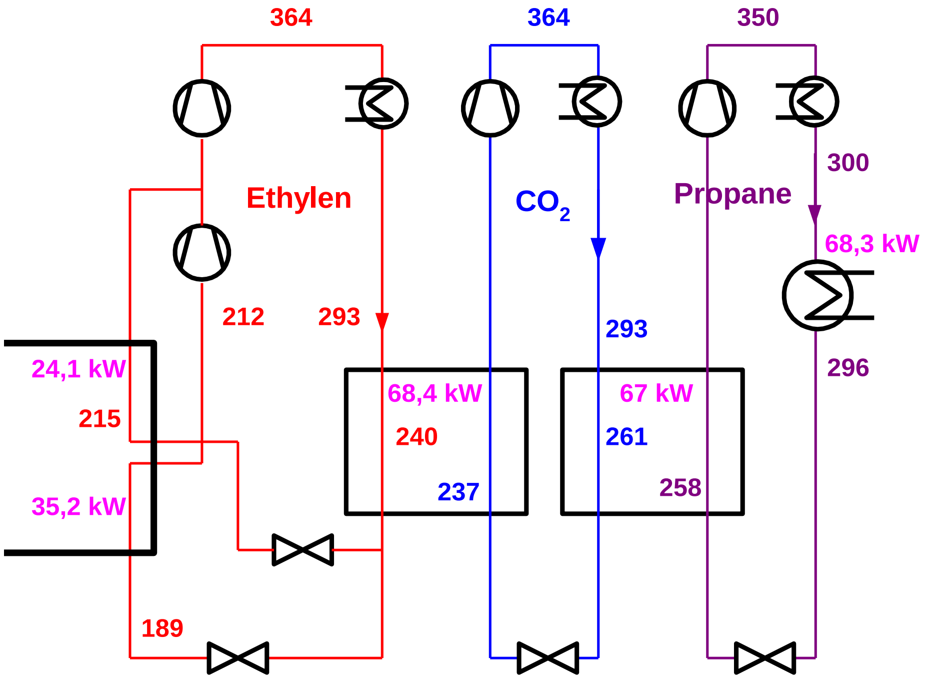

Figure 4. Flow diagram of the refrigerator
The figures in the diagram show heat flow rates in kW and temperatures in Kelvin.

The natural gas is cooled by boiling ethylene in two stages, first by ethylene boiling at 215 K and then by ethylene boiling at 189 K. The low pressure ethylene is compressed in the first stage compressor, then combined with the medium pressure stream and then compressed in the second stage compressor. The hot high pressure gas is used to produce hot water and is finally condensed at 240 K against boiling $CO_2$.
The $CO_2$ boils at 237 K. Then it is compressed and the hot gas is again used to produce hot water, before it is condensed at 261 K against boiling propane. The propane boils at 258 K. Then it is compressed and the superheated vapour is used to produce hot water before it is condensed against cooling water at 296 K.

## 5. ETHANE REMOVAL AND LIQUEFACTION

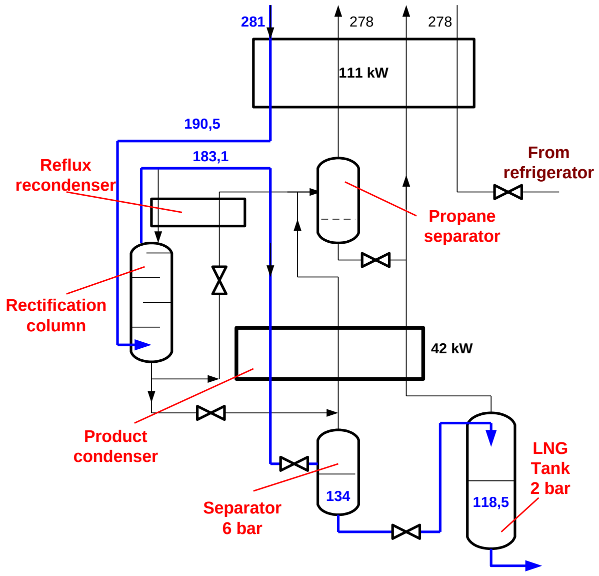

Figure 5. Liquefaction and ethane removal

Figure 5 shows the flow diagram of the equipment, which is contained in the cryogenic coldbox. The blue line shows the path of the feed to the product. The feed is cooled in the first heat exchanger by the two low pressure streams and the external refrigerator to about 190.5 K. At this point about one third of the feed is liquid. The two-phase mixture is guided to the bottom of the rectification column, the liquid flows downwards, the vapour upwards.

The vapour at the top of the column contains only little ethane and higher hydrocarbons. This vapour is condensed and sub-cooled in the “product condenser”. Then it is throttled into the 6 bar separator. The flash, which is generated in this throttling, contains most of the nitrogen. The liquid is throttled into the storage tank, in which the LNG is stored at 2 bar. The vapour generated in this second throttling contains the rest of the nitrogen.

The ethane-rich liquid from the bottom of the rectification column is throttled to 6 bar and is used to provide on one hand the reflux for the rectification column and on the other hand the cooling for the product condenser. Downstream of the condensers the two streams contain still some non-evaporated propane and higher hydrocarbons. These are separated in the propane separator and throttled into the two-bar stream, because these components are not helpful in the regeneration of the $CO_2$ adsorbers.

It is obvious from the flow diagram, that one has the option to use the liquid from the bottom of the column either for the reflux condenser or the product condenser. It turns out, that the division between these two flows has an influence on the ethane, nitrogen and $CO_2$ content in the LNG. Figure 6 shows the content of these components in the LNG in function of the heat removal in the reflux condenser for 3 and 5 theoretical stages of the rectification column.

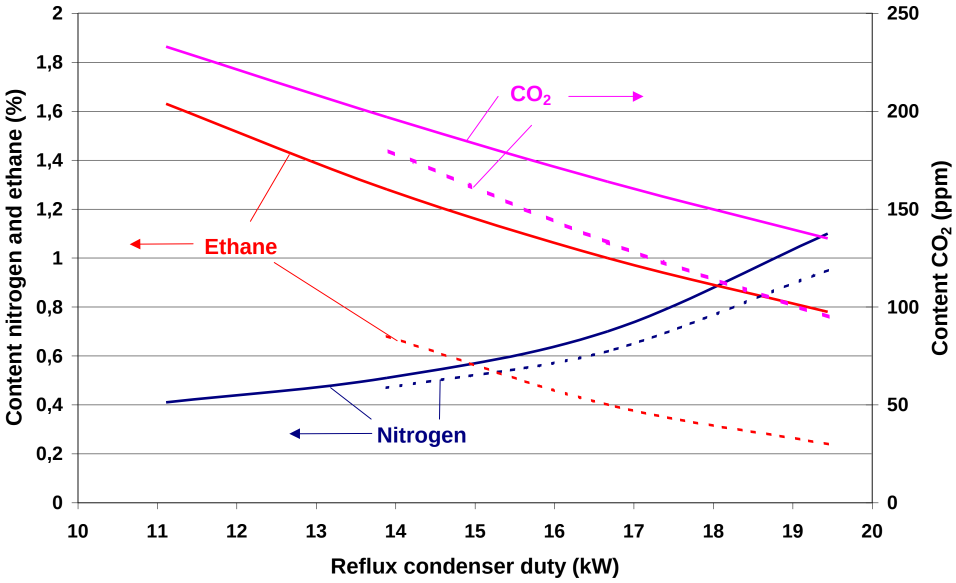

Figure 6. Content of ethane, nitrogen and $CO_2$ in function of the reflux condenser duty.
Full lines: 3 theoretical stages; dashed lines: 5 theoretical stages
Assumed content in the feed to the column: Ethane: 5 %, Nitrogen: 3 %, $CO_2$: 300 ppmv

From Figure 6 one obtains the information that the content of ethane can be reduced by increasing the reflux in the rectification column. With 5 instead of 3 theoretical stages the content in ethane can be reduced by another factor of two.

In the specification, which was chosen for the LNG on page 2, it had been specified, that the LNG should not contain more than 2.5 % of ethane. From Figure 9 one can deduct, that this goal can be reached already with 3 theoretical stages and a reflux duty of about 10 kW. The nitrogen content is sufficiently low anyway.

But there is another reason to consider a better column with a larger reflux. This is the $CO_2$ content. As mentioned in Figure 6, the $CO_2$ content of the feed to the coldbox, i.e. downstream of the pressure swing adsorption, was for this calculation assumed to be 300 ppmv. With 5 theoretical stages and a reflux condenser duty of 20 kW the $CO_2$ content can be reduced to below 100 ppmv, i.e. compared with the feed to the liquefier a factor of three. This means that the rectification can be considered as a backup for the purification in the PSA system!

A special feature of this rectification is, that it is performed at 39 bar, i.e. not far away from the critical pressure of the mixture. The density ratio between liquid and vapour is only about six!  But nevertheless, both sieve trays as well as structured packings can be used.

## 6. DISCUSSION

The place in the natural gas distribution system, where high pressure gas is throttled to a medium pressure local distribution system, is the ideal location for the installation of a small LNG production facility. Due to the Joule-Thomson cooling capacity of the part of the stream, which is not liquefied, the need for external mechanical refrigeration is rather low, in favourable circumstances even lower then in the very large bulk LNG liquefaction plant.

The gas, which is not liquefied can absorb those components of the gas, which are not desired in the LNG. So there is no need to vent any part of the gas to the outside or to a flare.

## 7. CONCLUSIONS

Since the need for natural gas as an automotive fuel is growing, the production of small capacity LNG production plants will probably be economic in many places, when the specific power consumption is as low as in the system proposed here. It can act as pre-runner for the import of bulk LNG from far away places.

041

# A Techno-Economic Optimization for Micro-Scale Liquefaction Plants

**Arteconi A.[*], Pacetti M.[**], Polonara F.[**]**

[*] Università degli Studi e-Campus, via Isimbardi 10, Novedrate (CO), 22060, Italy
[**] Dipartimento di Ingegneria Industriale e Scienze Matematiche, Università Politecnica delle Marche, via Brecce Bianche 1, Ancona, 60131, Italy

## ABSTRACT

Nowadays there is a growing interest towards small-scale natural gas liquefaction plants, mainly due to increasing energy demand and higher energy prices. This paper deals with the liquefaction of natural gas (NG) by micro-scale plants used to supply liquefied natural gas (LNG) to a refuelling station where it is used as heavy-duty vehicle's fuel. The liquefaction of pipeline natural gas on site is a possible supply option for this application, together with buying LNG at a regasification terminal. Linde cycle, Claude cycle and let-down plants are considered as potential technologies and a techno-economic optimization is performed in order to find out the feasibility of the mentioned supply option with particular reference to the Italian market.

## 1. INTRODUCTION

Nowadays there is a growing interest towards small-scale natural gas liquefaction plants, mainly due to increasing energy demand and higher energy prices, that make interesting and feasible on site applications and recovery of methane from various sources, as landfills, stranded wells, boil-off from LNG tanks. The feasibility of a liquefaction plant depends on several factors, amongst them reserve capacity, size of the plant and distance to the market. Typically, technologies for big scale plants are not suitable for small scale plants, where capital costs, efficiency and working conditions gain huge relevance. This paper deals with the liquefaction of natural gas (NG) by micro-scale plants used to supply liquefied natural gas (LNG) to a refuelling station where it is used as heavy-duty vehicle's fuel. In fact LNG as vehicle fuel is becoming attractive for its environmental benefits, mainly after many pilot projects proved their technical reliability and economical sustainability (Chrz et al., 2010). The liquefaction of pipeline natural gas on site is a possible supply option for this application, together with buying LNG at a regasification terminal. Linde cycle, Claude cycle and let-down plants are considered as potential technologies and a techno-economic optimization is performed in order to find out the feasibility of the abovementioned supply option, with particular reference to the Italian market.

## 2. MICRO SCALE LNG PLANTS

A micro-scale plants is a plant with a production rate lower than 60'000 liters of LNG per day (about 0.01 mtpa). At such a scale to find the right trade-off between capital and operating costs has a key role. In particular to keep the capital cost low has a paramount importance with the reduction of the plant size, while when the production rate increases the energy cost becomes more consistent, so it is worth complicating the process in order to increase the energy efficiency (Arteconi et al., 2011). The analysis refers to an LNG facility with a capacity of 10'000 liters of LNG per day, suitable for a final user with a fleet of about 25 trucks. The following sections are meant to study different liquefaction technologies in order to assess the LNG production cost.

### 2.1. Performance of the liquefaction technologies:

The liquefaction technologies analyzed are Linde cycle (Figure 1a) and Claude cycle (Figure 1b) with and without pre-cooling (Walker, 1983). Moreover for the considered application of supplying LNG to refuelling stations also let-down plants are analyzed (Figure 1c). A let-down plant is built at pressure reduction points along the pipeline network so that to exploit the pressure drop necessary to send the gas from the transmission to the distribution pipelines. Prototype units are available in the US (Chrz and Emmer, 2003).

The liquefaction cycles are compared on the basis of energy efficiency of each liquefier. The choice of these methane expansion cycles is due to their simplicity, that make them interesting for micro-scale applications.

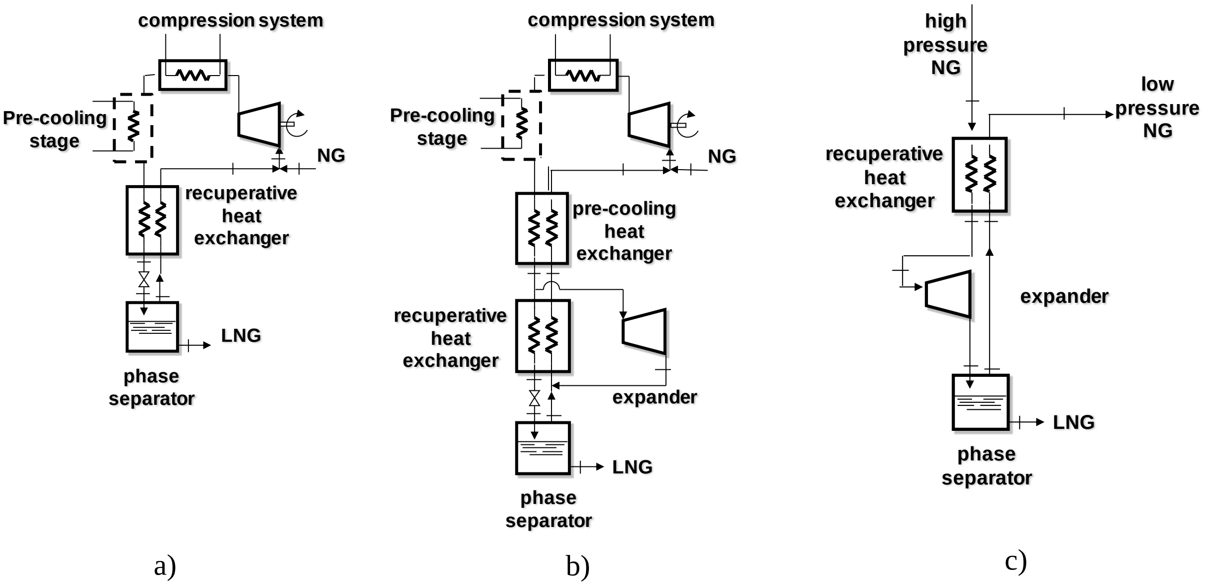

Figure 1. Liquefaction processes: a) Linde liquefaction cycle; b) Claude liquefaction cycle; c) Let-down plant.

The thermodynamic analysis and the thermodynamic optimization have been performed by means of Hysys, a software of Aspen Technology Inc. (Aspen Hysys, 2009). The Peng-Robinson-Stryjek-Vera (PRSV) equation of state (EOS) has been used to calculate the thermodynamic properties of the substances (Stryjek and Vera, 1986). It has been assumed that the natural gas stream is composed of 100% methane, available at 25°C and 0.1013MPa. Liquefied natural gas produced is at -161.6°C and 0.1013MPa. A minimum approach temperature of 5°C has been considered in the heat exchangers and compressor and expander have 75% of isentropic efficiencies, pressure drops have been neglected.

In the Linde cycle, natural gas is compressed with a multi-stage compressor to the maximum pressure of 20MPa, the heat of compression is rejected through an external refrigerant (e.g. water), and then it goes across the recuperative heat exchanger where it is precooled and subsequently expanded in a Joule-Thomson (J-T) valve. The stream coming from the J-T valve contains a small fraction of liquid, that is the final product, while the remaining gas is sent back through the heat exchanger in order to cool down the incoming compressed gas. It is possible to add a pre-cooling heat exchanger before the main recuperative heat exchanger in order to improve the cycle performance. The necessary cooling load can be provided by a vapour compression chiller, that should be available off-the shelf not to complicate the plant configuration. Reasonably, for such a unit, the minimum temperature achievable is -30°C with a coefficient of performance (COP) half of the ideal Carnot COP (COP=2).

In the Claude cycle it is possible to work at lower pressure than the previous case, thanks to the presence of the expander: part of the compressed gas is expanded in a turbine causing a decrease of the temperature and this low pressure gas is sent through the recuperative heat exchanger in order to pre-cool the main stream. The latter then is sent to the J-T valve whose outlet stream contains a greater liquid fraction (LNG) than the Linde cycle. The maximum pressure used in calculation and assessed by means of optimization methods is 5MPa. The fraction of NG entering the turbine is 75% of the total gas stream. In this case the possibility to add a pre-cooling heat exchanger is not interesting, due to the very low improvement in the cycle performance.

The last system analyzed is the let-down plant. In Italy the transmission pipeline has a pressure of about 7-8 MPa and it drops to 2.5 MPa going into the distribution network. A let-down plant does not need any compression phase because it takes the high pressure gas from the pipeline and expands it through a J-T valve or an expander down to the distribution pipeline pressure. The vapour fraction is first sent through the recuperative heat exchanger to precool the incoming gas and then into the distribution network, while the liquid fraction is the final product (LNG) that can be stored at said pressure or further expanded down to the necessary pressure.

In Table 1 main results of the energetic evaluation are reported. The net power ($\dot{\boldsymbol{W}}_{\boldsymbol{net}}$) has been assessed considering the power requested by the compressor plus the power requested by the chiller when the external pre-cooling is included and subtracting the power produced by the expander. The specific work has been expressed in terms of the necessary energy (kWh) to produce one kilogram of LNG. Moreover, considering to fuel the plant only with natural gas, it has been assessed the amount of fuel necessary to produce said liquefaction energy with an energy conversion efficiency of 0.3. In this way the specific work for liquefaction has been represented as the ratio between the produced LNG and the total natural gas entering into the liquefaction plant, considering also the gas used to fuel the liquefaction process. Thus an 80% of efficiency means that 80% of the natural gas becomes liquid and 20% is used as fuel in the process. As previously mentioned the pre-cooling phase has a positive impact on the Linde cycle performance, making it comparable with that of the Claude cycle, while its effect on the Claude cycle is negligible. The let-down plant, instead, does not need any external power nevertheless producing power by means of the gas expansion through the turbine.

Table 1. Results of the comparative analysis of the performance of the different liquefaction cycles.

| **Cycle** | $\mathbf{P_{max}}$ | $\mathbf{P_{min}}$ | $\mathbf{T_{pre\text{-}cooling}}$ | $\dot{W}_{comp}$ | $\dot{W}_{chille}$ | $\dot{W}_{exp}$ | $\dot{W}_{net}$ | **Specific work requirement** | |
|---|---|---|---|---|---|---|---|---|---|
| | MPa | MPa | °C | kW | kW | kW | kW | kWh/kg $_{LNG}$ | % |
| Linde | 20.00 | 0.10 | - | 370 | - | - | 370 | 2.10 | 66 |
| Linde+pre-cooling | 20.00 | 0.10 | -25°C | 189 | 18 | - | 207 | 1.18 | 78 |
| Claude | 5.00 | 0.10 | - | 214 | - | 37 | 177 | 1.01 | 80 |
| Claude+pre-cooling | 5.00 | 0.10 | -25°C | 181 | 17 | 27 | 171 | 0.98 | 81 |
| Let-down plant | 7.50 | 2.50 | - | - | - | 35 | -35 | - | 100 |

## 2.2. Economic evaluation of the liquefaction technologies:

The economic evaluation has been performed considering the capital cost of the plants and the operating costs composed of energy cost, labour, maintenance and all the other expenses that can be considered fixed costs. The hypothesis assumed in the analysis are:

- capital costs have been assessed on the basis of authors' knowledge (Arteconi et al, 2011);
- amortization period: 10 years;
- maintenance cost: 2.5% of capital investment;
- labour cost: 25€/h per person for 360 working days;
- energy price: natural gas 0.38 €/Sm$^3$ and electricity 0.14 €/kWh (prices on the Italian market).

In Table 2 the results of the economic analysis are reported. The Claude cycle with pre-cooling has not been included because considered not attractive due to the low energy efficiency improvement it produces while asking for a capital cost increase.

Table 2. Results of the economic evaluation of the different liquefaction cycles.

| | **Linde** | **Linde+precooling** | **Claude** | **Let-down** |
|---|---|---|---|---|
| Capital cost (1'000 €) | 1'000 | 1'200 | 1'500 | 1'000 |
| Annual operating cost (1'000 €) | 1'413 | 1'220 | 1'200 | 976 |
| Amortization (1'000 €) | 100 | 120 | 150 | 100 |
| Total annual cost (1'000 €) | 1'513 | 1,340 | 1'350 | 1'076 |
| LNG production cost (€/liter) | 0.420 | 0.372 | 0.375 | 0.299 |
| Mark up 10% (€/liter) | 0.463 | 0.410 | 0.413 | 0.329 |

Table 3. Results of the economic evaluation of the different liquefaction cycles.

| **Liquefaction cycle** | **LNG cost (€/liter)** |
|---|---|
| Linde | 0.463 |
| Linde + pre-cooling | 0.410 |
| Claude | 0.413 |
| Let-down | 0.329 |
| Regasification terminal | 0.214 |
| Regasification terminal – distance 200 km | 0.246 |
| Regasification terminal – distance 2'000 km | 0.435 |

For the considered application of supplying LNG to refuelling stations, it is necessary to compare the LNG production cost when it is liquefied from pipeline gas by means of a micro-scale liquefaction plant and when it is bought at a regasification terminal (Table 3). In the latter case, the LNG purchase price (0.21 €/liter, Waterborne Energy, 2012) has to include also the transportation costs for the delivery of the LNG from the terminal to the refuelling station. It ranges between 0.24-0.43 €/liter with varying the transportation distance between 200 and 2000 km (Arteconi and Polonara, 2012). Looking at Table 2, this means that when the liquefaction efficiency is about 80% (Linde cycle with pre-cooling or Claude cycle), the price of LNG from a micro-scale plant can be compared with the price of LNG from a regasification terminal, at least for terminals at great distance from the refuelling station site. Amongst the considered cycles, the let-down plant is the most competitive with the LNG purchased at the terminal. This solution is particularly interesting in Italy where the pipeline network is wide spread and the high pressure pipelines cross the Country from the North to the South, allowing to reach easily every place, as shown in Figure 2.

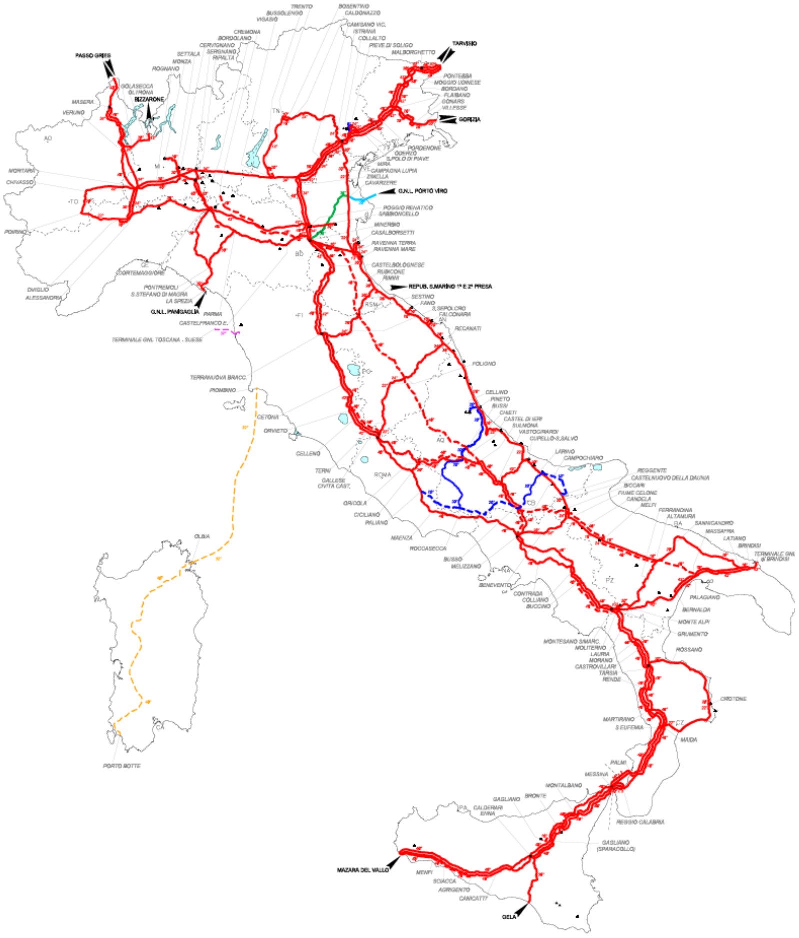

Figure 2. High pressure pipeline in Italy (Snam, 2009).

## 3. CONCLUSIONS

The present paper deals with the liquefaction of natural gas by means of micro-scale plants aimed at supplying LNG to refuelling stations. Liquefaction technologies through methane expansion have been considered for said application for their simple configuration, suitable at such small scale. Amongst them Linde cycle with a pre-cooling stage and Claude cycle have shown a good energy efficiency. Moreover it has been put in evidence that let-down plants, built to exploit the pressure reduction in the conjunction points between the higher pressure and the lower pressure pipelines, are the best option to produce LNG on site. In fact the LNG production cost is comparable with the current LNG purchase cost at the regasification terminal and the more the regasification terminal is distant from the refuelling station the more the liquefaction on site becomes a feasible option.

## 4. REFERENCES

Aspen Hysys, 2009, Aspen Technology Inc, Burlington MA USA, www.aspentech.com.

Arteconi A., Brandoni C., Santori G., Polonara F., 2011, Micro-scale LNG liquefaction plants, *Proceedings of the 23rd International Congress of Refrigeration*, paper 489, 21-26 August, Prague.

Arteconi A., Polonara F., 2012, LNG as vehicle fuel in Italy, *Proceedings of the 12th International Conference of Cryogenics*, paper 040, 11-14 September, Dresda.

Chrz V., Emmer C., 2003, Medium size LNG technology on progress, *Proceedings of the International Congress of Refrigeration*, paper 309, Washington, D.C.

Chrz V., Cermak T., Emmer C., 2010, LNG applications for fueling vehicles, *Proceedings of the 11th International Conference of Cryogenics*, paper 039, April 26-29, Bratislava.

Snam, 2008. Rete nazionale dei gasdotti (In Italian), www.snamretegas.it

Stryjek R., Vera J.H., 1986, PRSV: an improved Peng-Robinson equation of state of pure compounds and mixtures, *Canadian journal of chemical engineering*, vol. 64, 323-333.

Walker G. 1983, *Cryocoolers – Part1: Fundamentals*. Plenum Press, New York and London, 365p.

Waterborne Energy 2012, World LNG Estimated May 2012 Landed Prices, www.ferc.gov

040

# LNG as Vehicle Fuel in Italy

**Arteconi A.*, Polonara F.****

* Università degli Studi e-Campus, via Isimbardi 10, Novedrate (CO), 22060, Italy
** Dipartimento di Ingegneria Industriale e Scienze Matematiche, Università Politecnica delle Marche, via Brecce Bianche 1, Ancona, 60131, Italy

## ABSTRACT

Natural gas is considered a clean fuel. It can be used as compressed gas (CNG) or in the liquid phase (LNG). For heavy duty vehicles, particularly fleet vehicles, LNG becomes attractive because of reduced on-board weight and space requirements, thanks to its high energy density. LNG as vehicle fuel is already used both in the US and in Europe. The case of Italy is presented in this paper. An analysis showing strengths, weaknesses, threats and opportunities for the introduction of LNG as vehicle fuel in the Italian market is outlined. The analysis puts in evidence that the main issues to be addressed in order to introduce this new fuel concern the request of necessary authorizations to install any LNG facility and the problem of LNG supply, that can be purchased at regasification terminals or liquefied on site.

## 1. INTRODUCTION

Nowadays there is a growing interest in renewable energy sources and more sensitivity towards environmental issues. The transport sector represents a major item on the global balance of greenhouse gas (GHG) emissions. In Europe (EU-27) the GHG emissions due to the transport sector amounted to about 20% of the total emissions in 2009 (EEA, 2011) and between 1990 and 2007 emissions from transport rose by 29%. This increase was observed for both passenger transport and freight transport, mainly due to growing transport demand, in particular freight transport increased share of road freight transport as opposed to other transport modes. In an attempt to contain this phenomenon, European policies are being implemented to reduce GHG emissions, e.g. by promoting transport by rail, producing passenger cars with more limited GHG emissions and promoting the use of biofuels or alternative fuels. The European Union's Green Paper specifies the need to substitute 20% of conventional fuel consumption with alternative fuels by the year 2020 (EC, 2001a).

In this context alternative fuels have assumed more and more importance and a lot of incentives have been introduced to support them. Natural gas is considered the alternative fuel that, in the short-medium term, can best substitute conventional fuels in order to reduce their environmental impact (EC, 2001b), because it is readily available at a competitive price, using technologies already in widespread use (Hekkert et al. 2005). It can be used as compressed gas (CNG) or in the liquid phase (LNG). In small fuel tank sizes, which are suitable for small vehicles, CNG is generally more appropriate because space and weight are not critical criteria. For heavy duty vehicles, particularly fleet vehicles, LNG becomes attractive because of reduced on-board weight and space requirements, due to its higher energy density.

## 2. LNG IN ITALY: SWOT ANALYSIS

LNG as vehicle fuel is already used both in the US and in Europe. The case of Italy is presented in this paper. An analysis showing strengths, weaknesses, threats and opportunities for the introduction of LNG as vehicle fuel in the Italian market is outlined.

### 2.1. Strengths:

Main advantages of Natural Gas (NG) fuel are (Yeh, 2007): (i) environmental benefits for reducing local air pollution and GHG emissions, (ii) availability of natural gas resources and (iii) reduction of dependency on imported oil. In particular the reduced environmental impact has been the aspect that pushed the NG on the European market. In order to show such environmental benefits, a comparison among the well-to-wheel life cycle GHG emissions for CNG, LNG and Diesel has been performed (Arteconi et al, 2010). It has put into evidence that CNG reduces GHG emissions by 14% and LNG by 10% if compared with Diesel and the main GHG reduction is due to reduced emissions in the tank-to-wheel phase. Moreover CNG fuel cycle has lower emissions than LNG fuel cycle, because of the additional energy requested for natural gas liquefaction and shipping.

As already mentioned, LNG is the only choice for heavy duty trucks intended to do long distance, CNG is not valid because the required volume of CNG tanks is not compatible with the payload of the trucks. It is foreseen that LNG will cover about the 33% of the long distance road transport by 2035 (Lage, 2012).

In Italy the use of natural gas is well spread, thanks to the wide pipeline distribution. Italy has about 780'000 natural gas vehicles (NGVs), that is the 77% of the total number of NGVs in Europe, and the 30% of European natural gas refuelling stations (NGVA, 2011). Among the 860 Italian refuelling stations, 2 are LCNG stations, where LNG is stored liquid, pumped and vaporized to be used as CNG. They represent the first attempt to introduce LNG in the automotive market. Surely the uptake of LNG as fuel can benefit from the important role of NG in Italy. At this aim an association, Cryotrucks, of companies working in several fields, as automotive, storage, refuelling, was also established.

As far as the technology on board is concerned, it is mature and big companies of the automotive sector are developing their own trucks. Fiat Iveco, for example, launched its new LNG fuelled truck this year for applications carrying between 18 and 40 tons.

### 2.2. Weaknesses:

Natural gas pipelines are widely spread in a lot of regions but refuelling infrastructures are still facing the challenge of achieving the optimum ratio between NG vehicles and refuelling stations. Refuelling station distance and waiting time for refuelling are critical aspects for the public acceptance of NGVs. Different surveys have analyzed this point and they suggest that with a number of stations equal to 10-20% of conventional gasoline stations, refuelling is no longer seen as a major obstacle for the adoption of a NGV (Yeh, 2007). In order to overcome these barriers, a European project called GasHighWay (GHW, 2009) has been established, aiming at promoting the uptake of gaseous vehicle fuels, namely biomethane and CNG, and especially the realisation of a comprehensive network of filling stations for these fuels spanning Europe from the North, Finland and Sweden, to the South, Italy. Similarly, the Blue Corridor Project has the objective to establish transport corridors for heavy duty transport vehicles using liquid natural gas fuel instead of diesel, both because of its economic and environmental advantages. The Blue Corridor Project is included in the programmes of work of the United Nations Economic Commission for Europe Working Party on Gas and Inland Transport Committee (UNECE, 2003).

LNG has also to overcome another issue rather than the spread of refuelling infrastructures, that is how to supply the refuelling stations. There are two possibilities for LNG supply in Italy: (i) to buy it at LNG terminals or (ii) to liquefy pipeline natural gas directly on site.

Regarding the first option, there are two working LNG terminals in Italy at present: the on-shore terminal in Panigaglia (North, West coast) and the off-shore gravity based terminal in Rovigo (North, East coast). Other 7 terminals are planned and waiting for permissions to be issued, but the authorization process is not expected to be short. Moreover at the moment it is not possible to buy spot LNG cargos at the existing terminals, because all LNG is regasified and sent into the pipeline. The two existing LCNG refuelling stations in Italy are forced to buy LNG at Barcelona terminal. It is the closest to Italy (together with the French terminal at Fos-Sur-Mer), but nevertheless it is about 800 km far away the border and considering transportation costs and boil-off gas production during the delivery, this scheme does not seem very economical, at least for the Southernmost regions.

The second option deals with the liquefaction on site of pipeline gas. This solution is attractive because the LNG can be ready available where there is a request and the capillary pipeline network allows to reach almost every place. The main issue of this option concerns the availability of small-scale liquefaction plants and the necessity to find the right trade-off between capital costs and energy efficiency for plants at this scale (Arteconi et al, 2011).

Another critical aspect is the economy of the new fuel. Generally in most countries that have had a successful NGVs penetration the NG pump price is 40-60% below the gasoline price (Yeh, 2007) mainly due to reduced taxation. Surely the price difference between NG and conventional fuels is one of the most important factors in attracting users, together with the availability of a proper infrastructure. In Table 1 a breakdown of fuels costs is shown. The baseline LNG retail price has been assumed as 60% of the energy equivalent Diesel quantity, assessed considering the different energy content of LNG (25 MJ/liter) and

Diesel (38.3 MJ/liter). This baseline LNG price is meant to be the threshold value that could push customers to shift from Diesel to LNG. It has to be considered also that taxes on natural gas fuels are lower than those on traditional fuels, even if they have been recently increased.

Table 1. Fuels cost breakdown.

| Fuel | CNG | | LNG | | Diesel | | Gasoline | | LPG | |
|---|---|---|---|---|---|---|---|---|---|---|
| **Baseline price** | 0.5411 | €/m$^3$ | 0.5617 | €/liter | 0.8463 | €/liter | 0.8391 | €/liter | 0.4607 | €/liter |
| **Tax** | 0.0033 | €/m$^3$ | 0.0021 | €/liter | 0.5932 | €/liter | 0.7042 | €/liter | 0.2678 | €/liter |
| **VAT (21%)** | 0.1143 | €/m$^3$ | 0.1184 | €/liter | 0.3023 | €/liter | 0.3241 | €/liter | 0.1530 | €/liter |
| **Retail Price** | 0.6587 | €/m$^3$ | 0.6821 | €/liter | 1.7417 | €/liter | 1.8674 | €/liter | 0.8814 | €/liter |
| **Normalized price** | 0.0184 | €/MJ | 0.0273 | €/MJ | 0.0455 | €/MJ | 0.0541 | €/MJ | 0.0347 | €/MJ |

Considering the critical impact of the supply phase, a comparison between the two possible scenarios has been performed. The analysis refers to an LNG facility with a capacity of 10'000 liters of LNG per day, suitable for a final user with a fleet of about 25 trucks.

The first scenario considers that LNG is bought at the regasification terminal, then it is transported to the final user by LNG tanker trucks, where it is stored in the storage tank of an LNG refuelling station and supplied to the vehicles. A 20'000 liters tanker truck is used to deliver LNG to the refuelling station, so that 3 trips per week are necessary. At the refuelling station a storage of as minimum the same capacity as the tanker truck is available. The LNG is pumped from the truck to the storage and from the storage to the on board tanks.

In the second scenario, instead, the LNG is produced with a small scale liquefaction plant that takes natural gas from the pipeline and send the liquified natural gas to the storage tank of the refuelling station. For the considered final user, a daily LNG production of 10'000 liter is necessary. The plant efficiency is defined as the ratio between the produced LNG and the total natural gas entering into the liquefaction plant, considering that it is used also to fuel the liquefaction process. Thus an 80% of efficiency means that 80% of the natural gas becomes liquid and 20% is used as fuel in the process.

In Figure 1 and Figure 2 a schematic of the scenarios is shown, together with the cost breakdown along the supply chain. Values reported have been calculated with the following hypothesis. For the first scenario (Figure 1), the regasification terminal of Barcelona has been considered, that is about 800 km far away the Italian border, so that a distance of 900 km between the terminal and the LNG station has been assumed. The LNG selling price at the terminal is 11.5 \$/MMBTU, i.e. 0.21 €/liter (Waterborne Energy, 2012), and the final LNG baseline retail price (taxes and VAT excluded) has been assessed as 0.37 €/liter. In the second scenario (Figure 2), instead, natural gas comes from pipeline at the price of 0.38 €/m$^3$, i.e. 0.24 € per liter of LNG (MSE, 2012), while the LNG plant has an energy efficiency of 80%. The obtained LNG baseline retail price is 0.47 €/liter (taxes and VAT excluded). For a conservative evaluation, the possibility of boil off formation in the storage tanks has been considered: it can be reliquefied in the second scenario, while it is recovered as gas in the first scenario, representing a loss in the LNG value chain (Chen et al., 2004; Querol et a., 2010).

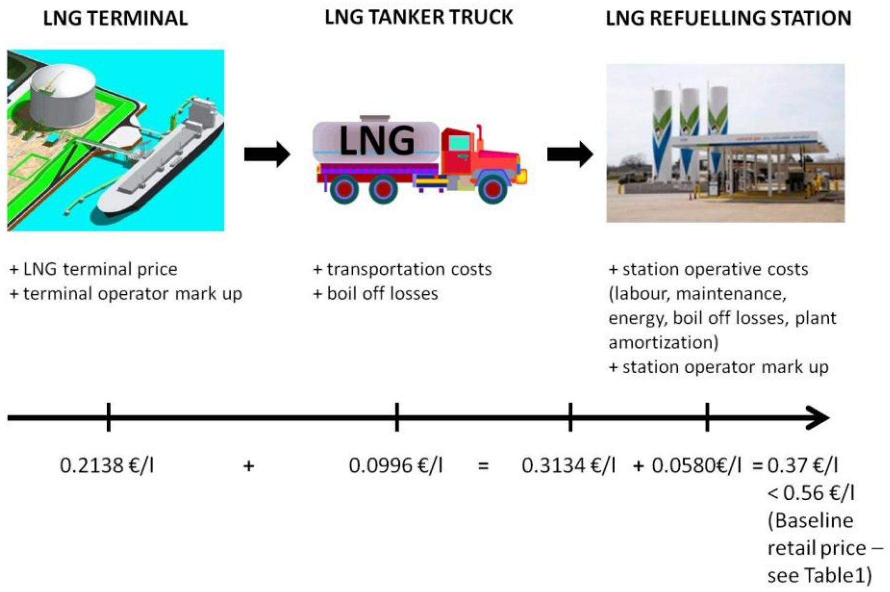

Figure 1. Scenario 1: cost breakdown.

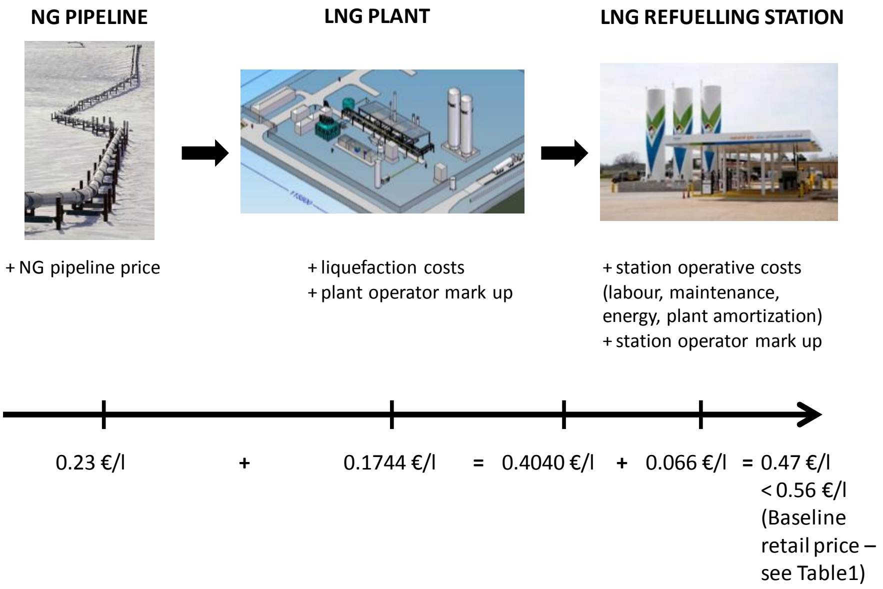

Figure 2. Scenario 2: cost breakdown.

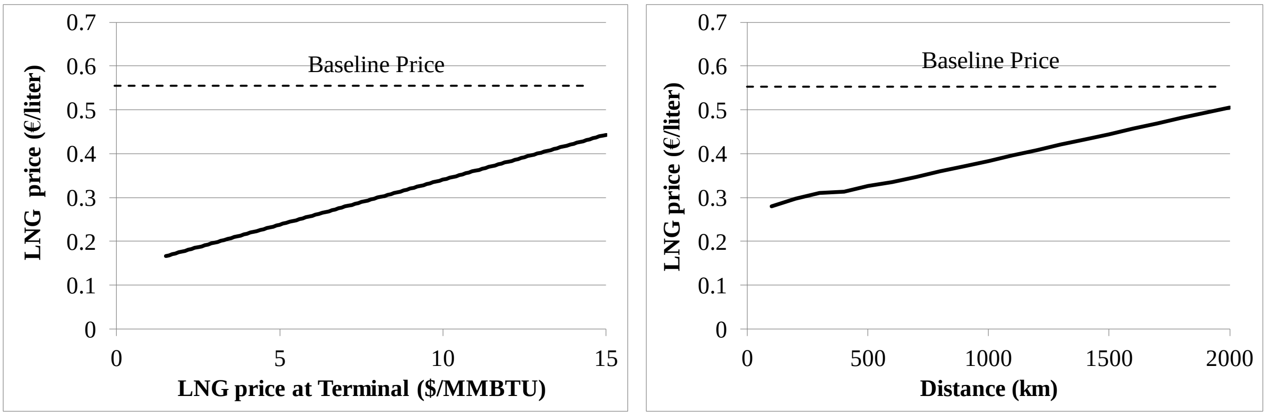

(a) (b)

Figure 3. Scenario 1: LNG baseline price trend varying the LNG selling price at the regasification terminal (a) and the distance between refuelling station and terminal (b).

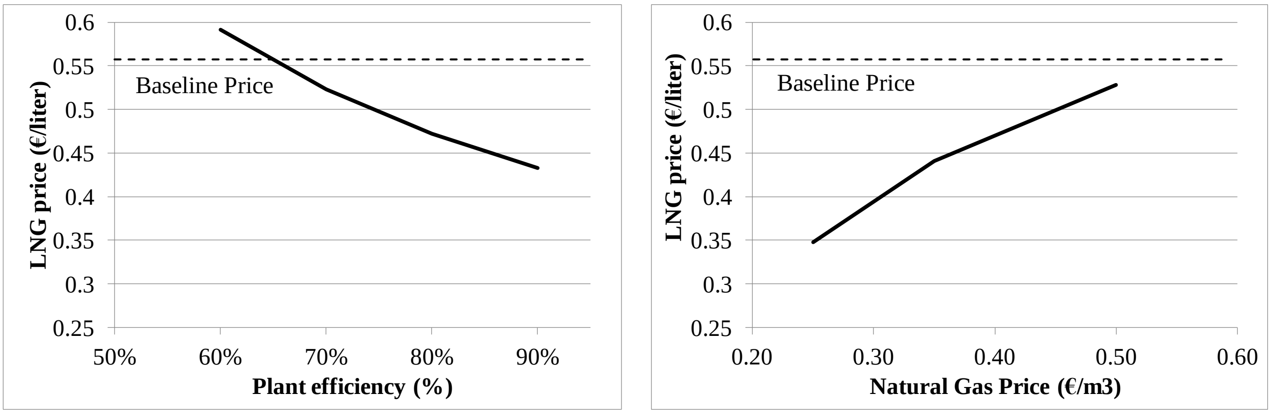

(a) (b)

Figure 4. Scenario 2: LNG baseline price trend varying the liquefaction plant efficiency (a) and natural gas pipeline price (b).

In Scenario 1 the LNG price depends mainly on the LNG selling price at the terminal and on the distance between the terminal and the station, as it is shown in Figure 3a and 3b respectively. In Scenario 2 the LNG price is affected by the NG pipeline price and by the energy efficiency of the liquefaction plant, as it is shown in Figure 4a and 4b respectively. Considering the reference baseline price that should not be overcome in order to assure economic competitiveness to LNG over Diesel, reported in Table 1 (0.5617€/l), it is possible to notice that the Scenario 1 represents the best supply option for distances below 2000 km, while the liquefaction on site is interesting only for plant efficiency above 70%.

## 2.3. Opportunities:

As several studies pointed out the market introduction of alternative fuels depends on the actions of many stakeholders, like car industry, fuel companies and consumers (Janssen et al. 2006; Engerer and Horn, 2009; Suurs et al., 2010). Also Governments have a central role for promoting NGVs by introducing regulations and incentive-based instruments. In Italy a policy to promote NGVs was carried on in the last years and it helped the diffusion of CNG vehicles. It consisted in incentive pay to convert traditional engines in natural gas fuelled engines. Moreover natural gas used as vehicle fuel can benefit of a reduced taxation (Table 1) and it is foreseen that the same regulations will be implemented also for LNG. Another positive contribution to the introduction of Government's help will come also from the European Union and the target of 20% share of alternative fuels by 2020.

Moreover, recently, a new boost to consider LNG as fuel is connected with the new rules in the marine sector, where increasing oil prices and new legislation are driving the technology towards ways of reducing emissions. In fact the Mediterranean area is going to become an Emission Control Area (ECA), that means it will be subjected to more stringent requirements for fuel quality and emissions. Currently, Baltic Sea and North Sea are the only ECA in the world, US coasts will become ECA in August 2012, while Mediterranean could become an ECA in 2015. Within ECA, ship owners need to switch to cleaner fuels (e.g. LNG) or to adopt alternative technologies (e.g. scrubber, after treatments). The use of LNG has been evaluated as the best solution by the involved stakeholders. The LNG powered propulsion can allow to achieve the following pollutants reduction: $CO_2$ -23%; $NO_x$ -92%; $SO_x$ -100%; Particulate -98/100% (Andreola, 2012). Mainly it completely avoids $SO_x$ emissions, because LNG does not contain sulfur, in accordance with ECA regulation that sets a 0.1% sulfur content as limit after 2015 (IMO, 2011). Therefore, considering the coast length in Italy and the economic relevance of shipping business, the introduction of the ECA in the Mediterranean area will contribute to build the necessary infrastructure for delivery LNG as fuel and solve the problem of LNG supply.

## 2.4. Threats:

The main threat for the uptake of LNG is the lack of a national regulation both for LNG technology on board and for its storage and delivery in the refuelling stations. The Italian law D.Lgs 334/1999, that comes from the European Directive 96/82/EC on the control of major-accident hazards involving dangerous substances, is a general reference for safety regulations in LNG installations. To cover all the other issues, the reference is represented by international regulations as it follows:

- ISO 12991 Liquefied natural gas (LNG) - Tanks for on-board storage as a fuel for automotive vehicles;
- EN 1160 Installations and equipment for liquefied natural gas - General characteristics of liquefied natural gas;
- EN 13645: Installations and equipment for liquefied natural gas - Design of onshore installations with a storage capacity between 5 t and 200 t;
- EN 1473: Installation and equipment for liquefied natural gas - Design of onshore installations (larger installations);
- NFPA 59A: Standard for the Production, Storage, and Handling of Liquefied Natural Gas (LNG);
- NFPA 52 Vehicular Fuel Systems Code;
- ISO 12617 (Draft International Standard in 2012) LNG connector;
- ISO 12614 (Draft International Standard in 2012) LNG vehicle onboard equipment;
- ISO 16924 (Committee Draft in 2012) LNG station for fuelling vehicles.

Because of the absence of a national law, the request for permissions to build LNG facilities, such as LCNG or LNG refuelling stations, becomes very complicated. The main difficulty is due to the fact that the permission process is local, that means that it depends on local authorities and local fire department. This aspect, together with the lack of information about the topic, does not help the build up of a standard procedure for the authorization procedure that can be shared on the whole Country and repeated everywhere in the same way.

## 3. CONCLUSIONS

In this paper the possibility of the introduction of LNG fuel in the Italian market has been considered. LNG is particularly attractive for heavy duty vehicles, because of reduced on-board weight and space requirements, thanks to its high energy density. An analysis showing strengths, weaknesses, threads and opportunities for the introduction of LNG fuel has been outlined. The analysis has put in evidence that in Italy the previous successful experience with CNG as fuel could be helpful for the uptake of the new fuel. Also the environmental concerns and the European environmental policy will represent a boost for LNG introduction, as well as the pollution restrictions in the maritime sector in the Mediterranean sea, that will help the establishment of a proper LNG supply chain. In fact the main weak point for LNG is the supply process. A comparison between the purchase at the regasification terminal or the liquefaction on site has been performed. It has shown that to buy LNG at the terminal is generally more economically attractive, at least for distances less than 2000 km.

## 4. REFERENCES

MSE, Ministry of Economic Development 2012, http://dgerm.sviluppoeconomico.gov.it/

Andreola M. 2012, Rolls Royce: the integrator for environ-shipping, *ENA Ecodesign Conference*, Ancona.

Arteconi A., Brandoni C., Bartolini C.M., Polonara F. 2010, Greenhouse Gas emissions of heavy-duty vehicles fuelled by natural gas, *IANGV 2010*, Roma

Arteconi A., Brandoni C., Santori G., Polonara F., Micro-scale LNG liquefaction plants, *Proceedings of the 23rd International Congress of Refrigeration*, paper 489, 21-26 August 2011, Prague.

Chen Q.-S., Wegrzyn J., Prasad V., 2004, Analysis of temperature and pressure changes in liquefied natural gas (LNG) cryogenic tanks, *Cryogenics* 44, 701-709.

Engerer H., Horn M. 2009, Natural gas vehicles: An option for Europe, *Energy Policy* 38: 1017–1029.

European Commission (EC) 2001a, *Green paper: towards a European strategy for the security of energy supply*, Luxembourg. 105 p.

European Commission (EC) 2001b, *White paper: European transport policy for 2010: time to decide*. Luxembourg. 119 p.

European Environment Agency (EEA) 2011, *Greenhouse gas emission trends and projections in Europe*, Report No 4/2011.

GHW, GasHighWay 2009, www.gashighway.net

Hekkert M.P., Hendriks F.H.J.F., Faaij A.P.C., Neelis M.L. 2005, Natural gas as an alternative to crude oil in automotive fuel chains well-to-wheel analysis and transition strategy development, *Energy Policy* 33: 579-794.

International Maritime Organization (IMO) 2011, Pollution prevention, www.imo.org

Janssen A., Lienin S.F., Gassmann F., Wokaun A. 2006, Model aided policy development for the market penetration of natural gas vehicles in Switzerland, *Transportation Research Part A* 40: 316–333.

Lage M. 2012, Is LNG the best solution for long-distance transport?, *The Small-Mid Scale LNG Summit 2012*, Amsterdam, The Netherlands.

NGVA Europe 2011, NGVs and refuelling stations in Europe, www.ngvaeurope.eu

Querol E., Gonzalez-Regueral B., García-Torrent J., García-Martínez M.J., 2010, Boil off gas (BOG) management in Spanish liquid natural gas (LNG) terminals, *Applied Energy* 87, 3384-3392.

Suurs R.A.A., Hekkert M.P., Kieboom S., Smits R.E.H.M. 2010, Understanding the formative stage of technological innovation system development: the case of natural gas as an automotive fuel, *Energy Policy* 38: 419-431.

Yeh S. 2007, An empirical analysis on the adoption of alternative fuel vehicles: The case of natural gas vehicles, *Energy Policy* 35: 5865–5875.

Waterborne Energy 2012, World LNG Estimated May 2012 Landed Prices, www.ferc.gov

UNECE, 2003, United Nations Economic Commission for Europe, Working Party on Gas and Inland Transport Committee, Blue corridor project – Final Report.

047

# Exergy Analysis to Determine Appropriate Design and Operating Parameters for Collins Refrigerator-Liquefier under Mixed Mode Operation

**Kundu A.[*], Thomas R.J.[**], Ghosh P.[*], Chowdhury K.[*]**

[*]Cryogenic Engineering Centre, Indian Institute of Technology, Kharagpur 721 302, India
[**]Dept. of Mechanical Engineering, SAINTGITS College of Engineering, Kottayam 686 532,India

## ABSTRACT

Helium plants operate as pure liquefier, pure refrigerator or as mixed-mode system where only a part of the liquid produced is extracted and the other part is vaporized by heat load. Each of these plants needs to be designed differently for achieving the highest cooling effect. In this paper, refrigerator, liquefier and mixed-mode (25/75, 50/50 and 75/25) plants, all having Collins Cycle configurations have been simulated on Aspen HYSYS® V7.0 for determining optimum compressor pressure, diversion of compressor flow through expanders and its distribution among the expanders and surface area required for each heat exchanger to achieve the highest possible exergy efficiency. A plant designed for a particular mixed mode operation (including liquefier and refrigerator) may suffer a large loss of efficiency if it is made to operate at off-design conditions. Detailed evaluation of deterioration in exergy efficiency may help one to choose the right mixed mode plant intended for a desired range of operation.

## 1. INTRODUCTION

In its simplest form, a helium liquefier or a refrigerator has Collins cycle based configurations. In helium liquefier, liquid is the output and it is taken out of the system for absorbing heat load. A continuous make-up helium gas at compressor suction maintains the mass flow of the system. Refrigerators, on the other hand, are closed systems, where the heat load is absorbed at a constant temperature and the boil-off from the helium bath returns to the compressor through the array of counterflow heat exchangers inside the cold box. However, in many applications like fusion reactors, particle accelerator or colliders, helium plant may operate in the liquefier-refrigerator mixed mode where only a part of the liquid produced is taken out as a liquefier and the other part is vaporized in-situ as a refrigerator, as illustrated as a Collins Cycle in Figure 1. For a pure refrigerator, $\dot{m}_{LL} = 0$. For a pure liquefier $\dot{m}_{LR} = 0$.

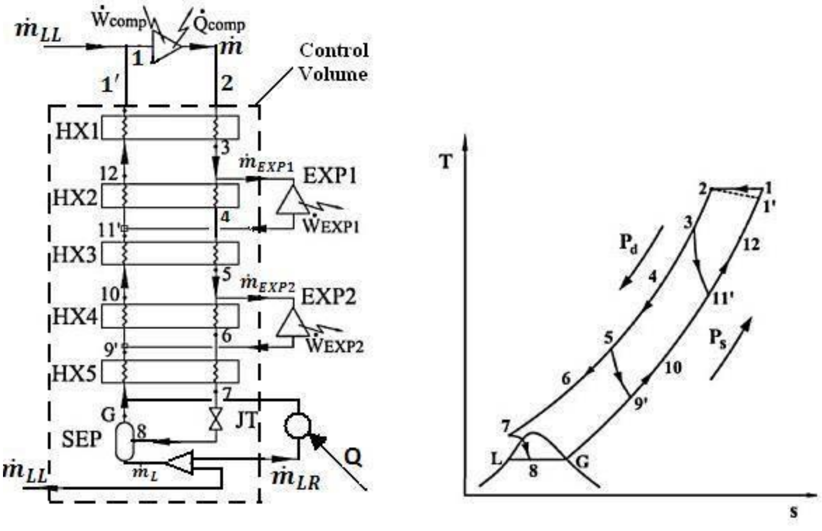

(a) (b)

Figure 1 (a): Schematic and (b) T-s diagrams of Collins Mixed Mode systems

The size of the heat exchangers, the discharge pressure of the compressor, flow through expanders etc., which are optimized for the highest plant performance of a liquefier, would produce a much worse performance as a refrigerator or a mixed-mode plant and vice versa. The purpose of the paper is to evaluate optimum geometric and operating parameters that would produce the highest performance at different modes of operation of helium plant and compare the values. The deterioration of the plant performance, where a plant optimized for a certain specific mode is operated in a different mode, has also been evaluated.

Defining X/Y Mixed mode

After its exit from the Joule-Thomson valve, all helium plants produce liquid. If in a particular mixed mode operation, X% of the liquid is drawn out from the system, and the remaining vapour returns to the compressor after absorbing the heat load, then the plant is operating at X/(100-X) mixed mode. Therefore, according to this definition, a liquefier operates at 100/0 mode, while a refrigerator is in 0/100 mode.

Exergy analysis has been found to be a useful tool to analyze and optimize complex thermal systems like helium plants. Trepp [1] in his study evaluated different exergy losses, particularly those associated with heat exchangers and expanders of helium refrigerators. Thirumaleshwar [2] used enthalpy-exergy diagram for helium and analyzed a helium refrigerator based on reverse Brayton cycle. Various other studies have used exergy analysis for determining the losses in helium refrigerators [3-5]. Optimum operating points for refrigerators are found not to be the same as those of liquefiers [6]. Many of the large-scale helium plants operate as liquefier-refrigerator mixed mode due to varying load requirements [7, 8]. Optimum system parameters for mixed mode plants are different from both liquefiers and refrigerators. Recent studies on helium liquefiers using Collins cycle as the configuration and exergy as the tool for analysis have provided more insight for designing helium liquefier plants [9, 10].

Objective of the present paper is to perform parametric evaluation of pure refrigerator, pure liquefier and some specific mixed-mode designs based on Collins cycle and to compare the optimum design and operating parameters. Evaluation of the loss of exergy efficiency at off-design operation for optimally-designed liquefier, refrigerator and mixed mode at 25/75, 50/50 and 75/25 also forms the objective of this paper.

## 2. GOVERNING EQUATIONS AND SOLUTION METHODOLOGY

The criteria used for determining the performance of the plant is cold box exergy efficiency. It is defined as the exergy output from the cold box divided by the exergy input to the cold box. Exergy based analysis combines both liquid production and refrigeration output into a single parameter; i.e. the exergy output. Also, the exergy destruction in various components of the cycle can be evaluated for possible improvement.

Simulation of the plant has been performed with Aspen HYSYS® V7.0 to perform all the parametric variations at steady state. The 32-term modified BWR Equation of State (EOS) which is a widely accepted EOS for helium is utilized for generating the thermo-physical properties of helium. Equations governing exergy analysis are given below:

$$\dot{E}x_{FLOW} = \dot{m} \times ex = \dot{m} \times [(h - h_0) - T_0(s - s_0)] \tag{1}$$

$$\dot{E}x_{IN} = \dot{m}ex_2 + \dot{m}_{EXP1}ex_{11'} + \dot{m}_{EXP2}ex_{9'} + \dot{m}_{LR}ex_G \tag{2}$$

$$\dot{E}x_{OUT} = (\dot{m} - \dot{m}_{LL})ex_{1'} + \dot{m}_{EXP1}ex_3 + \dot{m}_{EXP2}ex_5 + \dot{m}_{LR}ex_L + \dot{m}_{LL}ex_L + \dot{E}x_{Dest} \tag{3}$$

$$\dot{m}(ex_2 - ex_{1'}) = \dot{m}_{EXP1}(ex_3 - ex_{11'}) + \dot{m}_{EXP2}(ex_5 - ex_{9'}) + \dot{m}_{LL}(ex_L - ex_{1'}) + \dot{m}_{LR}(ex_L - ex_G) + \dot{E}x_{Dest} \tag{4}$$

$$\eta_{Ex\_ColdBox} = \frac{\dot{m}_{LL} \times ex_L + \dot{m}_{LR} \times (ex_L - ex_G)}{\dot{m} \times (ex_2 - ex_{1'})} \times 100\% \tag{5}$$

$$\eta_{Ex\_Cycle} = \frac{\dot{m}_{LL} \times ex_L + \dot{m}_{LR} \times (ex_L - ex_G)}{\dot{W}_{COMP}} \times 100\% \tag{6}$$

The general equation for exergy transfer accompanying mass flow ($\dot{m}$) is given as eq. (1) where $h$ and $s$ correspond to the specific enthalpy and specific entropy of the fluid respectively. $h_0$ and $s_0$ represent the specific enthalpy and specific entropy at the reference state ($T_0$, $P_0$) respectively. For this analysis, the atmospheric condition is taken as the reference state. ($T_0$ =300 K and $P_0$ =1.013 bar). Throughout the paper, the unit “bar” has been used to mean “bar absolute” i.e. bar gauge pressure plus atmospheric pressure.

For the control volume shown in Figure 1(a), exergy input is given by eq. (2) and exergy exit (including the exergy loss) is given by eq. (3). Equating eq. (2) and eq. (3), we get the exergy balance equation for the control volume as eq. (4).

In eq. (4), term I in the Left hand side (LHS) represents the net exergy input to the cold box, terms I and II in the Right hand side (RHS) gives the exergy utilization in the expanders, term III in the RHS is the exergy extracted through liquid, term IV in the RHS represents exergy obtained as refrigeration and term V in the RHS is the summation of all the exergy destructions in the cold box.
The exergy efficiency of the cold box is given by eq. (5) and the exergy efficiency of the entire plant is given by eq. (6). $\dot{W}_{COMP}$ is the electrical input to the compressor.

(Non-dimensional effective $UA$) $= \dfrac{UA}{\dot{m}c_P}$ where $\dot{m}$ is the mass flow rate at the exit of the compressor and the specific heat $c_P$ is calculated at 300 K and 1.013 bar. As the heat exchangers generally are non-counterflow and have many irreversibilities, such as, heat in-leak, flow maldistribution, specific heat variation of fluid, axial heat conduction etc., effective UA has been defined to include all such effects. Consequently, effective UA produces actual effectiveness when inserted in $N_{tu}$-effectiveness equation. The heat exchanger designer is expected to know the relationship between geometric UA and effective UA of the heat exchangers.

The system is assumed to be at steady state. In refrigerator mode, the fluid is at saturated vapor state after absorbing the external heat load using liquid helium. There is no heat in-leak or pressure drop present in the pipelines. There is no loss of exergy when fluids mix with each other. Specific power is defined as power input to the compressor per unit exergy output at the evaporator.

## 3. RESULTS

Figures 2, 3 and 4 show the results of the parametric evaluation of pure refrigerator. Exergy efficiency and specific power are presented in Figure 2. Figure 3 shows the influence of compressor pressure and expander flow rate on exergy efficiency. Figure 4 depicts the effect of increase of heat exchanger size (UA) on the performance of pure refrigerator. These results help to arrive at the optimum value of pure refrigerator.

Though similar results have been obtained through simulation studies for pure liquefier and mixed modes of 25/75, 50/50, 25/75 design, only the optimum values have been presented in Figures 5 and 6. These figures present the variation of optimum values of several important parameters, maximum attainable exergy efficiency and specific work input for mixed mode designs as plants change gradually from refrigerator to liquefier. Figure 7 highlights the deterioration of maximum attainable exergy efficiency when the plants operate away from their optimum design points at 0/100, 25/75, 50/50, 25/75 and 0/100 mixed modes.

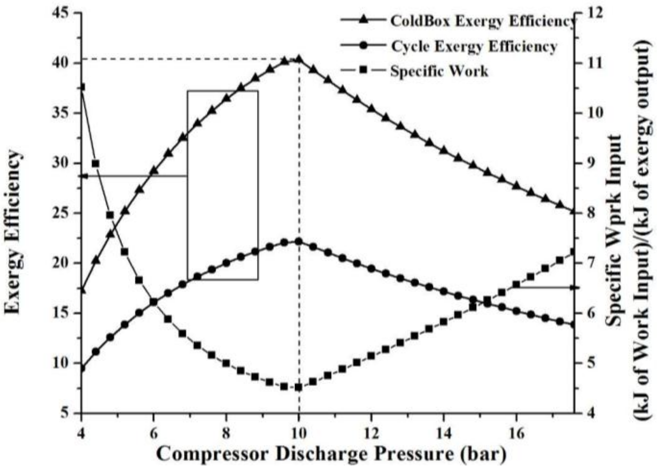

Figure 2: Effect of compressor discharge pressure on cold box exergy efficiency, cycle exergy efficiency and specific work for a pure refrigerator (0/100 Mixed Mode) [$P_s$=1.013 bar, Inlet temperature to 2-stage screw compressors =300K, $\eta_{COMP}$ = 55%, $\eta_{EXP1} = \eta_{EXP2}$ = 80%, $\dot{m}_{EXP1}$= 0.25$\dot{m}$, $\dot{m}_{EXP2}$=0.25$\dot{m}$, $\varepsilon_{HXs}$ = 0.97]

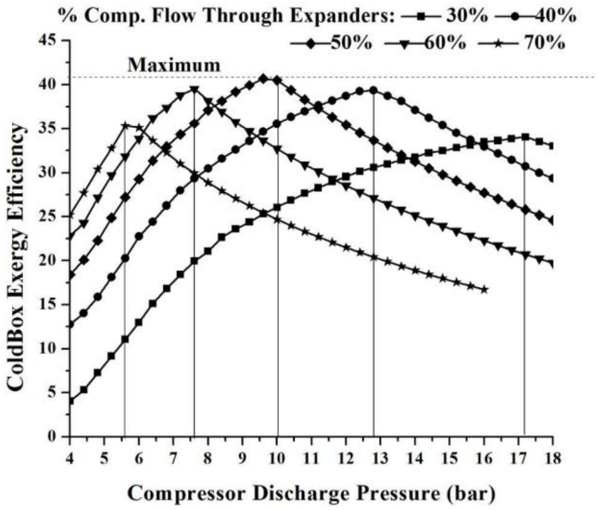

Figure 3: Effect of compressor discharge pressure on the cold box exergy efficiency at different expander mass flow rate for a pure refrigerator (0/100 Mixed Mode) [$P_s$=1.013 bar, Inlet temperature to compressor= 300 K, $\eta_{EXP1} = \eta_{EXP2}$ = 80%, $\dot{m}_{EXP1} = \dot{m}_{EXP2}$, $\varepsilon_{HXs}$=0.97]

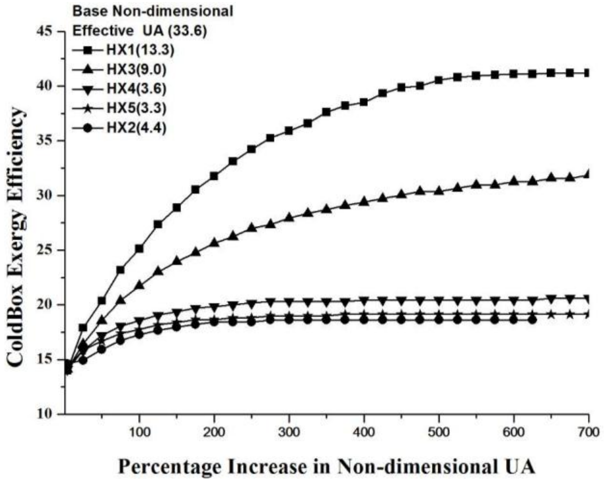

Figure 4: Variation of cold box exergy efficiency with increase in non-dimensional effective UA of HXs for pure refrigerator (0/100 Mixed Mode) [$P_s$= 1.013 bar, Inlet temperature to compressor= 300 K , $P_d$ = 10 bar, $\eta_{EXP1} = \eta_{EXP2}$ = 80%, $\dot{m}_{EXP1} = \dot{m}_{EXP2}$= 0.25$\dot{m}$, Base $\varepsilon_{HXs}$ = 0.93]

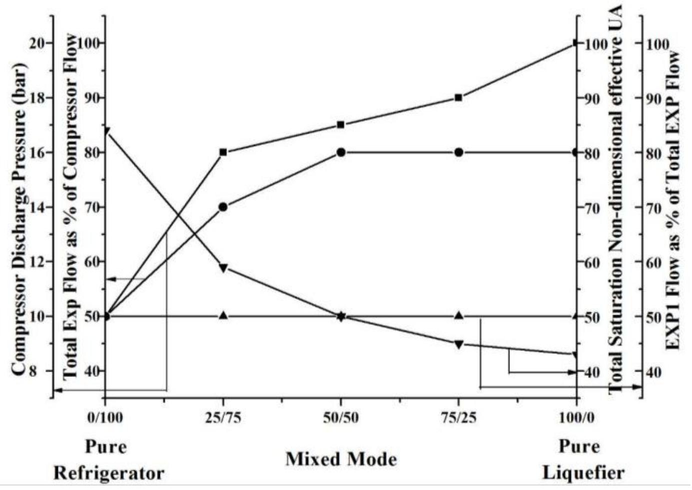

Figure 5: Variation of optimum values of compressor discharge pressure, total EXP flow, distribution of flow among the expanders and non-dimensional UA with change in mode of operation [$P_s$=1.013 bar, Inlet temperature to compressor = 300 K, $\eta_{EXP1} = \eta_{EXP2}$ = 80% ]

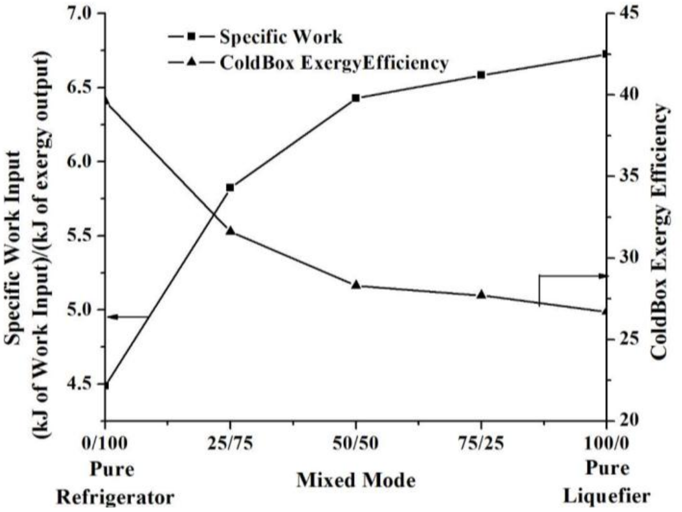

Figure 6: Variation of minimum specific power input and maximum attainable coldbox exergy efficiency at different modes of operation [$P_s$=1.013 bar, Inlet temperature to compressor = 300 K, $\eta_{COMP}$ = 55%, $\eta_{EXP1}$ = $\eta_{EXP2}$ = 80%, $\varepsilon_{HXs}$ = 0.97, other parameters same as optimum parameters at the respective modes of operation]

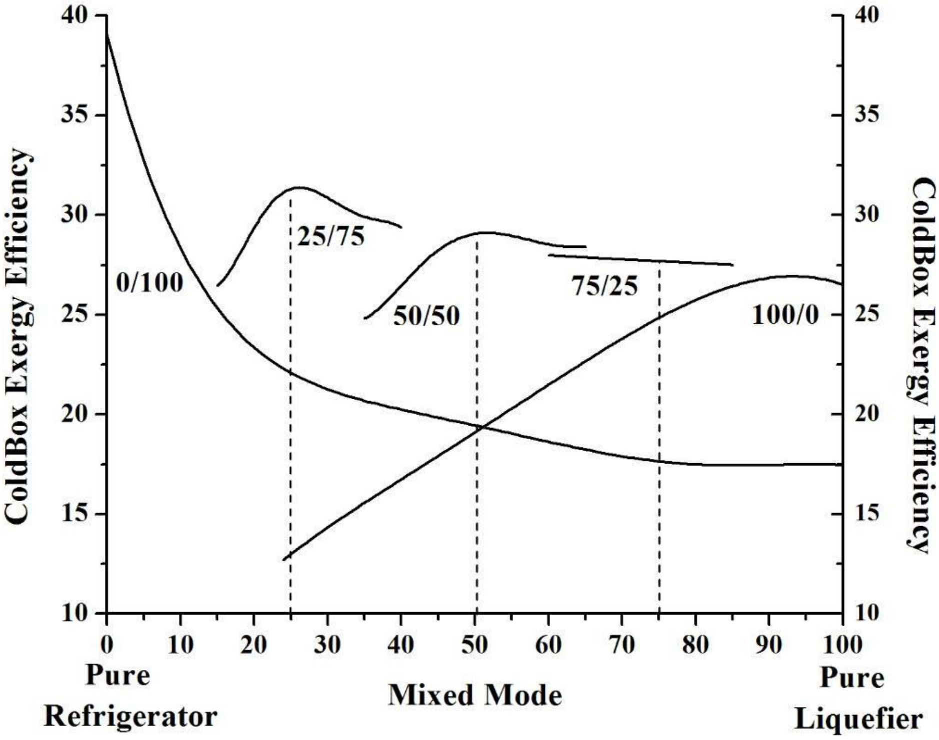

Figure 7: Variation of maximum attainable cold box exergy efficiency while helium plants operate away from their optimum points for 0/100, 25/75, 50/50, 75/25 and 100/0 mixed-mode plants [$P_s$=1.013 bar, Inlet temperature to compressor= 300K, $\eta_{EXP1} = \eta_{EXP2} = 80\%$, $\varepsilon_{HXs} = 0.97$]

## 4. DISCUSSIONS

Optimum pressure for refrigerator turns out to be 10 bar as shown in Figure 2. In Figure 3, liquid forms at inlet to JT for discharge pressure above 16 bar and for flow rate above 60% through expanders. Expander flow rate of 50% of compressor flow gives the highest efficiency, though the performance of 40% to 60% may be termed as acceptable.

In Figure 4, non-dimensional saturation effective UA has been defined as that UA at which exergy efficiency lies within 3% of the highest achievable exergy efficiency. Saturation or optimum value of each of the heat exchangers has been determined. If the size of heat exchanger is lower than its saturation value, the exergy efficiency is lower than the highest attainable exergy efficiency. However, designing heat exchangers above saturation UA is a waste as it does not give any improvement in the plant performance any further. Table 1 compares the performance of Collins helium refrigerator vis-à-vis Collins helium liquefier as they operate at their optimum points.

Table 1: Comparison of optimum parameters of pure liquefier and of pure refrigerator

| ` | Highest Exergy efficiency for a Collins Cycle | Compressor Discharge Pressure (bar) | Total EXP Flow as % of Total Comp Flow | EXP1 Flow as % of total flow EXP | Saturation Non-dimensional effective UA | | | | |
|---|---|---|---|---|---|---|---|---|---|
| | | | | | HX1 | HX2 | HX3 | HX4 | HX5 |
| Liquefier | 27% | 20 | 80 | 50 | 69 | 7 | 19 | 3 | 2 |
| Refrigerator | 40% | 10 | 50 | 50 | 73 | 11 | 54 | 12 | 9 |

In a liquefier, the exergy associated with the entire liquid is extracted out of the plant. Therefore, a liquefier needs a higher compressor pressure and higher flow rate through the expanders to make up the higher exit of exergy from the system when compared with a refrigerator. On the other hand, as a refrigerator returns the entire output from the JT valve as the saturated vapour to the system, a higher surface area of the heat exchangers is required to extract the higher amount of sensible cold than that in a liquefier. A higher amount of refrigeration available from returning stream helps pure refrigerator attain higher exergy efficiency.

In Figure 7, the extent of deterioration of exergy efficiency has been shown for optimally designed refrigerator and a liquefier, both made to operate along the entire range of mixed mode. Such extreme off-design operations may be inadvisable due to sharp decline in the plant performance. As a pure liquefier operates below 25/75 mode, liquid forms at the inlet of EXP2. This happens due to the larger refrigeration effect provided by the returning vapor stream. Further, if the range of the mode of operation is approximately known to the planner, the results shown in Figure 7 may be used to choose the mode for the plant at which the design should be made. For example, Figure 7 shows that for 40/60 mixed mode operation, it is wiser to design the plant as 25/75 mixed mode rather than 50/50 mixed mode. On the other hand for 50/50 mixed mode operation, a refrigerator and a liquefier are equally inefficient.

## 5. CONCLUSIONS

The achievable exergy efficiency and optimum parameters for a pure helium refrigerator, mixed mode plant and a liquefier are all different. There is a large reduction in plant efficiency when either a liquefier or a refrigerator is made to operate in the entire range of mixed mode. A mixed mode helium plant should be designed as close to the expected range of operation as possible.

## 6. REFERENCES

1. Trepp C. 1962, Refrigeration systems for temperatures below 25K with turbo-expanders, *Adv Cryog Engg.* 7: 251-61.
2. Thirumaleshwar M. 1979, Exergy method of analysis and its application, *Cryogenics* 19(6): 355-61.
3. Ziegler BO. 1986, Second law analysis of the helium refrigerators for HERA proton magnet ring, *Adv Cryog Engg.*31: 693-8.
4. Ziegler B, Quack H. 1992, Helium refrigeration at 40 percent efficiency, *Adv Cryog Engg.*37: 645-51.
5. Lohlein K, Fukano T. 1993, Exergy analysis of refrigerators for large scale cooling systems, *Fusion Engg. and Design* 20: 511-8.
6. Caillaud A, Crispel S, Grabie V, Delcayre F, Aigouy G. 2008, Evolution of the standard helium liquefier and refrigerator range designed by Air Liquide DTA, France 53: 830-7.
7. Marchand P. et al. 2006, Commisioning of the Soleil RF systems, *Proc. of European Particle Accelerator Conference (EPAC)*: MOPCH142.
8. Connor TG et al. 1997, Technical Specification for the 1.5 Tesla Superconducting Solenoid for the Babar Detector, *Lawrence Livermore National Laboratory*: UCRL-ID-126263 Rev1.
9. Thomas RJ 2012, Exergy Approach in Designing Large Scale Helium Liquefiers. Ph.D. Thesis, Indian Institute of Technology Kharagpur, India.
10. Thomas RJ, Ghosh P, Chowdhury K. 2012, Application of Exergy Analysis in Designing Helium Liquefiers, *Elsevier: Energy* 37(1): 207-219.

# CRYOBIOLOGY AND -TECHNOLOGY

046

# Analysis on Protein Stability in Tris Buffered Purified Bulk Solutions during the Freezing Process

**Heidingsfelder J., Reinsch H., Klier J., Herzog R.**

Hauptbereich Kryotechnik und Tieftemperaturphysik - Life Sciences;
Institut für Luft und Kältetechnik gemeinützige GmbH; Dresden; Germany

## ABSTRACT

Cryopreservation as a technique for the stabilization of solved biotechnologically produced pharmacological active agents (e. g. recombinant proteins) is gaining more and more importance as an industrial method. These recombinant proteins are solved in a buffer according to the fermentation process (upstream processing) and the purification process (downstream processing). Those buffered product solutions are named as purified bulk. Because of the time dependent loss of protein activity, the purified bulk gets frozen for reason of stabilization. But also the freezing process itself can damage the recombinant proteins in several ways. Possible mechanisms of protein damage are mechanical stress on the macromolecules due to ice formation, concentration effects and shifts of the buffer-pH depending on the change in temperature. The effects of changes in the pH are well known in proteins. The pH-dependent protein damage is related to the freezing process and can only be estimated by an analysis of the pH-properties of a purified bulk. The focus of this study is the discussion on the effect of the pH-shifts during the freezing of Tris(hydroxymethyl)-aminomethane (Tris) buffered purified bulk solutions and on the prevention of damaging effects on the protein agent.

## 1. INTRODUCTION

The biotechnological method of the production of pharmacological active agents is a important technique in the pharmaceutical industry. The common volume of one batch is 50 to 100 liters, that´s why there are large amounts of drug solutions. The solved products have to be stored after the purification process with minimum loss of activity. After running through the purification steps, the active agents are available in a highly-purified, concentrated form solved in a buffer. Such a medium is named as „purified bulk“ and should be stored at gentle conditions. There are lots of solution approaches to realize the storage and stabilisation of the purified bulk. Examples are the storage of the liquid medium at +4 °C, the lyophilisation or the cryopreservation [1].

Lyophilisation and the cryopreservation processes have one similar process step: the freezing of the medium. These techniques are some of the cryogenic storage-methods that study is focused on. Although the cryopreservation as a technique for storage stabilisation is gaining more and more importance, however the mechanisms of protein damage during the freezing process aren´t fully understood. In fact the application of cold reduces the activity of the protein agent, induced by mechanisms of protein damage (e. g. effects of salting-out processes, pH-change, aggregation, agglomeration, precipitation). Nevertheless the cryogenic preservation methods are getting more and more practical application in realizing an easy, safe and trouble-free storage and transport over long distances. For the implementation of the cryopreservation, one can choose between expensive *high end* – (e. g. high performance freezer, large scale freeze/ thaw systems) and cheaper *low budget – solutions* (freezing with common laboratory freezer) [2; 3; 4; 5; 6]. Latter ones are the focus of this study. However, there's a possibility of optimization for both available market solutions. But only with a knowledge about the damaging process an increase of the yield (in this case of the remaining enzyme activity) is possible. Therefore it's important to analyze the underlying mechanisms exactly. The pH and/or the pH-stability of a purified bulk is one of the main factors influencing the protein stability. In fact the pH directly affects the structure of proteins. For this reason the specific functions of enzyms are affected, too. This implies that the main demand on the buffer system is maintaining the constant pH. The pH-properties of a purified bulk are analyzed in detail below.

# 2. MATERIALS AND METHODS

## 2.1. Purified bulk

In essence, a purified bulk is a buffered, high purity and high potency active ingredient-containing solution. The downstream processing determines in which purity and concentration the pharmaceutical proteins are present in the purified bulk. For buffering the drug solution, a variety of buffer systems (e. g. phosphate-, citrate -, acetic – acetate -, Tris - buffer, etc.) can be used. This work is focused on a Tris/HCl (pH 7) buffered system, because Tris/HCl is a common buffer in many fields of biotechnology. In addition Tris (hydroxymethyl)-aminomethane also known as Trometamol is used as an additive in various pharmaceutical dosage forms (e. g. infusion, injections, eyedrops und creames) as well as a drug (treatment of acidosis). The focus of this study about the temperature dependency of the pH of a purified bulk is set only on the buffer system without protein.

## 2.2. Freezing experiments

The experimental setup is chosen to match a low budget freezing method. In fact it´s common practice to realize a bulk freezing putting the package filled with purified bulk into an ordinary laboratory freezer. In our case an ice cube M15 (Fa. Sylab) a laboratory freezer with LN2 cooling system realizes the process simulation. In the experiments the freezing chamber was precooled to a constant process temperature of – 30 °C via software. The chosen package is a 1000 ml polycarbonate (PC) that can filled up to 80 percent with purified bulk. After reaching process temperature, the measurement setup was put into the freezer.

## 2.3. pH measurements

The chosen experimental setup for the pH measurement is based on the assumption of a central freeze concentration. Thus the detection of the pH took place in the middle position of the package. The pH of the purified bulk was detected with a special pH-electrode (Mettler Toledo InLabCool). The electrode allows measurements from 80 °C to – 30 °C. The chosen freezing parameters were described above in subchapter 2.2.

# 3. RESULTS

## 3.1. The resulting pH-temperature-properties

It's well known that the dissociation constant depends on the temperature. In fact this leads to a temperature associated increase of pH while cooling the liquid buffer (for Tris that’s ~ 0.03 ΔpH/K) [7]. The purified bulk also shows such a behavior (figure 1). As long as the liquid bulk cools down there’s an increase of the pH of 0.026 ΔpH/K.

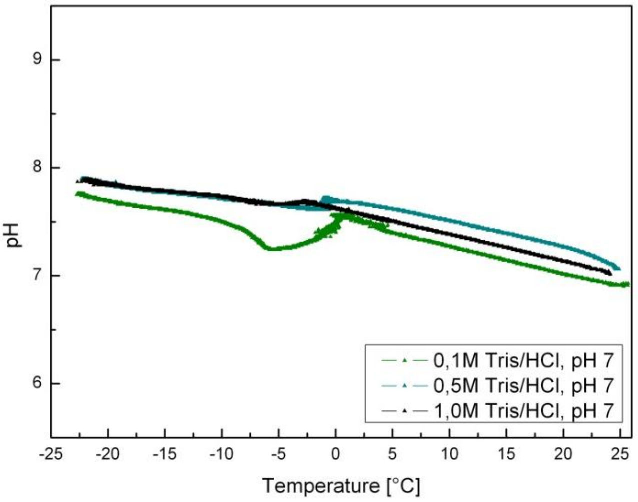

Figure 43 pH-temperature-progress of a Tris/HCl buffer with various molarities frozen with a process temperature of – 30°C

Compared with the value cited of literature [7] it is clear that the initial increase is triggered by the temperature-dependent dissociation constant. But the following decrease of the pH starting at about 0 °C to – 3 °C (depending on the molarities of the buffer) can't be explained by the temperature-dependent dissociation constant. Figure 2 leads to a better understanding of the mechanism that affects the pH shift. The diagram shows the temperature-time - and the pH-time - correlation of 0.1 M Tris / HCl buffer at a process temperature of 30 °C. After putting the measurement set up in the freezing chamber the purified bulk cools down until it reaches the crystallization temperature. The graph shows a constant temperature of 0 °C up to the liquid-solid transition after reaching the freezing point [8; 9]. During that temperature interval the ice grows toward the centre of the package. The crystallization of water leads to a freeze concentration of the ingredients in the centre and this leads to a shift in the pH during the freezing process.

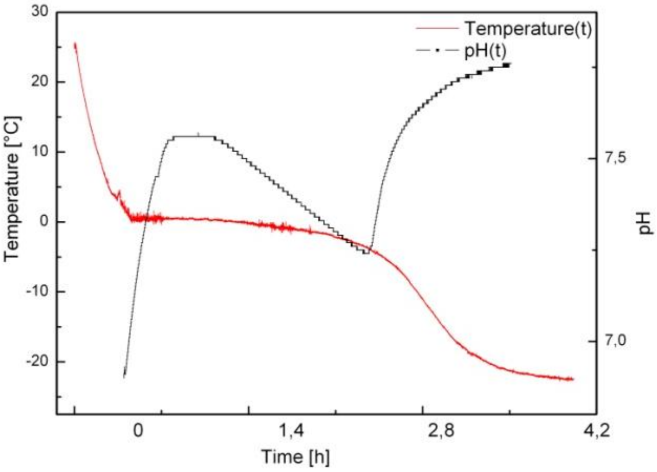

Figure 44 pH-time – and temperature-time – correlation of a 0.1 M Tris / HCl buffer is shown at a process temperature of 30 °C

However, considering the dependence between the freeze concentration and the cooling rate, it is clear that also the change of pH represents a function of cooling rate. In fact the higher the cooling rate the smaller is the freeze concentration. If the purified bulk reaches the solid phase the temperature decreases again up to the final temperature [8; 9]. In addition the resulting effect of a so-called pH-shift can be reduced by an increase in capacity of the buffer system. This context is also shown in figure 1. The diagram points out a direct dependence between the shift width and the buffer molarity. The higher the molarities the smaller is the pH shift. Nevertheless, too high concentrations of buffer substances can also lead to damage of the proteins. So there's a conflict between pH-stabilization of the purified bulk and the reduction of the caused damage for the proteins. If one takes account of the dependence of all possible damage mechanisms it's clear that the only option for the optimization is a statistical experimental design.

### 3.2. Is there a tool for the regulation of the pH shift?

The following chapter describes the search for a tool to regulate the pH shift. Figure 45 shows the pH correlation of a purified bulk, where a part of the hydrochloric acid has been replaced by phosphoric acid. The triprotic acid has a significant impact on the temperature-dependent dissociation constant. Comparing the case of 0.1 M purified bulk in figure 3 with the analogue system in figure 1, one can determine, that the phosphoric acid reduces the initial slope of the pH to 0.014 ΔpH/K. Also, the phosphoric acid leads to a greater pH shift. This is because of the lower capacity of the buffer system to counteract the higher freeze concentration of the triprotic acid. It is possible to reduce the shift width increasing the molarity of Tris. But a higher molarity leads also to a slope as it was in the initial state. That's a method to control the final pH by setting the mixing ratio of phosphoric acid / HCl. Also the pH shift that occurs during the freezing process can be controlled within a protein-specific tolerance range. However, the selective control is limited by the chosen buffer system and freezing parameters.

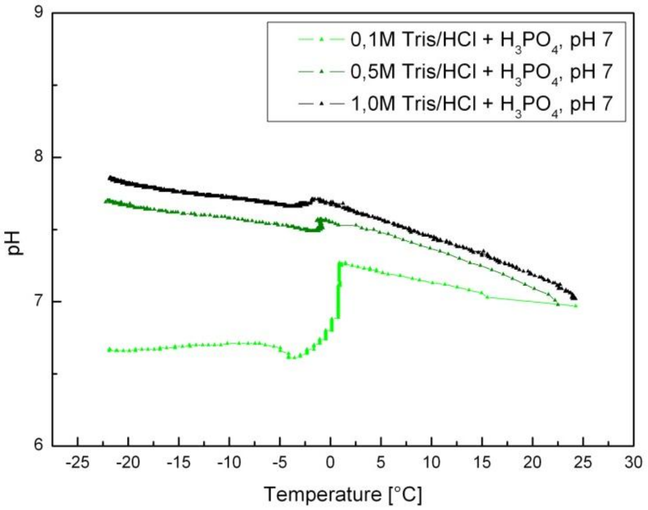

Figure 45 pH-temperature-progress of a Tris/HCl buffer with various molarities and phosphoric acid frozen with a process temperature of – 30 °C

In addition, the temperature at which the shift takes place can be controlled via the molarity of the buffer. The reason is a freezing point depression depended on the molarity of the buffer system. But as mentioned above, also high concentrations of the buffer components have a damaging effect on the solute proteins. This gives a tool to control the final pH, but there is always the question of benefits and harms.

## 4. DISCUSSION AND OUTLOOK

In pharmaceutical drugs, the degree of damage caused by a pH shift during the bulk freezing process depends mainly on their pH tolerance. A stabilization of the pH during a freezing process is possible by increasing the buffer capacity. However, higher buffer molarities are also associated with a damage potential for the enzymes. For a qualitative statement about the remaining product activity, an assessment about the damage depending on the freeze concentration of the buffer substances must be included. As example, a well known model enzyme can be mentioned the horseradish peroxidase (HRP). The HRP is having a pH stability in a pH interval of 3.0 to 12.5 [10], that means as long the pH of the purified bulk lays between that interval there is no damage effect. In addition the detected pH shift above has no influence on the activity of the enzyme. So if there is any loss of activity after a freezing, it has to be caused of any other mechanisms such as the freeze concentration.

Using the type of acid as a tool to control the final pH has a low importance in cryopreservation. But maybe it’s useful for a controlled cryogen isoelectric precipitation technique to separate proteins.

For this reason, the study about the pharmaceutical freezing at the Institute of Air and Refrigeration will be amplified to the field of the other damaging mechanisms. That study should consider a multiple factor of the various damage mechanisms. It occurs in form of a statistical experimental design to investigate the freeze concentration depending on the process temperature, package volume and molarity of the buffer. In addition, the interactions of the protein with each other molecules and the interactions of protein and ice interface should be analyzed.

## 5. REFERENCES

[1]. Pramik MJ. 1998, Cryopreservation Technologies: Application in Large Volumes of Biopharmaceutical Products. *Genetic Engeneering News.*, 18(4).

[2]. Wisniewski R. 1998, Developing Large-Scale Cryopreservation Systems for Biopharmaceutical Products. *BioPharm.*, 11(6).

[3]. Webb SD et al. 2002,Freezing Bulk-Scale Biopharmaceuticals Using Common Texhniques and the Manitude of Freeze-Concentration. *BioPharm.*, 15(5).

[4]. Singh KS et al. 2009, Large-Scale Freezing of Biologics A Practitioner´s Review, Part 2 Practical Advice. *BioProcess International.*.

[5]. Wilkins J, Sesin D, Wisniewski R. , Large-scale cryopreservation of biotherapeutic products. *Innovations in Pharmaceutical Technology*, 1(8).

[6]. Kantor A, Tchessolov PhDS, Warne PhDN. 2011, Quality-by Design for Freeze- Thaw of Biologics: Concepts and Application to Bottles of Drug Substance. *American Pharmaceutical Review*.

[7]. Sambrook EF, Fritsch T, Maniatis J. 1989, *Molecular Cloning: A Laboratory Manual 2nd ed. Cold Spring Harbor Laboratory*. Cold Spring Harbor New York.

[8]. Sackmann H**.** 1955, *Physikalische Chemie.* Fachbuchverlag Leipzig.

[9]. Franks F. 1982, The Properties of Aqueous Solutions at Subzero Temperatures. *Water A comprehensive Treatise, Volume 7, Water and Aqueous Solutions at Subzero Temperatures.* Plenum Press, New York.

[10]. Lemos MA, Oliveira JC, Saraiva JA. 2000, Influence of pH on the thermal inactivation kinetics of horseradish peroxidase in aqueous solution. *Lebensm.-Wiss. Technol.*, 33: 362-368.

003

# Coupled Transport of Water and Cryoprotectant across Cell Membranes and Applications to Cryopreservation

**Weng L., Li W.**

School of Energy and Power Engineering, Dalian University of Technology,
No.2 Linggong Road, Ganjingzi District, Dalian 116024, P. R. China

## ABSTRACT

The field of cryobiology has progressed as a fertile ground for new discoveries with important applications in cryopreservation over the past several decades. Some well-known thermodynamic models were proposed to predict the biophysical response of living cells and tissues in cryopreservation. This study, for the first time, develops a model that can calculate the coupled transport of water and cryoprotectants across cell membranes during the freezing and thawing protocols. The new model can eradicate the long-standing contradiction between the conventional Mazur model and the modern 2-P or K-K one. For cryobiological practice, the new model is applied to predict the volumetric change for human corneal keratocytes in the freezing protocol. The findings in this study will offer new insights into the biophysical response of biomaterials experiencing cryopreservation procedures.

## 1. INTRODUCTION

Cryobiology has progressed as a fertile ground for new discoveries with significant applications in both cryopreservation and cryosurgery. One of the most striking discoveries is the reveal of the cryoprotective function of glycerol in the cryopreservation of human spermatozoa (Polge, et al., 1949). Since then, the loading and removal of cryoprotective agents (CPAs) have been indispensible procedures to the efforts of preserving living cells and tissues at low temperatures. When cells are subjected to cryopreservation procedures, the transmembrane transport of water and permeable CPAs occurs due to the imbalance of chemical potentials between the extra- and intracellular media. For clarifying the mechanisms of the mass transfer across cell membranes, some thermodynamic models were proposed and their experimental verification was conducted (Mazur, 2010). These models (Weng, et al., 2010, Saenz, et al., 2009, Elliott, et al., 2007, Karlsson, et al., 1994, Toner, et al., 1990, Fahy, 1981, Mazur, 1963, Kedem and Katchalsky, 1958, Jacobs, 1933) can be generally categorized into two groups. They are: the isothermal models that determine the water and CPA movement across membranes during the addition and removal of permeable CPAs at a constant temperature; and the nonisothermal ones that calculate the water transport when cells are subjected to cooling and warming. These models have different application conditions, either for ideal solutions only or for both ideal and nonideal solutions.

By reviewing the commonly-used thermodynamic models in cryopreservation, one can notice that one issue remains to be addressed. Namely, studies have not yet been carried out so far to couple the transport of water and permeable CPAs of cells subjected to cooling and warming, particularly in cryomedia that are neither dilute nor ideal. The nonisothermal models such as the Mazur model (Mazur, 1963) typically assume that cell membranes are solely permeable to water during the freezing and thawing protocols. This assumption, on the contrary, is necessarily excluded in the isothermal models such as K-K and modern 2-P models (Kedem and Katchalsky, 1958, Jacobs, 1933) which are used to predict the loading and removal of CPAs at a constant temperature. Therefore, there exists a contradiction which has yet been resolved. One of the challenges, in our opinion, should be the difficulty in determining the changing concentration of the extracellular solution. But such a challenge can be undertaken based on the phase diagrams of cryoprotective solutions, which will be unravelled later in this paper.

This study develops a new set of equations that are able to calculate the coupled transport of water and permeable CPAs across cell membranes when living cells are subjected to cooling and warming in nondilute and nonideal solutions. To testify its effectiveness, the new model is applied to predict the volumetric change of human corneal keratocytes in various freezing protocols.

## 2. THEORY

The transmembrane mass transfer in cryopreservation is driven by the difference between the extra- and intracellular chemical potentials as shown by eqs. (1) and (2). A recently-developed expression for the chemical potential of solute $\mu_s$ is employed here (Elmoazzen, et al., 2009). A similar expression for the chemical potential of water $\mu_w$ is used to achieve the thermodynamic consistence.

$$\frac{dn_w}{dt} = k_w A\left(\mu_w^e - \mu_w^i\right) \tag{1}$$

$$\frac{dn_{CPA}}{dt} = k_{CPA} A\left(\mu_{CPA}^e - \mu_{CPA}^i\right) \tag{2}$$

where

$t$ is the time in min., $n_w$ and $n_{CPA}$ are the intracellular water and CPA contents, respectively, in mol, $A$ is the plasma membrane area in $\mu m^2$, $k_w$ and $k_{CPA}$ are water and CPA permeability coefficients, respectively, in $mol^2 \cdot min^{-1} \cdot atm^{-1} \cdot \mu m^{-5}$, $\mu$ is the chemical potential with the subscripts $w$ and $CPA$ indicating water and CPA, respectively, and with the superscripts $e$ and $i$ indicating the extra- and intracellular spaces, respectively, in $J \cdot mol^{-1}$.

### 2.1. The coupled transport of water and permeable CPAs across membranes

$\mu_w$ and $\mu_{CPA}$ in a real CPA-NaCl-water mixture can be calculated with eqs. (3) and (4) (Elliott, et al., 2007, Elmoazzen, et al., 2009, Abazari, et al., 2009).

$$\mu_w = \mu_w^0 - RT\left[\left(1 - x_w\right) + B_{CPA} {x_{CPA}}^2 + B_{salt} {x_{salt}}^2 + \left(B_{CPA} + B_{salt}\right) x_{CPA} x_{salt}\right] \tag{3}$$

$$\mu_{CPA} = \mu_{CPA}^0 + RT\left[\ln\left(x_{CPA}\right) + \left(\frac{1}{2} - B_{CPA}\right) x_w \left(1 - x_{CPA}\right) - \left(\frac{1}{2} - B_{salt}\right) x_w x_{salt}\right] \tag{4}$$

where

$\mu_w^0$ and $\mu_{CPA}^0$ are the chemical potentials of pure water and pure CPA, respectively, at the same temperature $T$ and pressure $P$ as the solution. $R$ is the universal gas constant. $x_w$, $x_{CPA}$ and $x_{salt}$ are the mole fractions of water, CPA and salt in the ternary mixture, respectively. $B_{CPA}$ and $B_{salt}$ are the osmotic virial coefficients for CPA and salt based on a virial expansion in mole fraction up to the second order. For example, $B_{CPA}$ is equal to 4.716 for DMSO and 3.415 for PG and $B_{salt}$ is equal to 2.759 for NaCl (Elmoazzen, et al., 2009).

Then, eqs. (1) and (2) would take the following forms by considering the freezing and thawing protocols with a rate $B\,(=\frac{dT}{dt})$.

$$\frac{dn_w}{dT} = -k_w ART \left[\begin{array}{l} \left(1 - x_w^e\right) + B_{CPA} {x_{CPA}^e}^2 + B_{salt} {x_{salt}^e}^2 + \left(B_{CPA} + B_{salt}\right) x_{CPA}^e x_{salt}^e - \\ \left(1 - x_w^i\right) - B_{CPA} {x_{CPA}^i}^2 - B_{salt} {x_{salt}^i}^2 - \left(B_{CPA} + B_{salt}\right) x_{CPA}^i x_{salt}^i \end{array}\right] \Big/ B \tag{5}$$

$$\frac{dn_{CPA}}{dT} = k_{CPA} ART \left[ \begin{array}{l} \ln\left(x_{CPA}^{e}\right) + \left(\frac{1}{2} - B_{CPA}\right) x_{w}^{e}\left(1 - x_{CPA}^{e}\right) - \left(\frac{1}{2} - B_{salt}\right) x_{w}^{e} x_{salt}^{e} \\ - \ln\left(x_{CPA}^{i}\right) - \left(\frac{1}{2} - B_{CPA}\right) x_{w}^{i}\left(1 - x_{CPA}^{i}\right) + \left(\frac{1}{2} - B_{salt}\right) x_{w}^{i} x_{salt}^{i} \end{array} \right] \Bigg/ B \tag{6}$$

where

$k_w$ and $k_{CPA}$ are temperature-dependent which can be determined by eqs. (7) and (8).

$$k_w = k_{wg} \exp\left[\frac{E_{kw}}{R}\left(\frac{1}{T_0} - \frac{1}{T}\right)\right] \tag{7}$$

$$k_{CPA} = k_{CPAg} \exp\left[\frac{E_{k\,CPA}}{R}\left(\frac{1}{T_0} - \frac{1}{T}\right)\right] \tag{8}$$

where

$k_{wg}$ and $k_{CPAg}$ are the water and CPA permeability coefficients at the reference temperature $T_0$, respectively, and $E_{kw}$ and $E_{kCPA}$ are the activation energies for $k_w$ and $k_{CPA}$ in kcal·mol$^{-1}$, respectively.

## 2.2 The mole fractions of water, CPA and salt in the extracellular space

For the CPA-NaCl-water mixture which is neither ideal nor dilute, $x_w^e$, $x_{CPA}^e$ and $x_{salt}^e$ can be determined based on its phase diagram by assuming that the ice is in equilibrium with the residual solution. The calculation of $x_w^e$, $x_{CPA}^e$ and $x_{salt}^e$ in the DMSO-NaCl-water mixture is illustrated as follows. The calculations for other complicated mixtures can be similarly done.

$T_m$ of the DMSO-NaCl-water mixture can be expressed as a function of its total solute concentration $S$ (g in 100g solution) and the mass ratio of DMSO and NaCl $R'$ (Pegg, 1986). Therefore $x_{CPA}^e$, $x_{salt}^e$ and $x_w^e$ at a given melting point $T_m$ are given by the following equations.

$$x_{CPA}^{e} = \frac{\left[S \cdot R'/(R'+1)\right]/M_{CPA}}{\left[S \cdot R'/(R'+1)\right]/M_{CPA} + \left[2 \cdot S/(R'+1)\right]/M_{salt} + (100 - S)/M_{w}} \tag{9}$$

$$x_{salt}^{e} = \frac{\left[2 \cdot S/(R'+1)\right]/M_{salt}}{\left[S \cdot R'/(R'+1)\right]/M_{CPA} + \left[2 \cdot S/(R'+1)\right]/M_{salt} + (100 - S)/M_{w}} \tag{10}$$

$$x_{w}^{e} = 1 - x_{CPA}^{e} - x_{salt}^{e} \tag{11}$$

where

$M_w$, $M_{CPA}$ and $M_{salt}$ are the molar mass of water, DMSO and NaCl in mol·g$^{-1}$, respectively.

# 3. RESULTS AND DISCUSSION

The model developed here is used to calculate the contents of water and CPAs in human corneal keratocytes in DMSO-NaCl-water and PG-NaCl-water mixtures, respectively, during the freezing protocol at 5 K·min$^{-1}$. The characteristics of membrane permeability of human corneal keratocytes were determined by Ebertz et al. (Ebertz and McGann, 2004) using the K-K model (Kedem and Katchalsky, 1958). In this study, we convert $L_p$, $P_s$ and $\sigma$ in the K-K model into $k_w$ and $k_{CPA}$ in eqs. (5) and (6). By fitting the values of $k_w$ and $k_{CPA}$

at different temperatures to eqs. (7) and (8), we obtain that $k_{wg}$ =2.71×10$^{-28}$ mol$^2$·μm$^{-5}$·min$^{-1}$·atm$^{-1}$, $E_{kw}$ = 14.16 kcal·mol$^{-1}$, $k_{CPAg}$ = 4.79×10$^{-32}$ mol$^2$·μm$^{-5}$·min$^{-1}$·atm$^{-1}$, $E_{kcpa}$= 17.03 kcal·mol$^{-1}$ for membrane water and DMSO permeabilities and $k_{wg}$ =2.54×10$^{-28}$ mol$^2$·μm$^{-5}$·min$^{-1}$·atm$^{-1}$, $E_{kw}$ = 15.24 kcal·mol$^{-1}$, $k_{CPAg}$ = 4.77×10$^{-32}$ mol$^2$·μm$^{-5}$·min$^{-1}$·atm$^{-1}$, $E_{kcpa}$= 17.48 kcal·mol$^{-1}$ for membrane water and PG permeabilities.

Figure 1 displays the change in the normalized water and DMSO contents $n_w/n_w^{iso}$ and $n_{CPA}/n_{CPA}^{iso}$ in human corneal keratocytes as they are cooled at 5 K·min$^{-1}$ after initially exposed to DMSO-NaCl-water mixtures with 0.25 and 2 mol·kg$^{-1}$ DMSO, respectively. It is shown in Figure 1(A) that as the temperature falls the intracellular water content decreases to as low as 8% of the isotonic water content. Correspondingly, the intracellular DMSO content experiences a rise-and-slightly-fall pattern with $n_{CPA}/n_{CPA}^{iso}$ reaching 1.78 at -7 °C and then falling to 1.59 at -20 °C. One can also observe in Figure 1(B) that $n_{CPA}/n_{CPA}^{iso}$ increases by only 3 percentage points as $n_w/n_w^{iso}$ decreases gradually to 36% at -20 °C. It is clear that in a more concentrated solution the transmembrane mass transfer would be gentler. This is mainly because that in the more concentrated solution the ice nucleation temperature is typically lower and the change in the solute concentration caused by the water loss can be less obvious.

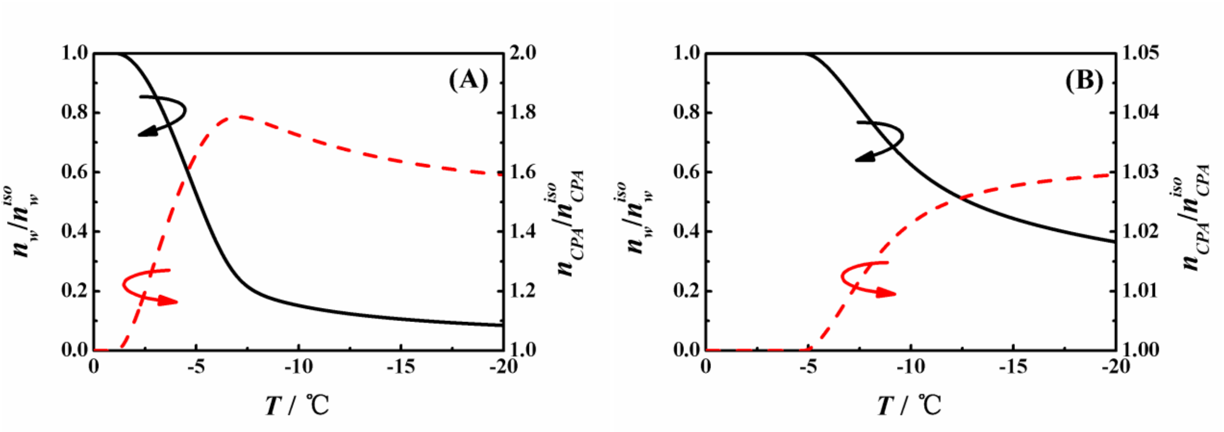

Figure 1. Normalized water and DMSO contents $n_w/n_w^{iso}$ and $n_{CPA}/n_{CPA}^{iso}$ in human corneal keratocytes as a function of temperature $T$ after exposed to DMSO-NaCl-water mixtures of 0.25 mol·kg$^{-1}$ (A) or 2 mol·kg$^{-1}$ (B) DMSO during a freezing protocol at 5 K·min$^{-1}$

Figure 2 displays the change in $V_c/V_c^{iso}$ of human corneal keratocytes as they are cooled at 5 K·min$^{-1}$ after an initial exposure to DMSO-NaCl-water and PG-NaCl-water mixtures with CPA molality of 1 and 2 mol·kg$^{-1}$, respectively. It is shown that the cell experiences shrinkage after the ice nucleation of the intracellular solution. For instance, the cell volume gradually decreases to 45.9% of the isotonic volume at -20°C with an initial exposure to the DMSO-NaCl-water mixture with a DMSO molality of 1 mol·kg$^{-1}$. Similarly, the cell volume accounts for 60.4% at -20 °C when the initial DMSO molality is 2 mol·kg$^{-1}$. One can also notice that the volume of human corneal keratocytes can change less dramatically when they are exposed to the PG-NaCl-water mixture than the DMSO-NaCl-water one at a given subzero temperature and with the same initial CPA molality. This is in part because that $k_w$ for PG is always smaller than that for DMSO at the same temperature. Since the water loss is the main contributor to the cellular volumetric change, the cellular change will be correspondingly less dramatic in the PG-NaCl-water mixture.

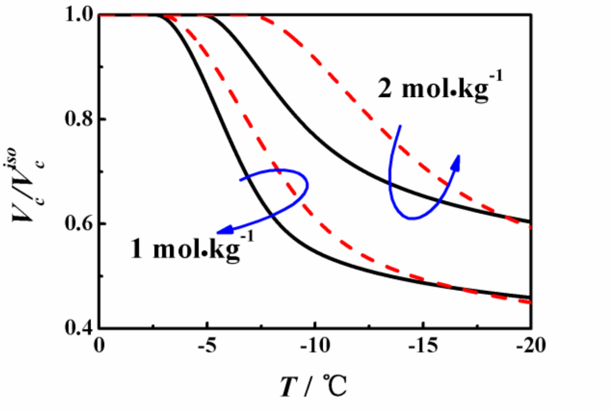

Figure 2. Volumetric response $V_c/V_c^{iso}$ as a function of temperature $T$ of human corneal keratocytes after exposed to CPA-NaCl-water mixtures of 1 and 2 mol·kg$^{-1}$ DMSO and PG, respectively, during a freezing protocol at 5 K·min$^{-1}$.
The black full lines represent the cases for DMSO and the red dashed lines represent the cases for PG.

## 4. CONCLUSIONS

Most thermodynamic models in cryobiology focus primarily on dilute and ideal solutions and cannot predict the coupled transport of water and CPAs across cell membranes during the freezing and thawing protocols. To overcome these limitations, this study develops a thermodynamic model that can calculate the transmembrane transport of both water and permeable CPAs when cells are subjected to cooling and warming. The new model is applicable to both ideal and dilute solutions and real ones. It can abandon the long-standing contradiction between the Mazur model and the modern 2-P or K-K one. It is proved that the intracellular content of DMSO or PG could be increased when human corneal keratocytes are cooled at 5 K·min$^{-1}$. The applications of the new model to the cryopreservation of human corneal keratocytes can expand our knowledge of the biophysical response of living cells during cryopreservation.

## REFERENCES

Polge, C., Smith, A. U., Parkes, A. S. 1949, Revival of spermatozoa after vitrification and dehydration at low temperatures, Nature, 164(4172): 666.

Mazur, P. 2010, A biologist's view of the relevance of thermodynamics and physical chemistry to cryobiology, Cryobiology, 60(1): 4-10.

Weng, L., Li, W., Zuo, J. 2010, Kinetics of osmotic water flow across cell membranes in non-ideal solutions during freezing and thawing, Cryobiology, 61(2): 194-203.

Saenz, J., Toner, M., Risco, R. 2009, Comparison between Ideal and Nonideal Solution Models for Single-Cell Cryopreservation Protocols, J. Phys. Chem. B, 113(14): 4853-4864.

Elliott, J. A. W., Prickett, R. C., Elmoazzen, H. Y., Porter, K. R., McGann, L. E. 2007, A multisolute osmotic virial equation for solutions of interest in biology, J. Phys. Chem. B, 111(7): 1775-1785.

Karlsson, J. O. M., Cravalho, E. G., Toner, M. 1994, A model of diffusion-limited ice growth inside biological cells during freezing, J. Appl. Phys., 75(9): 4442-4455.

Toner, M., Cravalho, E. G., Karel, M. 1990, Thermodynamics and kinetics of intracellular ice formation during freezing of biological cells, J. Appl. Phys., 67(3): 1582-1593.

Fahy, G. M. 1981, Simplified calculation of cell water content during freezing and thawing in nonideal solutions of cryoprotective agents and its possible application to the study of, Cryobiology, 18(5): 473-482.

Mazur, P. 1963, Kinetics of water loss from cells at subzero temperatures and the likelihood of intracellular freezing, J. Gen. Physiol., 47(2): 347-369.

Kedem, O., Katchalsky, A. 1958, Thermodynamic analysis of the permeability of biological membranes to non-electrolytes, Biochim. Biophys. Acta, 27(2): 229-246.

Jacobs, M. H. 1933, The simultaneous measurement of cell permeability to water and to dissolved substances, J. Cell. Comp. Physiol., 2(4): 427-444.

Elmoazzen, H. Y., Elliott, J. A. W., McGann, L. E. 2009, Osmotic transport across cell membranes in nondilute solutions: a new nondilute solute transport equation, Biophys. J., 96(7): 2559-2571.

Abazari, A., Elliott, J. A. W., Law, G. K., McGann, L. E., Jomha, N. M. 2009, A Biomechanical Triphasic Approach to the Transport of Nondilute Solutions in Articular Cartilage, Biophys. J., 97(12): 3054-3064.

Pegg, D. E. 1986, Equations for obtaining melting points and eutectic temperatures for the ternary system dimethyl sulphoxide/sodium chloride/water, Cryo Lett., 7(6): 387-394.

Ebertz, S. L., McGann, L. E. 2004, Cryoprotectant permeability parameters for cells used in a bioengineered human corneal equivalent and applications for cryopreservation, Cryobiology, 49(2): 169-180.

064

# Biological and Technological Challenges Establishing a Future-Proof Cryogenic Biomaterialbank

**Ciba P.[*], Böhmert B.[*], Lermen D.[**], Fuhr G.R.[**], Kruse C.[*]**

[*]Fraunhofer Research Institution for Marine Biotechnology, Paul-Ehrlich-Strasse 1-3, Lübeck, 23562, Germany
[**]Fraunhofer Institute for Biomedical Engineering, Ensheimer Straße 48, St. Ingbert, 66386, Germany

## ABSTRACT

To establish and maintain a cross generational cryogenic collection of rare animal biomaterial resources, several technological precautions need to be considered to ensure the usability of the stored samples at long-term. In the German Cell Bank for Wildlife “Alfred Brehm” (short: “CRYO-BREHM”) different biotechnological and cryotechnological features are applied that allow a sustainable scientific usability of the sample material. Further, a safe long-term storage of living cellular material and the sample related information is ensured.

## 1. INTRODUCTION

As the result of evolutionary adaptation to specific environmental conditions, each species exhibits extensive biological information. Adaptation, like resistance to pathogens or the ability to regenerate complex tissues, are realized through specific properties on the cellular level. This biological information can potentially be translated into various scientific and technological applications. Given the sustained loss of biodiversity, the preservation of cellular resources is imperative [1]. A continuous and sustainable use of rare cellular material, however, depends on the type of samples stored as well as on maintenance of the sample quality at long-term. The German Cell Bank for Wildlife “Alfred Brehm” (short: “CRYO-BREHM”) therefore focuses on the generation and preservation of cell cultures that can be extensively propagated and cryoconserved following standardized protocols. Latest cryotechnological equipment is used to preserve cell viability during long-term storage in liquid nitrogen atmosphere and accomplish a highly reliable storage of all sample related information.

## 2. RESULTS

Processing tissue samples from wildlife, various cell lines from different mammal, avian, fish and reptile species have been generated and cryogenically preserved [2, 3]. While in vitro culture of the cells requires adaptation of the culture conditions to the specific needs of cells from animals of different phylogenetic classes, all other steps from sample collection and sample processing to cryopreservation are highly standardized. Importantly, proliferative cell cultures with homogeneous characteristics from various taxa and tissue types are generated applying one robust, standardized protocol [4]. The cell cultures can be extensively propagated. Slow freezing and subsequent storage in liquid nitrogene atmosphere does not significantly affect cell viability. Frozen samples are not exposed to temperatures above -100 °C during sample stocking/withdrawl accomplished by a storage container with a working space that can be cooled down to deep temperatures [5]. Cryovials equipped with memory chips that are highly functional at low temperatures enable sample retrieval and inventory management and physically connect all sample and workflow related information with the sample [6].

## 3. DISCUSSION

The evolutionary adaptation of species to manifold abiotic (e.g. extreme habitats) or biotic (e.g. pathogens) environmental conditions accumulates to extensive biological information of a high scientific value. Cells represent these adaptations and therefore contain information, mechanisms and molecules relevant for various uses in biological, biochemical, pharmaceutical and technical research and development. Facing the continuous decline of biodiversity, the preservation of wildlife biomaterial resources is imperative to safe biological information that would be lost irrecoverably with the extinction of each species. Therefore, in the CRYO-BREHM project a collection is established exhibiting unique features that enable a long-term and sustainable usability of rare cellular resources. The applicability at long-term, firstly, is ensured by the type of samples. In the CRYO-BREHM, proliferative cell lines from wildlife species are generated and cryogenically stored. This enables a vast multiplication of the cellular material and thereby a sustainable scientific usability of each sample. Indeed, the generation of cell lines from tissue samples is a time-consuming procedure. In contrast to tissues, however, cell cultures can be reliably cryopreserved and thereby living and propagatable cellular material can be stored for long periods. Further, the usability at long-term depends on maintenance of the sample quality. Constant temperatures are obligatory as cell integrity can be affected when frozen samples are exposed to temperature changes. The use of storage containers equipped with a working space that can be cooled down to deep temperatures avoids significant changes in sample temperature, e.g. when racks are removed from the container to add new samples to the frozen stock. Thereby, the accumulation of subtle effects on cell viability is avoided enabling the CRYO-BREHM to provide viable samples to future generations. The scientific value of the samples further raises with the availability of the complete sample and workflow related data. The cryovials that are used in the CRYO-BREHM are equipped with memory chips that are highly functional at low temperatures. Thereby, all sample and workflow related information is physically connected to the sample and sample mistake is avoided. Moreover, every sample can be retrieved and assessed in stock and a mistake proof inventory management is provided.

## 4. CONCLUSIONS

Together, the biological and technological features of the CRYO-BREHM accumulate to a high quality, versatile, long-term and sustainable collection of rare living cellular material.

## 5. REFERENCES

[1] Lermen, D, Blömeke, B, Browne, R., Clarke, A., Dyce, P., Fixemer, T., Fuhr, G.R., Holt, W.V., Jewgenow, K., Lloyd, R.E., Lötters, S., Paulus, M., Reid, G.McG., Rapoport, D.H., Rawson, D., Ringleb. J., Ryder, O.A., Spörl, G., Schmitt, T., Veith, M., Müller, P. (2009): Cryobanking of viable biomaterials: implementation of new strategies for conservation purposes. Molecular Ecology (2009) Number 18, 1030–1033

[2] Ciba, P., Hering-Hagenbeck, S., Nagel U., Kruse, C., (2010). Examination and recording of stem cells from wild animals; here: Snow Leopard (Uncia uncia) and Giraffe (Giraffa camelopardalis rothschildi) - Article in German language. Der Zoologische Garten. 79 (2010), No.2-3, pp.132-139.

[3] Ciba, P., Schicktanz, S., Anders, E., Siegl, E., Stielow, A., Klink, E. and Kruse, C. (2008). Long-term culture of a cell population from Siberian sturgeon (Acipenser baerii) head kidney. Fish Physiol Biochem 34(4): 367-72

[4] Kruse, C., Birth, M., Rohwedel, J., Assmuth, K., Goepel, A. and Wedel, T. (2004). Pluripotency of adult stem cells derived from human and rat pancreas. Applied Physics Volume 79, Number 7: 1617-1624

[5] Ihmig, F.R., Shirley, S.G., Durst, C.H.P., Schulz, J.C., von Briesen, H., Zimmermann, H. (2009). The technology of the Global HIV Vaccine Research Cryorepository. Engineering in Life Sciences Volume 9, Issue 5, pages 376–383.

[6] Shirley, S.G., Durst, C.H.P. Fuchs, C.C., Zimmermann, H., Ihmig, F.R. (2008). A large-scale cryoelectronic system for biological sample banking. Cryogenics. 49 (2009), Nr.11, S.638-642.

087

# Cryopreservation of Mesenchymal Stromal Cells by Vitrification in Multicomponent Solutions

**Petrenko A.Yu., Trufanova N.A., Petrenko Yu.A.**

Institute for Problems of Cryobiology and Cryomedicine NAS, 23 Pereyaslavsky Str., Kharkov, 61015, Ukraine

## ABSTRACT

Due to capacity for differentiation into several cell lineages mesenchymal stromal cells (MSCs) are promising cellular components for cell therapy and tissue engineering that causes the need of cryopreservation of these cells. In the study combinations of cryoprotectants that allow avoiding ice formation during rapid cooling and rewarming as well as maintaining viability and unique properties of MSCs were discovered. The vitrification solutions consisted of dimethylsulfoxide, ethylene glycol, 1,2-propandiol and sucrose. Two vitrification multi-component solutions called DEPS-1 and DEPS-2, which prevented ice crystal formation in 2 ml cryovials during cooling and thawing were chosen for MSCs vitrification. After vitrification in DEPS-1 MSCs demonstrated higher viability and attachment rates than in DEPS-2. MSCs cryopreserved by vitrification in DEPS-1 were able to clonogenic growth and multilineage differentiation during culture. The vitrification protocol using DEPS-1 as CPA was adapted for cryopreservation of MSCs encapsulated in alginate microspheres.

## 1. INTRODUCTION

The capacity to multilineage differentiation makes mesenchymal stromal cells (MSCs) one of the most attractive cellular types for regenerative medicine and tissue engineering. For cryopreservation of MSCs the conventional cryopreservation protocol, including slow freezing in media containing 5-10% of dimethylsulfoxide ($Me_2SO$) as a cryoprotective agent (CPA) is usually used. However, since the conventional cryopreservation protocol is attended by the formation and growth of ice crystals, this approach can not ensure the preservation of cells within tissue engineered constructs. Moreover, we have shown previously, that conventional cryopreservation affects the differentiation properties of MSCs (Skorobogatova N. et al., 2010).

The alternative to conventional cryopreservation is vitrification. Vitrification as a process of glasslike solidification of the system is achieved without the formation of ice crystals, minimizing cell damage (Fahy GM et al. 1984) and represents the promising approach to cryopreservation of cells within natural (De Graaf IAM, Draaisma A, Schoeman O. et al. 2007) and artificial tissues (Song YC, Chen ZZ, Mukherjee N. et al. 2005). Successful vitrification requires high cooling rates, which is achieved by freezing of small volume of biological material in open type containers, such as open-pulled straws and cryoloops. These approaches greatly limit the size of the sample and do not meet GLP standards since the open containers not ensure sterility. The use of standard cryovials with screw cap allows preserving the biological material in the volume 0.5-2 ml and almost completely eliminates the risk of contamination during freezing and storage.

For vitrification it is necessary to use high concentrations of CPA that are toxic for cells. Taking into account that different CPAs have a specific mechanism of toxicity, reducing the overall toxic effect can be achieved by introducing a mixture of CPAs into cryoprotective medium.

The aim of the study was to discover the combinations of CPAs that are sufficiently non-toxic, able to avoid ice formation during cooling and rewarming, while maintaining the viability and unique properties of MSCs.

## 2. METHODS AND MATERIALS

### Cells isolation and culture

MSCs were obtained from human fetal mesodermal tissues after the patient informed consent under full Ethical guidelines. The study was approved by the Institute for Problems of Cryobiology and Cryomedicine Ethical Committee in accordance to the usage of biological material for research purposes. Adherent cells were resuspended in complete medium, which contained α-Minimum Essential Medium (α-MEM), supplemented with 15% fetal bovine serum, 50 units/ml penicillin, 50 μg/ml streptomycin, plated in T75 tissue culture treated flasks (Nunc, USA) and grown at 37°C in a humidified incubator at 5% $CO_2$. After reaching subconfluence, cells were harvested by trypsinization and replated 1:3 during 4 passages.

### Cells encapsulation

Before encapsulation, the cells were washed with a medium of 0.15 M NaCl, 25 mM HEPES (pH 7.4) and resuspended in 1.2% solution of activated charcoal purified and sterile filtered sodium alginate (Sigma). The obtained suspension with a concentration of $1{,}2 - 1{,}6 \times 10^6$ cells / ml was placed in a sterile syringe and sprayed in a solution containing 100 mM $CaCl_2$. Alginate microcapsules with cells left in the solution of $CaCl_2$ for 10 minutes for polymerization, and thereafter were washed out twice the excess of calcium ions with a solution of 0.15 M NaCl, 25 mM HEPES. The described method allowed obtaining microspheres with sizes in the range of 500-1000 microns.

### Vitrification solutions and procedure

Multicomponent vitrification solutions were prepared gravimetrically. The vitrification solutions contained $Me_2SO$ (Sigma, USA) in concentration of 10%, ethylene glycol (EG; 10, 15, 20 or 25%, Sigma, USA), 1,2-propandiol (1,2-PD; 10, 15, 20 or 25%, Sigma, USA) and sucrose (0.5, 1, 1.5 or 2 M, Serva, Germany). The primary screening of solutions was carried out using visual analysis.

Final concentrations of CPAs were obtained after mixing of vitrification solution with cell suspension in ratio 9:1. Vitrification solution was added in two stages at room temperature. At first stage 50 μl of cell suspension was put in a 1.8 ml cryovial (Nunc) and mixed with 50 μl of vitrification solution for 1 min. Then 400 μl of vitrification solution was added for 15 sec. Obtained samples were placed into liquid nitrogen. Samples were stored in liquid nitrogen during 1-3 days, and thawed on water bath at 40°C. For the removal of CPAs samples were diluted in ratio 1:10 with 0.5 M sucrose solution, then the obtained suspension was slowly mixed with equal volume of medium 199, supplemented by 10% FCS, and centrifugated at 450 g during 10 min. Obtained cell pellets were resuspended in culture medium.

### Viability and Alamar Blue assay

Viability was assessed by trypan blue staining (Sigma, USA). The adhesion ability of cells was determined under culture condition during 24 hrs. Metabolic activity was determined by Alamar Blue-test (AB; Serotec Ltd, USA). AB was added to culture medium in concentration of 10%. The reduced form of AB was determined after 24 hrs by fluorescence measurements at excitation wavelength of 550 nm and emission of 590 nm. Measurements were carried out using a Tecan Genios microplate reader (Tecan inc., Australia). Results were calculated as a difference between cells fluorescence and fluorescence of blank wells (with culture media supplemented 10% AB) and represented as the relative fluorescent units (RFU).

### Flow cytometry analysis

Cells were directly stained using FITC- or PE-conjugated monoclonal antibodies (mAbs). The following mAbs were used: CD29-PE (Serotec, USA), CD34-FITC (Dako, Denmark), CD45-PE (Serotec, USA), CD73-PE (BD Biosciences, UK), CD90-FITC (Serotec, UK), CD105-FITC (Serotec). Flow cytometry was carried out on a FACSCalibur (BD Biosciences, UK) and data were analyzed using WinMDI 2.8 software.

### Evaluation of the differentiation potential

To determine the differentiation capacity of MSCs before and after vitrification cells were seeded into 24-well plates and cultivated in osteogenic or adipogenic media. Osteogenic differentiation medium consisted of α-MEM supplemented with 10% FCS, 50 U/ml penicillin, 50 mg/ml streptomycin and 0.2 mM L-glutamine with special osteogenic supplements, like 20 mM ascorbic acid (Sigma), 10mM β-glycerolphosphate (Sigma) and 1 μM dexamethasone (Sigma). Following 21 days of culture with osteogenic supplements, two- and three-dimensional cultures were fixed in 4% neutral buffered formalin for 30 min at 4°C. Alkaline phosphatase expression was assessed using Fast Blue RR Salts / Naphtol kit (Sigma) during 30 min at room temperature in dark. Extracellular accumulation of calcium was assessed by von Kossa staining.

Adipogenic differentiation medium consisted of α-MEM supplemented with 10% FCS, 50 U/ml penicillin, 50 mg/ml streptomycin and 0,2 mM L-glutamine with adipogenic stimulants like 0.5mM 3-isobutyl-1-methyl-xanthine (Sigma), 1 μM dexamethasone (Sigma), 10 μg/ml insulin, and 100 μM indomethacin

(Sigma). Adipogenesis was evaluated morphologically after 21 days of culture by staining accumulated neutral lipids with Oil Red O (Sigma).

### Statistical analysis

Each experiment was performed in triplicate and repeated four times. Data was presented as M ± m. Statistical analysis was prepared using Student’s t-test. Data were considered significantly different if $p<0,05$.

## 3. RESULTS

### The choice of vitrification solution composition

At the first stage of study the mixtures of CPAs, which will prevent crystallization during rapid cooling and rewarming in the standard plastic cryovials were defined. Table 1 shows the results of visual analysis of crystallization during cooling and rewarming of CPA mixtures.

Table 1. Visual analysis of crystallization in CPA mixtures during rapid cooling and rewarming (n=5).

| Index | Solution composition | | | | | | | |
|---|---|---|---|---|---|---|---|---|
| | 10% Me$_2$SO | | | | | | | |
| | 0,5 M sucrose | | | | 1 M sucrose | | | |
| | 10% EG 10% 1,2-PD | 15% EG 15% 1,2-PD | 20% EG 20% 1,2-PD | 25% EG 25% 1,2-PD | 10% EG 10% 1,2-PD | 15% EG 15% 1,2-PD | 20% EG 20% 1,2-PD | 25% EG 25% 1,2-PD |
| Crystallization during cooling | + | – | – | – | – | – | – | – |
| Crystallization during rewarming | + | + | – | – | + | – | – | – |

Note: «+» - white and dimness sample;
«–» - transparent sample.

As shown in Table 1, crystallization was observed during cooling, when 0.5 M sucrose was combined with 10% EG and 10% 1.2-PD in the presence of 10% Me$_2$SO. Increasing concentrations of EG and 1.2-PD up to 15% in the medium eliminated crystallization during cooling, but ice crystals during rewarming were formed. Successful exclusion of the ice crystallization both at the cooling and rewarming stages was achieved by combining 0.5 M Sucrose with 20% or 25% EG and 1,2-PD. In the presence of 1 M sucrose and 10% Me$_2$SO no ice crystal formation was observed during cooling and rewarming, when concentrations of EG and 1.2-PD were equal to 5% or higher. As a result of screening two media containing the lowest concentrations of CPAs, which prevent crystallization during cooling and rewarming were chosen for following examination. Since the media contain Me$_2$SO, EG, 1.2-PD and sucrose they were named DEPS-1 and DEPS-2. The composition of the media is presented in Table 2.

Table 2. Composition of vitrification solutions

| Solution | Me$_2$SO | | EG | | 1,2-PD | | Sucrose | Total concentration of cryoprotectants, mol/L |
|---|---|---|---|---|---|---|---|---|
| | % w/v | mol/L | % w/v | mol/L | % w/v | mol/L | mol/L | |
| DEPS-1 | 10 | 1,4 | 20 | 4 | 20 | 2,6 | 0,5 | 8,5 |
| DEPS-2 | 10 | 1,4 | 15 | 2,4 | 15 | 2 | 1 | 6,8 |

### Characterization of MSCs

The defining characteristics of MSCs are appropriate immunophenotype, and the ability to differentiate along adipogenic, osteogenic and chondrogenic lineages in response to specific inductive stimuli. To confirm that isolated fetal fibroblast-like cells satisfy these criteria the immunophenotype and multilineage differentiation potential of these cells was assessed. The immunophenotypic analysis of 4 passage cells showed that they were 95% positive by CD29, CD73, CD90 and CD105 antigens and did not express hematopoietic markers CD34 and CD45.

After 21 days of osteogenic induction cells acquired several properties of bone cells - expressed alkaline phosphatase and accumulated mineralized extracellular matrix with calcium identified by von Kossa staining. In response to adipogenic stimuli cells accumulated intracellular lipid droplets, which were positively stained by Oil Red O.

### Effect of vitrification on MSCs viability rate, metabolic activity and specific properties

The viability rate of MSCs in control group (prior to cryopreservation) assessed by Trypan Blue was 90.3±2.9%. The intensity of AB fluorescence reflecting metabolic activity was 29630±3499 RFU and the ability to adhesion was 94.2±2.8% (Table 3). After exposure to both vitrification media and washing-out procedure (without cooling and rewarming) all viability parameters decreased for 20% comparing to control. More pronounced differences in solutions efficiency were revealed after vitrification and followed CPAs removal. After vitrification in DEPS-1 the viability of the cells decreased for 20%, metabolic activity – for 38%, adhesion ability – for 39% comparing to control. After Vitrification in DEPS-2 the viability dramatically decreased for 50%, metabolic activity – for 75%, adhesion ability – for 60% comparing to control. It should be mentioned that during thawing patterns of crystallization (dimness, white color) were visually detected for samples vitrified in DEPS-2.

Table 3. Effect of exposure to vitrification solutions and vitrification on viability of MSCs (n=15).

| Groups | Viability, % | Alamar Blue, RFU/well ×$10^3$ (% to the control) | Ability to adhesion,% |
|---|---|---|---|
| Control | 90,3 ± 2,9 | 29.6 ± 3.5 (100) | 94,2 ± 2,8 |
| Exposure to vitrification solutions + CPAs removal | | | |
| DEPS-1 | 71,7 ± 2,1* | 23.7 ± 3.9 (80) | 75,4 ± 4,1* |
| DEPS-2 | 71,8 ± 2,6* | 25.5 ± 2.5 (86) | 77,9 ± 4,4* |
| Exposure to vitrification solutions + vitrification + CPAs removal | | | |
| DEPS-1 | 70,6 ± 2,8* | 18.4 ± 4.9 (62)* | 55,1 ± 5,9* |
| DEPS-2 | 39,9 ± 4,1* | 7.4 ± 1.9 (25)* | 35,5 ± 3,5* |

Note: *- p<0,05 in comparison to the control.

Differences in the media efficiency were also revealed during culture of vitrified MSCs. After vitrification in DEPS-1 and further 24 hrs of culture about 60% of attached cells were flattened and had fibroblast-like morphology. After vitirification in DEPS-2 only 30% of attached cells were flattened, while the rest of cells remained rounded. During following culture, cells vitrified in DEPS-1 did not differ from control group, they proliferated and formed colonies. Cells vitrified in DEPS-2 had morphological properties of apoptosis and most of them degraded during further culture.

Taking into account that, DEPS-1 demonstrated higher cryopreservation efficiency, this medium was chosen for the evaluation of the differentiation capacity of MSCs after vitrification. It was revealed that vitrified in DEPS-1 cells under osteogenic stimuli expressed alkaline phosphatase and accumulated calcium (Von Kossa staining). After 21 days of culture in adipogenic medium the most cells were Oil Red O positive.

The suitability of the vitrification protocol with DEPS-1 was assessed for cryopreservation of MSCs encapsulated in alginate microspheres. Without further modification the protocol resulted in death of encapsulated cells. However, the viability and metabolic values similar to MSCs in suspension were achieved by increasing the time of exposure of alginate encapsulated cells with the multi-component solution.

## 4. DISCUSSION

Adherent cells isolated from human fetal tissues used in this study had the immunophenotype and multilineage differentiation potential that meet the criteria of mesenchymal stromal cells (Pittenger MF, Mackay AM, Beck SC, et al. 1999, Dominici M, Le Blanc K, Mueller I, et al. 2006). As a result of visual screening two multi-component CPA solutions, which avoided ice crystal formation during rapid cooling and rewarming were chosen for MSCs vitrification and called DEPS-1 and DEPS-2. The exposure of MSCs in both vitrification solutions and further CPAs removal procedure showed relatively low toxicity similar to other multi-component solutions described elsewhere (Takahashi T, et al. 1986, Wusteman M, et al. 2003). Further vitrification allowed identifying some advantages of DEPS-1. The application of DEPS-1 for vitrification can preserve the viability and metabolic activity of MSCs as well as their capacity to multilineage differentiation. It should be mentioned that values of viability obtained in the study after vitrification in standard plastic cryovials were similar to those when MSCs were vitrified in open-pulled straws (Todorov P, et al. 2010). The minimal adaptation of vitrification protocol by increasing the exposure time with DEPS-1 led to successful cryopreservation of MSCs encapsulated in alginate microspheres.

## 5. CONCLUSIONS

The protocol for vitrification of MSCs in multi-component CPA solutions, suitable for both cell in suspensions and encapsulated in alginate microspheres was developed. These multi-component solutions consisted of $Me_2SO$, EG, 1.2-PD and sucrose are promising for low temperature preservation of more complex MSCs – based tissue engineered constructs.

## 6. REFERENCES

Skorobogatova N, Novikov A, Fuller B, Petrenko A. 2010, Importance of a three-stage cooling regime and induced ice nucleation during cryopreservation on colony-forming potential and differentiation in mesenchymal stem/progenitor cells from human fetal liver, *CryoLetters*. 31(5): 371-379.

Fahy GM, MacFarlane DR, Angell CA et al. 1984, Vitrifications as an approach to cryopreservation, *Cryobiology*. 21(4): 407–426.

De Graaf IAM, Draaisma A, Schoeman O. et al. 2007, Cryopreservation of rat precision-cut liver and kidney slices by rapid freezing and vitrification, *Cryobiology*. 54(1): 1–12.

Song YC, Chen ZZ, Mukherjee N. et al. 2005, Vitrification of tissue engineered pancreatic substitute, *Transplant. Proc.* 37(1): 253–255.

Pittenger MF, Mackay AM, Beck SC, et al. 1999, Multilineage potential of adult human mesenchymal stem cells, *Science*. 284(5411): 143-147.

Dominici M, Le Blanc K, Mueller I, et al. 2006, Minimal criteria for defining multipotent mesenchymal stromal cells. The International Society for Cellular Therapy position statement. *Cytotherapy.* 8(4):315-317.

Takahashi T, Hirsh A, Erbe EF et al. 1986, Vitrification of human monocytes, *Cryobiology*. 23(2): 103–115.

Wusteman M, Pegg D, Wang L-H. et al. 2003, Vitrification of ECV304 cell suspensions using solutions containing propane-1,2-diol and trehalose, *Cryobiology*. 46(2): 135–145.

Todorov P, Hristova E, Konakchieva R, et al. 2010, Comparative studies of different cryopreservation methods for mesenchymal stem cells derived from human fetal liver, *Cell Biol Int.* 34(5):455-62.

070

# Safety and Quality Assurance in Donation, Harvest and Preservation of Cells and Tissues of Human Origin - A Review of Own Experience

**Měřička P., Straková H., Štěrba L.**

Tissue Bank University Hospital, Hradec Králové, 500 05 Hradec Králové, Czech Republic

## ABSTRACT

The authors review their own experience with implementation of the quality and safety assurance system in donation, harvest, further processing and distribution of cells and tissues of human origin intended for clinical application in man defined in the European Union by Directives 2004/23/EC, 2006/17/EC and 2006/86/EC. The issue of safety and quality has been systematically monitored and analyzed by authors with the aim to achieve compliance with the directives. In the year 2004 the Tissue Bank was granted the temporary licence by the Ministry of Health that covered both minimally manipulated cell and tissue grafts and cells expanded in vitro. As the new harmonized national legal norms came into force in 2008 the Tissue Bank was obliged to apply for a new licence at the State Institute for Drug Control. This licence was granted after 2.5 year lasting process and covered exclusively minimally manipulated grafts. In vitro expanded cells that are now classified as advanced medicinal products were a subject of separate licensing process that was successfully completed in 2011.

## 1. INTRODUCTION

Requirements on quality and safety assurance in donation, harvest, further processing and distribution of cells and tissues of human origin intended for clinical application in man were defined in the European Union (EU) by the Directive 2004/23/EC (European Parliament and Council, 2004) and by technical Directives 2006/17/EC and 2006/86/EC (European Commission 2006). The issue of the quality and safety of cell and tissue grafts was discussed earlier, however, especially within voluntary tissue bank associations (European Association of Tissue Banks, 1995) and within the European Council (Roscam Abbing, 1995). These discussions led to establishing and/or modifying existing standards of these organizations and to establishing of the Standards of the European Council (EC 2002). The existence of these standards helped in the process of preparation of EU Directives and harmonized national legal norms of the EU member states. In the Czech Republic temporary licences for tissue banks have been issued by the Ministry of Health since 2004, i.e. immediately after appearance of the Directive 2004/23/EC. After the harmonized national legal norms (Act No. 296/2008 and Decree of the Ministry of Health No. 422/2008, Ministry of Health of the Czech Republic, 2008) came into force all tissue banks were obliged to apply for a new licence issued by a State Institute for Drug Control, that became a competent authority for licensing tissue and procurement establishments. In the Tissue Bank of the University Hospital Hradec Králové the issue of safety and quality assurance was systematically monitored and analyzed with the aim to achieve compliance with the new quality and safety requirements (Měřička, 1984, Měřička et al., 2002,2003, Bláha et al., 2003, Měřička, 2006a,b, Měřička, Špatenka and Navrátil, 2011, Měřička, Navrátil and Špatenka, 2011) and to preserve the most of activities performed in the tissue bank before and reviewed in 2000 (Měřička, 2000). This paper is focused on safety and quality assurance of minimally manipulated grafts as substantially manipulated cells, i.e. cells expanded in vitro, such as cultured articular cartillage chondrocytes are now regarded as advanced medicinal products and are not regulated by the above mentioned directives and harmonized national norms.

## 2. METHODS

On basis of anticipated development of standards and legal norms regulating the process of harvesting and processing human cells and tissues the premises of the Tissue Bank of the University Hospital Hradec Králové established in 1952 by prof. R. Klen (Měřička 2000, 2008, 2011) were rebuilt in the years 2000-2002 (Měřička 2006 a,b., Měřička et al.2007). The standards of the International Society for Pharmaceutical Engineering (ISPE) (ISPE 1999) were applied in planning this reconstruction. Processing of cells and tissues is now made exclusively in the clean room facility of the tissue establishment with a processing area of grade A with background B checked regularly at rest and at operation conditions (Fig. 1). The bank was granted temporary multitissue bank licences of the Ministry of Health in the years 2004, 2006 and 2007 and received a registration number MTB 06. The last one was valid until completion of the new licensing process. In April 2009 the application for a new multitissue bank licence was sent to the State Institute for Drug Control. Many attachments documenting implementation of the quality assurance system were enclosed, such as Tissue Establishment and Diagnostic Laboratories Site master files, metrology master plans, specifications of the collected cells and tissues and processed cell and tissue grafts, validated standard operating procedures for processing of cell and tissue grafts, information leaflets for clinical users of cell and tissues grafts, template forms for reporting serious adverse reactions and events, references on clinical application of different types of cells and tissues, copies of existing contracts between the tissue establishment and procurement establishments and/or diagnostic laboratories. After withdrawal of all shortcomings in technology and documentation identified by the State Institute for Drug Control before and during inspection on place performed in 2010 the new licence was granted in November 2011.

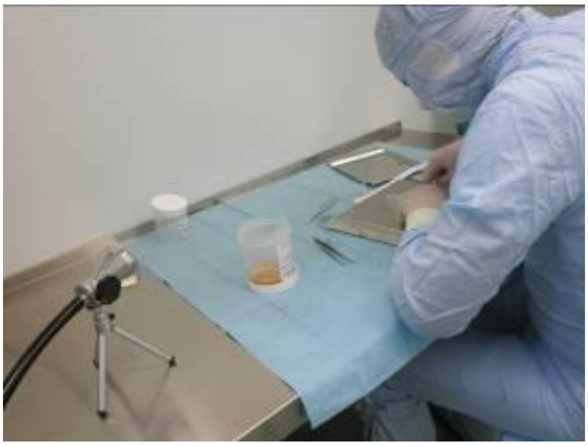

Figure 1a

Figure 1b

Figure 1a,b. Processing of solid tissue grafts is made on a stain-less steel table covered with sterile disposable sheets in a processing area of the grade A with the background B. The clean-room operator wears sterilized anti-emission garment. The quality of environment during operation can be checked by a portable particle counter equipped with a data analysis software (on the left) or by aeroscopy (on the right)

## RESULTS

The new licence was published on the website of the State Institute for Drug Control in November 2011 (State Institute for Drug Control, 2011). Spectrum of types of cells and tissues approved to be collected and processed in comparison with the previous situation is summarized in the Table I. Harvesting of solid tissues for implantation is approved to be performed exclusively at premises of operating rooms with controlled quality of environment and is followed by aseptic processing in the clean-room facility of the tissue establishment (Figure 1). The approved storage technology for cells and tissues is presented in Figures 2 and 3. Long–term storage of cryopreserved viable cells and tissues is performed at liquid nitrogen temperatures, preferably in the vapour phase of liquid nitrogen (Figure 2). The large liquid nitrogen storage containers are filled automatically from the low pressure back-up vessels connected with an external tank containing 10 tons of liquid nitrogen (Figure 4). In cryopreservation of cell suspensions, such as haematopoietic cells and in cryopreservation of vascular tissue grafts certified double bags are used exclusively. Deep frozen musculoskeletal tissues are stored typically in transparent certified plastic double bags at -80°C in the low temperature cabinets with the liquid nitrogen emergency back-up cooling system (Figures 2, 3).

Table I. Spectrum of collected and processed tissues

| Type of cells or tissues | Temporary licence by the Ministry of Health (until November 2011) | New licence by the State Institute for Drug Control (since November 2011) |
|---|---|---|
| Haematopoietic cells and donor lymphocytes | Yes | Yes |
| Reproductive cells (sperm) | Yes | Yes |
| Musculoskeletal tissue | Yes | Yes |
| Cardiovascular tissue | Yes | Yes |
| Biological skin covers (skin and chorioamnion) | Yes | Yes |
| Endocrine tissue-parathyreoid gland | Yes | No |
| Cultured cells (articular cartilage chondrocytes) | Yes (until December 2008) | No * |

* approved in March 2011 in a separate approval process

Figure 2. The cryostorage facility of the tissue establishment

Figure 3. Deep frozen musculoskeletal tissue grafts are stored in certified double plastic bags put into stain-less steel shelves

The spectrum of approved testing methods described in the European and/or Czech Pharmacopoiea (Czech Pharmacopoiea, 2009) is summarized in the Table II. Control of the environment in the procurement and processing facilities is performed by aeroscopy and particle counting. The grafts are distributed on basis of individual orders of physicians of potential hosts by ambulances of the Medical Emergency Service of the Hradec Králové District. The number of processed cell and tissue grafts in 2011 and the number of grafts delivered for clinical application in the same year is quoted in the Table III. The detailed data are available in the annual report of the tissue establishment (University Hospital Hradec Králové, 2012).

Table II. Application of viability and sterility tests in different types of cells and tissues

| Control test | Haematopoietic cells | Sperm | Solid tissue |
|---|---|---|---|
| Flow cytometry | Yes | Yes | N.A. |
| Colony formation | Yes | N.A. | N.A. |
| Sterility (Paul Ehrlich Institute method) | Yes | N.A. | Yes |

N.A. – not applicable

Table III. The number of cell and tissue grafts processed and delivered for clinical application in 2011

| Type of cells or tissues | No. of grafts processed | No. of grafts delivered | Type of user |
|---|---|---|---|
| Haematopietic cells and donor lymphocytes | 337 | 223 | Haematology transplantation unit |
| Reproductive cells (sperm) | 44 | 17 | IVF Centres |
| Musculoskeletal tissue | 365 | 378 | Orthopaedic, traumatology, neurosurgery and ophthalmology departments |
| Cardiovascular tissue | 2 | 1 | Vascular surgery department |

## 3. DISCUSSION

The new quality and safety requirements set by the European Union Directives and Czech national harmonized legal norms led to the most radical changes in the practice of the Tissue Bank University Hospital Hradec Králové in its 60-years old history. After completing of the licensing process the spectrum of collected and processed minimally manipulated grafts remained unchanged, however with the exception of parathyroid gland. On basis of this result the Ministry of Health of the Czech Republic confirmed the registration number of the multitissue bank MTB 06 for an unlimited time in January 2012. The cultured articular cartilage chondrocytes that were classified as advanced medicinal products were a subject of separate approval process successfully completed in 2011 (Table I). Although the principles of the quality and safety assurance system were implemented before the issue of national harmonized legal norms and the tissue bank has used clean-room technology since reconstruction completed in 2003 (Měřička 2006 a,b, Měřička et al., 2007) and self evaluation by comparison with the requirements of the European Quality System for Tissue Banking (European Commission, 2007) was performed many corrective actions were necessary to reach the quality and safety level set by the State Institute for Drug Control in the licensing process. The requirement to harvest solid tissues only in facilities with controlled environment led to considerable change in organization of tissue collection (Měřička, Špatenka and Navrátil, 2011). In banking of viable cells the corrective actions were aimed to establishing safe conditions for long-term storage of viable cells and tissues, using exclusively temperatures below -140°C and /or elimination of storage at temperature -80°C applied previously especially for storage of cells originating from patients with laboratory signs of severe infection (Měřička et al 2003, Měřička 2006) and to prevention of cross-contamination during storage by double bagging and preference of storage in the vapour phase of liquid nitrogen. Additional measures were establishing of continuous monitoring of temperatures inside equipment, setting temperature alert and alarm limits and 24 hour access of persons able to manage alarm situations. In banking musculoskeletal tissues the major change was replacing the packaging material - double peel packs (Steriking, Wipak Medical Finland) used since the end of the 80´s (Pařízek et al., 1989) by the newly developed certified transparent double freezing bags (Eva bags, Maco Pharma, France). This change made it possible to extend the shelf life of deep frozen grafts from 2 to 5 years. In evaluation of serious adverse reactions and events the Failure Mode and Effect Analysis method (FMEA) was introduced. The requirement of public availability of data on activities of the tissue establishment was met by publication of annual reports on the website of the University Hospital (University Hospital Hradec Králové, 2012). The major disadvantage of the process was considerable increase of liquid nitrogen consumption that required installation of 10-ton liquid nitrogen tank instead of the previously used 6-ton tank while the filling interval remained unchanged (Figure 4). The increase of manufacturing costs was caused also by using certified packaging materials and control tests upgraded according to the new requirements of the European Pharmacopoiea.

Figure 4. Filling of the external tank for 10 tons of liquid nitrogen from a mobile tank is performed in one month intervals

## 4. CONCLUSIONS

The new quality and safety requirements set by European Union Directives caused very radical changes in practice of tissue banks. The authors achieved compliance with the requirements before and during a 2.5year lasting licensing process due to following measures: reconstruction of the tissue bank making possible to combine cryotechnology with the clean-room technology, establishing of the quality assurance system, reorganization of tissue collection system, use of certified packaging material for collected and processed cells and tissues, establishing safe conditions for long-term storage of viable cells and tissues preventing cross-contamination, distribution of tissues in cooperation with the local medical emergency service, publication of annual reports on tissue bank activities on a website of the University Hospital.

## 5. REFERENCES

Bláha M. et al. 2003, The risk of infection transmission from blood progenitor cell concentrates. *Journal of Haemotherapy and Stem Cell Research* 12: 161-164.

Council of Europe 2002, *Guide to Safety and Quality Assurance for Organs, Tissues and Cells, 1st edition,* Council of Europe Publishing, Strasbourg: 87 p.

*Czech Pharmacopoeiea 6th edition* 2009, Grada Publishing, Praha: 3942 p. (In Czech).

European Association of Tissue Banks 1995, *General Standards for Tissue Banking,* ÖBIG – Transplant, Vienna.

European Commission 2006, *Commission Directive 2006/17/EC of 8 February 2006 implementing Directive 2004/23/EC of the European Parliament and Council as regards certain technical requirements for donation, procurement and testing of human tissues and cells,* O.J.L. 38: 40–52.

European Commission 2006, *Commission Directive 2006/86/EC of 24 October 2006 implementing Directive 2004/23/EC of the European Parliament and of the Council as regards traceability requirements, notification of serious adverse reactions and events and certain technical requirements for the coding, processing, preservation, storage and distribution of human tissues and cells,* O.J.L. 294: 32-50.

European Commission (EQSTB) 2007, De By T., Fernandez C., Navarro A. et al.: *Guide for Auditing Tissue Establishment,* Service Point Facilities Management Iberica, Barcelona: 113 p.

European Parliament and Council 2004, *The Council: Directive 2004/23/EC of the European Parliament and of the Council on Setting Standards of the Quality and Safety for the Donation, Procurement, Processing, Preservation, Storage and Distribution of Human Tissues and Cells,* Strasbourg, O.J.L.102: 48-58.

ISPE Headquaters/ISPE European Branch Office 1999, *Pharmaceutical Engineering Guides for New and Renovated Facilities, Vol. 3 Sterile Manufacturing Facilities, First Edition,* Tampa, Fl.,/The Hague, The Netherlands: 162 p.

Měřička P. 1984, Quality Control of Freeze-dried Tissue Grafts, In: *Proc. 16th Int. Congr. Refrig., Paris 1983, Fr.*, vol.3, International Institute of Refrigeration, Paris:161-165.

Měřička P. 2000, Brief History of the Tissue Bank, Charles University Hospital Hradec Králové, Czech Republic, *Cell and Tissue Baning* 1:17-25.

Měřička P., Straková H., Čermák P. et al. 2002, New Safety Assurance for Biological Skin Covers, *Acta Chir. Plast*. 44:23-29.

Měřička P., Bláha M., Vávra L., Štěpánová, V. 2003, Our System of Cross-contamination Prevention during Storage of Haematopoietic Progenitor Cells – Paper ICR 0302, In: Grof G., Menzer M. (eds), *CD: 21st IIR International Congress of Refrigeration, 1st edition, Washington D.C.*, International Institute of Refrigeration, Paris: 1-8.

Měřička P. 2006, *Contribution to Safety Assurance in the Cryopreservation of Cells and Tissues Used for Clinical Transplantation. Doctoral (Ph.D.) Thesis Summary*, Nucleus HK, Hradec Králové, 36 p.

Měřička P. 2006, Current Trends in Safety Assurance for Tissue Grafts Used in Burn Treatment, *Acta Chir. Plast.* 48 (2):51-58.

Měřička P., Bláha M., Straková H. et al. 2007, New Safety Assurance for Processing and Cryopreservation of Cells and Tissues used in Clinical Transplantation, *Transpl. Int*. 20 /Suppl.2: 325.

Měřička P. 2008, History of the Tissue Bank. Hradec Králové Medical Priorities (2), *Scan* 2:16-17 (In Czech).

Měřička P. 2011, Rudolf Klen. In:. *Encyclopaedia of the town Hradec Králové A-M*, Garamon Hradec Králové: 239 (In Czech).

Měřička P., Straková H., Lánská M., Vokurková D., Pecka M., Bláha M., Žák P., Jebavý L. 2011, Testing of cryopreserved concentrates at infusion leads to standardization of engraftment in autologous peripheral blood progenitor cell transplantation, *The 23rd IIR International Congress of Refrigeration Prague, 1st edition,* International Institute of Refrigeration IIR/IIF, Prague:1-4.

Měřička P., Navrátil P., Špatenka J. 2011, Legislation of Tissue Donation and Harvest in the Czech Republic. In: Baláž P., Janek J., Adamec M. et al. *Organ Harvests for Transplantation,* Karolinum Praha: 223-239 (In Czech).

Měřička P., Špatenka J., Navrátil P. 2011, Organization and Surgical Technique of Tissue Harvest within a Multi-organ Harvest. In: Baláž P., Janek J., Adamec M. et al. *Organ Harvests for Transplantation,* Karolinum Praha: 240-251 (In Czech).

Ministry of Health of the Czech Republic 2008, *Act No. 296/2008 Sb. on Setting Requirements for Assurance of Quality and Safety of Human Tissues and Cells Intended for Application in Man and on Change of Related Acts (Act on Human Tissues and Cells),* Act Collection of the Czech Republic, Part 97: 4441-4459 (In Czech).

Ministry of Health of the Czech Republic 2008, *Decree No. 422/2008 Sb. on Setting Requirement for Assurance of Quality and Safety of Human Tissues and Cells Intended for Application in Man*, Act Collection of the Czech Republic, Part 138:6941-6979 (In Czech).

Pařízek J., Měřička P., Špaček J., Němeček S., Eliáš P., Šercl, M. 1989, Xenogeneic Pericardium as a dural Substitute in Reconstruction of Suboccipital Dura Mater in Children, *J. Neurosurg*. 70:905-909.

Roscam Abbing H.D.C. 1995, Human Tissue and Clinical Medicine: An European Regulatory Perpective. In: Byk, C. jr., Lechat, A., von Versen, R (eds), *4th International Conference European Association of Tissue Banks Leuven, Belgium, October 15-18,* Monduzzi Editore, International Proceedings Division, Bologna: 3-9.

*State Institute for Drug Control website 2011,* List of licence holders in the domain of Human cells and tissues,http://www.sukl.cz/prehled-drzitelu-povoleni-cinnosti-v-oblasti-lidskych-tkani (In Czech).

*University Hospital Hradec Králové website 2011,* Tissue establishment annual report: http://www.fnhk.cz/tku/vyrocni-zpravy/vyrocni-zprava-za-rok-2011 (In Czech).

# LIQUID HYDROGEN

067

# Thermophysical Properties of Hydrogen and Deuterium at all Ortho-Para Compositions

**Leachman J., Richardson I.**

HYdrogen Properties for Energy Research (HYPER) Laboratory, Washington State University, PO Box 642920, Pullman, WA, 99164-2920, United States of America

## ABSTRACT

Hydrogen, deuterium, and tritium have two separable nuclear-spin isomers, denoted by ortho and para, with potentially significant differences in thermophysical properties. These differences are most apparent for storage applications at cryogenic temperatures where the equilibrium mixture concentration changes substantially with temperature. Property differences approaching 30 % can be observed between the ortho-para forms. Recent advances in the equations of state for hydrogen and deuterium have created an opportunity to couple statistical models of ideal-gas properties with real fluid models of non-ideal property behaviour. The resulting formulations are capable of high-accuracy property estimations at all ortho-para compositions. Methodologies for implementing the models are discussed and comparisons of the property calculations are presented.

## 1. INTRODUCTION

Discovering the allotropic nuclear spin-isomers of the hydrogen molecule was one of the greatest scientific accomplishments of the 20th century. The history of this discovery is an excellent story which was recently documented by Gearhart in 2010. In short, statistical derivation of hydrogen molecule heat capacities was a substantial proof of quantum mechanics such that the Nobel Committee awarded Werner Heisenberg the 1932 Nobel Prize in Physics, “for the creation of quantum mechanics, the application of which has, inter alia, *led to the discovery of the allotropic forms of hydrogen*” (emphasis added) (Nobelprize.org).

Isotopic molecules of hydrogen including protium, deuterium, and tritium, have a nuclear spin function that creates parity with the rotational function for the molecules. This parity requires hydrogen molecules to occupy either the even ($J = 0,2,4...$) or the odd ($J = 1,3,5...$) rotational energy levels. An additional energy is required to change the nuclear spin function thereby prohibiting exchange between the even and odd forms. In the absence of an intermediary catalyst these even and odd forms of hydrogen can be separated and preserved; forming pure fluids in quasi-equilibrium. Bonhoeffer and Harteck chose the names orthohydrogen and parahydrogen for the different fluids; “ortho” to represent the dominant concentration at room temperature, and “para” the lower concentration. This designation results in considerable confusion because the association changes between isotopes. Hydrogen and tritium obey Fermi-Dirac statistics so orthohydrogen and orthotritium have odd rotational energy levels and parahydrogen and paratritium have even rotational energy levels. Deuterium, having only one neutron in each nucleus, obeys Bose-Einstein statistics resulting in orthodeuterium with even rotational energy levels while paradeuterium has odd rotational energy levels. At least one hydrogen specific publication has made this error (Le Roy *et al.* 1990).

The differences in macroscopic thermophysical properties between ortho and para forms can approach 30 % for ideal-gas properties closely coupled to rotational energy. For example, Figure 1 shows ideal-gas isobaric heat capacity predictions for various orthohydrogen-parahydrogen and orthodeutrium-paradeuterium concentrations at cryogenic temperatures. A curve labelled “normal” has the ortho-para concentration of a sample in equilibrium at room temperature; for hydrogen and tritium the concentration is 3:1 ortho-para associated with the nuclear degeneracy of the molecule and for deuterium the ratio is 6:3 ortho-para. As the temperature of the sample is reduced, insufficient energy is available to occupy higher energy modes. Thus the equilibrium sample concentration will change if the fluid is allowed to slowly self-catalyze or is exposed to a catalyst. The equilibrium concentration at a given temperature is specified by the right hand axis of Figure 1. Below 30 K equilibrium samples will be nearly pure orthodeuterium and parahydrogen as these forms are associated with the J = 0 rotational energy level. Significant features of Figure 1 are the heat capacity curves labelled "equilibrium" displaying a substantial increase in heat capacities below 100 K. These curves are historically misleading and yet another source of significant confusion. If a sample of hydrogen is exposed to a perfect catalyst, the molecules can readily move between ortho and para forms and require an additional heat of conversion. Although the equilibrium curves reflect this change in heat capacity, the values should be thought of as effective heat capacities. A sample of hydrogen having the equilibrium concentration would display a heat capacity between the ortho and para curves unless perfectly catalyzed through a change in equilibrium composition. In practice it is more common to utilize non-equilibrium heat capacities, measure the change in mixture composition, and account for the heat of conversion.

The differences in thermophysical properties between ortho and para forms must be accounted for in the engineering of cryogenic systems that utilize these fluids. Recently, Equations of State (EOS) for hydrogen and deuterium have been developed that account for property differences between ortho and para forms (Leachman *et al.* 2009, Richardson *et al.* 2012). This development has enabled the opportunity to combine statistical thermodynamic predictions of ideal-gas properties with functions describing real-fluid behaviour to create the first ever reference quality property models applicable to hydrogen and deuterium at all ortho-para concentrations. Section 2 describes modern EOS formulations and how the separate ideal-gas functions and real-fluid functions are combined. Section 3 shows the results of this combination on thermophysical property predictions.

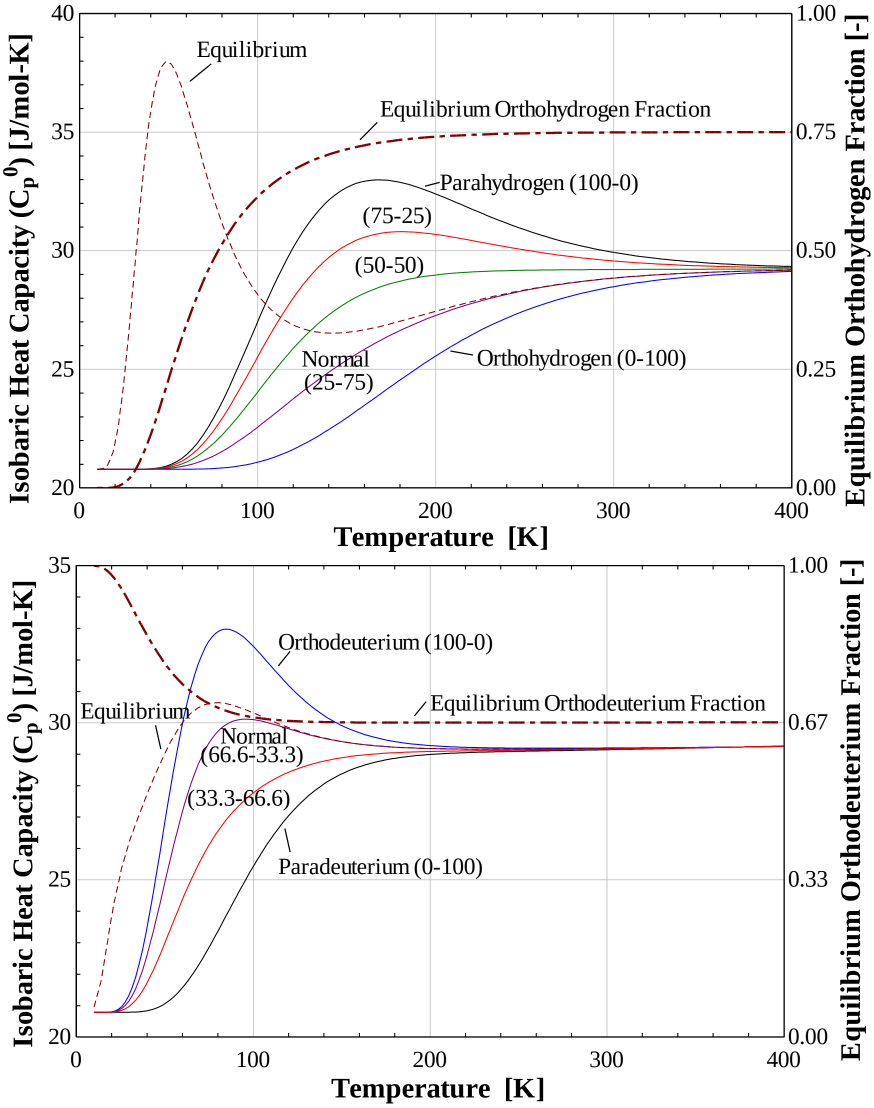

Figure 1. (Top) Ideal-gas isobaric heat capacities at various orthohydrogen-parahydrogen concentrations and equilibrium concentrations versus temperature. (Bottom) Ideal-gas isobaric heat capacities at various orthodeuterium-paradeuterium concentrations and equilibrium concentrations versus temperature. (this work)

## 2. HYBRID EQUATIONS OF STATE (EOS)

Reference quality Equations of State (EOS) for the para, ortho, and normal forms of hydrogen and deuterium have recently been developed (Leachman *et al.* 2009, Richardson *et al.* 2012). The details of these formulations can be found in the original publications and are not repeated here for brevity. The purpose of this section is to describe how to supplement the formulations with a statistical thermodynamics model to enable property calculations at all ortho-para compositions.

### 2.1. Ideal-Gas Properties:

It is standard for modern reference quality EOS to utilize the reduced Helmholtz free energy $\alpha$:

$$\frac{a(T,\rho)}{RT} = \alpha(\tau,\delta) , \tag{1}$$

Where $a$, $R$, $T$, $\tau$ , and $\delta$ are the Helmholtz free energy, ideal-gas constant, temperature, reciprocal reduced temperature, and reduced density, respectively:

$$\tau = \frac{T_\mathrm{c}}{T} , \tag{2}$$

$$\delta = \frac{\rho}{\rho_\mathrm{c}} . \tag{3}$$

The subscript c denotes a critical point property. The reduced Helmholtz free energy is composed of two parts, the ideal-gas contribution $\alpha^0$ and the residual contribution $\alpha^\mathrm{r}$:

$$\alpha(\tau,\delta) = \alpha^0(\tau,\delta) + \alpha^\mathrm{r}(\tau,\delta) . \tag{4}$$

The residual contribution to the Helmholtz free energy is based on nonlinear regressions of experimental data. The form and coefficients for the residual contribution should be utilized from the original publications (Leachman et al. 2009, Richardson et al. 2012). For most fluids, the ideal-gas contribution is also based on nonlinear regressions of experimentally determined ideal-gas heat capacity data to a function of the form:

$$\alpha^0 = \ln\delta + 1.5\ln\tau + a_1 + a_2\tau + \sum_{k=3}^{N} a_k \ln\left[1 - \exp\left(b_k\tau\right)\right] . \tag{5}$$

where $a_k$ and $b_k$ are fitted coefficients. Equation (5) is computationally efficient and utilizes different coefficients for the separate para, ortho, and normal forms. However, for the hydrogen and deuterium EOS formulations it was not necessary to fit Equation (5) to experimental measurements. The ideal-gas heat capacities for molecules as simple as hydrogen and deuterium can be calculated theoretically to orders of magnitude better accuracy than the very best experimental measurements. Therefore, calculated heat capacity data for the para, ortho, and normal forms were used in the regressions utilizing the most recent coupled ro-vibrational energy levels available (Le Roy *et al.* 1990).

The above approach allows for computationally efficient properties of the common para, ortho, and normal forms however does not allow for calculation at all mixture compositions due to an infinite set of coefficients that would be required for Equation (5). To enable researchers and industry to calculate properties at all para-ortho compositions it is necessary to calculate the ideal-gas contribution to the Helmholtz free energy, $\alpha^0$, directly from the ro-vibrational energy levels via statistical thermodynamics. Following the method established by Le Roy *et al.* 1990, the molecular partition function, $Z$, is written as

$$Z_n = \sum_v \sum_J i\left[(2J+1) {E_{vJ}}^n e^{-E_{vJ}/kT}\right] , \tag{6}$$

where $n$ denotes the moment 0-2 of the partition function, $v$ and $J$ are the respective vibrational and rotational energy levels, $i$ is the nuclear degeneracy, $E_{vj}$ is the tabulated energy level, $k$ is Boltzmann's constant, and $T$ is the temperature. For a sample in equilibrium, the moments of the partition function 0-2 are implemented directly as these include both ortho and para forms, however all other compositions must be summed for only even or odd rotational energy levels for the respective ortho-para forms and the result be treated as an ideal mixture. To utilize the partition function for calculation of the reduced ideal-gas Helmholtz free energy in Equation (4) several steps are necessary:

$$\alpha^0 = \frac{a^0}{Rm_wT} + \ln\left(\frac{\delta}{\delta^0}\right) \tag{7}$$

where $a^0$ is the ideal-gas Helmholtz free energy, $m_w$ is the molecular weight, and $\delta^0$ the reduced density of an ideal gas at the corresponding pressure and temperature. The ideal-gas Helmholtz free energy is:

$$a^0 = h^0 - RT - Ts^0 \tag{8}$$

where $h^0$, and $s^0$ are the ideal-gas enthalpy, and ideal-gas entropy respectively. These contributions are determined from the molecular partition function via:

$$h^0 = N_a\left[y_{para}\frac{Z_{para,1}}{Z_{para,0}} + y_{ortho}\frac{Z_{ortho,1}}{Z_{ortho,0}}\right] + \frac{5}{2}RT + h^0_{ref} \quad , \tag{9}$$

$$s^0 = -\left(\frac{g^0 - h^0}{T}\right) - R\ln\left(\frac{P}{P_{ref}}\right) + s^0_{ref} \tag{10}$$

where $y_{para}$ and $y_{ortho}$ are the respective molar fractions, $h^0_{ref}$ , $s^0_{ref}$ , $P_{ref}$ are arbitrary reference state values, and the ideal-gas Gibbs free energy, $g^0$ is

$$g^0 = -RT\ln\left[\left(y_{para}Z_{para,0} + y_{ortho}Z_{ortho,0}\right)\frac{\sqrt{m_w{}^3T^5}}{38.53986}\right]. \tag{11}$$

Equations (6)-(11) replace Equation (5) for calculating the ideal-gas contribution to the reduced Helmholtz free energy. The coefficients from Equation (5) were originally regressed utilizing data from Le Roy *et al.* 1990, therefore this is a substitution that may slightly increase the overall accuracy of the EOS formulations, although at a considerable increase in computational time.

## 2.2. Real-fluid Properties:

The difference in real-fluid properties between ortho-para forms is due to differences in rotational energies being substantial at low temperatures where limited energy levels are accessible. Although this difference primarily affects ideal-gas properties closely related to rotational energy levels, significant differences in real-fluid properties exist. The critical point and triple point are representative of these differences and listed in Table 1. The hydrogen points were measured by multiple experimentalists and the final points used by the EOS were tested for consistency with a Quantum Law of Corresponding States (QLCS) technique (Leachman *et al.* 2009). The differences between normal and equilibrium deuterium seem large compared with hydrogen considering the relatively small change in ortho-para concentration; this is likely due to experimental uncertainty and exemplifies the point that the differences in real fluid properties are small.

Several researchers have utilized differences in measured properties such as speed of sound or density to derive small differences in the Lennard-Jones potential for the ortho-para forms (Knaap and Beenakker 1961). The differences in Lennard-Jones potential between ortho-para forms are proportional to the molecular weights and have been utilized with the QLCS to estimate properties for other hydrogen forms (Souers 1985). As the molecular weight and temperature are increased, the momentum of the molecules is increased and the de Broglie wavelength, and associated effect of quantum mechanics, decreases. Thus, ortho-para effects for hydrogen are greater than deuterium, which are greater than tritium. A sufficient number of experimental measurements were available to account for these small differences when developing the EOS for orthohydrogen and parahydrogen. A true ortho-para mixture model for hydrogen must account for these differences in real-fluid properties and will be discussed in a separate publication (Leachman *et al.* 2012). Separate real-fluid models for the ortho-para forms of deuterium were not developed due to the estimated differences being smaller than the overall EOS uncertainty (Richardson et al. 2012).

Table 1. Critical and triple point properties for the ortho-para forms of hydrogen and deuterium.

| Fluid | $T_c$ [K] | $P_c$ [kPa] | $T_{tp}$ [K] | $P_{tp}$ [kPa] |
|---|---|---|---|---|
| Parahydrogen (Leachman *et al.* 2009) | 32.938 | 1285.8 | 13.8033 | 7.041 |
| Orthohydrogen (Leachman *et al.* 2009) | 33.22 | 1310.65 | 14.008 | 7.461 |
| Equilibrium deuterium (Souers 1985) | 38.262 | 1650 | 18.691 | 17.130 |
| Normal deuterium (Souers 1985) | 38.34 | 1665 | 18.73 | 17.150 |

## 3. PROPERTY PREDICTIONS FROM THE HYBRID EOS

In order to test the hybrid Equation of State (EOS), it is necessary to transform the reduced Helmholtz free energy to properties more useful to engineers. The entropy and enthalpy are determined via derivatives of the reduced Helmholtz free energy:

$$s = R\tau \left.\frac{d\alpha}{d\tau}\right|_{\delta} - R\alpha \quad , \tag{12}$$

$$h = \tau \left.\frac{d\alpha}{d\tau}\right|_{\delta} RT + \frac{P}{\rho} \quad . \tag{13}$$

The hybrid EOS is explicit in reduced density and temperature; however it is typically more convenient to utilize pressure as an input. The pressure is related to the reduced Helmholtz free energy via the equation

$$P = \rho RT\left(1 + \delta \left.\frac{d\alpha_r}{d\delta}\right|_{\tau}\right) , \tag{14}$$

which allows for the density to be implicitly solved with pressure and temperature inputs.

Figures 2 and 3 show the predicted entropies and enthalpies for the hybrid deuterium EOS versus temperature over a range of pressures. The residual contribution causes changes in pressure to have significant effects on the entropy and enthalpy. Below 70 K the entropy of paradeuterium is highest as the paradeuterium molecule remains locked in the first rotational energy level. The differences in predicted enthalpies shown in Figure 3 can be utilized to determine the enthalpy of conversion between paradeuterium and orthodeuterium. The enthalpy of conversion is only significant below 100 K because the molecules are primarily converting between the J = 0 and J = 1 rotational energy levels. Not enough energy is available to occupy higher rotational energy levels and the difference between the J = 0 and J = 1 levels is large. It should be noted that these are preliminary predictions as the full deuterium EOS is still pending review at the time this paper was written. The differences in enthalpies and entropies for the allotropic forms of hydrogen will be more significant than for deuterium. However the multiple real-fluid residuals for hydrogen require an extended scaling technique for reference quality predictions that will be presented in a separate publication (Leachman et al. 2012). However, the approach described here can readily be applied to hydrogen for the majority of engineering calculations as the real-fluid contributions are small.

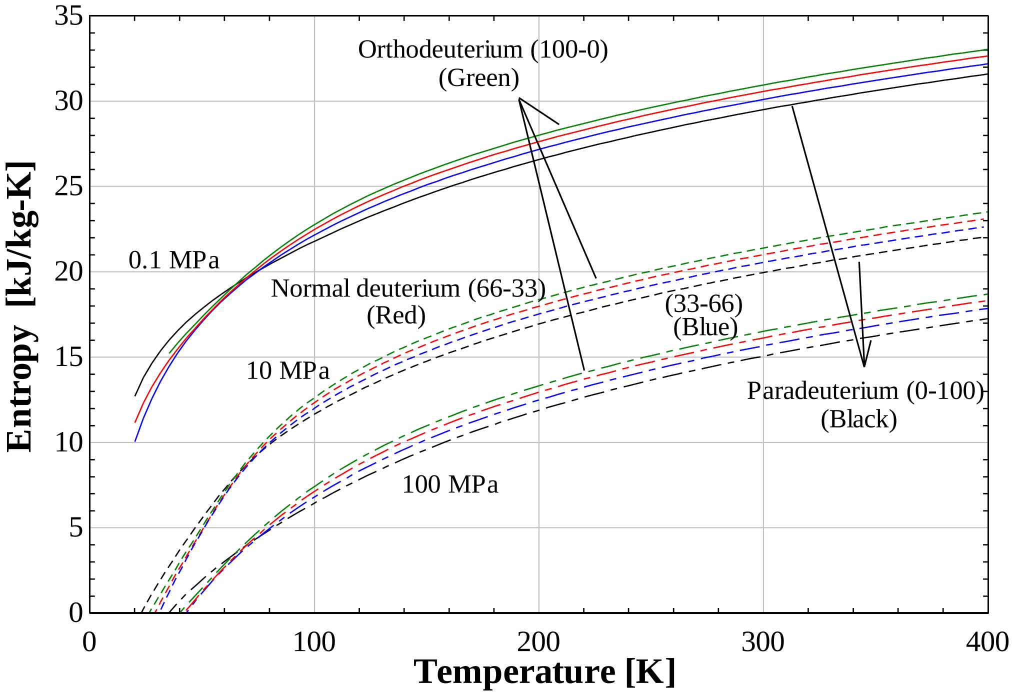

Figure 2. Predicted entropies plotted versus temperature for paradeuterium, a para-ortho deuterium mixture (33.3-66.6%), normal deuterium (66.6-33.3%), and orthodeuterium at 0.1, 10, and 100 MPa (this work).

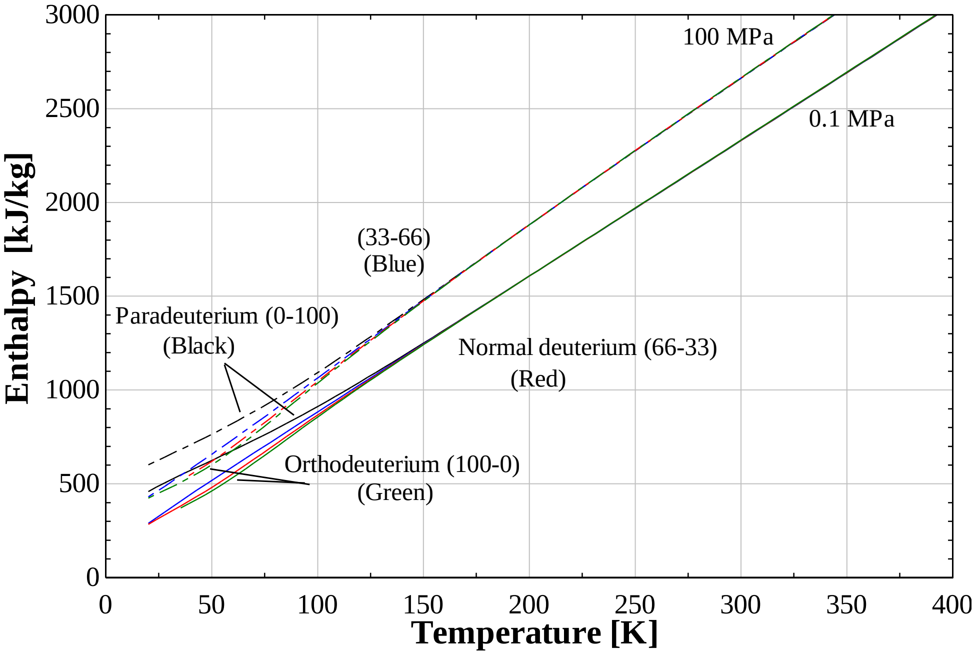

Figure 3. Predicted enthalpies plotted versus temperature for paradeuterium, a para-ortho deuterium mixture (33.3-66.6%), normal deuterium (66.6-33.3%), and orthodeuterium at 0.1, and 100 MPa (this work).

## 4. CONCLUSIONS

Recent developments in the equations of state for the allotropic nuclear spin isomers of hydrogen and deuterium have enabled development of an ideal mixture model applicable to all ortho-para concentrations. A hybrid equation of state was presented utilizing statistical thermodynamics to compute ideal-gas properties and an empirically regressed real-fluid residual function and predictions of the hybrid EOS for fluid deuterium were presented. The procedure has been implemented in the software package Engineering Equation Solver (EES) and is available as a distributable program (Klein 2011). Plans are in place to incorporate the model into the next release of REFPROP (Lemmon *et al.* 2008).

## 5. REFERENCES

Bonhoeffer K, Harteck P. 1929, Para-and ortho hydrogen, *Z. Phys. Chem. Abt.* 4(B):113.

Gearhart C. 2010, “Astonishing Successes” and “Bitter Disappointment”: The Specific Heat of Hydrogen in Quantum Theory, *Arch. Hist. Exact Sci.* 64: 113-202.

Klein S, 2011. Engineering Equation Solver (EES) Academic Professional V8.909-3D, F-Chart Software, Madison, WI.

Knaap H, Beenakker J. 1961, The Lennard-Jones 6-12 Potential Parameters of $H_2$ and $D_2$, *Physica* 27: 523-530.

Le Roy R, Chapman S, McCourt F. 1990, Accurate Thermodynamic Properties of the Six Isotopomers of Diatomic Hydrogen, *J. Phys. Chem.* 94: 923-929.

Leachman J, Jacobsen R, Penoncello S, Lemmon E. 2009, Fundamental Equations of State for Parahydrogen, Normal Hydrogen, and Orthohydrogen, *J. Phys. Chem. Ref. Data* 38(3): 721-748.

Leachman J, Richardson I, Essler J. 2012, Thermodynamic Properties of Parahydrogen-Orthohydrogen Mixtures, To be Submitted to *Fluid Phase Equilibria*.

Lemmon E, Huber M, McLinden M. (2008), Standard Reference Data Program #23, REFPROP Version 8.0. National Institute of Standards and Technology, Gaithersburg, Maryland.

Richardson I, Leachman J, Lemmon E. 2012, Fundamental Equations of State for Deuterium, To be submitted to *J. Phys. Chem. Ref. Data*.

Souers P, 1985. *Hydrogen Properties for Fusion Energy*, University of California Press, Berkeley, 375 p.

“Werner Heisenberg – Biography”. Nobelprize.org. 14 May 2012 http://www.nobelprize.org/nobel_prizes/physics/laureates/1932/heisenberg.html

080

# Principles for the Liquefaction of Hydrogen with Emphasis on Precooling Processes

**Walnum H.T.[*], Berstad D.[*], Drescher M.[*], Neksa P.[*], Quack H.[**], Haberstroh Ch.[**], Essler J.[**]**

[*]SINTEF Energy Research, Trondheim, Norway
[**]Technical University of Dresden, Dresden, Germany

## ABSTRACT

This paper elaborates a concept for designing efficient large scale hydrogen liquefaction plants, based on dividing the process into 4 independent stages and finding the optimum solution for each stage. The main focus is put on the precooling stage. Not because of its power consumption, but because it is the stage with the most degrees of freedom in design. Several processes have been discussed, mentioning some of the main advantages and disadvantages. One of the main challenges in efficient hydrogen liquefaction is light gas compression. This is unavoidable, since only light gases can provide cooling at the required temperature levels, but should be minimized by using heavier fluids where possible. Due to the higher exergy efficiency of compression compared to refrigeration, the hydrogen feed pressure should be as high as possible, as long as the pressure reduction in the liquefaction stage is performed by expansion machines instead of throttling.

## 1. INTRODUCTION

Hydrogen is considered to play an important role as an energy carrier in the future and could become an alternative to fuel, especially for the fossil fuel dependent passenger cars and utility vehicles [1]. Hence for the distribution of hydrogen and usage in the transport sector its energy density plays a considerable role. Even though hydrogen has a comparably high heating value its density is very low, which results in a rather low energy density compared to other fossil fuels. At its compressed state at 200 bar and 15 °C, hydrogen has an approximately 17 times lower energy density than liquid gasoline. Yet, the energy density can be increased significantly by liquefying hydrogen, which results in an approximately 5 times higher energy density at its liquid state than at its compressed state at 200 bar and 15 °C [2].

However, the liquefaction of hydrogen has its price, since hydrogen has the second lowest boiling point of all substances, with a boiling temperature of 20 K at atmospheric pressure. Only helium has a lower boiling point. On the other hand liquefied hydrogen provides advantages in efficient transport from the liquefaction site to a filling station. In addition it provides the flexibility of being provided either in liquid form or if needed vaporized and in compressed state. Here, a rather efficient pump could be applied for achieving the desired high pressure instead of a compressor. A study showing the competitiveness of liquefied hydrogen compared to distribution chain with compressed gas is show by Kramer [3].

Yet for hydrogen being able to play a major role in the transport sector a significant amount of liquid hydrogen must be available at a relatively competitive price. So far only a handful of liquefaction plants exist in Europe and Asia with a liquefaction capacity of 10.5 tons/day at the highest [4]. Hydrogen liquefaction plants with a capacity of up to 36 tons/day exist in the USA only [5]. Hydrogen liquefaction plants with higher capacity exist so far only on paper.

As a part of the EU-funded IDEALHY project a large scale liquefaction plant will be developed with a goal of reducing the required energy demand for liquefaction significantly compared to state of the art plants. Here the new process will make use of economy of scale as a capacity of 50 to 100 tons/day represents a scale-up of approximately 20 times to the most plants, which are in operation world wide. In addition, state-of the-art components and technologies will be applied.

However, before developing a new process the theoretical energy demand for the liquefaction process is investigated. For conduction this in a transparent approach, the liquefaction process is divided into several stages, such as: Hydrogen compression, pre-cooling, cryo-cooling and liquefaction. Each stage is individually discussed in a generic manner for illustrating the theoretical energy requirements and challenges.

Emphasis in this paper is placed on the pre-cooling stage of the liquefaction, which cools the hydrogen from ambient temperature to approximately 80 K. This stage represents a lot of variation possibilities as a number of different solutions may be applied. Furthermore, experience is drawn from large scale natural gas liquefaction plants which are commercially in operation all over the world and present a mature technology.

## 2. EVALUATION CONCEPT

The concept of dividing the liquefaction of hydrogen into several stages has been presented in earlier publications [6]. These stages are:

- Precompression (at ambient conditions)
- Precooling (ambient to about 80 K)
- Cryo-cooling (80 K to 30 K)
- Liquefaction (30 K to $LH_2$ at 1 atm)

Figure 46 shows where these stages are located in a generic process flow diagram (PFD) for a hydrogen liquefaction plant.

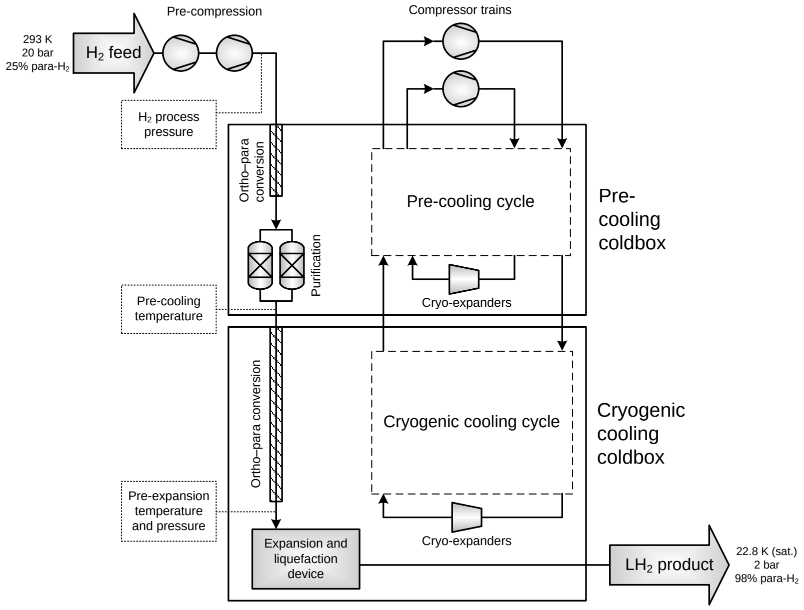

**Figure 46: Generic PFD of hydrogen liquefaction**

To be able to evaluate the different liquefaction stages separately, one has to assume that they are not influenced by each other. This is definitely not true for the precompression, as it heavily influences the cooling curve for hydrogen in the cryo-cooling and liquefaction stages. Figure 47 shows the distribution of the exergy requirement for each of the four liquefaction stages depending on the precompression outlet pressure. The total exergy requirement is 2.93 kWh/kg liquid product. It is assumed a feed pressure of 20 bar, which is typical from pressure swing absorption. If the inlet feed had atmospheric pressure, this would require 35 % higher exergy input due to increased compressor work.

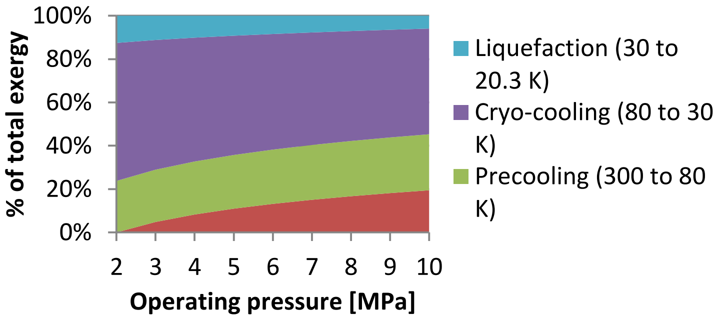

**Figure 47: Distribution of exergy requirement for each liquefaction stage**

The precooling is almost independent of the precompression outlet pressure. However, the influence of the choice of processes for the cryo-cooling and liquefaction stages on the precooling cycle must be investigated. One could however argue that refrigerants used in the low temperature stages (typically hydrogen or helium) are operating close to ideal gas in the precooling temperature range, which means that the enthalpy is a function of temperature only. The cooling curve for the refrigerant will therefore be independent of the pressure and the precooling duty of the refrigerant will therefore be cancelled out by the return flow.

Based on this, the precooling processes studied in this paper will be studied independent from the other liquefaction stages.

## 3. DISCUSSION OF THE PROCESS STAGES

### 3.1. Precompression

As discussed above, the precompression has a big influence on the low temperature part of the liquefaction process Figure 50. By compressing the feed to a higher pressure, part of the cooling demand can be supplied at a higher temperature, which reduces the necessary refrigeration work. The cost for this is then a higher compression work at ambient temperature.

Since one in general is able to compress at a higher efficiency than cooling the gas, one should compress to as high pressure as possible. However, for this to be true, the pressure reduction equipment in the liquefaction stage (see Section 3.4) has to be efficient (using an expander instead of a throttling valve). Yet the maximum pressure is normally limited by the heat exchangers.

The compression of hydrogen (with a molecular weight of 2 kg/kMol) is traditionally performed with piston or screw compressors. When moving towards larger scale liquefaction plants, turbo machinery might become more attractive, due to potentially higher efficiency and availability. Turbo compressors are however limited in pressure ratio per stage (due to the low molecular weight). With state of the art materials, the maximum pressure ratio for hydrogen is about 1.2 for Hydrogen [7]. This means that compression from atmospheric to 80 bar would require at least 24 stages. However, if the feed pressure is 20 bar (typical for pressure swing absorption purification) compression to 80 bar would require only 8 stages.

### 3.2. Precooling

All existing large scale hydrogen liquefiers utilise liquid nitrogen from an associated nitrogen/air liquefaction plant. For future very large scale plants this would not be the most likely option, since using pure liquid nitrogen for cooling down to 80 K is also fundamentally inefficient, due to the large temperature differences at low temperatures. The minimum exergy needed for production of liquid nitrogen is twice that needed for cooling of the hydrogen feed to 80 K. If one assumes an exergy efficiency of about 50 % for the liquid nitrogen process, the total exergy efficiency is 25 %.

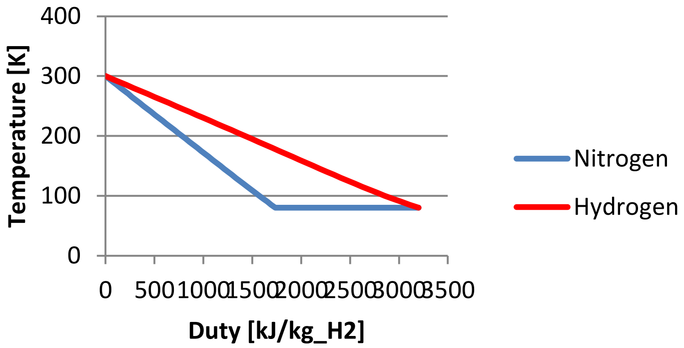

**Figure 48: Temperature profile for precooling with liquid nitrogen**

In the following section different solutions for precooling will be discussed.

**Closed nitrogen loop**

The most straight forward solution would be to integrate the nitrogen liquefaction cycle as a closed refrigeration loop, into the hydrogen liquefaction cycle. Compared to the utilization of liquefied nitrogen from a standalone plant, this gives the possibility of improved integration and temperature matches in the heat exchangers. This is done by shifting most of the liquid nitrogen production to cold gaseous nitrogen. In this way, the flat line in Figure 48 is shortened and the two lines will be more parallel, meaning better temperature adaptation and reduced losses. To further improve the efficiency, the liquid and gaseous nitrogen can be produced at multiple temperature levels.

**Helium/Hydrogen Brayton**

Since reversed Brayton or Claude cycles are necessary for the cryo-cooling stages, it might seem reasonable to add high temperature expansion stages to provide cooling in the precooling temperature range. However, as discussed in the precompression stage, compression of helium and hydrogen is generally much more complicated and power consuming than higher molecular weight gases.

As for compression, expansion is limited in pressure ratio. This is often stated in maximum enthalpy drop per stage, depending on maximum tip speed. This results in a vast number of compressor and expansion stages being necessary in the precooling refrigeration stages. This is exemplified by Valenti [8], utilizing 15 compressor stages and 7 expansion stages for cooling from ambient conditions to 90 K.

**Mixed refrigerant systems**

Mixed refrigerant (MR) concepts are common within the liquefied natural gas (LNG). Mixing refrigerants enables gliding temperatures during condensation and evaporation of the refrigerant (in contrast to the constant temperature phase change of single component refrigerants). By optimizing the refrigerant mixtures, one can adopt the evaporation curve to the cooling process to minimize the temperature differences and thereby the exergy losses. During the last decades several more or less complex and high efficiency processes have been developed to minimize the power consumption in LNG production.

The simplest MR process is the single stage process often referred to as the PRICO process [9].This process is commonly used for small scale LNG plants. However, due to the long temperature span of the hydrogen precooling (300 K to about 80 K) it will not be suitable, both because it is difficult to find a mixture with such long gliding evaporation temperature and because one would risk freeze-out of the least volatile fluids.

Berstad et al. [10] proposed a MR precooling cycle utilizing the Kleemenko auto-cascade principle. This concept enables removal of the heaviest components at a higher temperature level, and thereby automatically adjusting the mixed refrigerant to the temperature level and reducing the risk of freeze-out. Some of the challenges with such a process relates to optimizing and controlling the mixed refrigerant composition throughout the process.

A different approach would be to combine the MR concept with the cascade concept. Examples of this exist in the LNG industry [11, 12].

A possible layout of a mixed refrigerant cascade process for hydrogen precooling is shown in Figure 49. The upper MR cycle operates at normal natural gas liquefaction temperatures (300 K – 120 K), and the second cools the hydrogen down to about 80 K.

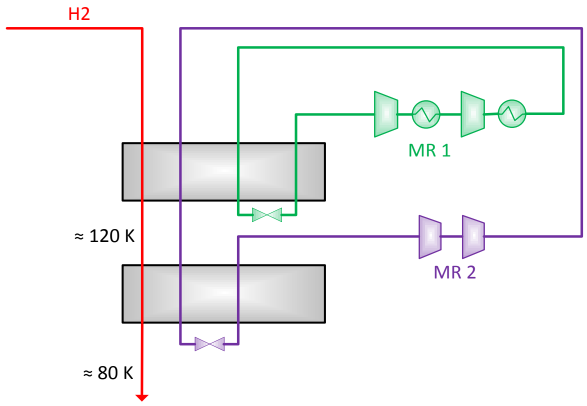

**Figure 49: Layout of mixed refrigerant cascade system**

Compared to a closed nitrogen system, a MR system usually needs larger heat exchanger surfaces, since the high internal heat exchange results in a lower relative refrigeration capacity (kW refrigeration power per kW transferred in the heat exchanger). This could partially or fully be compensated by the higher heat transfer coefficient of boiling or condensing fluids.

An important aspect is that compared to gas based cooling systems (nitrogen, hydrogen or helium), the number of compressor and expansion stages are drastically reduced. In Figure 49, throttling valves are utilized instead of expanders. This is partially because expanders for two-phase hydrocarbon mixtures are not commonly applied, but also because increase in efficiency by applying expanders is minor compared to Brayton or Claude cycles. This simplifies the system, since one does not need to handle power recovery through generators or coupling with compressors. Some savings are however possible, and Berstad et al. [10] showed a potential for 15 % reduction in MR compression work when replacing the JT-valves with expanders (without power recovery).

### 3.3. Cryo-cooling

For the cryo-cooling the possible processes are much more limited. The most common solution in state-of-the-art liquefaction plants are Hydrogen-Claude cycles [13]. Another possibility would be to use purely reversed Brayton cycles with Helium (possibly also with Hydrogen, but one is limited in minimum temperature).

As mentioned above, the main issue with using these light gasses for refrigeration is the compression. Quack [6] suggested to deal with this by adding neon to the refrigerant to increase the molecular weight. This reduces the compression problem, but on the other hand, it limits the minimum cooling temperature due to the triple point of neon at 24.6 K. The prediction of the behaviour of such mixtures is also difficult due to limited research within this field.

Another issue with utilizing neon, and possibly also helium, is that it is a very expensive gas, which requires a hermetic system to minimize leakage losses. This is possible with helium-neon systems, but difficult with Hydrogen, since the magnetic bearings are heavily subject to Hydrogen embrittlement.

The main challenge for the cryo-cooling cycle is to deal with the highly variable heat capacity of hydrogen around the critical point (Figure 50), which makes the temperature fit in the heat exchangers challenging. This is partially helped by increasing the pressure of the hydrogen feed (increasing the pre-compression), as this "flattens" the cooling demand at each temperature level. The variable cooling demand needs to be handled by adjusting the refrigeration power, e.g. by utilizing overlapping expander stages [14]. Another concept that was proposed by Valenti [8] is to fully separate the helium Brayton stages and do internal recuperation.

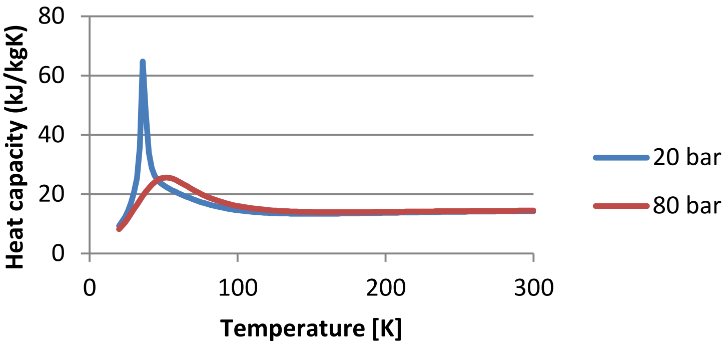

Figure 50: Heat capacity of equilibrium hydrogen at 20 and 80 bar.

### 3.4. Liquefaction

The main process decision for the liquefaction stage is if the process should be a "once-through" concept or with flash gas recycling. The most common industrial solution is to throttle the hydrogen into the two-phase region and then adding a liquefaction stage at storage pressure [5, 13]. Recent proposals for large scale liquefaction plants suggest to subcool the hydrogen to temperatures that assure only liquid at the outlet of the expansion [8, 14].

Figure 6 shows the vapour fraction after expansion depending on inlet temperature and pressure and expansion equipment (an isentropic efficiency of 0.9 is used for the expander). This shows the importance of utilizing expansion machines instead of isenthalpic throttling, especially when increasing the pre-compression pressure.

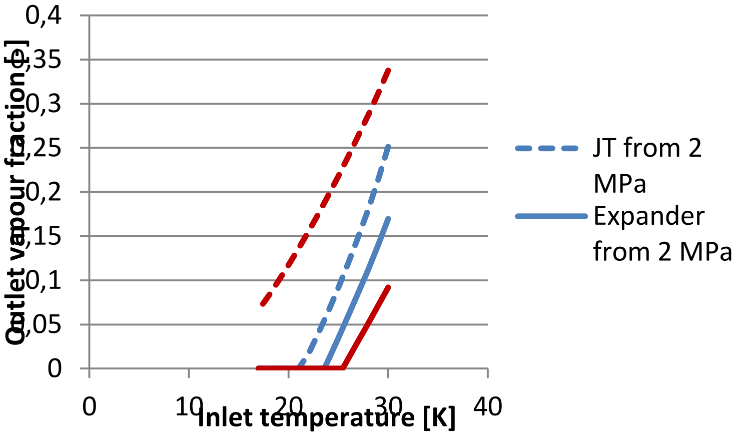

Figure 51: Vapour fraction from expansion of the hydrogen feed.

Another parameter to consider when choosing the liquefaction stage concept is the para-content. Often a very high para content (>98 %) is required in the product. This constrains the highest allowable cooling temperature. The equilibrium temperature for 98 % is about 28 K [15]. However one is probably not able to achieve fully equilibrium composition with continuous conversion, so with a 2K conversion delay one has to cool the hydrogen to at least 26 K.

## 4. CONCLUSIONS

This paper elaborates a method for designing an efficient large scale hydrogen liquefaction plant. The principal is to divide the process into 4 more or less independent stages, and find the optimum solution for each stage.

The main focus is put on the precooling stage. Not because it is the most power consuming stage, but because it is the stage with the most degrees of freedom in design. The standard concept of liquid nitrogen cooling is highly inefficient, and other concepts are needed for large scale applications. The two most promising concepts are integration of a nitrogen Claude cycle and a mixed refrigerants concept. Both systems have advantages and disadvantages that have to be further elaborated.

One of the main challenges in efficient hydrogen liquefaction is light gas compression. This is unavoidable, since only light gases can provide cooling at the required temperature levels, but should be minimized by using heavier fluids where it is possible.

Due to the higher exergy efficiency of compression compared to refrigeration, the pressure of the hydrogen feed should be as high as possible, as long as the pressure reduction in the liquefaction stage is performed by expansion machines instead of throttling valves. A higher pressure also beneficial for the cryo-cooling stages, since it reduces the peak in heat capacity above the critical point and makes it easier to achieve a good temperature fit in the heat exchangers.

## 5. ACKNOWLEDGEMENT

The research leading to these results has received funding from the European Union's Seventh Framework Program (FP7/2007-2013) for the Fuel Cells and Hydrogen Joint Technology Initiative under grant agreement n° [278177].

## 6. REFERENCES

1. GermanHy, *Studie zur Frage “Woher kommt der Wasserstoff in Deutschland bis 2050?* 2009, Im Auftrag des Bundesministerium für Verkehr, Bau und Stadtentwicklung.
2. *Hydrogen Fuel Cell Engines and Related Technologies Course Manual, Module 1: Hydrogen Properties*. 2001, College of the Desert.
3. Kramer, G.J., J.P.P. Huijsmanns, and D.M. Austen, *Clean and green hydrogen*, in *16th World hydrogen energy conference*. 2006: Lyon.
4. Verfondern, K., *Safety Considerations on Liquid Hydrogen*. Vol. 10. 2008: Jülich Forschungszentrum. 167.
5. Drnevich, R., *Hydrogen Delivery - Liquefaction & Compression*, in *Praxair, Strategic Initiatives for Hydrogen Delivery Workshop*. 2003.
6. Quack, H. *Conceptual design of a high efficiency large capacity hydrogen liquefier*. in *ADVANCES IN CRYOGENIC ENGINEERING: Proceedings of the Cryogenic Engineering Conference - CEC*. 2002. Madison, Wisconsin (USA): AIP.
7. Di Bella, F., P.E. Osborne, and C. Osborne. *Development of a Centrifugal Hydrogen Pipeline Gas Compresso*. in *Hydrogen Production and Delivery*. 2011: DOE Hydrogen Program.
8. Valenti, G.G., *Proposal of an innovative, high-efficiency, large-scale hydrogen liquefier*. International Journal of Hydrogen Energy, 2008. **33**(12): p. 3116-3121.
9. Maher, J.B. and J.W. Sudduth, *Method and apparatus for liquefying gases U.S. Patent 3,914,949*. 1975.
10. Berstad, D.O., J.H. Stang, and P. Nekså, *Large-scale hydrogen liquefier utilising mixed-refrigerant pre-cooling*. International Journal of Hydrogen Energy, 2010. **35**(10): p. 4512-4523.
11. Nibbelke, R., S. Kauffman, and B. Pek, *Double mixed refrigerant LNG process provides viable alternative for tropical conditions*. Oil&Gas Journal, 07/08/2002.
12. Linde AG, *LNG Technology*, in *Brochure from LINDE available from: http://www.linde-engineering.co.id/en/images/LNG_1_1_e_10_150dpi34-4577.pdf*. 2010.
13. Bracha, M. and L. Decker, *Grosstechnische Wasserstoffverflüssigung in Leuna*, in *Deutsche Kälte-Klima-Tagung*. 2008.

14. Shimko, M., *III.7 Innovative Hydrogen Liquefaction Cycle*, in *FY 2008 Annual Progress Report, DOE Hydrogen Program*. 2008, DOE.
15. McCarty, R.D., J. Hord, and H.M. Roder, *Selected properties of hydrogen (Engineering Design Data)*. 1981.

081

# Search for the Best Processes to Liquefy Hydrogen in Very Large Plants

**Quack H.[*], Essler J.[*], Haberstroh Ch.[*],**
**Walnum H.T.[**], Berstad D.[**], Drescher M.[**], Neksa P.[**]**

[*] Technische Universitaet Dresden, 01062 Dresden, Germany
[**]SINTEF Energy Research, Trondheim, Norway

## ABSTRACT

The goal of the IDEALHY project is to identify processes and components, which allow liquefying hydrogen with a power consumption much lower than with plants built so far. This requires comparing different possible processes concerning power efficiency, investment cost and compactness. The power consumption of a process depends on a number of boundary conditions. Without a clear overall definition of these boundary conditions, all statements and comparisons on the overall power consumption are questionable. So in the first step of the project the participants agreed on common boundary conditions.

Then it turned out, that the choice of the high pressure of the feed hydrogen influences strongly the rest of the liquefaction process, especially the region below 80 K. For this region there is an option between helium, hydrogen and neon as refrigerants and their mixtures. For the final choice of the working fluid and the process one has to identify the maximum possible circumferential speed of turbo compressors.

## 1. INTRODUCTION

The goal of the IDEALHY project is to identify the best processes for the liquefaction of hydrogen in very large plants, e.g. 50 t/d and larger. The first task was to check in literature for processes, which have been proposed in the past. A comparison of the collected cycles turned out to be difficult, because each author had selected different boundary conditions and component efficiencies. So the second task was to agree on a list of boundary conditions and component efficiencies, with which the most promising cycles were recalculated. Now a comparison was possible. Such a comparison leads to guidelines how to find an optimum processes.

## 2. CHOSEN BOUNDARY CONDITIONS

Table 1. Chosen boundary conditions.

| | | |
|---|---|---|
| Feed | Pressure | 20 bar |
| | Temperature | 293 K |
| | para-content | 25 % |
| | Purity | pure hydrogen |
| Product | Pressure | 2 bar |
| | Temperature | 22.8 K (saturated) |
| | para-content | 98 % |
| | Purity | pure hydrogen |
| Cooling water | Temperature | 293 K |
| | Temperature rise | 10 K |
| Heat leak | Process | none |
| | Storage | none |
| LN2 precooling | A closed cycle nitrogen plant has to be calculated | |

We are aware that the choices of a certain feed pressure of a certain product pressure have a quite a large influence on the power consumption. So after the comparison of the cycles with a set of preliminary values the influence of other pressures has to be evaluated.

It is expected, that the feed hydrogen will contain some impurities in the 100 ppm by volume range. These impurities will be removed by adsorption at the 80 K temperature level. We have estimated, that the refrigeration needed for the hydrogen loss and for the re-cooling of the adsorbers after the regeneration process is negligible compared to the overall power needs of the liquefaction.

## 3. PRELIMINARY ASSUMPTIONS FOR EFFICIENCIES OF COMPONENTS

Table 2. Selected efficiencies of components

| | | |
|---|---|---|
| Heat exchange | Cooling water pinch point temperature difference | 5 K |
| | i.e. outlet temperature from inter- and after-coolers of compressors | 298 K |
| | Condensing temperature of refrigerants like propane | 303 K |
| | Sub-cooling of condensate to | 298 K |
| | Whole cryogenic train | NTU < 120 |
| | Pinch point at warm end | 3 K |
| | Pinch point at 80 K level | 1 K |
| | Pinch point at cold end | 0.3 K |
| Pressure drop | Inter- and after-cooler | 0.2 bar |
| Cryogenic part | above 20 bar | 2 % |
| | medium pressure (4 bar) | 5 % |
| | low pressure | 20 % |
| | Linear interpolation between the pressure levels | |
| Compressor, isentropic efficiency | Piston and turbo-compressor | 85 % per stage |
| | Turbine brake compressor | 80 % |
| | Cold compressor | 70 % |
| Expander, isentropic efficiency | Expansion turbines below 120 kJ/kg enthalpy drop | 90 % |
| | Wet expander | 85 % |
| Ortho-para conversion | Temperature delay | 2 K |

These choices of boundary conditions and component efficiencies allow to re-calculate cycles on the same basis and to compare them.

## 4. PROCEDURE FOR THE SEARCH OF THE BEST PROCESSES [1]

6.1. The best process from a thermodynamic - i.e. a power consumption – point of view would be a reversible process. On paper there exist many reversible processes. One of them is sketched in Figure 1a. The background is a temperature-entropy diagram. At the top there is the ambient temperature and at the bottom the vapour dome is indicated with the saturated liquid on the left corner. The feed hydrogen is compressed at ambient temperature in many stages with inter-cooling in an ideal isothermal compression. This results in reduction of the entropy to a value, which corresponds to the entropy of the saturated liquid. Then the compressed gas undergoes an isentropic expansion with work recovery until the saturated liquid state is reached.

This simple process can not be realized, because there are no compressors and expanders for the required high pressure and it is difficult to include an ortho-para conversion in the isentropic expansion.

But it should be noted, that the process shown in Figure 1a does not contain any cryogenic heat transfer. So there is no potential for thermodynamic losses due to heat transfer. One search procedure could be to modify this process in the direction to implement realistic hardware while trying to minimize the amount of cryogenic heat transfer.

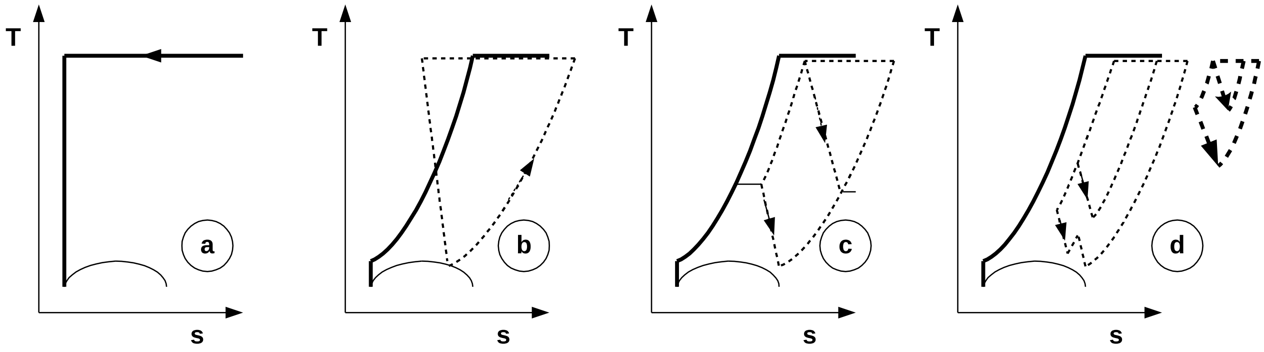

Figure 1. Steps from the ideal to a real process to liquefy hydrogen

In the next step, which is sketched in Figure 1b, the feed hydrogen is compressed only to the maximum pressure, which is compatible with currently existing compressors, heat exchangers and wet expanders, e.g. 80 bar. Then the hydrogen is cooled in a heat exchanger, in which the catalyst for the ortho-para conversion is integrated. At very low temperature the hydrogen is expanded in a "wet expander" with saturated liquid at the outlet.

The needed refrigeration for the cooling is provided by a closed cycle refrigerator, which is shown with dotted lines in Figure 1b. The cycle of this refrigerator includes an isothermal compression at ambient temperature, a work extracting expansion, which is as isentropic as technically possible, and a warm-up of the refrigerant in heat exchange with the hydrogen.

Again the maximum pressure, which can be handled in such refrigeration cycles is limited by today's technology. Therefore one has to stage several such cycles "above each other" as shown in Figure 1c. This arrangement is called a cascade. The cascade has the intended effect that the maximum pressure is reduced, but it also has the detrimental effect, that additional heat transfer is needed.

There is one additional effect, which complicates the refrigeration cycle: The needed cooling of the hydrogen is not constant over the temperature range. Figure 2 shows the specific heat of equilibrium hydrogen at 20 and 80 bar as a function of temperature with a 2 K deviation from the thermodynamic equilibrium as well as the para content.

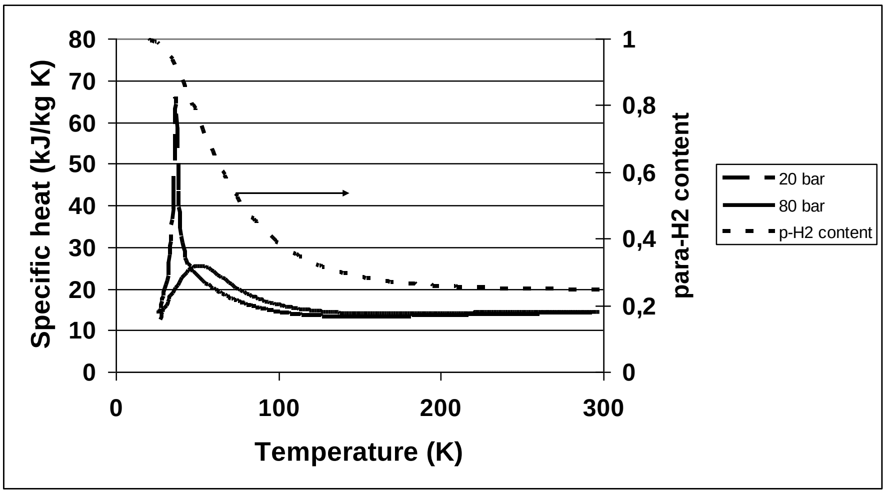

Figure 2. Specific heat of e-H2 at 20 and 80 bar and para content as function of the temperature

The specific heat of hydrogen at ambient temperature corresponds to the value for a two-atomic ideal gas. With falling temperature, the specific heat is first declining, because the rotational degrees of freedom have reached there lowest possible state. Hydrogen behaves then more and more like a one-atomic molecule. But below about 120 K the specific heat rises again due to two influences, the starting ortho-para conversion and the real-gas effects. The values of the specific heat rises to a maximum value, which is more pronounced at 20 bar than at 80 bar. Then the specific heat drops to the value of the liquid hydrogen.

A preferable refrigeration process must be designed such that the refrigeration power is produced just at, or only a little below the temperature where it is needed for cooling.
One example for a refrigeration process, which produces peak cooling in the 40 to 70 K region, is shown in Figure 1d. In this temperature range the expanders are partially overlapping in temperature.

## 5. CHOICE OF PRESSURES FOR BRAYTON REFRIGERATION CYCLES

The Brayton cycle consists of a compression at ambient temperature, a counter-current heat exchanger and one or more work extracting expanders. In principle one is free to choose the working fluid and the high and the low pressure. But there are a number of limitations, which have to be taken into account:

- Concerning the working fluid there is the choice between $N_2$, Ne, $H_2$, He or mixtures of these gases; but with $N_2$ and Ne one has to make sure that no liquid is generated at the outlet of the expander [2].
- From the heat transfer aspect, i.e. best heat transfer coefficients at a minimum pressure drop, one would prefer $H_2$ and He over Ne and $N_2$.
- Concerning turbo compressor, i.e. highest pressure ratio for a given circumferential speed of the impeller, one would prefer $N_2$ and Ne over He and $H_2$.
- Some materials of bearings and motors may not be compatible with hydrogen due to hydrogen embrittlement.
- To reduce heat transfer losses, one would prefer high pressure ratios with the smallest mass flow rates.
- To obtain the optimum working conditions for turbo compressors one would prefer low pressure ratios.
- The higher the low pressure of the cycle, the more compact are the heat exchangers.
- The higher the high pressure of the cycle, the closer one gets to the maximum allowed pressure of the heat exchangers.

From this list it is obvious, that it will not be possible to come up with one single “best” process. The choice of working fluid and operating pressures is always a compromise between conflicting requirements.

## 6. EXAMPLE OF A NEW PROCESS: IDEALHY TUD 5

For the cycle described in the following a number of choices have been made:

- Compression of the hydrogen feed in a two-stage piston compressor to 80 bar
- Continuous ortho-para conversion in the heat exchangers below 150 K
- Wet expander replacing the JT-valve
- The flash gas from the wet expander outlet is warmed up to ambient temperature and used for the regeneration of the upstream hydrogen purification
- Below 90 K a modified Brayton process with four expanders, which operate partially in series and partially in parallel. The working fluid can be either $H_2$ or He or a mixture of one of theses two gases with neon with a maximum neon content of 30 %
- Some temperature overlap in expansions in the temperature region between 70 and 40 K to cover the specific heat peak of the hydrogen
- Above 90 K a modified Brayton process with nitrogen as working fluid and again four expanders, which operate partially in series and partially in parallel.
- There are two cryogenic cold boxes: The upper one is perlite insulated, whereas in the lower one vacuum is used for insulation.
- A small part of the coldest nitrogen is used for the precooling of two helium heat exchangers, which are also located in the perlite box.
- The main power input occurs in the main nitrogen and helium turbo compressors. Both have the feature that a part of the return stream enters at elevated pressure. This has the effect, that the volumetric flow rate of the lower stages of the compressors are decreased, whereas the flows in the higher stages are increased compared to a system, where the full flow is compressed over the full pressure ratio.
- All eight expanders are directly coupled with one stage “brake” compressors, which take over part of the compression at ambient temperature.

- Expanders are partially arranged in parallel, whereas all brake compressors are arranged in series. This has the effect that the enthalpy increase in the compressors is only about half the enthalpy drop in the expanders. It is assumed that this arrangement gives the best operating conditions for both, expanders and compressors.

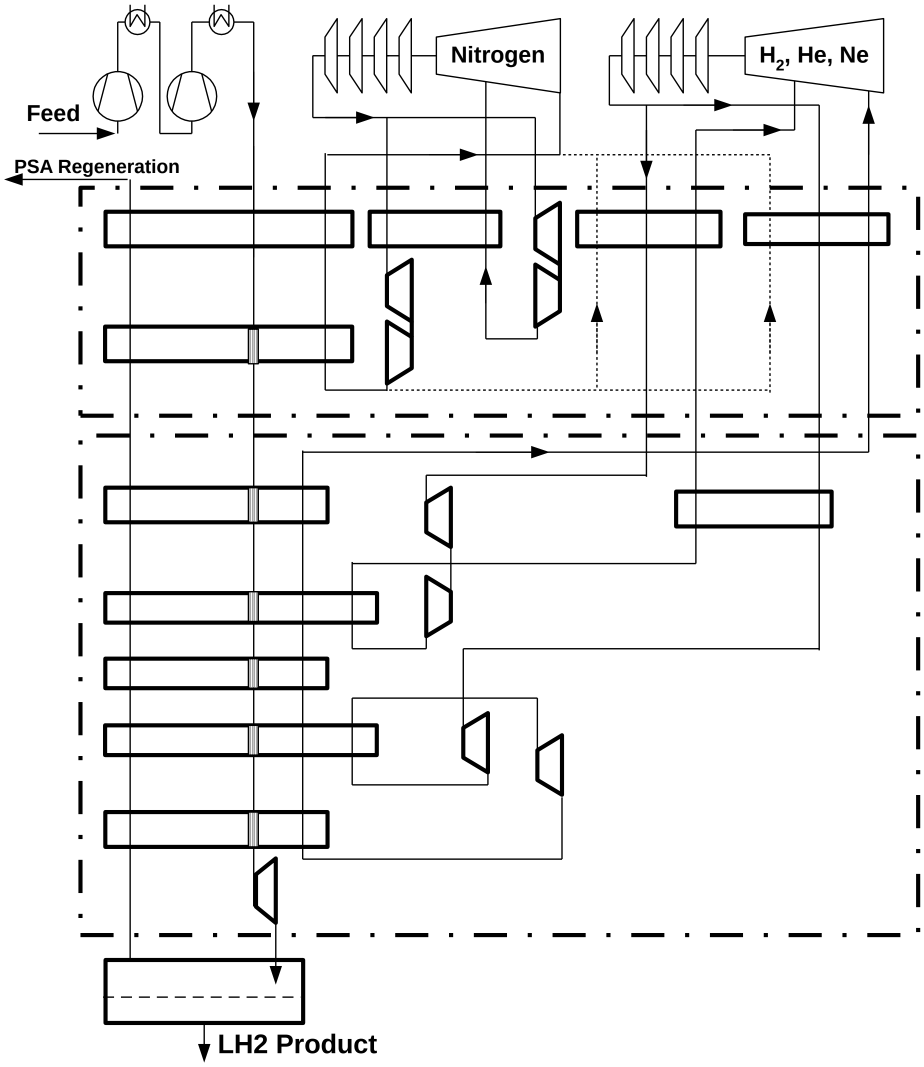

Figure 3. Flow diagram of the process IDEALHY TUD 5

It is not yet clear, whether the refrigerant in the low temperature cooling loop will be pure helium or a mixture of helium and neon. This depends on the available technology for the main turbo compressor. Pure helium requires very high circumferential speeds of the compressor blades. The addition of the neon would make this task easier. On the other hand pure helium would provide better heat transfer characteristics than a helium-neon mixture, i.e. lower pressure drop and better heat transfer coefficient.

The power consumption for the liquefaction depends on one hand on the boundary conditions (like the pressure and purity of the feed and the desired pressure of the product) and on the other hand on the efficiency of heat exchangers, expanders and compressors. This evaluation needs a number of iteration loops together with manufacturers of such equipment. This is presently under way.

Of course the process shown in Figure 3 is not unique. It could be of advantage to replace the nitrogen cycle – totally or partially – by a mixed-refrigerant throttle cycle [3].

## 7. CONCLUSIONS

When trying to find the optimum process for the liquefaction of hydrogen in large plants one recognizes, that the thermodynamic optimum leads to requirements, which surpass the present capabilities of state of the art machinery and heat exchangers. Thermodynamic aspects would e.g. lead to processes with a high pressure ratio. On the other hand, to obtain high pressure ratios for the light gases such as H2 and He the turbo compressors have to be operated at very high circumferential speed, limited by the strength of the used material.

Pushing machinery to its limits incorporates higher operational risks. So the process development procedure is to go to the limit on paper, and for the realization then go one step backwards towards higher operational reliability. It is clear that this approach requires an iterative procedure, which is still under way.

## 8. REFERENCES

[1] Berstad D. et al., *Design Principles for High Efficiency Liquefaction Processes*, World Hydrogen Energy Conference 2012, Toronto, June 2012

[2] Quack H.: *Die Schluesselrolle der Kryotechnik in der Wasserstoff-Energiewirtschaft*, Wiss. Zeitschrift der TU Dresden, 50 (2001) Heft 5/6 S. 112 – 117

[3] Walnum H. T. et al., *Mixed Refrigerants for High Efficiency Pre-cooling*, World Hydrogen Energy Conference 2012, Toronto, June 2012

061

# The Development of Methods and Means for Long-Term Storage of Liquid Hydrogen of High Purity (Extended Abstract)

**Cheremnykh O.Ya.**

JSC «Uralcryomash», Nizhny Tagil, Russian Federation, Sverdlovsk region, Vostochnoye shosse, 24

JSC «Uralcryomash» is well-known for its development, designing and manufacturing of vehicles for transportation and storage of liquefied low-temperature gases (nitrogen, oxygen, argon, ethylene, propane-butane mixtures, carbon dioxide, hydrogen, LNG).

Nowadays liquid hydrogen is widely used in different branches of industry: rocket and space engineering, aviation, radio and electronic industry, nuclear power engineering and others.

The main technical requirements for the capacity-depositories of liquid hydrogen are minimization of hydrogen losses and conservation of quality of hydrogen in the process of long-term storage. The conservation of quality of liquid hydrogen (presence of admixtures of nitrogen, oxygen, methane and others in liquids) depends on the value of daily losses of the cryogenic liquid content.

Decreasing of hydrogen losses in the storage tanks in the process of long-term storage is achieved first of all by usage of high-efficient thermal insulation in bulk storages.

The enterprise uses different types of thermal insulation for vehicles for transportation and storage of liquid hydrogen.

The most applicable type of the thermal insulation is the multilayer-vacuum thermal insulation. The usage of the multilayer-vacuum thermal insulation in 100-150 $м^3$ capacity liquid hydrogen storage tanks achieves the insulation quality expressed as hydrogen losses at the level 1% per day from the mass of hydrogen in the storage tank.

The further decreasing of hydrogen losses in the process of storage is achieved by use of the screen-layer-vacuum thermal insulation, where liquid nitrogen is used for aluminum screen as a cooling agent. Liquid nitrogen is in the nitrogen vessel, built-in the liquid hydrogen general bulk storage tank assembly (photo 1).

Photo 1. Overview of the liquid hydrogen storage tank with the screen-layer-vacuum thermal insulation at consignee site

Technical characteristics of the liquid hydrogen storage tank with the screen-layer-vacuum thermal insulation are presented in the table 1.

| Parameters | Values |
|---|---|
| Medium | Liquid hydrogen |
| Total capacity, $m^3$ | 102 |
| Working pressure in the vessel, MPa | 1,1 |
| Hydrogen mass in the vessel, kg | 6 300 |
| Type of the thermal insulation | Nitrogen screen with the multilayer-vacuum thermal insulation |
| Vacuum value in the walls-between clearance: | |
| - in warm condition | $1 \cdot 10^{-3}$ mm merc. column |
| - in cold condition | $1 \cdot 10^{-5}$ mm merc. column |
| Hydrogen losses at evaporation, % per day | 0,24 |
| Discharge method | Upper with blowing from the side source |
| Material of the tank storage: | |
| - vessel | Stainless steel 12x18H10T |
| - shell | Stainless steel 12x18H10T |
| - screen | Aluminum alloy AMg-5 |
| Overall dimensions, mm: | |
| - length | 22 480 |
| - width | 3 900 |
| - height | 3 812 |
| Total capacity of the nitrogen vessel, $m^3$ | 10,4 |
| Working pressure in the nitrogen vessel, MPa | 0,5 |
| Tare mass, kg | 8 430 |
| Material of nitrogen capacity: | |
| - vessel | Aluminum alloy AMg-5 |
| - shell | 09G2C |
| Period of nitrogen refueling, in days | 30 |

The results of experimental studies carried out with liquid nitrogen at first and then with liquid hydrogen have allowed to determine cooling time of the nitrogen screen and the rate of hydrogen evaporation in the 100 $m^3$ capacity storage tank with the screen-layer-vacuum thermal insulation at the level 0,24% per day.

Thus, at present the usage of the screen-layer-vacuum thermal insulation in the liquid hydrogen storage tanks of such design is more effective than widely applicable multilayer-vacuum thermal insulation.

050

# A New Cryogenic High-Pressure $H_2$ Test Area: First Results

**Klier J.[*], Rattey M.[*,**], Kaiser G.[*], Klupsch M.[*], Kade A.[*], Schneider M.[*], Herzog R.[*]**

* Institut für Luft- und Kältetechnik (ILK), Hauptbereich Kryotechnik und Tieftemperaturphysik, Bertolt-Brecht-Allee 20, 01309 Dresden, Germany
** Hochschule für Technik und Wirtschaft, Forschungsinstitut Fahrzeugtechnik, Dresden, Germany

## ABSTRACT

An innovative hydrogen test area for cryogenic high-pressure applications has been put into operation at the ILK Dresden. This test area allows fundamental investigations on hydrogen (in all its phase states) and on gaseous helium. Furthermore, tests and qualification of components of any kind in the temperature range from room temperature down to 10 K and under pressure conditions ranging from high vacuum to 1000 bar are possible. In the framework of a research project, investigations of the charging and discharging process of hydrogen tanks, and the development of new storage technologies to achieve a high hydrogen storage density up to 100 kg/m³ are feasible. Our experiments promote the intricate developments of new components in relation to the handling of supercritical mediums. Thereby, experiments on re-cooling systems in form of capillary expander or Joule-Thomson-cooler are performed as well as on special latent-heat storage systems based on eutectic mixtures. The current status of the development up to test set-ups and experimental results is presented. Furthermore, results of numerical calculations are shown regarding the optimization of process control.

This work has been supported by the BMWi (contract no. EURONORM VF090052).

## 1. INTRODUCTION

### 1.1. Hydrogen test areas

Hydrogen storage has become a field of rising interest in recent years due to its high capability for solving problems connected with non-continuous energy generation. Up to now, hydrogen test areas are often focussed on special experiments in pressure and temperature regimes. Therefore, fundamental results and scientific findings are still limited.

### 1.2. State of the Art of Hydrogen Storage

Numerous studies on hydrogen storage are focused on liquid hydrogen. However, liquid hydrogen requires cryogenic storage since it boils at about 20 K (under ambient pressure). Hence the storage vessels must be well insulated to prevent significant boil-off. For instance BMW has been working on a liquid tank for cars, producing for example the BMW Hydrogen 7 [1]. In another method, compressed hydrogen is stored in vessels up to 700 bar at room temperature used for mobile storage in hydrogen vehicles such as applied by Honda, Nissan, Toyota, or Mercedes [2, 3]. Both methods can be considered as an approach to enhance the specific energy in mobile applications.

### 1.3. Project Innovation

Calculations based on thermodynamic data [4] have shown that the density of hydrogen can be considerably increased by storing it in the supercritical state, *i.e.* above its critical point. So, in the following we present experimental setups for hydrogen storage in such a state. For that we have built up a new test area which enables investigations in the pressure range up to 1000 bar and down to cryogenic temperatures. The project includes also studies on additional components like re-cooling technologies and latent-heat storage systems in order to improve the performance of a combined hydrogen storage system. This kind of hydrogen storage was patented [5].

Supercritical storage is not limited to the case of hydrogen. For instance, in the case of methane, numerical simulations have revealed a storage density which is more than double at 220 K (supercritical state) compared to storage at room temperature under otherwise equivalent pressure (around 150 bar). In our experiments storing natural gas under the above conditions resulted in an increase of density by a factor of 2.2. Thus, supercritical storage is a very promising way to enhanced storage densities.

## 2. BASICS OF PROJECT

### 2.1. Hydrogen Phase Diagram

The phase boundaries of hydrogen are shown in Figure 1. The values for the transitions between solid, liquid and gaseous phases have been calculated [4]. Above the critical point ($T_{\mathrm{crit}}$ = 33.2 K, $p_{\mathrm{crit}}$ = 13.15 bar) the supercritical state (*i.e.* gas of high density) exists. At temperatures near but below the critical point, the liquid shows enhanced compressibility.

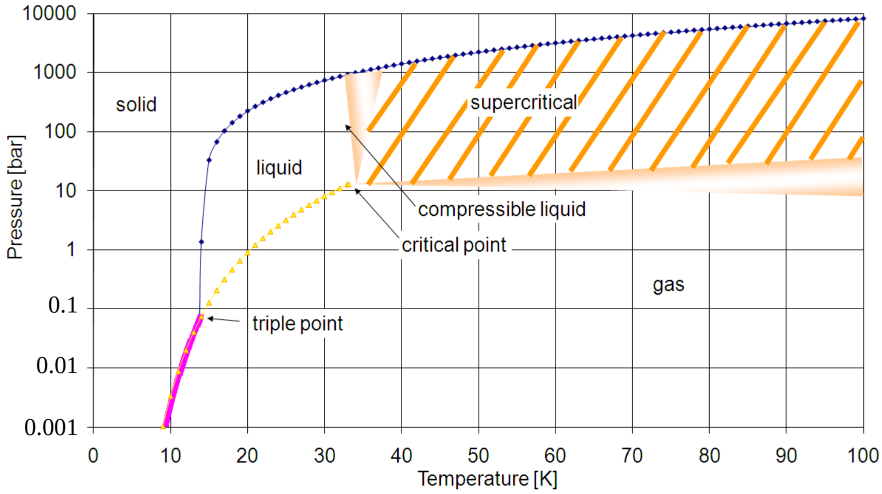

Figure 1. Phase diagram for hydrogen. The symbols correspond to numerical results [4]. Further transitions are shown schematically. The hatched area indicates the supercritical range (i.e. fluid of high density).

### 2.2. Cryogenic High-Pressure Hydrogen Storage

Figure 2 shows the hydrogen density depending on temperature and pressure.

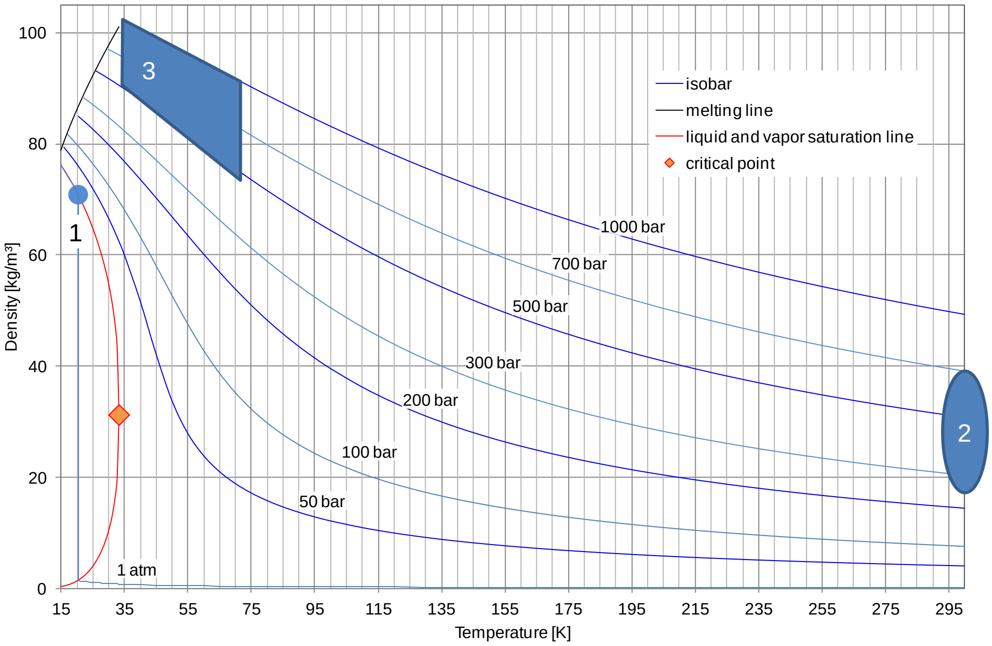

Figure 2. Shown is the hydrogen density as function of temperature at different pressures (lines). Highlighted areas mark state-of-the-art results: (1) liquid around 20 K, (2) pressurised gas around 300 K, and (3) cryogenic compressed gas, the project target of the ILK Dresden.

In general, the stored density rises with increasing pressure and decreasing temperature. Most pronounced changes are observed near the critical point. Well below $T_{\text{crit}}$, an increasing pressure does not enhance the density significantly due to the nearly "incompressible" liquid state.

The established storage concepts mentioned above, i.e., those in the liquid state around 20 K and in the gas state within the pressure range between 250 and 700 bar at room temperature, result in a stored density of approximately 70 kg/m$^3$ (liquid) and up to 40 kg/m$^3$ (gas), respectively. The advantages of supercritical storage (the target of the storage parameters of the ILK Dresden is between 500 to 1000 bar at $T_{\text{crit}} \leq T \leq 75$ K) are evidently: An increased density of up to 100 kg/m$^3$ and more is possible for temperatures well above those of the liquid storage thus reducing the cryogenic requirements and hydrogen losses. The latter is due to a lower boil-off which results from a higher maximum pressure compared with the liquid-storage parameters.

## 3. THE HYDROGEN TEST AREA OF THE ILK DRESDEN

Within the last two years, the hydrogen laboratory at the ILK Dresden has been designed and built. Some of its main components are shown in Figure 3. A high-pressure compressor enables the use of gases in the range up to 1000 bar. Minimum temperatures down to 10 K are achieved by a Gifford-McMahon cryocooler. Noteworthy, the gas supply also allows the utilisation of helium instead of hydrogen not only for inertisation but also for additional experiments in the mentioned range of pressure and temperature. Thus, a comparison of results on hydrogen with the properties of an inert gas is possible.

Figure 3. Some components of the hydrogen test area at the ILK Dresden: *e.g.* (1) – high-pressure compressor, (2) – dewar of the cryocooler, (3) – gas supply for hydrogen and helium, (4) and (5) – mass flow controller.

An overview of the hydrogen flow realized in the test area is given in Figure 4. The main components mentioned above are accompanied by a number of measuring instruments for mass flow, pressure, temperature, and safety equipment. The latter are connected with the exhaust line in order to establish a safe state in case of critical operation.

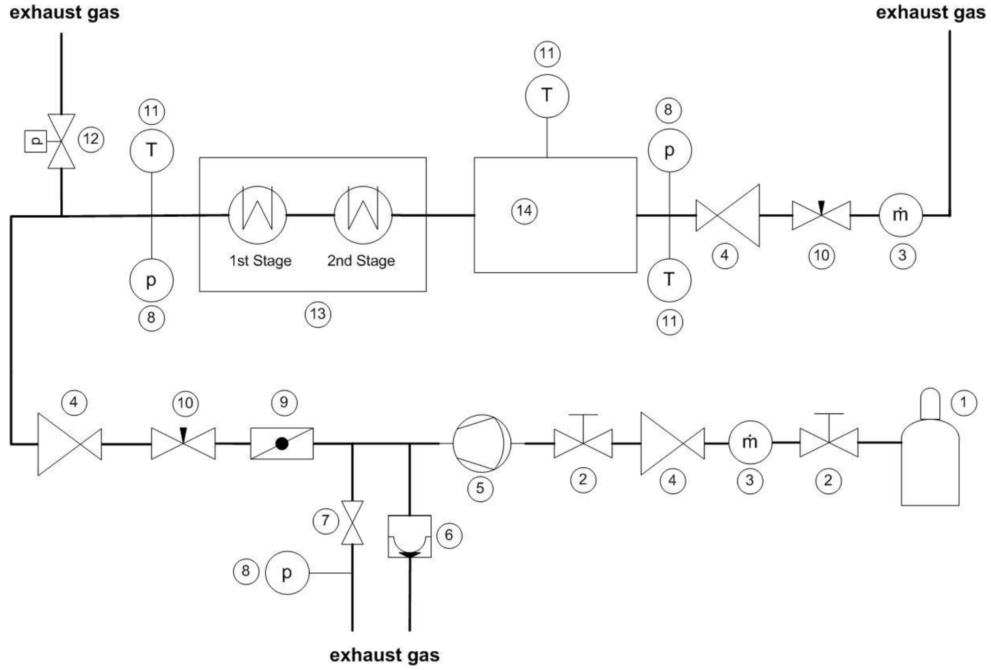

Figure 4. Schematic structure of the components within the main part of the hydrogen test area: (1) – $H_2$-source, (2) – lock valve, (3) – mass flow meter, (4) – pressure reducer, (5) – high-pressure compressor, (6) – rupture disc, (7) – safety valve, (8) – manometer, (9) – back-pressure valve, (10) – needle valve, (11) – thermometer, (12) – pneumatic valve, (13) – cryocooler, (14) – experiment (storage tank and additional components).

## 4. EXPERIMENTS

### 4.1. First Tests with Hydrogen

Within one of the first tests of the cryogenic high-pressure hydrogen test area, the melting line has been verified for a large pressure range. A typical pressure development is shown in Figure 5. A comparison between measured values and theoretical data is shown in Figure 6. Depending on temperature, the evolution of a pressure drop between inlet and outlet of the vessel clearly indicates the presence of a solid phase. The measurement gives reasonable agreement with the known phase diagram.

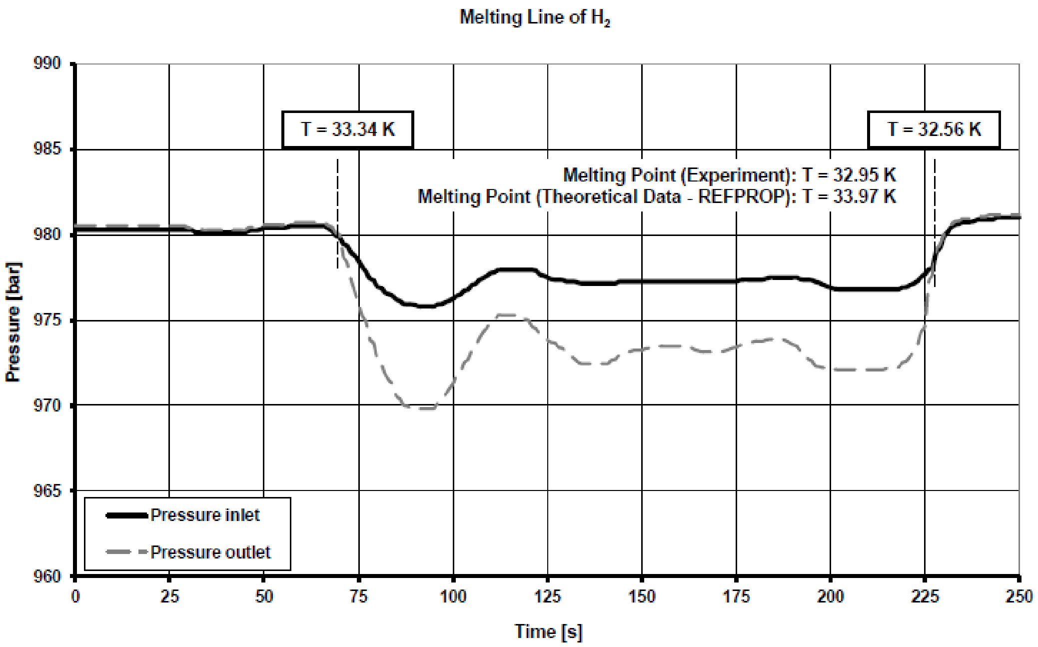

Figure 5. Typical pressure development at the melting point (temperature is varied; see text).

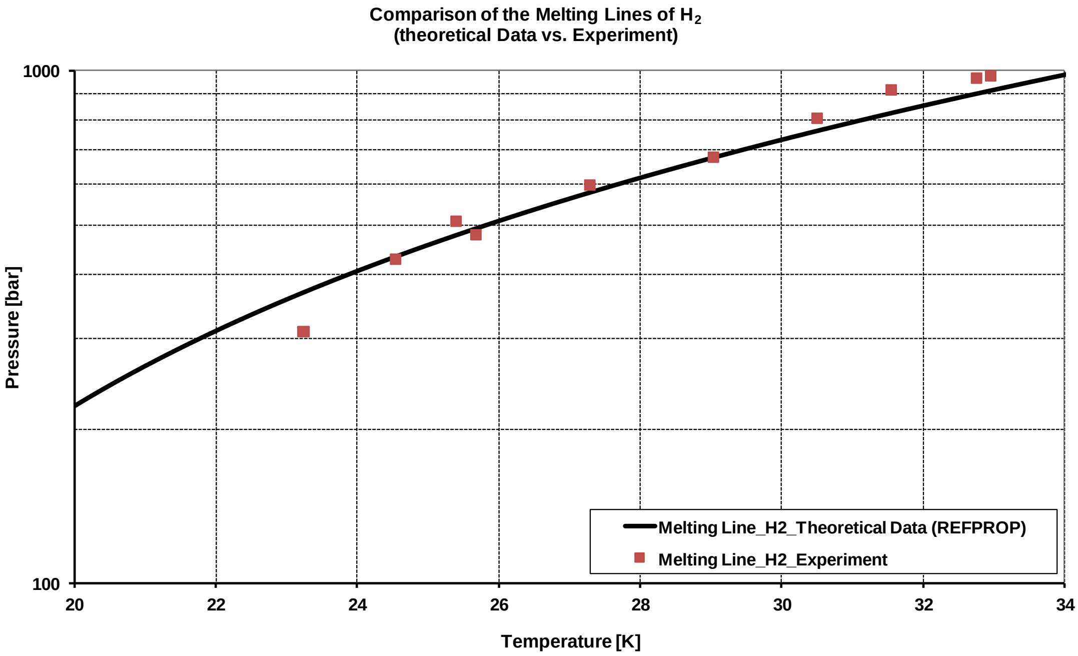

Figure 6. Comparison between measured values (squares) and theoretical data (thick line; [4]) for the melting line of hydrogen.

## 4.2. Latent-heat Storage

Due to a permanent heat flux into the hydrogen reservoir, a latent-heat storage system is used to guarantee a required storage temperature for a certain time. To develop and investigate such a storage system for these low-temperature conditions, an additional test area for material characterization has been built up, shown in Figure 7.

Interesting materials for latent-heat storages are typically eutectic mixtures of members of the alkane series as e.g. methan, ethan, and propan as well as a fraction of nitrogen. The measured solidification temperature of the tested mixtures is between 63 K and 65 K with a corresponding theoretical transformation-enthalpy of approximately 65 kJ/kg [6]. For example, the measured value for methane is 89.3 K with a latent heat of fusion of 59.2 kJ/kg which is in good agreement with literature data [6]. Currently a suitable latent-heat storage device for the integration in the whole hydrogen test area is under construction. In the final setup, the hydrocarbons will be stored in a separate vessel to serve as a working material but not as a material under test.

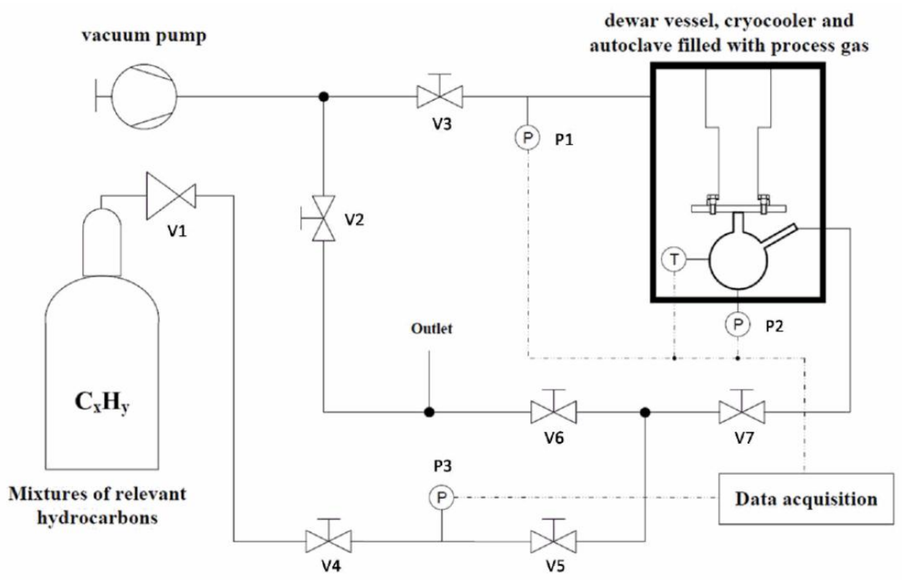

Figure 7. Schematic structure of the experimental station for material characterization

### 4.3. Re-cooler

First successful tests of a re-cooler have been performed using a separate experimental setup suited for gaseous nitrogen and gaseous neon. Nitrogen gas is taken from a standard gas cylinder. Its pressure is reduced to values of typically 5 bar. A pre-conditioner is used to assure defined and stable temperatures of the gas prior entering the cooler. In order to determine the cooling power, the cooler is kept at constant temperature by a heater whose power is measured. The data for pressure, temperature, heating power, and volume flow is collected and recorded. The measured cooling power was in agreement with calculated values. As expected, the best theoretical approximation of the measurement data can be obtained by use of a model considering both, the Bernoulli effect and the Joule-Thomson effect.

The next experiments will be performed with hydrogen within high-pressure $H_2$ test area.

## 5. CONCLUSIONS

A hydrogen test area for cryogenic high-pressure applications has been built up and tested. First experiments within the new $H_2$ test area show good results not only on the handling of cryogenic gases and liquids but also on potential benefits from additional components like re-cooling and latent-heat storage systems. Experiments on components like an integrated latent-heat store are on progress. A promising way of a high density hydrogen storage is described and patented [5]. Experimental investigations on the theoretically expected enhanced storage density in the supercritical state are currently performed.

## 6. REFERENCES

[1] http://www.bmw.com/com/en/insights/technology/efficient_dynamics/phase_2/clean_energy/bmw_hydrogen_7.html [2012-06-20]
[2] http://www.hycar.de/fahrzeuge.htm [2012-06-20]
[3] http://www.the-linde-group.com/en/news_and_media/press_releases/1483597.html [2012-06-20]
[4] NIST Reference Fluid Thermodynamic and Transport Properties Database (REFPROP 8.0), US National Institute of Standards and Technology, 2000
[5] ILK Dresden patent DE 10726881.5, PCT patent pending
[6] VDI - Ges. für Verfahrenstechnik und Chemieingenieurwesen. VDI-Wärmeatlas. Springer, 2006

# RARE GASES

059

# Assessment of the Storage of Crude Helium in Reserves in Europe or Elswehere

**Clarke R.H.*, Scurlock R.****

* $^4$He Consulting, 30 East Saint Helen St., Abingdon, Oxfordshire, OX14 5EB, UK
**Kryos Technology, 22 Brookvale Rd., Southampton, SO17 1QP, UK.

## ABSTRACT

Since the USA terminated its Helium Conservation Program, and started selling off its Federal Reserve helium, little action has been taken to counter the consequences to the international cryogenic industry. The Federal Reserve used to provide a “flywheel effect” which stabilised the global helium market; this stability is now lost and periodic shortages have emerged.

Two issues now dominate the helium market: (1) refining capacity in the short term and (2) long term resource availability. Market modelling (Nuttall et al. (eds.), “The Future of Helium as a Natural Resource”, 2012a) indicates how recurring under-supply is a serious threat to long term market sustainability. It will increasingly undermine the continuation of helium’s use, the development of new applications and the sustenance of existing ones.

The obvious need to re-establish the “flywheel effect” requires the replacement of the old and depleted US reserves with additional refining capacity and a number of large scale helium storage reservoirs inside and outside the USA

This paper will assess: (1) the sourcing of crude helium, surplus to demand, for filling long-life storage reservoirs, (2) the availability of suitable geological structures in Europe and elsewhere for the long term storage of crude helium, and (3) possible ownership and financing options.

## 1. INTRODUCTION

The helium market has grown at average rate of 3.5% since the early 1990s. Demand is constantly evolving. Some applications, such as the “dot.com” optic fibre boom, emerge and collapse while others, such as leak detection, persist. For the industrial gas industry it is hard to predict medium-term helium requirements. Coupled with the “fresh fruit market”, that is the liquid helium supply, industry disturbances can quickly propagate. Increasingly, the high technology users – cryogenics and MRI systems comprise nearly 30% of the market – are seeking ways to decouple their high value and high cost operations from the vagaries of helium supply.

Meanwhile, there are significant changes taking place upstream. The BLM Cliffside reserve is winding down towards a 2020 closure of its “open market” helium operations. Middle East and other LNG-based sources are increasing but a combination of “barriers to entry” and the industrial gas industry’s reticence to invest in helium refineries has limited access to molecules that are then vented.

It is this combination of changing and interconnected market dynamics that is leading to calls for more stability, an assurance of long term supply and less venting. This paper outlines some possible options which include the recovery of trace helium at natural gas fields, in natural gas networks and to look at geological storage of crude helium. In the related paper (Scurlock et al., 2012), a call for a new international arrangement for helium is made – to give the impetus, finance and organisation required to provide collective industry infra-structure of this kind.

## 2. HELIUM DEMAND AND PRICES

Figure 1 shows the trend in helium demand since the early 1990s. After the 1996 US Helium Privatisation Act came into operation demand has been erratic, although it is not (strongly) suggested the former led to the latter. Attempts have been made to explain these trends, albeit not very successfully. Here we suggest that there are two main components of the helium market: ‘traditional’ (largely industrial) users and ‘high technology’ (including cryogenic) users. Indices of these two sub-markets, the US Federal Reserve Bank’s Industrial Production and Utilisation (IPCU) data and the ArcaTech100 (NYSE:^PSE) index, when adjusted for a shift from traditional to high technology users (from 31% in 1990 to 48% in 2011) have been combined (grey squares). Even with the benefit of hindsight, such predictions might still have persuaded the industrial gas companies, one and all, to decline to bid for the Qatar-2 contract in 2003. The 2007 shortages were the result. The most reliable trend prediction has been a simple 3–3.5% growth, as shown.

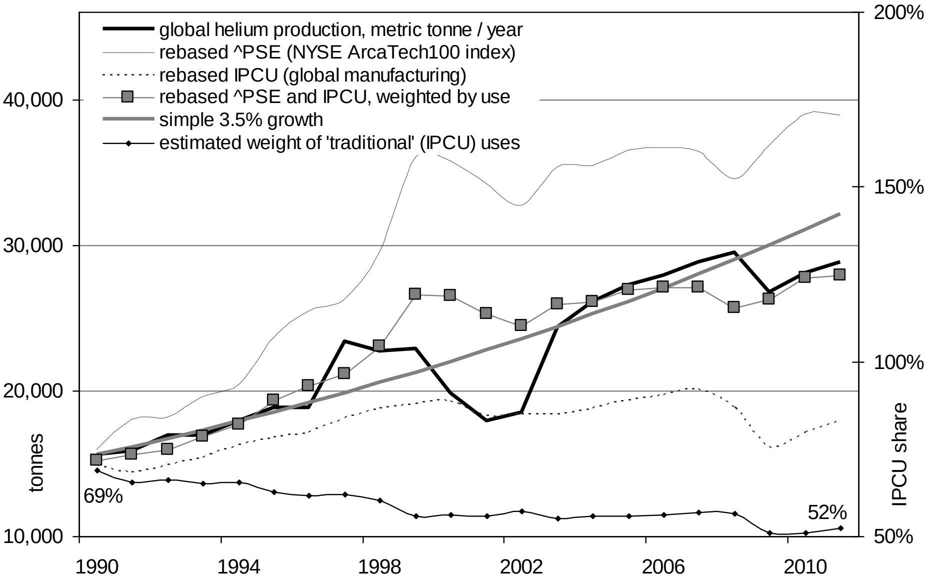

Figure 1. Global helium use: a 3.5% growth rate assumption is the most reliable indicator (source: USGS)

Helium price data (Figure 2) is understandably hard to obtain. However, under the Helium Privatisation Act, the price of federally-originated crude helium from the BLM Cliffside, Texas, facility was mandated to increase in line with the US consumer price index. This has artificially suppressed crude prices, not only in the US but in LNG projects that took their lead from the BLM. Recently, following the NAS (2010) review, US crude prices were raised and are now increasing at ~14%, a rate similar to that of estimated private industry Grade-A price rises. Note the 2004 breakout: to purify 1 Mcf of crude helium costs ~$10 (2000) rising to ~$20 today. The crude helium price has gone from being a ceiling to a floor, until recently. Yet, to see the growing difference between crude and private prices, it is not clear why there has not been enough investment in new helium refineries to adequately meet demand. As we shall see, belatedly most spare helium capacity at LNG plants has been taken up. Reaching other helium sources is harder.

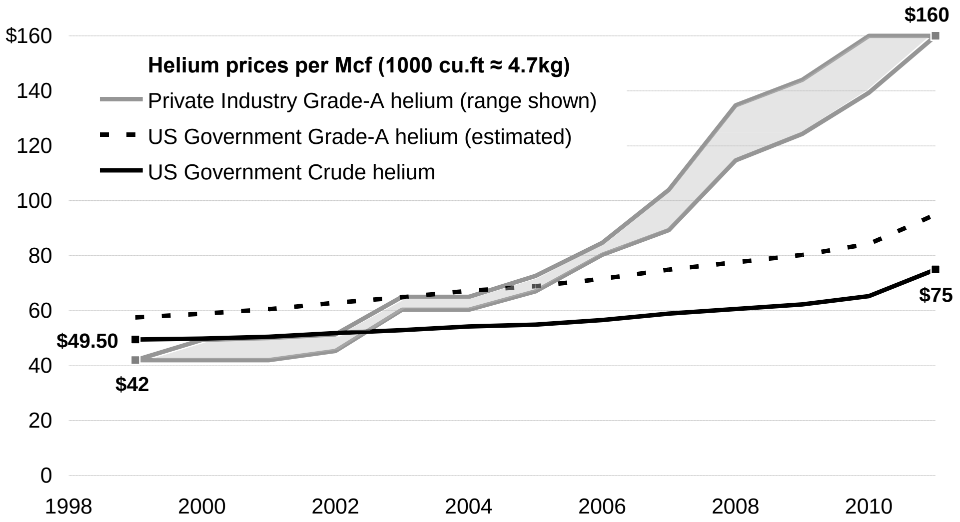

Figure 2. Helium prices: the BLM crude price was index-linked until 2010 (source: Washington Post/BLM)

## 3. SOURCING VENTED HELIUM

Cook (1979) suggested an algorithm for evaluating helium resources. The helium resources value unit (HRVU) = $G.z^2$ where G= natural gas flow rate (e.g. mmtpa LNG) and z= helium concentration. The square law reflects the difficulty of purifying a low grade helium feedstock. In LNG plants, helium is obtained from the main condenser purge gas and that can contain up to 50% helium which considerably reduces the capital cost of the helium purifier required. On this basis, the most promising prospects would appear to be LNG plants where helium is vented. However, as Table 1 shows, as of 2013 most of the resources will have been allocated. The only significant prospect is Shell's massive Pearl GTL complex: the natural gas feed contains 0.04% helium. It is not known what the helium concentration of the purge (vent) gas is, or what other contaminants it contains, but at first sight (given the location) it could be fed into the Qatar-2 helium plant which appears to have excess capacity for when the Qatar field is further developed.

Table 1. LNG and GTL plants as a source of high value crude helium (LNG data from: Flower, 2012)

| LNG / GTL exporter | LNG/NG volume in 2011 (mmtpa) | Field production status | Field He conc. (volume percent) | Helium available (tonne/y) | Helium production in 2013 (tonne/y) | Expected venting in 2013 (tonne/y) | Cook's HRVU | Comments: ( ~0.05 million cubic feet of natural gas (NG) per tonne LNG is assumed) |
|---|---|---|---|---|---|---|---|---|
| Qatar (Rasgas, Qatargas) | 74.0 | Flat* | 0.04 | 6900 | 9400 | -2500 | 11.8 | Qatar-2 He project appears to have reserve capacity. |
| Qatar (Pearl GTL) | 11.7 | Flat* | 0.04 | 1100 | 0 | 1100 | 1.9 | * Flat output until ~2015: ongoing field impact review |
| Algeria (Arzew, Skikda) | 12.8 | Declining | 0.19 | 5700 | 5600 | 100 | 46.2 | Hassi R'Mel field helium concentration. |
| Russia (Sakhalin) | 9 | Growing | 0 | 0 | 0 | 0 | 0 | Similarly at Yamal and Shtokman? |
| Indonesia | 21 | Declining | 0.02 ? | 1000 | 0 | 0 | 0.8 | He concentration is illustrative |
| Oman | 8 | Declining | 0.02 ? | 400 | 0 | 0 | 0.3 | " |
| Libya | 6 | Growing | 0.02 ? | 300 | 0 | 0 | 0.2 | " |
| Australia (Darwin) | 3.7 | Growing | ~0.08 [a] | 700 | 700 | 0 | 2.4 | Geography a significant factor n.b. Mt.Kitty prospect 0.6% He |
| Other LNG exporters examined were found to have negligible helium reported or inferred: Peru, Yemen, Norway, Equatorial Guinea, Egypt, Nigeria, Trinidad & Tobago, Malaysia, Brunei | | | | | | | | [a] deduced from mass balance |

If the LNG options are limited, what might the non-cryogenic options be? Looking at Europe, there is Russian gas from the east, Polish gas, LNG and Algerian gas from the south. In the case of the Russian gas, if there were trace helium it would be best removed before the flow is split. LNG has no helium, as it is removed or vented at source. This leaves the Polish and Algerian gas.

The Hassi R'Mel field, in northern Algeria, has a helium concentration of 0.19%. There are currently five customer groups to the north: Spain, Arzew (LNG), Algiers, Skikda (LNG) and Italy (Figure 3). Helium is extracted at the LNG plants but not on the other lines. This means that more than half the Hassi R'Mel helium molecules are vented by the end-users of the natural gas.

There are several ways to access these molecules, it is a combination of engineering and finance:

1. Separate crude helium (using membranes or large wound coil exchangers as used in the US Conservation Program) and re-inject it into the field – this would slowly build up the helium concentration possibly for capture at Arzew and Skikda if the LNG and helium plants can cope with the slowly increasing helium content
2. Separate the crude helium and send it by an old pipeline (e.g. to Spain) for underground storage and recovery to a new helium plant, a "flywheel" plant – this greatly depends on there being suitable geological (anhydrite) formations that are impermeable to helium
3. Separate crude helium and bring it straight to market via a purifier/liquefier at Hassi R'Mel or at the coast – the drawback is the lack of storage, but it is better than venting (although liquid helium can be transported in specialised containers for periods of up to 30 days, long-term storage of liquid would be very expensive)

The third option is closest to market but, while it helps meet helium demand, it does not conserve helium. A combination of the first and third options may be feasible.

A similar, but smaller scale, situation exists at the Odolanów helium plant in Poland. Blending of helium-rich and helium-lean gas, upstream, means that the Polish plant runs below capacity. In the longer term, developments in central Australia have helium production and storage potential.

Of all these prospects the Hassi R'Mel field offers the possibility to make a significant and beneficial impact on the helium market – particularly on the intermittency of supply problem. It is clear from our own researches that some of the ideas above have been mooted for previously, so what would encourage such developments to take place?

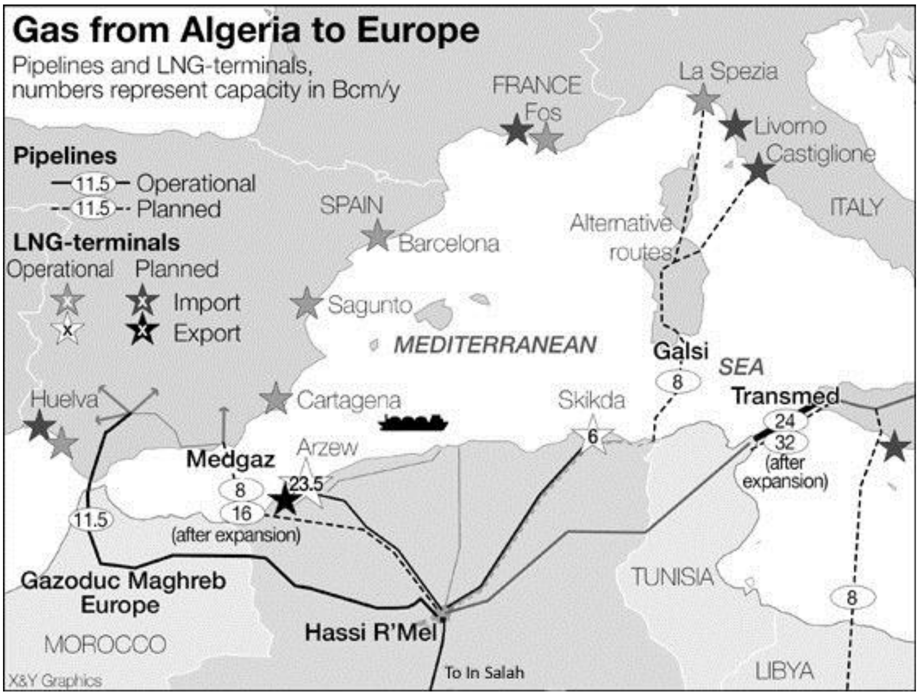

Figure 3. The Hassi R'Mel field, Algeria, and its pipelines (source: www.europeanenergyreview.eu)

## 4. DEVELOPING RECOVERY AND STORAGE AT HASSI R'MEL FIELD

The Hassi R'Mel field, in 2010, had estimated natural gas reserves of around 159 Tcf (Reinoehl, 2012) which, at 0.19% helium content, would be enough to meet projected global helium demand for more than 30 years (based on the work of Cai et al., 2010). This is the world's best prospect, now, as a helium resource and much of it is being lost. However, as was pointed out by Nuttall et al. (2012b), the global natural gas industry has a $1trillion turnover compared to the $1billion helium industry. In other words, any developments towards helium recovery or storage must not compromise the operation or revenue stream of the natural gas system. Tapping into and diverting a significant proportion of a country's natural gas supply needs studying carefully. Equally, what effect would re-injection of crude helium (albeit at low flow rates) have on the field itself?

Let us examine the store-and-produce option outlined above (items 1+3). This would require a helium purifier and liquefier with enough capacity to recover and purify most of the currently vented molecules. This could be in the same league as the $500 million Qatar-2 helium plant that will be capable of producing 17 tonne/day (1.3 Bcf/y) of helium. However, for much of the time the plant might be deliberately operated at reduced capacity so that, when needed, it could be ramped up i.e. it would be a “flywheel” plant. At times of reduced demand the recovered molecules, in the form of crude helium (~70% helium, ~30% methane + nitrogen) would be re-injected into the field at a suitable location. The expectation would be, if the geological work is done correctly, that the re-injected molecules would slowly increase the field’s helium concentration without any significant by-passing taking place. Effectively those molecules would be held in trust for future generations. Unless additional helium recovery is installed on the Arzew and Skikda lines, some medium term plan would be needed to adjust the processes and revenue at the two LNG plants; helium purifiers can be quite sensitive to changes in feed composition. Also, the Wobbe Index (a measure of the interchangability of gas sources) would need to be corrected after helium recovery, perhaps with a small quantity of nitrogen injection?

## 5. FINANCING

The above discussion, about new helium recovery and storage in Algeria, suggests that existing models of project development and financing have not proven sufficiently attractive for the idea to be developed. Some of the issues have been highlighted. The principal difficulty is finding a method of financing storage for the future.

This is where the ideas discussed in the related paper (Scurlock et al., 2012) take shape. What is needed is an oversight body that can lead helium industry action without reducing competiveness. That the BLM and US Federal Reserve has operated, and indeed led, the helium industry for most of the 20th century should be an encouraging precedent. The scale of the Hassi R’Mel field is such that, as the Cliffside field runs down, the Algerian production and recovery operation could ramp up. By 2020 there is projected to be a 14,000 tonne/year (3 Bcf/y) gap (Hooker, 2012) in helium supply that this project could help fill, at least a significant part of it.

It is proposed that new international arrangements for helium be established and, with the aim of bringing early focus, its first major project could be the Algerian proposal.

It is envisaged that there would be an operating agreement among the major industrial gas companies so, that in times of helium shortage or when other plants face upsets or maintenance, the Algerian “flywheel” helium plant can be ramped up or down by consent. Again, there is a model here. At Cliffside, the Crude Helium Enrichment Unit (CHEU) although providing a different role from that needed in Algeria is operated as private company (Cliffside Refiners LP).

## 6. CONCLUSIONS

In the context of proposed helium-industry-wide efforts to address the venting problem, we have examined here, in outline, the options for new developments. At first sight, the purge gas from LNG plants would appear the most attractive option but, as of 2013, there are only limited options amounting to a few hundred MMscf/y. An intriguing prospect is whether the helium rich purge gas at Shell’s GTL plant might be recovered into the Qatar-2 plant that comes online in 2013.

The most promising option, after LNG, turns out to be the Algerian Hassi R’Mel field that is already feeding two LNG plants with helium purifiers and liquefiers. The gas is rich in helium but more than half of the helium molecules are being vented through pipeline sales into southern Europe and elsewhere.

Helium gas recovery, storage and purification at the Hassi R’Mel field itself would appear to be a technically plausible option but, for various reasons, this has not yet happened.

It is proposed that the new international arrangements for helium outlined in the related paper (Scurlock et al., 2012) could pave the way for new mechanisms to be put in place to negotiate, engineer and finance further helium developments in Algeria or elsewhere.

Such a project could make a considerable and beneficial impact on helium market stability and long term helium availability.

# 7. REFERENCES

Cai Z., Clarke R.H., Glowacki B. A., Nuttall W. J. and Ward N. (2010) “Ongoing Ascent to the Helium Production Plateau – Insights from System Dynamics”, *Resources Policy*, Vol. 35, pp. 77–89

Cook E. (1979) “The Helium Question”, *Science*, Vol. 206, pp. 1141-7 (7 December 1979)

Flower A. (2012) “LNG – Liquid Natural Gas” in *The Future of Helium as a Natural Resource* (Nuttall W.J., Clarke R.H. and Glowacki B.A., Editors), Routledge, London and New York.

Hooker B. (2012) “Helium in Russia” in *The Future of Helium as a Natural Resource* (Nuttall W.J., Clarke R.H. and Glowacki B.A., Editors), Routledge, London and New York.

National Academy of Sciences (NAS) (2010) *Selling the Nation’s Helium Reserve,* National Academies Press, Washington, DC., USA.

Nuttall W.J., Clarke R.H. and Glowacki B.A. (Editors), (2012a), *The Future of Helium as a Natural Resource*, Routledge, London and New York.

Nuttall W.J., Clarke R.H. and Glowacki B.A. (2012b) “Resources: Stop Squandering Helium”, *Nature*, Vol. 485, No. 7400, pp. 573-575 (31st May 2012)

Reinoehl B. (2012) “Helium in Algeria” in *The Future of Helium as a Natural Resource* (Nuttall W.J., Clarke R.H. and Glowacki B.A., Editors), Routledge, London and New York.

Scurlock R., Nuttall W.J., Clarke R.H. and Glowacki B.A., (2012), “The Future of Helium? A Global Agency to Oversee Production, Storage, Supply and Use of Helium Gas and Liquid", Proc. Cryogenics 2012, IIR Conference, Dresden, Germany

024

# Cascade Units for Neon Isotopes Production by Rectification Method

**Bondarenko V.L.[*], Simonenko Yu.M.[**], Lyschik A.A.[***], Yemelyanov A.M.[***], Dalakov P.I.[***]**

[*]Moscow Bauman State Technical University, Moscow, Russia
[**]Odessa State Academy of Refrigeration, Odessa, Ukraine
[***]Iceblick, Ltd., 29, Odessa, Ukraine

## ABSTRACT

Mechanism of neon separation into isotope components by distillation method is considered. Influence of load characteristics of the upper and lower column on number of transfer units is shown. Characteristics of the packed rectification columns and their connection in the cascade chain are specified. Necessity of formation of initial steps of the cascade on the basis of several single-type rectification apparatus is proved.

## 1. INTRODUCTION

Nearly one hundred years ago A.J. Thomson by example of $^{20}$Ne and $^{22}$Ne determined for the first time existence of stable elements isotopes [1]. $^{21}$Ne was discovered in the 1920-ies. Neon isotopes are widely used in modern high technologies. $^{20}$Ne and $^{22}$Ne mixtures are object of research of the physicists, who study mechanism of photonuclear reactions. Isotope anomalies help to disclose secrets of our planetary system formation. In particular, astronomers found out that when some meteorites are heated $^{22}$Ne monoisotope is produced, at the same time the total contents of $^{21}$Ne and $^{20}$Ne doesn't exceed 1 % (almost twice as little as in neon extracted from Earth atmosphere). Neon isotopes gas mixture ($^{20}$Ne + $^{22}$Ne) is the active medium of gyroscopes, the operation of which is based on Zeeman's effect [2]. They are tolerant to mechanical influences and have stable scale factor. Besides navigation, such devices are in demand for researches in fundamental areas of physics. Very perspective is the sphere of application of the rarest $^{21}$Ne neon isotopes. Physicians believe that nuclear and physical properties of this element allow application as alternative of $^{3}$He isotope at MRI diagnostics of lungs ventilation.

## 2. NEON SEPARATION INTO ISOTOPES BY RECTIFICATION METHOD

In 1913 the first mass spectrometer, which was invented a year earlier, was used for separation of neon isotopes samples. Separation of $^{20}$Ne and $^{22}$Ne isotope pair for laboratory and industrial purposes is also possible by methods of thermo diffusion and chromatography [1, 3]. Neon is at the limit of application of distillation method, which is considered to be effective at molecular masses less than 20 [4]. Separation coefficient of $^{20}$Ne - $^{22}$Ne isotopes at liquid–vapor phase balance at temperatures $T = 27\ldots30$ K is $\alpha$=1,040…1,032 [5]. Despite this, low-temperature rectification is considered to be the most perspective method of neon separation [6]. This statement becomes even more powerful, if one of the target products is $^{21}$Ne.

Let's consider the process of binary mixture $^{20}$Ne - $^{22}$Ne separation. Illustratively let's use *y*-*x* diagram with reference to high-boiling isotope. 1-b figure shows, that the chart is symmetric to the typical diagram, made with reference to low-boiling component of mixture. Such decision allows avoiding unnecessary recalculations of concentration and gives direct information on the contents of the target product ($^{22}$Ne) in streams and sections of the column.

Table 1 shows the results of calculation of number of transfer units for the upper and lower sections of the column. Isotope concentrations of the streams, accepted at the solution of the task, are the following:

– initial mixture $x_0$=0,0925 (neon with natural isotope ratio 9,25% $^{22}$Ne);
– bottom section of the column product $x_p$=0,9999;
– waste stream, removed in the upper part of the column, $x_W$=0,015.

Under such concentrations the contents of W waste flow lose 15 % of the target product, and the level of extraction is $C$=0,85, where

$$C = \frac{(x_W - x_P)\cdot x_P}{(x_P - x_W)\cdot x_0}. \qquad (1)$$

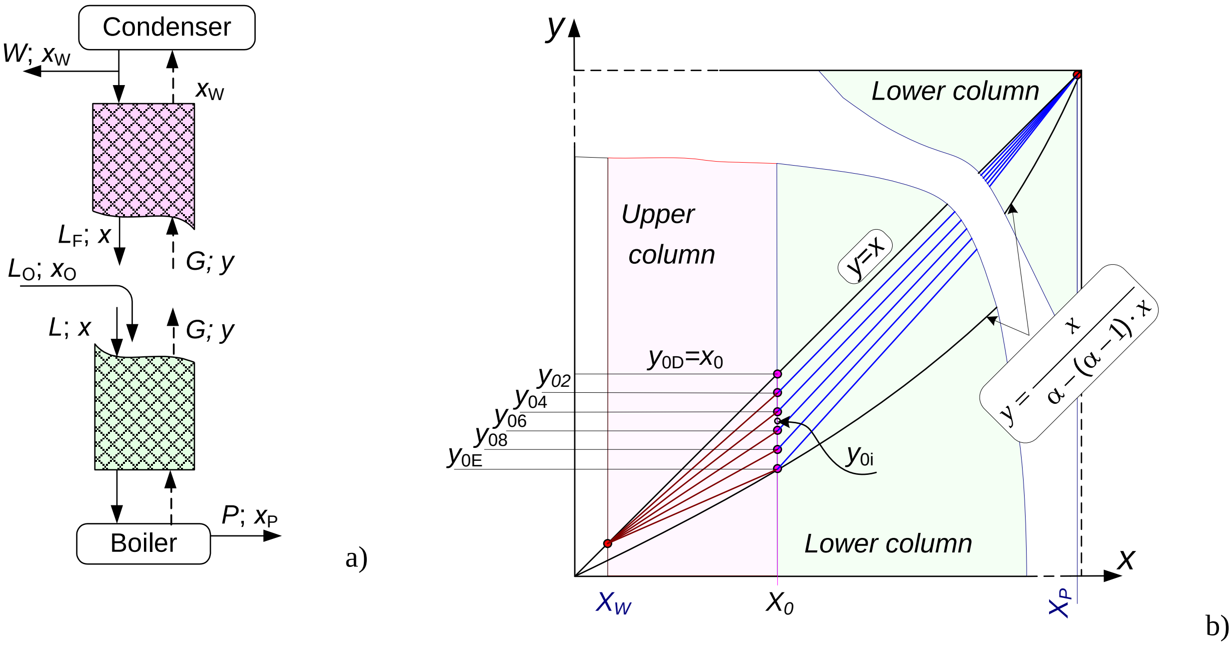

Fig.1. Material flows (a) for upper and lower sections of the column and operating lines (b) in $y$-$x$ diagram, made with reference to high-boiling component (representative scale); $L_0$, $W$ and $P$, correspondingly, flow rate of supply isotope mixture, waste (enriched with $^{20}$Ne) and product ($^{22}$Ne).

In accordance with number of «theoretical rectification stages» determination, it was accepted that liquid and vapor on each of elementary rectification stages unit are balanced. For general case equation of operating line for the upper column is:

$$y = \frac{L_F}{G}\cdot(x - x_W) + x_W, \qquad (2)$$

where
$L_F$ and $G$ – flow rate of liquid (phlegm) and vapor, [mol/s]; $x$ – concentration of liquid phase in the arbitrary section of the upper column, [mol/mol] (fig. 1-a).

The same is for the lower column

$$y = \left(\frac{L_F + L_0}{G}\right)\cdot(x - x_0) + y_{0i}. \qquad (3)$$

where
$L_0$ and $x_0$ – flow rate and concentration of supply vapor, [mol/s]; $x$ – concentration of liquid phase in the arbitrary section of the lower column, [mol/mol]; $y_{0i}$ – ordinate of intersection of tie lines of the upper and lower sections of the column (fig. 1-b).

In case the initial mixture is loaded to the column as liquid, the ordinate of points $y_{0i}$, where tie lines intersect, will be on the vertical line $x_0$=0,0925 within the limits of segment $y_{0D}$ - $y_{0E}$. In the calculation model there are considered: "no load" mode in case of selection of the product $P$=0 ($y_{0D}$=$x_0$), maximum possible loading in case of minimum phlegm ($y_{0E}$), and also four intermediate modes $y_{02}\ldots y_{08}$. Their characteristic tie lines are remoted from diagonal $y$=$x$ by 20, 40, 60 and 80 % comparing to the maximal distance, characteristic for the mode of minimum phlegm ($y_{0E}$). For the accepted concentrations of streams at the increase of the loading modes from $E$=0 up to $E$=1,0 the relative consumption of the product $P/L_0$ differs within the range of 0,0…0,0033. I.e., the volume of the produced product with isotopic concentration 99,99 % $^{22}$Ne does not exceed one third of a percent from the flow rate of the supply substance $L_0$.

Table 1. Descriptions of operating conditions in upper and lower sections at the liquid feed of rectification column with neon with the "natural" concentration of high-boiling component ($x_0$=0,0925) and output streams $x_W$=0,015 and $x_p$=0,9999.

| Description of the mode, degree of balance in stream delivery point $E=\dfrac{y_{0D}-y_{0i}}{y_{0D}-y_{0E}}$ | | Upper section | | | Lower section | | Total $N_T$, pcs. |
|---|---|---|---|---|---|---|---|
| | | Angular coefficient of lines on area $x_W$-$x_0$ $\lambda'_F=\dfrac{L_F}{G}$ | Number of transfer units (NTU) $N'_T$, pcs. | $y_{0i}$ – coordinate of crossing of working lines at $x=x_0$ | Angular coefficient of lines on area $x_0$-$x_P$ $\lambda''_F=\dfrac{L_F+L_0}{G}$ | Number of transfer units $N''_T$, pcs. | |
| No-load, *E*=0 | | 1,0 (diagonal) | 52,3 | $y_{0D}=x_0=0{,}0925$ | 1,0 | 316 | 368 |
| Intermediate conditions | *E*=0,2 | 0,992 | 59,8 | $y_{02}$= 0,0919 | 1,00066 | 327 | 387 |
| | *E*=0,4 | 0,984 | 70,6 | $y_{04}$= 0,0913 | 1,00132 | 340 | 411 |
| | *E*=0,6 | 0,977 | 88,3 | $y_{06}$= 0,0907 | 1,00199 | 357 | 445 |
| | *E*=0,8 | 0,969 | 125,6 | $y_{08}$= 0,0901 | 1,00265 | 384 | 510 |
| Minimum phlegm, *E*=1 | | 0,961 (equilibrium curve) | ∞ | $y_{0E}$= 0,0895 | 1,00331 | ∞ | |

As the results of calculation show, the number of theoretical rectification stages is calculated by hundreds. As the height of the transfer unit for the applied types of the packing makes dozens of millimeters (table 2), column for $^{22}$Ne production with isotopic quality 99,99 % and extraction coefficient *C*=0,85 has a considerable size. Height of mass exchange part can be 15...20 meters. Such sizes are the reason of considerable external heat leakage and complicates cryogenic support of the unit.

Table 2. Comparative descriptions of packing rectification columns, used by authors for neon separation into isotopes (in the mode of no-load *E*=0).

| Diameter, mm | $x_W$ | $x_P$ | NTU, $N_T$, pcs. (4) | Height of transfer units, mm | *q* – separation factor (4) | Specific surface area of packed bed, m$^2$/m$^3$ |
|---|---|---|---|---|---|---|
| 22 | 0,003 | 0,985 | 275 | 28,7 | 21 800 | 5470 – SP |
| 25 | 0,004 | 0,983 | 263 | 30,0 | 14 400 | 3430 – SP |
| 25 | 0,02 | 0,98 | 215 | 30,5 | 2 400 | 2720 – SP |
| 32 | 0,06 | 0,92 | 150 | 42,0 | 180 | 1520 – SC |
| 35 | 0,05 | 0,95 | 160 | 40,1 | 360 | 1980 – SC |
| 50 | 0,01 | 0,5 | 130 | 50,4 | 100 | 1000 – SP |
| 50 | 0,015 | 0,4 | 105 | 61,0 | 45 | 630 – SC |

Designations in the table 2: $x_W$ and $x_P$ are concentrations of high-boiling component ($^{22}$Ne); SP is spiral-prismatic packing; SC is spiral-cylindrical packing. Factor of separation *q* of column and number of theoretical rectification stages (transfer units) $N_T$ in case of no extraction of product (*P*=0) are specified in Fenske formula [7]

$$q=\frac{x_P}{x_W}\cdot\left(\frac{1-x_W}{1-x_P}\right)=\alpha^{N_T}\,, \tag{4}$$

where

α is separation coefficient of binary system (for isotope pair $^{20}$Ne- $^{22}$Ne α=1,037) [5].

## 3. SEPARATION OF NEON ISOTOPES IN CASCADE OF RECTIFICATION COLUMNS

If the height of a single column is limited (table 2), it is impossible to get the product of high quality $x_P$. Because of this separation of isotopic components has to be stage-by-stage. On some stage of separation it is occurs the accumulation ($^{21}$Ne) also, which kept in the initial mixture in concentration 0,28 %.
Fig. 2 shows the outlines of successive concentration of high-boiling ($^{22}$Ne) and intermediate ($^{21}$Ne + $^{22}$Ne) isotopic components. Naturally, $x_W$ mixtures enriched with low-boiling $^{20}$Ne are removed from the contours waste mixtures. The first outline (fig. 2-a) provides the frequent processing of intermediate fractions in the same column [6]. Obviously, the capacity of such method is low and to increase it cascade connection of several columns is used (fig. 2-b). The feature of the second outline is the return of waste fractions $x_{W2}$ and $x_{W3}$ to the previous sections (1 and 2) for reprocessing. For this purpose each next step has increased pressure $P_1<P_2<P_3$ in comparison with the previous one. Both in the first and the second case (fig. 2-a, b) supply of $x_{Pi}$ bottom section of the column product to the column for repeated separation is accompanied by a number of unproductive processes. The produced intermediate $x_{Pi}$ fractions have to be heated up to the temperature of ambient air, collect in gasholders, compress, purify from admixtures, cool down and supply to the next column (variant b) or to the same column (variant a). Unfortunately, these procedures result in the losses of expensive isotopic components, enriched by the target products ($^{21}$Ne + $^{22}$Ne).

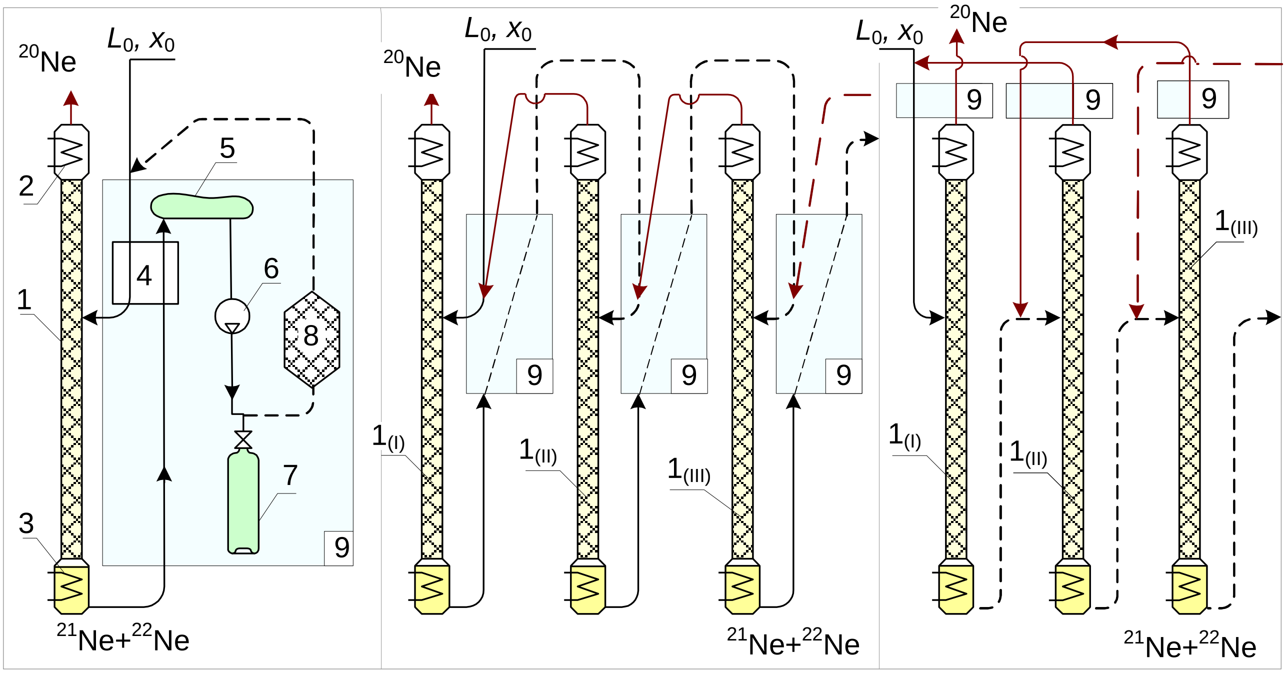

a) b) c)

Fig. 2. Variants of multistage separation of isotopic connections. a – on the basis of the same rectification column; b – cascade connection of columns with heating of intermediate fractions, enriched by target products; *c* – cascade connection of columns with heating of intermediate fractions, leant by target products. Designations: 1– rectification columns; (I)…(III) – # of the stage; 2 – condenser; 3 – vaporizer of bottom section of the column; 4 – heat-exchanger; 5 – gasholder; 6 – compressor; 7 – receiver; 8 – adsorber; 9 – collection, storage and purification fraction block.

More perspective, in our opinion, is the third variant (fig. 2-c), because valuable products are supplied directly to the subsequent stages of cascade ($x_{P1}$ – to the column 2, $x_{P2}$ – to the column 3, etc.) in cold state. Thus, less valuable products, enriched by prevailing component $^{20}$Ne are supplied to the block 9 (collection, storage and purification of fraction). The outline (fig. 2-c) can function without return of waste streams. In this case $x_{Wi}$ fractions are collected and used, e.g. for preparation of mixtures with modified (different from natural) isotopic ratio.

For providing of outline operation, showed on fig. 2-c, it is necessary to support the propulsive difference of pressures between the stages $P_1>P_2>P_3$. Such pressure difference can be achieved through the different thermal loading in vaporizers of bottom section of the column 3 (fig. 3-a). Important operating advantage of the outline, shown on fig. 2-b and 3-a, is decreased pressure in the end column III. Thus coefficient of relative volatility (separation factor) of isotope pair $^{20}$Ne - $^{22}$Ne with reduction of the working pressure is increased [5].

All stages on figures 2 and 3 are shown as columns with the identical diameter. Meantime most cascade units use the outlines with the step decreasing productivity of elements [8]. Decrease of consumption $x_{01} > x_{02} > x_{03} \ldots$. allows decreasing of time of achievement of stationary state in the columns of cascade. For illustration of this phenomenon we will introduce the special factor – relative productivity of rectification devices:

$$\omega = \frac{L_0}{V} = \frac{L_0}{k \cdot \varphi \cdot (v_1 + v_2 + v_3)}, \text{ [1/h]} \qquad (5)$$

where
$L_0$ – consumption of processed product, [norm. dm$^3$/h]; $(v_1 + v_2 + v_3)$ – total hydraulic volume of column, [dm$^3$], that consists of volumes of packing section (1), condenser (2) and bottom section of the column (3), correspondingly (see fig. 2 and 3); $\varphi$ = 0,16…0,18 – fraction of filling of volumes 1, 2, 3 by liquid neon; $k = \rho_G / \rho_L$ = 1 450 – volume of neon [norm. dm$^3$], that is produced at evaporation of 1 dm$^3$ of liquid ($\rho_G$ = 0,829 g/dm$^3$ – density of gaseous neon at $P$=0,1 MPa and $T$=293 K; $\rho_L$ = 1206 g/dm$^3$– density of liquid neon).

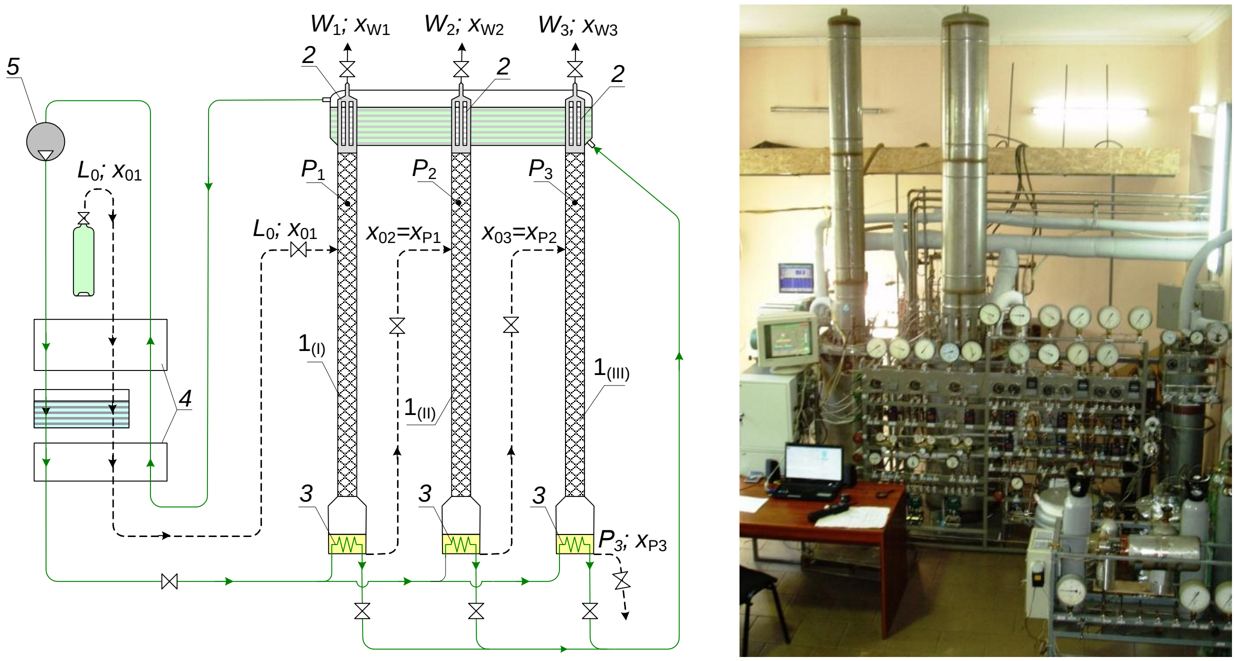

a) b)

Fig. 3.Outline of cryogenic supply of cascade unit identical to fig. 2-c. Designations: 1...4 –correspondingly fig. 2; 5 – compressor of neon throttle cycle with nitrogen cooling.

As follows from data [6] and results of the tests, received by the authors, the size ω for the primary column of cascade in the mode of $^{22}$Ne production is $\omega_{22}$=0,10…0,12 . When $^{21}$Ne is the target product, the relative consumption is decreased up to $\omega_{21}$=0,014…0,018. Being a nominal index, factor ω, at the same time, demonstrates what time consumption is necessary for the primary accumulation of the target product in columns. If this factor is not taken into account and there is no replacement of isotope products in phlegm, which fills the cavities of devices, it is possible to produce only partly enriched products. Production of concentrated substances is possible only as a result of accumulation of sufficient volume of target product in the columns (especially end sections). Minimum time (hours), required for stabilizing of concentrations, in the initial approximation is

$$\tau = \frac{1}{\varpi \cdot x_{01}}, \text{ [h]} \tag{6}$$

where
$x_{01}$ is concentration of the target product in initial mixture, which is supplied to the first column of the cascade, [mol/mol].

Taking into account $\omega_{22}$ empiric values and $^{22}$Ne contents in the initial neon stream with natural composition ($x_0$=0,0925), we will get $\tau_{22}\approx$ 100 hours. By analogy $\tau_{21}$>20 000 hours is necessary for $^{21}$Ne ($x_0$=0,0028) production! For reduction of this period deep concentration (satiation of phlegm by target product) is applied only in the end columns of the cascade. The same result can be got by reduction of volume (diameter) of columns of end cascades and increase of initial section size. According to (4) and (5) the initial section determines quality of the target product, supplied to the contour of separation. In other words, only high-performance initial stage can provide operation of low-capacity output column.

Meantime, this technical solution, put into operation, doesn't give the expected result. The attempt to increase the flow rate of initial column due to increase of its section (diameter) results in the sharp drop of separation factor *q* (table 2). The degree of extraction of target products (1) that accumulate in the packing as phlegm is decreased. This negative phenomenon can be leveled by forming of the initial stages of cascade due to several small-scale columns (fig. 4-a). Theoretically, all columns of the cascade can be unified, and their amount as part of the steps must be gradually decreased. Such reduction will lead to the redistribution of streams between sections. In its turn, it will influence on inclination of the operating lines, shown in formula (3) (fig.4-b).

Undertaken research allowed to create the series of industrial units for production of neon isotopes with concentration up to 99,99 %.

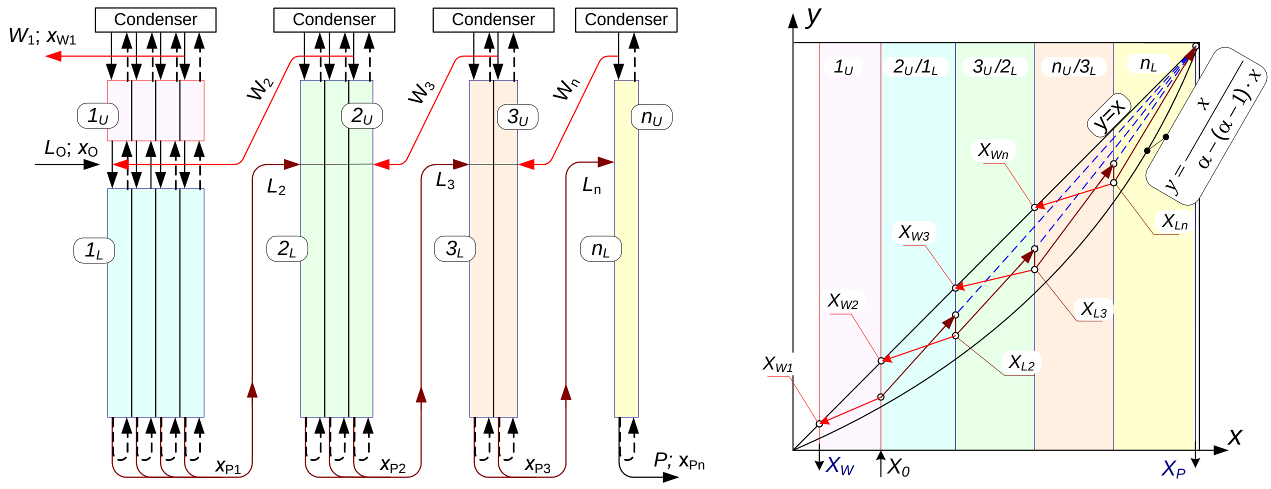

a) b)

Fig. 4.Outline of cascade unit (fig. 2-c and 3-a), formed from single-type columns (a) and character of operating lines (b) in *y*-*x* diagram on high-boiling component (representative scale).

## 4. REFERENCES

1. Brodsky A.I. 1988, Stable isotopes of light elements, *Success of physical sciences*, т.XX, edition. 2: 153-182.
2. Azarova V.V., Golyaev Yu. D. et al. 1999, In: *Optical Gyros and their Application* (RTO AGARDograph 339: 5-1).
3. Arkharov A. M., Arkharov I.A. Bondarenko V.L. et al. 2004, Non-traditional technologies of production of $^{20}$Ne isotope concentrate, *Proc. 8 Int. Conf. «Cryogenics 2004»*, Prague: 175-183.
4. Benedikt M., Pigford T. 1960, *Chemical technology of nuclear materials*, Tr. from English, M.: Atomizdat, 529 p.

5. Andreev B.M., Zelvensky Ya.D., Katalnikov S.G. 1982, *Separation of stable isotopes by physics-chemical methods*, Energoatomizdat, 208 p.
6. Bewilogua L. Verges P., Vinzelberg H. 1977, *Isotopenpraxis*, Bd.9: 97.
7. Fenske M. 1932, *Industrial & Engineering Chemistry*, 24: 482.
8. Rozen A.M. 1960, *Theory of isotope separation in columns*. M.: Atomizdat, 439 p.

022

# Enrichment of Rare Gases Concentrates with Application of Diaphragm Technologies

**Bondarenko V.L.**[*]**, Losyakov N.P.**[**]**, Simonenko Yu.M.**[***]**, Chuklin A.P.**[***]

[*] Bauman Moscow State Technical University, Moscow, Russia
[**] Iceblick Ltd, Odessa, Ukraine
[***] Odessa State Academy of Refrigeration, Odessa, Ukraine

## ABSTRACT

Examples of membrane separation of the streams containing nitrogen, oxygen and inert gases are considered. The simplified methods of calculation of membranes for a number of applied tasks are offered. Dependence of concentration of the target product on extent of extraction in case of enrichment of neon-helium mixture is shown. Comparison of membrane technologies and condensation methods of enrichment of inert gases is carried out. Results of a pilot study of membrane modules on the basis of hollow fibers are given.

## 1. INTRODUCTION

Membrane processes take a special place in technologies of enrichment of gas products. Component separation of streams in membranes takes place at the expense of selective permeability of porous material and doesn't need thermostating. In most cases membrane separators are capable to work effectively at temperature level of ambient air. This operational feature promoted expansion of the sphere of membranes application [1, 2]. Application of membrane devices instead of reflux condenser will allow expanding of the number of inert gases sources at the expense of air separation units (ASU) with limited delivery of liquid cryoproducts.

Diaphragm gas separator is shown in figure 1. The most important element of the device is the firm partition (membrane/diaphragm). It divides the case into two cavities: space over diaphragm and drain channel.

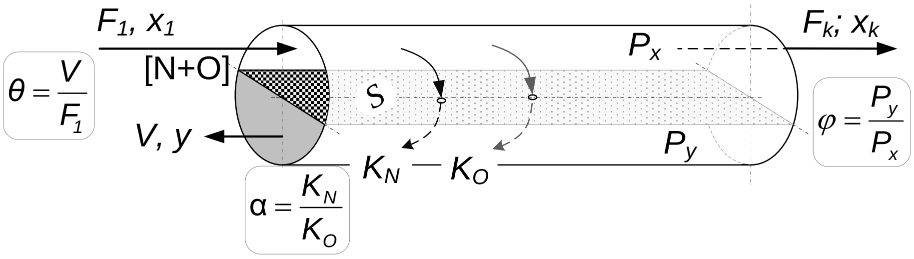

Figure 1. The simplified scheme of diaphragm module and main designations.
$N$ and $O$ - binary mixture components; $F_1$ and $F_k$ –mixture consumption at the input and output of the space over diaphragm; $V = F_1 - F_k$ – consumption of penetrating (permeating) stream; $x_1$, $x_k$ and $y$ – concentration of less penetrating component; $P_x$ and $P_y$ – pressure in space over diaphragm and in drain channel;
$K_N < K_O$ – permeability coefficients of mixture components, $S$ – area of selective surface.

Figure 1 shows the outline of diaphragm working surface in the form of $S$ rectangle. In reality in devices with hollow fibers the total $S$ selective layer is formed by lateral cylindrical surface of hundreds thousands of tubes with diameter of about 0,1 mm. For such devices such term as “space over diaphragm” is considered to be very relative. Generally this term is used for designation of space, where the separated mixture with $F_1$ consumption and $x_1$ initial concentration is supplied. This mixture passes along the surface of $S$ diaphragm and, having $P_x$ high pressure tends to penetrate to cavity of low pressure – drain channel. The material of $S$ partition has different permeability in relation to mixture components (fig. 2). Therefore in process of movement in space over diaphragm the consumption of stream not only decreases the stream consumption by V quantity, but also its concentration changes (the share of less penetrating N component is increased; $x_k > x_1$). Thus pressure of the stream over diaphragm corresponds to pressure of initial mixture $P_{x1} \approx P_{xk}$. In drain channel the permeating stream with V consumption and $y < x_1$ concentration is formed by elementary volumes of penetrating gas.

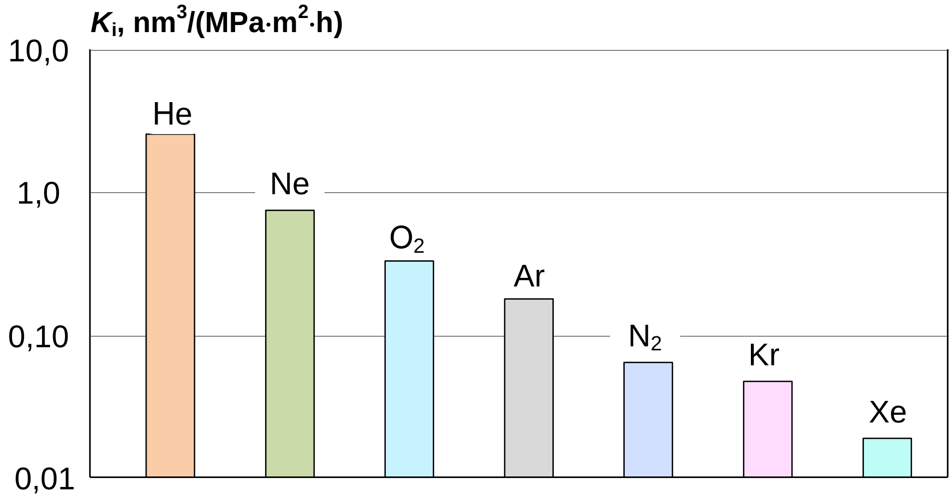

Figure 2. Permeability coefficients of pure substances – air separation products.

Relative consumption of permeating stream $\theta = V/F_1$ is the most important operational parameter of diaphragm installations. Difference of pressure $\Delta P = P_x - P_y$ between cavities (fig. 1-a) is the main motive power of process of baromembrane gas separation. This factor is often characterized by $\varphi = P_y/P_x < 1$.

## 2. CALCULATION OF BAROMEMBRANE SEPARATION OF BINARY MIXTURE

Let’s consider the mechanism of separation of binary mixture in N - O in the diaphragm module. The following formula can be got from material balance in relation to less penetrating N component taking into account the designations (fig. 1).

The received formula [3, 4]

$$\frac{y}{1-y} = \alpha \cdot \frac{\tilde{x} - \varphi \cdot y}{1 - \tilde{x} - \varphi \cdot (1-y)}, \qquad (1)$$

is called diaphragm state equation. It shows the connection between the average concentration of mixture in the cavity over diaphragm $\tilde{x} = \frac{x_1 + x_k}{2}$ and composition of permeating stream (y) depending on the disposed relation of pressures φ. Dimensionless quantity α is the factor of separation of the specified couple of components. It shows the way this membrane is able to "distinguish" the molecules of "N" and "O" gases. The further α value from the unity is the higher diaphragm selectivity is. For example, α = 0,15 is better, than α = 0,25.

The expression (1) is quadratic formula in relation to y (concentration of permeating stream). For $K_N < K_O$ ($\alpha < 1$) its solution is

$$y = \frac{1}{2} \cdot \left[ -\frac{B}{A} + \sqrt{\left(\frac{B}{A}\right)^2 - 4 \cdot \frac{C}{A}} \right], \qquad (2)$$

where

$$A = (1-\alpha) \cdot \left[ 2 \cdot \varphi \cdot (1-\theta) + \theta \right]; \qquad (3\text{-a})$$

$$B = 2\cdot(1-\theta) - 2\cdot\varphi\cdot(1-\alpha)\cdot(1-\theta) - 2\cdot x_1\cdot(1-\alpha) + \theta\cdot x_1\cdot(1-\alpha) + \alpha\cdot\theta; \qquad \text{(3-b)}$$

$$C = \alpha\cdot x_1\cdot(\theta-2), \qquad \text{(3-c)}$$

The example of calculation of binary mixture separation in diaphragm module is presented in table 1 in the column IV. Air is chosen as object for modeling of process of separation in diaphragm module. The choice of this mixture is justifiable, because for a first approximation it can be considered as two-componential product. Besides, considerable number of industrial membrane installations is intended for air separation to produce nitrogen and enriched oxygen.

Table 1. Solving of equation (1) for mixtures containing $N_2$: air and nitrogen-neon-helium concentrate at the same operational parameters. Definition of the complex factor of $\alpha_3$ separation for three-componential mixture of $N_2$-(He-Ne) is presented below in table 2.

| # | Definable parameter | | Formula, description | Nitrogen-oxygen | Nitrogen – (neon-helium) |
|---|---|---|---|---|---|
| I | II | | III | IV | V |
| 1. | Nitrogen concentration in the input | | Initial data | $x_1$=0,79 (air) | $x_1$=0,5 |
| 2. | Separation factor | | | $\alpha$=0,185 | $\alpha_3$=0,0485 |
| 3. | Pressure (abs.) | Over diaphragm | | $P_x$=1,0 MPa | |
| 4. | | permeate | | $P_y$=0,1 MPa | |
| 5. | Pressure ratio | | $\varphi = P_y / P_x$ | $\varphi$ = 0,1 | |
| 6. | Relative consumption of permeating stream | | $\theta = V / F_1$ | $\theta$ = 0,55 | |
| 7. | Coefficients of equation (2) | | (3-a)…(3-в) | A = 0,5215;<br>B = – 0,00485<br>C = – 0,2121 | A = 0,6090;<br>B = 0,1512;<br>C = – 0,0352 |
| 8. | Fraction of nitrogen in permeate | | (2) | $y$=0,643 | $y$=0,146 |
| 9. | Fraction of nitrogen in residual stream (over diaphragm) | | $x_k = \dfrac{F_1\cdot x_1 - V\cdot y}{F_k}$ | $x_k$ =0,970 | $x_k$ = 0,932 |
| 10 | Concentration of more penetrating components in permeate | | $Y$=1-$y$ | $Y_{O2}$= 0,357 = **35,7**% | $Y_{(NE+HE)}$= 0,854= **85,4**% |
| 11 | Concentration of more penetrating components in residual stream | | $X_k$=1-$x_k$ | $X_{O2}$= 0,03 = **3** % | $X_{(NE+HE)}$= 0,068=**6,8**% |

## 3. CONCENTRATION OF Ne-He-$N_2$ MIXTURE IN DIAPHRAGM MODULE

The majority of large air separation units are able to produce neon-helium mixture with concentration beside 50 %. Reflux condensers, which enrich concentrate up to 90…95 % [5], are established in the output of ASU. At this expense the transportation costs on delivery of neon-helium product to production facility, where pure neon and helium [6] are produced, are decreased. Operation of reflux condensers is based on enrichment of target substances by $N_2$ condensation, which is the main impurity. External coolant (liquid nitrogen) is consumed for cryogenic provision of condensation process.

In recent years air separation units with limited production of liquid cryoproducts have appeared. Application of standard reflux condensers of neon-helium mixture on such objects is complicated. In the absence of liquid $N_2$ membrane devices can be considered as alternative of concentrate enrichment.

It should be noted that diaphragm separators, intended for separation of certain gases (for example, $N_2$ and $O_2$), in many cases appear to be suitable for solution of other applied tasks. Under certain conditions it is possible to "borrow" not only devices, but also methods of their calculation. The target product in three-componential mixture Ne-He-$N_2$ is the complex (Ne+He), and the by-product is nitrogen. It is possible to assume that for preliminary analysis of neon-helium enrichment of neon-helium mixture the method of calculation of binary mixture separation (see table 1, column IV) can be applied. For the current task the close analog is the separation of $N_2$ - $O_2$ where $\alpha<1$ factor is compared to less penetrating component – nitrogen. The same as in the above-mentioned example with nitrogen-oxygen system, calculation is focused on assessment of concentration of one of components ($N_2$) in permeate. This parameter unequivocally defines structure of the enriched target product $Y_{(NE+HE)}$ . Differences in penetration of Ne and He are considered by the complex factor of $\alpha_3$ separation for three-componential mixture. Its physical sense is shown in table 2.

Table 2. The given factor of separation for calculation of three-componential mixture (to table 1).

| Mixture type | Two component $N_2$ - $O_2$ (residual product is nitrogen) | | Three component $N_2$-(Ne+He) (residual product is nitrogen) | | |
|---|---|---|---|---|---|
| Penetration coefficients, $m^3/(MPa\cdot m^2\cdot h)$ | $K_{N2}$ | $K_{O2}$ | $K_{N2}$ | $K_{NE}$ | $K_{HE}$ |
| | 0,070 | 0,378 | 0,07 | 0,88 | 4,0 |
| Factors of separation of components | $[N_2\leftrightarrow O_2]$; $\alpha_2 = \frac{K_{N2}}{K_{O2}} = 0{,}185$ | | $[N_2\leftrightarrow Ne]$; $\alpha_2' = \frac{K_{N2}}{K_{NE}} = 0{,}0795$ | | |
| | | | $[N_2\leftrightarrow He]$; $\alpha_2'' = \frac{K_{N2}}{K_{HE}} = 0{,}0175$ | | |
| | | | $[N_2\leftrightarrow(Ne+He)]$; $\alpha_3 = \frac{\alpha_2' + \alpha_2''}{2} = 0{,}0485$ | | |

The example of calculation of diaphragm enrichment of neon-helium mixture (table 1) shows that the residual stream, which goes out of cavity over diaphragm, unfortunately, contains some percent of the target product $X_{(NE+HE)}$.More visually dependence of extraction degree is shown graphically in figure 3. Reflux condensers characteristics are given at various temperatures of phase balance [5] for comparison. Diagrams show that the reflux condenser provides the minimum content of nitrogen in the product at very moderate losses of the product. However, membrane installation is simple and technological, while the standard reflux condenser is rather difficult and metal-consuming product, which consumes liquid nitrogen for cooling. It consists of a set of expensive fittings, several regulators of coolant level and constantly working vacuum pump.

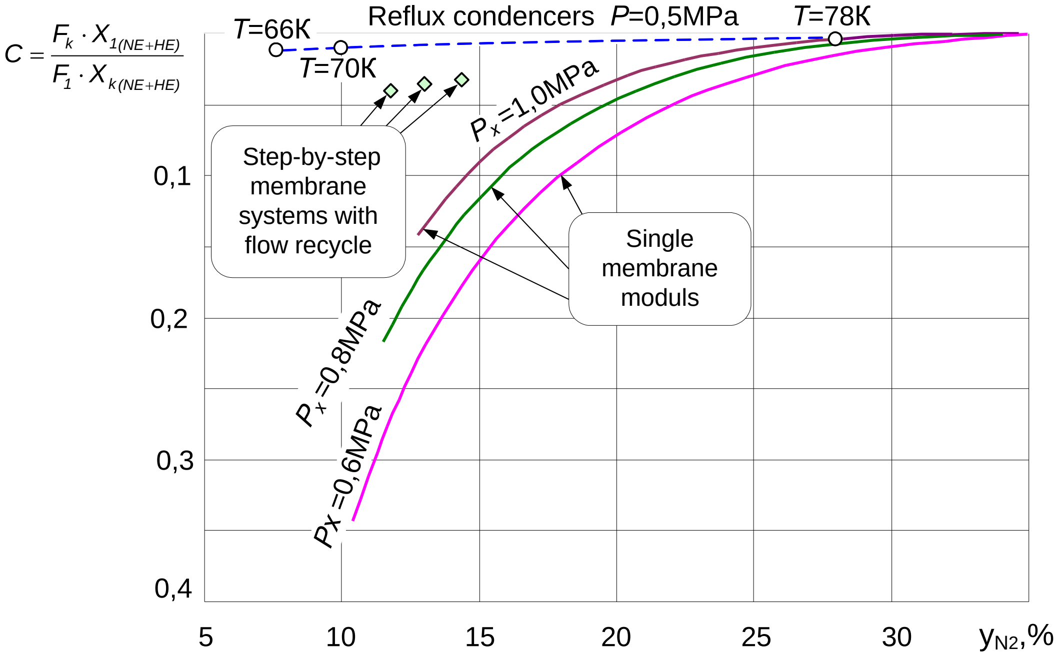

Figure 3. Dependence of degree extraction of $C_{(Ne+He)}$ on contents of $y_{N2}$ admixture in the stream of the target products in the process of neon-helium mixture enrichment in diaphragm devices at T=300 K and reflux condencers at T = 66…78 K.

Undoubtedly, a single diaphragm yields to the reflux condensers. However, operating drawbacks of diaphragm separators can be partly removed due to application of stage devices. As shown on fig. 3, descriptions of such devices are close to designations of reflux condensers. Stage installations usually provides the repeated separation of one of the streams in the additional diaphragm, and special compressors are used for recirculation. Fig. 4 shows the outline and description of one of such units, where permeating stream of the second section is returned by $C_2$ compressor to the input of the first module. Channel over diaphragm appears to be divided into two parts. The remaining stream in the output from the second section is thrown out. Mixture, which goes through the diaphragm in the first section, is taken away as the product, and the mixture at the second section is directed to the input of the unit. $C_1$ compressor is applied for increase of operating pressure, which increase the selectivity of the device.

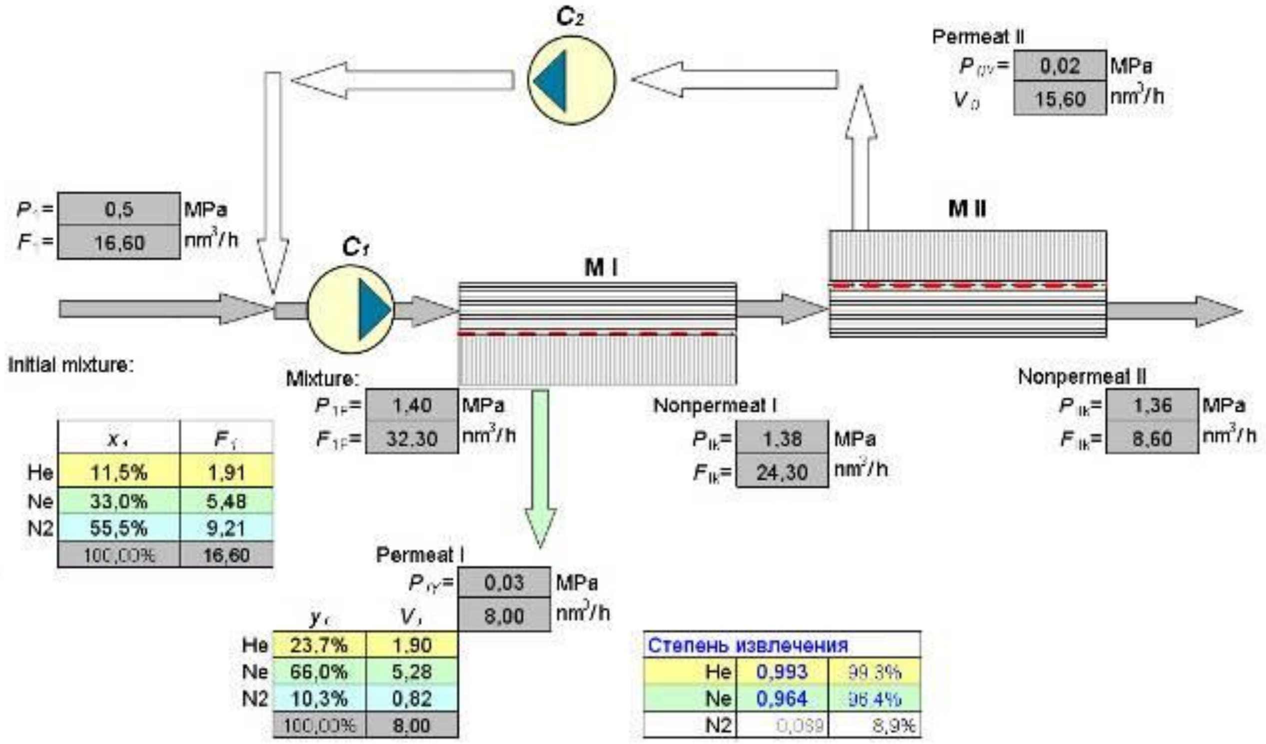

Figure 4. Schemes of diaphragm units with recirculation of permeating stream.

The carried out experiments gives the possibility to create a set of experimental-industrial units for neon-helium mixture concentration (fig. 5). In most cases the operating pressure in module is provided due to potential of pressure of low column of air-separation unit.

Figure 5. Laboratory and industrial diaphragm units for enrichment of neon-helium mixture.

## 4. CONCLUSIONS

The simplified method of analysis shows the process of air separation in diaphragms with hollow fibres quite vividly. The offered methodology of calculation of binary mixture separation is suitable also for prognosticating of parameters of diaphragm enrichment of concentrate ($N_2$-Ne-He).

In process of enrichment of neon-helium mixture one-step baromembrane units, which use technological pressure difference, yields to reflux condensers in economy and not always guarantee the necessary level of mixture concentration. Cascade diaphragm units with recirculation can compete with reflux condensers, but at the objects with limited output of liquid cryoproducts such diaphragm systems practically don't have alternatives [7].

## 5. REFERENCES

1. S.-T. Khvang, K. Kammermayer. 1981, *Membrane separation processes*, M.: Mir,. 464 p.
2. Baker R.W. 2002, Future directions of membrane gas separation technology, *End. Eng. Chem. Res.* 41: 1393-1411.
3. Dytnersky Yu.I. 1986, *Baromembrane processes,* M.: Khimiya, 272 p.
4. Hogsett E.J., Mazur W.H. Estimate membrane system area, *Hydrocarbon Processing,* 9(A): 52-54.
5. Simonenko Yu.M. 2000, Preliminary enrichment of Ne-He mixture in reflux condensers, *Proc. 6 Int. Conf. Cryogenics'2000,* Praha: 177-180.
6. Bondarenko V.L., Simonenko Yu.M. 2010, Cryogenic technologies of light inert gases production. The reserves and prospects for the raw materials complex. *Proc. 11 Int. Conf. «Cryogenics 2010»,* Bratislava: 124-129.
7. Bondarenko V.L., Losyakov N.P., Simonenko Yu.M. etc. 2012, Application of membrane processes in the technology of separation gas mixtures based of air components, *Technical gases,* 2: 19-30.

060

# The Future of Helium? A Global Agency to Oversee Production, Storage, Supply and Use of Helium Gas and Liquid

**Scurlock R.[*], Clarke R.H.[**], Glowacki B.A.[***], Nuttall W.J.[****]**

[*] Kryos Technology, 22 Brookvale Rd., Southampton, SO17 1QP, UK.
[**] $^4$He Consulting, 30 East Saint Helen St., Abingdon, Oxon, OX14 5EB, UK
[***] Department of Materials Science and Metallurgy, University of Cambridge, Pembroke Street, Cambridge CB2 3QZ, UK
[****] Judge Business School, University of Cambridge, Cambridge CB2 1AG, UK

## ABSTRACT

Since the USA abandoned its Helium Conservation Programme, global markets for helium have become increasingly unstable, and there are growing concerns about the future of cryogenics and its applications.

Work in the last three years, since an International Helium Workshop at Cambridge, UK, has led to the publication of “The Future of Helium as a Natural Resource” (Nuttall et al., 2012) a record of facts, discussions and proposals regarding the question of helium supply, demand and application. For the first time ever, the World has to face the fact that a readily available natural resource, helium from natural gas, is unsustainable.

We believe there is therefore a need to set up some form of new international arrangements for helium. In this paper we present and expand upon some of the ideas that have been proposed.

## 1. INTRODUCTION

The last conference Cryogenics 2010, Bratislava, included discussions of the growing scarcity of helium supply throughout the cryogenic industry. These discussions arose from the findings of the Helium Workshop, Cambridge, 2009, which was in the process of being written up as a publication entitled “The Future of Helium as a Natural Resource,” and the more recent US NAS 2010 report “Selling the Nation’s Helium Reserve.” Considerable concern was raised at Bratislava by these findings, and by the serious nature of the future outlook for all cryogenic projects, namely intermittent supplies and rapidly escalating prices.

Two years on, in 2012, the problem of helium supply has grown worse, including examples of non-availability of helium for on-going research projects.

## 2. HELIUM - A NATURAL RESOURCE

Helium is the natural product of alpha-particle decay by natural radio-activity in the whole of the Earth. With its low density and correspondingly high diffusivity, helium diffuses out of the Earth’s core, mantle and crust into the atmosphere and then into space, so that the equilibrium amount in the atmosphere is now only 5.2 parts per million. While atmospheric helium is abundant and might economically be extracted in small quantities as part of a range of future air products, large scale-extraction from the atmosphere would not be economically viable. Over geological time, 100–500 million years, some of the diffusing helium became trapped within the Earth’s crust together with other gases, including hydrocarbons produced by biological decay.

## 3. FIRST STORAGE PROGRAMME AND ITS END IN 1996

During the Twentieth Century helium was discovered in recoverable quantities, in the range of 0.1% to 5% and more, in a small number of natural hydrocarbon gas fields within the Earth’s crust. This discovery first made in North America has led to a considerable industry, whereby helium bearing natural gas, if it was economical to do so, was first stripped of the helium by large cryogenic separation plants before being distributed as fuel gas or chemical feedstock. This crude helium, in excess of immediate usage, was stored in depleted gas fields as a strategic reserve, and this US federal storage programme was the first example of the conservation of a natural resource by long term storage, beginning in the 1920's.

The US Helium Act of 1960 established a debt financed helium conservation programme. Stored helium grew to high levels and so did the debt. The programme was terminated in 1996 via the Helium Privatization Act and it was legislated that the bulk of the federal store of helium must be sold off. Today, about half of that helium has been sold. There is the possibility that the US will need to import helium in competition with the rest of the world from the smaller production plants around the world. Meanwhile much available helium is going to be vented, by the expanding natural gas industry.

Both demand and supply of helium are internationalising, but the administrative arrangements around this most unsustainable resource are not keeping pace. Something should be done and this paper puts forward some options.

## 4. CURRENT PRODUCTION OF CRUDE HELIUM

Some of the plants left over from the US programme are still producing some helium for direct sale to US customers. However, the plants feeding the Cliffside in-ground helium store are over 50 years old and need expensive replacement to be competitive with more modern, energy efficient designs. Some pipelines are being dismantled anyway, partly because the fuel gas and helium content from the nearby gas wells have been exhausted.

New, yet to be discovered, natural gas fields including fracking gas fields, may, or may not, contain recoverable helium. If they do contain helium, then large-scale cryogenic extraction plants will require considerable additional capital expenditure. On the other hand, useful sources can, in principle, be provided by LNG plants which liquefy natural gas for export, for example, in Algeria and Qatar. The tail gases of uncondensed components contain any helium from the original natural gas. With the necessary additional, relatively small scale cryogenic plant, these tail gases can be used to recover the helium present in initial concentrations down to 0.015%, at relatively low additional capital expenditure.

## 5. FUTURE STORAGE OF CRUDE HELIUM

At present, there are no in-ground storage programmes in operation anywhere in the World. The local storage of crude helium, containing 50% or more helium, may be possible in or at existing gas fields (see related paper, by Clarke and Scurlock). There are a number of natural storage possibilities to be studied and developed for low cost operation, such as old ex-salt mines, depleted gas wells and underground caves. The volumes that would need to be stored are large, in the range of 25 to 250 Bcf., or 1 to 10 billion cubic meters, together with minimum loss rates to enable long storage times of many years to be practicable. Logistically, there are questions as to where these stores are best sited: perhaps near major centres of helium bearing natural gas in Europe, Australia, the Far East, as well as in North America; perhaps near LNG plants or natural gas extraction plants; or perhaps near to major industrial users of helium as far as geology and pipelines can permit. Such arrangements on the supply side need to be accompanied by more responsible use and recycling of helium on the demand side.

## 6. FIRST THOUGHTS ON INTERNATIONALISATION

As one of the first people to comment on the need for a more internationalised policy, the late Art Francis (1996) proposed that any world helium policy should include the following 10 criteria:

1. *Current world needs should be met by extracting helium from natural gases exploited for fuel use.*
2. *Helium, contained in low grade natural gases, should preferably remain in place, and not to be exploited until supplies of helium-bearing fuel gases are fully depleted and helium supply has substantially decreased due to that depletion.*

3. *Helium extracted from fuel gases and not immediately required for current consumption should be stored and not be vented, unless this is technically impractical.*
4. *Opportunities should be sought to establish low-cost storage at locations of major helium extraction operations, or at other sites connected by spare pipelines.*
5. *Crude helium from storage should be made available to supplement normal supply from extraction plants, when the production of helium-bearing fuel gas is insufficient to meet the needs of helium consumers.*
6. *All sources of economically extractable helium-bearing fuel gases and helium-consuming applications should be identified and continuously monitored.*
7. *Forecasts of supply and demand, and inventory changes should be made at regular intervals and publicly reported.*
8. *Governments involved in helium conservation should utilise economic mechanisms to encourage the private sector to accomplish the previously stated objectives.*
9. *These objectives should be pursued by means of information exchange and discussion, with minimum reliance on formal agreements, contracts and statutory law.*
10. *The private sector can more effectively introduce new technology to improve the efficiency of helium production, distribution and application. Private enterprise can also more effectively integrate helium with the supply and marketing activities of related commodities. Thus private enterprise should have the primary responsibility for normal worldwide helium supply.*

## 7. WORLD HELIUM COUNCIL AND BANK

One of us, Ralph Scurlock, has complemented the advice from Francis in recently proposing an International Helium Council or IHC (Scurlock and Francis, 2012). The IHC would include an executive committee to exercise planning, control, conservation, storage and marketing of helium as a diminishing earth resource. The International Helium Council would involve both national and institutional interests and give a strong voice to private sector stakeholders. The IHC would interface to a new World Helium Bank. This would be a new single entity, albeit with interests in many parts of the world. It would hold assets of helium and shares in the Bank would be traded to assist with project finance and helium-related infrastructure development. The Council would represent and co-ordinate various stakeholder interests from governments, private industry and those representing end users of helium.

The World Helium Bank would purchase all surplus helium not immediately sold after extraction, for conservation and storage as a derivative product. Helium taken from storage would then be sold to meet additional demand at a price determined by the market and its full storage costs, similar to other derivative products on the world markets. It may take a World Helium Bank up to ten years to begin a world conservation programme, which therefore, in this scenario should aim to be operational before 2025.

We assess the main advantage of this proposal to be that it would have the potential to administer a complex matter with efficiency and due concern to all key issues. The disadvantage of the proposal is the degree of ambition it represents. Entities of the type suggested are not easily established. Given the limited scale of the helium industry, however, it is not an impossible goal.

## 8. INTERNATIONAL HELIUM AGENCY

Others of us, Nuttall, Clarke and Glowacki have suggested an International Helium Agency (IHA) akin to the International Energy Agency (Nuttall et al., 2012). The IEA is an intergovernmental organisation established under the Organisation of Economic Cooperation and Development. The OECD is based on a Convention between governments signed in 1960.

The International Energy Agency was established in November 1974 (Scott, 1994). As Scott explains the origins of the IEA were an economic and political crisis in the period 1973-1974. The crisis emerged from the 1973 ‘Yom Kippur’ war and the response of the Organisation of Arab Petroleum Exporting Countries (OAPEC) (Scott, 1994, p. 28). OAPEC was distinct from ‘OPEC’, a broader body established earlier in 1960, including, for instance, Venezuela and other non-middle eastern states. The industrialised west had become dependent upon petroleum imports from Arab countries and in the face of OAPEC production cuts, prices rose dramatically.

As Scott notes: "*The industrial countries permitted excessive and even wasteful and inefficient use of energy and of oil in particular. Energy conservation measures in those countries were woefully underdeveloped. Their oil production potential was not fully realized, nor was sufficient investment devoted to the development of other energy sources as alternatives to oil. They had yet to devise a workable system for responding to serious disruptions in oil supply; and their organizational arrangements for co-operation could not enable them to cope effectively with the institutional implications of those situations.*" (Scott, 1994 p. 11)

The IEA itself is based upon an international treaty: The International Energy Program Agreement of 1974 and amended in 1992 (Scott, 1994 p. 353). The measures included a legally binding oil sharing mechanism and the creation of a strong Secretariat based in Paris. Chapter 6 of the IEP Agreement established a 'framework of consultation with oil companies'.

The IEA member states are required to maintain strategic petroleum reserves among which the US has the largest. Formally IEA members operate their strategic petroleum reserves autonomously and may use their stocks for national purposes. US emergency draw-downs from its Strategic Petroleum Reserves have historically been coordinated with the IEA (DOE, n.d.).

In suggesting an IHA reminiscent of the IEA, Nuttall et al. (2012) are not drawing parallels between upstream oil cartels of the early 1970s and today's industrial gases industry, notwithstanding the degree of market power that individual industry players can exert in certain territories. Rather the suggestion is for an intergovernmental framework and agreement preserving high levels of national discretion. Separate national strategic reserves would be established, not a single global reserve. The IEA established its membership from among the major industrialised countries, both oil importing and exporting (but mostly importing). The balance of membership of a possible IHA might reflect those willing and able to implement strategic helium reserves. The balance between producer states and consumer states, however, takes us back to a question posed in section 5 and unanswered for now.

The advantage of the IHA approach is that it seems plausible to establish an international agreement between concerned governments. The IHA might grow from a relatively small core of countries. The disadvantages are that it can be difficult to establish new treaty based organisations and also by its very nature the IHA would be a creature of governments with all that entails.

## 9. CONCLUSIONS

The primary objective of all concerned parties should be to reach an effective agreement that defines the goals of helium conservation and the respective roles of governments and the private sector worldwide.

Throughout the twentieth century the United States led on policy and technology for helium storage and market management. Some mistakes were made and lessons learned. In the twenty-first century those lessons must inform the creation of new international arrangements. The United States will always be an important country in the global helium business, but it can no longer shoulder the burden of helium policy alone (see: (NAS, 2010)).

An internationalisation of helium is well underway and policy for helium must catch up. This paper puts forward some ideas which we hope will be of benefit as the international community gets to grip with pioneering this important and time sensitive topic.

Otherwise, the helium crises we have today may evolve into a helium famine. Please help to start a rolling programme of actions.

## 10. REFERENCES

Department of Energy, USA, *Strategic Petroleum Reserve – Profile*, DOE website, no date, http://fossil.energy.gov/programs/reserves/spr/

Francis A.,1996, *Helium at the Crossroads*, unpublished manuscript.

National Academy of Sciences (NAS) (2010) *Selling the Nation's Helium Reserve,* National Academies Press, Washington, DC., USA.

Nuttall, W.J., Clarke, R.H. and Glowacki B.A., *Stop Squandering Helium*, Nature, 31 May 2012, vol. 485. pp.573-575 (2012).

Scott R, *The History of the International Energy Agency, Volume 1 the first twenty years 1974-1994,* 1994, available at: http://www.iea.org/Textbase/nppdf/free/1-ieahistory.pdf

Scurlock R. and Francis, A. *Is there a helium problem? Ways forward,* in Nuttall W.J., Clarke R.H. and Glowacki B.A., (editors), *The Future of Helium as a Natural Resource*, Routledge, London and New York, pp. 296-306 (2012).

# POSTER SESSION - SUPERCONDUCTIVE MATERIALS AND MAGNETS

013

# Design of a Superconducting Inductor for Axial Concentration Flux Motor

**Ailam E., Hachama M., Benallal M.N., Hocine A.**

Laboratoire de l'Energie et des Systèmes Intelligents LESI,
Université de Khemis Miliana, 44225, Khemis Miliana, Algeria

## ABSTRACT

In this paper, a superconducting inductor based on the magnetic flux concentration for axial motor is designed. The inductor is made of an NbTi superconducting solenoid and YBaCuO bulk superconductors. We are interested to principally study the influence of the number of poles for an NbTi wire solenoid. A high magnetic flux density is created using the superconducting solenoid. Its spatial variation is obtained thanks to YBaCuO bulk superconductors. To raise the torque, the flux density in the air-gap of the motor has to be increased. This flux density depends on the inductor dimensions and the superconducting solenoid current density. The influence of the number of inductor poles is studied. We present the cases of two and four poles. Calculations are carried out using Monte Carlo methods. Calculations of the flux density must take into account the J-B characteristic of the superconducting wire used in the realization of the solenoid.

## 1. INTRODUCTION

In the last decade, several realizations of superconducting rotating motors around the world have demonstrated the benefits of these materials. In fact, using superconductors, more lightweight and smaller motors can be obtained, and electrical performances of the motor can be significantly improved [1] and [2]. Three configurations of motors are possible depending on the used superconductors, HTS, LTS, wire or bulk [3], [4] and [5]. In the first one, superconducting wires are used in the inductor when a DC current supply is needed, and no AC losses are considered. This is equivalent to a synchronous conventional motor. The performances of these motors depend on the current density of the used wire. High values have been recorded recently with HTS wires. In the second category, permanent magnets are replaced by magnetized bulk superconductors. A high trapped flux density in bulk superconductors increases the torque and the power of the motor in comparison to conventional permanent magnet motors. In the third category, a high magnetic flux density is obtained on the basis of the magnetic concentration principle. The GREEN Laboratory of Nancy has a long experience in this kind of motors. A first prototype based on a full saturation of moving ferromagnetic plugs was made in 1984 [6]. In 2002 and 2006 an eight-pole superconducting inductor and a 20 kW eight-pole superconducting motor have been realized, respectively [7], [8] and [9]. For both projects, the inductor is radial and is made of two opposed superconducting solenoids and YBaCuO single domain bulk to modulate the magnetic flux density in the air-gap of the motor. For the last of the realized machines, the tests in alternator operation show quasi-sinusoidal waves of the three-phase voltages. Our interest in this paper is the axial superconducting motor with a magnetic concentration inductor.

## 2. THE REALIZED RADIAL SUPERCONDUCTING MOTOR

The realized superconducting motor is an eight-pole synchronous one. It is made of a fixed superconducting inductor and a rotating three-phase conventional copper armature. The inductor is made of two opposed NbTi solenoids and eight YBaCuO bulk plates. The role of the solenoids is the creation of a high magnetic flux density. The created flux density is modulated thanks to the YBaCuO bulk plates when the maximal value is obtained between two YBaCuO plates and the minimal one is obtained behind an YBaCuO plate. This configuration allows a quasi-sinusoidal variation of the magnetic flux density in the air-gap of the motor. In figure 1, the principle of the realized inductor is illustrated. In figure 2 and figure 3, the realized inductor and the realized superconducting motor are shown. The parameters of the realized inductor are presented in table 1.

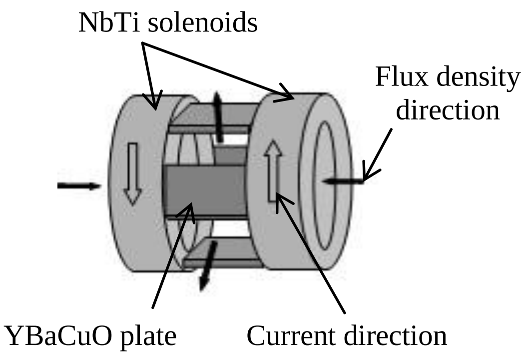

Figure 1. Principle of the radial flux superconducting inductor

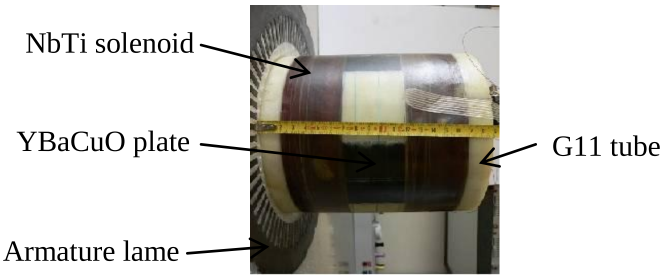

Figure 2. The realised radial flux superconducting inductor

Table 1. Parameters of the realized superconducting motor.

| | |
|---|---|
| Inner diameter of a solenoid | 105 mm |
| Outer diameter of a solenoid | 210 mm |
| Length of a solenoid | 50 mm |
| Distance between the two solenoids | 50 mm |
| Current density in the NbTi wire | 460 A/mm$^2$ |
| Maximal flux density on the NbTi wire | 6.9 T |
| Flux density for 15 mm air-gap thickness | 2.5 T |

The two solenoids are made of NbTi wire, so helium gas is used to cool the inductor. A fixed cryostat has been designed and realized. The cryostat is inserted in the air-gap of the motor. Sliding contacts are used to supply the three-phase rotating armature. Tests results under alternator mode of the realized machine showed a three-phase generated voltage. The first more important result is the validation of an original design of the machine based on the magnetic flux concentration principle. Figure 3 illustrates the experimental results of phase to phase generated voltages [8].

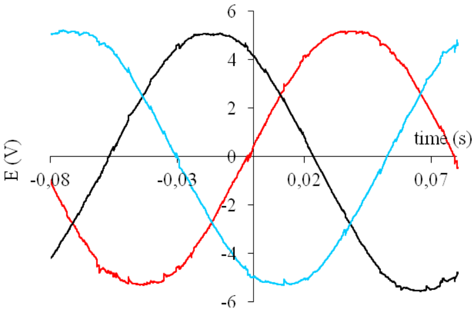

Figure 3. The phase to phase generated voltages (93 rpm and 10 A in the NbTi solenoids)

## 3. TOPOLOGY OF THE AXIAL SUPERCONDUCTING MOTOR

The studied superconducting motor is an axial one. It is made of two parts: a three-phase cooper axial armature and a magnetic concentration axial flux superconducting inductor. The armature of the motor rotates, and the inductor is fixed. The topology of the superconducting motor is illustrated in figure 4.

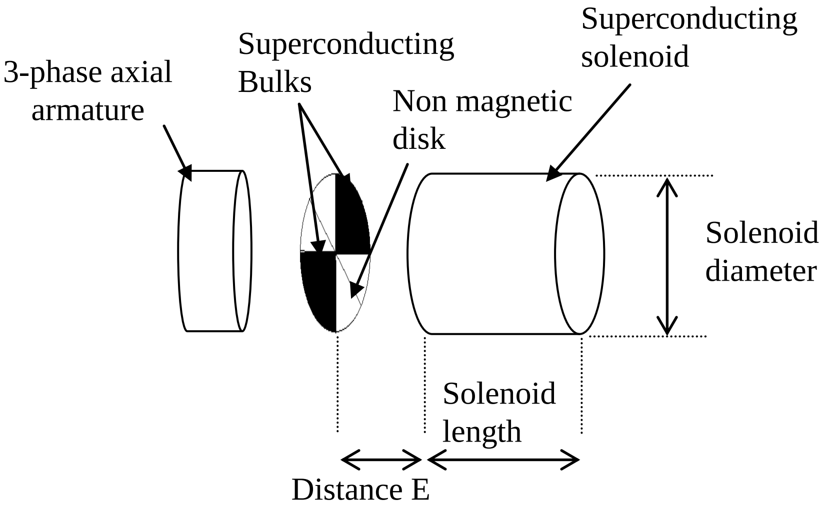

Figure 4. Topology of the axial flux superconducting motor

The nominal operation parameters are the current density in the superconducting solenoid and the maximal flux density on the superconducting wire using the J-B curve of the NbTi wire. Using the FEMM software, the current density and the maximal flux density are calculated. The obtained values are 526 A/mm$^2$ and 6.6 T, respectively. Figure 5 and figure 6 illustrate the J-B characteristic and the FEMM magnetic calculations for the studied superconducting solenoid.

Duo to the 3D geometry, software based on the Monte Carlo method is developed to carry out the magnetic calculations. First, the magnetic scalar potential is calculated on two axes situated behind a superconducting bulk and between two bulks. Secondly, the magnetic scalar potential is derived to obtain the flux density. The developed software is validated by comparing the obtained results and an analytical curve on the axis of a solenoid. Figure 7 illustrates the comparison between the developed software and an analytical solution.

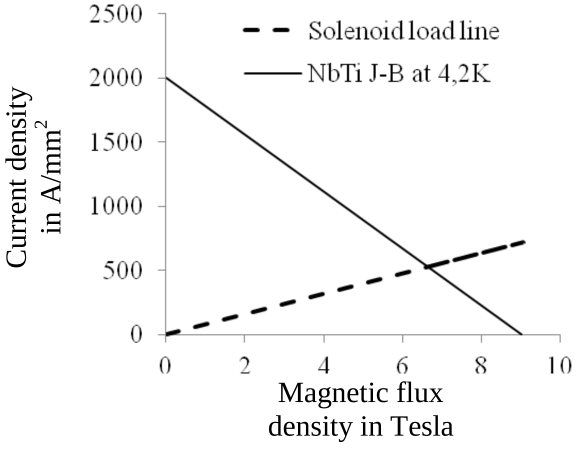

Figure 5. J-B characteristic of NbTi wire and the line load of the studied superconducting solenoid

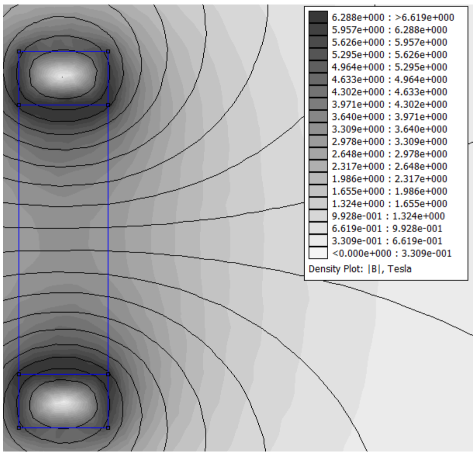

Figure 6. The maximal magnetic flux density calculation for an NbTi superconducting wire using FEMM software.

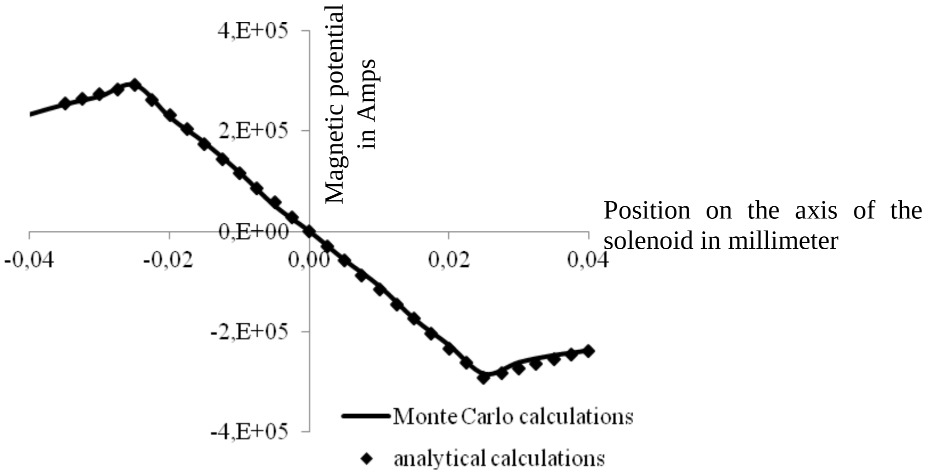

Figure 7. Comparison between the results obtained using the developed software and an analytical solution (variation of the magnetic potential in Amps for a given position on the axis of the solenoid in meter)

At present, the developed software is validated, and it can be applied in two specific regions of the studied geometry. The scalar potential is calculated on the first axis situated behind a bulk and on the second axis situated on the middle distance between two bulks. Calculations are made in the case of two-pole and four-pole inductors, and results are illustrated in figure 8. The flux density is obtained by the derivation of the curves of figure 8. $B_{min}$ and $B_{max}$ are the magnetic flux density behind a bulk and between two bulks respectively. The difference between $B_{min}$ and $B_{max}$ is called $\Delta B$. The variation of $\Delta B$ in the air-gap of the motor for two-pole and four-pole inductor is illustrated in figure 9.

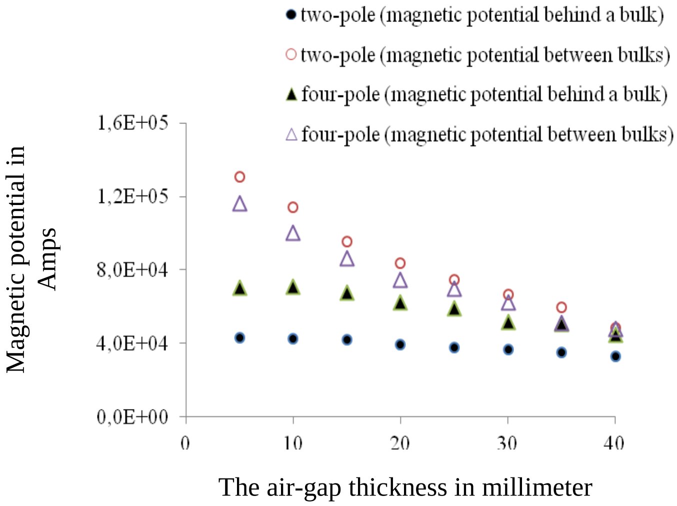

Figure 8. Variation of the magnetic potential in Amps with the air-gap thickness in millimeter for a two-pole and four-pole inductor

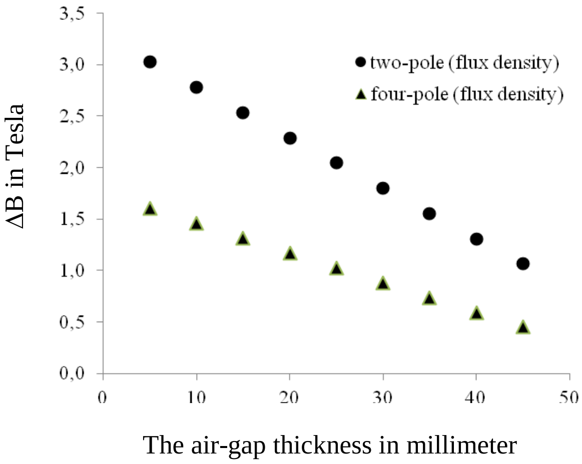

Figure 9. Variation of the flux density in Tesla with the air-gap thickness in millimetre for a two-pole and four pole inductor

In figure 9, we can see clearly that the flux density is approximately two times larger in the case of the two-pole inductor in comparison to a four-pole inductor. The other conclusion is that the flux density decreases when the air-gap of the motor increases. The variation of the flux density for an air-gap of 5 mm between 0° and 360° is illustrated in figure 10.

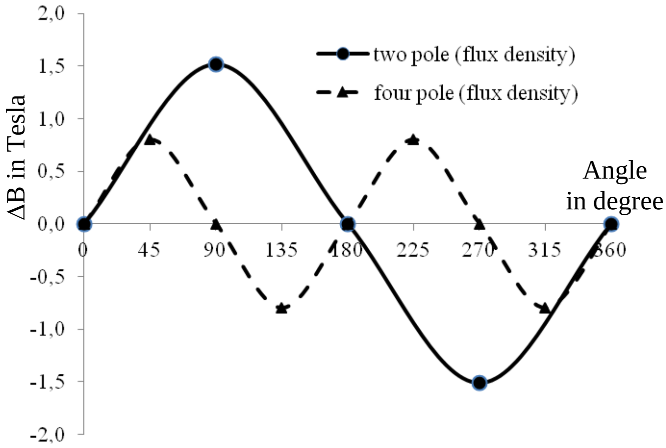

Figure 10. Variation of the flux density for an air-gap of 5 mm

In table 2 we present the comparison between three cases of magnetic concentration motors. The flux density is calculated for an eight-pole radial flux motor, a two-pole and a four-pole axial motor.

Table 2. Flux density in the air-gap of a four-pole radial motor, a two-pole and a four-pole axial motor.

| Type of the motor | Flux density in the air-gap of the motor (T) |
|---|---|
| Eight-pole radial motor | 1.25 |
| Two-pole axial motor | 1.5 |
| Four-pole axial motor | 0.8 |

## 4. CONCLUSION

In this paper the principle of an axial flux motor based on the magnetic concentration principle is studied. Software using the Monte Carlo method is developed and the obtained results are compared to an analytical solution for a simple case. Two conclusions can be noted. First, the principle of an axial flux motor based on magnetic concentration is validated. Second, we note that the two-pole axial motor has higher flux density in the air-gap of the motor in comparison to a four-pole axial motor.

## 5. REFERENCES

[1] Philippe J. Masson and Cesar A. Luongo, 2007, HTS Machines for Applications in All-Electric Aircraft, *IEEE Power Engineering Society General Meeting*, 1-6.

[2] Clive Lewis and Jens Müller, 2007, A Direct Drive Wind Turbine HTS Generator, *IEEE Power Engineering Society General Meeting*, 1-8.

[3] X. Granados et al., 2006, Iron-YBCO Heterostructures and their application for trapped field superconducting motor, *Journal of Physics: Conference,* (43): 788–791.

[4] Hiroyuki Ohsaki et al., 2001, *Study on electric motors with bulk superconductors in the rotor, Journal of Materials Processing Technology*, (108): 148-151.

[5] Q Jiang et al., 2006, Design and AC loss analysis of a superconducting synchronous motor, *Superconductor Science and Technology,* (19): 1164–1168.

[6] A. Rezzoug, A. Mailfert and P. Manfe, 1984, Cryogenic Supersaturated Synchronous Machine Optimization And First Experiment Results, *IEEE Transactions on Magnetics*, 20(5): 1795-1797.

[7] Philippe J. Masson et al., 2007, Design of HTS Axial Flux Motor for Aircraft Propulsion, *IEEE Transactions on Applied Superconductivity*, 17(2): 1533-1536.

[8] El Hadj Ailam et al., 2007, Design and Testing of a Superconducting Rotating Machine, *IEEE Transactions on Applied Superconductivity*, 17(1): 27-33.

[9] Renaud Moulin et al., 2010, Superconducting Multistack Inductor for Synchronous Motors Using the Diamagnetism Property of Bulk Material, *IEEE Transactions on Applied Superconductivity*, 57(1): 146-153.

016

# Stability of YBCO Coated Conductor according to Cu Stabilizer Thickness for Cryogenic Applications

**Joonhan B., Beomyong E., Haejong K., Kichul S.**

Korea Electrotechnology Research Institute, Seongjudong, Changwon, 641-120, Korea

## ABSTRACT

The studies on the conduction-cooled superconducting magnets are actively underway with rapid advancement in refrigeration technology recently. YBCO coated conductor (CC) is one of the promising conductor for conduction-cooled superconducting magnets because of increasing the operation temperature of magnets and being able to have cost competiveness with conventional copper conductor in the future. However, it is known that quench propagation velocity in high-temperature superconductor (HTS) is two or three orders of magnitude slower than that in low-temperature superconductor (LTS) because of its large heat capacity and the high operating temperature. The hot spot will emerge in local region if the critical current is non-uniform along the length of HTS tape and eventually, it causes permanent destroy for the whole HTS tape. Based on the protection of YBCO CC, it is necessary to determine a suitable copper stabilizer thickness for YBCO CC so that the temperature of hot spot in local area does not exceed the permissible temperature. In this study, we analyzed the thermal properties of YBCO CC in the adiabatic condition. Also, we measured minimum quench energy (MQE) of the three kinds of YBCO CC samples with different copper stabilizer thickness fabricated by Superpower Incorporated.

## 1. INTRODUCTION

The studies on the conduction-cooled superconducting magnets are actively underway with rapid advancement in refrigeration technology recently. YBCO coated conductor (CC) is one of the promising conductor for conduction-cooled superconducting magnets because of increasing the operation temperature of magnets and being able to have cost competiveness with conventional copper conductor in the future. However, it is known that quench propagation velocity in high-temperature superconductor (HTS) is two or three orders of magnitude slower than that in low-temperature superconductor (LTS) because of its large heat capacity and the high operating temperature. Although the stability of HTS is better than LTS, because the normal-zone propagation of HTS is too low, the hot spot will emerge in local region, which have the lowest critical current along the length of HTS and eventually, it causes permanent destroy for the whole HTS. Therefore, based on the protection of the HTS magnet, it is necessary to determine a suitable stabilizer thickness for the YBCO CC so that the temperature of hot spot in local regime does not exceed the permissible temperature.

In this study, the thermal stability of YBCO CC was investigated numerically. We have established a suitable thermal analysis model, and analyzed transient thermal properties of YBCO CC using finite element method. Also, we measured the minimum quench energy (MQE) of YBCO CC samples with different copper stabilizer thickness at various operating temperature and current.

## 2. NUMERICAL ANALYSYS

Assuming that all of transport current flow in the stabilizer layer when a local quench is induced in the YBCO CC, the thermal behaviors of YBCO CC is governed by the following heat balance equation.

$$C(T)\frac{\partial T}{\partial t} = \nabla \cdot (k(T)\nabla T) + \rho_{stab}(T) \cdot J^{2}_{stab} \quad (1)$$

Here, C is the volumetric heat capacity, k is the volumetric thermal conductivity. $\rho_{stab}$ and $J_{stab}$ are the electrical resistivity and the current density of stabilizer, respectively. Fig. 1 shows the schematic view of the solid model to analysis thermal behaviors of YBCO CC. It is composed of hastelloy substrate, buffer, YBCO, silver and copper stabilizer layers. A heater that drives YBCO CC to quench is located in the middle of the sample tape.

Considering the spatial symmetry of the temperature distribution induced by the heater, we adopt a half of the whole sample as thermal analysis model. The one end of model was fixed to the operating temperature ($T_{op}$) (i.e. Dirichlet condition), and the rest of the boundaries were considered as thermally adiabatic (i.e. Neumann condition) in the simulation. The quench simulation for the YBCO CC model proceeded with the following process. $T_0$ initiate a local quench in YBCO CC, the heater energy is applied to the model carrying transport current for 0.7 second. The temperature profiles are numerically computed at $T_1$ and $T_3$ in Fig. 1.

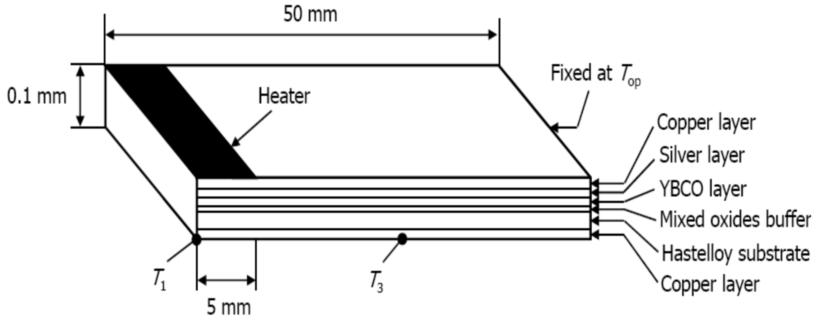

Figure 1. Thermal analysis model of the YBCO CC

## 3. EXPERIMENT

We conducted experiments on MQE characteristics of YBCO tapes according to transport current and temperature. In the experiment, we prepared three kinds of YBCO sample tapes, which have copper stabilizers with different thicknesses of 40 μm, 60 μm, and 100 μm. These sample were produced by Superpower Incorporated using MOCVD technique. The specifications of these sample tapes are listed in Table I. The minimum input energy of heater that drives a tape to quench is defined as the minimum quench energy (MQE). The input energy in the experiment was calculated according to $E = I^2 R t$, where E is the input energy, I is the constant current in the heater, R is the resistance of the heater, and t is the pulse width. Since the amount of the Stycast 2850FT used to fix the heater was small, we assumed that all energy the heater generated was deposited in the tape.

Fig. 2 shows the schematic drawing of the experimental setup. A conduction cooling system with a Gifford-McMahon cryocooler was adopted for the experiment. Both ends of YBCO tape sample were thermally connected to the copper blocks fixed to the second stage of the Gifford-McMahon cryocooler through fiberglass reinforced plastics insulation sheet. The copper blocks were electrically connected to HTS current leads. Since the sample tape was installed into the vacuum vessel, it was isolated thermally and electrically except at the current lead points.

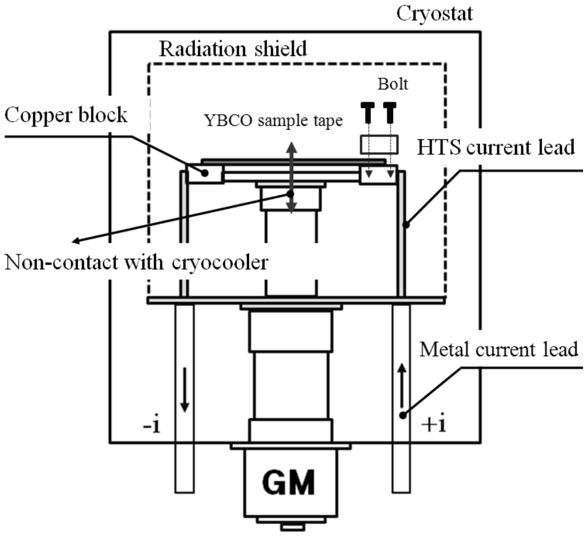

Figure 2. Experimental setup for MQE test of YBCO samples

Table 1. Specifications of YBCO CC Samples

| | Sample 1 | Sample 2 | Sample 3 |
|---|---|---|---|
| Length (mm) | 100 | | |
| Width (mm) | 4.2 | | |
| Thickness of Cu Stabilizer (μm) | 40 | 60 | 100 |
| Thickness of Silver (μm) | 2.5 | | |
| Thickness of YBCO (μm) | 1.0 | | |
| Thickness of Buffer (μm) | 0.16 | | |
| Thickness of Substrate (μm) | 50.8 | | |
| Critical Current (77K) (A) | 104 | 113 | 108 |
| N-value (77K) | 20 | | |
| Minimum Bending Diameter (mm) | 11 | | |

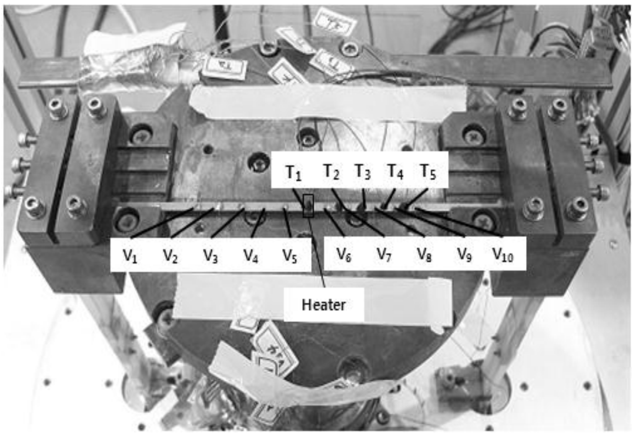

Figure 3. YBCO sample tape fixed to copper blocks cooled by cryocooler and arrangement of voltage taps and the heater for thermal disturbance

Fig. 3 shows the experimental setup for the MQE test of the samples. A strain gauge as a heater to trigger the thermal quench was installed at the center of the sample tape. All voltage taps, thermometers, and the heater were attached on the Cu surface of the sample tape. $V_5$ and $V_6$ were attached at 20 mm away from the heater, and the rest of voltage taps, $V_1$ ~ $V_4$, and $V_7$ ~ $V_{10}$ were attached at intervals of 10 mm. Thermocouples ($T_1$ ~ $T_5$) were attached in the center between adjacent voltage taps. Measurements were carried out for operating temperatures of 45 K, 50 K, 60 K, 70 K, and 77 K.

## 4. RESULTS AND DISCUSSION

The critical currents of nine different zones in the longitudinal direction of three sample tapes were measured by applying the triangular wave current pulse at the rate of 2 A/s using 1μV/cm criterion. In MQE test, the critical current of each sample is determined from the minimum critical current of each sample at operating temperature.

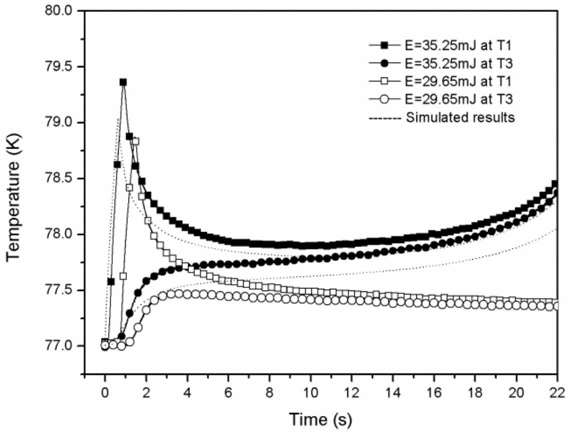

Figure 4. Temperature variations at $T_1$ and $T_3$ after the heater quench of the sample 1 carrying 100 A of transport current at 77 K

Fig. 4 shows the temperature traces of sample 1 at $T_1$ and $T_3$ for different quench energy at 77 K and 96% of minimum critical current of sample 1 (100A). In result, it is observed that when quench energy is 29.65 mJ, the YBCO CC is recovered to superconducting state after quench. Whereas, when quench energy is 35.25 mJ, the temperature of the YBCO CC rise gradually and the quench has been propagated without recovering. Therefore, it can be estimated that the minimum quench energy is 35.25 mJ. The dotted lines in Fig. 4 show temperature traces of sample 1 calculated by quench simulation. It is seen that the calculated results makes good agreement with the experimental data relatively. Fig. 5 shows MQE of three YBCO samples at 77 K as a function of $I_t/I_c$ where $I_t$ is the transport current and $I_c$ is the critical current of each sample.

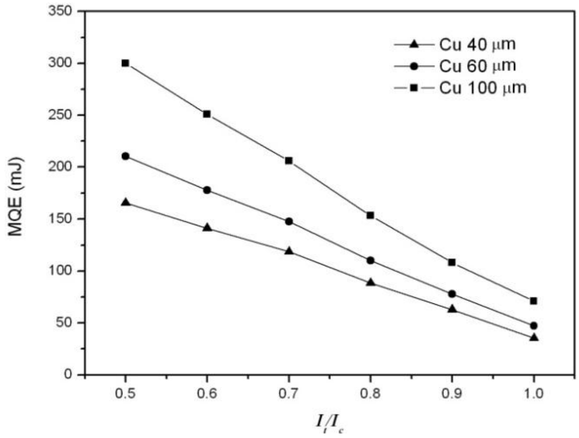

Figure 5. MQE of three samples at 77 K as a function of $I_t/I_c$, where $I_t$ is the transport current and $I_c$ is the critical current

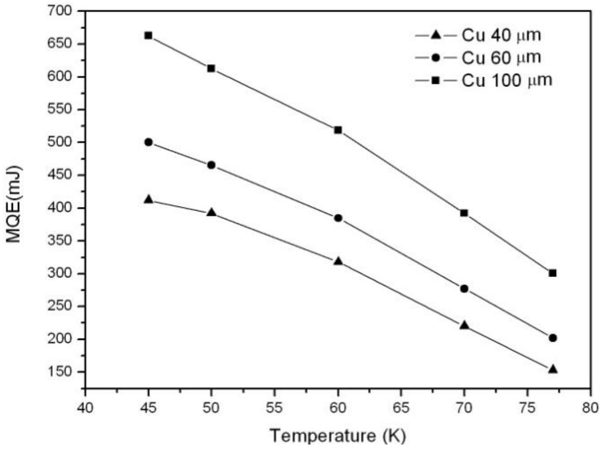

Figure 6. MQE of three samples as a function of temperature at $I_t/I_c = 0.5$

It can be seen that the MQE decline along with the increase of current. This is because the joule heat is in square proportion to transport current, that is, quench propagation is more easily induced when carrying larger current in YBCO CC. Also, it is shown that MQE becomes larger due to the increment of heat capacity of YBCO CC with increasing the thickness of copper stabilizer. As $I_t/I_c$ approaches 1.0, the difference of MQE among three samples is shortened. It means that the thickness of cooper stabilizer does not contribute to the improvement of endurance against thermal disturbance of YBCO CC in case of applying the transport current close to $I_{c.}$

Fig. 6 presents MQE of three samples as a function of temperature when $I_t/I_c$ is fixed to 0.5 The MQE becomes larger with decreasing operating temperature. The reason is that the difference between operating temperature and current sharing temperature become larger with falling down the operating temperature, that is, a larger amount of resistive heating in copper stabilizer is needed to induce the quench in YBCO CC.

## 5. CONCLUSIONS

The results are as follows. In this paper, the thermal stability of three YBCO CC samples, which have copper stabilizer with different thicknesses, was investigated. We have established a suitable thermal analysis model, and analyzed transient thermal properties of YBCO CC using finite element method. Also, we measured the minimum quench energy of YBCO CC samples with different copper stabilizer thickness at various operating temperature and current. The results are follows.

a) MQE decline along with the increment of transport current because the joule heat is in square proportion to transport current.
b) MQE becomes larger due to the increment of heat capacity of YBCO CC with increasing the thickness of copper stabilizer.
c) The dependency of thickness of cooper stabilizer on the thermal stability of the YBCO CC decrease as the transport current approaches the critical current.

As the difference between operating temperature and current sharing temperature become larger with falling down the operating temperature, MQE becomes larger with decreasing operating temperature.

The results through this research will be utilized to determine the operating current of the conduction-cooled HTS magnet and to design the external protection circuit to keep HTS magnet from damage by thermal quench.

## 6. ACKNOWLEDGEMENT

This work was supported by the  Power Generation & Electricity Deliveryof the Korea Institute of Energy Technology Evaluation and Planning(KETEP) grant funded by the Korea government Ministry of Knowledge Economy (No.R-2004-1-144).

## 7. REFERENCES

G. Snitchler, S. S. Kalsi, M. Manlief, R. E. Schwall, A. Sidi-Yekhlef, S. Ige, R. Medeiros, T. L. Francavilla, and D. U. Gubser, 1999, High-field warm-bore HTS conduction cooled magnet, IEEE Trans. Appl. Supercond. 9: 553-558

H. Kumara, T. Ohara, H. Kitaguchi, K. Togano, H. Wada, H. Mukai, K. Ohmatsu, H. Takei, and H. Okada, 2001, Development of Bi-2223 magnetic separation system, IEEE Trans Appl. Supercond. 11: 2519-2522

Giebeler, G. Thummes, and K.-J. Best, 2004, A 5 T persistent current niobium-titanium magnet with a 4 K pulse tube cryocooler, Supercond. Sci. Technol. 17: S135-S139

R. H. Bellis, Y. Iwasa, 1994, Quench propagation in high Tc superconductor, Cryogenics  34(2): 129-144

Y. Fu, O. Tsukamoto, M. Furuse, 2003, Copper Stabilization of YBCO Coated Conductor for Quench Protection, IEEE Trans. Magn. 13(2): 1780-1783

A. Ishiyama, H. Ueda, T. Ando, H. Naka, S. Bamba, and Y. Shinohara, 2007, A Criterion for Determining Stabilizer Thickness of YBCO Coated Conductors Based on Coil Protection, IEEE Trans. Appl. Supercond. 17(2): 2430-2433

033

# Properties of Impregnated Superconducting Coils Made from YBCO Coated Conductor Using Different Technology of Impregnation

**Frolek L., Seiler E., Šouc J., Pardo E.**

Institute of Electrical Engineering, Slovak Academy of Sciences, Dúbravská cesta 9, Bratislava, 84104, Slovak Republic

## ABSTRACT

Superconducting coils are very important components in various applications like e.g. superconducting magnets, superconducting magnetic energy storage systems ( SMES ), superconducting fault current limiters, transformers, motors and generators. There is a strong worldwide effort to use the high temperature superconductors in these applications. The aim of our work is to build a self-contained coil without coil frame by resin impregnation. In addition, impregnation is necessary for conduction-cooled systems. In this article, we present the properties of three superconducting coils made from YBCO coated conductor. These coils have identical inner diameter and number of turns while the thicknesses of windings are slightly different. Their inner diameter is 60 mm and they have 10 turns. The coils were impregnated using different resins and technologies of impregnation. Coils were characterized in the liquid nitrogen bath and their parameters like the critical currents, *E(I)* characteristics, inductances and AC losses at frequencies 36 Hz, 72 Hz and 144 Hz were compared. In conclusion, none of the impregnation techniques disqualifies the coils for AC applications. However, for one impregnation method the coil is not rigid.

## 1. INTRODUCTION

In applications, low-temperature superconductors ( LTS ) were used as first. LTS, as multifilamentary niobium-titanium ( NbTi ) or niobium-tin ( $Nb_3Sn$ ) wires were successfully used in different types of windings. High-temperature superconductors ( HTS ) can operate at much higher temperatures, providing much larger thermal margin and simpler cooling systems. This opens new possibilities in applications such as superconducting magnets [1], superconducting magnetic energy storage systems ( SMES ) [2], superconducting fault current limiters [3], transformers [4], motors [5] and generators [6]. The tapes based on the $Bi_2Sr_2Ca_2Cu_3O_{10}$ superconductor embedded in Ag-based matrix are called the first generation wires. Superconducting wires of the second generation ( 2G ) comprise of a thin ( ~1 μm ) layer of $YBa_2Cu_3O_8$ ( YBCO ) superconductor deposited on a metallic substrate tape covered by a protective layer. These tapes are usually also covered with stabilizing metallic strips on both sides and have much higher current carrying capacity in magnetic field and bend tolerance. Using YBCO-coated conductor, current density in superconducting coils can be increased and their volumes reduced. Recently, various YBCO coils have been designed and fabricated [7, 8, 9]. Epoxy impregnation can substantially degrade the performance of coils made from YBCO-coated conductors [10]. Successful resolving of this problem is very important as many applications require impregnated, mechanically stabilized windings.

In this work, three superconducting coils made from YBCO coated conductor were constructed using three different technologies of impregnation and resins. These coils were self-contained without coil frame, cooled down several times and characterized in the liquid nitrogen bath. Important parameters as dependences of electrical field on current ( *E(I)* characteristics ), critical currents ( $I_c$ ), inductances and AC losses at frequencies 36 Hz, 72 Hz and 144 Hz were measured and compared.

## 2. DESCRIPTION OF COILS

### 2.1. Common parameters

The investigated pancake coils had inner diameter 60 mm and 10 turns of superconducting tape. They have been made from Super Power's YBCO coated conductor SCS12050-AP which has a copper stabilizing strip on both surfaces. Cross section of the coated conductor was 0.1 mm x 12 mm and the self-field critical current ( $I_c$ ) was 447 A at the temperature of liquid nitrogen ( 77K ). The coils are shown in figure 1. Two different alternatives of current leads configurations were tested, as described in other sub-sections. The thicknesses of windings were measured in 5 points on each coil and average value for each coil is listed in table 1. Here we can see that thicknesses of windings are very similar. However, the thickness of coil no. 3 is only for 9 turns of superconducting tape, because one turn has been damaged at current lead during manipulation and was removed afterwards. Higher thickness in this case is a consequence of the winding technique, described in sub-section 2.4. The inductances were measured using very sensitive RLCG meter. Higher difference is again for coil no. 3 because it was measured for 9 turns.

Table 1. Thickness of winding and inductance for each coil.

| Coil number | 1 | 2 | 3 |
|---|---|---|---|
| Thickness of winding ( mm ) | 3.9 | 3.8 | 4 |
| Inductance ( μH ) | 10 | 9.9 | 8.2 |

### 2.2. Coil number 1

In this coil, polyesterimide resin dissolved in styrene VUKI NK 50/30 was used for impregnation. The individual turns of the coated tape were insulated with a textile tape 0.25 mm thick and 12 mm wide, which was wound simultaneously with the superconducting tape. A flat copper braid was used for current leads. As first, one current lead was soldered on the superconducting tape and together with the textile tape it was wound into the coil. After the winding, the coil mounted on a special holder was immersed in the resin. The vessel with the coil and resin was then kept in vacuum for 20 minutes. After this time, the coil was removed from the vessel with resin and cured in air for 3 hours at 140 ºC. This coil is quite soft and compressible because some of the volume of the resin flowed out after impregnation. The complete coil is shown in figure 1 a).

### 2.3. Coil number 2

In this coil, epoxy resin ARALDIT F was used for impregnation. The individual turns of the coated tape were insulated with a textile tape 0.25 mm thick and 12 mm wide and a flat copper braid was used for current leads as well. This coil was wound the same way as coil no. 1. After the winding, the coil has been placed in a special casting form which was then filled with the resin so that the coil was completely immersed. The form with coil was then heated to 60 ºC and kept in vacuum for 20 minutes, then in the air at the atmospheric pressure for 20 minutes. This sequence was repeated 3 times. After this treatment the coil in the casting form has been cured in air at 90 ºC for 6 hour and at 120 ºC for 12 hours. After the curing, the coil was taken out from the special casting form. Complete coil is hard and stable and is shown in figure 1 b).

### 2.4. Coil number 3

In this coil, epoxy resin STYCAST 2850 FT BLUE was used for impregnation. The individual turns of the coated tape were insulated with a fiberglass tape 0.12 mm thick and 12 mm wide and 0.2 mm thick a flat copper plate was used for current leads. This coil was wound in a different way as coil no. 1 and coil no. 2. Superconducting tape together with fiberglass tape was wound into the coil and impregnated simultaneously during the winding. One current lead was soldered on the superconducting tape before the winding and other one after the winding. After the winding, the coil was cured at room temperature. The vacuum was not used. Complete coil is hard and stable and is shown in figure 1 c).

Figure 1. View of all coils: a) Coil no. 1, b) Coil no. 2, c) Coil no. 3.

## 3. RESULTS AND DISCUSSION

### 3.1. E(I) characteristics and critical currents

First were measured *E(I)* characteristics for all coils. The potential taps were soldered approximately 50 mm from current leads. The coils were measured in liquid nitrogen bath until exceeding the coil terminal voltage corresponding to an electric field of 1 μV per 1 cm of tape and slightly over $I_c$. For this criterion, the critical currents and *n* parameters were determined. The *E(I)* characteristic in measured current interval were fitted with the power law dependence given by the equation (1).

$$E(I) = E_0 \left( \frac{I}{I_c} \right)^n \tag{1}$$

where
$E$ = electric field [μV/cm], $E_0$ = 1 [μV/cm], $I$ = current [A], $I_c$ = critical current [A], $n$ = parameter

Table 2. Critical current and *n* parameter for each coil.

| Coil number | 1 | 2 | 3 |
|---|---|---|---|
| Critical current ( A ) | 282 | 267 | 270 |
| *n* parameter | 24.7 | 20 | 28.6 |

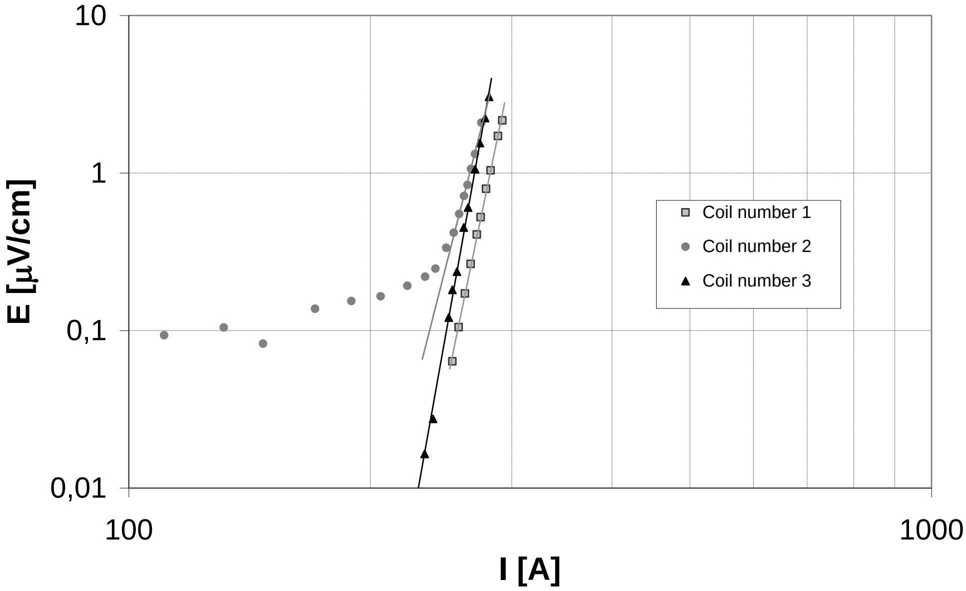

Figure 2. Graph of the *E(I)* characteristics of all coils.

The measured *E(I)* characteristics are shown in figure 2 and critical currents and *n* parameters are listed in table 2. From these measurements it is evident that coil no. 1 has highest $I_c$ from given coils and thus best transport properties in DC regime. Its mechanical properties are unfortunately the worst. This coil is very soft and contains very small volume of the resin. Coil no. 2 has the lowest $I_c$ but very similar as the coil no. 3. Some resistive part is visible in *E(I)* characteristic of coil no. 2 at currents lower than $I_c$ . It can be caused by some microcrack in the superconducting tape. Coil no. 3 has higher $I_c$ than coil no. 2 and lower $I_c$ than coil no. 1. The *n* parameter of coil no. 3 is the highest from all the coils. This coil is mechanically stable. However, the difference between the highest and the lowest critical current is 15 A, which is 5.3% of the maximum $I_c$. This decrease is not significant and none of the tested impregnation technologies is thus being disqualified. Although below $I_c$ the coil 2 presents a resistive component, its AC loss properties are not appreciably affected (see section 3.2).

### 3.2. Transport AC loss

Transport AC losses were measured by the lock-in technique. The coil was fed with harmonic AC transport current and the RMS values of the current and the voltage in-phase with current were measured. The AC loss of the coil was calculated by multiplying these values [8]. The measurements of the AC losses were performed at three frequencies, 36 Hz, 72 Hz and 144 Hz. The measured dependences of the AC loss per cycle $Q$ on the transport AC current RMS value $I_{rms}$ are plotted in the figure 3 for all three frequencies and all three coils. These measurements are compared to calculated AC loss. Methodology of calculation is described in [11, 12]. The calculations require as input the dependence of the critical current density, $J_c$, on the magnetic field B and its orientation. In this article, we directly use an interpolation of the measured average critical current density of the tape [13].

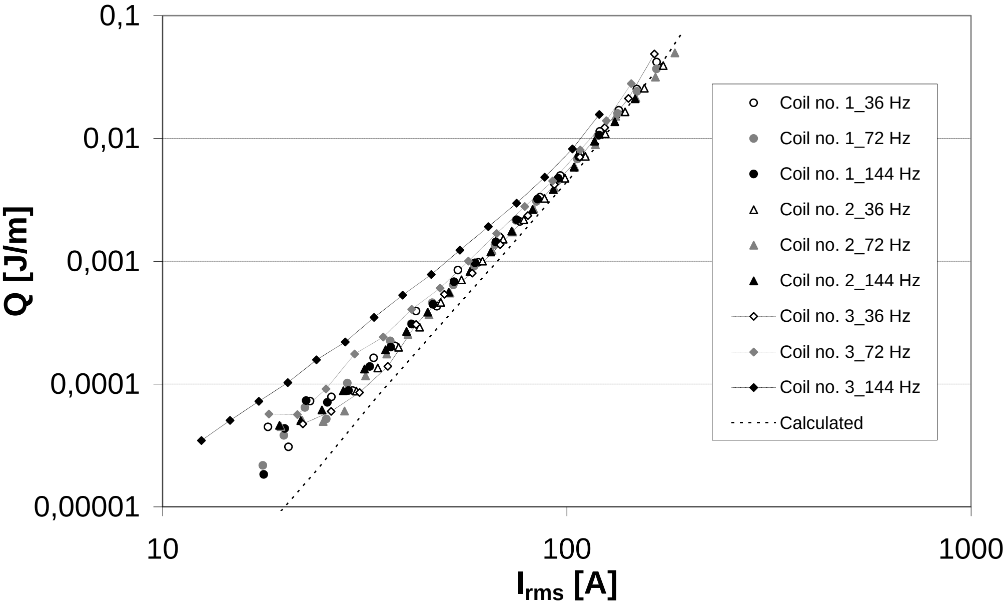

Figure 3. Graph of the transport AC losses of the all three coils, $Q$, expressed as loss energy per cycle and per 1 meter of the tape length in dependence on the RMS current value $I_{rms}$. Losses were measured at frequencies 36 Hz, 72 Hz and 144 Hz. AC loss calculated for coil no. 1 is also shown.

As can be seen, transport AC losses of coil no. 1 and coil no. 2 are frequency independent and are practically identical. Their character is hysteretic and there is an obvious discrepancy between the calculated and measured curves. At high $I_{rms}$, the calculations agree with the measurements, confirming that the impregnation process did not appreciably degrade the coils. The calculations under-estimate the AC loss at low $I_{\rm rms}$. The reason is that the model assumes a uniform tape, while $J_{\rm c}$ is degraded on the edges [13]. More complicated is the case of coil no. 3. The losses are evidently dependent on frequency and increase with frequency. With increasing frequency the maximum safe transport current has been decreasing because of the excessive heating of the coil. This coil includes highest volume of the resin and it can be the reason of the intensive heating. The frequency dependence of the loss indicates the presence of a loss with non-hysteretic character. It can be eddy current loss in current leads because in this case the flat copper plate was used for current leads as one of tested alternatives.

## 4. CONCLUSIONS

Three self-contained coils without coil frame were made from YBCO coated conductor using three different technologies of impregnation and resins. Coil no. 1 impregnated by the resin VUKI NK 50/30 has highest $I_c$ from given coils and transport AC loss is according to the expectation. The electrical parameters are the best from the tested coils but this coil is very soft and compressible and thus in many applications it is unusable. Coil no. 2, impregnated by the resin ARALDIT F, has the lowest $I_c$ and transport AC loss is practically identical to the coil no. 1. This coil is more suitable for AC applications because its properties are better in AC than in DC regime. The coil is hard and mechanically stable and usable in more ambitious applications.

Its manufacturing is the most complicated. Coil no. 3, impregnated by the resin STYCAST 2850 FT BLUE, has the $I_c$ higher than the coil no. 2 and lower than the coil no. 1. Its transport AC loss is dependent on frequency and increases with frequency. It is because the coil has copper plate current leads. This coil has the highest thickness of the winding. It is suitable for DC applications and, if using braided conductors in the current leads instead of a solid plate, also for AC applications, it’s hard and mechanically stable and usable in more ambitious applications. Its manufacturing is the simplest. However, the difference between the critical currents of the mentioned coils is about 5 %, which is not very much and thus all the given technologies of impregnation can be used under certain circumstances. Actually, 5 % is within the usual variation of the critical current in the tape length given by the manufacturer.

## 5. ACKNOWLEDGMENT

This work has been supported by the Agency of the SF of EU from the Ministry of Education, Science, Research and Sport of Slovakia (ITMS 26240220028).

## 6. REFERENCES

[1] Zhang H, Li Q, Zong J, Dong N. 2004, Development of a 1.5 T Ag-sheathed Bi-2223 magnet, *Physica C*, 469: 1799-1803

[2] Kim WS, Kwak SY, Lee JK, Choi KD, Jung HK, Seong KCh, Hahn SY. 2006, Design of HTS Magnets for a 600 kJ SMES, *IEEE Transactions on Applied Superconductivity*, 16: 620-623

[3] Chen M, Paul W, Lakner M, Donzel L, Hoidis M, Unternaehrer P, Weder R, Mendik M. 2002, 6.4 MVA resistive fault current limiter based on Bi-2212 superconductor, *Physica C*, 372-376: 1657-1663

[4] Bohno T, Tomioka A, Imaizumi M, Sanuki Y, Yamamoto T, Yasukawa Y, Ono H, Yagi Y, Iwadate K. 2005, Development of 66 kV/6.9 kV 2 MV A prototype HTS power transformer, *Physica C*, 426-431: 1402-1407

[5] Jiang Q, Majoros M, Hong Z, Campbell AM, Coombs TA. 2006, Design and AC loss analysis of a superconducting synchronous motor, *Supercond. Sci. Technol.* 19: 1164-1168

[6] Goddard KF, Lukasik B, Sykulski JK. 2009, Alternative Designs of High-Temperature Superconducting Synchronous Generators, *IEEE Transactions on Applied Superconductivity*, 19: 3805-3811

[7] Grilli F, Ashworth SP. 2007, Quantifying AC Losses in YBCO Coated Conductor Coils, *IEEE Transactions on Applied Superconductivity*, 17: 3187-3190

[8] Seiler E, Abrahamsen AB, Kováč J, Wichmann M, Træholt Ch. 2012, Measurement of AC losses in a racetrak superconducting coil made from YBCO coated conductor, *Physics Procedia*, In press

[9] Okamoto H, Hayashi H, Tomioka A, Konno M, Owa M, Kawagoe A, Sumiyoshi F, Iwakuma M, Suzuki K, Izumi T, Yamada Y, Shiohara Y. 2008, AC loss properties in YBCO model coils for loss reduction, *Physica C*, 468: 1731-1733

[10] Takematsu T, Hu R, Takao T, Yanagisawa Y, Nakagome H, Uglietti D, Kiyoshi T, Takahashi M, Maeda H. 2010, Degradation of the performance of a YBCO-coated conductor double pancake coil due to epoxy impregnation, *Physica C*, 470: 674-677

[11] Pardo E. 2008, Modeling of coated conductor pancake coils with a large number of turns, *Supercond. Sci. Technol.*, 21: 065014

[12] Pardo E, Šouc J, Kováč J. 2012, AC loss in ReBCO pancake coils and stacks of them: modelling and measurement, *Supercond. Sci. Technol.*, 25: 035003

[13] Gömöry F, Solovyov M, Pardo E, Šouc J, Seiler E, Frolek L, Macroscopic AC loss in a superconducting coil, *to be published*

049

# Study of Heat Electrodynamic Processes in High Temperature Superconductors (HTSC) Taking into Account Defects of Their Internal Structure

**Arkharov A., Romanovskiy V., Dontsova E.**

Bauman Moscow State Technical University, 2-aya Baumanskaya, 5, 105005, Moscow, Russia

## ABSTRACT

The approaches to HTSC modeling according to their defects have been examined. A computer modeling of the quality of HTSC superconducting properties with the aim to obtain data on the permissible parameters of the crystal defects disposition, which guarantee the critical current, was carried out. The obtained data can be used to manage the process in order to produce a superconductor with a guaranteed quality of its superconducting properties. As a result of the experiment the sum areas of defects at which a superconducting cluster is formed, were estimated. The maximum total area of defects when superconductivity was formed is 80%. When a superconducting cluster was formed the area of defects was at the average 40%. We compared the influence of horizontal and vertical defects on the superconductor quality. During the experiment the maximal number of horizontal defects when the superconductivity was formed, was 270849, the maximal number of vertical defects was 367642. The number of horizontal defects influences more on the cluster formation. The conclusions are the following: the sum area of defects observed of the HTSC material is admitted to 40%; at technological processing it should be taken into account that the material may be stretched out but not twist.

## 1. INTRODUCTION

The weak points of all superconducting ceramics samples are contacts between the granules. They determine the critical current in such materials. In the work the model of a superconductor's structure is presented.

## 2. MAIN PART: HTSC MODEL

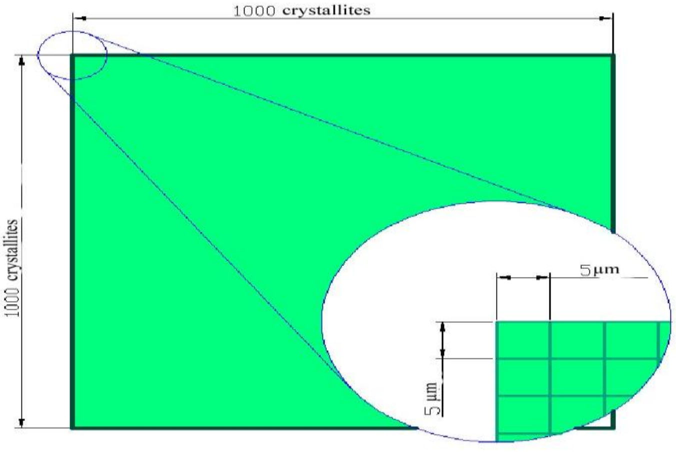

Figure 1 – Model of a superconductor's ideal structure

The green field of the two-dimensional model denotes the model of polycrystal. It corresponds to a material particle of HTSC, sized five by five millimeters. Each pixel on this field is matched to one crystal.

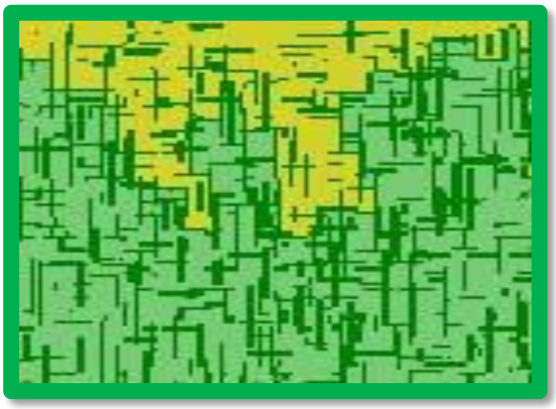

Figure 2 – Model of a superconductor's structure with defects

The horizontal and vertical segments are inflicted on the ideal structure of the conductor – this is simulation of the structural defects. The yellow color means the appearance of the percolation cluster. The dark green color is a defect, and light green one is an ideal structure.

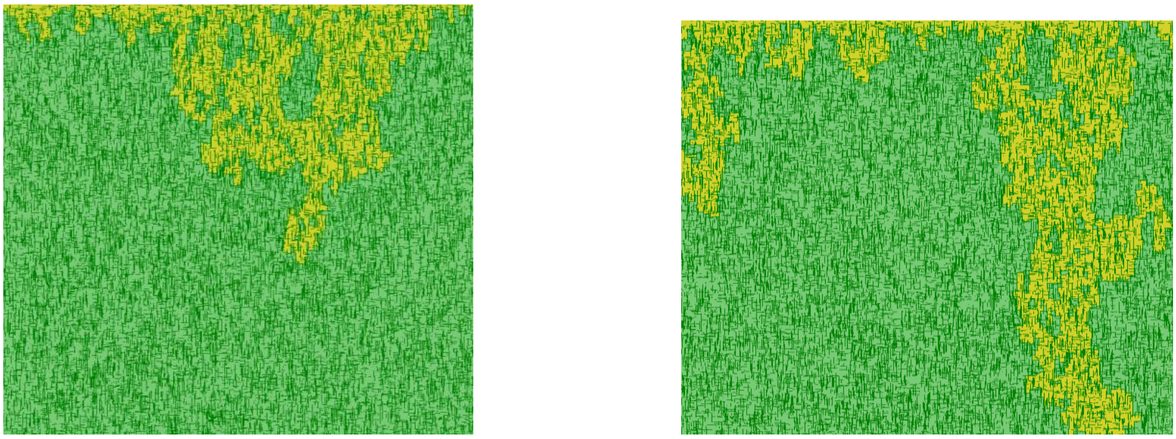

Figure 3 – examples of the program implementation

In the left picture the examples show the situation then the cluster is not formed. The amount and the dislocation of the defects don't allow the superconductor's current to cross the sample. And in the right picture the current can flow from the top to the bottom of the sample. In each case of the program fulfillment the computer registers the amount of the horizontal and vertical defects.

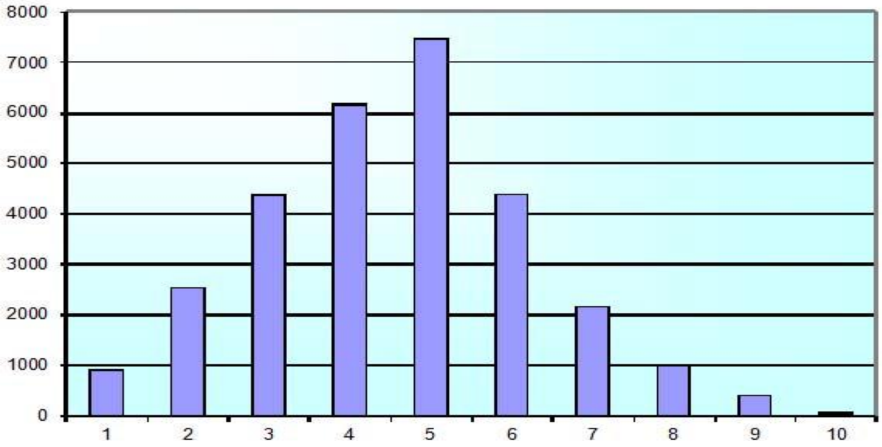

Figure 4. Diagram of quantity defects distribution

This is a histogram displaying the size of the defects area in case of successful formation of superconducting clusters. The maximum total area of defects is 80 %. On average, when a superconducting cluster appears the surface of the defects is equal to 40%.

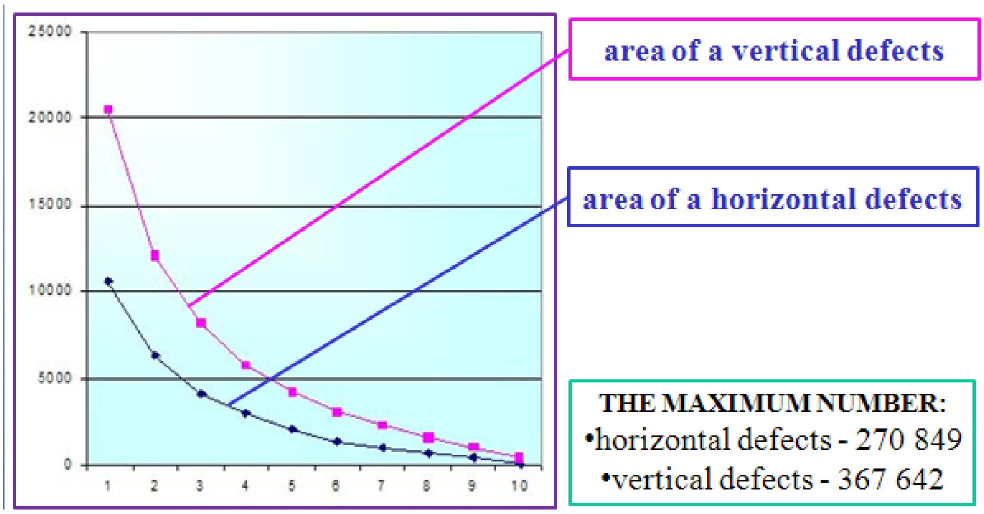

area of a vertical defects

area of a horizontal defects

THE MAXIMUM NUMBER:
•horizontal defects - 270 849
•vertical defects - 367 642

Figure 5. Diagram of horizontal and vertical defects distribution

The curves on the figure 5 show the differences between the affects vertical and horizontal defects on the HTSC quality.

## 3. CONCLUSIONS

1.The total area of the observed defects in material HTS can be up to 40 %.
2.When the conductors are processed one should pay attention to the reducing of the number of horizontal defects , so you can stretch the material but not twist it.

086

# Critical Current Degradation Analysis in Irradiated Superconducting Materials

**Sosnowski J.**

Joint Institute for Nuclear Research, Dubna, Russia
and Electrotechnical Institute, Warsaw, Poland

## ABSTRACT

Influence of the heavy ions or fast neutron irradiation on the current-voltage characteristics and critical current of high temperature superconducting materials is considered. Elaborated model based on an energy balance analysis for the system of the vortex captured on pinning centre is described and used for the critical current determination. The regular arrangement of caused by irradiation columnar type defects has been regarded. In critical current analysis has been taken into account the Lorentz force induced by current flow and elasticity energy of deformed vortex lattice, and especially nano-defects concentration and dimensions. The results of calculations indicate in which way the degradation of critical current occurs under the irradiation process. For optimally prepared tapes the irradiation leads to the decrease of critical current and appropriate change of the current-voltage characteristics. Elaborated model has been applied to the second generation tapes, while it is possible extend it also on tapes of the first generation and low temperature wires.

## 1. INTRODUCTION

Superconducting materials, both high temperature HTc as well as low temperature LTc superconductors are more and more frequently applied in nuclear physics devices, especially in accelerators, as current leads and in the windings of the superconducting magnets, as it has place in Nuclotron in Dubna. These materials are frequently exposed to the direct irradiation by the heavy ions or fast neutrons, creating defects of the nanometric size, it is nano-defects. Also in the winding process of the superconducting coils the defects in the superconductors will arise in the form of the micro crushes. These defects appearing in the superconducting tapes used in accelerators windings influence their proper work, so it is important task to investigate role and mechanism of the degradation of the critical current under their existence. It concerns especially HTc superconducting tapes, as well as $Nb_3Sn$, which are sensitive to irradiation creating disorder in linear chains of Nb atoms, responsible for superconductivity. For NbTi materials indicating 3d mechanism of superconductivity irradiation effects should be not so important from superconducting point of view.

## 2. MODEL OF THE CURRENT-VOLTAGE CHARACTERISTICS

Theoretical analysis has been performed of an influence of fast neutrons and heavy ions irradiation on the critical current of superconducting tapes working in the nuclear devices. The energy balance, of the system of vortex captured on the pinning centre, created just during an irradiation process was analyzed. Described geometry is presented in Fig. 1. Cylindrical defects shown here schematically are caused by irradiation of superconducting tape by heavy ions or fast neutrons, while rectangular defects can arise during the wounding procedure of the superconducting coils, leading to the micro-crashes creation. Movement of the vortex from the captured, equilibrium position, as shown in Fig. 1 causes an increase of the normal energy of the system. From the other side pinning of an individual vortex leads to its displacement in the regular vortex lattice and causes an increase of the elasticity energy of the system [1-2], because the regular vortex lattice is disturbed then. Current flow leads to arising of the Lorentz force. An increase of the energy of system related to the normal state development during the movement of the pancake type vortex, is given for cylindrical defects by an expression:

$$U = \frac{\mu_0 H_c^2 l}{2}\left[\xi^2\left(\alpha - \pi - \frac{\sin 2\alpha}{2}\right) - R_0^2\left(\beta - \frac{\sin 2\beta}{2}\right)\right] \tag{1}$$

In eq. (1) has been applied notation shown in Fig. 1. In the case of large defects diameters and especially micro-crushes flat geometry of the pinning centres shown in Fig. 1 can be considered. For that geometry potential well shape is given by:

$$U = \frac{\mu_0 H_c^2 l \xi^2}{2}\left(\alpha - \pi - \frac{\sin 2\alpha}{2}\right) \tag{2}$$

In eqs. (1-2) has been used energy scaling in such a way that normal state energy is on zero level. Then the depth of the pinning potential well is equal to the condensation energy because it is just the gain of the system free energy with totally pinned vortex. $H_c$ denotes thermodynamic magnetic field, angles $\alpha$ and $\beta$, shown in Fig. 1, describe the deflection of the vortex core against the pinning center. $R_0$ is the radius of the pinning center – columnar defect, $\xi$ is coherence length and describes the radius of the core of the vortex, while $l$ is the thickness of the vortex, for HTc superconductors of the thin pancake form. The pinning potential determined above is supplemented by the Lorentz force potential, connected with the interaction of the local current density at vortex and magnetic induction $B$. The Lorentz force acts on the volume $v_c$ of the captured vortex, tearing it off from an initial equilibrium position. In the paper has been considered an initial captured vortex position for the depth of the coherence length $\xi$ inside the pinning centre, which is favorable from the point of view of the shielding currents configuration. Others initial vortex positions could be considered in model too. The tilting of the potential energy wells, given by eq. (2) caused by the current flow and existence of the Lorentz force potential leads to the expression for an energy barrier, which should cross vortex in the flux creep process, in the function already of the reduced current density $\boldsymbol{i = j/j_c}$. $\boldsymbol{j}$ is here transport current density, while $j_c$ critical current density expressing the transitions between flux creep and flux flow states:

$$j_c = \frac{\mu_0 H_c^2}{\pi \xi B} * \frac{S(1 - S/d^2)}{d^2} \tag{3}$$

$\boldsymbol{B}$ is applied magnetic induction, $\mu_0$ magnetic permeability. Parameter $\boldsymbol{S}$ is the cross-section of nano-defect, while $\boldsymbol{d}$ the lattice constant of the regularly arranged nano-defects into the square lattice. Potential barrier height is given then as follows for flat defects:

$$\Delta U = \frac{\mu_0 H_c^2}{2} l \xi^2 \left[-\arcsin\left(\frac{j}{j_c}\right) + \frac{\pi}{2} - \frac{j}{j_c}\sqrt{1 - \left(\frac{j}{j_c}\right)^2}\,\right]$$

(4)

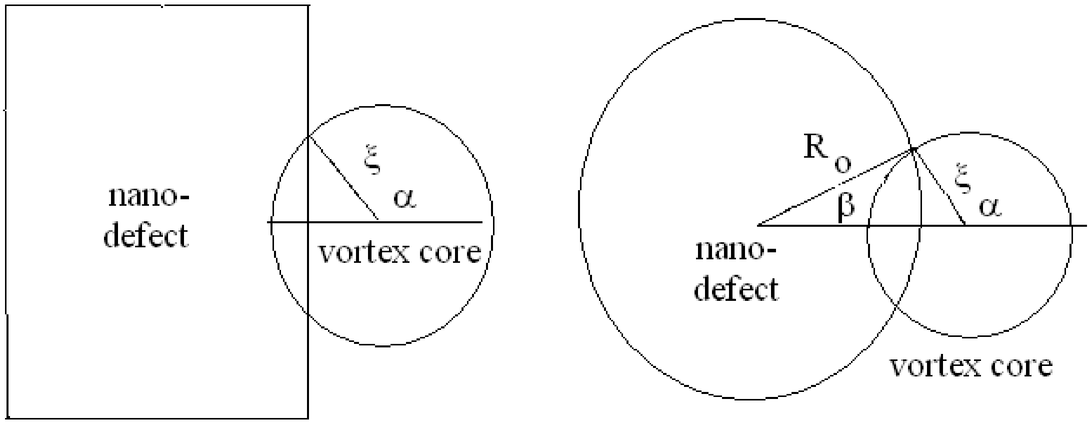

Fig. 1. Scheme of the geometry of the interaction of the vortex of the core radius equal to the coherence length ξ captured on the rectangular (left) and cylindrical (right) defect.

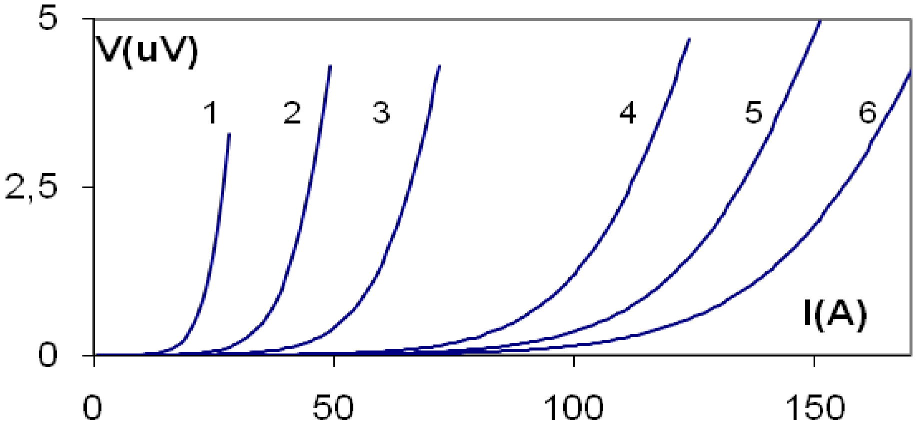

Fig. 2. The influence of the nano-defects on the current-voltage characteristic of HTc superconductor for surface concentration of defects equal to: (1) 105 $\cdot 10^{10}$ cm$^{-2}$, (2) 99$\cdot 10^{10}$ cm$^{-2}$, (3) 92,5$\cdot 10^{10}$ cm$^{-2}$, (4) 80$\cdot 10^{10}$ cm$^{-2}$, (5) 74$\cdot 10^{10}$ cm$^{-2}$, (6) 68$\cdot 10^{10}$ cm$^{-2}$.

Potential barrier given by eq. (4) is strongly dependent on the kind of defects and their size and concentration and determines the shape of the current-voltage characteristics of the superconductors:

$$E = -B\omega d\left[\exp\left[-\frac{\Delta U(0)}{k_B T}\left(1+\frac{j}{j_C}\right)\right]-\exp\left(-\frac{\Delta U}{k_B T}\right)\right] \tag{5}$$

$E$ is electric field, while $\omega$ the flux creep frequency, $k_B$ Boltzmann's constant, $T$ temperature. Eq. (5) describes both forward as well as backward flux creep processes and is used according to presented model for investigations of the critical current, filling resistivity criterion, dependence on the heavy ions irradiation.

## 3. INFLUENCE OF CREATED BY HEAVY IONS IRRADIATION DEFECTS ON THE CRITICAL CURRENT

Above presented mathematical model has been used for determining the influence of the irradiation by heavy ions and fast neutrons on the current-voltage characteristics and critical current of HTc tapes. This task has great importance for an improvement of our knowledge on the work of the superconducting windings in accelerators used in nuclear physics investigations. As the result of irradiation the columnar defects are created in superconducting tapes. In model it was assumed that these defects, acting as pinning centres form square array. Their lattice constant is inversely proportional then to the square root from the surface concentration of the defects. The change of the lattice constant of the defects array influences the critical current density given by eq. (3) as well as critical current filling real resistivity criterion, described by eq. (5). Selected results of numerical calculations describing the influence of the pinning centres concentration on the current-voltage characteristics are presented in Fig. 2. From given here curves it can be deduced strong decrease of the critical current with irradiation. Simplified model leading to the expression (3) for critical current, based on single interaction of vortices with pinning centres has been extended on the case of the regular ordering of defects into lattice. Then HTc superconducting tape of the second generation has been treated as long thin film composed from the regions of smaller cross-section, in which defects appear and regions non-deformed. The same current *I* flows through both of these connected in raw domains, but different is already the current density *j*. Because both these regions are electrically connected, so total electric field registered on voltage taps is superposition of fields induced on each of them. For simplifying the calculations, especially concerning the separating of these two parts it has been assumed the square shape of the defects. On importance of this effect of division of tape, on the critical current indicates the Fig. 3 showing the comparison of the dependence of the critical current received in the simple homogeneous approximation given by eq. (3) with modified inhomogeneous approach taking into account just existence of these two electrically connected in raw regions. Such approximation concerns especially the HTc superconducting tapes of the second generation (2G), in which superconducting current flows mainly in thin superconducting layer. On the other hand in the case of the first generation wires, thin filaments are immersed into the silver matrix. Then beside the division effect should be additionally treated parallel connection of both un-deformed and deformed regions with the silver matrix. This should additionally modify the critical current dependence on irradiation. In Fig. 4 is shown the critical current dependence not only on irradiation defects concentration but also on their dimension, which is other important parameter.

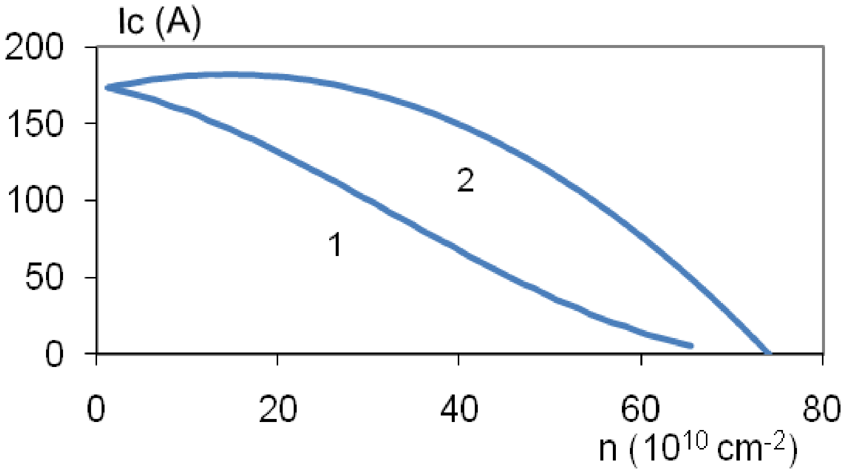

Fig. 3. Theoretically predicted influence of the fast neutron irradiation on the critical current of the HTc superconducting tape for the model: (1) of connected in raw regions and (2) basing on the relation (3).

Summing up we state that results of presented investigations indicate on the relevant meaning of ions irradiation for the proper work of superconducting windings used in cryogenic accelerators. The case of HTc superconducting tapes of second generation was investigated, while this model can be applied too for the first generation tapes, as well low temperature superconductors, especially for $Nb_3Sn$ wires.

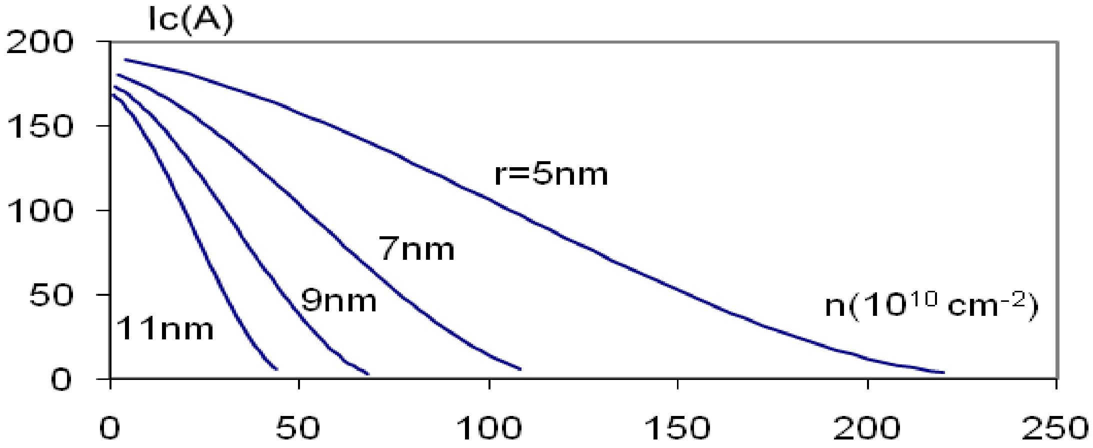

Fig. 4. Calculated influence of the irradiation dose, creating nano-defects of the dimensions given at each curve, on the critical current of HTc superconducting tape.

## 4. REFERENCES

[1] Sosnowski J. 2008, *Superconducting materials: modelling and properties*, Electrotechnical Institute Book Publisher, Warsaw, 200 p. (in polish)

[2] Sosnowski J. 2003, *Superconductivity: properties and applications*, Electrotechnical Institute Book Publisher, Warsaw, 208 p. (in polish)

093

# Opportunities for Improving the Electrochemical Characteristics of Ni-Zn Batteries using High Temperature Superconducting Ceramic

**Ivanova G.*, Stoyanova-Ivanova A.**, Terzieva S.**, Kovacheva D.***,**
**Mladenov M.*, Blagoev B.****, Dimitrov D.****

*Institute of Electrochemistry and Energy Systems, BAS, G. Bonchev Street, bl.10, 1113 Sofia, Bulgaria;
**Institute of Solid State Physics, BAS, Tsarigradsko Chaussee 72, 1784 Sofia, Bulgaria;
***Institute of Physical Chemistry, BAS, G. Bonchev street, bl.11, 1113 Sofia, Bulgaria;
****Institute of Electronics, BAS, Tzarigradsko Chaussee 72, 1784 Sofia, Bulgaria.

## ABSTRACT

Conductive ceramics powders can be used as an additive to form a „highly conductive" network between particles, which help to improve the electrical contact between "charge carrying" electrochemical active materials in the system. Superconducting ceramics are used as additives in order to insure greater longevity of Ni-Zn batteries and to provide an alternative replacement to the widely used Ni-Cd batteries. Such a ceramic powder with the nominal chemical composition of $Y_{0.95}Pr_{0.05}Ba_2Cu_3O_{6.96}$ (YPrBCO) was used as a conductivity additive to the active mass of the Zn electrode. For electrochemical studies electrochemical cells with demountable "button" were developed to simulate real metal body constructions. So, the cell with $Y_{0.95}Pr_{0.05}Ba_2Cu_3O_{6.96}$ superconducting ceramic in the zinc electrode exhibits generally good cyclic operation ability and performance stability. The specific capacity of 150 mAh/g (active mass) opens a real chance to use this material in Ni/Zn system.

## 1. INTRODUCTION

During the last years investigations have been carried out to develop the electrochemical properties of the nickel/zinc (Ni/Zn) rechargeable batteries for various applications such as power sources for hybrid/electric vehicles and new portable devices at low temperatures, worldwide. Zink oxide, commonly used as the anode material of Ni-Zn rechargeable batteries, has considerable advantages like low toxicity, low costs and abundant resources. Ni/Zn batteries are offered as a commercial product despite relatively small numbers of charge-discharge cycles compared to Ni/Cd (McLarnon, Cairns, 1991; Einerhand, Visscher, 1991; Huang et a., 2008). The short cycle life due to dendrite growth and shape change of the zinc electrode is the main problem which needs to be overcome. Many efforts have been done about improvement of electrochemical performance of Ni-Zn batteries using metal oxides or metal hydroxides (McBreen et al., 1981; McBreen et al., 1985; Renuka et al., 1992; Shivkumar et al., 1998; Coates et al., 1997; Yu et al., 2001). So, $Ca(OH)_2$ reduces the Zn concentration in the electrolyte and others as carbon-graphite and acetylene black increase the electronic conductivity and current distribution (Yuan et al., 2006a; Yuan et al., 2006b; Zheng et al., 2004). The most recent laboratory experiments show that the application of superconducting ceramics as materials for electrochemical power sources contribute to longer battery life by reducing gas control during charging of the cell (Battery and Energy Technologies, 2010). In the present work, the conductive ceramic powder of the superconducting system $Y_{0.95}Pr_{0.05}Ba_2Cu_3O_{6.96}$ is studied as a supplement to the Zn anode of Ni/Zn rechargeable batteries in order to form a highly conductive network between the particles, which helps to improve the electrochemical contact between power generating materials in the system.

## 2. EXPERIMENTAL

### 2.1. Preparation of conductive ceramic $Y_{0.95}Pr_{0.05}Ba_2Cu_3O_{6.96}$ powder.

A sample of $Y_{0.95}Pr_{0.05}Ba_2Cu_3O_{6.96}$ was prepared by the standard solid state reaction. The appropriate amounts of high purity (all 99.99% pure) powders of $Y_2O_3$, $Pr_6O_{11}$, $BaCO_3$ and CuO were mixed together and ground, pressed into pellets and annealed in oxygen atmosphere. This calcination was repeated three times. The first sintering was performed at 900 ºC in flowing oxygen for 21 h. After grinding the powder was sintered at 930 °C for the second time at the same atmosphere followed by a slow cooling and additional annealing to

450 °C for 2 h. The pellets were pressed at 5-6 MPa, sintered for the third time 950 °C for 23 h and subsequently annealed at 450 °C for 23 h.

## 2.2. Preparation of the zinc electrode and electrochemical tests

2.2.1. Preparation of a composite for paste electrode.
Literature data suggests that ZnO with smaller particle size (higher specific surface area) has a higher electrochemical activity and a longer life in charge-discharge cycles compared to larger particles. It is shown that the modification of the morphology of the material during charge-discharge cycles depends on the initial particle size. For smaller particles the growth is epitaxial, leading to longer maintenance of the initial morphology of the material and the later on formation of dendrites. Based on our own electrochemical motivation as well as on some literature sources, ZnO synthesized by solution combustion method is used after thermal treatment on air at 600 °C during 1 hour. The average crystallite size of this material is about 35 and 45 nanometers. The paste composite contains $Bi_2O_3$ and activated carbon as well.

2.2.2. Preparation of the zinc paste.
The used paste consists of: Zn-composite mass with additives- carboxymethylcellulose (CMC 3% solution), polytetrafluorethylene (suspension of PTFE 60%). Appropriate amounts of the composite for one electrode in the developed experimental cell (3 g anode mass) are initially wetted with diluted PTFE (5%) solution and treated in an ultrasonic bath during 6-10 minutes. Thereafter CMC is added under intensive stirring during 4 to 6 min and finally the concentrated PTFE (60%) emulsion is added to the mixture and stirred for 10-15 min until receiving paste with homogeneous consistence. The weight ratio of the paste composite to the CMC (3% solution) to the (60% suspension) is 81:14:5.

2.2.3. Pasted electrodes and battery assembling.
Zinc electrode is prepared by inserting the zinc paste on the matrix (modified metallic or conductive ceramic composite). The paste is uniformly spread on the preliminary configured Cu current collector (15 mm diameter, non-covered or covered with zinc layer). The pasted electrode is dried at 90 °C for 2 hours and then is pressed under 30 MPa for 2 min (or sintered at 320-360 °C during 40 min).
A solution of 7 M KOH, 0.9 M KF and 0.1 M LiOH, saturated with ZnO was used as the electrolyte. In assembling the experimental Ni-Zn cell, sintered carbonyl-nickel electrodes engineered for nickel-cadmium battery 2KNB-2 (2.5 V - 2.0 Ah) were applied as most appropriate. These electrodes are characterized by long charge-discharge cycling life. The capacity of the $Ni(OH)_2$ electrode was far more than of the Zn electrode.
Before assembling the cell, the electrodes are soaked under vacuum with electrolyte during 10 min. For comparison, similar zinc electrode with pure nanosized ZnO was also fabricated. Separator Celgard 3501 was used as the separator to retard Zn dendrite penetration and prevent the electrodes from shorting. The Zn electrode and Ni $(OH)_2$ electrode were assembled into a cell and placed in a coin-type cell container made of transparent material.

2.2.4. Electrochemical tests
Cyclic charge-discharge characteristics are recorded using specialized laboratory equipment allowing galvanostatic mode charge / discharge, as well as mixed mode cycling - constant current/constant voltage (CC/CV). The cell package consists of two disk-type electrodes with a diameter of 15 mm, separated by a micro porous separator and immersed in alkaline electrolyte.
The charge/discharge cycling tests were performed at room temperature. The cells were charged at 0.5 C for 6 h, and then discharged at 0.2 C down to 1.3 V cut-off. The CV experiments were carried out on an electrochemical workstation Arbin MSTAT with a scanning rate of 0.1 $mVs^{-1}$.

# 3. RESULT AND DISCUSSION

Powder X-ray diffraction patterns were collected within the range from 5.3 to 80◦2 theta (deg.) with a constant step of 0.02 2theta (deg.) on Bruker D8 Advance diffractometer with Cu Kα radiation and LynxEye detector. Phase identification was performed with the Diffracplus EVA using ICDD-PDF2 Database. The total oxygen content of the YBCO phase was obtained by the spectrophotometric method described previously (Stoyanova-Ivanova et al., 2005a and 2005b). The critical temperature of superconducting transition, $T_c$ is 90.8 K measured by four probe contact method.

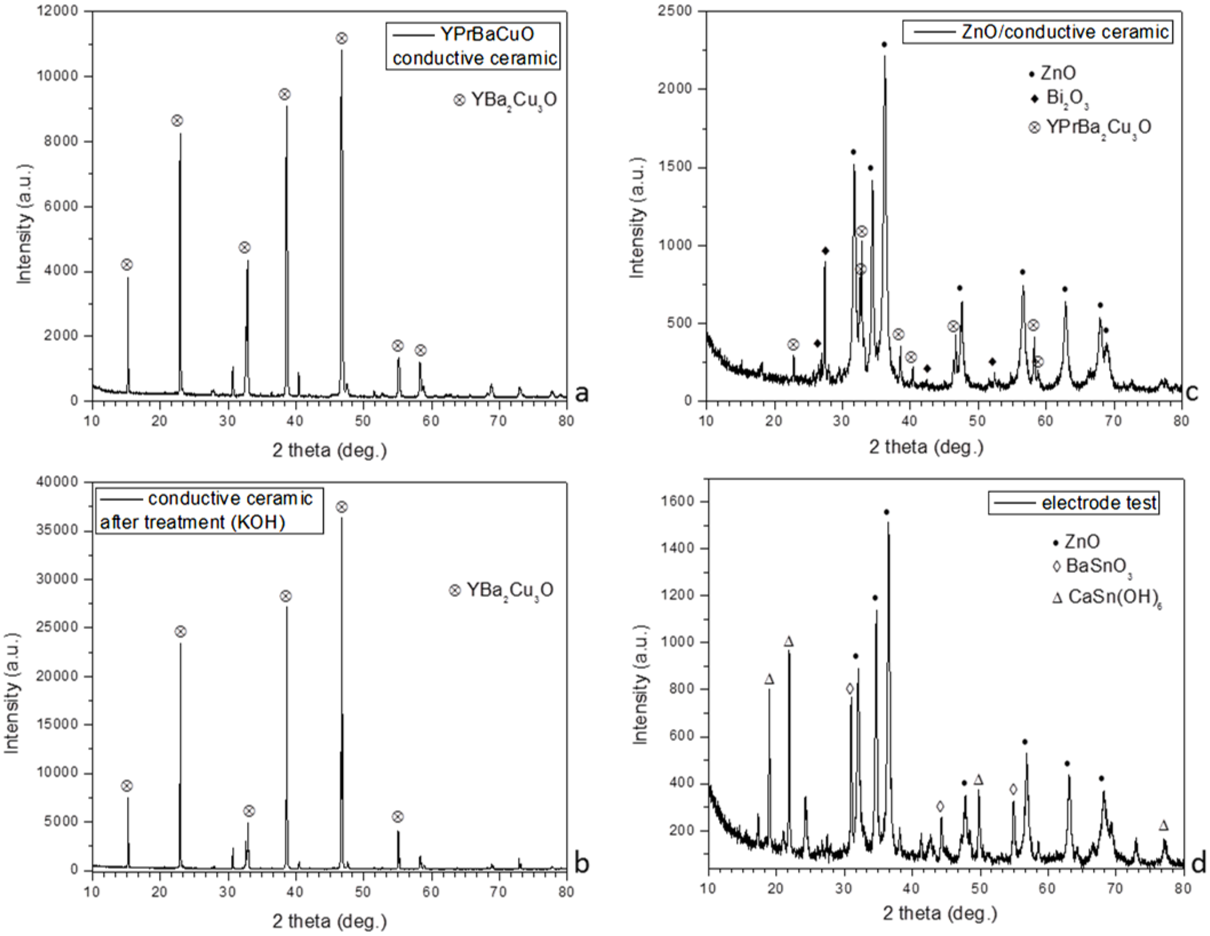

Figure 1. XRD patterns for obtained superconducting $Y_{0.95}Pr_{0.05}Ba_2Cu_3O_{6.96}$ ceramic (a), after 96 hours in electrolyte solution (b) and after electrochemical test (c, d).

According to the X-ray powder patterns, the superconducting ceramic material is homogeneous, without a second phase and well crystallized. The XRD spectra (Figure 1 (a-b)) show that the single phase 123 structure typical of high temperature superconducting ceramic is preserved after treatment in electrolyte solution of KOH (b). Figure 1 (c and d) show the XRD patterns of ZnO/conductive-ceramic composite. The main diffraction peaks are attributed to ZnO and others $Bi_2O_3$ and $Y_1Ba_2Cu_3O$ phases (c). During the electrochemical tests of the electrode the conductive ceramics is absorbed and its phase was not detected in XRD spectra (d).

Figure 2 shows the SEM images of conductive HTS ceramic and Zn/conductive-ceramic paste (composite), respectively. Pure HTS ceramic has “plate like” surface morphology and grain sizes from 2 to 15 μm (a). The structure of ZnO/ conductive-ceramic paste (composite) is homogenous with uniformly finer particles (b).

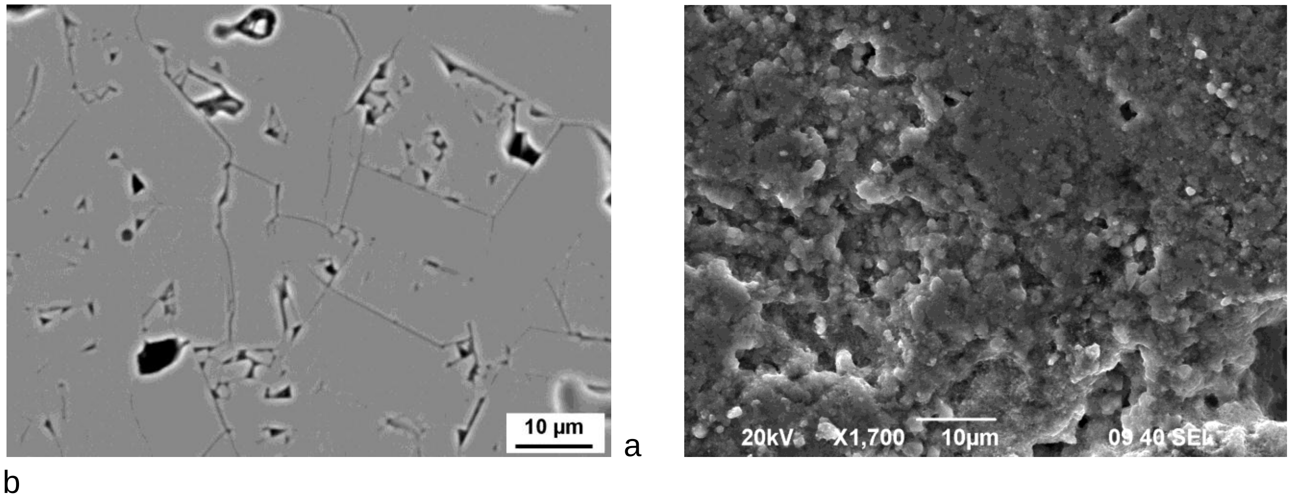

Figure 2. SEM images of $Y_{0.95}Pr_{0.05}Ba_2Cu_3O_z$ superconducting ceramic sample (a) and ZnO/conductive ceramic paste (composite) (b).

Typical charge/discharge voltage curves for the cell (with electrode paste containing $Y_{0.95}Pr_{0.05}Ba_2Cu_3O_{6.96}$ superconducting ceramic) during cycling are presented in Figure 3. Cyclic charge-discharge characteristics are obtained using specialized laboratory equipment allowing galvanostatic mode charge and discharge, as well as mixed –mode constant voltage. High temperature superconducting ceramics in powder form mixed with active materials and additives are applied to galvanized copper foam to obtain a Zn electrode. Electrode of the cell envelope consists of two disk electrodes with a diameter of 15 mm, separated by a porous separator (with pores of microns in size) and immersed in alkaline electrolyte as mentioned in paragraph 2.2.3. The tenth cycle of the voltage-time curves of both tested electrodes are presented in the inset. It can be seen that the voltage of the cell (i.e. the potential of the zinc electrode) increases very slowly during charging. The low charging voltage leads to improvement of the efficiency of the charging process and reducing the gas evolution. The cycling efficiency of the cell is over 90%.

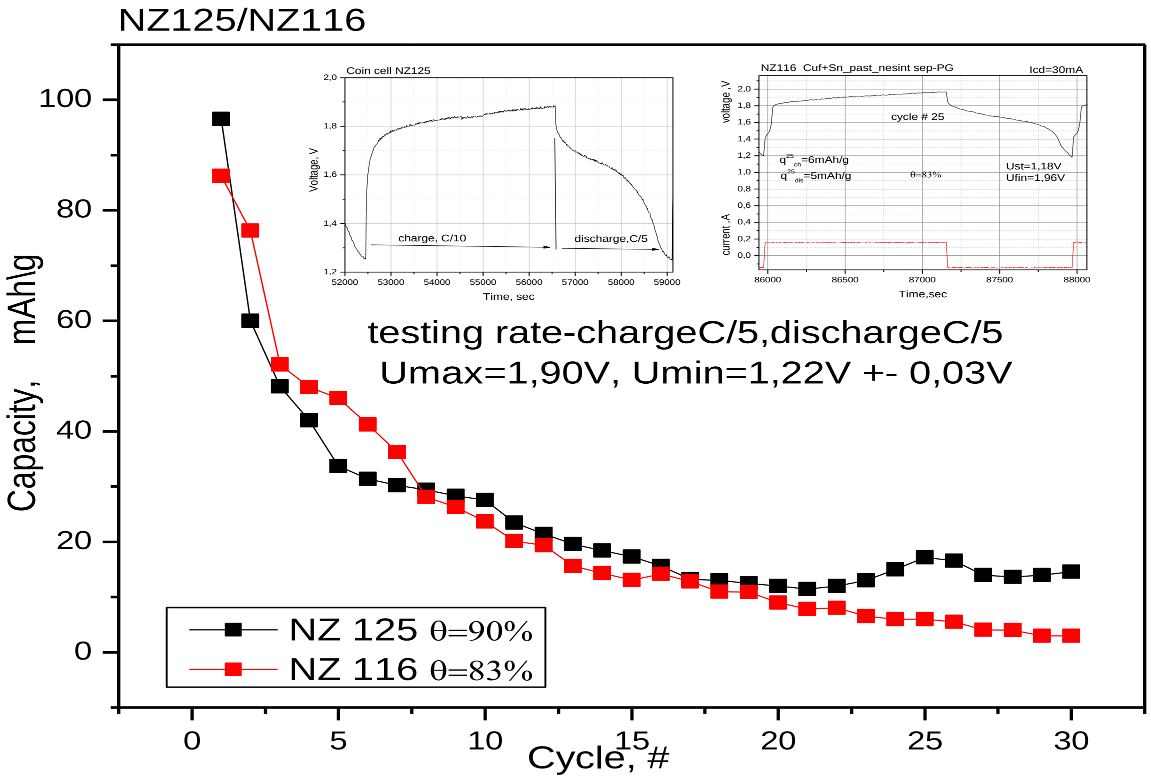

Figure 3. Electrochemical characteristics of Zn –electrodes:- cell 125 – with $Y_{0.95}Pr_{0.05}Ba_2Cu_3O_{6.96}$ superconducting ceramic- cell 116- without superconducting ceramic.

In figure 3 insets shows typical charge/discharge voltage curves for the cell with electrode paste containing $Y_{0.95}Pr_{0.05}Ba_2Cu_3O_{6.96}$ superconducting ceramic (left) and a control cell without superconducting ceramic additives to the electrode mass (right). The cell was charged up to end voltage ($U_{end\ ch}$=1.88 V) for the first 10 cycles and after that the charging continued to the higher end voltage ($U_{end\ ch}$=1.9V), while the discharge finished always to the cut-off voltage 1.25 V. At the 10th cycle, the cycling efficiency of the cell containing $Y_{0.95}Pr_{0.05}Ba_2Cu_3O_{6.9}$ is over 90% while that of the control cell is about 83%. Plots of discharge capacity vs. cycle number of the both cells are presented in the same figure. Comparing the capacity of the cell, containing superconducting ceramic composite electrode, with that of the cell without $Y_{0.95}Pr_{0.05}Ba_2Cu_3O_{6.96}$ superconducting ceramic leads to the conclusion, that additives of superconducting ceramic to the electrode mass improve the retention of the cell capacity to a higher values after prolonged cycling . The discharge capacity of Ni-Zn cell without $Y_{0.95}Pr_{0.05}Ba_2Cu_3O_z$ superconducting ceramic in higher during first 7- 8 cycles but after that decreases more rapidly. The results suggest that the cell with $Y_{0.95}Pr_{0.05}Ba_2Cu_3O_{6.96}$ superconducting ceramic in the zinc electrode exhibits generally good cyclic operation ability and performance stability. The testing of this type of cell continues.

## 4. CONCLUSIONS

Initial attempts are made for the application of superconducting ceramics as an additive to form a highly conductive network to improve the electrochemical contact between materials composing zinc electrode in Ni-Zn batteries. X-ray analyses of phase YBCO demonstrated that it is remarkably stable in the electrolyte solutions used for this type of batteries. XRDs of electrode material before and after cycling (during the real “work” of the battery) show that the YBCO phase decomposes during cycling to its building elements forming new phases, which obviously play positive role in cell performance. The initial electrochemical characteristics of Ni-Zn battery give reason to believe that the additive of superconducting ceramic to the composite improves the capacity retention of the cells, thus assists the prolongation of battery life.

## 5. ACKNOWLEDGEMENTS

This work was financially supported by the Institute of Solid State Physics - BAS (Grant BK -01-12/29.03.2012).

## 6. REFERENCES

McLarnon FR, Cairns EJ. 1991, *J. Elecrochem. Soc.* 138 645.

Einerhand R, Visscher W. 1991, *J. Electrochem. Soc*. 138 (1) 7.

Huang H, Zhang L, Zhang W.K. Gan Y, SHao H. 2008, θ*Journal of Power Sources* 184 663-667.

McBreen J, Gannon E. 1981, *Electrochim. Acta* 26 1439.

McBreen J, Gannon E. 1985, *J. Power Sources* 15 169.

Renuka A, Veluchamy A, Venkatakrishman N. 1992, *J. Appl. Electrochem.* 22 182.

Shivkumar R, Kalaigan G, Vasudevan T. 1998 *J. Power Sources* 75 90.

Coates D, Ferreira E, Charkey A. 1997, *J.Power Sources* 65 109.

Yu JX, Yang H, Ai XP, Zhu XM. 2001, *J.Power Sources* 103 93.

Yuan YF, Tu JP, Wu HM, Zhang B, Huang XH, Zhao XB. 2006a, *Electrochem. Commun*. 8 653.

Yuan YF, Tu JP, Wu HM, Yang YZ, Shi DQ, Zhao XB. 2006b, *J. Power Sources* 159 357.

Zheng Y, Wang JM, Chen H, Zhang JQ, Cao CN. 2004, *Mater. Chem. Phys*. 84 99.

Battery and Energy Technologies-Recharchable batteries, 2010, *Electroapaedia, Woodbank, Comunications* LTD.

Stoyanova-Ivanova AK, Nedelcheva TK, Vladimirova LK. 2005a, *Central European J. Chem,* 3 (3), 432-440.

Stoyanova-Ivanova AK, Terzieva S, Zalamova K, Angelov Ch, Zahariev A, Ignatov H, Kovachev V. 2005b, *Journal of Optoelectronics and Advanced Materials* Vol 7, №1, 477-480.

056

# Superconducting Unclosed Shields for Improving Homogeneity of the Magnetic Field in Magnetic Systems

**Kulikov E.[*], Agapov N.[*], Dorofeev G.[**], Drobin V.[*], Malinovski H.[*], Prokofichev Yu.[*], Smirnov A.[*], Trubnikov G.[*]**

*Joint Institute for Nuclear Research, Dubna, Russia;
**National Research Centre "Kurchatov Institute", Moscow, Russia;

## ABSTRACT

The homogeneity of the magnetic field is a very important task for such practical applications as MRI, NMR spectroscopy and particle accelerators (electron cooling systems etc.). An axisymmetric solenoid is often used as a source of the magnetic field. This work presents the experimental results of the influence of the superconducting unclosed shield on homogeneity of the solenoid magnetic field. The developed mathematical model adequately describes the shielding of the radial component of the external non homogeneous field. These results open up an opportunity of designing the efficient superconducting unclosed shields to form highly homogeneous magnetic fields in big volumes. The results of this work are supposed to be used for the electron cooling system of the NICA (the Nuclotron-based Ion Collider fAcility) which is being developed at JINR.

## 1. INTRODUCTION

The high current-carrying capacity of type-II superconductors allows one to use such superconductors for magnetic field shielding purposes.

Generation of the highly homogeneous magnetic field makes it possible to construct an electron cooling system for charged-particle beams, as a part of NICA accelerator complex [**1**]. For that, the magnetic field homogeneity has to be at least $10^{-5}$, with the length of the cooling system solenoid of about 6 m and the magnetic field of up to 2 T. However, it is very expensive due to the complexity of the precision winding. Moreover, multiple sections will inevitably lead to the non-uniform field at solenoid junctions. Using a superconductor shield could help to solve this problem.

The experiments on the superconductor solenoids with the superconducting shield inside have been conducted to determine if it is possible to use superconductivity when generating highly homogenous magnetic fields in large-sized devices. The shield is a multilayer unclosed winding made of the superconducting foil.

A mathematical model of such shield, which takes into account particular properties of the type-II superconductors and gives an adequate description of the very mechanism of shielding with the material like that, has been developed. To prove that the model is correct, the radial component of the field has been measured, and the experimental data have been compared with the theoretical calculations.

## 2. MEASURING OF THE MAGNETIC FIELD LONGITUDINAL COMPONENT

Multiple experiments with the shields of different design made of the NbTi strip - typical type-II superconductor alloy were performed at the Laboratory of High Energy Physics. The longitudinal component of the field was measured on the axis of the magnetic system using the one-component Hall sensor in 5 mm increments. The sensitivity of the Hall sensor was 73 mV/T. Liquid helium was used to cool the solenoid and the shield. The schematic diagram of the installation is given in Fig. 1.

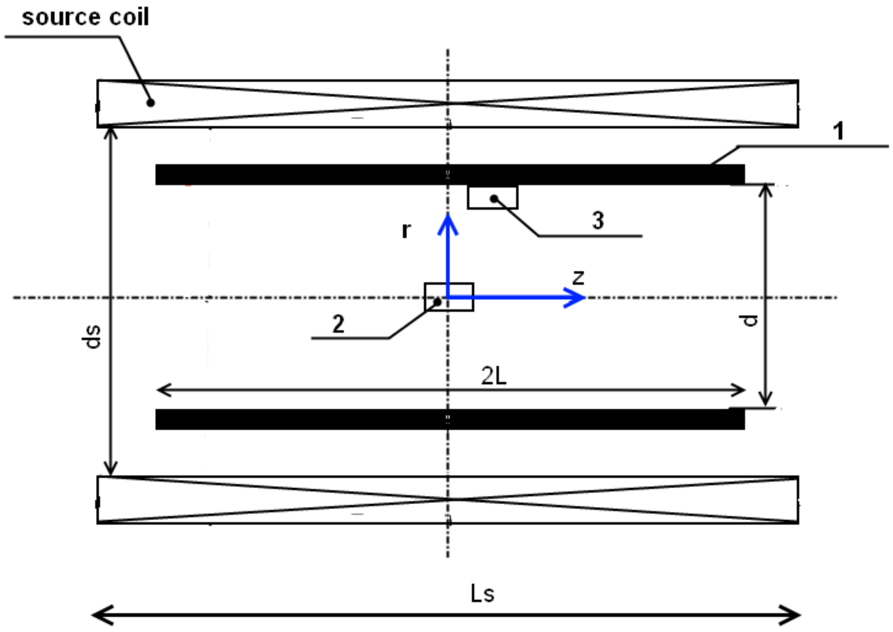

Figure 1. Experimental set-up. 1- superconducting unclosed shield; a) 2- Hall sensor to measure the longitudinal field component , Ls=150mm, ds=100mm, 2L=138mm; b) 3- Hall sensor to measure the radial field component, Ls=60mm, ds=15mm, 2L=60mm.

The tailor-made superconducting solenoid made at the laboratory was used in the first run of measurements, and its parameters are given in Fig. 1.a. The shield had five layers each 150 µm thick spirally wounded on the coil tube with diameter d = 78 mm. The experiments were carried out at different values of DC field formed by the solenoid, and the results are given in Fig. 2.

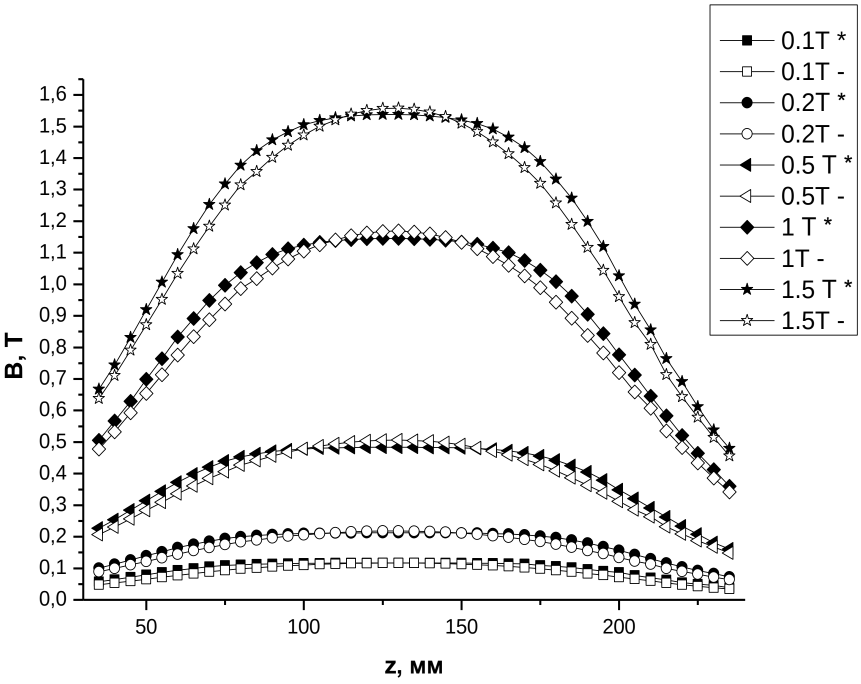

Figure 2. Longitudinal magnetic field as a function of z- coordinate for different applied induction (from 0.1 to 1.5 T) with shield (*) and without it (-).

The use of the superconducting shield results in a significantly larger area of highly homogeneous field, even with the solenoid having a small length-to-diameter ratio. With the increase of the magnetic field, the homogeneity area decreases due to the saturation of the superconducting shield with the critical density currents. The accuracy of magnetic field the measurements was about $\Delta B/B \sim 10^{-3}$, which was basically determined by the stability of the solenoid power supply.

## 3. MEASURING OF THE MAGNETIC FIELD RADIAL COMPONENT

Along with the first set of experiments (described in Part 2), the radial component of the magnetic field was measured on the inner surface of the shield. For this purpose, the 15-layer shield made of NbTi foil 20 µm thick spirally wounded on the tube with diameter d = 11 mm, was used (see Fig. 1.b).
As it may be seen from Fig. 3, the radial component of the field goes to zero near the centre of the shield, while the field penetrates the shield at the edges since this area is in the critical state.

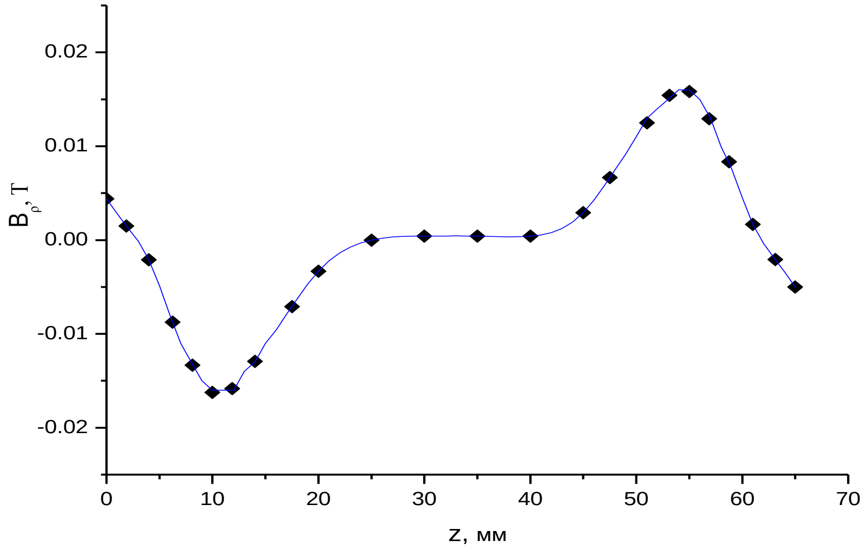

Figure 3. Radial magnetic field as a function of z- coordinate on the inner shield surface under applied induction of 1.5 T.

As it will be illustrated further, the measurements have qualitative confirmed the model offered in Part 4.

## 4. A MATHEMATICAL MODEL OF THE UNCLOSED SHIELD

It is known that type-II superconductor has two critical fields $B_{c1}$ and $B_{c2}$. We assume that $B_{c1} < B_{ext} < B_{c2}$, in other words, the superconductor is in the mixed state [2,3]. A mathematical model of the unclosed shield has been proposed because standard programs to calculate the magnetic fields calculating don't allow to carry out accurate modeling of this behavior of the material.
From the physical point of view, the existence of the area with the homogenous longitudinal component of the magnetic field results from the screening of the external field radial component by the superconducting unclosed shield.
To simplify the task, we consider that the shield material is isotropic, initially not magnetized and the shield thickness is much smaller than its radius: $\delta \ll R$. This assumption makes it possible to calculate the radial field component of the multilayer shield using the magnetic field of the infinite linear current-carrying conductor.
In the first approximation, the multilayer foil superconducting shield is similar to the plate that is not rolled in a tube yet and located in the external normal magnetic field. The radial component of the magnetic field vanishes in the centre of the solenoid. The magnetic field change induces two closed image currents in the two areas of the plate with the opposite external fields that have only the azimuth component, $J_\varphi$. Each of these currents screens the corresponding radial component of the magnetic field in the centre of the solenoid and is closed by the opposite currents flowing on the end of the shield surface.

According to the critical-state model, the density of these closing currents which flow in the shield areas penetrated by the radial component of the solenoid field, is supposed to be critical [3]. This determines the width of the flow area for the closing currents and, consequently, the operational integrity of the shield. For the sake of simplicity, let us assume that the critical current density does not depend on the local induction of the applied field and represents a certain constant value. Mathematically, it will have the following view:

$$\int_{-a}^{a} \frac{\mu_0}{2\pi} \frac{I(z)}{\delta} \frac{dz}{z-x} + \frac{\mu_0}{2\pi} J_c \delta \times \ln \left| \frac{L-x}{L+x} \frac{a+x}{a-x} \right| - B_{ext}(x) = 0 \tag{1}$$

where

$a$ [m] refers to the half-width of the area occupied by the non-saturated currents $I(z)$ [A] which are to be determined, $L$ [m] refers to the half-length of the shield.

The second summand in equation (1) is the normal magnetic field which was produced by the closing critical density currents $J_c$ [A/m$^2$]. The external field $B_{ext}(x)$ [T] is approximated by a polynomial of uneven degree $P_{2n+1}(x)$ and $P_{2n+1}(0)=0$. Substituting $a \times t$ for z in integral equation (1) we get the singular equation with Cauchy`s kernel. To unambiguously determine all the unknowns (the limit of integration $a$ is also unknown), the total current conservation equation has to be added (2):

$$\int_{-a}^{a} \frac{I(z)}{\delta} dz = 2 J_c \delta (L-a) \tag{2}$$

Thus we have a system of equations (1) - (2); it is solved with the Multhopp- Kalandia method (See Ref. [4,5] ). The determined current $I(x)$ is represented by a series described with function (3) quite well:

$$I(x) = \frac{C_0 \cdot x^2}{\sqrt{a^2 - x^2}} \quad \text{as} \quad x \neq \pm a \tag{3}$$

Here $C_0$ [A/m] is an approximation coefficient.

At point $x=\pm a$, the current equals to the critical current, so the singularity is eliminated. Solution (3) is a good approximation to the actual current flowing within the shield to provided condition (4) to be fulfilled

$$a > \frac{L}{2} \tag{4}$$

Thus, for the solenoid and the shield from the first experiment with the maximum applied field of 1 T and the average critical current density $2.6 \times 10^6$ A/m$^2$, it was found that $C_0 \approx 93.10$ A/m and $a$ =35 mm. As it follows from (3), the current in the geometrical centre of the shield equals to zero and is saturated to the critical level when $|x| \to a$. The calculated total field formed by the image current configuration (1) and the external field of the solenoid has the shape similar to the experimentally measured curve shown in Fig. 3.

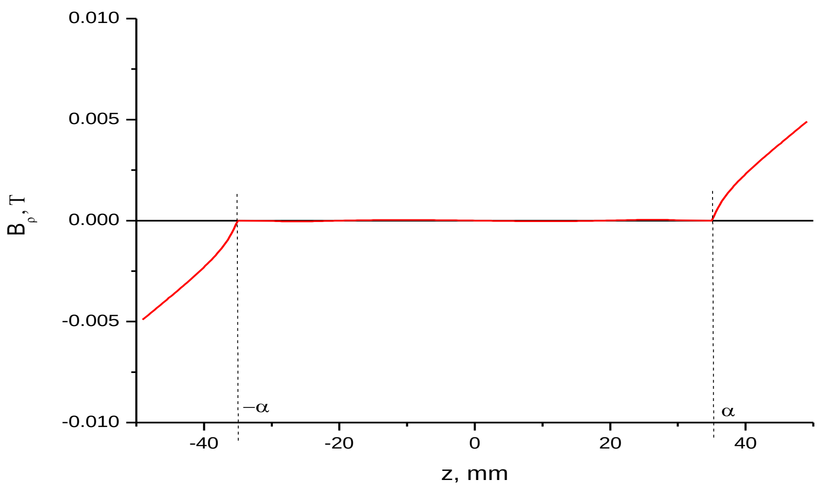

Figure 4. Radial magnetic field on the shield surface in the vicinity of the unsaturated area.

The obtained mathematical model gives an opportunity to make the following important conclusion. As $B_{ext}(x)$ increases (or the critical current density decreases), the unsaturated currents area is also shrinking, which is indirectly confirmed by the results given in Part 2 because the bigger the unsaturated area size - the wider the homogenous field region is (see Fig. 2).

## 5. CONCLUSIONS

The experiments have demonstrated an opportunity to use the superconducting shield for increasing the homogeneity of the magnetic field in the linear solenoid.

Although the model is rather simple, it, however, gives a correct qualitative description of the mechanism of shielding the magnetic field with the unclosed shield made of type-II superconductor. The quantities and the distribution of the image currents on the surface of the superconducting foil have been obtained.

Note that the currents on the end of the shield flow in the same direction as the major solenoid currents, while in the center they have an opposite direction, which explains the formation of the typical homogenous field areas shown in Fig. 2.

## 6. REFERENCES

Meshkov I., et al. 2009, Application of Cooling Methods to NICA Project, *Proc. of COOL'09 Workshop, China*.

Rose-Innes A., et al. (edited by Schmidt V. V.) 1972, *Introduction to the physics of superconductivity*, Mir, Moscow, 272 p.

Brandt E.H. 1998, Superconductor disks and cylinders in an axial magnetic field, *Phys. Rev. B.* 58(10): 6506-6522.

Polyanin A.D., Manzhirov A.V. 1998, *Handbook of Integral Equations*, CRC Press, Boca Raton-London, 272 p.

Muskhelishvily N. I. 1968, *Singular integral equations*, Nauka, Moscow, 512 p.

# POSTER SESSION - CRYOCOOLERS AND COOLING OF SUPERCONDUCTIVE SYSTEMS

019

# Cool-Down Processes of the NICA Accelerator Complex

**Mitrofanova Y., Emelianov N., Nikiforov D.**

Joint Institute for Nuclear Research, 141980 Dubna, Russia

## ABSTRACT

A new accelerator complex NICA (The Nuclotron-based Ion Collider fAcility) will be constructed in the next four years on the base of the Nuclotron. It will include, except the Nuclotron, a superconducting booster and a collider. Additional new accelerator rings will be cooled by two “satellite” refrigerators and a 1000 l/h helium liquefier located at the central cryogenic plant. In this paper we describe flow-schemes for the cool-down of the NICA superconducting magnets. According to these schemes, in addition to their main purpose, “satellite” refrigerators are used as a cool-down apparatus. At the first stage of the cool-down process, the refrigerator capacity will be produced by nitrogen refrigerators and the liquid helium flow from the central cryogenic plant at the second stage. Calculations of basic parameters of cool-down processes for the new accelerators are presented.

## 1. INTRODUCTION

The magnets of the NICA accelerator complex are constructed by the technology developed for the Nuclotron. For them there are no constrains on the cooling time usual for the majority of superconducting magnets arising from thermal gradients and stresses in constructions: all structural elements have been tested while cooling time till the liquid helium temperature up to 10 hours. Therefore, in the cool-down period the limiting factor will be only the refrigerator capacity of the cryogenic system. During more than 40 runs of the Nuclotron (with the “cold” mass of 80 tons) the usual cooling time amounted about 100 hours [1]. This time was mainly determined by the quantity of liquid nitrogen intended for the cool-down period. About 100 tonnes of liquid nitrogen are usually stored for this purpose.

## 2. FLOW SCHEME FOR COOL-DOWN

The cooling scheme of the booster and collider is shown in Fig. 1. This scheme has no special cool-down apparatus: their roles will be fulfilled via helium satellite refrigerators [2] with the heat-exchange equipment specially designed according to this task.

The cool-down processes of booster and collider are divided in two stages. At the first stage (Fig. 1a) the cooling source is the nitrogen refrigerator RA – 0.5 (with the capacity of 500 kg/h of liquid nitrogen), which provides the temperature of the cooling helium near 80 K. The liquid helium from the central liquefier OG–1000 is used at the second stage of cool-down (Fig. 1b).

## 3. CALCULATIONS OF BASIC PARAMETERS OF COOL-DOWN

It is assumed that cryostating of magnetic systems of booster and collider will be the same as cryostating of the Nuclotron. It is implemented by circulation of a vapor-liquid flow of helium inside the parallel channels located within the windings of the magnets [3].

The magnets are connected in parallel to the supply and return headers. The liquid helium from the refrigerator goes to the supply header of the accelerator and then it is distributed through cooling channels of individual magneto-cryostat modules. In each module, the vapor-liquid helium flow sequentially passes through the cooling channels of superconducting cables of electrical connection of adjacent magnets, magnet windings, and after cooling of the supply header and iron yoke of the magnet it enters the return header. While passing through the channels of the modules and removing the heat load the mass vapor content of helium varies from 0 at the input to the module to 0.9 at its exit. Cooling of the supply header necessary to maintain the helium inside in a single-phase state is provided by subcoolers installed at the outlet of windings

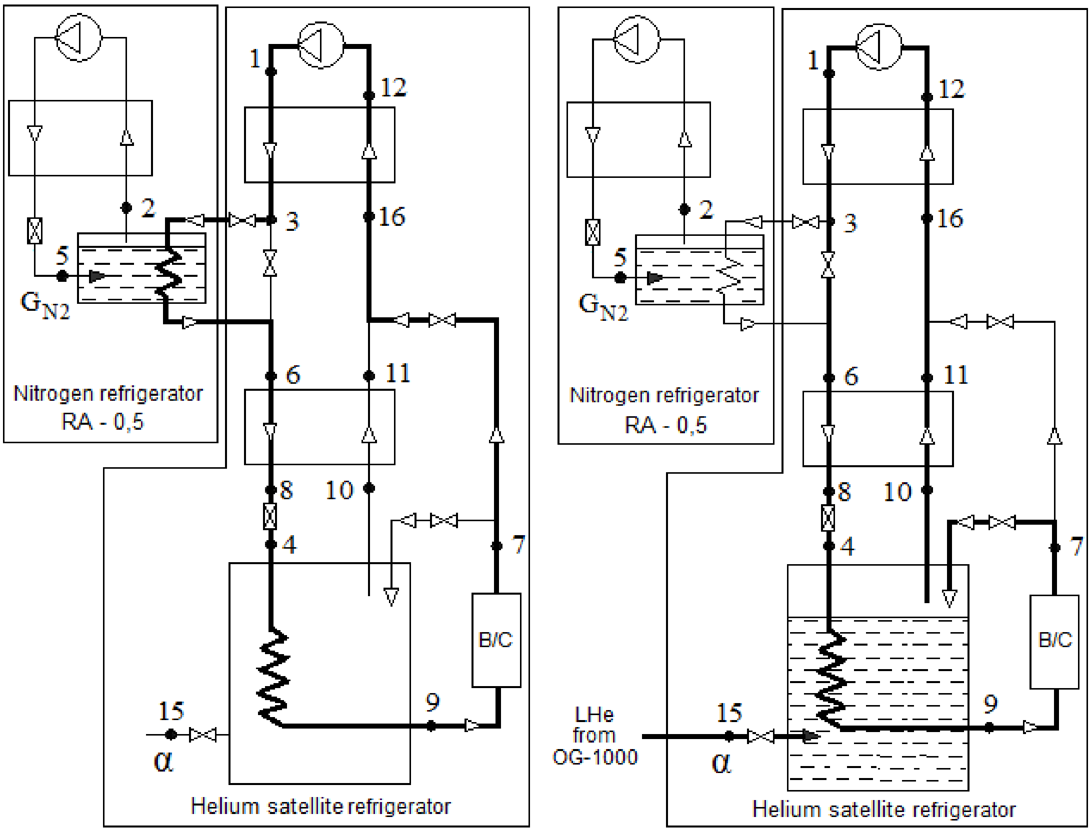

a b

Figure 1. Flow scheme for cool-down of the booster B and collider C: a) at the first stage of cooling, b) at the second stage of cooling

of each magnet. Usage of the header subcoolers results in significant temperature changing gas supplied to the cooling of magnets along the perimeter in cool-down period.

To perform the calculations, it is necessary to determine the relation between the temperature of magnetic elements and the temperature of helium at the outlet of the return header in the cool-down period.

As a first approximation, we used the data of typical cooling processes at the Nuclotron: an array of the helium flow temperature at the outlet of the magnet as a function of time for each magnet; an array of the helium flow temperature at the outlet of the return header as a function of time.

The average temperature of the Nuclotron magnetic system is approximately described by the relation:

$$\overline{T} = \frac{m_d \cdot \sum T_{out\_d} + m_q \cdot \sum T_{out\_q}}{m_d \cdot N_d + m_q \cdot N_q} \qquad (1)$$

where $m_d$, $m_q$ – the mass of the dipole and quadrupole magnets [kg]; $N_d$, $N_q$ – the number of the dipole and quadrupole magnets in the accelerator ring, $T_{out\_d}$, $T_{out\_q}$ – the experimental helium flow temperature at the outlet of the dipole and quadrupole magnets [K], respectively. In this case it is assumed that the temperature of the material of each of the magnetic element is equal to the helium flow temperature at the outlet of it.

Dependence of the average temperature of the magnetic system on the helium flow temperature at the outlet of the return header is shown in Fig. 2. This ratio of temperatures is used while calculating of the cooling processes of the magnet systems of the booster and collider in the first approximation. In the future the parameters of the cool-down processes of rings of these accelerators will be updated.

The range of the average temperature of the magnets from the initial (300 K) up to operating value (4.5 K) was divided by the number of intervals. For each value of the temperature of this array we have determined the appropriate value of the helium flow temperature at the outlet of the return header (Fig. 2), as well as the value of the specific heat of the construction material of the magnets [4].

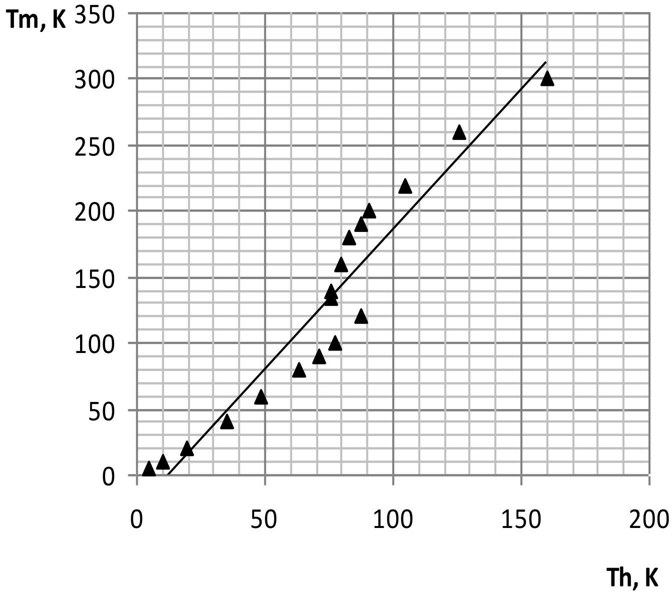

Fig. 2. Dependence of the average temperature of the magnetic system $T_m$ on the helium flow temperature at the outlet of the return header $T_h$

### 3.1. Mass flow rate of helium in the cycle

In the operating mode the mass flow rate of helium is determined by the heat load of a cryostating object, which consists of the dynamic heat releases of the magnets and heat leakages from the environment. At the current stage of the project the heat load is estimated to be 1000 W and 3000 W at the temperature of 4.5 K for the booster and collider, respectively.

In the operating mode the corresponding flow rate of helium is determined from the following ratio:

$$G_{He} = \frac{Q_{oper}}{r \cdot x_7 - i_{9oper}} \tag{2}$$

and is equal to 0.175 kg/s for the collider and 0.059 kg/s for the booster: where $Q_{oper}$ – the heat load in the operating mode [W], r – the specific heat of vaporization of helium [J/kg], $x_7 = 90\%$ – the mass vapor content of helium at the outlet of the return header, $i_{9oper}$ – the specific enthalpy of helium at point 9 of the scheme [J/kg] (Fig. 1).

In the cool-down period the mass flow rate of helium is determined by the capacity of the nitrogen refrigerator and the temperature of helium flow at the inlet of the nitrogen bath (Fig. 1, point 3).

The mass flow rate of helium in the cool-down period determined from the equation of the energy balance of pre-cooling stage:

$$G_{Hek} = \frac{G_{N2} \cdot (i_5 - i_2)}{i_1 - i_6 + i_{7k} - i_{12}} \tag{3}$$

where $G_{N2}$=500 kg/h – the mass flow rate of liquid nitrogen; $i_1$, $i_6$, $i_7$, $i_{12}$ – the specific enthalpy of helium at corresponding points of the scheme (Fig. 1) [J/kg], $i_2$, $i_5$ – the specific enthalpy of nitrogen at corresponding points of the scheme (Fig. 1) [J/kg], k – the array index of the helium flow temperature at the outlet of the return header.

For the collider in the cool-down period, starting with the value corresponding to the temperature at point 7 equal to 300 K, the flow rate of helium increases smoothly up to the operating value of 0.175 kg/s. For the booster, in view of its relatively small mass, the flow rate of helium during the cool-down period is equal to 0.059 kg/s.

### 3.2. The first stage of cooling

At the first stage of cooling the helium flow temperature at the inlet of supply header (point 9) is constant and amounts to about 80 K. The heat load withdrawn from the magnetic system of the accelerator and the cooling rate will decrease with the reduction of temperature of the helium flow at the outlet of the return header. To avoid delaying the cooling process at the temperature of the helium flow at the outlet of the return header (point 7) with a certain value, it is necessary to pass to the second stage of cooling with the satellite refrigerator operation according to the scheme shown in Fig. 1b.

Under this scheme, the reduction of the helium flow temperature at the inlet of the supply header (point 9) is provided by the flow of the liquid cooling agent from the liquefier OG – 1000 into the separator of the satellite refrigerator. The absence of sharp fluctuations of this temperature is provided by the supply of the return flow of the cooling agent (point 7) into the separator of the satellite refrigerator.

The specific enthalpy of helium at point 7 when transition to the second stage of cooling is determined from the equation of energy balance of the separator taking into account the constancy of the temperature at point 9 (80 K):

$$i_{7trans} = \frac{i_{10} \cdot (G_{He} + \alpha) - i_{15} \cdot \alpha}{G_{He}} \tag{4}$$

where α – the mass flow rate of the liquid helium supplied from the liquefier OG – 1000 (500 l/h for the collider, 300 l/h for the booster); $i_{10}$, $i_{15}$ – the specific enthalpy of helium at points 10 ($T_{10}$=80 K) and 15 of the scheme [J/kg] (Fig. 1).

The calculated temperature of helium flow at point 7 when transition to the second stage of cooling is 88 K and 94 K for the collider and booster, respectively.

As stated above, the range of the average temperature of magnets from 300 K to 4.5 K was divided into some number of intervals. While calculating the parameters of the first stage of cooling of the accelerator we used the array of temperatures from 300 K up to the temperature corresponding to the transition to the second stage.

The heat load withdrawn by the helium flow from the magnetic system of the accelerator was calculated by the formula:

$$Q_k = G_{Hek} \cdot (i_{7k} - i_9) \tag{5}$$

where $G_{He}$ – the mass flow rate of helium [kg/s]; k – the array index of helium flow temperature at the outlet of return collector; $i_7$, $i_9$ – the specific enthalpy of helium at points 7 and 9 of scheme [J/kg] (Fig. 1).

The cooling rate at each temperature interval was determined from the relation:

$$\left(\frac{dT}{d\tau}\right)_z = \left(\frac{Q_z + Q_{z+1}}{2}\right) \Bigg/ \left(M \cdot \frac{Cp_z + Cp_{z+1}}{2}\right) \tag{6}$$

where z – the array index of temperature ranges, $C_p$ – the specific heat of the construction material of accelerator [J/(kg·K)], M – the "cold" mass of accelerator (40 tons – booster, 100 tons – collider) [kg].

The cooling time at each temperature interval was determined from the relation:

$$\tau_z = \left(Tm_z - Tm_{z+1}\right) \Bigg/ \left(\frac{dT}{d\tau}\right)_z \tag{7}$$

where $T_m$ – the average temperature of magnets of the accelerator [K].

Thus the duration of the first stage of cooling calculated by the formula:

$$\tau = \sum_z \tau_z \tag{8}$$

amounts to 78 and 43 hours for the collider and for the booster, respectively.

### 3.3. The second stage of cooling

The parameters of the second stage of cooling of the magnetic system of the accelerator were determined by the same method as for the first stage. For calculations we used the array of the average temperature of magnets from the value corresponding to the transition to the second stage up to the operating value (4.5 K).
During the second stage of cooling the helium flow temperature at the inlet of the supply header (point 9) gradually decreases from 80 K to 4.5 K. In order to determine its dependence on the temperature of helium at the outlet of the return header (point 7), the array of values of the helium enthalpy at point 10 was determined by the equation:

$$i_{10k} = \frac{\alpha \cdot i_s + i_{7k} \cdot G_{He}}{G_{He} + \alpha} \tag{9}$$

where α – the mass flow rate of the liquid helium supplied from the liquefier OG – 1000 [kg/s]; $i_7$ – the specific enthalpy of helium at point 7 of the scheme (Fig. 1) [J/kg]; $i_s$ – the specific enthalpy of saturated vapor of helium [J/kg]; k – the array index of the helium flow temperature at the outlet of the return header; $G_{He}$ – the mass flow rate of helium [kg/s].
The array of temperature values at point 8 was determined by the following equation:

$$T_{8k} = (1 + s) \cdot T_{10k} \tag{10}$$

where s = 0.015 – the coefficient of the temperature difference at the cold end of the second heat exchanger, $T_{10}$ – the temperature at point 10 of the scheme (Fig. 1) [K].
The array of values of the enthalpy of helium at the inlet of the supply header was determined by the equation of energy balance of the separator:

$$i_{9k} = \frac{i_{8k} \cdot G_{He} + i_{15} \cdot \alpha + i_{7k} \cdot G_{He} - i_{10k} \cdot (G_{He} + \alpha)}{G_{He}} \tag{11}$$

where α – the mass flow rate of the liquid helium supplied from the liquefier OG – 1000 [kg/s]; $i_7$, $i_8$, $i_{10}$, $i_{15}$ – the specific enthalpy of helium at the corresponding points of the scheme (Fig. 1) [J/kg]; $G_{He}$ – the mass flow rate of helium [kg/s].
Thus the heat load withdrawn by the helium flow from the magnetic system of the accelerator was calculated by the following formula:

$$Q_k = G_{He} \cdot (i_{7k} - i_{9k}) \tag{12}$$

where $G_{He}$ – the mass flow rate of helium [kg/s]; $i_7$, $i_9$ – the specific enthalpy of helium at the points 7 and 9 of scheme [J/kg] (Fig. 1).
The cooling rate and the cooling time at each temperature interval were determined from the equations (6) and (7), respectively.
As a result the calculated duration of the second stage of cooling (eq. 8) amounts to 250 and 176 hours for the collider and for the booster, respectively.

## 4. CONCLUSIONS

This article has presented first results of calculations of basic parameters of superconducting magnets cooling of the NICA accelerator complex to the operating temperature (Tab. 1). In this case, we used data of typical cooling processes at the Nuclotron.
The results of calculations of duration of cool-down processes are presented in Fig. 3. As it can be seen from the graphs, the cool-down time calculated for the collider with the “cold” mass of 100 tons is 328 hours. For the booster with “cold” mass of 40 tons – 219 hours.

Table 1. Calculation results of cool-down periods for the booster and collider

| | Booster | Collider |
|---|---|---|
| Mass flow rate of helium direct flow of the satellite refrigerator in the operating mode, kg/h | 210 | 630 |
| Helium flow temperature at the outlet of the return header while the transition to the second stage of cooling, K | 94 | 88 |
| Average temperature of the accelerator magnets while transition to the second stage of cooling, K | 200 | 190 |
| Moment of transition to the second stage of cooling, h from the beginning of cool-down | 43 | 78 |
| Total calculated time of the accelerator cooling to the temperature of 4.5 K, h | 219 | 328 |

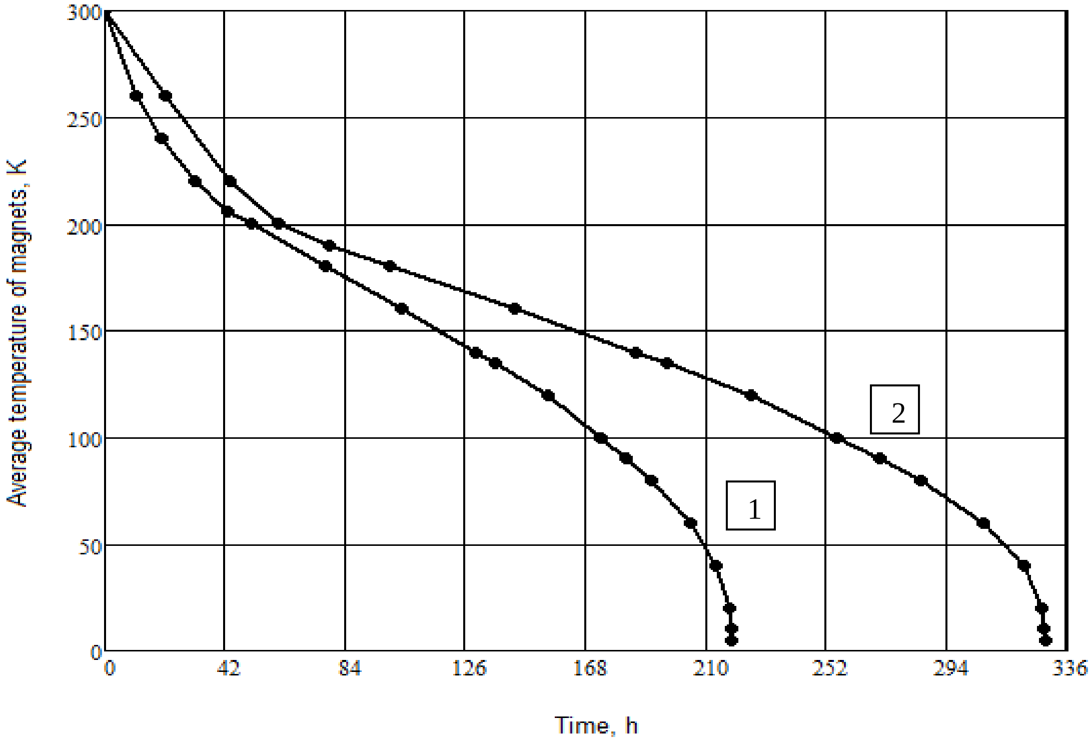

Figure 3. The average temperature of the booster (1) and collider (2) magnetic systems during the cool-down period

## 5. REFERENCES

Agapov N. 1999, Cryogenic Technologies of the Nuclotron – Superconducting Accelerator of Relativistic Nuclei, Physics of Elementary particles and Atomic Nuclei. 30(3): 760-804.

Agapov N., Mitrofanova Yu. et al. 2012, Development and Reconstruction of VBLHE Cryogenic System for NICA Accelerator Complex (2012–2015), JINR Communications. R8-2012-14, Dubna.

Agapov N, Vaseneva Yu. et al. 2004, Nuclotron Cryogenic System: Status and Recent Development, Proc. of Eight IIR Conference, Prague: 57-65.

Malkov M., et al. 1985, Handbook of physical and technical fundamentals of cryogenics, Energoatomizdat, Moscow, 431 p.

021

# Liquid Cryogen Targets for Experiments in Nuclear Relativistic and Particle Physics

**Konstantinov A.** [*]**, Borzunov U.** [*]**, Shimanskiy S.** [*]**, Varava A.** [**]

[*]Joint Institute for Nuclear Research, 141980, Dubna, Moscow region, Russia;
[**]Moscow Power Energetic Institute, 111250, Moscow, Russia.

## ABSTRACT

Now liquid cryogen targets are used and constructed for experiments being performed at JINR. These devices are needed to provide physical experiments with nuclei of the lightest elements (H2, D2, 4He) as targets. A cryogenic target is a cylindrical vessel made of polymer film filled with liquid H2, D2, or 4He.
The vacuum vessel for the cryogenic target is made of polyfoam. These solutions are used to reduce interactions of the beam and environmental matter (In case of the metal vessel there are too many irrelevant effects). This paper reviews the development of some liquid cryogen targets constructed at JINR, and gives the physical results obtained in these experiments. This paper describes a method of liquefaction of deuterium and hydrogen by using helium and helium - by helium. It also presents the results of using polymer materials while constructing cryogenic targets and vacuum vessels.

## 1. INTRODUCTION

Different types of targets are used at the particle accelerators in experiments with extracted beams of leptons, hadrons and nuclei. The type of the target used in experiments depends on the physical tasks. In some experiments it is necessary to use the lightest nuclei of $H_2$, $D_2$, $^4He$ as targets. Working substances in these targets are hydrogen, deuterium and helium [1].

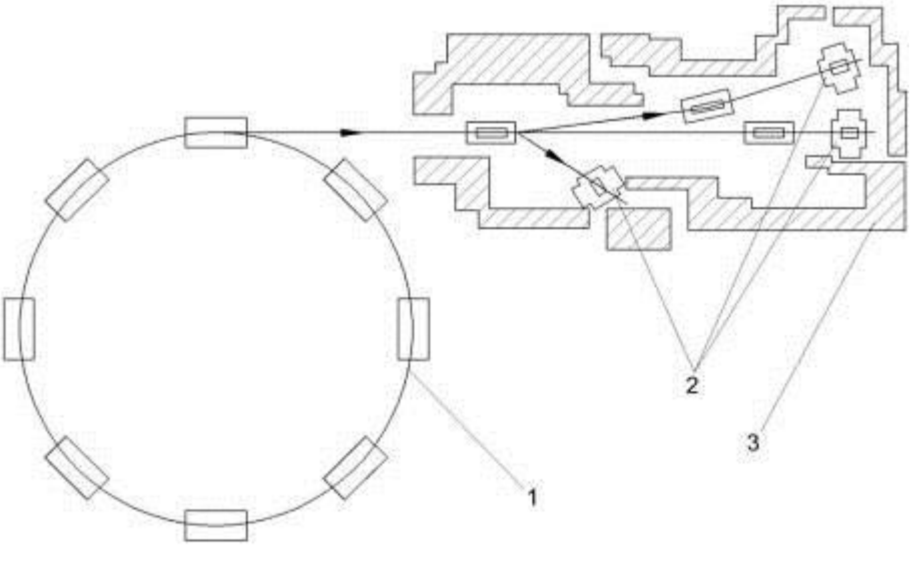

Fig.1. Scheme of the extracted beam experiments at the Laboratory of High Energy Physics (LHEP) at the Joint Institute for Nucear Research (JINR).
1. The accelerator (Nuclotron), 2. Targets for extracted beams, 3. Radiation shield.

Number of interactions (I) projectile particles on to a target is directly proportonal tothe density (ρ) of the target substance, intensity of falling bunch (i) and length of the target (l):

$$I \sim \rho \cdot i \cdot l.$$

The experiments required the number of effective interactions with the working substance to be possibly bigger therefore they use the beams with the maximum intensity and targets with the maximum density of the working substance. The length of the target is limited by the configuration of a physical facility. The problem to increase the beams intensity belongs to the problems of accelerator equipment and that is why it is important to construct the targets of the lightest nuclei with the maximum density.

Hydrogen, deuterium and helium are in a gaseous state under normal conditions. The increase of the density of the working substance can be reached by gas cooling before its transition to a liquid state or its compression. The lightest gases pass to a liquid state at temperatures below 21 K. The density of any liquid is approximately by 700-800 times more than the density of the gas being under normal conditions. The same density can be reached by compressing gas at the pressure of about 100 MPa. To keep gas under this pressure, it is necessary to make targets with thick walls.

The quality of the target is defined by the number of projectile particles interacting with the working substance of the target (effective events) and also by the number of their interactions with the extraneous substance (material from which the target is made) - background events. The quantity of background events should be minimum therefore the type and quantity of the extraneous substance are defining parameters to make targets. The quantity of the extraneous substance is characterized by parameter (c), depends on density and thickness of the material from which the target is made of and defined by the following expression:

$$c = \rho \cdot \delta \ [\mathrm{g/cm^2}],$$

here $\rho$ - density of the material, g/cm$^3$, $\delta$ - thickness of the material, cm.

Let us compare the quantity of the extraneous substance of the target with the compressed gas and the cryogenic target. The material of the walls of the vessel will be extraneous substance of the target with the compressed gas. The thickness of the walls of the vessel made of stainless steel (density $\rho = 7.7$ g/cm3), will be about 160 mm. Extraneous substance in the cryogenic target is the material from which the vacuum jacket is made of, the thermal screen and the internal vessel of the target. The vacuum jacket is made of polyfoam 10-15 mm thick and density $\rho = 0.081$ g/cm$^3$. The internal vessel – from mylar 0.08-0.13 mm thick and density $\rho = 1.33$ g/cm$^3$. The thermal screen is made of copper foil 0.5 mm thick and density of 8.93 g/cm$^3$. Thus, the quantity of the extraneous substance for the target with the compressed gas will be 123 g/cm$^2$ and 0.585 g/cm$^2$ – for the cryogenic target. The cryogenic target contains extraneous substance by 200 times less than the target of compressed gas and it is the best option for providing experiments.

The scheme of the cryogenic target developed at LHEP JINR, is presented in Fig. 2. It consists of the internal vessel (1), containing the working substance of the target, and vacuum jackets (2) and (4). The thermal screen (3) is installed between the internal vessel and the vacuum jacket. It is used to decrease the radiation heat flow. The target is filled with the working substance by means of the pipeline (5). Pumping of the vacuum volume (6) is provided by means of the joint (7).

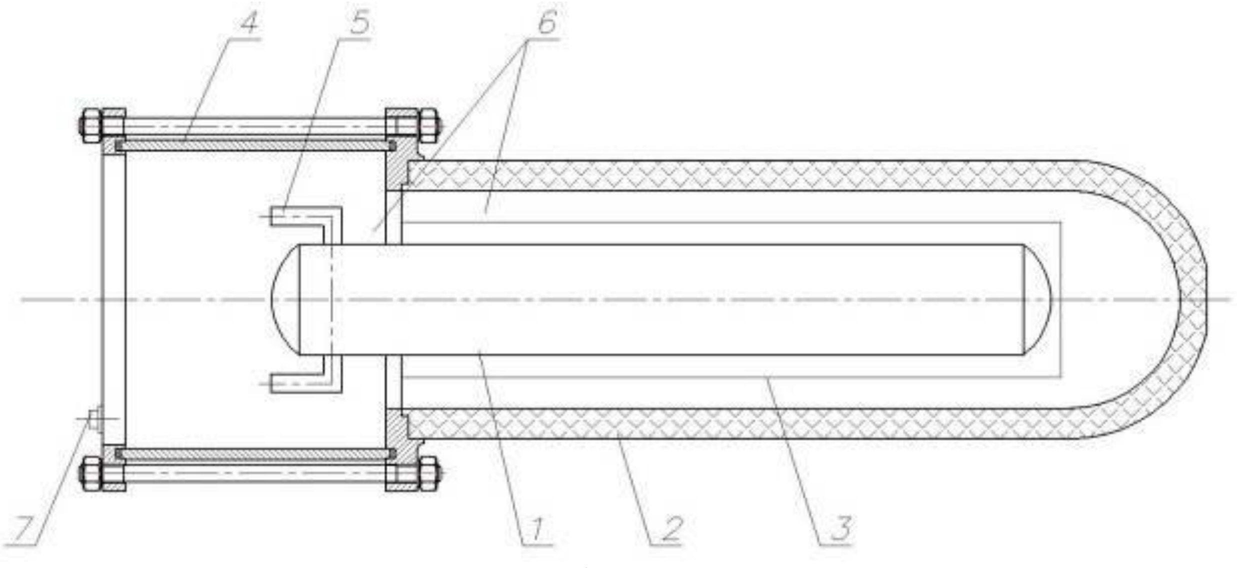

Fig. 2. Design of the cryogenic target.

1. internal vessel; 2. polyfoam vacuum jacket; 3. thermal screen; 4. stainless steel vacuum jacket; 5. the pipeline for filling the target with working substance; 6. vacuum volume; 7. vacuum pumping joint.

## 2. THE CRYOGENIC TARGET DESIGN FEATURES.

Let us consider the design features while constructing separate elements of the cryogenic target. Let us begin with the internal vessel (1, Fig. 2.). The internal vessel of the cryogenic target is filled with working substance in the liquid state. The requirements to the internal vessel are as follows:

1. The internal vessel should work at temperatures from 4.2 to 21 K;
2. It should be resistant difference of pressure up to 0.1 MPa between the vacuum volume and the vessel;
3. The vessel should contain a minimum quantity of substance of the walls.

The last item is define the material choice for manufacturing the internal vessels of the target.

The material properties can be characterized by the radiating length ($X_0$) which is defined by the following expression:

$$X_0 = \frac{716 \cdot A}{Z \cdot (Z+1) \ln(287/Z)} \text{ [g/cm}^2\text{]},$$

here Z – the charge of the nucleus and A – the nuclear weight of the material. The radiating length ($X_0$) is the efficient distance at which intensity of the gamma radiation and the high energy electrons stream are weakened by *e* times. The material background is possible to determine by parameter (q) which is equal to the following expression:

$$q = \rho \cdot \delta / X_0,$$

here ρ - density of the material, g/cm$^3$, δ - thickness of the material, cm, $X_0$ - radiation length, g/cm$^2$.

The first targets developed at LHEP JINR had an internal vessels made of stainless steel foil. The radiation length of stainless steel is equal to $X_0$ = 15.3 g/cm$^2$. Development of new polymeric materials, especially mylar, allows one to give up using metals to manufacture internal vessels. Mylar possesses good mechanical properties, has low density and contains elements with lower number of Z. It makes possible to construct internal vessels with bigger radiation lengths ($X_0$ = 39.95 g/cm$^2$). The internal vessel of the target, made of metallized mylar, has been developed at LHEP JINR, presented in Fig. 3.

Fig. 3. Internal vessel of the cryogenic target.

Another important construction element of the target is the vacuum jacket (2, Fig. 2). The vacuum jacket of the target is loaded with the external pressure (difference up to 0.1 MPa) under operation conditions and works for compression. It should be resistant the pressure upon a rupture of about 0.5 MPa in case of a failure. The first vacuum jackets of the targets developed at LHEP JINR, were made of stainless steel. Later, in the results of testing various materials polyfoam was recognized to be the best material for this purpose.

Polyfoam has small density, and its mechanical properties provide necessary durability. The vacuum jacket made of polyfoam for the internal vessel (Fig. 3), developed at LHEP JINR, is shown in Fig. 4. Application of polyfoams and mylar for manufacturing the elements of the target allows one to reduce quantity of the material by 5-10 times on the way of particles.

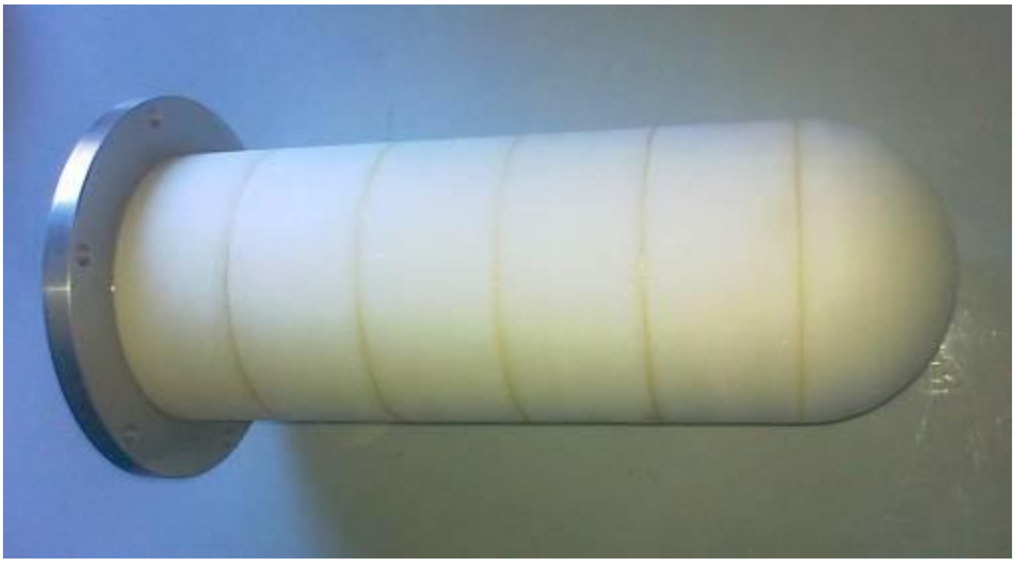

Fig. 4. The cryogenic target vacuum jacket.

## 3. FEATURES OF THERMAL INSULATION FOR TARGETS

The heat flow from environment and heat evaporation due to energy loss of the particles passing through the target, lead to the working substance vaporization. The heat from environment to working substance is transferred by means of residual gases, radiation from warm surfaces and the thermal conductivity of the target materials. To decrease the heat flow defining evaporation speed of the working substance some types of the thermal insulation are used.

To reduce the heat flow from the residual gases to the working substance, it is necessary to provide vacuum in vacuum volume of the target not less than 0.1Pa. To support the vacuum they use the adsorbents located on cold pipelines of the target.

Radiation heat flow is reduced by using the screens cooled with vapor of the liquid which has evaporated from the target. The thermal screen is a cylindrical construction made of the thin sheet material.

The screen material and its thickness have been chosen to provide the working temperature of the screen below 100 K, and the minimum quantity of the screen substance on the way of particles. Depending on the sizes of the screen and the way of its cooling, it is possible to use the metal foil with high thermal conductivity or mylar film with metallization of various thickness.

To reduce the heat flow caused by the material thermal conductivity they use the pipelines with minimally thick walls.

## 4. FILLING OF THE TARGETS WITH THE WORKING SUBSTANCE.

As the working substance in the target constantly evaporates, it is necessary to have a system of filling to support a constant level of the working substance in the target.

One of the ways of continuous providing targets with the working liquid – its replenishment from the vessel where it is already is in the liquid state. The advantage of this method is simplicity of the operation. The main disadvantage is the necessity to have a large amount of the cryogenic liquid. That is especially dangerous at work with explosive hydrogen and deuterium.

In case when the target has small sizes or it works in strong electric fields, it is expedient to carry out condensation of hydrogen (deuterium) by using liquid helium.

The condenser - heat exchanger for liquefaction of hydrogen (deuterium) has been developed at LHEP JINR [2]. It uses thermal capacity of the steam and warmth of evaporation of liquid helium. The facility automatically supports the pressure in the target filled with liquid hydrogen (deuterium), with a precision

±980 Pa. The condenser - heat exchanger and automatic equipment provide stabile work of the target at the heat flow of up to 30 W. The scheme of the automatic control of pressure in the target is shown in Fig. 5. While filling the target (1) the gaseous hydrogen (deuterium) comes to the condenser - heat exchanger (8) from the receiver (16) and, having passed through it, the hydrogen (deuterium) flows down into the target. Liquid helium comes to the condenser - heat exchanger from the vessel (5) and then – to the gasholding system. Having filled the target with liquid hydrogen (deuterium), helium from the condenser - heat exchanger passes through the consumption regulator (19), (RCH). As soon as the pressure increases in the target (that signals about the increased evaporation of the liquid in the target) the pneumatic signal comes in the measuring block (4) of the differential manometer where it amplifies the signal which opens RCH. The amount of the helium passing through the condenser - heat exchanger, thus, increases, and the pressure in the target falls as a result of hydrogen (deuterium) condensation. The pressure drops, and RCH is closed. The operation control of the condenser - heat exchanger is carried out by means of the manometers. At sharp increase of the hydrogen (deuterium) pressure in the target, the safety valve works, and hydrogen (deuterium) goes to the emergency dumping line.

The developed system also allows one to liquefy helium by helium. By means of this method allows one to liquefy all working substances with one condenser - heat exchanger. In this case there is no need to have vessels with each type of the working substances in the liquid state. The target takes small room, that is important for physical facilities.

To liquefy helium by helium, it is necessary to have different temperatures of the helium in the target and the helium which it is liquefied with. It can be reached by increased pressure in the target. The increase of the helium pressure in the target by 0.1 MPa increases its transition temperature to the liquid state from 4.2 K to 5.2 K. This method has shown efficiency and reliability while operating at many targets.

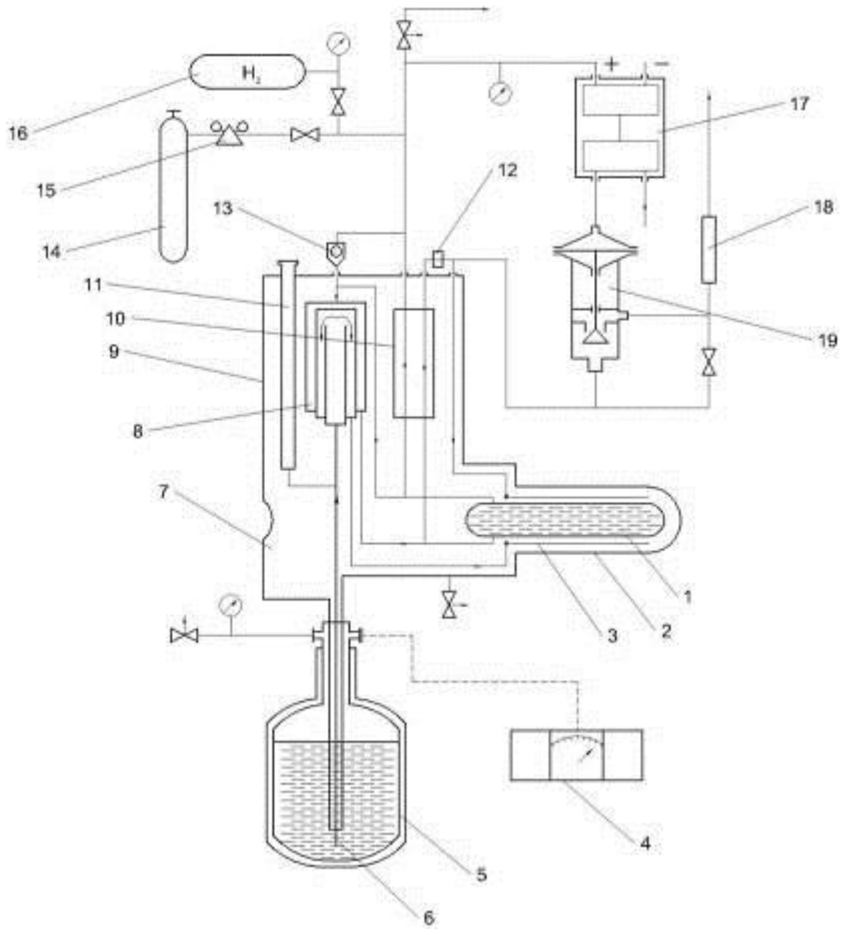

Fig. 5. Scheme of providing the target by cryogenic liquid.

1. working volume of the target; 2. polyfoam vacuum jacket; 3. thermal screen; 4. the block of measurement the liquid helium level and pressure maintenance in the Dewar vessel; 5. the Dewar vessel; 6. tube of helium supply; 7. mylar window; 8. condenser - heat exchanger; 9. vacuum jacket; 10. heat exchanger of preliminary cooling; 11. pipeline for helium; 12. diaphragm; 13. reverse valve; 14. vessel with the

compressed gas; 15. reducer; 16. receiver; 17. differential manometer; 18. rotameter; 19. regulator of helium consumption (RCH).

## 5. CRYOGENIC TARGET WITH LIQUID HELIUM, HYDROGEN, AND DEUTERIUM

This target developed at LHEP JINR, is a basic element of the “Disk” facility, to study cumulative effects [3]. The feature of the target is that it`s the single vacuum jacket has simultaneously vessels with liquid $H_2$, $D_2$ and He, and also a vessel for background measurements. The scheme of the designed target is shown in Fig. 6. The cylindrical vacuum jacket (1) is made of stainless steel and has four identical rectangular windows located one under another. The windows are closed by the cylindrical jacket (2) made of mylar film 0.12 mm thick. Opposite to each window there are internal vessels made of the same mylar film. In general two targets of this type were made: one target with internal vessels 50 mm long, another – 140 mm. Deuterium liquefying proving by means of liquid hydrogen in the condenser - heat exchanger (5) which is consist of two coaxial cylinders made of stainless steel. Minimization of the heat flow is reached by using a copper polished screen and three layers of the metallized mylar 0.012 mm thick which wrapped up cold surfaces of the target. Besides, the helium vessel is protected by the screen (6) which has a thermal connection to the condenser - heat exchanger (5).

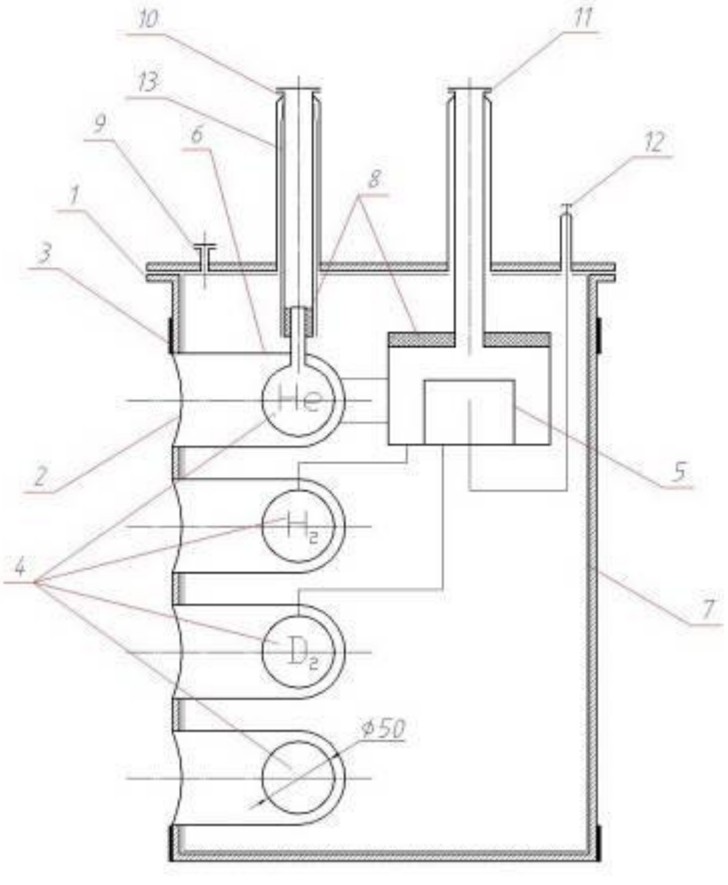

Fig. 6. Design of the cryogenic target containing liquid helium, hydrogen, and deuterium. 1. vacuum jacket; 2. mylar jacket; 3. nylon filament bandage; 4. internal vessels from mylar; 5. condenser - heat exchanger; 6. thermal screen for helium vessel; 7. radiation screen; 8. adsorber; 9. union of vacuum pumping; 10. pipeline for He; 11. pipeline for $H_2$; 12. pipeline for $D_2$

Let us list the main advantages of this installation.

a) target replenishment by helium and hydrogen is carried out by the liquid drift of intermediate vessels without any regulators.
b) there is no need to load deuterium to receivers after each run on the accelerator because capacities for emergency dumping of deuterium serve and for its storage between runs.
c) there is no need to use liquid nitrogen for cooling of thermal screens because the screens are cooled with helium and hydrogen evaporation.
d) The air cannot penetrate to deuterium communications because the minimum pressure in the system is always higher than the atmospheric one.

## 6. CRYOGENIC TARGET WORKING AT LHEP JINR

Liquid cryogenic target used for providing physical experiments at "NIS-GIBS" facility is shown in Fig. 7.

Fig. 7. General view of the cryogenic target.

There are two identical target were made. One target for providing experiments, another – for background measurements (Fig. 8).

Fig. 8. Cryogenic target.

The target operation control is provided by means of the control console (Fig. 9).

Fig. 9. Cryogenic target control console.

## 7. REFERENCES

1. N. N. Agapov et all 1982, *Kriogennie pribory i ustroystva v yadernoy fizike*,(in Russian) energoatomizdat, p27-68

2. Yu. T. Borzunov, L. B. Golovanov (Dubna, JINR) 1985, *Liquid Hydrogen Target With Recondensation Of Hydrogen By Helium*, Instrum. Exp. Tech. 27 (1984), p542-546

3. L. B. Golovanov, V. L. Mazarsky, A. P. Tsvinev (Dubna, JINR) 1980, *Cryogenic Target Containing Liquid Helium, Hydrogen, and Deuterium*, Instrum. Exp. Tech. 21(1978), p593

062

# Studies of Performance Characteristics of Twin Thermoacoustic Prime Mover with Gas Mixtures as Working Fluids

**Behera U.[*], Kasthurirengan S.[*], Kamble B.[**], Kuzhiveli B.[**], Krishnamoorthy V.[***]**

[*] Centre for Cryogenic Technology, Indian Institute of Science, Bangalore 560012, India.
[**] Mechanical Engineering Department, National Institute of Technology, Calicut 673601, India.
[***]I-Design Engineering Solutions Ltd., Wagholi, Pune 412207, India.

## ABSTRACT

Thermoacoustically driven Pulse Tube Cryocooler totally eliminates the moving components and hence it is highly reliable towards end applications. In our objective to develop such a system, we have designed and fabricated twin standing wave type Thermoacoustic Prime Mover (TAPM). However, this needs to be optimized in terms of its operational parameters. In this paper we present the performance characteristics of twin standing wave type TAPM with gas mixtures of different working fluids, namely nitrogen, argon and helium. The operating frequency, pressure, pressure amplitude, and temperature difference between the stack ends have been studied at different operating pressures by varying gas mixture compositions. Simulation studies have been carried out using DELTAEC software for He-Ar system. The simulation and the experimental results compare fairly well and are presented here. It is observed that He-Ar mixture leads to very stable low frequency oscillations suitable to drive the Pulse Tube Cryocooler.

## 1. INTRODUCTION

The thermoacoustic prime mover (TAPM) is an attractive alternative to the conventional pressure wave generator (compressor) used in pulse tube cryocooler/refrigerator (PTR), owing to no moving components, eliminating problems associated with conventional drives such as wear and tear and vibrations, simplicity in construction, reasonable thermodynamic efficiency and use of environment friendly working fluids. Many researchers [1-8] have investigated the standing wave TAPM with different designs and suitable modifications to achieve low operational frequency and high efficiency. Towards matching the operational frequencies of TAPM and PTR, experiments are carried out with two different working fluids, one in TAPM and the other in PTR separated by an elastic partition [9]. The influence of the working fluids on the performance of TAPM has been studied by Hao et. al. [8], in particular to decrease the operating frequency of TAPM to match that of PTR. Based on the design guidelines [1, 10], a twin standing wave TAPM setup has been built and detailed experimental studies have been conducted with the same. In this work, we report the experimental studies carried out on the performance characteristics of TAPM using pure working fluids namely nitrogen, argon and helium and their mixtures. The experimental studies show that for the best performance of TAPM, correct binary mixture of working fluids should be used. Further, simulation studies have been carried out using DELTAEC (Design Environment for Low Amplitude Thermoacoustic Energy Conversion), free software from Los Alamos National Laboratory, USA. The experimental results are found to be in reasonably good agreement with the simulation studies.

## 2. EXPERIMENTAL SETUP

The twin standing wave TAPM is a symmetric structure having two prime movers located at the either end of the resonator tube. Each prime mover consists of a hot heat exchanger, a stack and an ambient heat exchanger. The buffer volume is a part of the hot end of the prime mover. The design of system has been carried out using the guidelines of Swift [1] and Tijani [10].

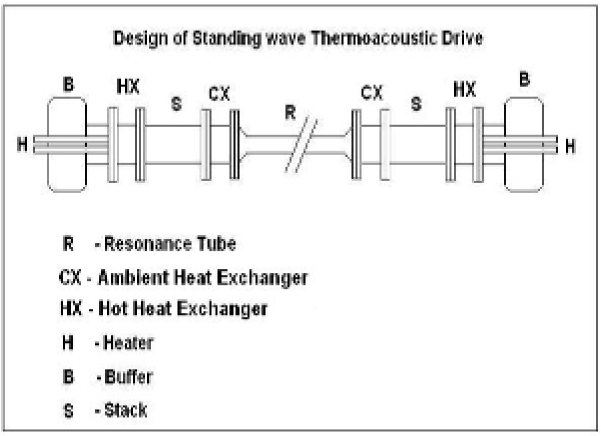

Figure 1. Schematic of the twin standing wave TAPM.

Figure 2. Photo of the twin standing wave TAPM.

The schematic of the twin standing wave TAPM is shown Figure 1. The photograph of the experimental system is shown in Figure 2. The diameter of the resonator tube is reduced at appropriate location to enable shortening the overall length of the system. The resonator is a copper tube of appropriate dimension with stainless steel end flanges and the prime movers are attached to it at either ends. The electrical resistance heater powered by an AC supply is mounted on the zone of hot end heat exchanger. K-type thermocouples are used to monitor the temperatures at different locations of the thermoacoustic prime mover. The heat loss by radiation and convection from the hot zones are reduced by the use of ceramic wool insulation and aluminum foil.

Stacks are fabricated from stainless steel plates of 0.5 mm thickness with 1 mm spacers and TIG welded at their edges. They are arranged parallel to the axis of the prime mover. The hot end and ambient heat exchangers are fabricated in a similar way but with copper plates. The ambient heat exchanger is equipped with external aluminum fins with forced air cooling. The oscillations of the TAPM were monitored using microphone transducers along with a digital storage oscilloscope. The average pressure and its amplitudes were measured using GEFRAN make pressure transducers. Detail dimensions of the twin standing TAPM are given in Table 1.

Table 1. Dimensions of twin standing wave TAPM.

| Parameter | Hot End HE | Stack | Ambient HE | Resonator | Buffer volume |
|---|---|---|---|---|---|
| Diameter (mm) | 51 | 51 | 51 | 37.5 | 1 litre |
| Length (mm ) | 80 | 200 | 40 | 3300 | |

## 3. SIMULATION USING DELTAEC

The simulation of the twin standing wave TAPM has been attempted using DELTAEC. This software has been adopted in a suitable form to obtain the solutions of acoustic pressure amplitude, temperature difference across the stack and frequency of oscillation. Wherever possible, the experimental results have been compared with the simulation studies and they are discussed along with the experimental results.

## 4. RESULTS AND DISCUSSION

Experimental studies have been performed at different working pressures with fluids such as nitrogen, argon and helium. They have been used both in pure form as well as binary mixtures. The operating frequencies, the pressure amplitudes and the temperature differences $\Delta T$ across the stack have been monitored during the experimental studies.

### 4.1 Studies with Pure Working Fluids

4.1.1 Frequency dependence of TAPM

The resonance frequency of a TAPM depends on the working fluid used. The resonance frequencies measured with different working fluids namely nitrogen, helium and argon are plotted as a function of operating pressure in Figure 3. It is observed that the resonance frequency is nearly constant with the operating pressure for all working fluids. The operating frequency increases with the decreasing mass number of the working fluid. DELTAEC is found to predict a higher frequency than the measured experimental value.

4.1.2 Pressure amplitude dependence of TAPM

Figure 4 plots the oscillation pressure amplitudes as a function of operating pressure of TAPM for different pure working fluids. The measured pressure amplitudes are found to increase with the pressure of the working fluid. This is also predicted by the simulation. The pressure amplitudes are found to be maximum for argon, minimum for helium and intermediate for nitrogen. As before, the simulation predicts higher values of pressure amplitudes compared to the experimental data.

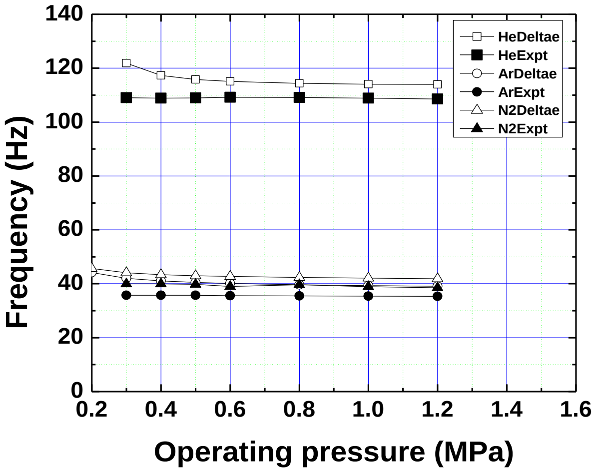

Figure 3. Frequency variation for different pure working fluids.

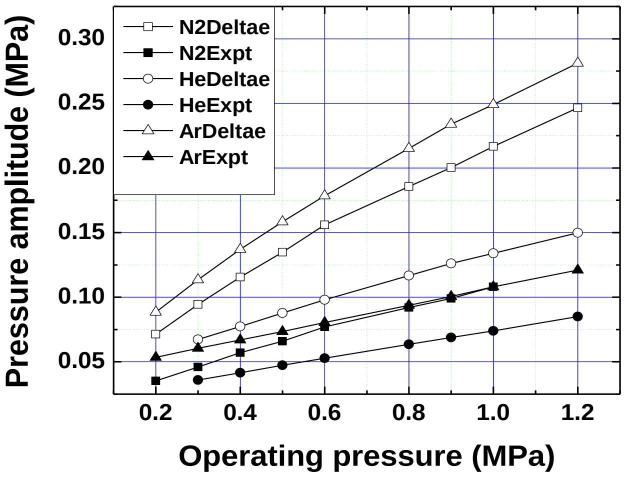

Figure 4. Variation of pressure amplitudes for different pure working fluids.

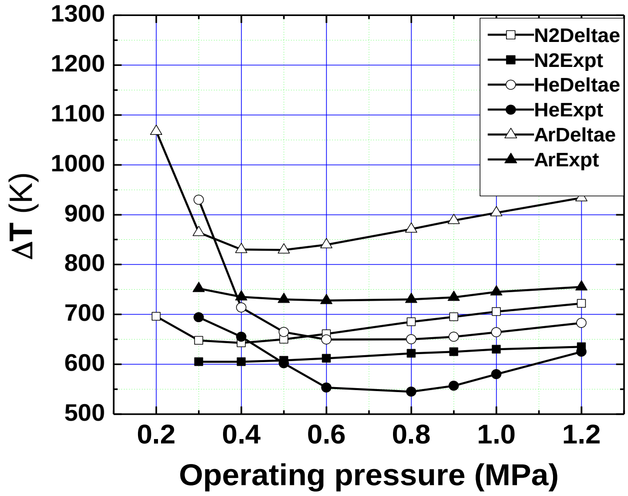

Figure 5. Temperature difference across the stack for different pure working fluids.

### 4.1.3 Dependence of temperature difference across the stack for TAPM

Figure 5 plots the temperature difference ΔT across the stack as a function of the operating pressure for different pure working fluids. It is observed that the ΔT values gradually increase with the operating pressure. Further, for a given working pressure, argon leads to the highest ΔT and helium to the lowest. The ΔT values for nitrogen falls in between them. In all cases, the simulation predicts higher values of ΔT compared to the experimental values.

## 4.2 Studies with Binary Mixtures of Working Fluids

Experimental studies have been performed with binary gas mixtures such as helium - argon, helium - nitrogen and nitrogen – argon of varying compositions. Since the number of experimental data is quite high, we present here the experimental results for specific compositions of gas mixtures only. These are (a) helium-argon (60:40), (b) helium-nitrogen (60:40) and (c) nitrogen-argon (60:40). As before, in the following we discuss the experimental results relating to the operating frequency, pressure amplitude and the temperature difference across the stack.

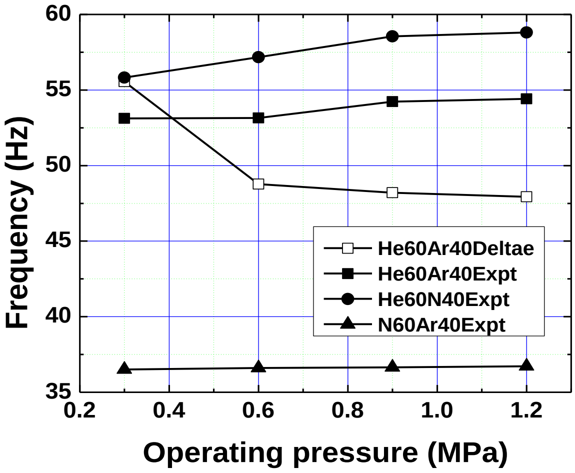

Figure 6. Frequency variation for different binary gas mixtures.

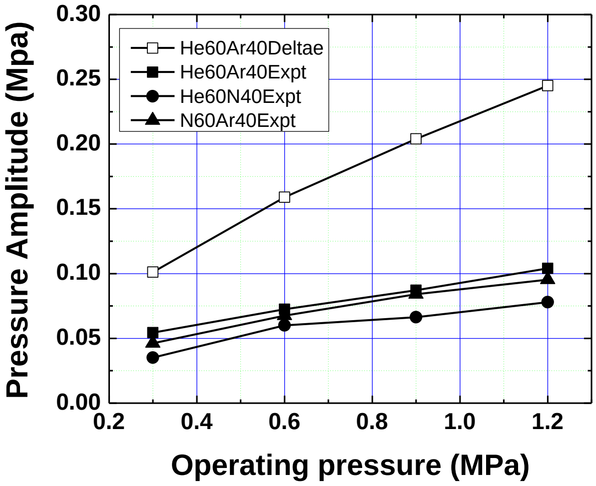

Figure 7. Variation of pressure amplitudes for different binary gas mixtures.

### 4.2.1 Frequency dependence of TAPM

The resonance frequencies measured with the above mentioned specific binary gas mixtures are plotted in Figure 6. As before, the resonance frequencies are found to be nearly independent of the operating pressure. Similar to the pure working fluids, the operating frequency is found to decrease with the increasing mass number of the composition in the gas mixture. Since in the present case, DELTAEC simulation is possible only for helium-argon mixture, their results are presented. The simulation predicts the frequency values close to that of the experimental values.

### 4.2.2 Pressure amplitude dependence of TAPM

Figure 7 plots the pressure amplitudes as a function of the operating pressure for the binary gas mixtures of specific compositions mentioned earlier. The pressure amplitudes are found to increase with increasing operating pressure of the working fluid. Experimental results show the same trend of having higher pressure amplitudes for argon based mixtures. The simulation predicts higher pressure amplitudes than the experimental values.

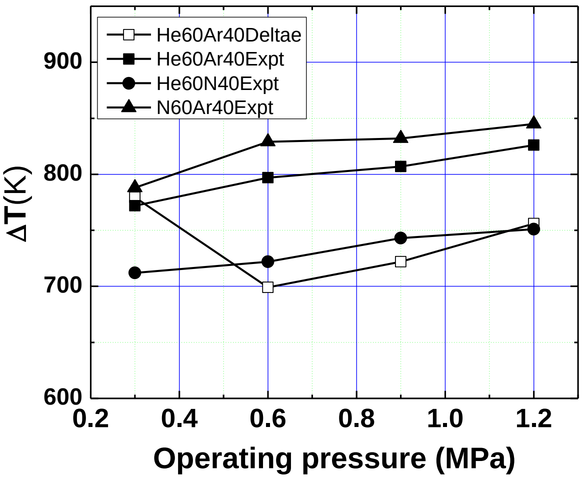

Figure 8. Temperature difference across the stack for different binary gas mixtures.

### 4.2.3 Dependence of temperature difference across the stack for TAPM

Figure 8 plots the temperature difference ΔT across the stack as a function of the operating pressure for binary gas mixtures of specific compositions. For all mixtures of working fluids experimental ΔT values increase with increasing working pressure. Experimental results show the same trend of having higher ΔT values for argon based mixtures. The simulation predicts lower values of ΔT compared to the experimental values.

## 5. CONCLUSIONS

The influence of different pure working fluids and their binary mixtures on the performance of the twin standing wave TAPM has been experimentally studied and simulated using DELTAEC wherever possible. These studies indicate;

- The resonance frequency of the TAPM increases with the acoustic velocity of the working fluid. The minimum resonance frequency can be achieved using argon as the working fluid.
- The pressure amplitude and temperature difference across the stack increases with the operating pressure of the working fluid.
- The pressure amplitude is high when argon is used as the working fluid. However ΔT across the stack is also high for argon. In view of this, an optimal mixture of helium to argon in the ratio of 60:40 can be chosen to obtain the best performance.
- Both nitrogen and argon produce low frequencies of oscillation, when used as working fluid. However the temperature difference across the stack increases in the order: helium, nitrogen, argon.

## 6. ACKNOWLEDGEMENTS

The authors acknowledge the financial support provided by CSIR, New Delhi, which enabled this research work and thank the staff of the Centre for Cryogenic Technology for their help in the fabrication of the experimental setup.

## 7. REFERENCES

1. Swift G.W., P 1988, Thermoacoustic engines, *J Acoust Soc Am*, Vol. 84, pp 1146-1180.
2. Zhou S., Matsubara Y., P 1998, Experimental research of thermoacoustic prime mover, *Cryogenics*, Vol. 38, pp 813-822.
3. Chen G.B., Jin T., P 1999, Experimental investigation on the onset and damping behavior of the oscillation in a thermoacoustic prime mover, *Cryogenics*, Vol. 39, pp 843-846.
4. Jin T., Chen G.B., Shen Y., P 2001, Thermoacoustically driven pulse tube refrigerator capable of working below 120 K, *Cryogenics*, Vol. 41, pp 595-601.
5. Tang K., Chen G.B., Kong B., P 2004, A 115 K thermoacoustically driven pulse tube refrigerator with low onset temperature, *Cryogenics*, Vol. 42, pp 287-291.
6. Tang K., Chen G.B., Qiu L.M., P 2005, Influence of resonance tube length on performance of thermoacoustically driven pulse tube refrigerator, *Cryogenics*, Vol. 45, pp185-195.
7. Chen G.B., Jiang J.L., Shi T., Tang K., Jiang Y.L., Jiang N., Huang Y.H., P 2002, Influence of buffer on resonance frequency of thermoacoustic engine, *Cryogenics*, Vol. 42, pp 223-227.
8. Hao X., Behera U., Kasthurirengan S., P 2011, Influence of working fluid on the performance of standing wave thermoacoustic prime mover, *Cryogenics*, Vol. 51, pp 559-561.
9. Hu J., Luo E., Dai W., P 2005, An innovative configuration for thermoacoustically driven pulse tube coolers, *Cryogenics*, Vol. 45, pp 523-527.
10. Tijani M.E.H., Zeeger J.C.H., Waele A.T.A.M.de., P 2002, Design of thermoacoustic refrigerator, *Cryogenics*, Vol. 42, pp 49-57.

065

# Cryogenic System of Superconducting Separator for Kaon Channel of IHEP Accelerator

**Kozub S., Ageyev A., Bakay A., Orlov A., Stolyarov M., Zinchenko S.**

Institute for High Energy Physics, Nauka Sqr.1, Protvino, Moscow Region, Russia

## ABSTRACT

A cryogenic system for cooling a superconducting separator of a new Kaon channel of an accelerator was developed and commissioned at the Institute for High Energy Physics (IHEP). The separator consists of two superconducting RF (Radio Frequency) cavities placed at 76 m distance between them. The cryogenic system cools these cavities by superfluid helium at a temperature of 1.8 K and has about 300 W refrigeration capacity at 1.8 K. The design of the cryogenic system and experience of its operation are presented in this article.

## 1. INTRODUCTION

For the U-70 accelerator complex, IHEP designed and implemented the RF Separated Kaon Beam Project to study rare decays of these particles. The proposal to create this channel using superconducting separator is stated by Obraztsov and Landsberg (2001), the technical parameters are given by Garkusha *et al* (2003). The kaon beam is produced using a beam separator consisting of two superconducting RF cavities. The distance between the cavities is 76 m, the expected heat release in the deflectors due to RF load is 20 watts at the 1.8 K temperature level.

The cryogenic system under construction is to provide simultaneous operation of two deflectors RF1 and RF2 at a temperature of 1.8 K. The use of the existing at the Institute cryogenic plant KGU500-4.5/140 with the capacity of 150 l/h in liquefaction mode and of 500 W in refrigeration mode at a temperature of 4.5 K, as well as of helium compressors, of the of gaseous helium storage, of the low-temperature helium purification system, located at a distance of about 850 m from the KGU500-4.5/140, has allowed to significantly reduce time and cost of the cooling system construction.

## 2. SCHEME OF CRYOGENIC COOLING SYSTEM FOR SUPERCONDUCTING RF SEPARATOR

The cryogenic system for cooling the superconducting RF separator (Fig. 1) described by Ageyev *et al* (2006) is built as a system with satellite refrigerator, where the KGU500-4.5/140 plant is used as a cold generating installation. This plant consumes 60 g/s of helium gas at a pressure of 2.5 MPa and produces 5 g/s of liquid helium, part of which is supplied through the valve CV2 into the intermediate cooling bath (ICB); cold helium vapor returns from the bath to the KGU plant (refrigeration load). Liquid helium is used in the ICB in the heat exchanger HX1 for cooling the direct flow to be sent for the cooling of RF1 and RF2. The rest of the helium from the KGU is throttled in the valve CV3 and after cooling in the heat exchanger HX2, located in the ICB, is fed into the satellite refrigerator return flow, providing the excess flow rate. This part of the helium flow does not return to the KGU plant and it represents its liquefaction load.

The main flow of helium for cooling the cavities is produced by the satellite refrigerator, which is based on the large vacuum heat exchanger (HEX), which cools the flow of compressed helium (7-10 g / s, 2.5 MPa) from room temperature to a temperature close to the liquid helium temperature. After HEX the helium stream is sent to the ICB, where it is throttled in the valve CV4, cooled in the heat exchanger CHX1 and then merges with the flow from the KGU plant after it passed the heat exchanger CHX2. After the ICB helium flows along the transfer line to the distribution box, where it is divided into two parts, each one is sent in its own cryogenic transfer line to the cryostats RF1 and RF2, before them it is cooled in the low temperature heat exchangers of RF1 and RF2 and throttled in the valves CV5 and CV6 into the helium vessels of the RF1 and RF2, respectively.

The reverse flow of the helium vapour from the helium vessels cools the direct flow in the low-temperature heat exchangers, then in the HEX, then it is pumped out and pressurized by the compressor, and then it is sent to the KGU plant and to the HEX and the cycle repeats. Reaching and maintaining of the required temperature in the RF1 and RF2 cryostats below 4.3 K is realized by pumping the helium vapour from the helium vessels by vacuum compressors ("pumping machine").

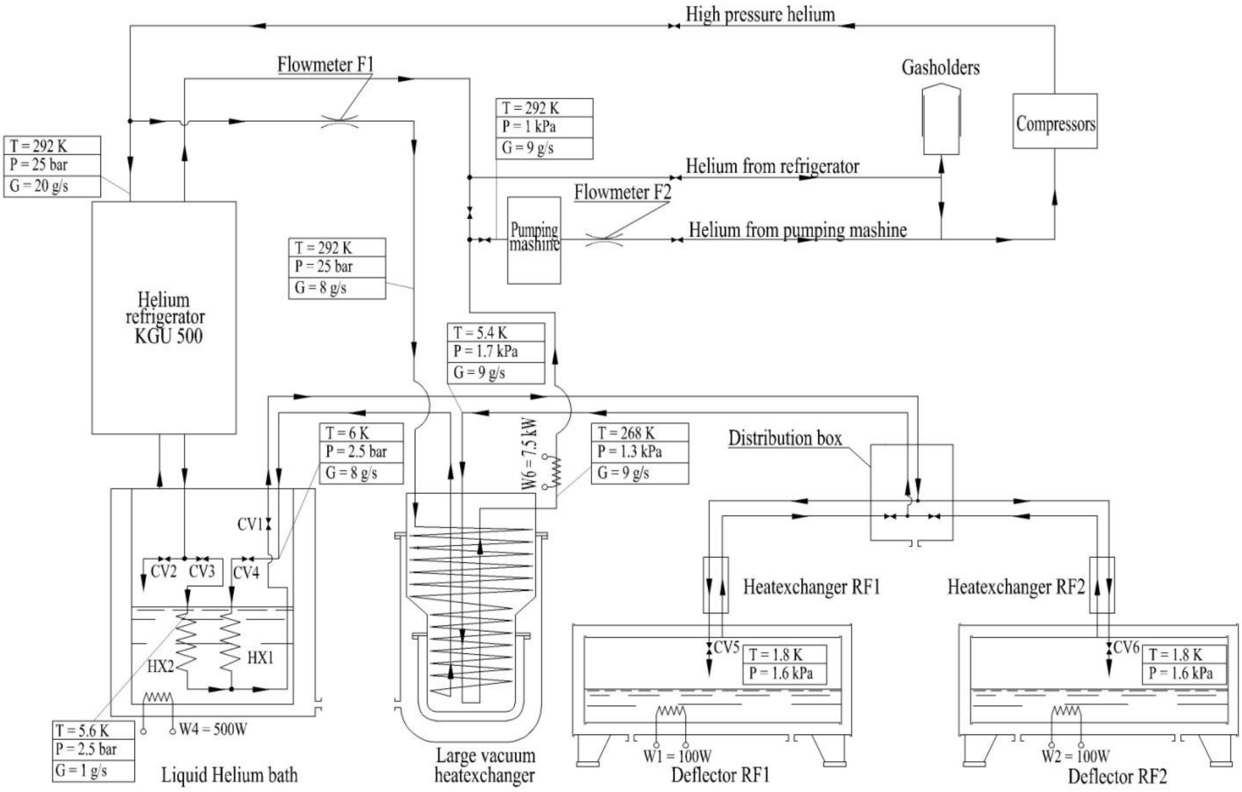

Figure 1. Flow chart of the cryogenic and vacuum plant cooling the superconducting RF deflectors.

## 3. CRYOGENIC SYSTEM EQUIPMENT

Deflector is placed in the helium vessel of a cryostat with superfluid helium, which provides the necessary stabilization of the temperature of its surface. The main parameters of the deflector and of the cryostat are presented in Table 1 by Barth and Lehmann (1976).

Table 1. Main parameters of the deflector and of the cryostat.

| Parameter | Value |
|---|---|
| Operating frequency, GHz | 3 |
| The strength of the deflecting field, MV/m | 1 |
| Deflector weight 260, kg | 260 |
| Length (diameter) of the deflector, m | 2.7 (0.14) |
| Length (diameter) of the helium vessel, m | 3.5 (0.51) |
| Length (diameter) of the vacuum vessel, m | 4.2 (0.92) |
| Operating temperature of the deflector, K | 1.8 |
| Working level (volume) of helium,% (l) | 78 (415) |

The intermediate cooling bath cools the supercritical helium below the critical temperature after throttling in the valves CV3 (heat exchanger HX2) and CV4 (heat exchanger HX1). Heat exchangers are immersed in liquid helium boiling at a temperature of 4.6 K, and their main characteristics are presented in Table 2.

In the large vacuum heat exchanger the flow of compressed helium for cryostating the deflectors must be cooled from room temperature to a temperature close to liquid helium temperature. Low hydraulic resistance of the reverse flow is an important requirement for such a heat exchanger. To ensure the low pressure loss the velocity of reverse flow is reduced, the flow mode is close to a laminar flow with low values of Reynolds number and, consequently, low heat transfer coefficients. Means for improving the heat transfer in laminar flow are very limited. Basically, they are the use of channels with a small equivalent diameter and the increase of the heat transfer surface area with fins.

Table 2. Parameters of the heat exchangers.

| Parameter | HX1 | HX2 |
|---|---|---|
| The pressure of helium flow in pipes, MPa | 0.25 | 0.25 |
| The temperature of helium in ICB, K | 4.6 | 4.6 |
| Helium temperature at the heat exchanger inlet, K | 6.0 | 5.6 |
| Helium flow through the pipes, kg/s | 0.010 | 0.002 |
| The outer diameter of the pipe, m | 0.006 | 0.006 |
| The inner diameter of the pipe, m | 0.004 | 0.004 |
| The number of pipes | 10 | 2 |
| Pipes length, m | 20 | 20 |

The heat exchanger was designed by Kashtanov *et al* (2000) which satisfies the requirements referred to above. It is made of a tightly coiled copper tubes, finned by a spiral of copper wire. This finning acts as a spacer, providing a fairly uniform distance between the pipes, and it is useful for intensive mixing of the flow, thus preventing the flow of helium breakthrough. On the other hand, the spiral of wire up to 10 times increases the heat exchange surface area. HEX is divided into upper and lower part, to compensate for the significant dependence of the properties of helium on the temperature. Direct "warm" helium stream passes inside the pipes, then goes to the throttle valve CV4, located in the ICB. The return "cold" helium stream flows up in the annular intertubular space of the heat exchanger. Main characteristics of the heat exchanger are presented in Table. 3.

Tab. 3. Main characteristics of the large vacuum heat exchanger.

| Parameter | Value |
|---|---|
| The outer diameter of the pipe, m | 0.004 |
| The inner pipe diameter, m | 0.0032 |
| The diameter of the spiral fin, m | 0.005 |
| The diameter of the fin wire, m | 0.8 |
| Mass flow rate, kg/s | 0.01 |
| The pressure drop in the forward flow, Pa | 1100 |
| The pressure drop in return flow, Pa | 270 |
| Low pressure heat transfer area, $m^2$ | 275 |
| High pressure heat transfer area, $m^2$ | 32.3 |

HXRF1 and HXRF2 heat exchangers are used to lower the temperature of the helium flows before throttling into the deflector helium vessels. Heat exchangers are made of copper tubes finned with a copper wire spiral. They are located in the low pressure tubes of the cryogenic transfer lines. High pressure helium flow is moving inside the pipes, the low pressure helium flows between the pipes. The main characteristics of low-temperature heat exchangers are presented in Table 4.

The temperature of 1.8 K in the deflector helium vessel is achieved by pumping the helium vapour to a pressure of 1.6 kPa with a vacuum compressors, and the helium flow rate through each deflector cryostat is about 5 g/s and a vacuum compressors flow rate - 10 g/s. “Pumping machine” consists of twenty-four vacuum pumps, grouped in three stages. The first stage of the eight Roots vacuum pumps 2DVN-1500 provides compression of up to 3 kPa. The second stage uses eight 2DVN-500 and compresses helium to

5 kPa. The third stage of the eight backing pump AVZ-180 compresses helium to 100 kPa. After each pump of the first and the second stages the flow of helium is cooled with water down to 30 Celsius degree in the heat exchangers developed and produced at IHEP.

Table 4. Main parameters of the heat exchangers HXRF1 and HXRF2.

| Parameter | Value |
|---|---|
| The outer diameter of the pipe, m | 0.004 |
| The inner pipe diameter, m | 0.0032 |
| The diameter of the spiral fin, m | 0.005 |
| The diameter of the fin wire, m | 0.8 |
| The inner diameter of the winding, m | 0.1 |
| The outer diameter of the winding, m | 0.176 |
| Winding length, m | 0.56 |
| The number of winding layers | 3 |
| Mass flow rate, kg/s | 0.005 |
| Low pressure heat transfer area, $m^2$ | 3.7 |
| High pressure heat transfer area, $m^2$ | 0.43 |
| The pressure drop in return flow, Pa | 5 |

The first stage of the control system built by IHEP and reported by Alferov *et al* (2010) includes 240 channels of data collection and remote control, 72 electronics unit in 14 frames and in 8cabinets, the output of data on 5 PCs in the two control rooms. The control system provides measurement of the following parameters:
helium flow temperature in the 72 points and vacuum compressors temperature in the 42 locations,
low helium pressure between the stages of the “pumping machine” in three locations,
insulation vacuum at 32 points,
the level of liquid helium in 3 tanks,
helium pressure at 11 points,
helium flow rate at 2 points,
phase currents of the “pumping machine” pumps motors by 72 channels,
the reading of the digital signals by 12 channels (status).
To control these parameters, a system of remote monitoring and analysis with the function of archiving data was developed by Lobov *et al* (2010) and built. For storage and accumulation of data MS SQL-server is used, the software to display the archived data (graphs, tables) was created with the help of the software package NI Developer Suit Core. To display the current settings online in order to control the cryogenic and vacuum system there is a special web-server with the interactive mnemonic diagrams mechanism created in IHEP developed original software.

## 4. ANALYSIS OF MAIN MODES OF CRYOGENIC SYSTEM OPERATION

Cooling capacity of the cryogenic system is to compensate for the heat loads to the equipment of the system and to provide the required cooling down rate of the superconducting RF separator. The measured values of heat loads in the system are presented in Table 5.

Table 5. Cryogenic system heat loads at 1.8 K.

| Elements of the cryogenic system | Heat load, W |
|---|---|
| Intermediate cooling bath (ICB) | 8 |
| Cryogenic transfer line between the ICB and the RF1 and RF2 | 135 |
| RF1 helium vessel | 15 |
| RF2 helium vessel | 22 |
| Superconducting deflectors RF1 and RF2 RF heat release | 20 |
| Total heat load | 200 |

The cooling down time of the separator is determined by the relation between the cooling capacity of the cold generating installation, mass and heat capacity of the refrigerated structures, and by the constraints on the cooling down rate imposed by the design of the deflectors.

The main cold generating installation in a temperature range from room temperature down to 20 K is the KGU 500-4.5/140 helium plant. The satellite refrigerator starts working at temperatures below 40 K (inversion temperature of helium). At a temperature of 1.8 K the direct helium flow rate after ICB is of 9.15 g/s, which corresponds to the cooling capacity of 280 W. From this flow rate 6.26 g/s are spent to ensure the operating mode of the deflectors and 2.89 g/s (86 l/h) are used for accumulation of liquid helium in the cryostats of deflectors.

The only devices for which the restrictions are imposed on the cooling down rate, are the superconducting deflectors: in the temperature range from room temperature down to 150 K - 10 K per hour, from 150 K to 90 K - 20 K per hour and below 90 K - 10 K per hour. Table 6 shows the duration of the different steps for deflectors to reach the operating temperature as given by Ageyev et al (2008).

Table 6. Duration of the deflectors cooling down to the operating temperature.

| Name of stage | Time, hour |
|---|---|
| KGU 500-4.5/140 helium plant and ICB cooling down | 10 |
| Cryogenic transfer line cooling down | 4 |
| Cooling down of the cavities from 290 to 4.3 K | 38 |
| accumulation of liquid helium in the cryostats of deflectors<br>at 4.3 K<br>at 1.8 K | <br>9<br>4 |
| Total | 65 |

Cryogenic and vacuum system power consumption is associated with the work of the high pressure compressors (256 kW) and vacuum compressors (280 kW). In the steady state cryogenic system consumes 4 tons per day of liquid nitrogen, for both KGU plant and for the thermal shields of the ICB, HEX, cavities cryostats and for the transfer line with the distribution box.

For emergencies, the elimination of which requires a long time, a special operation mode was developed. When the cryogenic helium plant is stopped the large vacuum heat exchanger continues to operate as a satellite refrigerator, using as a source of cold the helium vapor evaporating from the deflector cryostats due to the heat leaks. In this case, the amount of liquid helium in the deflector cryostats decreases, but it is sufficient for continuous operation in such a way. In this mode, the cryogenic transfer line is heated up by no more than 12 K, which when re-starting the cryogenic system allows one to keep the liquid helium in the cryostats RF1 and RF2, and does not lead to an increase in the cavities temperature. For example, when using this mode the level of the liquid helium in the deflector cryostats was 70% before stopping the helium plant. In 12 hours the helium plant has been started and in 4 more hours the cryogenic system was brought into a stationary mode, while the temperature in the helium vessels RF1 and RF2 maintained at 1.8 K and the level of liquid helium in the deflector cryostats did not drop below 40%.

In the 2010 run the installation worked for 50 days. From that time, 54 hours were spent on cooling down from room temperature to 4.3 K and filling the cryostats RF1 and RF2 with liquid helium. Preparation of deflectors to work at temperatures of 3 K, 2.5 K and 2 K lasted about 5.5 hours, after that the RF1 and RF2 work continued at a temperature of 1.8 K within 40 days. Heating up of the system to a temperature of 250 K took 2 days. During this run over a million of events on the OKA experimental installation had been registered. The study of kaon decays continued in 2011.

## 5. CONCLUSIONS

Building and successful start of the operation of the Russia's largest cryogenic system, cooling superconducting devices with superfluid helium, at the IHEP U-70 accelerator complex can be stated. The effective operation of the system with the cooling capacity of 280 W at 1.8 K allowed to provide the necessary parameters of the superconducting RF particle separator in the channel 21K, to receive over one million events on the OKA installation and to plan collection of a large number of kaon decays, which is necessary to research them on a new level.

## 6. REFERENCES

Obraztsov, V., Landsberg L. Prospects for CP-violation Searches in the Future Experiment with RF-separated K+/- beam at U-70, Nucl.Phys.Proc.Suppl.99B, 2001, p. 257-264

Garkusha V., et al., "Calculated Characteristics of the Separated Kaon Beam for OKA Experiment at the U-70 Accelerator", IHEP Preprint 2003-4, 17 p.

Ageyev A., et al. Commissioning of Superconducting Radiofrequency Separator Cryogenic System, *Proc. RUPAC-2006*, Novosibirsk, Russia, pp. 79-81.

Barth W., Lehmann W. Experience with Two Large-Scale HeII-Cryostats for a Superconducting r.f. Particle Separator Working in Closed Cycle with a 300 W Refrigerator, *Proc. ICEC-6*, Grenoble, France, 1976, p.144-149.

Kashtanov E., et al. Large Low Pressure Heat Exchanger for the TTF Cryogenic System, *Proc. ICEC-18*, Mumbai, India, 2000, p.315-318.

Alferov V., et al., LabView Control System of the Cryogenic Complex for the Kaon RF-Separator at IHEP, *Proc. RUPAC-2010*, p 257-259.

Lobov I., et al., Software Service for Cryogenic Data Representation and Analysis, Proc. RUPAC-2010, p. 263-265.

Ageyev A., et al. Starting -Up and Adjustment Works on Cryogenic and Vacuum System of the Superconducting Radio-Frequency Separator, *Proc. RUPAC-2008*, p. 282-284

068

# High-Power Stirling-Type Pulse Tube Cryocooler for Operation Near 80 K

**Sun J.**[*,**,+], **Dietrich M.**[*,**], **Thummes G.**[*,**]

*Institute of Applied Physics, University of Giessen, D-35392 Giessen, Germany
**TransMIT-Centre for Adaptive Cryotechnology and Sensors, D-35392 Giessen, Germany
+Institute of Refrigeration and Cryogenics, Zhejiang University, Hangzhou, 310027, China

## ABSTRACT

High-power cryocoolers are used in many superconductor and gas liquefying applications. Stirling-type pulse-tube cryocoolers (PTCs) offer the advantage of high reliability, high efficiency and low maintenance compared to other cooler types. An in-house made single-stage Stirling-type pulse-tube cryocooler with inline configuration of regenerator and pulse tube was optimized for high cooling power near 80 K. The cooler is driven by a 10 kW-class linear compressor with dual opposed pistons (QDrive model 42SM-2S297W PWG). In order to reduce losses from pressure drop, the regenerator is designed with a small length to diameter ratio, thus making it susceptible to internal streaming losses. These losses manifest themselves in a measureable temperature inhomogeneity around the circumference of the regenerator and in a low cooling performance. To overcome these losses, the transverse heat conductance in the regenerator was increased by use of sandwich type fillings, where a part of the original stainless wire mesh was replaced by materials with higher thermal conductance, such as copper and brass mesh. Several types of sandwich fillings were experimentally investigated. Using these types of regenerator fillings, the losses from streaming were significantly reduced and the minimum no-load temperature was lowered from 54 to 47.5 K. The mean pressure and frequency of the pressure oscillation were also optimized. Up to now, a cooling power of 413 W at 80 K is available with an acoustic power (pV-power) of 7.8 kW at a frequency of 56 Hz.

## 1. INTRODUCTION

The needs for large scale cryocoolers are increasing with the development of High-Temperature-Superconducting (HTS) power applications. The demands on cooling power is in the range of 300 W up to several kW at 80 K for HTS fault current limiters, transformers and cables [Gromoll 2004]. Among all kinds of closed-cycle cryocoolers, high frequency Stirling-type PTCs with oil-free linear compressors became more attractive since they promise better cooling performance than GM-type coolers as well as longer maintenance intervals. During the past few years, several large scale single-stage Stirling-type PTCs for operating temperatures between 60 and 80 K have been successfully developed [Zia 2007, Potratz 2008, Ercolani 2008].

The work presented in this paper is based on our previous efforts to develop a single-stage Stirling-type pulse-tube cryocooler with inline configuration of regenerator and pulse tube [Dietrich 2007]. To overcome the negative effect of circulating streaming, the transverse heat conductance in the regenerator was increased by use of sandwich type fillings, where a part of the original stainless screens was replaced by materials with higher thermal conductance. Cooling powers of 50 W at 45 K and 200W at 70 K were available with electric input powers of 6.3 kW and 8.6 kW, respectively [Dietrich 2007].

In the present work, the length of the regenerator is has been reduced to optimize the performance of the cryocooler near 80 K. Following our previous experience, different sandwich fillings of stainless steel screens in combination with wire mesh of higher thermal conductivity have been tested.

## 2. EXPERIMENTAL SETUP AND MEASUREMENT SYSTEM

In order to improve the cooling performance of the pulse tube cryocooler near 80 K, a regenerator with a small length to diameter ratio of 0.4 was used. The diameter and length of the regenerator was chosen to be 117 mm and 49 mm respectively, according to our theoretical analysis based on the simulation software Sage [Gedeon 1994]. The present length to diameter ratio of the regenerator is only half of that in our previous single-stage PTC configuration that was designed for cooling near 30 K [Dietrich 2007].

The PTC setup consists of a commercial linear compressor with dual opposed pistons (QDrive model 42SM-2S297W PWG) and an in-house made pulse tube cold head with inline configuration, as schematically shown in Figure 52. The compressor has a nominal electrical input power of 10 kW and is able to provide an acoustical power of 8 kW under optimal conditions. The main components of the cold head are: primary shell-and-tube aftercooler (AC), secondary slot aftercooler and flow straightener (FS), regenerator (REG), slot cold heat exchanger (CHX), pulse tube (PT), warm heat exchanger (HHX), and phase shifter consisting of inertance tube with buffer volume. The compressor, the first and second after cooler and the warm heat exchanger are water cooled.

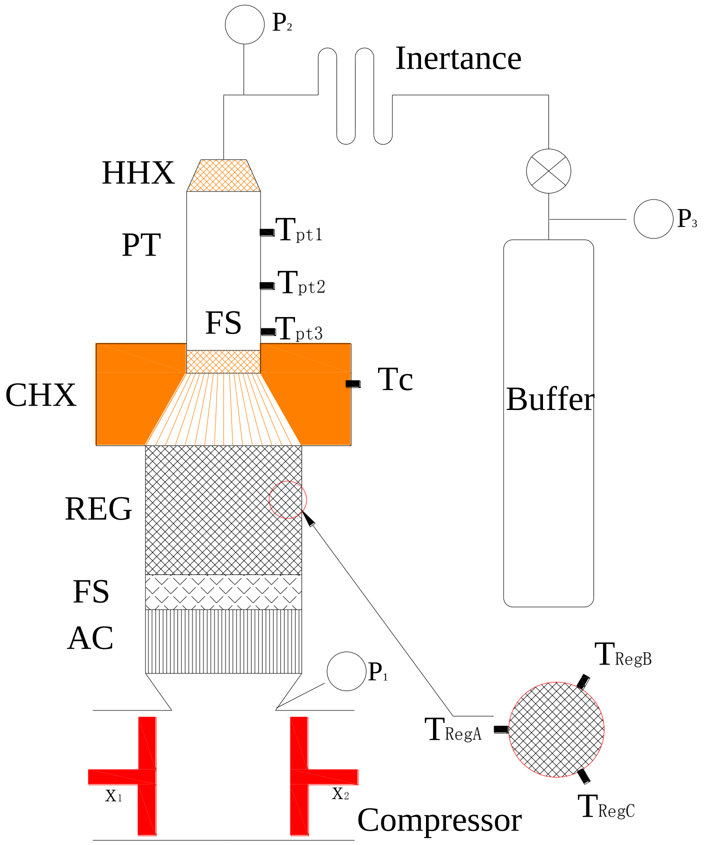

**Figure 52. Schematic of the inline PTC with linear compressor (see text for details).**

The compressor is equipped with two position sensors (X1 and X2) and a pressure sensor (P1) to measure the generated pV-power $W_{pV}$. Two additional pressure sensors (P2 and P3) are installed close to the warm heat exchanger and at the main buffer. In order to determine the efficiency of the compressor and of the cold head, the electrical input power $W_{in}$ is also monitored. The refrigeration temperature $T_c$ is measured at the cold heat exchanger by means of a Pt-100 resistance thermometer. A number of Pt-100 resistance thermometers are installed along the regenerator and pulse tube wall, to measure the temperature profiles. As illustrated in the chart of Figure 52, three Pt-100 sensors ($T_{RegA}$, $T_{RegB}$, $T_{RegC}$) are equidistantly mounted on the circumference of the regenerator tube at half of its length in order to measure the azimuthal temperature distribution.

## 3. EXPERIMENTAL RESULTS AND DISCUSSIONS

### 3.1. Sandwich regenerator fillings

Based on the past experience of benefiting from sandwich fillings of the regenerator [Dietrich 2007], the radial heat conductance was enhanced by replacing part of the stainless steel (SS) screens by copper-screens (mesh #80) or brass-screens (mesh #352). Four modified sandwich fillings, as shown in Table 10, were applied to reduce the temperature inhomogeneity and the associated losses in the regenerator by increasing the transverse heat conductance.

Table 10 compares the effective radial and axial thermal conductivities, estimated at an average temperature of 200 K, of the four conduction enhanced matrices. The porosity and length fraction of each wire mesh are also listed. In case of matrices no. 1-3, where copper screens are chosen, the transverse thermal conductivity is larger than in matrix no. 4 that contains no copper screens. The copper screens in matrices no. 1-3 are positioned in the middle of the regenerator, where the maximum temperature inhomogeneity along the regenerator circumference can be expected [Dietrich 2007]. In matrix 4, the brass screens and stainless steels screens are stacked piece by piece. Whereas the #400 mesh stainless steel screens in matrix no. 1 and 2 are made of 30 μm thick wires, the wire diameter of the #400 mesh stainless steel screens in matrices no. 3 and 4 is only 25 μm, which results in a higher porosity.

**Table 10. Composition and estimated heat conductivities of the different regenerator fillings.**

| Matrix No | 1 | 2 | 3 | 4 |
|---|---|---|---|---|
| Material | SS screens #400 (30 μm)<br>+ Cu screens #80<br>+ Brass screens #353 | SS screens #400 (30 μm)<br>+ Cu screens #80 | SS screens #400 (25 μm)<br>+ Cu screens #80 | SS screens #400 (25μm)<br>+ Brass screens #353 |
| Length fraction(%) | 60+19+21 | 78+22 | 79+21 | 56+44 |
| Porosity | 0.59 / 0.61 / 0.62 | 0.59 / 0.61 | 0.68 / 0.62 | 0.68 / 0.62 |
| Average hydraulic diameter (μm) | 14.4 | 14.2 | 14.4 | 8.1 |
| Total radial conductivity at 200 K (W/m K) | 54 | 39 | 37 | 21 |
| Total axial conductivity at 200 K (W/m K) | 11 | 3.9 | 4.9 | 7.3 |

### 3.2. Azimuthal temperature variation:

Figure 53 shows the azimuthal temperature variation $\Delta T_{Reg,0.5}$ (defined as the maximum difference of $T_{RegA}$, $T_{RegB}$, and $T_{RegC}$, see Figure 1) as function of pV-power for the four different matrices. The data were measured in stationary state without additional heat load. The corresponding no-load refrigeration temperatures are shown in Figure 3. For the whole range of pV-power, matrix no. 4 exhibits the highest temperature non-uniformity of the four fillings. This can be related to the low radial conductivity of matrix 4 because of the lack of copper screens (see Table 1). In contrast, matrix 1 with the highest radial conductivity shows the lowest azimuthal temperature difference in the middle of the regenerator. Higher radial conduction does not only help to lower the temperature non-uniformity, it also reduces the sensitivity of the azimuthal temperature variation to pV-power, as shown in Figure 53. This result clearly shows the effectiveness of an enhanced radial conduction in reducing the temperature inhomogeneity in the regenerator.

However, radial heat conduction is not the only parameter that influences the temperature inhomogeneity. As seen from Table 1, matrices 2 and 3 have similar compositions of stainless steel and copper mesh, and their radial thermal conductivities differ only slightly. In contrast, the azimuthal temperature variations for matrix 2 and 3 in Figure 53 are much more different than one would expect from the slightly different radial conductivities.

The wire diameter and the porosity of the stainless steel screens, which are different for matrix 2 and 3, are believed to be the reason. Further investigation of the effect of matrix porosity on the temperature inhomogeneity is needed.

### 3.3. Refrigeration temperature:

Figure 54 shows the dependence of the refrigeration temperature on pV-power for the four tested regenerator matrices. The effect of radial conduction on no-load refrigeration temperature is not as clear as its effect on the azimuthal temperature difference. The no-load refrigeration temperature for the different fillings is in the range between 49.5 K and 57 K. Matrix 2 yields the lowest minimum refrigeration temperature among the four tested fillings.

Although the temperature inhomogeneity for matrix 4 is the highest, a low minimum temperature of 52 K is obtained with matrix 4 despite the rather high losses from the temperature asymmetry (Figure 53). This is most probably related to the high heat transfer area caused by the low average hydraulic diameter of this matrix (see Table 1), which leads to comparatively low regenerator losses from incomplete heat transfer and also to a low pressure drop. However, the minimum refrigeration temperature for matrix 4 slightly rises when the pV-power exceeds 3.3 kW (Figure 3). Compared with the other matrices, this rise in $T_c$ shows the effect of the large temperature inhomogeneity in matrix 4.

With matrix 3, which contains stainless steel screens with a wire diameter of 25 µm and copper screens of mesh #80, the minimum temperature is only 57 K. This rather high temperature is attributed to the reduced heat transfer area caused by the coarse copper screens which have a wire diameter of 140 µm. Matrix 1 has higher axial conduction losses than matrix 2. This can be the reason that matrix 1 gives a higher $T_c$ than matrix 2 in Figure 3, although the temperature inhomogeneity is smaller than that with matrix 2 in Figure 2.

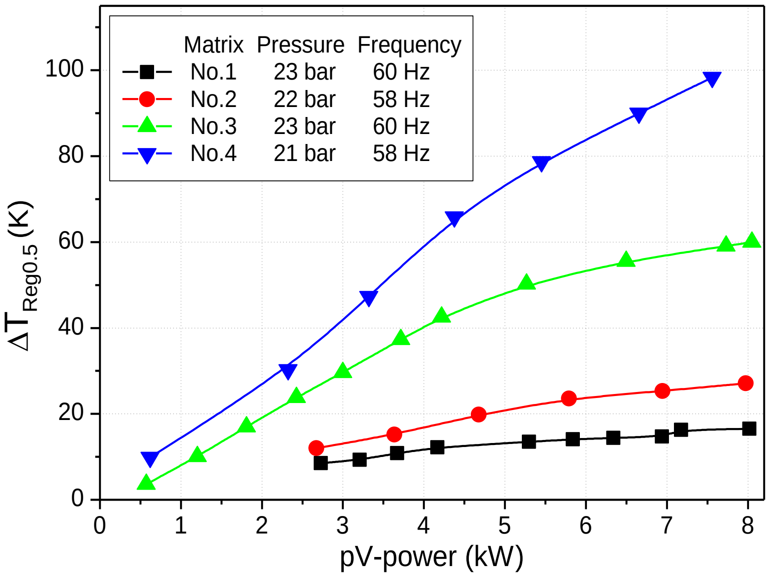

Figure 53. Measured azimuthal temperature variation $\Delta T_{Reg0.5}$ for the four different matrices.

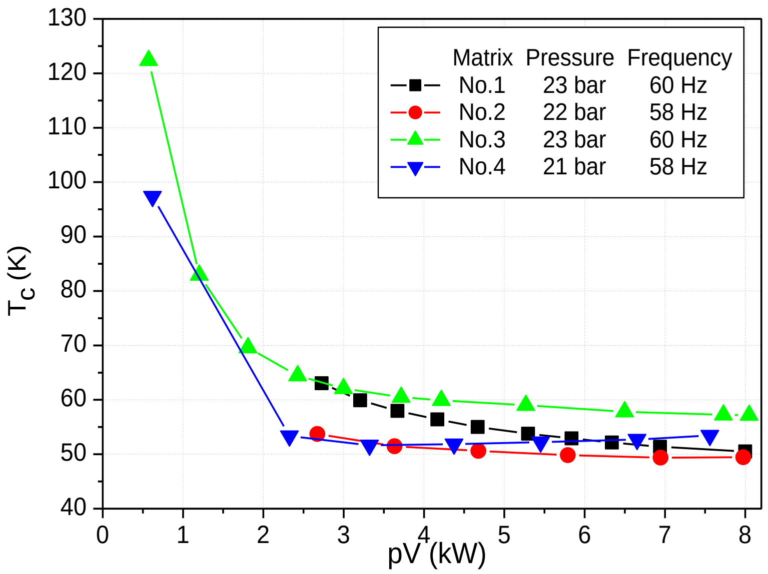

Figure 54. Measured refrigeration temperature versus pV-power for the four tested regenerator matrices.

## 3.4. Cooling power:

Figure 55 displays the measured cooling power versus $T_c$ that was obtained with the four sandwich matrices at a pV-power of 7.6-8 kW. Due to the different porosities of the regenerator matrices, the maximum electrical input power in these tests was either limited by compressor input current or by piston stroke.

Different frequencies and charging pressures are tested for each type of sandwich fillings. In Figure 4, the cooling power is shown for the optimum frequency and charge pressure of a particular regenerator filling.

As seen from Figure 55, the slopes of the load lines for matrices 1-3 are rather similar, approximately 12.7 W/K. With matrix 1 and 2, a lowest no-load temperature of 47.5 K is reached. Therefore, a high cooling power of 300 W is achieved at 71 K for matrix 2 and at 72 K for matrix 1. By linear extrapolation of the load lines, the available cooling power for matrix 1 and 2 is 405 W and 413 W at 80 K, respectively. The corresponding coefficients of performance (COP = cooling power/compressor input power) for matrix 1 and 2 are 4.55% and 4.54% at 80 K, respectively. The cooling powers with matrix 1 and 2 are considerably higher than that with matrix 3, which amounts to 330 W at 80 K. With matrix 3, the cryocooler exhibits the worst performance. The COP at 80 K is only 3.7%.

With matrix 4, the minimum refrigeration temperature is only 52 K. However, the load curve has the largest slope of 14.5 W/K. As seen from Figure 2, the azimuthal temperature inhomogeneity is highest for matrix 4. The variation of $\Delta T_{Reg0.5}$ as function of $T_c$, as shown in Figure 56, indicate that for matrix 4 the inhomogeneity considerably decreases with increasing refrigeration temperature. Therefore, the high slope is ascribed to the decrease of losses from the temperature inhomogeneity with increasing $T_c$. As a result, the cryocooler with matrix 4 can provide a comparatively high cooling power of 411 W at 80 K, which is similar to that with matrix 1 and 2, even though the no-load refrigeration temperature is higher. The cooling power of 411 W at 80 K for matrix 4 is achieved with an electrical input power of 8.9 kW corresponding to the highest COP of 4.65%.

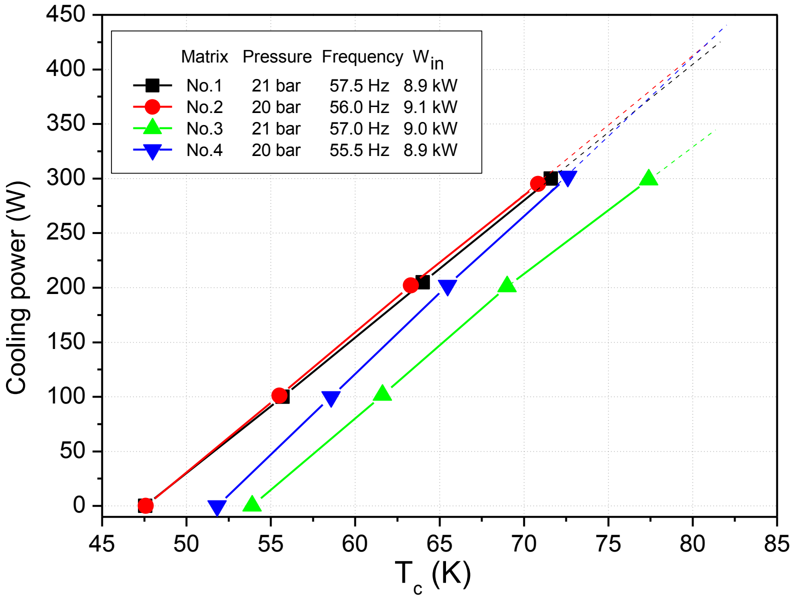

Figure 55. Measured cooling power as function of refrigeration temperature for the four regenerator matrices

## 4. CONCLUSIONS

A high-power single-stage Stirling-type pulse-tube cryocooler was optimized for operation near 80 K. Four different sandwich regenerator fillings were comparatively tested. The experimental results show the effect of an enhanced radial heat conductance on reducing the azimuthal temperature inhomogeneity in the regenerator. With the sandwich fillings, the cryocooler has reached a no-load refrigeration temperature of 47.5 K, and a maximum cooling power of 413 W at 80 K is available with a pV-power of 7.8 kW.

However, the overall performance was sacrificed to some extent by enhancing the radial conductivity by the use of coarse copper screens that have a large thermal conductivity, but also have a large hydraulic diameter that reduces the heat transfer area. Thus, the reduction of temperature inhomogeneity and the heat transfer ability of the sandwich matrices have both to be considered in more detail. The conduction enhanced sandwich matrices that were tested up to now still exhibit potential to improve the overall performance, which will be the subject of future investigations.

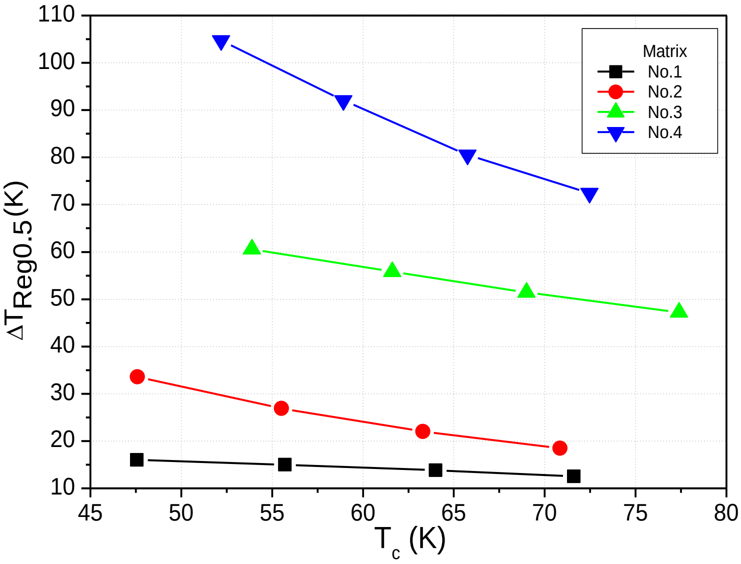

Figure 56. Measured azimuthal temperature variation as the function of refrigeration temperature.

## 5. REFERENCES

Gromoll, B. 2004, Technical and Economical Demands on 25K -- 77K Refrigerators for Future HTS --- Series Products in Power Engineering, *Advances in Cryogenic Engineering* 49B: 1797-1804.

Zia, J.H. 2007, A Pulse Tube Cooler with 300 W Refrigeration at 80 K and an Operating Efficiency of 19% Carnot, In: *Cryocoolers 14*: 141-147.

Potratz, S.A., et al. 2008, Stirling-Type Pulse Tube Cryocooler with 1 kW of Refrigeration at 77 K, *Advances in Cryogenic Engineering* 53A: 42-48.

Ercolani, E., et al. 2008, Design and Prototyping of a Large Capacity High Frequency Pulse Tube, *Cryogenics* 48(9-10): 439-447.

Dietrich, M., Yang L.W., Thummes, G. 2007, High-Power Stirling-Type Pulse Tube Cryocooler: Observation and Reduction of Regenerator Temperature-Inhomogeneities, *Cryogenics* 47(5-6): 306-314.

Gedeon, D. 1994, Sage: Object orientated Software for Stirling-Type Machine Design, *Proc. 29th Intersociety Energy Conversion and Engineering Conference* vol. 4, American Institute for Aeronautics sand Astronautics: 1902-1907.

090

# Status of the Cryogenic System for the ARIEL E-Linac at TRIUMF

**Sitnikov A., Bylinskii I., Koscielniak S., Koveshnikov A., Laxdal R., Yosifov D.**

TRIUMF, Vancouver, B.C., Canada

## ABSTRACT

A new cryogenic system will be installed at TRIUMF to supply liquid helium (LHe) for three accelerator cryomodules containing superconducting radio frequency (SRF) cavities operating at 2 Kelvin. The system is a part of the ARIEL e-linac particle accelerator project [1].

The cryogenic plant is designed to provide LHe at maximum liquefaction performance of 288 l/h at 4.6 K into a supply Dewar. The transition from Helium I to Helium II below Lambda point ($\lambda \sim 2.17$ K) occurs inside each cryomodule via Joule-Thomson expansion to sub-atmospheric pressure. The operational objective is 24/7 continuous supply of LHe during eleven months per year. This paper outlines our strategy on the configuration of the cryogenic system for different scenarios of operation and the challenges these pose; as well as the technical solutions adopted.

A key ingredient for operational longevity is control of helium purity, and the gas management system is described. The paper concludes with a description of the ARIEL e-linac project status, focusing particularly on the cryogenic equipment procurement and the civil construction for the new compressor building.

## 1. INTRODUCTION

The Advanced Rare IsotopE Laboratory (ARIEL) provides a new front end to the existing ISAC radioactive beam facility that will eventually triple TRIUMF's rare isotope production capability for the needs of the international scientific community. The key features of ARIEL are a new proton beamline and an electron linac that provide drive beams for two new target stations. The linac will be constructed first, followed by the proton line. The 50 MeV 10 mA continuous-wave (CW) electron linear accelerator (e-linac) is based around 1.3 GHz TTF-style 2K superconducting cavity technology, but with many modifications for c.w. operation. The three new cryogenic modules are a development of the top-loading design employed at the ISAC-II facility at TRIUMF modified for 2K operation. All cryomodules will require cooling by liquid helium supplied from an independent cryogenic system. This article presents details of the cryogenic system: estimated heat loads, the layout at the e-linac hall and compressor building with the helium and nitrogen distribution piping and storages, description of all major components and operating requirements.

## 2. CRYOGENIC SYSTEM COMPONENTS

The e-Linac cryogenic system will consist of the following major subsystems and components (see Figures 1 and 2):

- Injector (EINJ) and accelerator (EACA and EACB) cryomodules (1);
- Helium cryoplant consisting of the turbine-based Cold Box (2), main compressor (10), recovery (purification) compressor (11), and oil removal/gas management systems (OR/GMS) (14);
- Helium distribution system including, vacuum-jacketed, liquid nitrogen shielded *'cold'* transfer lines (4a), cold valves, helium ambient vaporizer (6), warm HP and LP plumbing (18);
- Sub-atmospheric system including sub-atmospheric pumps (12), sub-atmospheric helium line (13) with heater (8), and pressure control system;
- Purification system including standalone full-flow freeze-out purifier (16) with a dedicated compressor (11) (serving also a helium recovery function) equipped with OR/GMS, helium multi-component purity analyzer (17), start-up purifiers (cryoadsorbers) (15);
- Liquid Nitrogen (LN2) distribution systems including $LN_2$ tank (21), vacuum jacketed transfer lines (4b), cold valves, phase separator (5), LN2 ambient vaporizer (7), and exhaust plumbing;
- Helium Storage: Liquid He Dewar (3) and two helium storage tanks (19, 20)
- Temperature, pressure, liquid level and flow instrumentation;

- Safety systems;
- EPICS based control system.

Beginning in 2012 and culminating in 2017, one E-linac Injector Cryomodule (EINJ) and two E-linac Accelerator Cryomodules (EACA & EACB), will be gradually installed and comissioned [2]. The e-linac cryogenic system has to be sized to accomodate all three **cryomodules** (1).

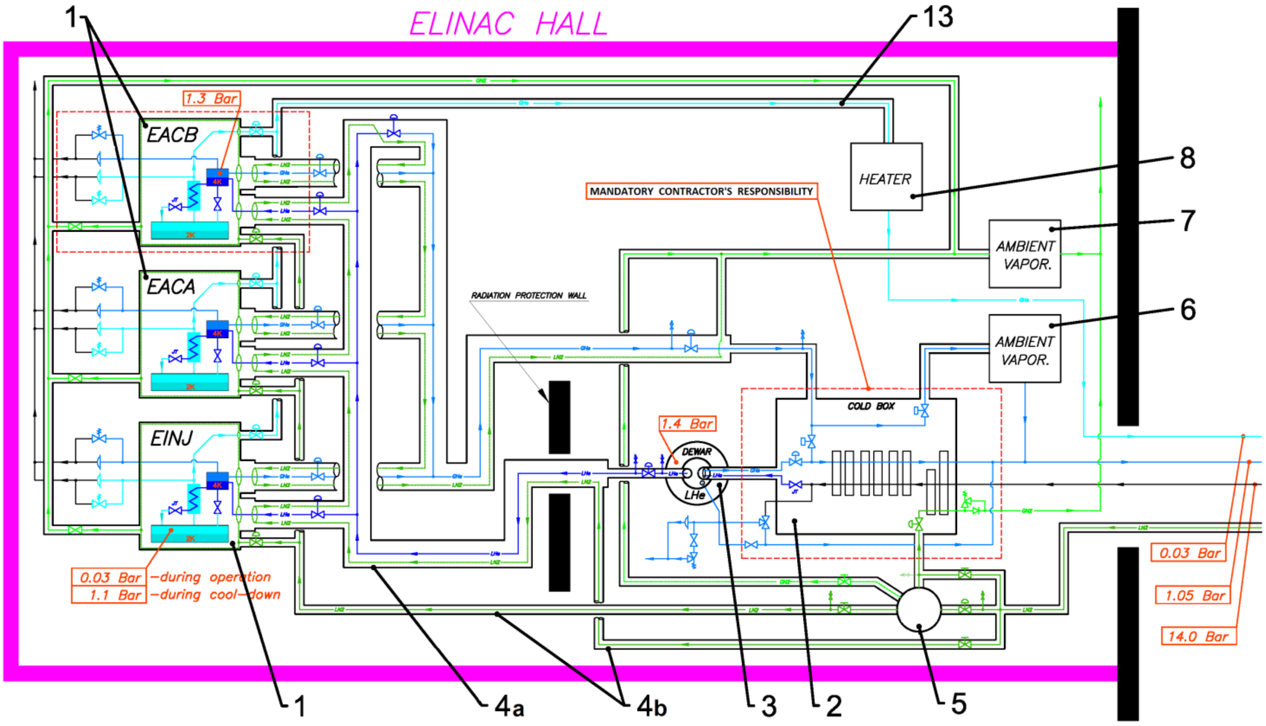

Figure 1. Process Flow Diagram (e-linac hall)

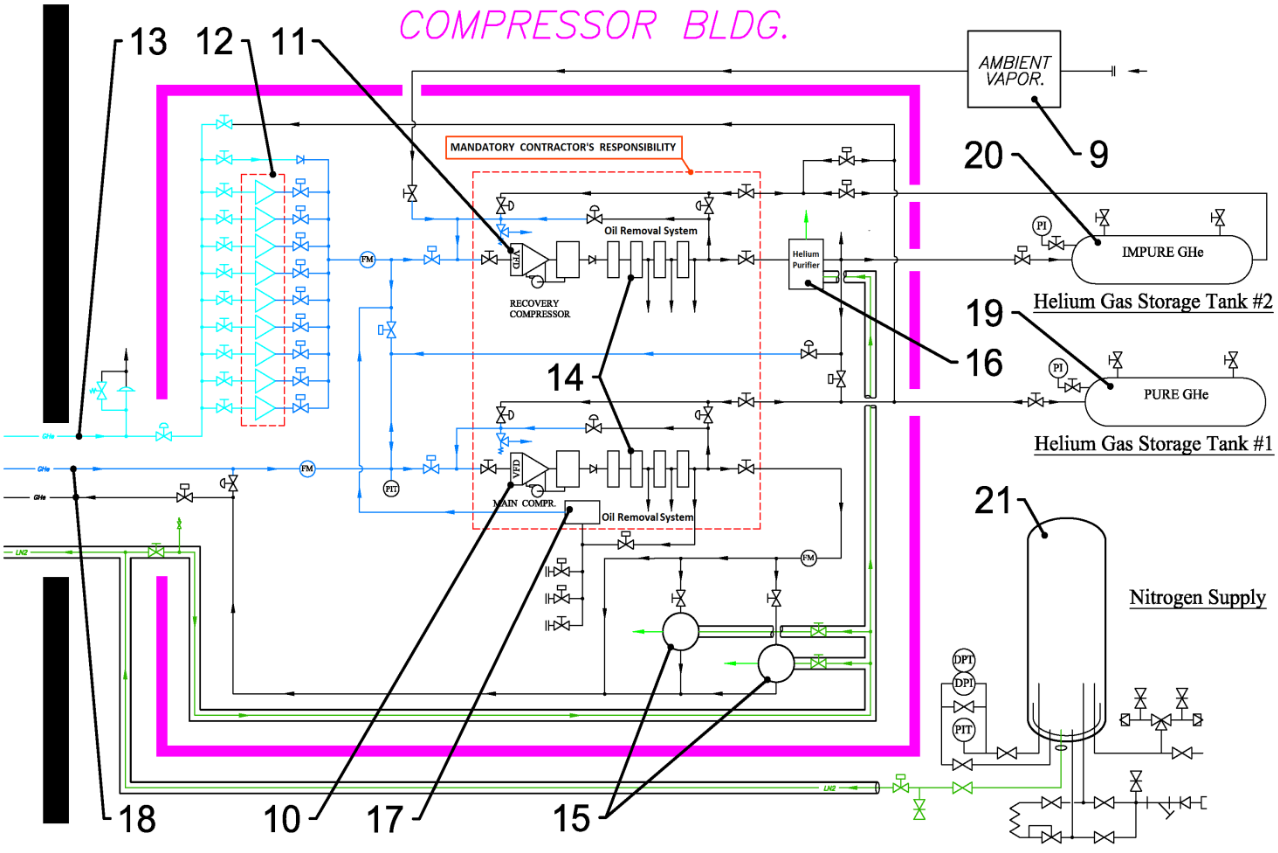

Figure 2. Process Flow Diagram (compressor building)

The LHe Liquefier HELIAL LL - turbine-based **Cold Box** (2) from Air Liquide Advance Technologies - ALAT (France) will produce LHe in Dewar of 1000 litters volume at 1.4 Bar (corresponding to 4.6 K). The contract for the supply of helium liquefier was awarded to ALAT in November 2011.

The design of the cryoplant has been approved during the final design review (FDR) in June 2012 giving a green light for the fabrication. The delivery is scheduled for Q2 2013. Installation, acceptance tests and commissioning is scheduled for Q3 2012.

The whole cryogenic system with cryomodules and infrastructure is planned to commission by 2014.

The turbine-based Cold Box (2) and Dewar (3) together represent the Liquefaction/Refrigeration unit. The guaranteed performances from [3] are the following:

| | |
|---|---|
| - Cold Box refrigeration & liquefaction with LN2 pre-cooling | > 242 L/h @4.6K & 130 W |
| - Cold Box liquefaction with LN2 pre-cooling | > 288 L/h @4.6K. |

The LHe will be delivered via cold distribution lines (4) to all three cryomodules (1) representing the heat loads for the cryogenic system. The heat loads summary is shown in Table 1 below.

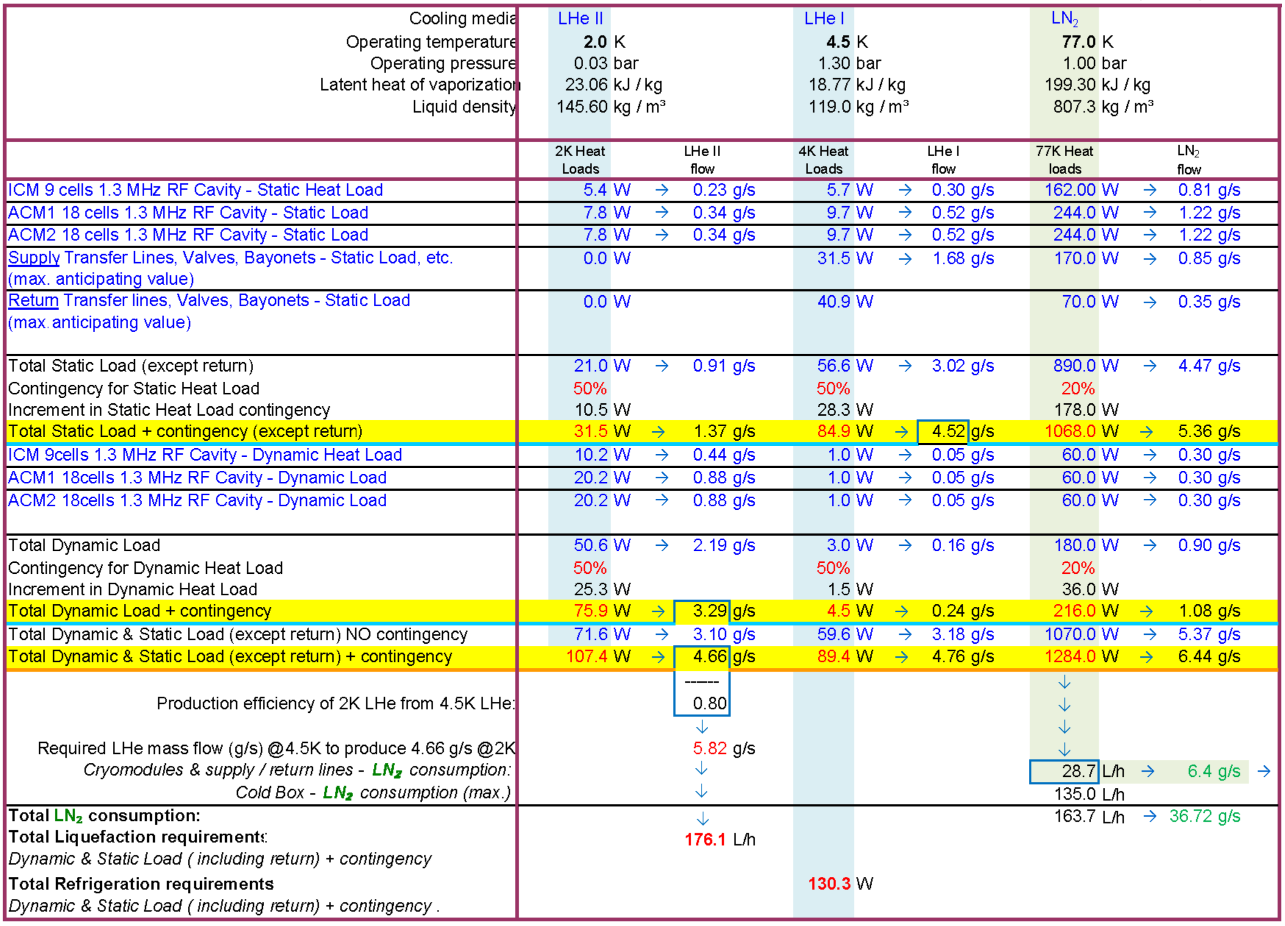

| | 2K Heat Loads | LHe II flow | 4K Heat Loads | LHe I flow | 77K Heat loads | $LN_2$ flow |
|---|---|---|---|---|---|---|
| Cooling media | LHe II | | LHe I | | $LN_2$ | |
| Operating temperature | **2.0** K | | **4.5** K | | **77.0** K | |
| Operating pressure | 0.03 bar | | 1.30 bar | | 1.00 bar | |
| Latent heat of vaporization | 23.06 kJ / kg | | 18.77 kJ / kg | | 199.30 kJ / kg | |
| Liquid density | 145.60 kg / m³ | | 119.0 kg / m³ | | 807.3 kg / m³ | |
| ICM 9 cells 1.3 MHz RF Cavity - Static Heat Load | 5.4 W | → 0.23 g/s | 5.7 W | → 0.30 g/s | 162.00 W | → 0.81 g/s |
| ACM1 18 cells 1.3 MHz RF Cavity - Static Load | 7.8 W | → 0.34 g/s | 9.7 W | → 0.52 g/s | 244.0 W | → 1.22 g/s |
| ACM2 18 cells 1.3 MHz RF Cavity - Static Load | 7.8 W | → 0.34 g/s | 9.7 W | → 0.52 g/s | 244.0 W | → 1.22 g/s |
| Supply Transfer Lines, Valves, Bayonets - Static Load, etc. (max. anticipating value) | 0.0 W | | 31.5 W | → 1.68 g/s | 170.0 W | → 0.85 g/s |
| Return Transfer lines, Valves, Bayonets - Static Load (max. anticipating value) | 0.0 W | | 40.9 W | | 70.0 W | → 0.35 g/s |
| Total Static Load (except return) | 21.0 W | → 0.91 g/s | 56.6 W | → 3.02 g/s | 890.0 W | → 4.47 g/s |
| Contingency for Static Heat Load | 50% | | 50% | | 20% | |
| Increment in Static Heat Load contingency | 10.5 W | | 28.3 W | | 178.0 W | |
| Total Static Load + contingency (except return) | 31.5 W | → 1.37 g/s | 84.9 W | → 4.52 g/s | 1068.0 W | → 5.36 g/s |
| ICM 9cells 1.3 MHz RF Cavity - Dynamic Heat Load | 10.2 W | → 0.44 g/s | 1.0 W | → 0.05 g/s | 60.0 W | → 0.30 g/s |
| ACM1 18cells 1.3 MHz RF Cavity - Dynamic Load | 20.2 W | → 0.88 g/s | 1.0 W | → 0.05 g/s | 60.0 W | → 0.30 g/s |
| ACM2 18cells 1.3 MHz RF Cavity - Dynamic Load | 20.2 W | → 0.88 g/s | 1.0 W | → 0.05 g/s | 60.0 W | → 0.30 g/s |
| Total Dynamic Load | 50.6 W | → 2.19 g/s | 3.0 W | → 0.16 g/s | 180.0 W | → 0.90 g/s |
| Contingency for Dynamic Heat Load | 50% | | 50% | | 20% | |
| Increment in Dynamic Heat Load | 25.3 W | | 1.5 W | | 36.0 W | |
| Total Dynamic Load + contingency | 75.9 W | → 3.29 g/s | 4.5 W | → 0.24 g/s | 216.0 W | → 1.08 g/s |
| Total Dynamic & Static Load (except return) NO contingency | 71.6 W | → 3.10 g/s | 59.6 W | → 3.18 g/s | 1070.0 W | → 5.37 g/s |
| Total Dynamic & Static Load (except return) + contingency | 107.4 W | → 4.66 g/s | 89.4 W | → 4.76 g/s | 1284.0 W | → 6.44 g/s |
| Production efficiency of 2K LHe from 4.5K LHe: | | ------<br>0.80<br>↓ | | | ↓<br>↓<br>↓<br>↓ | |
| Required LHe mass flow (g/s) @4.5K to produce 4.66 g/s @2K | | 5.82 g/s | | | | |
| *Cryomodules & supply / return lines - **$LN_2$** consumption:* | | ↓ | | | 28.7 L/h | → 6.4 g/s → |
| *Cold Box - **$LN_2$** consumption (max.)* | | ↓ | | | 135.0 L/h | |
| **Total $LN_2$ consumption:** | | ↓ | | | 163.7 L/h | → 36.72 g/s |
| **Total Liquefaction requirements:** *Dynamic & Static Load ( including return) + contingency* | | **176.1** L/h | | | | |
| **Total Refrigeration requirements** *Dynamic & Static Load ( including return) + contingency .* | | | **130.3** W | | | |

Table 1. **Heat Loads** for 10 MV/m Operating Mode with 50% contingency.

The Liquefaction/Refrigeration unit will be located in the e-linac hall. The Cold Box and Dewar will be able to form a closed loop system with an immersed heater as a load. Such an arrangement will allow plant's performance evaluation during acceptance test and will provide LHe level control during normal operation. Two independent heaters in Dewar will be used for redundancy in case one fails.

The **cold distribution lines** (4a) for LHe (with the nitrogen shielding jackets) and for nitrogen (4b) are about 16 m long each and specified to have a heat leak less than 0.5 W/meter for nitrogen shielding and 0.05 W/meter for helium [4]. The concept and design is based on our previous experience with ISAC II heavy ion superconducting linac built and operating at TRIUMF since 2005 for Phase I and Phase II.

For the Liquid Nitrogen (LN2) supply two vacuum jacketed feeds from LN2 storage (21) are envisaged: one goes to the compressor room to support purification installations; the other one is sent to the e-Hall, see Fig.2 and Fig.3. The thermal shields of the cryomodules require high quality LN2 to prevent vibrations caused by the dual phase flow. The LN2 **phase separator** (5) will deliver steady temperature liquid to the cryomodule shields. The cold box supply by LN2 (135 l/h) can be either from the phase separator or from the main LN2 flow in a dual phase. The internal thermal shields of the LHe distribution line will be fed from the main LN2 flow in a dual phase as well.The consumption in LN2 of the process purifier (16) in the compressor building is unknown yet and may vary from 20 to 60 l/h. Nitrogen vapours from the trunk, phase separator, and cryomodules will be carried by vacuum jacketed lines to the ambient heat exchanger and then exhausted to the atmosphere.

The **helium ambient vaporizer** (6) will be required during cool down of the cryomodules and distribution lines to bring temperature of the returning helium gas from ~10 K up to ambient temperature. For the returning helium gas flow of 5 g/s the required performance of the ambient vaporizer would be 16 kW (during 8 hours maximum). The nitrogen ambient vaporizer (7) will operate in continues mode warming up about 6.5 g/s of nitrogen gas (~5.5 kW) coming from 80 K shielding. The gas heater (8) is not defined yet. It will be required to warm up the helium gas flow maximum 8g/s in continues mode. The challenge in designing of this heater is to keep the channel aperture open enough with minimum twists for the sub-atmospheric flow at ~30 hPa (mBar). However, heat exchange in this kind of channel is not efficient, and so. The use of an active heater instead of ambient vaporizer is under consideration. The last ambient vaporizer (9) will serve to warm up the helium gas from Dewar during refilling our helium inventory.

The **Main Compressor** (10) is a medium pressure screw-type oil-flooded Kaeser compressor FSD 571 (water cooled) equipped with a variable frequency drive (VFD) and capable of supplying up to 112 g/s of the helium gas to the cold box at 14.7 Bar. An important point is the compressor suction pressure which should be retained above atmospheric to reduce a risk of air contamination in case a leak develops in the suction line plumbing.

In addition to the main compressor, a smaller Kaeser helium compressor CSD 85 (air-cooled) of the same screw-type, oil-flooded, will be supplied. This **Recovery/Purification Compressor** (11) is intended to be used for a dual purpose. In the event of a power failure the Recovery Compressor working from an emergency power generator shall handle all boiled off helium (~ 4.6 g/s) and send it in the Gaseous Helium (GHe) storage tank (19). Additionally, this same compressor should be capable to handle the throughput of the sub-atmospheric pumps ~9.0 g/s when this gas flow would need to go through the purifier in case of a minor leak in the sub-atmospheric line.

Warm helium **sub-atmospheric pumps** (12) have to be able to remove helium vapours from the cryomodules 2K reservoirs keeping 31.5 ± 0.5 hPa (mBar) pressure independent of RF load. The decision for a modular pumping system configuration was based on the experience from other labs. Having several pumps in parallel will allow us to increase the pumping capacity gradually (up to nine pumps) in accordance with actual demand. It’s important that the modular approach can allow a rotation of pumps during the maintenance. An additional variable frequency drive (VFD) might be considered to optimize electrical power consumption by motor and provide coarse pumping speed control.

The warm part of **sub-atmospheric line** (13) is sized to have the pressure drop below 1.5 hPa (mBar) over the distance ~90 m between the compressor building and e-linac hall. With estimated total pressure drop for ‘cold’ components of sub-atmospheric line less than 3 hPa (mBar) and combined pressure drop for the heater and pressure control system ~ 3.5 hPa (mBar) the sub-atmospheric pumping system shall provide adequate pumping capacity at 24 hPa (mBar) base pressure . There is a rigid requirement to the leak tightness. Having the radiation within e-linac hall we are going to employ the special, not sensitive to radiation, Helicoflex® gaskets for all ANSI B16.5 flanges proved to be leak tight.

The purity required for the process helium gas in [3] is 99.9995% or better. This implies that after each compressor an additional **ORS** (14) shall be installed. The ORS shall remove any oil vapours/aerosol particles from the process gas. From our experience with the ISAC II helium cryoplant and troubleshooting reviews of other facilities [5, 6] the decision was made that the sizing of the coalescers and charcoal adsorber shall be increased, e.g. [5]. For this purpose each ORS has to be equipped with three coalescers (not two as it was before), bigger charcoal adsorber and a micro-particle filter to capture particulates > 5μm. The criteria for the design of the oil removal system are the following. The gas flow speed through the filtering elements shall be between 5 and 8 cm/s; the annular gas speed along the filtering elements shall be before the turbulent region to prevent the oil particles catching. The charcoal bed shall provide maintenance service not often than ones in two years. The gas flow speed through the charcoal bed shall not exceed 5 cm/s.

The **start up purifiers** (15) are required after maintenance (e.g. oil change) on the main compressor to engage the clean up loop. This is not expensive purifiers with several hours of operation (before regeneration). Each purifier can handle the portion (~5 g/s) of the gas flow stream from the main compressor. Two units will be required for regeneration purposes.

One pass stand-alone **process purifier** (16) shall be capable of handling minimum ~ 9 g/s mass flow. This purifier is necessary if there is a leak in the sub-atmospheric line. In this case, operation can be continuous until the nearest shutdown.

The multi-component helium **purity analyzer** (17) will be capable of measuring online a content of nitrogen ($N_2$), water ($H_2O$), and hydrocarbons ($C_nH_m$) with a resolution of 0.1 vpm within anticipated range of 1 to 100 vpm. As for the oil aerosol the measurement range will be within 1 - 30 vpm and the lower level detection of 10 ppb mass. With an online measurement of the circulating He gas purity an interlock signal will be provided for the cold box protection. The set of reliable and fast responding to impurities levels moisture and nitrogen or oxygen sensors will also required to monitor various branches of helium system. The on-line leak detector (by nitrogen) in the sub-atmospheric line is under consideration.

To provide ample provision for storage of boiled-off helium from the system during the power outage, the gaseous **storage tank** (19) of ~113 $m^3$ volume (~30,000 gallons) for the pure helium will be installed in February 2013 and certified for the maximum operating pressure of 1.72 MPa (250 PSI). The storage tank will be capable to store about 268 kg of the pressurized helium gas at 1.47 MPa (the main compressor maximum operating pressure – 14.7 Bar). This amount of the gaseous helium is equivalent to ~2154 litres of LHe. For references, we will have the total LHe inventory about 1077 litres (max. 800 litres in Dewar plus ~277 litres in cryomodules). The rational for this choice were considerations like the optimum between volume and fabrication efforts, cost and delivery schedule. A storage tank (20) of the same size for impure helium will be installed above the storage tank (19).

The **control system** at the high operator level is EPICS running under the Linux operating system. All Programmable Logic Controllers (PLC's) will be Siemens and designed to interface with the TRIUMF EPICS control system. Networked instrumentation will be isolated over a separate network with independent switches. The design will provide option that a restart of all Input /Output controllers would not interrupt the operation of the system.

## 3. OTHER CONSIDERATIONS

The cryogenic system shall remain safe for all personnel and equipment in the event of a power failure or loss of insulating vacuum. Consideration shall be made for the hazards at each stage of the equipment life, including: installation, commissioning, operation, maintenance, repair, component failure, decommissioning and disposal of all potentially hazardous materials. The design must be in compliance with the safety requirements of all applicable documents [7] in the procurement packages including American Society of Mechanical Engineers (ASME) Boiler and Pressure Vessel Code (2010) and ASME Code B31.3 "Process Piping" (2008).

All components and transfer lines will be designed to eliminate all trapped volumes leading to a spontaneous expansion of cryogens and pressure increase in the case of any unexpected shutdown, such as a power outage. To prevent this, pressure relief valves and/or rupture disks will be adopted.

Within the e-linac hall, all sensitive electronics shall be protected against radiation exposure. For example, all controllers of the cryogenic valves have to be either locally shielded or removed from the high radiation area. For references, it is expected ~1-5 mSv/h radiation level within e-linac hall and ~0.1 mSv/h behind the shielding wall at the cryogenic equipment location. Similar considerations for the pressure transducers, capacitance manometers and vacuum gauges shall apply. All polymers used in the wire insulation materials or gaskets, etc. shall have radiation index above 4.5 as per [9] and [10].

## 4. CONCLUSIONS

The concept and design of the new cryogenic system for the e-linac was based on the in-house designed ISAC-II linac cryogenic system that has been operational since 2005. An expertise gained with the ISAC-II operation has allowed thorough evaluation of the cryogenic loads to specify cryoplant capacity. A significant liquefaction rate contingency has been applied against e-linac design parameters (accelerating gradient of 10 MV/m) that may allow future energy upgrade with increased gradients of up to 16 MV/m. Also, an operational experience at TRIUMF and other facilities [5], [6], [8] provided a good reference regarding the sizing and required performance of the ORS that was reflected in the specification requirements for e-linac cryogenic system. Again, as in the past, TRIUMF has taken a path of ordering the subcomponents from different suppliers while maintaining overall responsibility for the system integration. That allows more economical solution for the tight budget project compared to the turn-key system. The design effort and components procurement are following the schedule.

## 5. REFERENCES

1. Bylinskii I., Kishi D., Koveshnikov A., Laxdal R., Sekachev I., Sitnikov A., Yosifov D., 2011, *Overview of the Cryogenic System for the ARIEL e-linac at TRIUMF,* in CEC Proceedings C3OrC-05, Spokane
2. Laxdal B. 2011, *Design Considerations for the e-Linac Cryogenic System*, TRI-DN-11-04.
3. Air Liquide Advance Technologies Technical Proposal C1256 NT 001 (1) 2011.
4. Bylinskii Yu., Koscielniak S., Koveshnikov A., Laxdal R., Sekachev I., Sitnikov A., Yosifov D., *ARIEL e-linac cryogenic system development at TRIUMF*, in proceedings of International Cryogenic Engineering Conference, ICEC'24, 2012, Fukuoka, Japan, - to be published.
5. Satti, R. A. and Andrews, R. A., "*Fermilab Satellite Refrigerator Compressors With the Oil and Moisture Removal Systems*" in CEC Proceedings (1983), Vol.29, p.453
6. Pflueckhahn D. , Anders W. , Knobloch J. , Rotterdam S. 2010, *"Operational experience with a helium plant and distribution system at BESSY II"* , Vancouver, Workshop presentation at TRIUMF.
7. American Society of Mechanical Engineers (ASME) Boiler and Pressure Vessel Code (2007, 2010) (see: http://campaign.asme.org/bpvc10/home.cfm?track=go.asme.org)
8. Thiering R., Taylor D., Lu W. 2011, *Helium Refrigerator Maintenance and Reliability at the Opal Cold Neutron Source, in CEC Proceedings (2011), C3OrA-01.*
9. Nuclear and Space Radiation Effects of Materials, NASA
10. Appendix T28: Radiation Resistance, LAPP Group

# POSTER SESSION
# - HEAT TRANSFER

017

# The Cryogenic Insulation Characteristics of GFRP in Liquid Nitrogen

**Kim H.J.[*], Seong K.C.[*], Choi J.H.[**], Kim W.J.[**], Kim S.H.[**]**

[*]Korea Electrotechnology Research Institute, Changwon, Korea
[**]Gyeongsang National University, Jinju, Korea

## ABSTRACT

A power apparatus applying superconductivity is operated in a specific environment of cryogenic temperature. The conventional solid insulator was not able to maintain its performance of insulation due to its cracking or transformation from contraction under cryogenic temperature. However, GFRP has excellent mechanical and electrical properties even in extremely low temperature, so it has been frequently used as a bobbin or insulator for the superconducting power apparatus such as the superconducting transformer, fault current limiter, and HTS SMES. In this paper, we have investigated the electrical characteristics of insulation according to the thickness and shape of GFRP. In conclusion, a rod shape showed worse insulation properties than a plate shape. As a plan to complement this point, a shape using collars was effective. A shape applied collar is a useful element to help flashover discharge improve withstand voltage. And regulating the ratio of thickness to collars can expect better insulation performance.

## 1. INTRODUCTION

Superconducting power devices use superconductors instead of generally used copper. A superconductor can flow several ten or several hundred times of electric currents compared to copper. Thus it has advantages such as increase of device efficiency, reduction of weight and volume, increase of overload withstand ability, etc. However, a superconductor has superconductivity only at a cryogenic critical temperature. It is hard to use a general insulation material at a cryogenic temperature. Cold energy results in contraction, destruction or deformation of materials, for which insulation withstand ability reduce, failing to act like at a normal temperature. For this, it is very important to research the insulation properties of materials for cryogenic temperature. Especially, glass fiber reinforced plastics (GFRP) has small thermal contraction and excellent mechanical strength at a cryogenic temperature. In addition, it has excellent electric insulation properties, attracting attention as a cryogenic insulation material or structure. This paper researched breakdown properties depending on the thickness, length, shape, etc. of GFRP. These research results will be used usefully as data for the insulation design of superconducting power devices.

## 2. EXPERIMENT

An experimental apparatus to research the insulation properties of GFRP at a cryogenic temperature is largely made up of electrode systems and power supplier. The electrode systems are diverse depending on the discharge properties of an insulation experiment, the shape of samples, the kind of materials, the level of applied voltage, etc. Fig. 1 shows the simulated electrode systems for insulation experiments. Plane-plane electrodes were used for puncture breakdown properties depending on changes in thickness. The upper electrode to which high voltage was applied was made of stainless steel of 25 mm diameter and 5 mm corner curvature radius. The lower electrode connected to the ground has 75 mm diameter and 5 mm corner curvature radius. GFRP plates were inserted into between the two electrodes, and then the insulation properties of the various thickness plates. A rod type of electrode system was used for the breakdown properties depending on the shape of materials. Glass fiber was wound around a copper rod of 30 mm diameter, to make GFRP. The copper inside the rod electrode system was connected to high voltage, and the exterior GFRP surface was grounded. The insulation properties of various thicknesses were researched by varying the number of glass fiber windings. The experiment used AC and lightning impulse generator. The maximum AC voltage is 100 kV, and its frequency is 60 Hz. The lightning impulse generator has $1.2\times50$ $\mu$s standard waveforms, 400 kV maximum voltage, and 20 kJ storage energy. The electrode system was dipped in liquid nitrogen and cooled enough for insulation tests at a cryogenic temperature. AC voltage was applied at a rise speed of 2 kV per second until breakdowns took place. The lightning impulse voltage was increased by 4 kV in a step-up method.

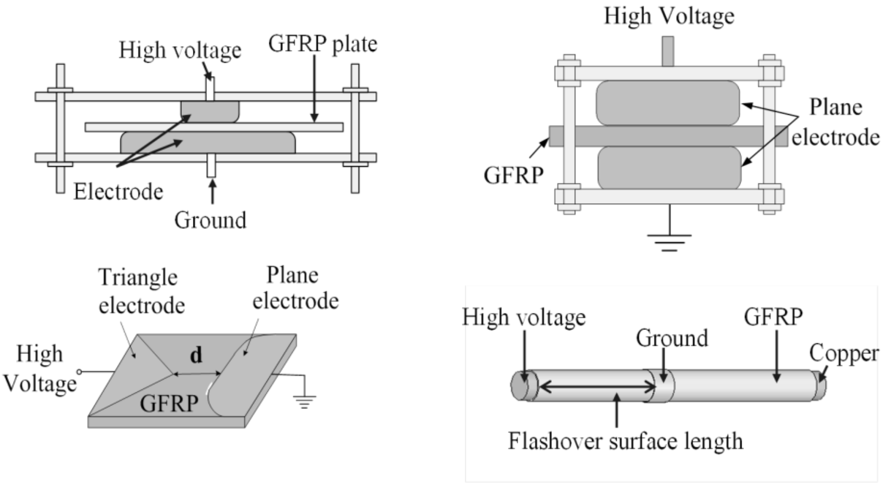

Figure 1. The simulated electrode systems for insulation experiment.

## 3. RESULT AND DISCUSSION

Fig.2 shows the lightning impulse puncture breakdown properties of GFRP depending on thickness. A GFRP plate of 0.5-5 mm thickness was inserted into between a 25 mm plane electrode and a 75 mm plane electrode, and then broken down. As thickness increased, the breakdown voltage increased almost linearly. As shown in the figure, it has very superior electric strength of approximately 40-50 kV/mm. Due to the limit in experimental apparatuses, over 5 mm insulation properties could not be assessed, but it is suitable as an insulation material for high voltage power devices, so additional research on a thicker sample is necessary.

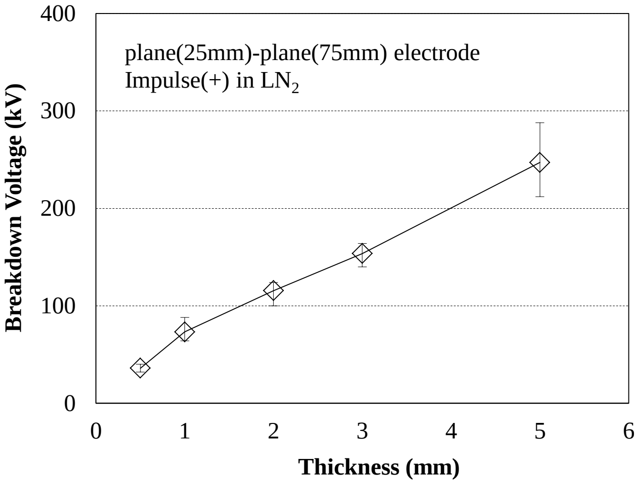

Figure 2. Impulse breakdown of the GFRP depending on thickness.

Fig.3 shows the lightning impulse flashover discharge properties of GFRP depending on length. Triangular and plane electrodes were attached on a GFRP plate with a uniform surface, to examine their flashover discharge properties. The angle of the apex in the triangular electrode is 90°, and its radius of curvature is 25 $\mu$m. 10 times of experiments were performed each while changing the gap between the two electrodes to 50-300 mm. The results of flashover discharge properties were not better than those of puncture breakdowns. As shown in the figure, approximately 1-2 kV/mm of weak electric strength was confirmed. Thus it is important to design GFRP so that it may have no structure of flashover discharge when using GFRP as an insulation material at a cryogenic temperature.

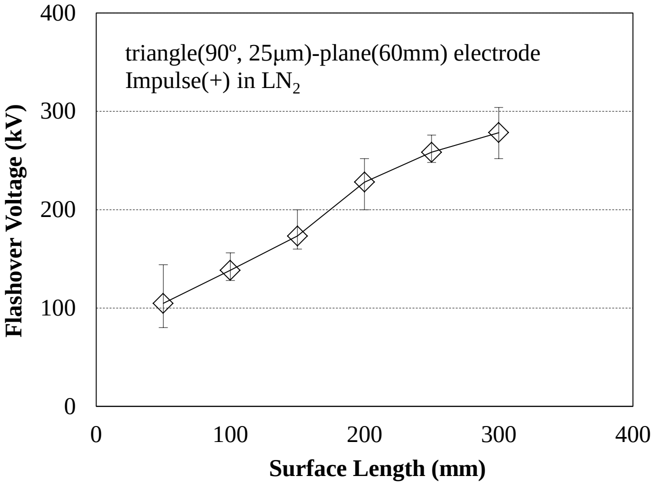

Figure 3. Impulse flashover of the GFRP depending on length

Fig.4 shows the lightning impulse puncture breakdown properties of GFRP depending on its shapes. This is an experiment to examine the effect of a rod type and a plate type of shape for the GFRP samples of the same thickness. The rod type sample has a structure that GFRP is covered on a copper rod of 30 mm diameter in a pipe shape. The plate type has a structure that both surfaces are uniform and flat. According to the experimental results, the breakdown voltage of a rod type GFRP is approximately 1.5 times lower than that of a plate type GFRP. Thus it seems that the devices such as the bushings and current leads with a rod type of insulation structure should be carefully designed.

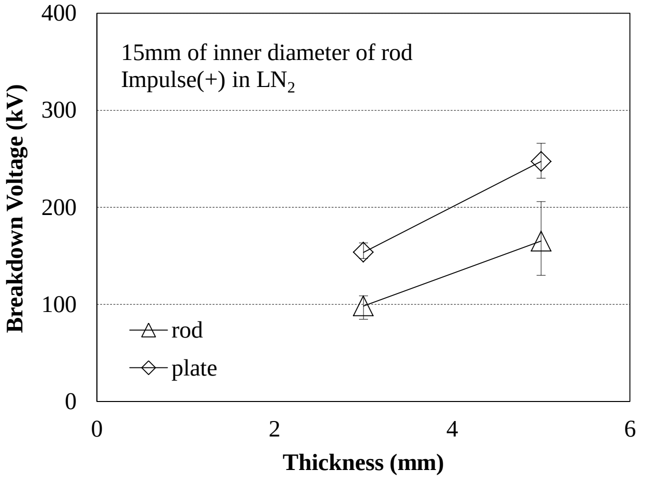

Figure 4.  Impulse breakdown of the GFRP depending on shape

Fig.5 shows the lightning impulse flashover discharge properties of GFRP depending on its shapes. Electrodes were attached to the surface of the same samples that were used in the previous experiment, to measure flashover discharge voltage. The gap between electrodes was set to 50 mm equally. Similarly to the result of puncture breakdowns, a plate type showed higher voltage than a rod type. However, voltage difference was not big, and there was an approximately 10-15% effect in average. Even the error in a plate type is larger to show lower voltage than that in a rod type. In flashover discharge, a plate type has a little better insulation properties, but as mentioned before, it has low intrinsic breakdown voltage, so be careful in applying it to insulation.

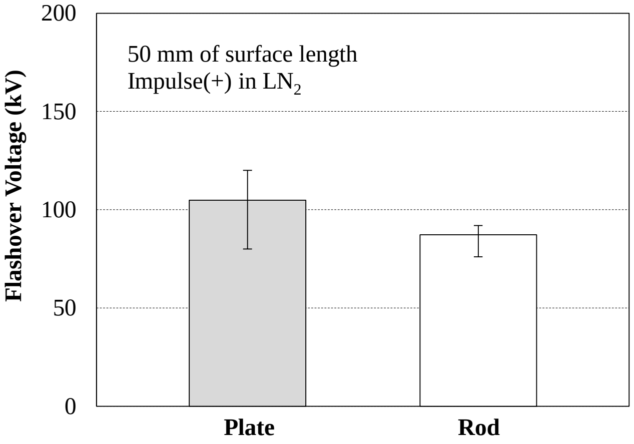

Figure 5. Impulse flashover of the GFRP depending on shape.

Fig.6 shows the puncture breakdown properties of GFRP depending on the kind of voltage source. A plate sample of 1 mm thickness was inserted into between two plane electrodes of 25 mm and 75 mm diameter, and AC and impulse voltages were applied to each. As shown in the figure, the impulse voltage was approximately 2~2.5 times higher than the AC voltage. The impulse voltage was divided into positive polarity and negative polarity and examined, and they were confirmed to have almost the same values.

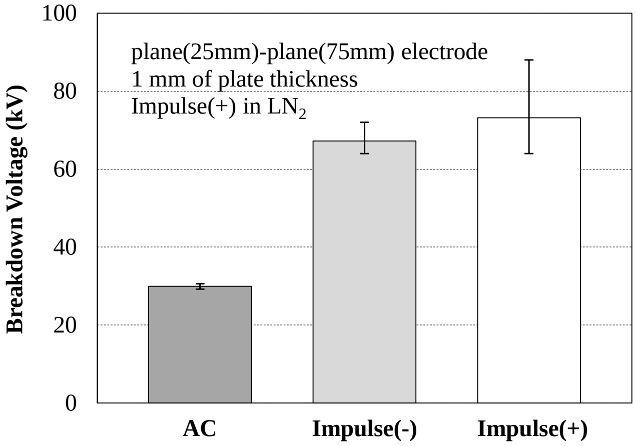

Figure 6. Puncture breakdown of GFRP depending on voltage source.

Fig.7 shows the AC flashover discharge properties of GFRP depending on its collar length. With various collar lengths of a GFRP plate having constant thickness, its total surface length was varied. Its thickness was set to 1, 2, 5 mm, and its collar length was varied up to 1-6 mm. As shown in the figure, its total surface length is equal, but there is a difference in voltage depending on its ratio of thickness to collar. If the ratios of thickness *t* to collar *c* are 1:6, 2:5, 5:2, their total surface lengths are equally 7 mm, but their voltages are different. The voltage for 2 mm thickness is highest, and those for 5 mm and 1 mm thicknesses are next. In addition, according to the results in Fig.3 and Fig.6, the electric strength of lightning impulses with higher breakdown voltage than AC is 1-2 kV/mm. To the contrary, a shape using collars showed 4-9 kV/mm of high electric strength despite being AC. From this result, it can be inferred that the effect of shapes on breakdowns is substantially big. Thus it is expected that utilizing this usefully can contribute to designing an insulation structure of excellent performance.

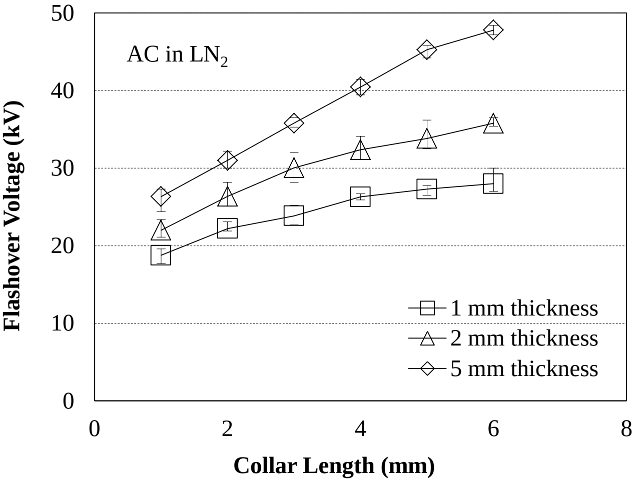

Figure 7. AC flashover of GFRP depending on collar length

## 4. CONCLUSIONS

This paper researched the breakdown properties depending on the thickness, length and shape of GFRP widely used as a cryogenic material. GFRP has very excellent puncture breakdown withstand voltage. However, it has a disadvantage of weak flashover discharge properties as well. A rod shape showed worse insulation properties than a plate shape. As a plan to complement this point, a shape using collars was effective. A shape applied collar is a useful element to help flashover discharge improve withstand voltage. And regulating the ratio of thickness to collars can expect better insulation performance. The above experimental results were expected to be applicable as data for insulation design of superconducting device such as transformer, fault current limiter and SMES. And it is thought that designing the safe of cryogenic GFRP structures can contribute to the improvement of insulation performance. However, it is thought that additional researches on lifespan properties for improving insulation reliability and security of extensive breakdown data should be realized.

## 5. ACKNOWLEDGEMENT

This work was supported by the Power Generation & Electricity Delivery of the Korea Institute of Energy Technology Evaluation and Planning(KETEP) grant funded by the Korea government Ministry of Knowledge Economy (No.R-2004-1-144).

## 6. REFERENCES

D. R. James, and I. Sauers, “Electrical Insulation Materials for Superconducting Coil Applications,” *2004 IEEE Power Engineering Society General Meeting*, vol. 2, pp. 2062-2064, 2004

C. H. Park, T. Kaneko, M. Hara, and M. Akazaki, “Effects of Mechanical Stresses on the Dielectric Breakdown Strengths of Pet and FRP,” *IEEE Trans. Electrical Insulation*, vol. EI-17, no.3, pp. 234-240, Jun. 1982

E. Tuncer, I. Sauers, D. R. James, and A. R. Ellis, “Electrical Insulation Characteristics of Glass Fiber Reinforced Resins,” *IEEE Trans. Appl. Supercond.*, vol. 19, no. 3, pp. 2359-2362, Jun. 2009.

V. Bondarenko, S. Egorov, E. Lamzin, V. Korsunsky, I. Rodin, and N. Voronin, “Components of Thermal and Electrical Insulations for the Superconducting Magnet Systems,” *IEEE Trans. Appl. Supercond.*, vol. 15, no. 2, pp. 1435-1438, Jun. 2005.

J. K. Walsh, M. W. Hooker, M. J. Lizotte, E. Tuncer, and I. Sauers, “Nanocomposite Insulation for HTS Applications,” *IEEE Trans. Appl. Supercond.*, vol. 19, no. 3, pp. 2363-2366, Jun. 2009.

071

# Cryogenic He experiment on Natural Turbulent Convection

**Kralik T., Urban P., Musilova V., Hanzelka P., Srnka A., Repisky A.**

Institute of Scientific Instruments of the ASCR, v.v.i., Kralovopolska 147, Brno, 612 64 Czech Republic

## ABSTRACT

Cryogenic helium gas is a suitable fluid for study of natural turbulent convection at very high Rayleigh numbers. We present an experimental method and a new result on Reynolds and Péclet numbers characterizing large scale circulation (LSC) of fluid at Rayleigh numbers within the range from 1011 to 1015. Observation of LSC is based on measurement of local temperature fluctuations of convecting helium. For experiments we used a specially designed cylindrical cell of height L = 0.3 m and diameter D = 0.3 m with minimized parasitic effects on studied convection, previously published on conf. CryoPrague 2006.

## 1. INTRODUCTION

Natural turbulent convection is a ubiquities phenomenon and its study is of great importance for various fields of science and technology. The basic parameter of thermally driven convection is the dimensionless Rayleigh number, *Ra*, which characterises intensity of this phenomenon similarly to the Reynolds number, *Re*, in connection with forced flow. Value of the Rayleigh number increases with the dimension of convection flow achieving thus values $10^{17}$ in the Earth's atmosphere, $10^{20}$ in oceanic streams or $10^{21}$ for observed effects on the Sun, e.g. The highest value of Rayleigh number in a laboratory was achieved using cryogenic helium gas ($Ra = 10^{17}$) [1].

Due to its low viscosity and thermal diffusivity in comparison with other commonly used fluids, cryogenic helium gas (~ 5 K) enables to achieve very high values of Rayleigh number in laboratory conditions and it is thus a very useful working fluid for experimental studies of turbulent flow (see definition of *Ra* number in Eq. 1 and Table 1). Moreover, owing to the strong dependence of helium properties on the pressure and temperature in the vicinity of helium critical point (5.195 K, 227.5 kPa and 69.64 kg/m$^3$) the flow can be studied in a wide range of *Ra* numbers.

Table 1. The ratio of the fluids properties in Ra number

| Fluid | Temperature | $\alpha/\nu\kappa$ ($K^{-1}cm^{-4}s^{-2}$) |
|---|---|---|
| Air | 20 °C | 0.122 |
| Water | 20 °C | 14.4 |
| Mercury | 20 °C (SVP) | 3.43 |
| Hydrogen (para, liquid) | 20.2 K (100 kPa) | $5.9\times10^{3}$ |
| $SF_6$ | 50 °C (5 MPa) | $7.5\times10^{5}$ |
| Helium (gas) | 5.5 K (100 kPa ) | $1.05\times10^{5}$ |
| Helium (gas) | 5.5 K (280 kPa ) | $1.41\times10^{8}$ |

For study of thermally driven turbulent flow the model of Rayleigh-Bénard convection (RBC) is used. A fluid confined between two horizontally infinite plates kept at a constant temperature, is heated with the lower plate and cooled via the upper one. In experiments, RBC is realized using a container of height *L*, often of cylindrical shape with the diameter *D*. Ideally, the vertical walls of the container are adiabatic, non-influencing the flow.

Such a system is possible to study experimentally, theoretically or by direct numerical simulation. When the study is conducted under the conditions of nearly incompressible fluid (more exactly under the Boussinesq conditions [2]) the RBC is fully described by three dimensionless numbers, the Rayleigh and Prandtl numbers and aspect ratio (*Ra*, *Pr* and *Γ*).

$$Ra = g\frac{\alpha}{\nu\kappa}\Delta T L^3,\ Pr = \frac{\nu}{\kappa},\ \Gamma = \frac{D}{L}, \tag{1}$$

where g stands for the acceleration due to gravity, and $\Delta$T is the temperature difference between the parallel bottom and top plates separated by vertical distance L. The properties of the working fluid are characterized by a combination of $\alpha /\nu\ \kappa$, where $\alpha$ is the isobaric thermal expansion, $\nu$ is the kinematic viscosity, and $\kappa$ denotes the thermal diffusivity.

On the principle of similarity, all the properties of RBC, including transferred heat as an important consequence of the convection, can be assigned to the given values of those three numbers via Nusselt number. The dimensionless Nusselt number which characterises "intensity" of heat transfer is the ratio of the heat flux, $H$, transferred by convection to the heat, $H_0$, transferred by a quiescent fluid

$$Nu = \frac{H}{H_0},\quad H_0 = \lambda\frac{\Delta T}{L} \tag{2}$$

where $\lambda$ is the heat conductivity of the fluid. The dependence $Nu(Ra, Pr, \Gamma)$ is usually expressed as a scaling law $Nu \sim Ra^{\gamma}Pr^{\beta}$ [Ahlers 2009]. Values of exponent $\gamma \approx$ from 2/7 to1/3 were obtained for $Ra < 10^{11}$. One of the important concerns of RBC studies is the possible existence of the so called „ultimate" (asymptotic, Kraichnan) regime (with $\gamma = ½$) which, possibly, might enable extrapolations to the values of $Ra$ higher than are the laboratory ones. Contemporary theory [2] predicts occurrence of this effect at Rayleigh numbers of about $10^{13}$-$10^{14}$. Although such a values of $Ra$ were obtained in laboratory, the results on $Nu(Ra, Pr, \Gamma)$ dependence at such a high $Ra$ values are still contradictory.

In connection with "seeking" for the ultimate regime, the experimental studies using various fluids focus on the $Nu(Ra, Pr, \Gamma)$ dependence, structure and dynamics of the boundary layers (difficult task due to their submilimeter thickness) and on dynamics of the large scale circulation in the convection turbulent flow [2], Fig. 1.

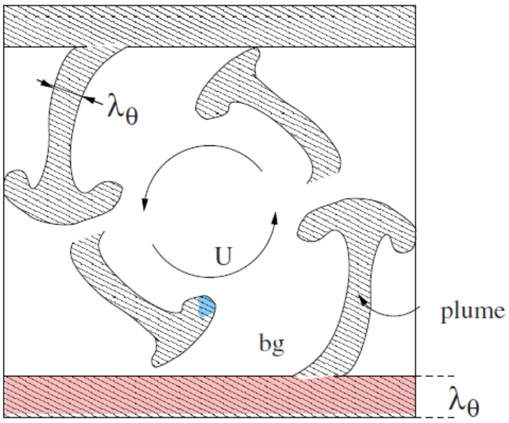

Figure 1. Scheme of main structures in RBC with aspect ratio $\Gamma = 1$ [2]. Outlined are thermal boundary layers (thickness $\lambda_\theta$), large scale circulation (velocity $U$) and hot and cold plumes emitted from thermal boundary layers.

The large scale circulation (LSC) is relatively easy to recognise via measurement of the temperature fluctuations. A scheme of LSC in the convection cell with $\Gamma = 1$ is in Fig. 1. At higher Rayleigh numbers LSC starts to coexist with the thermal structures called "plumes" which are emitted from the thermal boundary layers [3] and together with heat diffusion via boundary layers they drive LSC [2]. When the characteristic period $T_p$ of detection of plumes is derived from the temperature fluctuation spectra (or from the autocorrelation function) the Reynolds or Péclet dimensionless numbers can be defined for LSC [2]:

$$Re \equiv \frac{2L^2}{\nu T_p},\quad Pe \equiv Pr \cdot Re\ . \tag{3}$$

An approximate scaling law was theoretically predicted and experimentally observed as power law $Re \sim Ra^{1/2}$ or $Pe \sim Ra^{1/2}$ [2, 4]. In a study of convection in cryogenic helium, the plumes were detected up to Rayleigh numbers $Ra = 10^{13}$ by Niemela et al. [4] who remarked in [4] that above $Ra=10^{13}$ the coherent structures are hard to distinguish.

In this paper we present preliminary results on detection of large scale circulation (LSC). Aim of this study is to recognise LSC and its variations with *Ra* numbers increasing up to values of $10^{15}$. We present shortly experimental method of convection study and show an example of observation of a coherent structure in time record of temperature fluctuations measured locally in the vertical stream of LSC.

## 2. EXPERIMENT

A helium cryostat with cylindrical experimental cell has been developed at the Institute of Scientific Instruments in Brno in cooperation with the Department of low temperature physics at MFF of Charles University, Prague, for study of turbulent convection [5, 6]. Parameters of this unique apparatus enable to study thermally driven convection over the wide span of *Ra* numbers, from $10^6$ up to $10^{15}$, with minimum influence of the convection cell construction on *Nu(Ra, Pr)* dependence.

The $\Gamma = 1$ cell, 0.3 m in diameter, has thin stainless steel sidewalls (of thickness 0.5 mm in the bottom and upper part, see Fig. 2) of relatively low thermal conductivity. The top and bottom plates are made of 28 mm thick annealed OFHC copper (Outokumpu) of high thermal conductivity, at least 2 $\mathrm{kWm^{-1}K^{-1}}$ (at 5 K). The upper plate is thermally connected to the liquid helium (LHe) vessel via a heat exchange chamber (GHe) filled with gaseous $^4$He. The total external parasitic heat leak to the cell (both radiative and conductive) is suppressed to < 1% of the lowest convective heat flux used in the experiment. Design of the electrical heaters ensures better than 1 mK temperature homogeneity of the internal side of plates, under the assumption that the heat is uniformly supplied or removed. Four calibrated Lake Shore GR-200A-1500-1.4B Ge temperature sensors are imbedded in the centre and near the edge of Cu plates. Two of them, with 5 mK absolute accuracy guaranteed by the manufacturer, measure temperature of top and bottom plates, while additional comparative calibration among the sensors allows determination of $\Delta T$ with accuracy within 2 mK. The pressure in the cell is measured with a MKS Baratron 690 A (calibration traceable to NIST) with 0.08 % reading accuracy. Helium properties are gained from the NIST database [7], based on the actual pressure in the cell and the mean temperature $T_{\mathrm{m}}$ assessed as arithmetic average of the plate temperatures.

Two stainless steel tubes thermally anchored to the LHe vessel [5, 6] are used for venting. A needle valve connecting He convection cell with a LHe bath enables to vary He fluid density in the convection cell operatively.

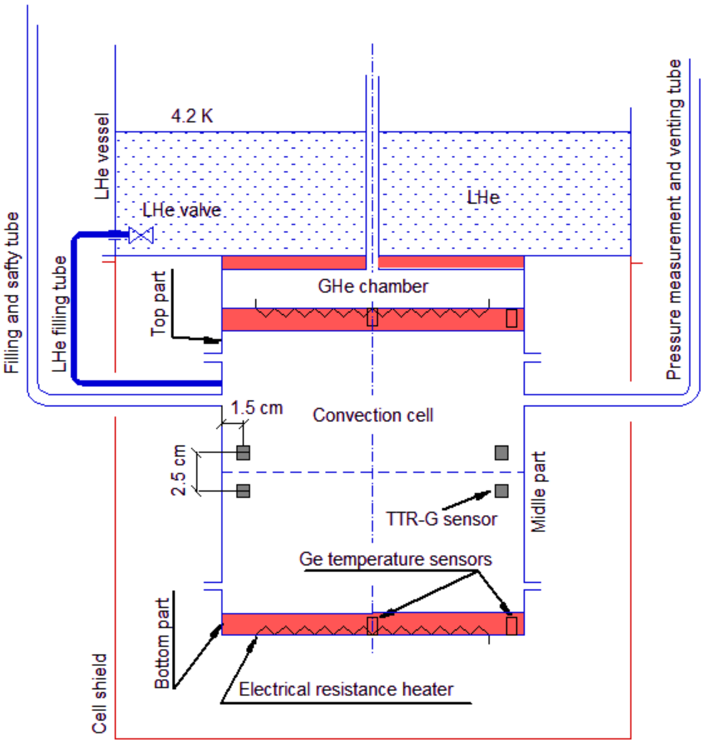

Figure 2. Scheme of the experimental cell with the temperature sensors inside of the cell [6]

Inside the convection sell, four miniature temperature sensors are localised. The sensors TTR-G (Institute of Semiconductor Physics, Kiev, Ukraine) are 0.2 mm cubes of doped Ge. At 5 K their electrical resistance and sensitivity are of about 6 kΩ and $10^3$ Ω/K respectively. The pairs of sensors are fixed near the horizontal middle plane in 1.5 cm distance from the wall (Fig. 2). The sensors of each pair are positioned one by 2.5 cm vertically away from the other. This configuration is designed for the method of derivation fluid velocity from correlations between the pairing temperature signals.

Small changes of resistance of temperature sensor are measured using a phase sensitive (lock-in) amplifiers Stanford Research Systems SR830 combined with Wheatstone „resistance bridge“ which is balanced both resistively and capacitively. The bridge is fed by an adjustable sinusoidal signal generated by SR 830. We have used amplitude 50 mV and frequency 20 kHz. Measured voltage at the bridge was sampled with frequency 32 Hz, data were recorded by PC via GP-IB interface, integration time of SR 830 was correspondingly set to 10 ms. Data records are typically from 30 to 60 minutes long. Matrix oriented programs Matlab (or Octave alternatively) were used for data processing. In this paper we present results of single sensor measurement obtained within experiment focused on $Nu(Ra, Pr)$ dependence.

## 3. RESULTS

Fig. 3 shows an example of autocorrelation function obtained at $Ra = 1.6\times10^{14}$. In the inserted plots we can clearly see a coherent structure with the period $T_p$=14 s which we interpret as the time derived from the period of revolution of large scale circulation [2]. Taking into account the helium viscosity and diffusivity, we obtain the dimensionless numbers $Re = 3.1\times10^5$ and $Pe = 1.15\times10^6$.

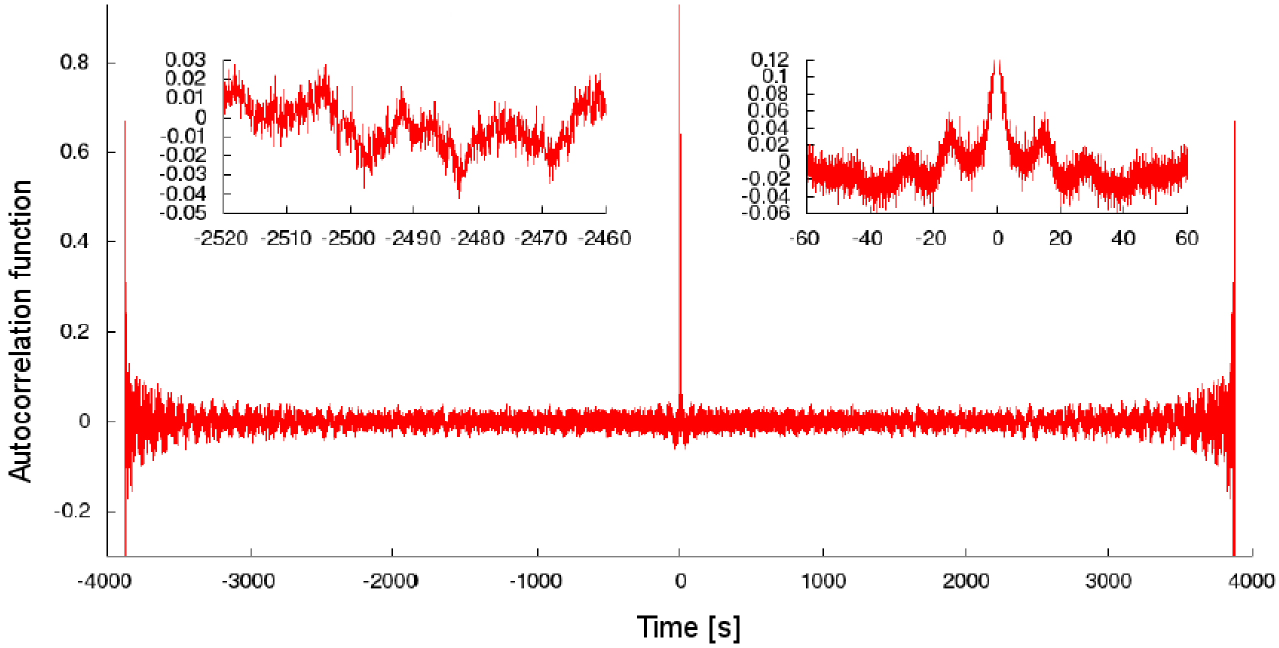

Figure 3. Autocorrelation function of temperature fluctuations measured in the LSC at $Ra = 1.6\times10^{14}$, $Pr$ =3.9 and $\Gamma = 1$. Temperature sensor was located near the horizontal middle plane in a distance of 1.5 cm from the sidewall.

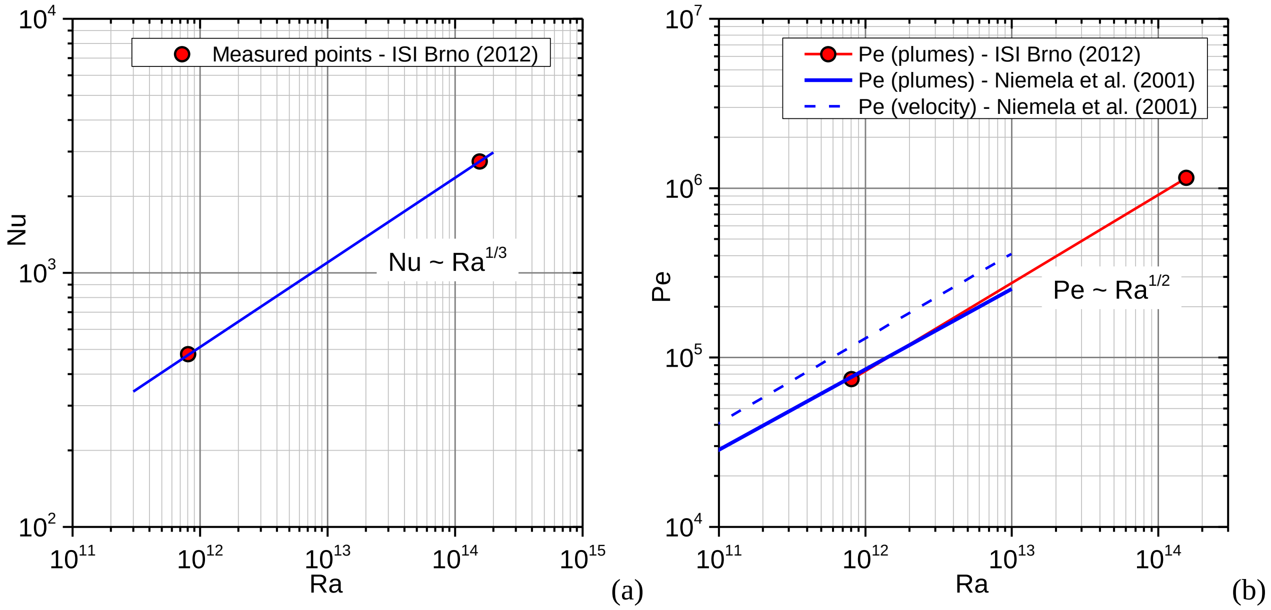

(a) (b)

Figure 4. *Nu*(*Ra*) and *Pe*(*Ra*) scaling laws. Circles – *Pe*, *Nu* numbers obtained in here presented experiment. a) line: $Nu = 0.051\ Ra^{1/3}$ [7]; b) full line: Niemela et al.[4] (one sensor measurement), dashed line: Niemela et al.[4] (pair sensors measurement).

The values of *Nu* and *Pe* numbers obtained for $Ra = 8\times10^{11}$ and $Ra = 1.6\times10^{14}$ are plotted in Figs. 4 a) and b) versus *Ra* together with the power law $Nu \sim 0.051\ Ra^{1/3}$ [8]. Fig. 4 b) shows the results obtained by LSC velocity measurement using two temperature sensors ($Pe \sim 0.13\ Ra^{1/2}$) [4] and somewhat lower values, derived from one temperature sensor, published as well in [4]. Péclet number follows the extrapolated dependence $Ra^{1/2}$ obtained by Niemela et al. [4] from both pair of sensors and one sensor measurement. We can conclude that we have observed LSC in RBC at $Ra = 1.6\times10^{14}$ which is one order of magnitude above the *Ra* where LSC was observed by Niemela et al. [4] in the cryogenic He convection in the vessel with height and diameter of 0.5 m.

## 4. CONCLUSION

During the course of the experiment which focused on the study of the scaling law *Nu*(*Ra*, *Pr*) up to $Ra = 10^{15}$, we have recorded several temperature time signals measured by the temperature sensor located in convecting helium gas. In the autocorrelation function of the signal we could observe a coherent structure which we have attributed to the large scale circulation of He in the experimental vessel. This coherent structure, having a period of 14 s, was observed at very high value of Rayleigh number, $Ra = 1.6\times10^{14}$. The Péclet number follows approximately the extrapolated dependence $Pe \sim Ra^{1/2}$ previously observed by other laboratory for $Ra \leq 10^{13}$ [4]. To our knowledge, it is the first observation of large scale circulation at Rayleigh numbers above $Ra = 10^{13}$ in RBC in laboratory conditions. In the next course of the experiment we are concerning on measurement of temperature fluctuations in convecting He using two pairs of sensors in regime of Rayleigh numbers up to $10^{15}$.

## 5. ACKNOWLEDGEMENT

This work was financially supported by grant GACR 203/12/P897 and MEYS CR (CZ.1.05/2.1.00/01.0017).

## 6. REFERENCES

[1] J. J. Niemela, L. Skrbek, K. R. Sreenivasan, R. J. Donnelly, Turbulent convection at very high Rayleigh numbers. Nature, 2000, n. 404, pp. 837-840. - ISSN 0028-0836.

[2] G. Ahlers, S. Grossmann, D. Lohse, Heat transfer and large scale dynamics in turbulent Rayleigh-Bénard convection, Rev. Mod. Phys. 81, 503 (2009).

[3] G. Zocchi, E: Moses, A. Libchaber, Coherent structures in turbulent convection, an experimental study, Physica A, Volume 166, Issue 3, 387 (1990).

[4] J. J. Niemela, L. Skrbek, K. R. Sreenivasan, R. J. Donnelly, The wind in confined thermal convection, J. Fluid Mech., 449, 169 (2001).

[5] A. Srnka, P. Hanzelka, V. Musilova, P. Urban, L. Skrbek, Design of a Helium cryostat for the study of turbulent thermal convection at cryogenic temperatures. In: *Proceedings of the 21st International Cryogenic Engineering Conference : CryoPrague 2006*. Praha : Icaris, 2006 pp. 661-664. - ISBN 978-80-239-8883-3.

[6] P. Urban, P. Hanzelka, T. Kralik, V. Musilova, L. Skrbek, A. Srnka, Helium cryostat for experimental study of natural turbulent convection, Rev. Sci. Instrum. 81, 085103 (2010).

[7] NIST Reference Fluid Thermodynamic and Transport Properties Database (REFPROP), Version 8.0, National Institute of Standards and Technology, USA, 2000.

[8] P. Urban, V. Musilova, L. Skrbek, Efficiency of Heat Transfer in Turbulent Rayleigh-Bénard Convection, Phys. Rev. Lett. 107, 014302 (2011).

072

# Radiative Heat Transfer at Low Temperatures over Microscopic Distances in Vacuum

**Kralik T., Musilova V., Hanzelka P., Horak M., Srnka A.**

Institute of Scientific Instruments of the ASCR, v.v.i., Kralovopolska 147, Brno, 612 64 Czech Republic

## ABSTRACT

We present experimental results on heat transfer between plane parallel surfaces of samples separated by a microscopic vacuum gap. The radiative heat flux between metallic samples exceeding the heat flux between black surfaces was observed for gaps of several micrometres at temperatures below 50 K. Comparison with near field theory of radiative heat transfer is presented.

## 1. INTRODUCTION

In vacuum, heat can be exchanged between two surfaces through emission and absorption of thermal radiation. The Stefan-Boltzmann law states that the radiative heat flux between two flat plates separated by a vacuum gap is equal to $\sigma(T_2^4\text{-}T_1^4)$ where σ is the Stefan-Boltzmann constant and $T_1$ and $T_2$ are the temperatures of the two media, respectively. However, this law is applicable when the width $d$ of the vacuum gap is greater than the characteristic wavelength of thermal radiation $\lambda_m$ that can be obtained from Wien's displacement law. As the distance decreases and becomes comparable with or shorter than $\lambda_m$, near-field effects become important and the radiative heat transfer can be significantly increased.

From the microscopic point of view, the thermal radiation originates from the random thermal motion of electric charges inside the medium that induces fluctuating currents, and these currents enter as field sources in Maxwell equations. The fluctuational electrodynamics, pioneered by Rytov and co-workers in 1950s, combined the fluctuation–dissipation theorem with Maxwell's equations to fully describe the emission, propagation, and absorption of thermal radiation in both the near and far field [1]. For given geometry and temperature distribution, Maxwell's equations should be solved to obtain the electric and magnetic fields. Although the mean value of the fluctuating current $\left( j(r,\omega)\right)$ is zero, the correlation functions of the components of the current density $\left( j_i(r,\omega)\, j_k(r',\omega')\right)$ are non-zero and the same is true also for the correlation functions of electromagnetic fields like $\left( E_i(r,\omega)\, E_k(r',\omega')\right)$ and for the mean value of the Poynting vector component perpendicular to the planar interface $\left( S_Z(r,\omega)\right) = (1/2)\,\mathrm{Re}\left\{\left(E_x H_y - E_y H_x\right)\right\}$ which is the key quantity in heat transfer calculation.

An anomalous radiative heat transfer between flat metallic surfaces was reported by Domoto [2] at cryogenic temperatures and by Hargreaves [3] at room temperature. In both cases, an increase of the flux was measured for separation gaps in the micrometre range. A theoretical explanation was given by Polder and Van Hove [4] within the framework of fluctuational electrodynamics. More recently, the heat exchange through evanescent phonon tunnelling modes (near field) as well as by freely propagating modes (far field) was theoretically studied by Pendry [5]. A large number of papers about near field transfer were published in last years; we refer to several review papers and literature cited herein [6, 7, 8, 9]. It seems now that the near field radiative heat transfer between two planar objects including multilayers is well understood, while that between curved or more general objects seems to be still not as clear; the radiative heat transfer between two spheres, dielectric sphere and plate, between plate and spheroid or plate and various kinds of sharp objects (cylinders, cones, tips) or the effect of surface roughness are the subjects of recent theoretical research.

Although many theoretical calculations have been published about the effect of near field on heat transfer, experimental works are rare. Measurements between plan-parallel metallic surfaces have been done by Domoto et al. [2] at temperatures from 10 K to 15 K and by Hargreaves [3] between 130 K and 300 K; however, the observed heat power enhancement was less than one order of magnitude. Experiments on radiative heat transfer between a sphere and a plate, both made of silica, were conducted in [10]. More recently, Ottens et al. [11] have measured the heat transfer at temperatures near 300 K between two macroscopic sapphire plates.

## 2. EXPERIMENTAL SETUP

The design of the apparatus previously used for measurements of emissivities in far field [12, 13] was adapted for the measurement of the heat flow over a plane parallel vacuum gap, the width of which can be varied from two millimetres down to micrometres (Fig. 1). The heat flow $Q_R$ between the surfaces of two plane parallel concentric disks (samples at temperatures $T_2$ and $T_1$), each 35 mm in diameter, is conducted through a calibrated thermal resistor (heat flow meter) into a liquid helium bath and is evaluated from the temperature drop ($T_1$–$T_S$) on this resistor (Fig. 1). The sensitivity of the heat flow meter is 30 µW/K at 5 K. The stability of the foot of the thermal resistor ($T_S$) together with a resolution of 50 µK of the temperature measurement enables to measure heat flows from 20 nW to 1 mW.

The lower part of the apparatus vacuum casing is inserted in the LHe bath in the wide neck Dewar vessel. The LHe bath keeps the temperature of the measurement chamber below 5 K. In the apparatus, pressure lower than $10^{-8}$ Pa is kept by cryopumping. Thus, the heat transferred by molecular flow is reduced below measurable values.

The width of the vacuum gap between samples is set up with a differential screw (100 µm/rev) acting on a hot sample suspension (Fig. 1). The sample suspension bears the sample assembly consisting of a sample holder with a heater and a temperature sensor measuring the temperature $T_2$ of the hot sample, a plane parallelism equalizer and the hot sample. Preservation of plane parallelism of the gap during movement of the hot sample is ensured by two flexure membranes, part of hot sample suspension, that bear the sample holder in axial position [14].

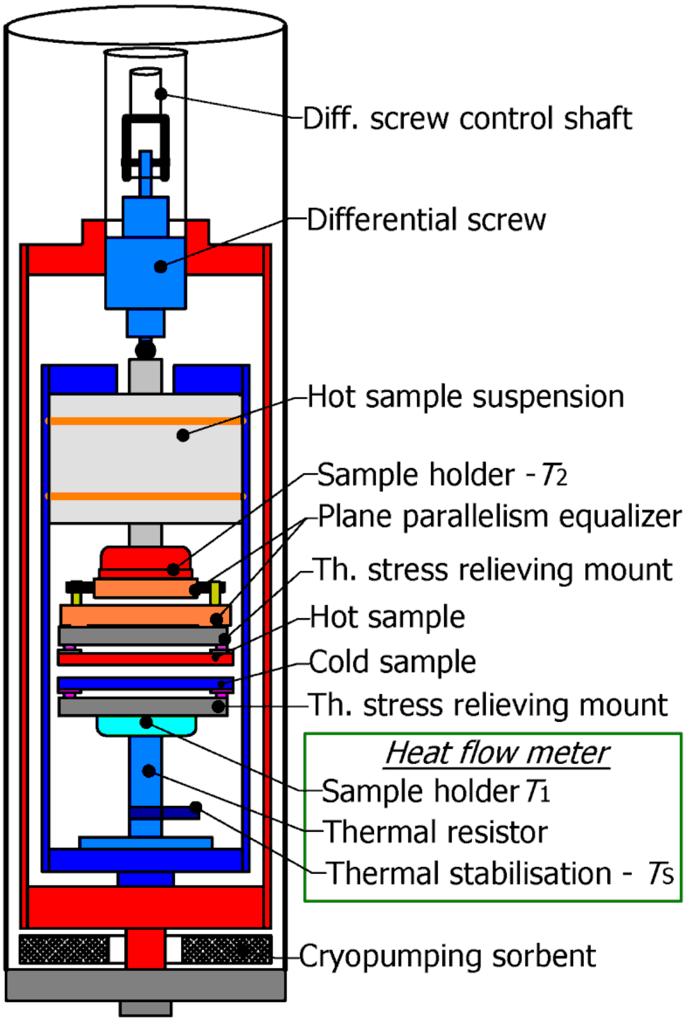

Figure 1. Schema of the apparatus

Adjustment of the plane parallel position of the samples is solved by the plane parallelism equalizer (PPE) (Fig. 2a) inserted between the hot sample and its holder. The function of the PPE is based on friction between three pairs of pins which are perpendicular to each other creating three friction locks (Fig. 2a). Moving the hot sample towards the cold one, the samples come into contact. Further shifting of the suspension down by several hundred micrometres let slip the friction locks of the plane-parallelism equalizer and samples can align parallel to each other with zero gap. When the gap size is increased the hot sample is kept fixed to the moving part by friction locks of PPE. The zero gap is indicated by vanishing of electrical contact between samples. A copper braid connecting the fixed and sliding part of the PPE ensures that the temperature difference between the heater and the sample is less than 0.1 K. The plane parallelism can be established several times until the fixed and sliding part of the PPE come into contact. The PPE can be reset by restoring the gap between moving and fixed part by shifting of the suspension in its highest position.

The position of the hot sample is read on the scale of the differential screw with a precision of 0.5 μm or more precisely from capacitance measurement. The positioning system enables to set plane-parallelism and distance between samples with an accuracy of ~1 μm.

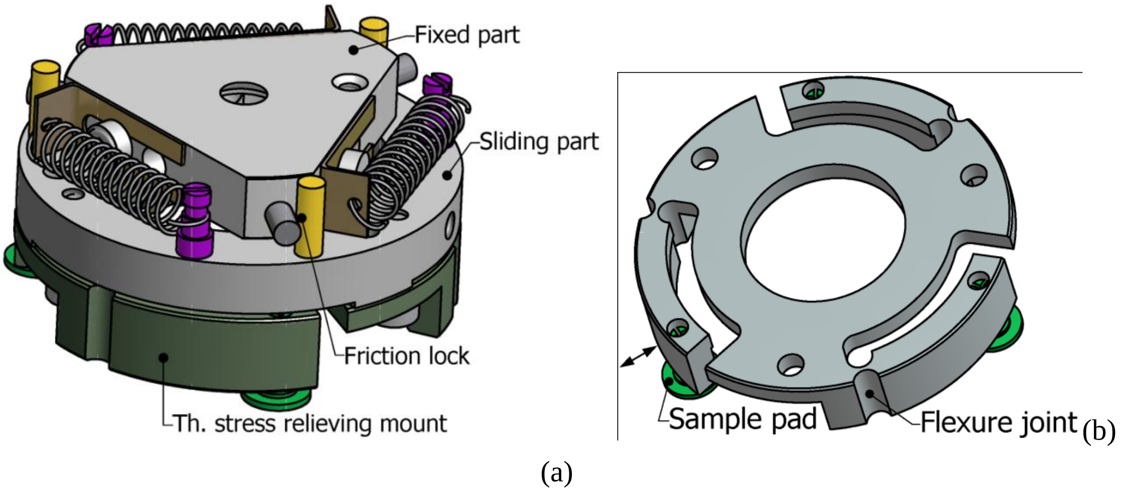

Figure 2. (a) Plan parallelism equalizer (PPE) and Thermal stress relieving mount (b)

## 3. SAMPLES

For manufacturing of samples we have chosen tungsten (nonmagnetic material, mechanically hard, providing normal skin-effect). Samples have shape of a disc, 2.5 mm thick and 35 mm in diameter.

One sample, made of polished pure tungsten metallic disc, labelled "*W bulk*", has slightly convex shape with planarity ~7 μm (Fig. 3).

Two samples, labelled "*W layer*", were prepared by sputtering of 150 nm thick tungsten layer on polished pure alumina substrates ($Al_2O_3$ of 99.8% purity, density of 3.87 g/cm$^3$). A planarity of 0.6 μm and 0.1 μm. (slightly concave shape) of the two samples was determined by the HeNe laser interferometry (Fig. 3).

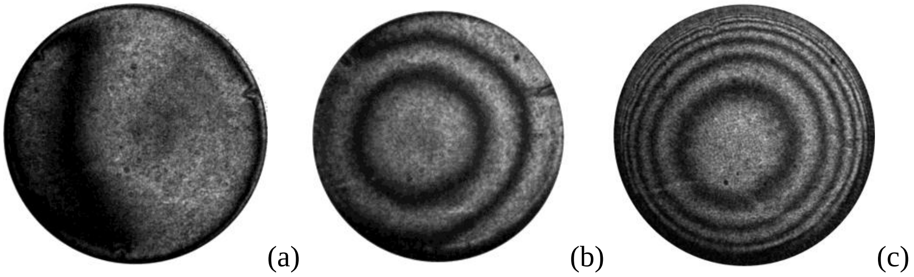

Figure 3. Image from the HeNe laser interferometer (628 nm) of the samples surface (a)-cold sample, (b)-hot sample, (c)-W bulk.

Alumina has been used as a familiar material, UHV compatible, solderable and possessing high thermal conductivity. Sample surface is optically smooth except small pits (due to small voids in alumina ceramics).

The back sides and cylindrical sides of “W layer” samples were aluminized to decrease their emissivity. A 100 µm wide separation strip along the sample circumferential edge electrically isolates the tungsten layer.
The samples were cleaned just before their installation by a method used for cleaning of silicon wafers before electron lithography processing. The samples were put face to face together immediately after the cleaning to prevent contamination by dust. Before installation in the measurement chamber, samples are glued to a thermal stress relieving mount (Fig. 2b) to prevent sample deformation or detachment due to mismatch in thermal contractions when cooling down the apparatus. The procedure of apparatus evacuation, cooling down and measurement ensures that samples are not contaminated by water.

## 4. RESULTS

Fig. 4 a) shows the dependence of mutual emissivity on distance *d* between samples. Mutual emissivity $\varepsilon_{21} \equiv q_R / q_{BB}$ here characterises the heat flux transferred between samples $q_R$ normalised to the far field heat flux between black surfaces $q_{BB} = \sigma\,(T_2^4 - T_1^4)$. Two pairs of samples were measured. Measurement A is for “*W bulk*” sample opposite to “*W layer*” on alumina and measurement B is for “the pair of two samples “*W layer*”. The sample “*W layer*” was heated to $T_2 = 30$ K in both measurements, the cold sample was kept at $T_1 \approx 5$ K.

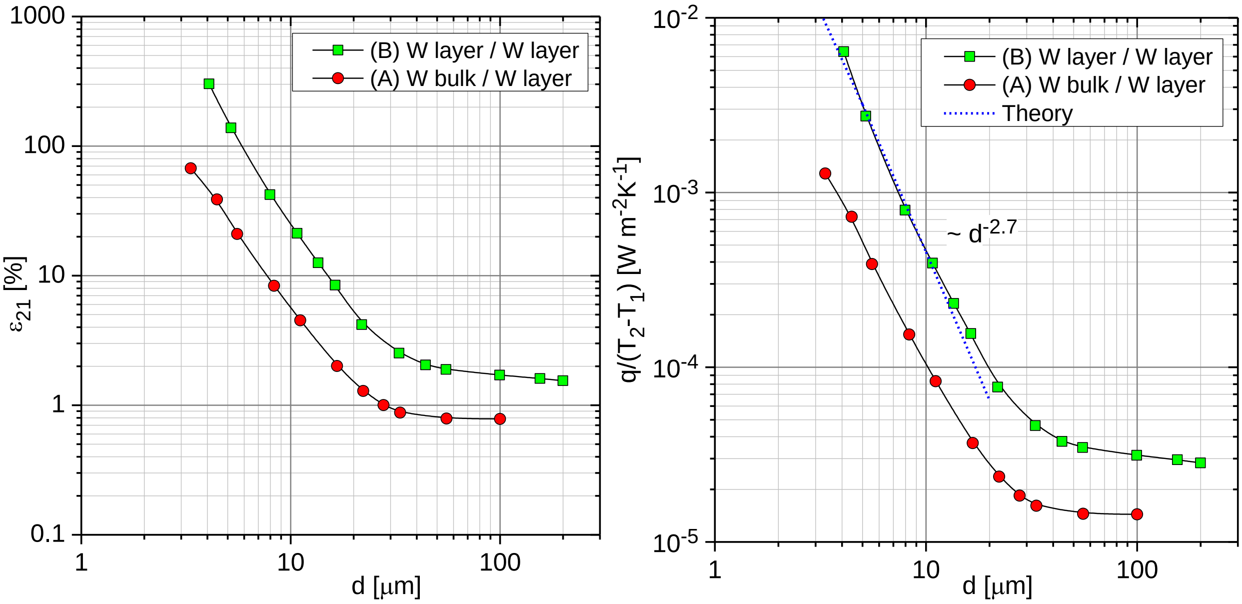

(a)

(b)

Figure 4. a) Measured “mutual emissivity” $\varepsilon_{21} \equiv q_R / q_{BB}$ (transferred radiative heat normalised to the one between black surfaces in far field) in dependence of the distance *d* between samples. Temperature of the hot and cold sample were $T_2 = 30$ K and $T_1 = 5$ K, respectively.
b) Transferred heat flux divided by temperature difference between surfaces of the samples.

The measurements started in the far field regime, at $d = 200$ µm. The two presented measurements differ by far field mutual emissivity, one being $\varepsilon_{21A} \approx 0.7\%$ (measurement A) and the other $\varepsilon_{21B} \approx 1.7\%$ (measurement B). Hargreaves (the only one published near field experiment on plane parallel metallic samples, far field emissivity $\varepsilon_{12H} \sim 3\,\%$) defined onset of near field effect by the distance *d*(10%) at which heat transfer exceeds the far field value by 10 %. We can observe the onsets at $d_A(10\%) \approx 30$ µm and $d_B(10\%) \approx 40$ µm approximately.
In the following semi quantitative discussion we suppose metallic samples, optical properties of which do not depend or depend only slightly on the temperature. This is valid from the practical point of view of radiative heat transfer for many materials. Further we suppose that the temperature of the cold sample is quite bit lower than the temperature of the hot sample. Then according to theoretical formulas for radiative far and near field heat transfer, the onset depends approximately on the temperature of the hot sample as $d(10\,\%) = C/T$, where $C$ is the material dependent constant. Then we can find $C_H = 780$ µm/K for Hargreaves’ experiment ($T_R = 150 \div 300$ K) with chromium layers [3] and $C_A = 900$ µm/K and $C_B = 1200$ µm/K for the here presented measurement on tungsten samples. Comparing the near field onset with the wavelength

$\lambda_m \approx 3000/T$ [μm/K] at the maximum of blackbody radiation (Wien's law), we obtain $d_H(10\%) \approx \lambda_m/3.8$, $d_A(10\%) \approx \lambda_m/3.3$ and $d_B(10\%) \approx \lambda_m/2.5$.

From Fig. 4 a) we can read the distance $d$(BB) at which the heat flow achieves the value of heat flow exchanged between black surfaces in the far field (emissivity of 100 %). We obtain $d_A(\mathrm{BB}) \approx 3.0$ μm and $d_B(\mathrm{BB}) \approx 5.5$ μm for measurements A and B, respectively. This is the first experiment where "black body limit" was experimentally perceptibly exceeded.

Fig.4 b) plots the radiative heat flux $q$ divided by the difference $T_2 - T_1$ between temperatures of the samples. This quantity showed up, within wide span of its values above near field onset, to be weakly dependent on the samples temperature. From $q_B/(30 - 5) = 5\times10^{-4}$ W/m$^2$/K measured at $d = 10$ μm, e.g., we can guess the value $5\times10^{-4}\times(80 - 5) = 0.038$ W/m$^2$ of heat flux between surfaces of present samples at temperatures 80 K and 5 K. The temperature independence of the quantity $q/(T_2 - T_1)$ would mean that the heat flux transferred in the near field regime at a fixed vacuum gap increases linearly with the temperature $T_2$, while the heat flux transferred in far field regime increases with forth power of $T_2$. The approximately linear temperature dependence of heat flux was observed by Hargreaves at a distance of 1.5 μm and temperatures between ~150 and 250 K ($\lambda_m > 12$ μm) [3].

The full line in Fig. 4 b) presents theoretical contribution of near field heat transfer. The fit was achieved by choice of an appropriate value of relaxation time ($8\times10^{-15}$ s) in Drude model of tungsten. Both theoretical and experimental values follow the dependence ~ $d^{-2.7}$.

## 5. SUMMARY

We have used a cryogenic apparatus for demonstration of the near field effect in radiative heat transfer.

Radiative heat transfer over a vacuum gap between plane parallel tungsten samples with reflectivity of ≈ 97 % or higher was observed. At distances of few micrometers the transferred heat flux exceeds the "black body limit" (mutual emissivity exceeds 100 %).

The near-field heat transfer becomes significant when the vacuum gap is lower than a fraction of the wavelength $\lambda_m$ given by Wien's displacement law for the thermal radiation of the hot sample. This value is dependent on material of the samples. We have found the onset at about $\lambda_m/3$.

Experimental data on near field heat fluxes are in good agreement with theoretical calculation. Under not very strict assumptions, heat flux, in some region after onset of near field regime, increases approximately linearly with temperature of the hot sample at a fixed distance between samples (except very narrow gaps). It contrasts with the far field, which increases typically with the fourth power of temperature.

Heat transfer strongly enhanced by the near field could find application in situations where the physical contact between bodies should be avoided and the far field thermal radiation can not transfer sufficient heat flux from or into a body. This method was proposed as an alternative thermal coupling for cooling of the gravitational waves detectors where detecting mass is hanging on thin fibres and is held at low temperature [11]. Using our data, a heat flux of 13 mW transferred without physical contact between plates 300 mm in diameter with a gap of 5 μm can be achieved when the plates are kept at temperatures 10 K and 30 K. The near field effect can also provide a dynamic thermal coupling when varying the gap width between two objects (e.g. for $T_1 = 5$ K, $T_2 = 20$ K and $d = 10$ μm is $\mathrm{d}q/\mathrm{d}d = 1$ mW m$^{-2}$ μm$^{-1}$).

## 6. ACKNOWLEDGEMENT

This work was partially supported by European Commission and Ministry of Education, Youth, and Sports of the Czech Republic (project No. CZ.1.05/2.1.00/01.0017).

027

# Design of a Cryogenic Helium Plate-Fin Heat Exchanger

**Hu Z.J.[*], Qiu Y.N.[*], Zhang N.[**], Li Q.[*]**

[*] Key Laboratory of Cryogenics, Technical Institute of Physics and Chemistry Chinese Academy of Sciences, No.29 Zhongguancun East Road, Beijing, 100190, China
[**] Huazhong University of Science and Technology, Wuhan, 430074, China

## ABSTRACT

A cryogenic helium plate-fin heat exchanger had been designed and tested operating at 20 K and 0.8 MPa. The total leak rate of this plate fin heat exchanger was less than $1.0\times10^{-9}$ Pa·m$^3$/s on the room temperature. The characteristic parameters of the serrated fins were optimized in order to increase heat transfer performance. The channels' distribution and array were the key design issues for plate-fin heat exchangers. According to the heat transfer coefficient and the flow fluids resistance to calculated the fluids mass velocity, the channel amount and the efficient breadth of the heat exchanger. The heat transfer design included to calculate heat transfer coefficient, the fins' efficiency and the total heat transfer area. After the efficient length of the heat exchanger had been determined, the pressure loss and temperature distribution of the fluids flowed in different channels were calculated. Because this heater exchanger was used in a 20 K helium turbine refrigeration cryogenic system, the leak rate was the most important parameter to avoid the impurity polluted the helium working gas. The leak rate of the plate-fin heat exchangers depended on the manufacturing techniques. Aluminum plate-fin heat exchangers require high level of technology, strict quality control and inspection measures. Manufacturing process included parts preparation, plate-beam assembly, brazing, and head arc welding processes. The temperature difference between the warm and cold fluids on the hot end of the cryogenic heat exchanger was tested, which relative error between the experimental value and the designed value was less than 2.5%.

## 1. INTRODUCTION

The plate-fin helium cryogenic heat exchanger is one of the key equipment in large-scale helium refrigeration cryogenic system. Because the plate-fin heat exchanger has some advantages, such as small size, light weight and high efficiency. The lowest temperature difference on the hot end of the plate-fin heat exchanger was only 0.5K. So the irreversible loss caused by temperature difference would be reduced. And the efficiency of the cryogenic refrigeration system would be improved.

Special structure of the fin was adopted for the plate-fin heat exchanger. So the helium streaming in the channel would form a strong turbulence. The boundary layer will be reduced, thus the thermal resistance was reduced effectively. In result, the heat transfer efficiency was improved. The heat transfer area per unit volume of plate-fin helium cryogenic heat exchanger could be 1200 to 5600 m$^2$/m$^3$. However, due to the helium flow channel was so narrow that the solidification of impurity gases at low temperature brought blockage. So the added purification system should be introduced into a helium liquefaction system to remove the impurities.

The plate-fin helium cryogenic heat exchanger, produced by Norton Company, France and Chart United States had a very low leak rate of $1.0\times10^{-10}$ Pa·m$^3$/s at room temperature. But the leakage rate of the cryogenic plate-fin heat exchanger in air separation cold box in Chinese major manufacture companies could only reach $1.0\times10^{-6}$ Pa·m$^3$/s. With an improve brazing process, the Technical Institute of Physics, Chinese Academy of Sciences, and Hangzhou Zhongthai Process Equipment Co., Ltd. developed and produced the first plate-fin helium cryogenic heat exchanger with low leak rate of $1.0\times10^{-10}$ Pa·m$^3$/s.

## 2. HEAT EXCHANGER DESIGN

Aimed the cryogenic system in the Chinese Spallation Neutron Source (Abbreviated as CSNS), the two stage plate-fin helium cryogenic heat exchanger had been designed, built and test. CSNS had two cooling capability of different accelerators. There were two kinds of operating capacity for the CSNS cryogenic system. A simple idea to satisfy the two accelerator cooling capacity was to operate the cryogenic cycle with or without the liquid nitrogen. So the helium cryogenic heat exchanger should be designed with the liquid nitrogen pre-cooling and the checking condition was to remove the liquid nitrogen.

The design of a plate-fin helium cryogenic heat exchanger included design calculations and performance check. Design conditions for the plate-fin helium cryogenic heat exchanger of this project was shown in Figure 1-2 and Table 1-2. As shown in Figure 1 and Table 1, the heat exchanger should be designed to meet the requirements the parameters with the liquid nitrogen pre-cooling. In Figure 1, the pressure on the state spot 7 should be calculated by the pressure of 8 and the loss of the piping resistance of the nitrogen channel. And the temperature of 7 was the saturation temperature corresponding to the corresponding pressure. As shown in Figure 2 and Table 2, the heat exchanger parameters were different if the liquid nitrogen was closed.

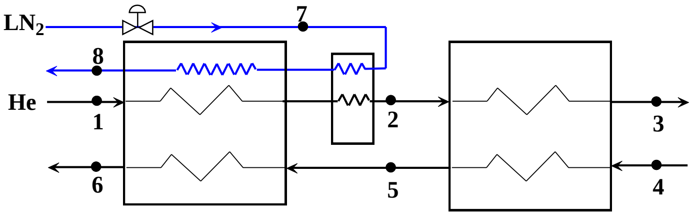

Figure 1. Helium cryogenic flow diagram with the liquid nitrogen pre-cooling

Table 1. Design parameters of pressure and temperature with the liquid nitrogen pre-cooling

| | 1 | 2 | 3 | 4 | 5 | 6 | 8 |
|---|---|---|---|---|---|---|---|
| Temperature/K | 313 | 82 | 22.17 | 20 | 80.7 | 298 | 283 |
| Pressure/bar | 7.2 | 7.17 | 7.16 | 1.15 | 1.13 | 1.08 | 1.05 |

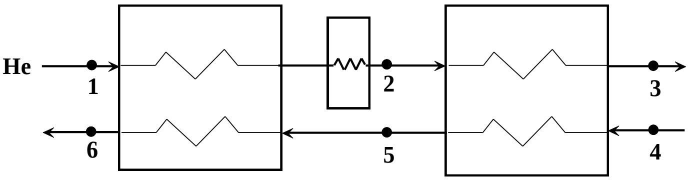

Figure 2. Helium cryogenic flow diagram without the liquid nitrogen pre-cooling

Table 2. Design parameters of pressure and temperature without the liquid nitrogen pre-cooling

| | 1 | 2 | 3 | 4 | 5 | 6 |
|---|---|---|---|---|---|---|
| Temperature/K | 313 | 171.4 | 24.55 | 20 | 167.7 | 309.4 |
| Pressure/bar | 7.2 | 7.17 | 7.16 | 1.15 | 1.13 | 1.08 |

It was complicated to design the plate-fin heat exchanger, and it was difficult to design the channel. Air separation industry had developed feasible design calculations and procedures, such as the MUSEI calculation procedures and the U.S. SW procedures. Helium was the only working gas when the plate-fin heat exchanger operating below the liquid hydrogen temperature. Due to the lack of helium property data, MUSEI procedures couldn’t design a helium heat exchanger directly. The special design program for a helium cryogenic heat exchanger had been developed, and the helium physical parameters were introduced.

The design procedures were used for how to determination the fin types, the channel arrangement and heat transfer area. Detailed steps were mentioned as follows.
1) The fin types were selected and the geometric parameters of the fins were determined;
2) The integral average temperature difference was calculated;
3) The mass flow rate was determined, and the amount of channels and the effective width were designed, based on the coefficient of heat transfer and fluid resistance;
4) According to the principle of channel layout, the channel arrangement was determined;
5) The effective length of the heat exchanger were determined, including as below,
   i. The numbers of criteria of Re, St and Pr were calculated;
   ii. The fin efficiency and the surface efficiency were calculated;
   iii. The heat transfer coefficient K was calculated;
   iv. The heat transfer area was calculated;
   v. The fluid pressure loss was calculated.

For example, the calculated results were shown in Table 3, which was a helium cryogenic heat exchanger with the liquid nitrogen pre-cooling. The detailed parameters in different fluid channels were all described.

Table 3. Calculation results of a helium cryogenic heat exchanger with the liquid nitrogen pre-cooling

| **Main Heat Exchanger 1** | | | | | |
|---|---|---|---|---|---|
| Stream | | | A | B | C |
| Fluid Description | | | He | He | $LN_2/N_2$ |
| Type of Stream | | | Hot | Cold | Cold |
| Total Flow | | Kg/h | 273.6 | 273.6 | 36.1 |
| Molar Weight | | | 4.003 | 4.003 | 28.01 |
| Temperature In/Out | | K | 310/82 | 79.63/298 | 77.9/298 |
| Operating Pressure | | MPa(a) | 0.72 | 0.115 | 0.108 |
| Heat Exchanged Per Stream | | KW | -90.2 | 86 | 4.2 |
| Max Allow Pressure Drop | | KPa | 4 | 10 | 3 |
| Design Temperature | | K | 438/15 | 438/15 | 438/15 |
| Design Pressure | | MPa(g) | 1.32 | 0.15 | 0.15 |
| Parting Sheet Thickness | | 1.6mm | Outside Sheet Thickness | | 5 mm |
| Number of Passages | | | 21 | 36 | 6 |
| Fin | height × thick mm × mm | | 6.35X0.18 | 6.35X0.15 | 5.0X0.15 |
| Exchange | Density | FPI | 909 | 909 | 909 |
| Fins Efficiency | | | 92% | 84% | 94% |
| K | $W / m^2 \cdot K$ | | 438 | 375 | 134 |
| Heat Transfer Area | | $m^2$ | 133 | 228 | 32 |
| Design Pressure Drop | | KPa | 2.8 | 7.5 | 1.8 |
| Nozzle Size In/Out | | mm | 80/50 | 80/100 | 15/25 |

The shape of the fins was selected according to the performance of the fluid and operating conditions. In the large scale helium refrigeration cryogenic equipments, the temperature difference between the hot and the cold fluids was small. The serrated fin, also known as high-performance fin was appropriate for this counter-flow cryogenic heat exchanger, which detailed structure was described in the first reference. The heat transfer coefficient of serrated fins could be increased by more 30% than the straight fins.

The channel design was the key issue of the plate-fin heat exchangers, because the channel allocation and arrangement directly determined the plate-fin heat exchanger performance. If the channel was arranged improperly, the imbalance of local heat would be caused and the heat exchanger efficiency would be reduced.

As shown in Table 4, the experimental results were accordant with the design simulations. The temperature difference between the warm and cold fluids on the hot end of the cryogenic heat exchanger was tested, which relative error between the experimental value and the designed value was less than 2.5%.

Table 4. The simulation and experimental results without the liquid nitrogen pre-cooling

| | | 1 | 2 | 3 | 4 | 5 | 6 |
|---|---|---|---|---|---|---|---|
| TEMPERATURE K | DESIGN | 313 | 171.4 | 24.55 | 20 | 167.7 | 309.4 |
| | TEST | 284.95 | 188.1 | 24 | 19.5 | 184.2 | 280.8 |
| | SIMULATION | 284.95 | 188.1 | 24 | 19.5 | 184.45 | 281.08 |
| PRESSURE BAR | DESIGN | 7.2 | 7.17 | 7.16 | 1.15 | 1.13 | 1.08 |
| | TEST | 6.77 | 6.72 | 6.67 | 1.13 | 1.1 | 1.07 |
| | SIMULATION | 6.77 | 6.75 | 6.73 | 1.13 | 1.115 | 1.086 |

## 3. MANUFACTURING PROCESS IMPROVEMENTS

Vacuum aluminum brazing process has been widely used in plate-fin heat exchanger manufacturers. For the helium cryogenic heat exchanger, the leak is the most important quality defects, because the high vacuum insulation allowed the leak rate requirement is lower than $1.0\times10^{-10}$ Pa·m$^3$/s. The leak rate in the ordinary heat exchangers used in air separation devices was often only $1.0\times10^{-7}$ Pa·m$^3$/s. Therefore some special aluminum brazing processes were required in the production of helium cryogenic heat exchangers.

In order to obtain good brazing quality, the components on the surface of the oxide film and grease should be thoroughly cleaned. Oxide film was the origin of pores and slags, because it easily absorbed moisture and then prevented the brazing seam. Oxide film was wiped off using the method of specific lye and acid chemical cleaning. The machining accuracy of the component itself could also cause the brazing defects. For example, brazing seam gap would cause weld brazing seam discontinuities phenomenon between the fins. Each component surface roughness also affected the capillary force of the flow of the brazing filler metal. In the process of vacuum brazing, the brazing temperature and holding time were the most important process parameters, which directly influenced on the melting of the solder and caulking effect.

In the manufacture of helium cryogenic heat exchangers, the vacuum in the furnaces, was the most important impact of the quality of brazing factors, which should be higher than the degree of vacuum of $1.0\times10^{-3}$ Pa. In the process of brazing heating always accompanied by gas release, which affects the vacuum. The degree of vacuum was most difficult to control process parameters. An effective method was adopted to trap water vapor in a vacuum furnace using a liquid nitrogen cold trap before the mechanical pump. According to the above brazing process, the helium plate-fin heat exchanger were successfully developed with a leak rate of $1.0\times10^{-10}$ Pa·m$^3$/s.

## 4. CONCLUSIONS

A helium plate-fin cryogenic heat exchanger had been designed and built, with a leak rate of $1\times10^{-10}$ Pa·m$^3$/s. Combined with helium physical parameters, a helium cryogenic heat exchanger design procedures was developed. The fin types and the channel arrangement were the key issues of the plate-fin heat exchanger, which directly determined the performance. The experimental results were accordant with the design simulations. In order to reduce the leakage rate of the of heat exchangers, a serial vacuum brazing process had been improved, including the surface treatment, the brazing temperature, holding time and the high vacuum, and so on.

## 5. REFERENCES

Chen C.Q., Shen Y.H. 1993, *Cryogenic heat exchanger*, Machinery Industry Press, Beijing.148 p

Wang H.S. 1984, *Plate-fin heat exchange* , Chemical Industry Press, Beijing. 246 p

Ji X.D.1998, Progress on the plate-fin heat exchangers, *Temperature and Specialty Gases*. (1): 22-27.

Sun R., Ma Y., Yi W. G. J. 2009, Leakage of vacuum brazing of aluminum alloy plate heat exchanger, *Light Alloy Fabrication Technology.* 37 (3) :47-50.

# POSTER SESSION
# - LIQUID HYDROGEN

025

# Cryogenic hydrogen storage in highly porous materials – A modelling approach – (Extended Abstract)

**Schlemminger Ch., Naess E., Bünger U.**

Department of Energy and Process Engineering, Norwegian University of Science and Technology,
Trondheim, Norway

Sustainable hydrogen as energy carrier can be a promising way to reduce carbon dioxide emissions and meet user requirements such as low cost, long range travel, quick and easy filling capacities in the automotive sector. Therefore, the automotive industry has invested substantial efforts to develop and make available such technologies. There are several possible storage options for hydrogen, e.g. as compressed gas, as liquid, ab- and adsorption, and cryo-compressed. At NTNU -Trondheim an investigation of heat and mass transfer in cryogenic adsorption hydrogen storage with highly porous materials is ongoing.

To predict the transient storage behaviour a three dimensional numerical model is under development. The implementation of adsorption characteristics for the used adsorbent (Fe-BTC-xerogel) presented in [1] is crucial for successful modelling. Two approaches, namely Langmuir and Sips models are compared to implement the sorption characteristics into the numerical model. The Sips model is a purely empirical approach established in 1948 [2] and is based on derivation of an integral equation of the local Langmuir isotherm equation [2]. Therefore, the approach covers the average of the local Langmuir isotherm equation over an energy distribution at the surface. The applied energy distribution follows a Gaussian shape [2]. This leads to an additional exponent in the equation compared to the Langmuir approach, which can be treated as a fit parameter and represents the surface heterogeneity of the adsorption material. In addition the saturation capacity of the adsorbent is defined as a temperature dependent variable. Therefore, an additional fit parameter is present, which can be applied in the Langmuir approach as well. The details of the equations can be found in [2]. A least squared error minimisation is applied to find the optimal fit parameters for the Langmuir and the Sips approaches.

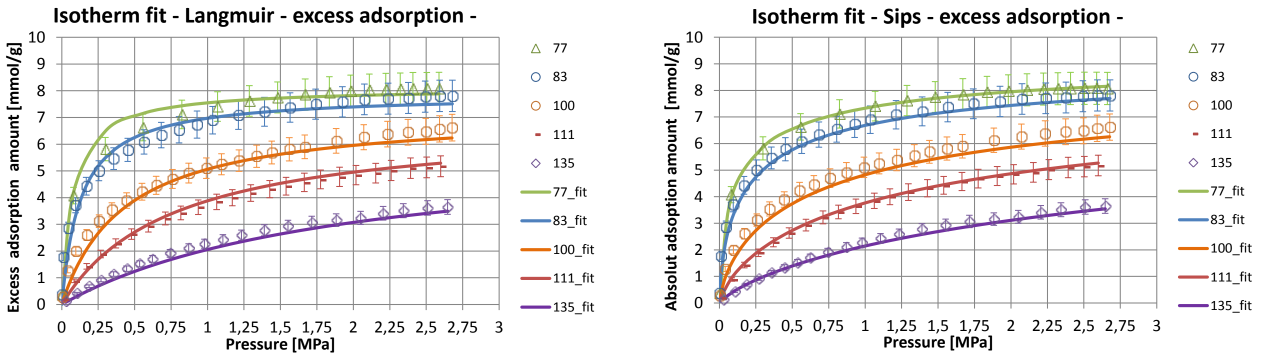

Figure 1 a) Langmuir isotherm fit of excess adsorption Fe-btc-xerogel (residual=6.32)

b) Sips isotherm fit of excess adsorption Fe-btc-xerogel (residual =1.47)

Figure 1 visualizes the isotherm fits (coloured lines) of the two approaches for five isotherms from 77 K to 135 K up to 2.6 MPa in comparison to the measured hydrogen excess uptake isotherms with error bars (coloured circles). A typical working range of a cryo-adsorption storage will be in this temperature range and in a pressure range of 0.2 MPa to 2.5 MPa. At 77 K a typical IUPAC type I isotherm with a steep increase at low pressure followed by a plateau at high pressure is observed. Whereas, at 135 K the smooth increase of the excess adsorption amount even at low pressures occurs and at 2.6 MPa still no adsorption maxima is reached.

The quality of the parameter fits are expressed in the residual (square error sum). It shows clearly the advantage of the Sips parameter fit, where the residual is 1.47 compared to the Langmuir residual with a value of 6.32. This indicates the importance of the surface heterogeneity of the material. As visible in Figure 1 a) the major uncertainty of the Langmuir isotherm fit occurs at low temperatures e.g. 77 K and 83 K and in a pressure range between 0.2 MPa and 1 MPa. In comparison to this the Sips approach fits better in this region, which leads to the lower residual.

Therefore, the Sips adsorption model was selected to describe the thermodynamics of the adsorbent / adsorbate interaction. Relevant thermo-physical properties of the adsorbate used in the model were measured at NTNU and published in [3]. A local thermal equilibrium between the gas-, adsorbed- and solid phase was assumed simplifying the mathematical model. The complete model was implemented in to the commercial finite element code COMSOL Multiphysics® Version 4.2a. For the selected geometry shown in Figure 2 and 3, a 2D axial symmetric approach was chosen to reduce amount of computational work. Furthermore, the boundary conditions e.g. axial symmetry, wall temperature, in-/outlet mass flow rate adsorption properties and initial conditions together with thermo-physical properties were set.

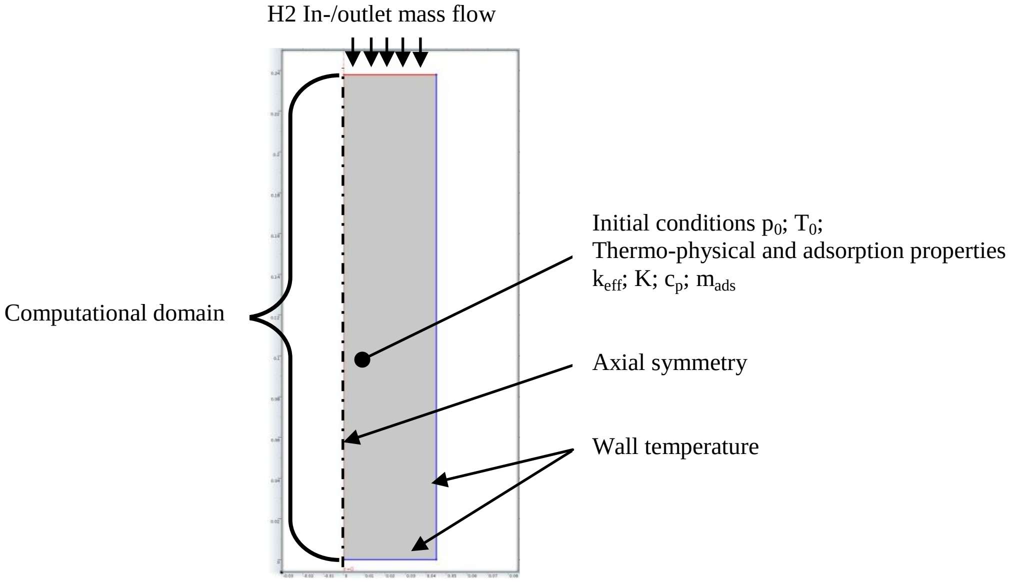

Figure 2 Computational domain and boundary conditions

For model validation a test setup was designed. This setup consists of a gas handling section for charging and discharging of the tank, including hydrogen pre-cooling to 80 K. In addition a data acquisition section (NI cFP) logs mass flow rates, pressures and temperatures in the test section during the measurements with a time resolution of 0.5 s. Measurement uncertainties are given in [3]. Furthermore, the test section, as shown in Figure 3, consists of cylindrical inner tank (Aluminium 1100) and an outer tank (SS 316). This test section is fully covered by liquid nitrogen at ambient pressure during measurements. A separate hydrogen in-/outlet for the inner tank allows independent hydrogen mass flow measurements for the inner tank. The coiled aluminium (Aluminium 1100) tube around the inner tank is filled with liquid nitrogen during operation. Enclosure, the outer tank with the massive top flange works as a pressure containment and withstands pressures up to 6 MPa. Only the inner tank is filled with highly porous material, therefore only the results for the inner tank are taken in to account.

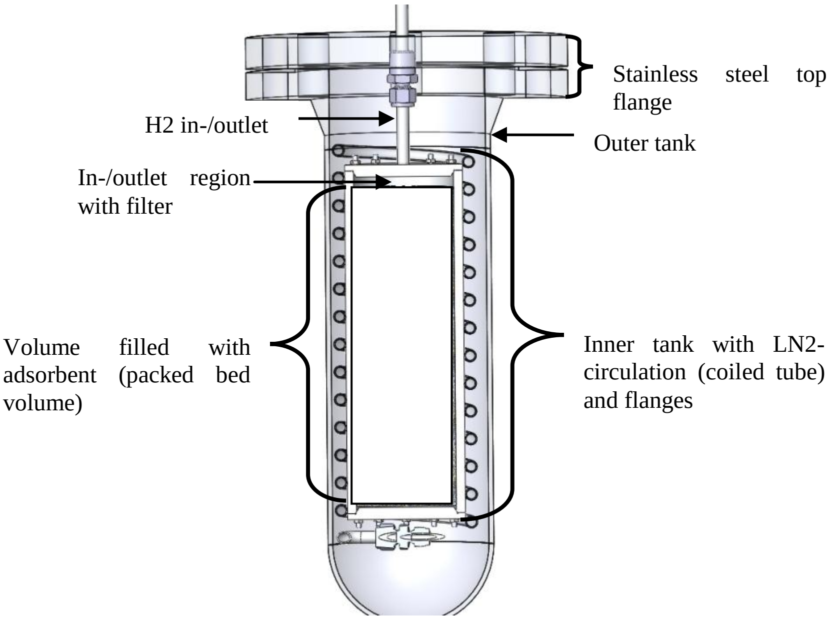

Figure 3 Test section

Dimensions of the part filled with adsorbent are outer diameter 100 mm, inner diameter 90 mm a total height of 238 mm, giving a total packed bed volume of 1.514 l. The total internal inner tank volume is 1.527 l. In the upper region a space of 12 mm is used for a filter element (3 mm), which shall prevent material losses due to convective transport at the in-/outlet region and to manifold the hydrogen. Furthermore, the spot-like influence of the cold (~80 K)H2 gas inlet stream is reduced by the 10 mm inlet region. The modelling domain shown in Figure 2 has the dimensions of the volume filled with adsorbent.

In the poster the status of modelling work in comparison to experimental data is shown to demonstrate the validity of the modelling approach. Due to low thermal conductivity of the adsorbent bed an effective heat management system is crucial to fulfill the user requirements of e.g. automotive customers.

Funding of the work by the European collaboration program HyCo and The Research Council of Norway is gratefully acknowledged. We also acknowledge the support from Statoil ASA for funding the conference participation.

## 6. REFERENCES

[1] Schlichtenmayer, M. 2012, Wasserstoffspeicherkapazität poröser Materialien in Kryoadsorptionstanks, *PhD thesis*, University of Stuttgart

[2] Do, D. D. 1998, *Adsorption analysis: equilibria and kinetics vol. 2,* Imperial College Press, London, 49-64

[3] Schlemminger, C. et al., 2012, Advanced MOFs for hydrogen storage in cryo adsorption tanks, *WHEC 19th*, Toronto, June 3-7 2012

069

# The Development of Methods and Means of Gasification of Liquid Hydrogen under Supercritical Parameters (Extended Abstract)

**Cheremnykh O.Ya.**

JSC «Uralcryomash», Nizhny Tagil, Russian Federation, Sverdlovsk region, Vostochnoye shosse, 24

For the last ten years hydrogen is actively used as fuel for hydrogen-oxygen electrochemical generators power supply system (ECG PSS) of both transportation vehicles and stationary installations in different branches of industry: in energetics of space ships and apparatus, sea ships and deep sea objects, electric actuators of cars, loaders and tractors in the USA, Germany, Japan, the Great Britain, Russia.

The storage and preparation of reagents system is the obligatory component of any type of power plant on the ECG base.

Purity reagents, pressure, temperature and expense of supply hydrogen and oxygen influence the energetic characteristic of ECG. Requirements for purity reagents are explained by accumulation of admixtures on the ECG electrodes that decreases the energetic characteristic of ECG.

In consequence of the change of the dynamic load of the ECG PSS the expense of reagents supplied for ECG has got the difficult changing in time characteristic.

The influence on the voltage-current characteristic of the fuel element of the ECG hydrogen pressure led to the necessity of creation of the pressure 1,1÷2,5 MPa before the energy module for long period of time.

The total combination of these requirements led to the necessity of creation of the hydrogen storage and gasification system of both before critical and supercritical parameters in storage tanks and gasifiers for hydrogen.

The gasifier of liquid hydrogen with supercritical parameters (photo 1) in working conditions is considered as the system of variable mass, that is the open system, in which the process of exchange of work, heat and mass of working body with the environment is happened.

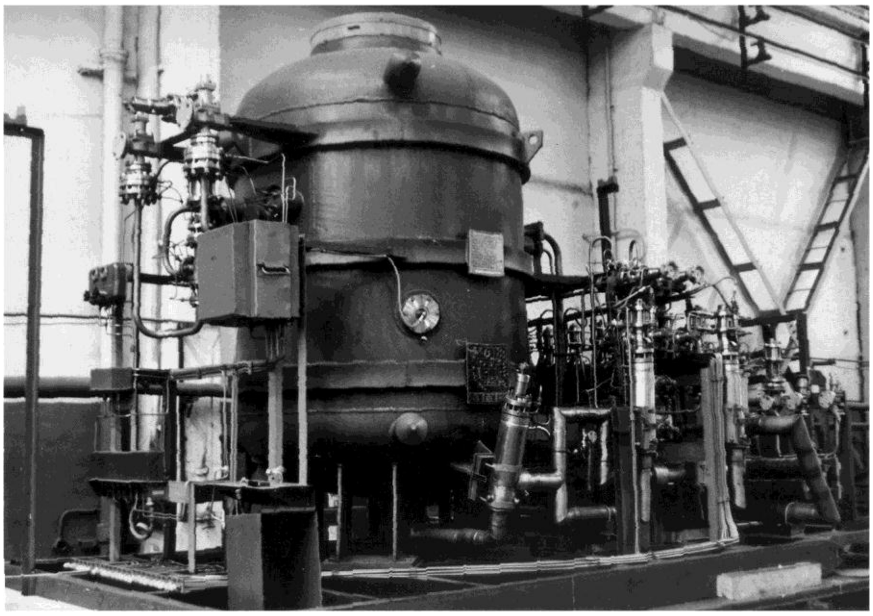

Photo 1. Overview of gasifier of liquid hydrogen with supercritical parameters

The account of heat and mass exchange in the gasifier was made from the first beginning of thermodynamics for open system.
The distinguish feature of the gasifier is regulated heat supply for hydrogen in the storage tank during the discharge of product to consumer depending on changing pressure what is achieved by the introduction of the internal and two external heat exchangers into the schematic circuit.

That constructive solution allows redistributing hydrogen expense delivered to consumer in such way that the part of hydrogen expense is used for the heating of liquid in the capacity to support the isobaric flow of the product from the liquid in the process of its discharge to consumer.

In the present contribution there is the description of the mechanism of convey of heat flow and thermodynamic of the working process of the gasifier (the technical characteristics are given in the table 1) according to the problem of hydrogen storage under supercritical parameters, the quantity characteristics of the changing thermodynamic parameters during the working process of the gasifier are determinated, the results of gasifier's tests are given.

The table 1. The technical characteristics of the gasifier of liquid hydrogen with supercritical parameters

| Parameters | Values |
|---|---|
| Medium | liquid hydrogen |
| Total capacity of the vessel, $m^3$ | 2,0 |
| Working pressure in the vessel, MPa | 2,5 |
| Hydrogen mass in the vessel, kg | 126 |
| Hydrogen losses at evaporation, % per day | 1,0 |
| Type of the thermal insulation | the multilayer-vacuum thermal insulation |
| Material of the vessel | Stainless steel 12x18H10T |
| Material of the shell | Steel 09G2C |
| Hydrogen expense from the capacity, kg/h | 2,16 |
| Mass of the capacity, kg | 3 300 |
| Overall dimensions, mm: | |
| - length | 1 700 |
| - width | 1 700 |
| - height | 2 835 |
| Time of pressure rise till working pressure 1,8 MPa under expense o heating medium 0,005 kg/sec., min | 5÷7 |
| Hydrogen consumption under pressure 1,7÷1,9MPa, nl/min | 400÷450 |

## 7. REFERENCES

[1] Rytov S.M., Krastov Yu. A., Tatarskii V.I., Principles of Statistical Radiophysics. Springer-Verlag: New York, 1987.

[2] Domoto, G. A., Boehm, R. F. & Tien, C. L., Experimental investigation of radiative transfer between metallic surfaces at cryogenic temperatures. J. Heat Transfer 92 (1970), 412.

[3] Hargreaves, C. M., Anomalous radiative transfer between closely-spaced bodies. Phys. Lett. A 30 (1969), 491–492; Radiative heat transfer between closely spaced bodies, Thesis, Univ. of Leiden, 1973.

[4] Polder D, van Hove D, Theory of Radiative Heat Transfer between Closely Spaced Bodies, Phys. Rev. B 4 (1971) 3303-3314.

[5] Pendry J.B., Radiative exchange of heat between nanostructures, J. Phys.: Condens. Matter 11 (1999) 6621–6633.

[6] Joulain K, Mulet J. P, Marquier F, Carminati R, Greffet J.-J, Surface electromagnetic waves thermally excited: Radiative heat transfer, coherence properties and Casimir forces revisited in the near field, Surface Science Reports 5 (2005), 59-112

[7] Basu S., Zhang Z. M., Fu C. J., Review of near-field thermal radiation and its application to energy conversion, Int. J. Energy Res. 33 (2009), pp. 1203-1232.

[8] Francoeur M., Mengüc M. P.¸ Vaillon R., Solution of near-field thermal radiation in one-dimensional layered media using dyadic Green's functions and the scattering matrix method, J. Quantitative Spectroscopy & Radiative Transfer 110 (2009), 2002-2018.

[9] Biehs S. A, Ben-Abdallah P, Rosa F. S. S, Nanoscale Radiative Heat Transfer and Its Applications. In: Infrared Radiation, Edited by Vasyl Morozhenko, ISBN 978-953-51-0060-7, InTech Publisher 2012, Chap. 1.

[10] Rousseau E., Siria A., Jourdan G., Volz S., Comin F., Chevrier J., Greffet J.-J., Radiative heat transfer at the nanoscale, Nature Photonics 3 (2009) 514-517.

[11] Ottens R. S, Quetschke V, Wise S., Alemi A. A, Lundock R, Mueller G., Reitze D. H., Tanner D. B, Whiting B. F, Near-Field Radiative Heat Transfer between Macroscopic Planar Surfaces. Phys. Rev. Lett. (2011) 107, 014301

[12] Musilova, V., Hanzelka, P. Kralik, T., Srnka, A., Low temperature radiative properties of materials used in cryogenics. Cryogenics 45 (2005), 529–536

[13] Hanzelka P, Kralik T, Maskova A, Musilova V, Vyskocil J, Thermal radiative properties of a DLC coating. Cryogenics 48 (2008), 455-457.

[14] Kralik T, Hanzelka P, Musilova V, Srnka A, Zobac M, Cryogenic apparatus for study of near-field heat transfer. Rev. Sci. Instrum. 82 (2011), 055106

[15] Derjaguin B. V, Abrikosova I. I, Lifshitz E. M, Direct measurement of molecular attraction between solids separated by narrow gap, Quart. Rev. 10, 295 (1956).

[16] Biehs S. A., Greffet J.-J, Influence of roughness on near-field heat transfer between two plates, Phys. Rev. B 82 (2010), 245410.

082

# The development of methods and means of evacuation of hydrogen from tanks of a space flying apparatus under supercritical parameters (Extended Abstract)

**Cheremnykh O.Ya.**

JSC «Uralcryomash», Nizhny Tagil, Russian Federation, Sverdlovsk region, Vostochnoye shosse, 24

In the process of the preparation for start and after-flight service of a space orbital ship, that uses hydrogen-oxygen electrochemical generators as source of electric power, liquid hydrogen is under supercritical parameters in storage tanks of the preparation and gasification of reagents system.

In the case of postponement or failure of start and also an official after-flight service of an orbital ship there is the problem of evacuation of hydrogen from tanks of the system of energy supply of the ship under supercritical parameters.

Depending on the program of the flight of the orbital ship the primary quantity of hydrogen in tanks may be different (50%, 75%, 100% - fuelling), but under returning of the orbital ship on the landing complex the remainder of hydrogen in tanks of the ship will be 10%-15% from the primary quantity.

The number of tanks with hydrogen and mass of component in them of the storage and preparation of reagents system of the power supply system of the orbital ship is determined by the program of flight and according to that may be different.

At the first moment of discharge of hydrogen to ground technological systems the condition of hydrogen is determined by the following thermophysical properties: pressure, temperature and density of component and consequently by the physical condition of hydrogen (liquid, gas or intermediate condition: vapor-liquid, vapor).

Depending on that condition of hydrogen in tanks of the orbital ship they use the appropriate technology of discharge of hydrogen to ground technological systems of launch and landing complexes.

At the period of after-start works on the rocket-space complex there is the same problem of evacuation of hydrogen under supercritical parameters from the storage tank of the ground technological system.

The schematic circuit of discharge of hydrogen from 2 $m^3$ ground liquid hydrogen storage tank, with working pressure 2,6M Pa, the coefficient of filling 0,85 and hydrogen mass 119 kg is given at the picture 1.

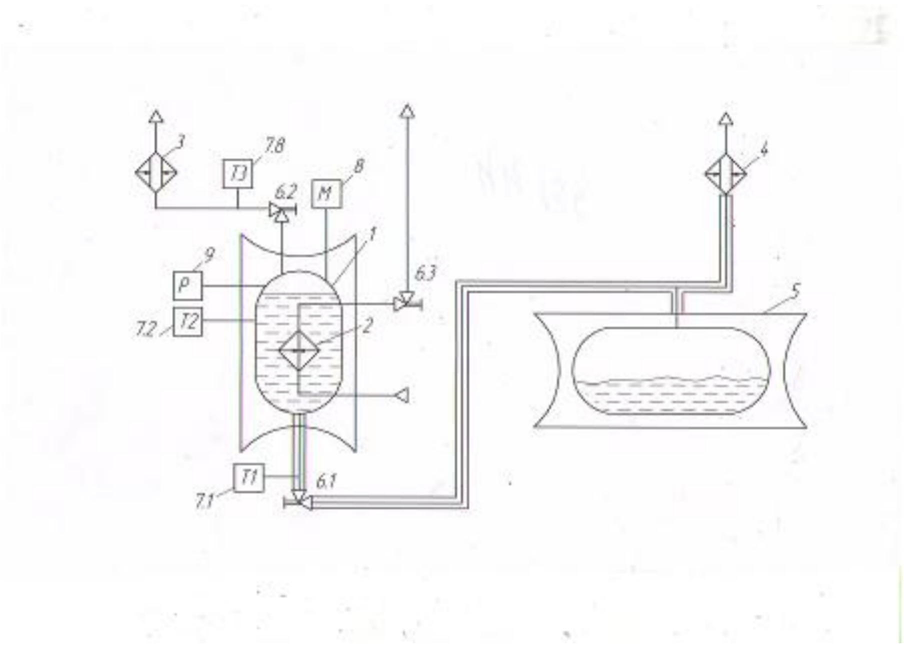

Picture 1. The schematic circuit of evacuation of hydrogen from the storage tank under supercritical parameters: 1 – storage tank; 2 – heat exchanger with hydrogen heat carrier; 3 - heat exchanger of drainage main line; 4 - heat exchanger of drainage main-line; 5 – drain tank; 6.1, 6,2, 6.3 – the flow components; 7.1, 7.2, 7.3 – temperature sensors; 8 – sensor of hydrogen mass.

The primary condition of hydrogen in the tank before discharge is characterized by following parameters: pressure – 2,6 MPa, temperature – 31,2 K. Under such parameters we have got hydrogen in tank expressed as one-phase liquid all over the tank volume.

According to "T-S" diagram we find pressure of separating of phase under crossing through the line of saturation. Under such parameters we have got pressure – 0,7 MPa, density of the product – 56,8 kg/m$^3$, specific volume – 35,5 cm$^3$/moll and mass of remaining liquid – 113,6 kg.

Thus, at first we discharge hydrogen to drainage main-line with heat exchanger 3 to pressure of separating of phase 0,7 MPa, after that we discharge hydrogen over discharge main-line to drain tank 5 and then we discharge hydrogen through heat exchanger 4 on drainage plug.

The condition of hydrogen in the tank is controlled by pressure sensor 9, temperature sensor 7.2 and sensor of hydrogen mass 8. Temperature of hydrogen in the process of discharge and in the drain tank is controlled by temperature sensors7.1 and 7.3.

At the primary coefficient of filling of the tank K=0,5 mass of hydrogen is 69,9 kg and pressure is 2,6 MPa, temperature of product is 38,7K. Under such parameters we have got hydrogen expressed as gaseous state all over the tank volume.

According to "T-S" diagram the crossing over the line of saturation is made under these primary parameters and under pressure 1,3 MPa (density of the product is 28,8 kg/cm$^3$, i.e. we have got the condition of hydrogen expressed as gas all over the tank volume).

In that case we carry out evacuation of hydrogen from the tank through the drainage main-line, then on heat exchanger 3 and on drainage plug to creation of minimum excess pressure 0,13÷0,15 MPa in the tank.

# POSTER SESSION
# - LNG

091

# Computer Program for Simulating the Rollover Phenomenon during the Storage of the Stratified Layers of Liquefied Natural Gas

**Belgacem A.*, Rebiai R.*, Belmedani M.***

* USTHB-Faculté Génie Mécanique et Génie des Procédés
Laboratoire Phénomènes de Transfert
Equipe Cryoprocédés
BP.32 El Alia-Bab Ezzouar-16111- Algiers- Algeria

## ABSTRACT

The rollover phenomenon occurs when two stratified layers of Liquefied Natural Gas (LNG) with different temperatures and/or densities are stored for a long period in the same tank. The stratification will appear when the light layer is stored above the heavier one, or when the cold layer is stored on the warm one.

The incoming of heat from the surroundings and from the bottom of the tank is the source of the evaporation of both layers. As the upper layer in contact with the free surface of the tank, the evaporation of its components (the light hydrocarbons and the nitrogen) causes an increase in its density. However, this heat will be trapped in the lower layer which can't evaporate, so the density will stay slightly constant. After a period of storage the two densities will equalize, this result in a rollover and a sudden mixing, followed by an important evaporation called « boil off ».

In fact, our study is based essentially on the comprehension and interpretation of the phenomenon of rollover and its evolution in the time. It allowed us to develop a mathematical model leading to a computer program whose purpose is to predict in advance the time of the mixing and the intensity of evaporation rates.

The program can also be performed to evaluate the variation of the properties (temperature, density, compositions ...) of each layer before, during and after the rollover.

For validation of the model we compared our results with two existing theoretical models (HMS, Sugawara) and the practical results of the best documented incident occurred in the complex of La Spezia (Italy).

From the results of the simulation, solutions can be proposed in order to predict and possibly prevent the development of rollover due to the change of the temperature and/or density in storage conditions.

## 1. INTRODUCTION

In the recent decades Natural Gas has become one of the most coveted sources of energy. Through its behavior towards the environment, its heating value and its appreciable abundance, natural gas continues to compete with the other forms of energy (oil, coal, nuclear, renewables), and presents the best alternative.

The large-scale storage of LNG from various sources with different compositions reveals some unexpected phenomena not yet explained, related to the instability of the liquid, and whose consequences can be disastrous.

Among the most important phenomena, subject of this study, we distinguish the rollover, which corresponds to a vortex mixture, representing a long and fairly complex process describing the changeover of stratified layers of LNG as a result of equalization of densities.

This phenomenon is accompanied by a sudden increase in the rate of surface evaporation, which in some cases, may have fatal effects on plants.

Although the notion of stratification was observed as developed natural phenomenon in the atmosphere and lakes [1], its use is much more important in the LNG storage tanks.

By definition, stratification is the superposition of two or more layers of a similar liquid but with different physical characteristics. These layers are separated by one or more interfaces of zero thickness.

In this sense there are two types of stratification: those induced by filling and those induced by nitrogen or autostratification.

Mathematical models for predicting mixtures are used to simulate the behavior of LNG storage tanks and take into account the heat and mass balance between the stratified layers during the storage of LNG.
The use of such models for predicting the rollover is very complicated because the coefficients of heat and mass transfer across the interface liquid - liquid are not sufficiently well established.
In this sense, experimental results obtained with salt solutions [1], were used to predict the corresponding values in LNG.
Among the most studied models belongs to Chatterjee and Geist [2] [3] which was the first mathematical models defining the phenomenon of rollover. The authors, in their first model consider LNG as a mixture of two components: methane and ethane. The other hydrocarbons and nitrogen are not considered. They subsequently modified their model by taking into account the influence of the nitrogen which is considered as the most volatile component [4].
The Model of Heestand, Meader and Shipman (HMS) [5] differs from the previous in the consideration of the coefficients of mass and heat transfer across interfaces; in fact the authors replaced the coefficients determined by Turner for the saline solution by others approximations.
The model of Y. Sugawara et al. [6] is simulated from an experimental study using Freon as fluid of simulation. The authors, in this model, are mostly interested to the interface conditions between the upper and lower layers

## 2. MATHEMATICAL MODELING

After studying and analysing the different mathematical models proposed in the literature and after taking into account the results of their simulations, we proposed, on the base of similar assumptions, a mathematical model defining the LNG as a multi component bringing it closer to reality.
For the determination of heat and mass balances, we consider a storage tank of known dimensions, in which coexist in unstable stratification two layers of LNG.
The model involves a liquefied natural gas (LNG) composed by five (5) components (methane, ethane, propane, butane and nitrogen).
The stored LNG has two distinct layers with different properties separated by a rigid interface of zero thickness (figure 1).

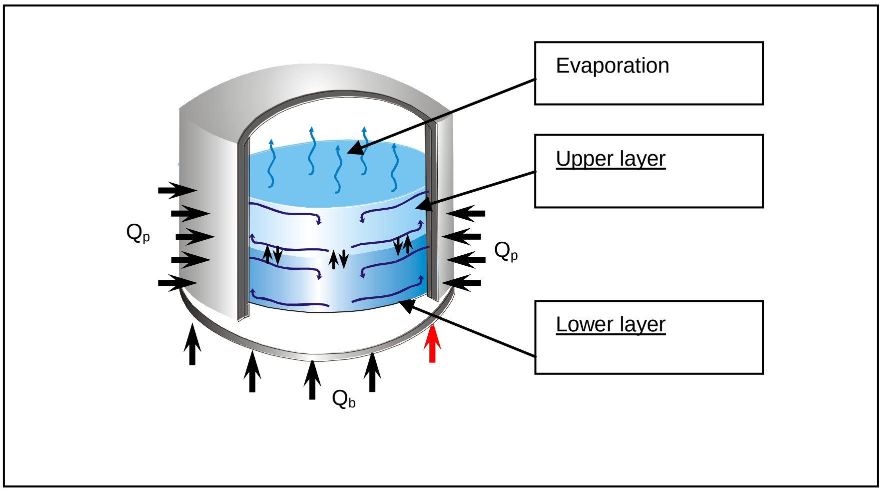

Figure 1. Stratified layers of LNG during the storage

### 2.1. Assumptions :

To simplify the problem it is necessary to express some assumptions:

- The physical properties of the two layers are taken as averages
- The interface is stationary implying stable layer heights.

### 2.2 Equations

The reasoning is based on a dimensional model.
From these data the mass and energy balances for the two layers are written as follows:

***Energy Balance***

- Upper layer:

$$\frac{\delta}{\delta t}\left(AH_H\rho_H Cp_H T_H\right) \;=\; \pi D Q_P H_H + 0 + A\rho_H Cp K_T\left(T_B - T_H\right) - AL_V b$$

- Lower layer:

$$\frac{\delta}{\delta t}\left(AH_B\rho_B Cp_B T_B\right) \;=\; \pi D Q_P H_B + AQ_B - A\rho_B Cp K_T\left(T_B - T_H\right)$$

***Mass Balance***

- Upper layer:

$$\frac{\delta}{\delta t}\left(AH_H\rho_H\frac{M_i}{M_H}y_i\right) = A\rho_H K_M\left(x_i - y_i\right) + Aby_i$$

- Lower layer:

$$\frac{\delta}{\delta t}\left(AH_B\rho_B\frac{M_i}{M_B}x_i\right) = -A\rho_B K_M\left(x_i - y_i\right)$$

Where :

| | |
|---|---|
| A | Surface, [m$^2$] |
| Cp | Specific heat, |
| D | Diameter of the tank , [ m] |
| H | Height of the layer,[ m] |
| $K_M$ | Mass transfer coefficient across the interface |
| $K_T$ | Heat transfer coefficient across the interface |
| $L_V$ | Latent heat, [kcal/m$^2$K] |
| M | Masse, [kg] |
| $Q_p$ | Heat from surrounding, [kcal/m$^2$h] |
| $Q_B$ | Heat from the bottom, [kcal/m$^2$h] |
| T | Temperature of the layer, [ K] |
| x | Molar fraction of lower layer |
| y | Molar fraction of upper layer |

*Subscripts*

| | |
|---|---|
| B | Bottom layer |
| H | Upper layer |
| i | Component i |

The established mathematical system for the five components of LNG includes twelve (12) equations and thirteen (13) unknowns (molar fractions (compositions), temperatures of each layer, and the rate of evaporation in the upper layer). To remove the indetermination, we use Hashemi and Wesson relation to estimate the rate of evaporation noted b.

$$\boldsymbol{b = 0.0672\frac{\rho_H C_{pH}}{L_V}\left(\frac{g\alpha k^2}{\rho\,\mu\,C_p^2}\right)^{1/3}\left(T_H - T_{sat}\right)^{4/3}}$$

Where

| | |
|---|---|
| $\rho$ | Mass density, [kg/m$^3$] |
| $\alpha$ | Coefficient of thermal expansion |
| $\mu$ | Dynamic viscosity |
| b | Boil off rate, [ kg/h] |
| k | Thermal conductivity |
| $T_{sat}$ | Temperature of saturation |

To solve the system of equations of heat and mass balances we have developed a computer program (application) written in Fortran language (figure 2).

Figure 2 : program interface for rollover simulation

## 3. RESULTS AND DISCUSSION

The best documented incident on the phenomenon of Rollover is that occurred in 1971 in the terminal of La Spezia in Italy. Indeed the addition of LNG with different characteristics on the LNG heel remaining in the storage tank, automatically led to an unstable stratification. After a period of storage, the equalization of the two densities has led to a considerable rate of evaporation. From the data provided by Sarsten [7] (Table1)

Table 1.Conditions of La Spezia simulation

| Pressure | Heat from surrounding : Qp | Heat from bottom : Qb | Tank Diameter |
|---|---|---|---|
| 1.025 kg/cm$^2$ | 6.94 kcal/m$^2$.h | 20.82 kcal/m$^2$.h | 49 m |

| | Composition (% mol) | | | | | | $\rho$ (kg/m$^3$) | T (°C) [K] | H (m) |
|---|---|---|---|---|---|---|---|---|---|
| | C1 | C2 | C3 | C4 | C5 | N2 | | | |
| Lower layer | 62.26 | 21.85 | 12.66 | 3.14 | 0.07 | 0.02 | 541.118 | -158.2 [114.356] | 12.802 |
| Upper layer | 63.62 | 24.16 | 9.36 | 2.35 | 0.16 | 0.35 | 537.316 | -154.5 [118.994] | 5.029 |

From these data we could simulate the variations of the parameters managing the phenomenon of rollover, as well as their monitoring, during and after the mixing of the stratified layers

The results are compared with two existing models, the first one (HMS) which is purely theoretical, while the second (Sugawara) combines the experimental one and the theory.

This paper concerns only the variation of the temperature and density for the two layers, as well as the rate of boil off.

The mixing is due either of the equalization of density or the equalization of temperature of the two stratified layers but not the two parameters at the same time.

### 3.1 Variation of the density

For our model, we notice a light increase in the value of the density for the upper layer, which in contact with the free surface, evaporates while releasing the most volatile component i.e the methane, this involves an increase in the composition of heavy hydrocarbons, and consequently, an increase in its density.

Theoretically, the lower layer should not change, but on the graph we notice an appreciably weak variation, this is due to the various imperfections which exist in all the industrial facilities and amongst other things the insulation.

The comparison with the first model (figure 3) shows that the shapes of the curves in the two models resemble to each other, in spite of the light change in the calculation of the initial densities.

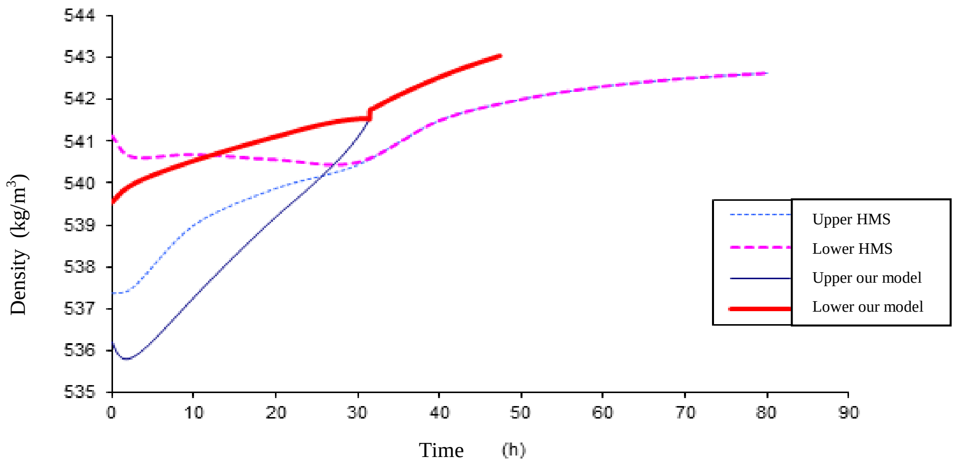

Figure 3: comparison of the variation of the density between our model and that of HMS

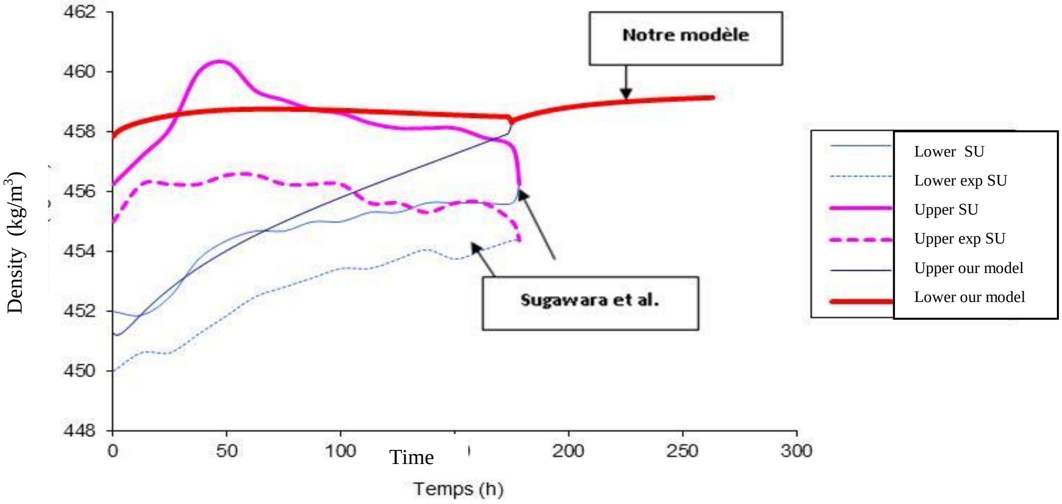

Figure 4: comparison of the variation of the density between our model and that of Sugawara

This change is due mainly to the method of calculating used; indeed, while we use the method of Klosek-McKinley for the estimate of the density, HMS use the tables of Boyles.

With regard to the second model (figure 4), it is clear that the shapes of the curves of our model coincide with those of the theoretical data cited by the authors and they are slightly spaced compared to the experimental ones. This is due also to the estimate of the density by using two different methods.

### 3.2 Variation of the temperature

Concerning the variation of the temperature, we see that in our model, the reduction in the temperature of the lower layer can be explained by the fact that heat exchange through the interface is much more important than the mass exchange. Thus, the transmission of the cold by the upper layer towards the lower layer is done more quickly than of heat coming from this latter.

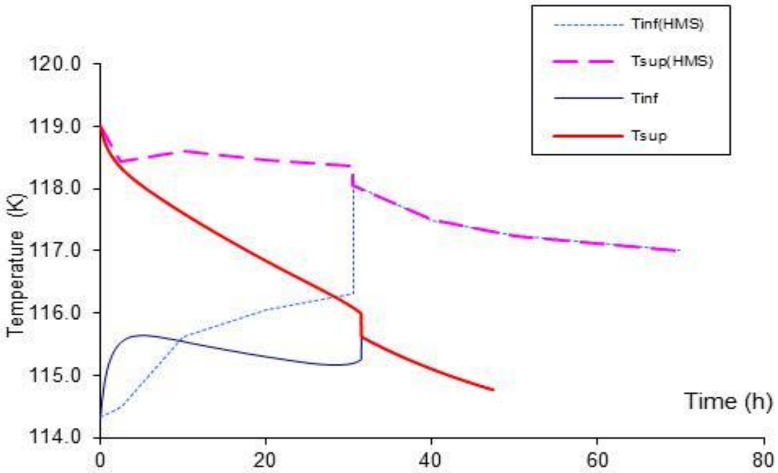

Figure 5: comparison of the variation in the temperature between our model and that of HMS

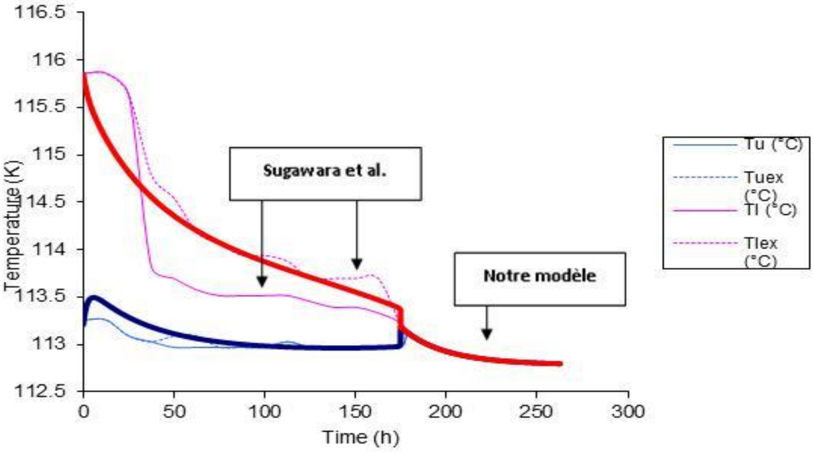

Figure 6: comparison of the variation in the temperature between our model and that of Sugawara

With regard to the comparison with HMS (figure 5), the shapes of the curves of the two models are different through the variation in the temperature from the lower layer, which is cooled in our case, while it remains practically constant for HMS model. We estimate for the explanation of this case that the heat transfer to the interface is more important than the mass transfer, which leads to this type of cooling.

While for the model of Sugawara and al (figure 6), we notice that the temperature variations of the two layers in our model are appreciably equivalent to those drawed by the authors, and more particularly with the experimental parts.

Concerning the rate of boil off we note that the peak of boil off is the illustration of the Rollover phenomenon, indeed, the sensible heat accumulated during the period preceding the Rollover is suddenly released immediately after the equalization of densities of both layers. The peak value of boil off is roughly equal to twenty times the normal rate of evaporation (Figure 7).

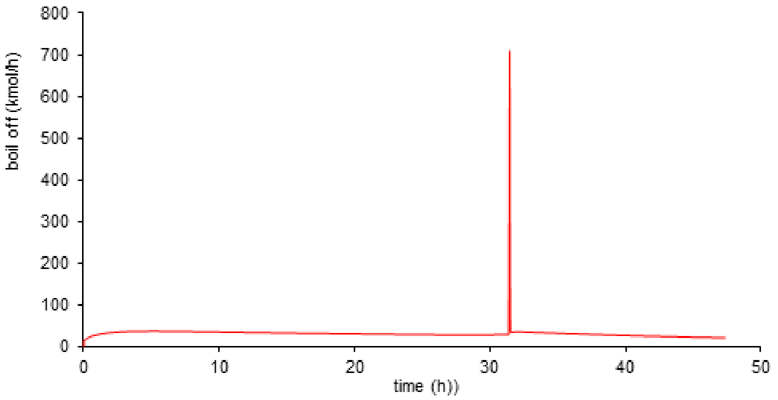

Figure 7 : simulation of the boil off before, during and after rollover 1

In reality, the return to normal evaporation does not happen instantly, but it occurs gradually, as the vapours released are discharged by the safety valve and in small quantities. In our case we assume that the entire amount of exhaust steam when released which explains the linearity of the peak of the boil off
The comparison of results obtained by simulating with those of Sarsten statements during the incident in La Spezia are given in Table 2. We see that the results from our model are closer to those recorded by Sarsten.

Table 2 : Results of simulation and comparison

| | Time before Rollover (hours) | Boil off Peak (kmol/h) | Initial rate (kmol/h) |
|---|---|---|---|
| **Our model** | **30.914** | **720.166** | **37** |
| Sarsten | 31.00 | 620 -1500 | 30.06 |

## 4. CONCLUSIONS

The model, we developed in the form of software is based on heat and mass balances of stratified layers of LNG stored or transported, approaches and significantly raised practical results in the single incident at La Spezia in Italy.
It is designed to accurately determine the two most important parameters which occur during the rollover, ie, the time of arrival of rollover and the intensity of evaporation rates during this time. It can also provide graphically the evolution of all other parameters necessary for the storage of LNG. The model realized in this study represents a reliable, more profitable and therefore less costly tool allowing users to have enough time to take decisions and appropriate action to avoid any incident that may be caused by the rollover phenomenon

## 5. REFERENCES

[1] TURNER J.S., 1974 “Laboratory experiments one doubles diffusive instabilities”, I.J.H.M.T, flight 40, N° 8, p 1870-1884, Elsevier Science Ltd, London,.

[2] CHATTERJEE NR, GEIST J.M., 1972 “The effect off stratification one boil-off spleens in LNG tanks” Pipeline & Gas Newspaper, vol. 199, pp.40-47, the USA.

[3] CHATTERJEE NR, GEIST J.M., 1972 “Nitrogen induced stratification in LNG storage tanks” A.G.A. Transmission Conference,Las Vegas, Nevada.

[4] CHATTERJEE NR., GEIST J.M., 1976“Spontaneous stratification in LNG tanks containing nitrogen” A.S.M.E. Meeting,New York

[5] HEESTAND J., MEADER J.W, SHIPMAN C.W. , 1983 “predictive model for rollover in stratified LNG tanks has”, BAITS Newspaper, flight 29, N° 2, PPP 199-207 6New York.

[6] SUGAWARA Y. & experimental Al, 1984 “study one LNG rollover using liquid Freon”, Technical Review, flight 21, n° 3.

[7] SARSTEN, J.S., "LNG Stratification and Rollover", Pipeline and Gas Journal, 199, Page: 37-42, 1972

# POSTER SESSION
# - AIR SEPARATION

023

# Mixtures on Basis of Rare Gases. Application and Methods of Production

**Bondarenko V.L.**[*]**, Diachenko O.V.**[**]**, Simonenko Yu.M.**[***]

[*] Bauman Moscow State Technical University, Moscow, Russia;
[**] Iceblick Ltd., Odessa, Ukraine;
[***]Odessa State Academy of Refrigeration, Odessa, Ukraine

## ABSTRACT

Neon, helium and heavy rare gases possess a number of unique properties and can be a part of various mixtures used in lasers, welding process, diving, medicine and precision engineering [1]. The basic methods of preparation of compound substances with specified concentration of components, including rare gases and their stable isotopes are considered in the work. The examples of the mixtures components amounts obtained by manometric and gravimetric methods are given. The areas of potential preferred use of volume and flow mixers are shown. Industrial and laboratory methods of mixtures preparation in the form of cryogenic liquids are also studied in the research.

## 1. INTRODUCTION

The growing consumption of mixtures and the variety of their composition have given rise to a great number of mixing devices of different types. The most important operational features of mixers are their metering (flow) characteristics and accuracy of the components composition. Very often the combination of the definitions of “high flow” and “high accuracy” is not possible in one mixer. For instance, the methods of analysis gas mixtures preparation are not exactly applicable for preparation of big volumes of protective gases. On the other hand, high-flow mixers are characterized by relatively high errors which are not compatible with requirements for laser and breathing mixtures. Besides, when making mixtures on the basis of rare gases and their stable isotopes, it becomes important to use saving technologies in order to use sparingly the expensive components. The study of the physical methods of compound substances preparation will expand the sphere of application of the mixing devices and will enable to make devices with the compromise between the flow and accuracy characteristics of the produced products components.

## 2. DOZERS OF CONTINUOUS ACTION

The most important application of the man-made mixtures is the creation of the protective (shielding) atmosphere. In particular, the protective features of the mixtures have helped to increase the life duration for lighting equipment, to adopt modern technologies in electric arc welding and to save natural quality of food products in pressure packages with modified gas atmosphere.

For two-component flows and multi-component flows with the flow rate of tens and hundreds of $m^3$/hour, special mixing devices are used, in which the concentration of some substances are defined by the value of hydraulic resistance of the corresponding channels. If the correlation of the pressures is higher than critical, then the gas rate through the nozzle is clearly defined by the gas parameters in the input.

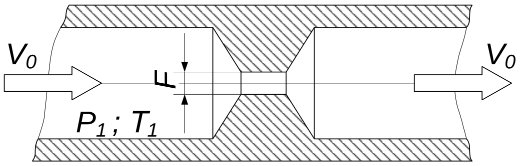

$$F = 0{,}095 \cdot \frac{V_0}{P_1} \cdot \sqrt{\frac{M \cdot T_1}{R \cdot \frac{2 \cdot k}{k+1}\left(\frac{2}{k+1}\right)^{\frac{2}{k-1}}}}, \tag{1}$$

where
$V_0$ – gas flow rate, $m^3$ (led to conditions $P_0 = 0{,}1$ MPa and $T_0 = 293$ K); $P_1$ – pressure, MPa and $T_1$ – temperature, K – gas parameters at the nozzle, $M$ – molecular mass of gas, kg/kmole; $R = 8314$ J/(кmole·K) – uni-

versal gas constant; $k$ – adiabat line (for mono-atomic gases (He, Ne, Ar, Kr, Xe) $k_1 = 1{,}67\ldots1{,}68$; for diatomic gases ($O_2$, $N_2$, $H_2$) $k_2 = 1{,}4\ldots1{,}41$; for polyatomic gases ($CO_2$, $CH_4$, $NH_3$) $k_n = 1{,}31\ldots1{,}32$.
The correlations (1) are applicable to the majority of the components, because usually moderate pressures are used in flow dozers. At the ambient temperature and $P < 1$ MPa, deviations of density from the ideal gas parameters become evident only in Kr, Xe and $CO_2$ (Table 1), The difference in the components properties will effect the flow temperature changes after their throttling in reducing devices R1 and R2 (Picture 1). To make the temperatures even, there is a stabilizer T located in front of the reducing devices D1 и D2. The fluctuations of pressure in the outlet can also cause an imbalance of the system and may require manual adjustment of the concentration with the help of Rv. This drawback is compensated by a receiver Rc. But its leveling functions are limited to some extend.

In case of exclusive demands to the accuracy of the product components, it’s recommended to use the system of continuous mixture analysis on the basis of the comparator unit. As Figure 1 shows, a small portion of the ready product is sampled after the receiver, and comes through one of the lines of the comparator unit K. If there is a deviation of the mixture thermal conductivity from the standard product (AGM), which comes through the other line of the comparator unit, the bridge connection of the comparator unit generates a certain signal. The signal is amplified and causes the cross-section change in valve Dv. The level of the effects of the automatic control contour (circuit) is defined by valve Rv.

Table 1. Cross-section of the dozer F flow part (mm$^2$) for different gases,
when $P_H = 1{,}0$ MPa; $T_H = 285$ K; $V_0 = 100$ m$^3$/h.

| Mixture components: | He | Ne | $N_2$ | Kr | Xe | $CO_2$ |
|---|---|---|---|---|---|---|
| Cross-section $F$ in accordance with (1) | 4,9 | 11,0 | 13,8 | 22,3 | 28,3 | 17,7 |
| Errors of calculations according to (1), caused by gas compressibility, % | -0,27 | -0,23 | 0,14 | 2,1 | 2,8 | 3,0 |

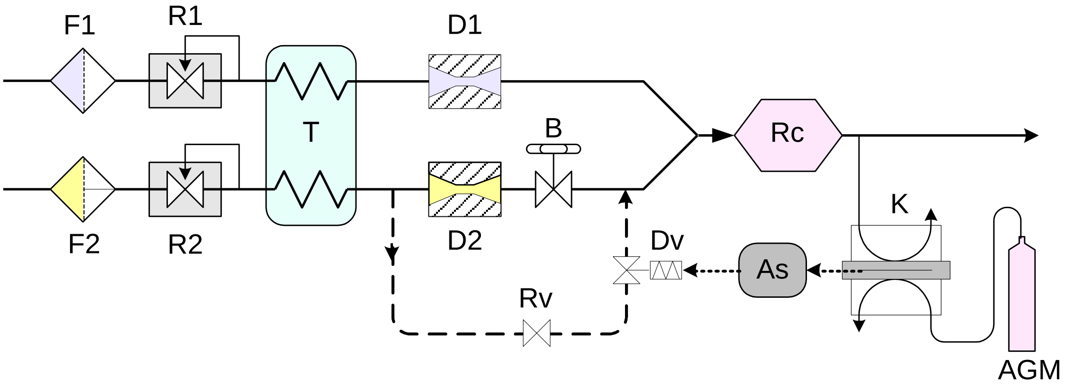

Figure 1. Diagram of binary mixture preparation of flow type with the feed-back.
«1» и «2» are referred to separate components of the mixture.

Indications: F1, F2 – filters, R1, R2 – reducers; T – temperature stabilizer; D1, D2 – dozing elements of constant cross-section; Dv – dozing valve of component «2»; Rc – receiver; K – comparator on the basis of the thermal conductivity detector ; As –signal amplifier; Rv – control valve; AGM – control gas mixture; B – bypass.

## 3. METHODS OF MIXING IN AN ENCLOSED VOLUME

Mixing of gases in cylinders guarantees high quality of the mixtures produced. But because of the sporadic character of filling, mixing and composition analysis, such procedure is not efficient. Gravimetric method (Figure 2-a) is based on cylinder weighting after the addition of each component (Table 2, point 2.1…2.4) [2]. To increase accuracy, the method of repeated dilution is used. The procedure of several sequent dilutions is especially necessary at the low (less than 1%) concentrations of the target components. Provided that electronic high-precision scales and pure primary components are used, the mass method enables to reach the accuracy of the mixture components up to 0,5%.

The manometric method is based on the pressure control in the mixing chamber with the known hydraulic volume [3]. Portions of the gaseous components are introduced gradually into the chamber. To reduce the influence of compressibility, the pressure is limited to several atmospheres. The ready-made mixture is pump-over from the mixing chamber to cylinders. The procedure is repeated till the required amount of the product is achieved. (Figure 2-b).

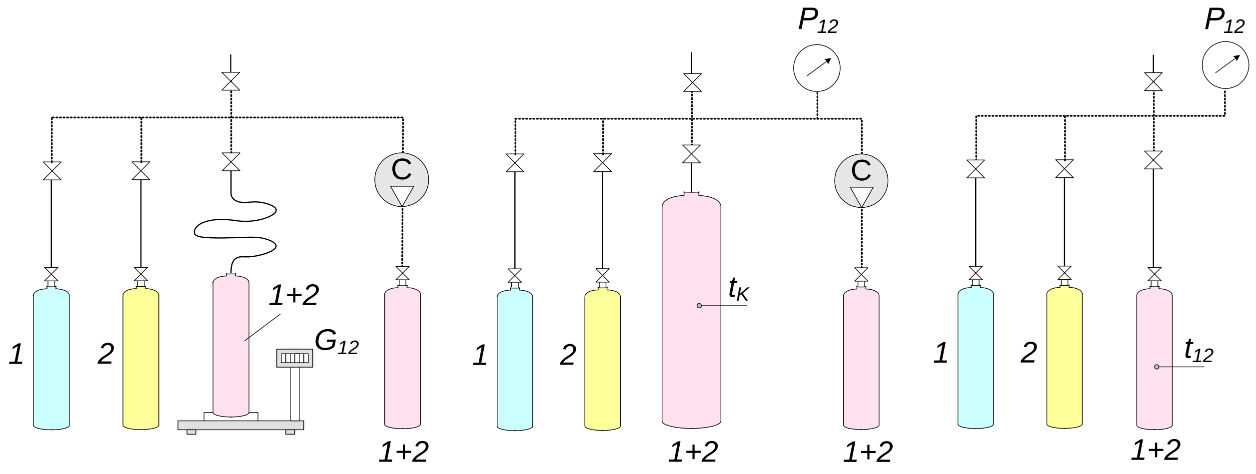

a b c

Figure 2. Diagrams of the stands for gravimetric (a) and manometric (b and c) methods of mixture preparation. C – compressor; $P_{12}$ – manometer (pressure gauge).

Table 2. Sequence of preparation of ternary (three-component) mixture of the increased pressure at $T = 290$ К.

| Components → | Nitrogen | Oxygen | Argon | Mixture |
|---|---|---|---|---|
| 1. Initial data | | | | |
| 1.1. Hydraulic volume of the mixing cylinder $V_\Sigma$, м$^3$ | | | | 0,05 |
| 1.2. Set amount of ready-made mixture $m_\Sigma$, кг | | | | 6 |
| 1.3. Mixture density $\rho_\Sigma = m_\Sigma / V_\Sigma$, кг/м$^3$ | | | | 120 |
| 1.4. Required volume concentration of the mixture $y_i$, % | 78,11 | 20,96 | 0,93 | 100 |
| 2. Components Mass weighing (gravimetric method) | | | | |
| 2.1. Molecular weight of the components $\mu_i$, кg/ kmole | 28,01 | 32 | 39,95 | |
| 2.2. Apparent molecular weight of the mixture $\mu_\Sigma = y_{N2}\ \mu_{N2} + y_{O2}\ \mu_{O2} + y_{Ar}\ \mu_{Ar}$, kg/mole | | | | 28,96 |
| 2.3. Mass concentration of the components $c_i = \frac{y_i \cdot \mu_i}{\mu_\Sigma}$, % | 75,56 | 23,16 | 1,28 | 100 |
| 2.4. Components mass in the mixture $m_i = y_i\ m_\Sigma$, kg | 4,533 | 1,390 | 0,077 | 6,0 |
| 3. Calculation of the components pressures (manometric method) | | | | |
| 3.1. Components density $\rho_i$ (provided that each of the components is placed into the cylinder separately $V_\Sigma$), kg/m$^3$ | 90,67 | 27,79 | 1,54 | |
| 3.2. Components pressure according to the reference data for pure substances at $\rho_i$ and $T = 290$ К $P_i$, bar | 77,589 | 20,639 | 0,929 | |
| 3.3. Estimated pressure of the mixture $P_\Sigma = P_{N2} + P_{O2} + P_{Ar}$, bar | | | | **99,157** |
| 3.4. Sequence of pressure build-up in the mixing cylinder, bar | Argon | | | I - 0,929 |
| | Oxygen + Argon (20,639+0,929) | | | II - 21,568 |
| | Nitrogen + Oxygen + Argon (77,589+20,639+0,929) | | | III - 99,157 |

CHECKING: Actual air density according to reference data for estimated pressure $P_{\Sigma} = 99{,}157$ bar and $T = 290$ K makes $\rho^{т}_{\Sigma} = 120{,}85$ kg/m$^3$ [6], Deviation from the density $\rho_{\Sigma}$ (see point 1.3) makes 0,71%.

The preparation of mixture at low pressures in the mixing chamber does not guarantee high accuracy. Because of the "reality" of the components and the influence of armature and instruments, the error of a single-shot mixing on pressure can achieve as much as 5%. The necessity of correction, long period of temperature stabilization and possibility of foreign impurities contamination when using compressors, proves this method to be inefficient and not reliable.

At the sufficient available pressure of the primary components there is a possibility to receive the target substances directly in cylinders [4, 5]. This method is applicable to mixtures composed of several pure gases if the concentration of separate components $y_i \geq 1\%$. It is assumed that the reference data on physical properties of each of the components are available. The procedure of mixture preparation is shown in Table 2 by the example of "synthetic air" preparation. The product is chosen for illustrative purposes and because of the availability of mixture properties, necessary for checking the correctness of the calculation method.

When making volume mixing (lines 2.2…2.4, see Table 2) as well as making gravimetric mixing of pure substances, the mass of each component $m_i$ is determined. These values for the set amount of the product $m_{\Sigma}$ are calculated by volume $y_i$ and mass $c_i$ concentrations according to the known ratios [1]. Lines 3.1…3.4 in Table 2 show the calculations of components pressures at which the set concentration is achieved by the manometric method.

The method described was evaluated by us when receiving the mixture of $^{20}$Ne - $^{22}$Ne with the given isotopic ratio. In most cases, the desired result was achieved after one corrective action planned on the basis of isotopic composition control. The main advantage of this method is exclusively economic consumption of high-valued products, for instance, isotopes of rare gases. Picture 3 shows the equipment used for manufacturing mixtures by the manometric method.


a b c

Figure 3. Separate blocks of the mixer for Ne production with the given isotopic ratio by the manometric method: a – compressor variant (see picture 2-b); b – direct mixing; c – mass spectrometer ЭМГ-20-1, used for isotopic composition control.

## 4. MANUFACTURING AND STORAGE OF MIXTURES IN THE LIQUID STATE

Methods based on phase equilibrium of the components, enable to receive significant amount of mainly binary mixtures (Figure 4) [7, 8]. For this method, special units with thermo isolation and temperature stabilizer circuit (Figure 5) are needed. The mixture composition is set by pressure and temperature of phases [9]. The obtained solution is taken from the reservoir mainly in liquid state and is gasified. The drawback of the process is a limited range of possible values of concentration, because in the obtained mixtures the high-boiling component predominates.

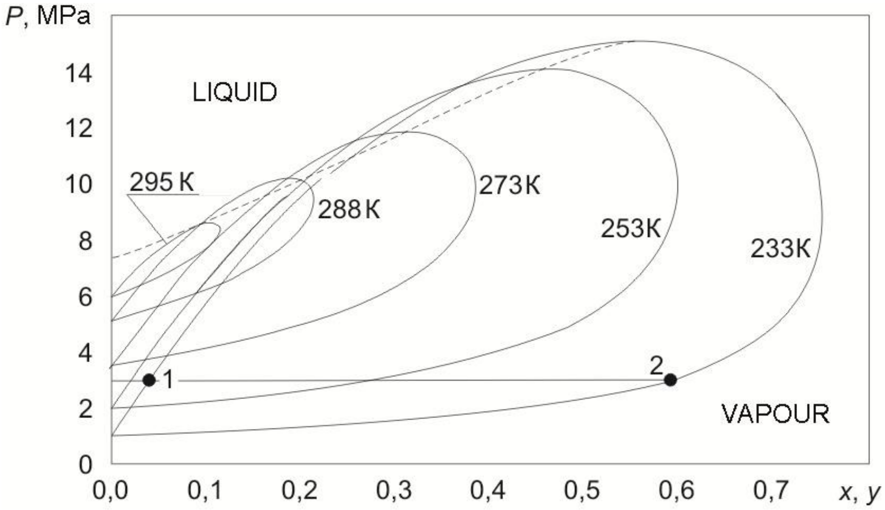

Figure 4. Equilibrium isotherms liquid-vapor for argon-carbon dioxide mixture.

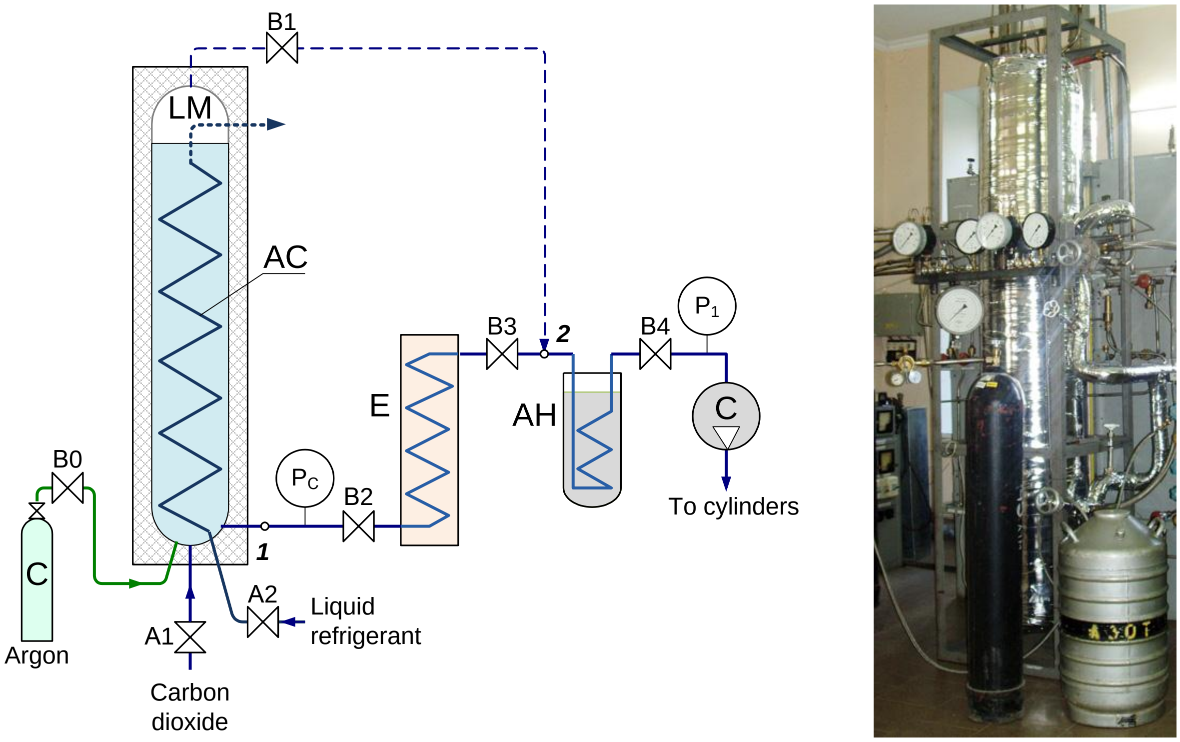

*a* *b*

Figure 5. Diagram (a) and photo (b) of the unit for preparation and storage of mixtures in liquid state [9] (by the example of mixture Ar-$CO_2$). C – cylinder with argon; LM – device for mixture preparation in liquid state; AC –after-cooler; E – evaporator; AH – additional heater; $P_C$, $P_1$ – manometers; A1, A2, B0-B4 – shut-off valves.

In case you need to prepare the mixture with the significant portion of a low-boiling substance, the bleeding is made during the gas-phase with the continuous feeding of a low-boiling component from cylinder C (see Figure 5). To obtain the composition close to equilibrium, the said feeding is made by the barbotage method through the liquid layer. Also, to ensure the continuous work, it’s necessary to have a stock of high-boiling substance to refill the mixer LM.

## CONCLUSION

All the mixing methods described above, are used in the laboratory and production activities of Iceblick Ltd. We have a good collection of standard gas mixtures and unique instruments for gas and isotopic analysis. The construction of the unit for the preparation of combined gas products has made it possible to increase the number of rare gases consumers.

## REFERENCES

1. Bondarenko V.L., Simonenko Yu. M. 2009, *Cryogenic technologies of rare gases recovery*, Odessa: Publishing House «Izdatelskiy centr», 232 p.
2. State standard documents (GOST R ISO 6142-2008) *Gas analysis. Preparation of a calibrate gas mixtures. Gravimetric method*, 30 p.
3. State standard documents (GOST R ISO 6144-2008) *Gas analysis. Preparation of a calibrate gas mixtures. Static volumetric method*, 23 p.
4. Kirillin V.A., Sychev V.V., Sheydlin A.E. 1983, *Technical thermodynamics: Textbook for higher educational institutions*, Moscow: Publishing House “Energoatomizdat”, 416 p.
5. Vukalovich M.P., Novikov I.M. 1968, *Technical thermodynamics*, Moscow: Publishing House «Energiya», 496 p.
6. Vasserman A.A., Kazavchinskiy Ya.Z., Rabinovich V.A. 1966, *Thermal characteristics of air and its components*, Moscow: Publishing House «Nauka», 375 p.
7. Coquelet C., Valts A., Dieu F. *et al.* 2008, Isothermal P, x, y data for the argon + carbon dioxide system at six temperatures from 233.32 to 299.21 K and pressures up to 14 MPa , *Fluid phase equilibria*, 273: 38-43.
8. Wei Y.S., Sadus R.J. 1996, Vapour-liquid and liquid-liquid phase equilibrium of binary mixtures containing helium: comparison of experimental data with predictions using equations of state, *Fluid phase equilibrium*. 122: 1-15.
9. Bondarenko V.L., Losyakov N.P., Diachenko T.V. *et al.* 2011, New technologies extraction concentrates of rare gases, *Industrial gases*. 1: 42-52.

028

# Development of an Equation of State for the Representation of Solid-Liquid, Solid-Vapour, and Liquid-Vapour Equilibria of Substances of Interest for the Air Distillation Process

**Stringari P.[*], Campestrini M.[*], Coquelet C.[*], Arpentinier P.[**]**

[*] MINES ParisTech, Laboratoire CEP/TEP, 35 Rue Saint Honoré, 77305 Fontainebleau, France
[**] Air Liquide – Centre de Recherche Claude-Delorme, 1 chemin de la Porte des Loges BP 126,
78354 Jouy-en-Josas, France

## ABSTRACT

A common problem in the industrial cryogenic processes, as cryogenic air distillation, is the solidification of some impurities. Consequently, a thermodynamic model suitable for being applied in the simulation of cryogenic processes should account for the solid-fluid equilibrium. The capability of the Yokozeki equation of state in representing phase equilibrium experimental values of pure compounds has been verified. Some limits have been found with respect to the solid-liquid equilibrium. In order to overcome these limits the Solid Liquid Vapour Peng-Robinson equation of state (SLV PR EoS) has been proposed. A comparison between the SLV PR EoS and the experimental values has been presented for nitrogen, oxygen, argon, krypton, xenon, neon, carbon dioxide, nitrous oxide, methane, ethane, ethylene, propane and propylene, and a good agreement has been found. Furthermore, the equation proposed has been used for representing the phase equilibria of the binary mixtures methane-carbon dioxide and ethane-carbon dioxide.

## 1. INTRODUCTION

Air is a mixture of approximately 79 mol% nitrogen and 21 mol% oxygen; it also contains a little less than 1 mol% argon, carbon dioxide and trace quantities for the other rare gases such as helium, neon, xenon and krypton. Nitrogen and oxygen are among the most common commodity chemicals produced all over the world; consequently, their production via air separation is of major importance in the chemical industry.

Cryogenic distillation of air is the oldest but most highly developed separation technology for the industrial production of oxygen. This technology has not changed fundamentally from that initially developed by Carl von Linde (Germany) and Georges Claude (France) at the beginning of the twentieth century.

Cryogenic air separation is based on fractional distillation in which components of the air mixture are separated on the basis of differences in boiling point. The basic principles are similar to those applicable to distillation separation at higher temperatures. This technique consists in boiling a liquid mixture of the components at the bottom of a column by heat addition, followed by staged condensation of the vapour as it rises up the column. One significant difference is that, in cryogenic distillation, the work of separation is provided by feed compression as opposed to heat addition in high-temperature distillation. The use of very low temperatures owing to the fact that the separated gases only liquefy necessitates additional steps such as refrigeration production and air contaminant removal.

Atmospheric air contains undesirable contaminants that, upon cooling, become solids and foul the heat transfer surfaces, impeding the heat exchange and increasing the pressure drops through the process. Water and carbon dioxide must be removed as their freezing points are above the temperatures required for air liquefaction and they will freeze out in the heat exchanger and block the equipment. Furthermore, air distillation plants are generally installed on industrial sites and this contributes to air contamination by different types of pollutants (nitrous oxide, light hydrocarbons).

Significant efforts are made by the oxygen producing companies to ensure the safety of cryogenic air separation unit. Their aim is to avoid that undetected contaminants reach the vaporizer-condenser, are concentrated in liquid oxygen and form a critical mass of solid deposit which could lead to an explosion [1], [2]. Global approaches are developed by these companies to minimize and control that risk. These latter have led to the development of processes equipped with liquid oxygen filters, the development of new adsorbents in the front-end purification unit and monitoring strategies to track accurately the most volatile contaminants from the feed air to the liquid oxygen.

Thus, it is clear that a complete knowledge of solid-fluid equilibrium, contaminants nature and behaviour in gaseous and liquid streams of a cryogenic air separation unit is a key issue for efficient and safe operation.

## 2. MODELING METHODS FOR SOLID-FLUID EQUILIBRIUM

Many methods have been proposed for representing the solid-fluid equilibrium, by imposing an EoS to respect different experimental properties at the triple point, such as the temperature, the molar volume change of melting, the heat of melting, the solid density, and the change in the specific heat upon fusion. Despite that, it has been demonstrated that each of these methods present some limits.

In the approach reported by Prausnitz et al. [3], and Twu [4], the fugacity of the solid phase is evaluated in terms of a liquid-phase reference. In [3] the limits are the impossibility to predict thermodynamic properties of the solid phase – such as density or heat capacity – and, for the mixtures, the insolubility of the solvent in the solid solute.

Kan [5], and Wenzel and Schmidt [6] modified cubic EoSs by adding respectively a 9-order term in the repulsive part of the Van der Waals EoS and a term with a six power in volume in the Redlich-Kwong EoS. The behaviour of these two modified EoSs gives at some temperature and pressure conditions a solid-liquid critical point and this fact is not in agreement with the experimental observations.

Geaña and Wenzel [7], Lang and Wenzel [8], and Heidemann and Prausnitz [9] suggested to consider the dense phases as results of the partial association of different monomers that compose the pure substance. In this way, the solid and the liquid phases are represented as self-associated molecular aggregates. Their EoSs are finally applied alternatively to the monomer for representing the vapour phase and to $N$-mers with different values of $N$ for representing the liquid and the solid phases. Consequently these approaches do not represent solid, liquid, and vapour phases at the same time.

This limit is shown also in the Salim and Trebble [10] method. Indeed, they used twice a cubic equation of state, one for the liquid-vapour equilibrium and the other for the solid-vapour equilibrium, considering the dense branch valid alternatively for the liquid or for the solid phase.

Yokozeki [11] proposed a non-cubic analytical EoS, eq. (1), for describing the phase behaviour of three states (solid, liquid, and vapour) of matter at the same time. This equation is the first introducing a discontinuity for the fluid-solid transition in the isothermal P-$v$ behaviour of a fluid.

$$P = \frac{RT}{v-c}\left(\frac{v-d}{v-b}\right)^k - \frac{a}{v^2 + qcv + rc^2} \tag{1}$$

In eq. (1) $P$ is the pressure, $R$ is the gas constant, $T$ is the temperature, $v$ the molar volume, $b$ the liquid covolume, $c$ the solid covolume, $a$ the parameter for the attractive term, $d$, $k$, $q$ and $r$ are parameters. Two important relations introduced by Yokozeki for using his EoS are $c < d < b$, $k \geq 1$ and integer.

Concerning the exponent $k$, Lee and Yoo [12] found that the model violates at least two physically important behaviours. The first problem concerns the hard-sphere behaviour as described by the Yokozeki EoS. The Yokozeki EoS can be applied for representing the hard-sphere behaviour imposing $a = 0$ in the attractive term of eq. (1). For odd values of $k$ the EoS shows a negative pressure in the regions $c < v < b$. Molecular simulation results [13] confirmed that a hard-sphere fluid without attraction has a positive pressure in all density regions, including the solid-fluid transition region. This is in contrast with the Yokozeki model for hard-sphere which presents a negative pressure in the solid phase branch.

The second problem concerns the application of the Maxwell's equal area rule to the solid-liquid phase transition. For the application of the Maxwell's equal area rule, the Helmholtz energy must be convergent in the phase transition region. The case with $k$ even and greater than one in eq. (1) cannot be applied for modelling the solid-liquid phase transition via the Maxwell's equal area rule because the Helmholtz energy is not convergent in the phase transition region.

Despite these problems, the Yokozeki EoS maintains a simple form, useful for engineering purposes. Using eq. (1) with $k = 1$ allows using the Maxwell's equal area rule for calculating solid-fluid equilibrium.

In this work, the capability of the Yokozeki EoS (with $k = 1$, and the Peng-Robinson values for $q$ and $r$ in the attractive term, $q = 2$, $r = -1$) of representing quantitatively the phase equilibrium experimental values has been evaluated. Accurate auxiliary equations [14] have been used for generating values for solid-vapour (SVE), solid-liquid (SLE), and liquid-vapour equilibria (VLE) of some substances of interest for the air distillation process.

The model proposed by Yokozeki was forced to reproduce the values generated with the auxiliary equations and to represent exactly the critical point and the triple point temperature and pressure. The comparisons between the phase equilibrium values calculated with the Yokozeki EoS and the values obtained from the auxiliary equations are shown for oxygen and argon in Figure 1.

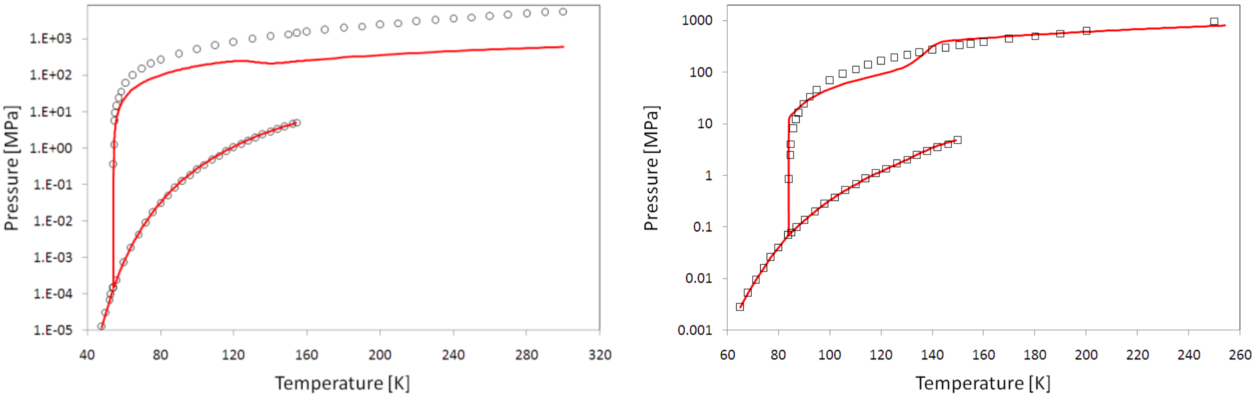

Figure 1. Comparison of the pressure-temperature equilibrium values obtained with the Yokozeki EoS and values from auxiliary equations for oxygen and argon. Yokozeki EoS: –; auxiliary equation: ○ (oxygen) and □ (argon).

Figure 1 shows high deviation values for the solid-liquid equilibrium (the SVE and the VLE are well represented). The behaviour is incorrect also from the qualitative point of view; negative step (oxygen) and positive step (argon) are located on the SLE branch near the critical temperature.

Consequently, a modification has been proposed to overcome the limits of the Yokozeki EoS. The modification regards the substitution of the solid covolume *c* with the liquid covolume *b* in the attractive term. The Solid Liquid Vapour Peng-Robinson equation of state (SLV PR EoS) is presented in eq. (2).

$$P = \frac{RT}{v-c}\left(\frac{v-d}{v-b}\right) - \frac{a}{v^2 + 2bv - b^2} \qquad (2)$$

This equation leads to a correct representation of the entire phase diagram, from both the quantitative and the qualitative side. For understanding the improvement in representing the phase equilibrium values, in Figure 2 are shown the comparisons – for oxygen and argon – between the phase equilibrium values calculated with the SLV PR EoS and the values obtained from the auxiliary equations.

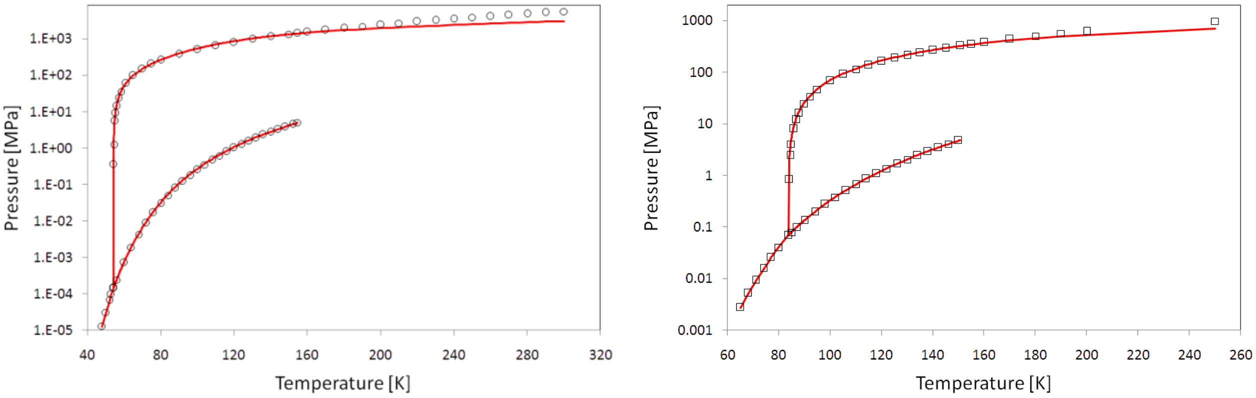

Figure 2. Comparison of the pressure-temperature equilibrium values obtained with the SLV PR EoS and values from auxiliary equations for oxygen and argon. SLV PR EoS: –; auxiliary values ○ (oxygen) and □ (argon).

Using the SLV PR EoS the representation of the SLE branch is improved avoiding unphysical behaviour and without losing the capability in representing the SVE and the VLE.

## 3. RESULTS

The SLV PR EoS has been used for representing phase equilibria of the following pure compounds: nitrogen, oxygen, argon, krypton, xenon, neon, carbon dioxide, nitrous oxide, methane, ethane, ethylene, propane and propylene. For each compound, a pressure-temperature range has been fixed; each range extends from a minimum, located on the SVE branch, to a maximum, located on the SLE branch. The minimum and the maximum values for all the pure compounds studied are indicated in Table 1. The VLE is instead studied between the triple and the critical points for all the pure compounds. For the hydrocarbons, except methane, the lower limits correspond to the triple point coordinates.

Table 1. Temperature and pressure ranges for the comparison of the phase equilibria calculated with the SLV PR EoS and the auxiliary equations for each compound studied.

| Compound | SVE | | SLE | |
|---|---|---|---|---|
| | Tmin / K | Pmin /MPa | Tmax / K | Pmax /MPa |
| $N_2$ | 40 | 11 | 130 | 400 |
| $O_2$ | 48 | 12 | 160 | 1500 |
| Ar | 50 | 37 | 160 | 380 |
| Kr | 65 | 12 | 220 | 430 |
| Xe | 90 | 17 | 300 | 440 |
| Ne | 15 | 14 | 45 | 170 |
| $CO_2$ | 125 | 11 | 310 | 610 |
| $N_2O$ | 130 | 140 | 310 | 1500 |
| $CH_4$ | 60 | 16 | 200 | 600 |
| $C_2H_6$ | 90.37 | 1.1 | 340 | 4100 |
| $C_2H_4$ | 103.99 | 122.0 | 330 | 3500 |
| $C_3H_8$ | 85.53 | $2\cdot10^{-4}$ | 380 | 4100 |
| $C_3H_6$ | 87.95 | $7\cdot10^{-4}$ | 370 | 17500 |

The quantitative comparison of the phase equilibrium values obtained with the SLV PR EoS and the values obtained from the auxiliary equations has been evaluated with reference to the common statistical indexes: AAD%, Bias% and MAD%.

Table 2 represents these errors obtained calculating the equilibrium temperature at fixed pressure. The last line of Table 2 represents a summary of the results obtained for all the compounds. In this line the AAD% and the Bias% values are mathematical average of the values for each compound; instead, MAD% is the percentage maximum absolute deviation considering all the fluids.

Table 2. Summary of the statistical errors in calculating equilibrium temperatures at fixed pressures for all the pure compounds studied. Errors are evaluated with respect to the auxiliary equations.

| Compound | VLE | | | SVE | | | SLE | | |
|---|---|---|---|---|---|---|---|---|---|
| | AAD% | BIAS% | MAD% | AAD% | BIAS% | MAD% | AAD% | BIAS% | MAD% |
| $N_2$ | 0.12 | -0.1 | 0.31 | 0.05 | 0.02 | 0.1 | 0.47 | 0.03 | 0.91 |
| $O_2$ | 0.41 | -0.37 | 0.81 | 0.26 | 0.24 | 0.38 | 1.08 | -0.79 | 2.56 |
| Ar | 0.20 | -0.18 | 0.29 | 0.13 | 0.04 | 0.29 | 0.46 | -0.33 | 1.62 |
| Kr | 0.32 | 0.22 | 0.69 | 0.57 | 0.45 | 0.83 | 1.24 | 1.03 | 3.02 |
| Xe | 0.22 | 0.21 | 0.45 | 0.65 | -0.14 | 2.13 | 0.41 | 0.05 | 0.7 |
| Ne | 0.25 | -0.25 | 0.46 | 0.06 | 0.03 | 0.13 | 0.62 | 0.23 | 1.18 |
| $CO_2$ | 0.43 | -0.28 | 0.82 | 0.16 | 0.04 | 0.29 | 0.44 | -0.21 | 1.49 |
| $N_2O$ | 0.21 | -0.05 | 0.50 | 1.25 | -1.22 | 2.66 | 0.56 | 0.19 | 2.09 |
| $CH_4$ | 0.05 | -0.01 | 0.1 | 0.06 | -0.06 | 0.22 | 0.08 | 0.03 | 1.25 |
| $C_2H_6$ | 0.12 | -0.004 | 0.22 | | | | 0.49 | 0.47 | 0.95 |
| $C_2H_4$ | 0.02 | -0.02 | 0.14 | | | | 1.12 | -0.9 | 3.29 |
| $C_3H_8$ | 0.18 | 0.03 | 0.52 | | | | 1.47 | 0.08 | 4.32 |
| $C_3H_6$ | 0.32 | -0.17 | 0.9 | | | | 1.53 | -1.34 | 5.69 |
| **Overall** | **0.22** | **-0.07** | **0.90** | **0.35** | **-0.07** | **2.66** | **0.77** | **-0.11** | **5.69** |

For VLE the AAD% averaged with respect to all the compounds is about 0.2% with a Bias% close to zero. The percentage maximum absolute deviation (MAD%) is less than 1%. For SVE the AAD% averaged with respect to all the compounds is less than 0.4%. Also in this case the Bias% is close to zero. The maximum value of MAD% is found for nitrous oxide at very low pressure and it is less than 3%. AAD% for SLE is about 0.8% with a Bias% of -0.11%. The maximum MAD% is about 6%.

Successively, extension of the SLV PR EoS to binary mixture has been considered. The classical mixing rules proposed by Yokozeki [15] have been used for the mixture parameters. Figure 3 shows the pressure-temperature equilibrium behaviour for the mixture methane-carbon dioxide. The SLV PR EoS allows a well representation of the experimental values of the triple line [16], [17], of the critical line [16] and of the phase envelope for a fixed mixture composition [18].

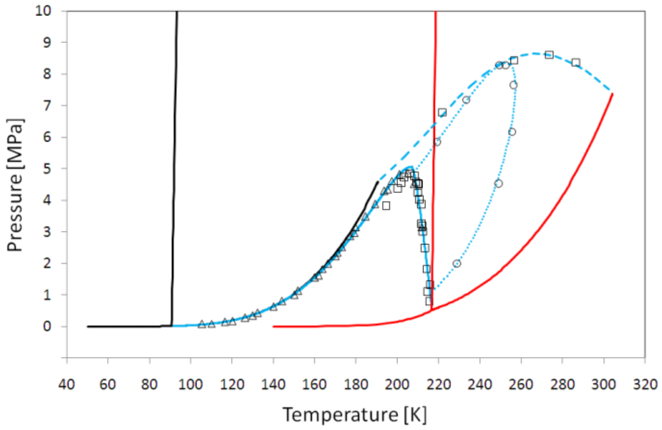

Figure 3. Pressure-temperature equilibrium behaviour for the mixture $CH_4$-$CO_2$.
Calculated values: — $CH_4$; — $CO_2$; — triple line; - - critical line; ···· phase envelope ($x_{CH4}$=0.524).
Experimental values: □ Donnelly and Katz [16]; △ Davis et al. [17]; ○ Esper et al. [18].

Besides representing the pressure-temperature equilibrium behaviour, the SLV PR EoS has been tested for representing both Px and Tx cross sections. An example is shown in Figure 4; the left side presents the temperature-composition equilibrium behaviour for the mixture $CH_4$-$CO_2$ at 6.2 MPa, while the right side of Figure 4 shows the pressure-composition equilibrium behaviours for the binary mixture $CO_2$-$C_2H_6$ at 223 K.

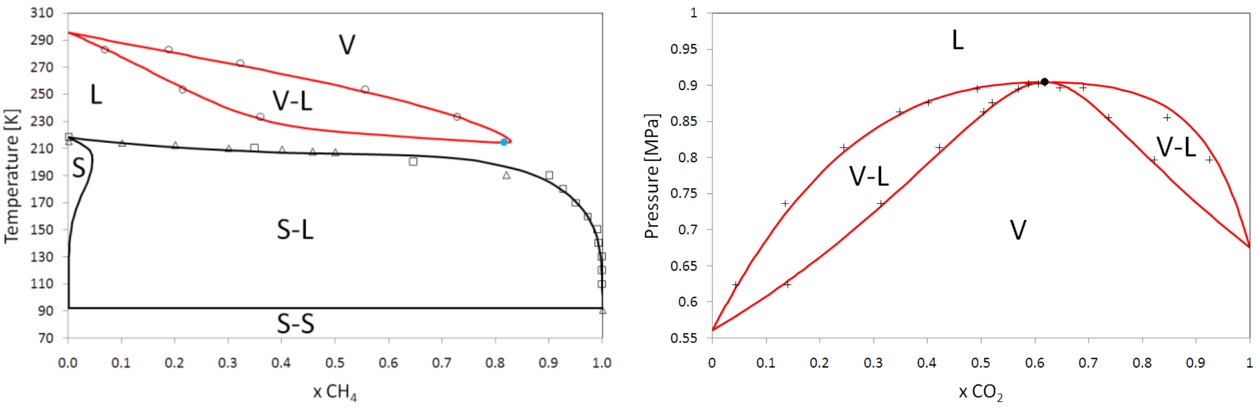

Figure 4. Left side: Tx diagram at P = 6.2 MPa for the system $CH_4$-$CO_2$.
Right side: Px diagram at T = 223.15 K for the system $CO_2$-$C_2H_6$.
Calculated values: — SLE; — VLE; ● VLE critical point; ● VL azeotrope. Experimental values:
□ Streich [19]; △ Brewer and Kurata [20]; ○ Kaminishi et al. [21]; + Fredenslund and Mollerup [22].

## 4. CONCLUSIONS

Suitable modification has been proposed in order to overcome some limitations that the Yokozeki EoS shows especially in the SLE near the critical temperature; a new equation of state has been developed, and named Solid Liquid Vapour PR EoS. With this EoS it has been possible to obtain a good representation of the SLE, SVE, and VLE in a wide range of temperature and pressure for $N_2$, $O_2$, Ar, Kr, Xe, Ne, $CO_2$, $N_2O$, $CH_4$, $C_2H_6$, $C_2H_4$, $C_3H_8$ and $C_3H_6$. Using the SLV PR EoS it is possible to achieve continuous representations of the pressure-temperature equilibrium behaviours of pure compounds and to evaluate the derived properties. Therefore the intention of the authors is to extend the study to other pure compounds of interest in the cryogenic domain and to reduce the number of the parameters included in the SLV PR EoS for an industrial application of this equation. The EoS proposed can be extended to mixtures, and allows evaluating their thermodynamic behaviour in the cryogenic field. This could be an important aid for designing and optimizing industrial cryogenic processes; knowing at which conditions in a mixture the solid-fluid equilibria (where fluid means either the liquid or the vapour phases) appears represents an opportunity of great interest, because it could be used for improving the cryogenic processes and for avoiding some drawbacks as solidification of the impurities. The phase diagrams, as Px and Tx cross section at cryogenic conditions, can give important information for evaluating new air separation techniques, exploiting the capability of the SLV PR EoS in representing phase equilibrium values in which also the solid phase is involved.

## 5. ACKNOWLEDGEMENTS

The authors are grateful to Air Liquide for the financial support to the development of this equation.

## 6. REFERENCES

[1] De Stefani V, Baba-Ahmed A, Richon D. 2003, Experimental Determination of Carbon Dioxide and Nitrous Oxide co-Solubility in Liquid Oxygen, *Fluid Phase Equilibria*, 207: 131-142.

[2] Millet C, Bourgeois P, Kraus G, Gabillard JP. 2001, Process for Purifying Air by Adsorption Before Cryogenic Distillation, United States Patent, Patent No.: US6270557B1.

[3] Prausnitz JM, Lichtenthaler RN, de Azevedo EG. 1985, Molecular Thermodynamics of Fluid-Phase Equilibria, 2nd edn., Chap. 9, Prentice-Hall, Englewood Cliffs, NJ.

[4] Twu CH, Tassone V, Sim WD. 2003, New Solid Equation of State Combining Excess Energy Mixing Rule for Solid-Liquid equilibria, *AIChE Journal*, 49(11): 2957-2965.

[5] Kan KC. 1979, An Equation of State and the Gas-Liquid-Solid Equilibrium in Argon, *Chinese Journal of Physics*, 17: 32-43.

[6] Wenzel H, Schmidt G. 1980, A Modified Van der Waals Equation of State for the Representation of Phase Equilibria Between Solids, Liquids, and Gases, *Fluid Phase Equilibria*, 5: 3-17.

[7] Geaña D, Wenzel H. 1999, Solid-Liquid-Gas Equilibrium by Cubic Equations of State and Association, *Journal of Supercritical Fluids*, 15: 97-108.

[8] Lang E, Wenzel H. 1989, Extension of a Cubic Equation of State to Solids, *Fluid Phase Equilibria*, 51: 101-117.

[9] Heidemann A, Prausnitz JM. 1976, A Van der Waals-type Equation of State for Fluids With Associating Molecules, *Proc. Natl. Acad. Sci*., USA, 73: 1773-1776.

[10] Salim PH, Trebble MA. 1994, Modeling of Solid Phases in Thermodynamic Calculations via Translation of a Cubic Equation of State at the Triple Point, *Fluid Phase Equilibria*, 93: 75-99.

[11] Yokozeki A. 2003, Analytical Equation of State for Solid-Liquid-Vapour Phases, *International Journal of Thermophysics*, 24: 589-620.

[12] Lee HJ, Yoo KP. 2011, Comments on Analytic Equation of State for Solid-Liquid-Vapour Phases, *International Journal of Thermophysics*, 32: 553-558.

[13] Alder BJ, Wainwright TE. 1957, *Journal of Chemical Physics*, 27: 1208-1209.

[14] Huber ML, McLinden MO, Lemmon EW. 2007, NIST Standard Reference Database 23, Reference Fluid Thermodynamic and Transport Properties-REFPROP, Version 8.0, National Institute of Standards and Technology, Standard Reference Data Program, Gaithersburg.

[15] Yokozeki A. 2004, Phase Behaviors of Binary Hard Sphere Mixtures Using Simple Analytical Equation of State, *International Journal of Thermophysics*, 25: 643-667.

[16] Donnelly HG, Katz DL. 1954, Phase Equilibria in the Carbon Dioxide-Methane System, *Industrial and Engineering Chemistry*, 46: 511-517.

[17] Davis JA, Rodewals N, Kurata F. 1962, *AIChE Journal*, 8: 537.

[18] Esper GJ, Bailey DM, Holste JC, Hall KR. 1989, Volumetric Behavior of Near-Equimolar Mixtures for $CO_2$+$CH_4$ and $CO_2$+$N_2$, *Fluid Phase Equilibria*, 49: 35-47.

[19] Streich M. 1970, *Hydrocarbon Processing*, 49: 86-88.

[20] Brewer J, Kurata F. 1958, *AIChE Journal*, 3: 317-318.

[21] Kaminishi GI, Arai Y, Saito S, Maeda S. 1968, Vapor-Liquid Equilibria for Binary and Ternary System Containing Carbon Dioxide, *Journal of Chemical Engineering of Japan*, 1(2): 109-116.

[22] Fredenslund A, Mollerup J. 1974, *Journal of the Chemical Society, Faraday Trans. 1*, 70: 1653-1660.

029

# Study Concerning the Possibility for Increasing Argon Recovery from a Cryogenic Air Separation Process

**Cuzic M.**[*], **Serban Al.**[**], **Popa V.**[***]

[*] Criomec SA, 63 Drumul de Centura, Galati, Zip code, Romania
[**] Transilvania University, 29 Eroilor Av., Brasov, 500036, Romania
[***] "Dunarea de Jos" University, 47 Domneasca Street, Galati, 800008, Romania

## ABSTRACT

Argon recovery is an important challenge for cryogenic industry. Its recovery is maximized by optimizing the number of theoretical stages in each section of low pressure air separation column and argon column and also the flow rates of the streams. For increasing argon recovery in a cryogenic air separation process, the crude argon column have a condenser in the top and the trays are a combination of conventional sieve trays and structured packing. The condenser is feed with oxygen enriched liquid from the kettle of high pressure column.

## 1. INTRODUCTION

Argon is a highly inert element over a very wide range of conditions, both at cryogenic and very high temperatures. The major source of argon is air. Therefore, argon is typically produced using cryogenic air separation unit. The small amount of argon present in air (nearly 1%) creates a very high value for argon produced from cryogenic oxygen plants. Other sources of argon such as ammonia purge gas require a much greater energy input and capital costs to effect the separation. Thus, the production of additional argon from an air separation plant constitutes a very large economic benefit to the operation of the process. Argon is therefore valued at a substantial premium over the corresponding oxygen production from the process.

Because argon is a valuable product, its recovery is maximized by optimizing the number of theoretical stages in each section of low pressure air separation column and argon column and also the flow rates of the streams. The optimization of the number of theoretical stages depends of contact efficiency and pressure drop per tray. The ratio of these parameters is the pressure drop ($\Delta p$) per theoretical stage. The total pressure drop available for operation of the argon column limits the number of theoretical stages. The relative volatility of argon with respect of oxygen ($\alpha$) is about 1.5 at the bottom of the argon column and about 1.1 at the top of this column. This low value of relative volatility at the top of the column makes it difficult to produce crude argon with low concentration of oxygen in high recoveries. That means that it is difficult to obtain oxygen lean argon at high recovery rates. In the conventional air separation unit, the number of theoretical stages typically used in an argon column is 30-50.

## 2. ARGON RECOVERY LINDE METHOD

The traditional method to purify argon is that the gas from the argon transfer of the upper column is purified in a side column, the so called crude argon column to approx. 2 % $O_2$ and 1 % $N_2$. This method is presented in figure 1.

The remainder of the oxygen part is removed by chemical purification. Then the nitrogen part is removed in the pure argon column. The reason why not all of the oxygen is removed in the crude argon column, is that it demands so many trays that the pressure drop would be too large. But structured packing in the column has been shown to be competitive in recent times, because of its low pressure drop. This makes it possible to increase the number of theoretical trays and not to use chemical purification.

A crude argon column is a column with a condenser but without a reboiler, so it must take in gas in the bottom. This gas comes from the argon transfer and contain approx. 90 % oxygen, 10 % argon and 0,1 % nitrogen. As there is much oxygen which we want to remove and we know that it is difficult to separate oxygen and argon, a large number of trays and a large reflux ratio (=reflux flow/crude argon flow) is required. There is around 50-60 trays and a reflux ratio = 30-40 (i.e. 30-40 times as much column reflux as crude argon production). Crude argon with 2 % oxygen is taken out as gas from the top.

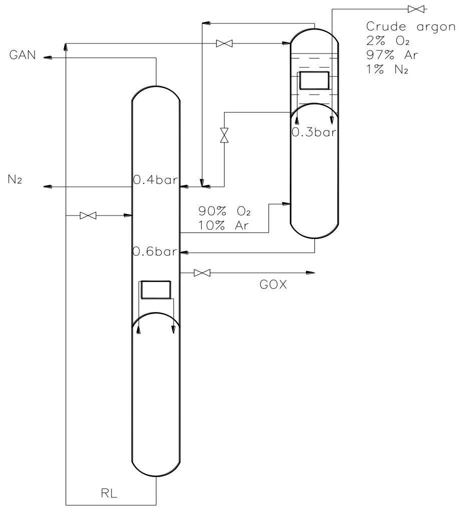

Figure 1. Linde cryogenic air separation unit with crude argon column

Column reflux runs from the bottom of the column to the argon transfer in the upper column. The evaporated rich liquid is fed to the upper column at a lower point than the liquid with the same composition. This is so that each feed shall be added where the concentrations are as alike as is possible. This means that why the rich liquid is added at the tray where the liquid contains approx. 35 % oxygen and the evaporated part is added above the tray where the gas has approx. 35 % oxygen, which occurs at a lower point.

## 3. ENHANCED RECOVERY OF ARGON FROM CRYOGENIC AIR SEPARATION CYCLES

In our study, the theoretical number of stages for the argon column is considered. This number of theoretical stages was obtained as to produce a crude argon product with concentration of oxygen less or equal to 0.5 % molar concentration, because it is sufficiently low for effective separation of oxygen in the downstream steps of argon purification, but it still ensures a reasonable argon recovery. This method is presented in figure 2.

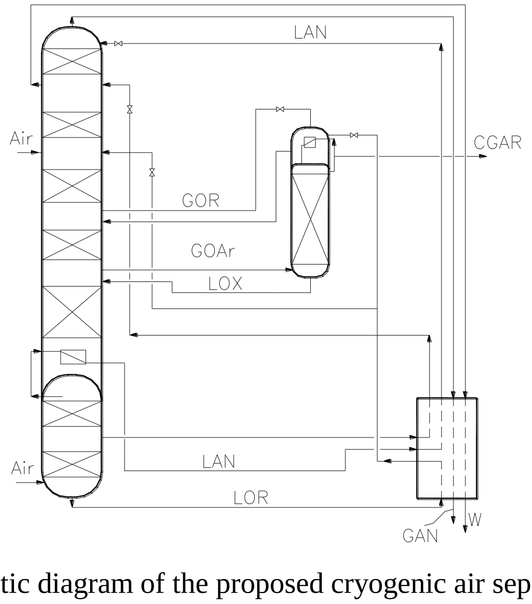

Figure 2. Schematic diagram of the proposed cryogenic air separation process

The oxygen enriched liquid from the bottom of the high pressure column is sent to the condenser located in the top of the argon column. This flow rate is greater than the theoretical minimum flow rate of oxygen enriched liquid. The theoretical minimum flow rate is defined as the oxygen enriched liquid flow rate which pass through the condenser placed at the top of crude argon column such that it is completely vaporized by the condensing argon flow. That oxygen enriched liquid flow will leave the condenser like saturated vapour flow and it is introduced in low pressure air separation column.

It optimizes the fraction of oxygen liquid flow from the bottom of high pressure air separation column which is fed directly to the upper intermediate location of the low pressure distillation column. This fraction of oxygen enriched liquid from the bottom of high pressure column acts as impure feed to the low pressure column and increase argon recovery from the low pressure column to the crude argon column without reducing argon recovery in the argon column.

The crude argon column is operated so as to achieve a pressure at the top of the argon column such that the flow of oxygen enriched liquid to the condenser located in the top of the column total vaporizes. There are two ways to do this. The best way is to ensure a direct contact between vapour flux and liquid reflux in the argon column, using a combination of conventional sieve trays and structured packing. In that situation, the pressure drop in the argon column is lower that in the case when all the trays are conventional. The conventional trays will provide a supplementary pressure drop, so the pressure in the top of argon column can be adjusted. By reducing the pressure in the top of crude argon column lead to the reducing de temperature difference in the condenser placed at the top of this column.

## 4. DISCUSSION

The process shown in figure 2 was simulated. The basis for the simulation is that the plant produces all gaseous products. Two cases were considered: one case when all the trays are conventional sieve trays, and second case, where in the crude argon column there is a combination of conventional sieve trays and packing trays. The temperature difference in the condenser located at the top of crude argon column was considered $\Delta T = 3$ K. In the first case, the simulation show that a crude argon product having an oxygen concentration of 3 % and an argon recovery of 91%. If the oxygen concentration in crude argon is 1.5 %, the argon recovery will be 82 %. In the second case, a crude argon product having an oxygen concentration of 0.7 % should be obtained and an argon recovery of 90 %. By using packing trays, the pressure drop in the crude argon column decreases, so we can use a larger number of trays without any energy penalty.

In figure 3, argon recovery is presented like a function of pressure at the top of crude argon column. From this figure, a maximum argon recovery will exist, depending of the pressure at the top of crude argon column.

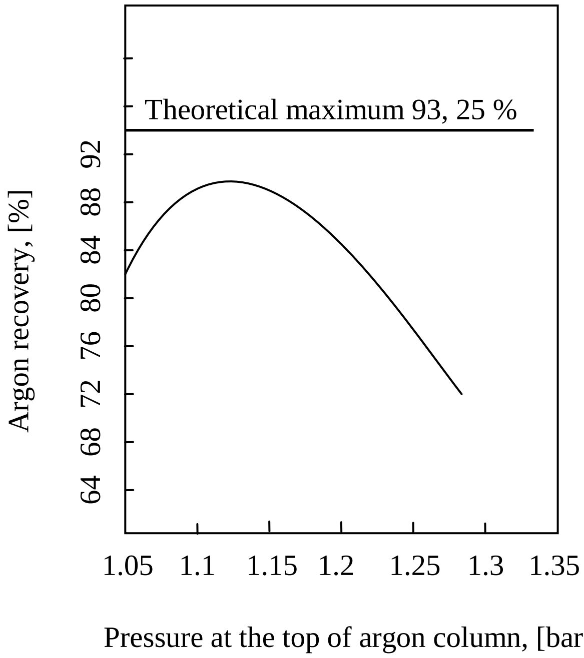

Figure 3. Argon recovery versus pressure at the top of crude argon column

Normally, it is expected that the separation process is better when pressure at the top of the argon column is low. That because when the pressure is reduced, the relative volatility of argon with respect of oxygen is increasing. Due to this low value of the relative volatility, a large number of theoretical stages or a value for reflux factor L/V approaching the unity are required to produce crude argon with low concentration of oxygen.

## 5. CONCLUSIONS

In order to increase argon recovery in a cryogenic air separation plant, the oxygen enriched liquid from the bottom of high pressure column passed through the condenser placed at the top of argon column, and it will leave like saturated vapours. In order to reduce the pressure drop in the argon column, part of the trays should be structured packing and some conventional sieve trays placed at the bottom of the crude argon column. The conventional sieve trays reduce the pressure at the top of crude argon column, for controlling the temperature difference in the condenser.

## 6. REFERENCES

Lenneskog A. 1995. *Air separation techniques course*, AGA AB, Lidingö, Sweden.

Bernstein J. CRYOGENIC ARGON PRODUCTION, Modern Air Separation Plant Technology Conference, Chengdu, China, 1999.

Arkharov A. M. 2001, *Cryogenic Systems*, Bauman Moscow State Technical University Press, Moscow.

Isalsky, W.H., 1989, *Air Separation Processes*, Separation of Gases, Clarendon Press, Oxford.

034

# Test Procedures for Cryogenic Components and Considerations for Leakage Measurement

**Boersch M., Holdener F., Iten E.,Oertig D.**

WEKA AG, Baeretswil, Switzerland

## ABSTRACT

Engineering components in cryo-technological plants have to meet demanding requirements derived from functional needs or prescribed in relating standards.
For cryogenic components such as cryogenic valves and couplings some of the most important characteristics are defined in tightness requirements and pressure stability. However the performance is needed at service under cryogenic conditions, specific time-tested procedures are established since long time and carried out under ambient temperature level. Whereas for pressure tests it can be followed to the international standards and regulations, the preconditions for definition, testing and interpretation of acceptable leakage rates are based on limits of detectibility of the methods and lastly the experiences in the field. Corresponding specifications and test procedures for test objects to their encircling vacuum insulation, their ambient and their function related pipe connections has been established.

## 1. INTRODUCTION

There are very high tightness requirements on cryogenic control and shut-off valves as well as on other cryogenic components such as check valves, couplings and ejectors. These default settings are necessary since the components must ensure shut-off, on the one hand, and practically no medium must escape into the insulation vacuum, on the other. No medium may also reach the environment. This applies especially to expensive or hazardous gases. The high tightness requirements are a result of the very small molecular size of frequently used cryogenic media. The requirements are specified through permissible leak rates.

## 2. MEASURING METHOD TO DETECT THE SMALLEST LEAK RATES

Tightness tests on cryogenic systems and components are usually carried out at ambient temperature using helium as test gas. The test gas pressure corresponds to the specified operating or design pressure.

### 2.1. Tightness test in the overpressure method

The test gas is connected to the object to be tested and generates an internal pressure in the object.
Tests are carried out on important checkpoints such as housing, welding seams and O-ring gaskets to check whether test gas is escaping. When the helium concentration is increased, the attached measuring device (helium detector) calculates the leak rate. A distinction between local and integral leak detection is made.
While the entire test object is included in integral leak detection, local leak detection investigates individual components of the test object. This makes leak detection easy. However, the test object is only partially tested and the detectable leak rates are limited because of the background concentration of helium in the measuring environment.

The principle explained below is the simplest method for determining the tightness of a test object. It can be used in the qualitative testing of a weld seam, for example.

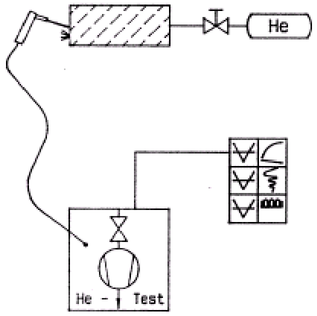

Figure 1. Local leak searching with helium sniffling device

The following method can be used to determine the local quantitative leak rate. It is used as the standard test procedure for cryogenic valves to test welding seams, metallic bellows seals or O-ring seals, for example. The smallest detectable leak rate is Q ≤ 1*10-7 mbar*l/s.

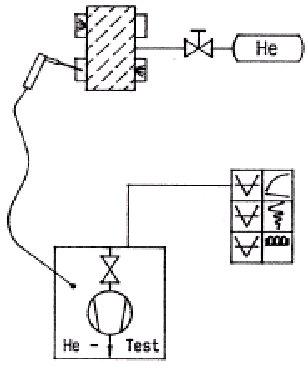

Figure 2. Integral-method, local with plastic bag

The next method can be used to check the integral leakiness of a test object.
It is used in the testing of valve bodies, for example. If there is a leak, however, its position cannot be located.
The smallest detectable leak rate is Q ≤ 1*10-7 mbar*l/s.

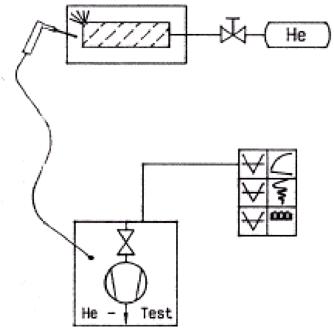

Figure 3. Integral-method with plastic bag

If tightness requirements are especially stringent, the test object is tested in a vacuum chamber.
The vacuum environment allows even the smallest helium concentrations in the range of Q ≥ 1*10-9 mbar*l/s to be detected, and even lower concentrations using suitable measuring instruments.
However, the position of a possible leak also cannot be determined using this method.
The principle of vacuum measurement is the standard procedure for determining the seat tightness of a cryogenic valve.

The vacuum method is also suitable for tightness tests at cryogenic temperatures. The valve seat and seat housing are indirectly cooled to 80K in the test chamber using an LN2 cooling medium (with a heat exchanger).

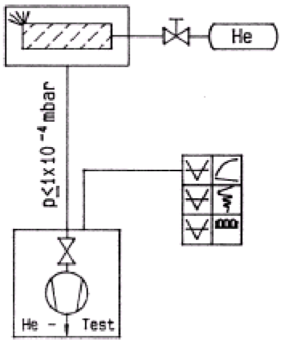

Figure 4. Integral-method with vacuum envelope

## 2.2. Tightness test in the vacuum method

The vacuum method is also used as the second essential method for tightness tests. Here the test object is connected to the helium detector and the air in the inner test chamber is evacuated. This creates a vacuum in the test object. The test gas is applied from outside, penetrating the test vacuum if there are leaks. The method allows quantitative calculation of the leak rate. It is used especially if the design complicates accessibility, that is, measurement using the overpressure method cannot be done or valves used in vacuum operation have to be tested.

Since the leak rate is determined inside a test vacuum, very low concentrations and leak rates can also be detected using this method.

The following principle, in turn, represents the simplest method for determining the tightness of a test object. The leak rate can also be quantitatively determined using this method.

It is often used to determine leak location but also to test welding seams.

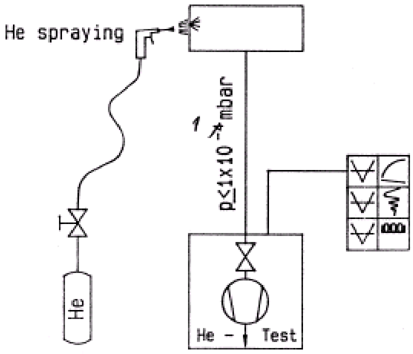

Figure 5. Local leak searching

The leak rate in a locally demarcated area can be calculated quantitatively using the following method. It is used in welding seam testing, for example.

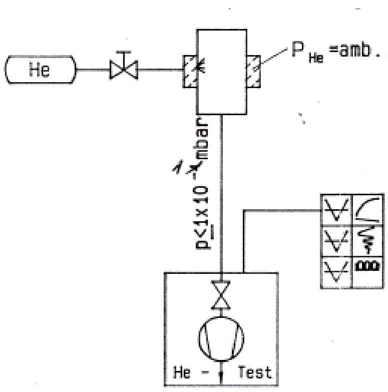

Figure 6. Integral-method, local with plastic bag

The next method can be used to check the integral leakiness of a test object.
The leak rate can be calculated quantitatively. The method is used in the testing of valve bodies intended for media under vacuum, for example.

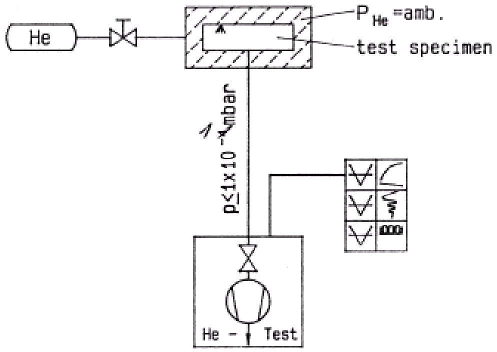

Figure 7. Integral-method with plastic bag

## 3. VALVE TIGHTNESS

### 3.1. Tightness of the valve seat

The tightness of cryogenic valves is determined in various tests. To demonstrate the shut-off function, the valve seat is first checked.
For this purpose, the valve is closed with the specified closure force and the helium test gas at the prescribed operating pressure and at ambient temperature is fed to the valve input. The helium detector is connected to the valve output. The detector's vacuum pump generates a test vacuum in the range of $p \leq 1*10\text{-}4$ mbar. The helium detector measures the concentration of helium test gas entering and calculates the existing leak rate based on the increase in concentration. The accumulation test during which the test is executed is at least 10 minutes.
High levels of valve tightness are reached using soft seat seals. Their leak rate lies in the range of $Q \leq 1*10\text{-}4$ mbar*l/s.
The procedure essentially corresponds to the drawing in Figure 4.

### 3.2. Tightness of the valve body to the environment

The tightness of the valve body against the environment can be tested in two different ways. In both methods the valve is placed in the open position and filled with helium test gas at the prescribed operating pressure at ambient temperature.

In the integral test shown in Figure 4 the entire valve is in the vacuum chamber right up to the valve's vacuum flange. The helium detector is connected to the vacuum chamber and detects the increase in helium concentration during a retention period of at least 10 minutes. The leak rate of the valve body with welding seams lies in the range of $Q \leq 1*10\text{-}7$ mbar*l/s.

The method shown in Figure 2 is used as an alternative to this procedure. The advantage lies in the flexibility with which the most varied kinds and sizes of valves can be tested as well as in the fact that leak locations can be directly determined.

### 3.3. Tightness of safety sealing

The movable valve inset of cryogenic valves has double sealing against the environment on the valve stem. When using valves for low-molecular or rare gases, metal bellows seals are often used together with a downstream static gasket to form a dynamic seal. Testing is carried out in the intermediate chamber of both gaskets (cf. to Figure 1).

## 4. TIGHTNESS OF COUPLINGS AND OTHER COMPONENTS

Other cryogenic components are tested in similar fashion. The tests should mirror the application in the best possible way, that means components under internal pressure are also connected and loaded accordingly during the tightness test. Important functional characteristics are likewise loaded according to the operating conditions.

Cryogenic couplings are also always tested for tightness against the environment in the plugged-in and secure state.

In check valves tightness is also tested in the reverse direction.

## 5. INTERPRETATION OF RESULTS

The leak rates of test gases can be converted to various process gases using formulas and available tables.

In these calculations, however, the different leak types which have other properties in cracks and pores in metals compared to leaks in plastic seals must be considered.

In principle, conclusions can also be drawn for cryogenic media. However, it has been known and demonstrated from decades of practical application that the leak rates described above - which are determined at ambient temperature - also ensure adequate tightness in the operating range of cryogenic temperatures.

## 6. REFERENCES

WEKA AG Baeretswil, Switzerland, *Standard Delivery of Cryogenic Components*.

WEKA AG Baeretswil, Switzerland, *Helium Tightness Test, Pressurized Procedure and Vacuum Procedure*.

083

# Study on the Miniature Turbo-Expander Reverse Brayton Cryocooler Designed for Operation at 100 K

**Hou Y.**[**], **Lai T.**[*], **Zhao H.**[*], **Chen R.**[*]

[*] School of Energy and Power Engineering, Xi'an Jiaotong University, Xi'an, China
[**] State Key Laboratory of Multiphase Flow in Power Engineering, Xi'an Jiaotong University, Xi'an, China

## ABSTRACT

For the demands of space application, the prototype of the reverse Brayton cycle cryocooler was developed. The designed lowest temperature of this cryocooler is 80 K and a cooling capacity of 10 W @ 100 K is expected. The main components of the cryocooler are a woven wire screen matrix heat exchanger and a gas bearing turbo-expander (GBTP). The heat transfer performance of a woven wire screen matrix heat exchanger was introduced; especially the overall performance of the miniature high speed turbo-expander was studied experimentally. A 9 mm diameter radial impeller is applied to drive the rotor and the normal speed of this GBTP is about 300,000 rpm. The experimental results show that the turbine maintains very stable running, small vibration and high efficiency.

Keywords: Reverse Brayton cycle; Cryocooler; Turbo expander

## 1. INTRODUCTION

The application of high speed turbine machinery in a Reverse Brayton cycle(RBC) cryocooler makes it not only possess many advantages, such as miniaturization, long lifetime, wide range of cooling temperature and wide range of cooling capacity, but is also an ideal way to realize high thermal efficiency, and high reliability of a space cryocooler[Swift 1999]. In order to promote the exploration of key technology of miniature turbo-expanders, a -50℃ Reverse Brayton cycle air refrigerator, a range of 190 K/170 K/100 K RBC cryocoolers, an 80 K RBC cryocooler test rig and a 10 W @ 100 K miniature RBC cryocooler prototype were set up by the institute of Refrigeration and Cryogenics of Xi'an Jiaotong University who is the beginner in the study of RBC cryocooler in China[Hou 2006]. In the meantime, a series of turbo-expanders with rotating speed at 80 krpm (rotor diameter 35 mm), 100 krpm (rotor diameter 25 mm), 170 krpm (rotor diameter 17 mm), 220 krpm (rotor diameter 12 mm) and 480 krpm (rotor diameter 6 mm) were fabricated.

## 2. REVERSE BRAYTON CYOCOOLER SYSTEM

The ideal fundamental cycle of the single stage turbo-expander RBC consists of four parts including isentropic compression, isobaric cooling, isentropic expansion and isobaric heating. With the above four parts a RBC cryocooler migrates the heat load from a low temperature body to a high temperature object. Nitrogen was used as the working fluid for the 10 W @ 100 K RBC cryocooler proposed in this paper; the system diagram and the design parameters are shown in Fig. 1. The system shown in Fig.1 is constituted by turbo-expander 8, brake wheel 9, matrix heat exchanger 6, three water coolers 3, 5 and 10, and a two stage compressor 1 and 2.

## 3. HEAT EXCHANGER

The demands of high efficiency and light weight require a heat exchanger with high compactness and small terminal temperature difference. A highly compact and high efficiency wire screen matrix heat exchanger (seen from Fig. 2) was employed in the proposed RBC cryocooler. The right photograph of Fig.2 is an overall view of the wire screen matrix heat exchanger, totally 500 spacer-screen pairs (as shown in the left of Fig.2) constitute the whole heat exchanger, the curly tubes in the matrix heat exchanger body are fixed for pressure measurement. The detailed thermal performance and pressure loss of the designed matrix heat exchanger were investigated experimentally by Chen et al. [Chen 2009]. Figure 3 shows the vacuum cryo-trap test rig. With a thermal efficiency of 95% at the condition of 260 W/230 K(seen from Fig. 4) and a pressure loss of 6 kPa the tested matrix heat exchanger can meet the requirements of the cryocooler. Two matrix heat exchangers are configured in the RBC cryocooler system in parallel in order to determine the thermal efficiency.

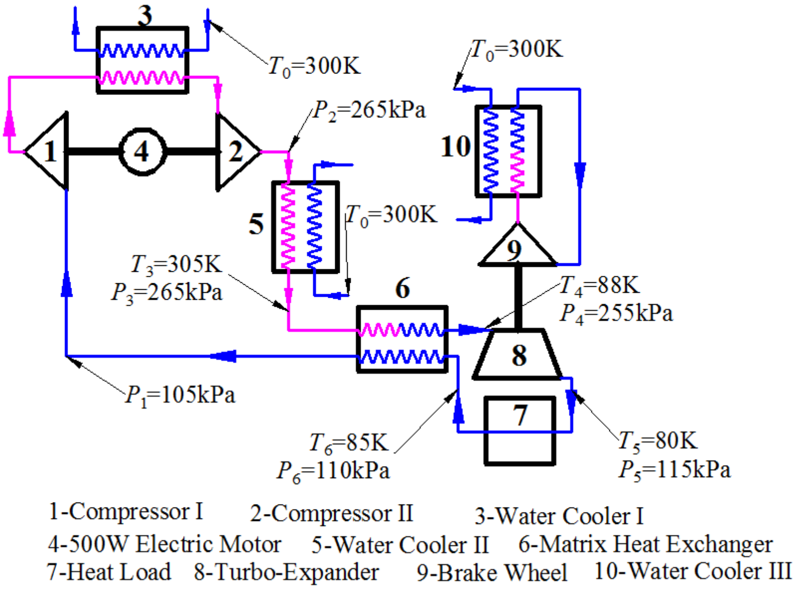

Figure 1 System diagram of 10 W/100 K single stage RBC cryocooler

Figure 2 Matrix heat exchanger and its heat transfer unit

## 4. GAS BEARING TURBOEXPANDER

As the key component, the turbo-expander can supply most of the capacity to remove heat for the whole system; therefore good thermal performance and good mechanical performance become vital to a high efficiency and high reliability turbo-expander. A gas bearing was applied to achieve the high speed from 100 krpm to 500 krpm which to some extent means high efficiency [Chen 2010]. A turbo-expander with a rotor diameter of 6mm and a working wheel diameter of 9 mm was fabricated. Two integrative throttle orifice type aerostatic thrust and journal bearings were employed as supporting elements. Fig. 5 and Fig. 6 show the photos of the turbo-expander and parts of its components, respectively.

Figure 7 shows the measured frequency distribution and rotor centreline orbit of the turbo-expander at 342328 rpm. The results show that the synchronous frequency component occupies the major part compared to the subsynchronous frequencies; in addition, the rotor has a regular centreline orbit and small vibration amplitude (right chart in Fig. 7). It is can be seen from Fig. 8 that the turbo-expander can achieve stable running with maximum vibration amplitude of 3.1 μm. According to the real inlet and outlet temperature of the turbo-expander, the proposed RBC cryocooler presents good stability, and high cooling rate (seen from Fig. 9). Finally, a system thermal efficiency of 50% and a maximum temperature drop of 42 K were achieved at 0.27 MPa system inlet pressure and 296 K ambient temperature.

Figure 3 Matrix heat exchanger test rig

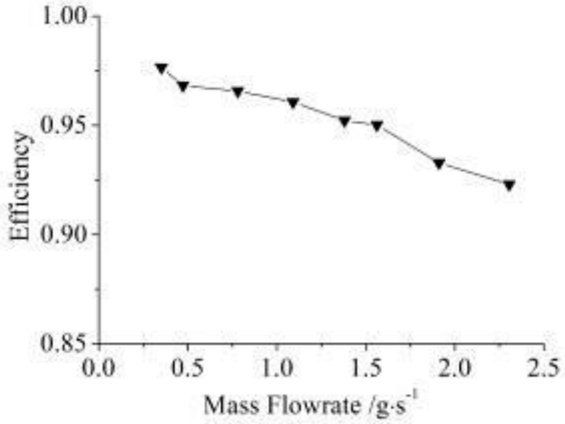

Figure 4 Efficiency versus mass flow rate

Figure 5 Miniature turbo-expander

Figure 6 Rotor and nozzle ring

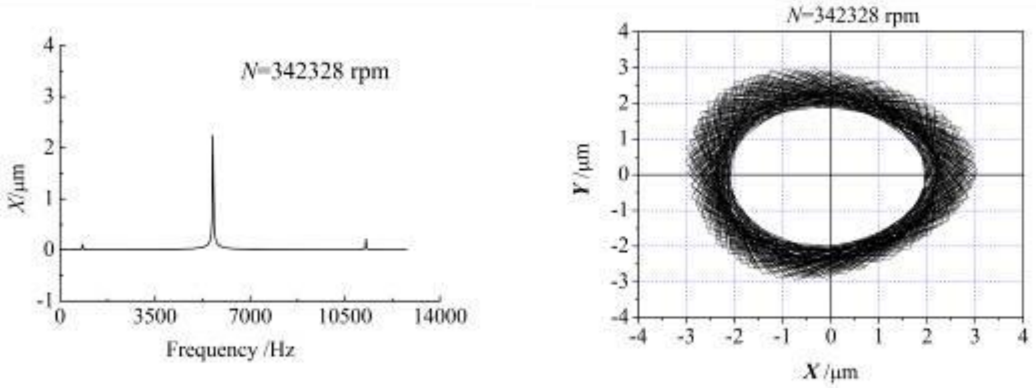

Figure 7 Frequency distribution and rotor centreline orbit of turbo-expander

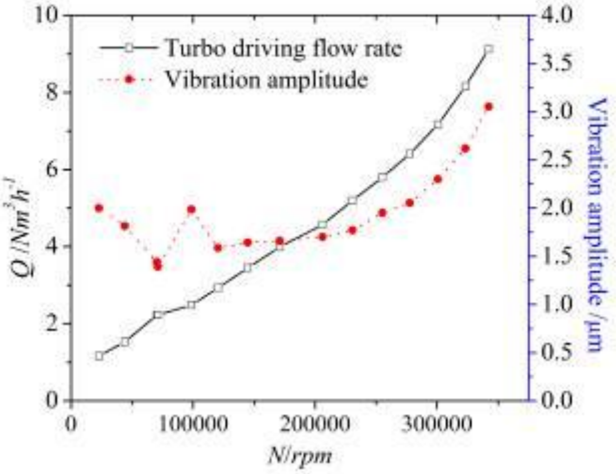

Figure 8 Tubine flow rate $Q$ and vibration amplitude versus speed of rotor $N$

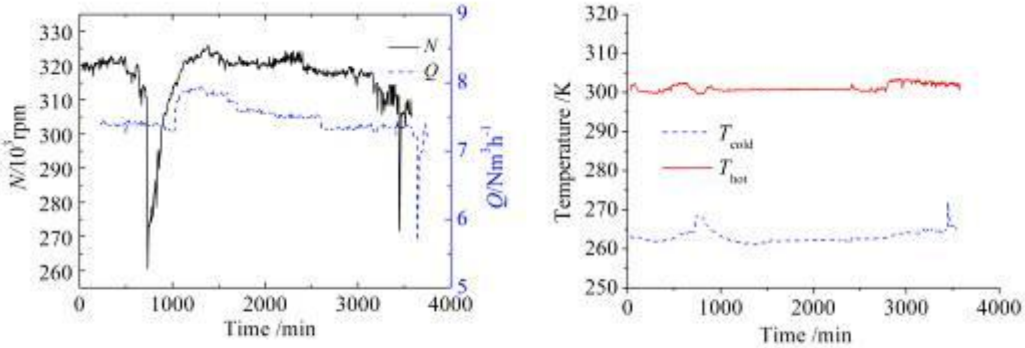

Figure 9 Experimental thermal performance of the expander in environment

## 5. CONCLUSIONS

The experiment verified that the mechanical and thermal performance of this turbo-expander, and the thermal performance and pressure loss of the applied matrix heat exchanger can meet the requirements of the cryocooler and is feasible to be widely applied to the reverse Brayton cryocooler at lower temperature. Furthermore, the 100 K cryogenic temperature test of the designed RBC cryocooler is in progress.

## 6. ACKNOWLEDGEMENT

This project was supported by National Nature Science Foundation of China (50976082) and the Specialized Research Fund for the Doctoral Program of Higher Education (20090201110006).

## 7. REFERENCES

Swift WL, Zagarola MV, Nellis GF, McCormic JA, Sixsmith H, Gibbon JA. 1999, Developments in turbo Brayton technology for low temperature applications, *Cryogenics*. 39(12): 989-995.

Hou Y, Zhao HL, Chen CZ, Xiong LY. 2006, Developments in Reverse Brayton Cycle Cryocooler in China, *Cryogenics*. 46(5), 403-407.

Chen ST, Hou Y, Zhao HL, Xi L. 2009, A numerical model of thermal analysis for woven wire screen matrix heat exchanger, *Cryogenics*. 49(9), 482-489.

Chen RG, Hou Y, Chen CZ. 2010, Study of miniature high speed turboexpander with gas lubricated bearing, *Journal of Xi'an Jiaotong University*. 44(1), 61-65.

084

# Experimental Investigation on the Thermodynamic Performance of Turbo-Expander in Two Phases

**Lai T.[*], Hou Y.[**], Niu L.[*], Liu J.[*]**

[*] School of Energy and Power Engineering, Xi'an Jiaotong University, Xi'an, China
[**] State Key Laboratory of Multiphase Flow in Power Engineering, Xi'an Jiaotong University, Xi'an, China

## ABSTRACT

Experiment has been carried out on a two-phase air turboexpander under pre-cooling operation in order to enhance the efficiency of expander working in two-phase state. The temperature at the inlet of turboexpander is controlled through regulating the heat transfer rate of front heat exchanger. The outlet temperature, rotating speed and thermodynamic efficiency of the tested turboexpander with respect to inlet temperature have been instrumented and studied. When the turboexpander stepped into two-phase state, the outlet temperature tends towards stability which is independent with air inlet temperature. The isotropic efficiency of turboexpander with relative low liquid ratio maintains a high level and a system hysteresis shows up in the experiment. The working principle of turboexpander transiting from single phase to two phases has been investigated which may provides more reliable design criteria for turboexpanders working in two-phase.
Keywords: two-phase, turboexpander, thermodynamic efficiency, low liquid ratio

## 1. INTRODUCTION

Isentropic expansion is recognized as one of the most important approaches for cryogenic refrigeration, and the quasi-isentropic process can be efficiently realized through the expansion in a turboexpander. In the air separation and liquefaction plants, the performance including the extraction ratio and units energy consumption can be improved by replacing the throttle with a two-phase turboexpander which possesses higher refrigeration effect and retrieves a portion of the expansion work. However, the complex phase transition and two phase flow in a cryogenic two phase turbo-expander will bring down its thermodynamic performance and lead to cavitations and aerodynamic performance degradation.

Research and development of two-phase turboexpander has been focused on the gas-liquid or gas-solid flows. In 1970, a design criterion that droplet or micro particles force direction at any location of the flow trajectory should be parallel with flow path structure surface has been proposed by a research institute from USA, a two-phase turboexpander was developed and applied successfully, and its efficiency reached 82% with a power output of 895kW. 1984, Ardashev raised the liquid ratio of turboexpander up to 20% by controlling gas condensation point, which provided basic research foundations for high liquid ratio turboexpander in air separation systems. Kevin from O.C. Turboexpanders concise discussed and validated the reliability of two phase turboexpander with high liquid ratio by means of experiment in respect of operation reliability, efficiency and precise two-phase flow design.

To obtain the characteristics of thermodynamic and aerodynamic performance of a two-phase turbo-expander, experiment was carried out on a back stream expansion turboexpander in a low pressure air separation system.

## 2. EXPERIMENTAL SYSTEM

### 2.1. Main Experimental Equipment

The experiment was conducted on the low pressure liquid nitrogen air separation system with an air handling capacity of 20L/h liquid nitrogen. The experimental diagram is shown in Fig. 1 and the tested turboexpanders are shown in Fig. 2.

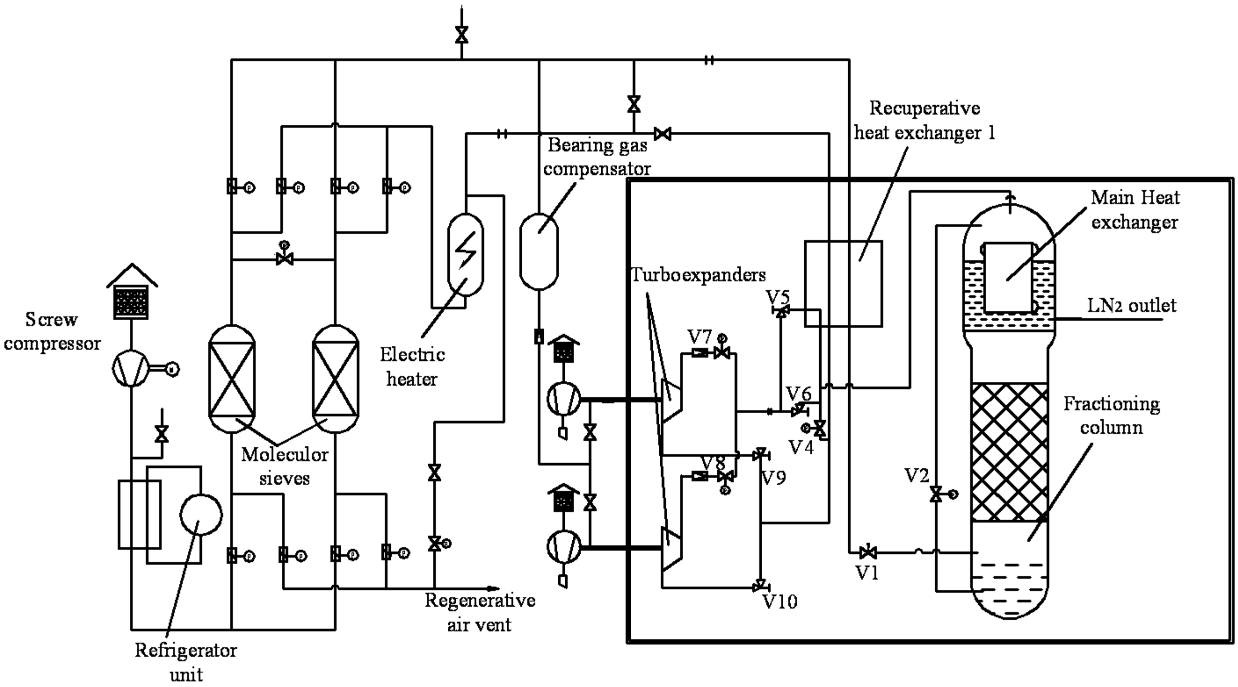

Figure 1 Flow diagram of $LN_2$ low pressure air separation system

Figure 2 Two phase turboexpander setup

## 2.2. Experimental method

The air temperature at the inlet of expander is adjusted through regulating the fluid flow rate through recuperator heat exchanger 1 ( seen from Fig.1). The procedure in the experiment is as follows:
Step 1 Open up the bypass valve V6 in Fig. 1 gradually at an interval of 1 minute, record the expander outlet air temperature and rotational speed until V6 fully opened;
Step 2 Close down the inlet valve of turboexpander V5 gradually at an interval of 1 minute, record the expander outlet air temperature and rotational speed until V5 fully closed;
Step 3 Monitor and record the expander outlet air temperature and rotational speed at an interval of 1 minute until the parameters are stabilized.
Step 4 Restore the original process by reversing the above mentioned steps and shut down the system.

## 3. RESULTS AND DISCUSSIONS

## 3.1. System operation states

The main parameters of the experiment are presented in table 1. The inlet and outlet fluid temperatures of the experiment are lower compare to the designed condition while the inlet pressure is higher.

Table 1 Working parameters and corresponding saturation phase states(60% nitrogen mass ratio)

| Opearting parameter | Inlet temperature/ K | Inlet pressure/ MPa | Outlet pressure/ MPa | Gas saturation temperature / K |
|---|---|---|---|---|
| Designed | 121 | 0.41 | 0.13 | 86.65 |
| Experiment | 105.7 | 0.35 | 0.13 | -- |

### 3.2. Experimental results

The inlet and outlet temperatures in the experiment are displayed in Fig. 3. In step 1 and 2, the outlet fluid temperatures of turboexpander decreased with the cooling down of inlet temperature and the two curves kept similar trend. In step 3, the outlet temperature dropped spontaneously due to system inertia from the moment at 30 minute. During the initial period of self cooling, the inlet temperature decreased and the outlet temperature went into a relative stable state which means that the turboexpander had entered into two-phase state. At the end of self cooling, both temperatures at inlet and outlet kept stabilized and the system went into an equilibrium state since 45 minute. The outlet temperature in the experiment appeared stable around 88.9K and the corresponding inlet temperature was 106K.

The relationship between outlet and inlet temperatures is shown in Fig. 4. The theoretical and experimental temperatures kept stabilized to respective values with the decrease of inlet temperature which follows the similar trend. The theoretical results predict well when inlet temperature is higher than 115K, and deviate a little afterwards. The two phase onset of the experiment is 110K for inlet temperature and 88K for outlet.

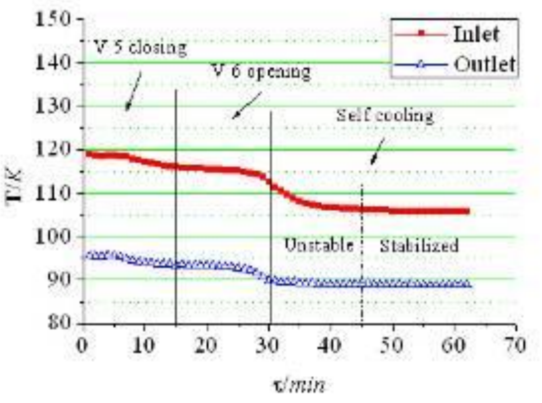

Figure 3 Inlet and outlet temperatures

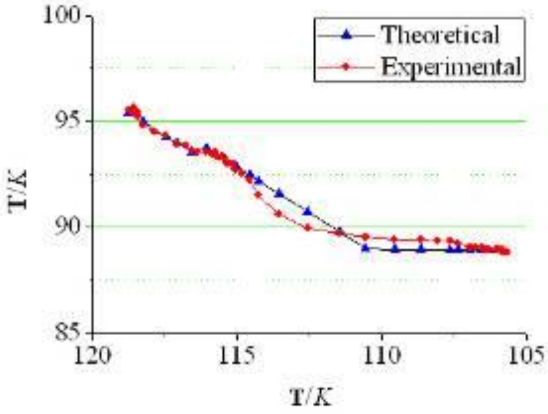

Figure 4 Outlet temperature VS. inlet temperatures

The trends of isentropic efficiency curves from experiment and theoretical ideal condition are displayed in Fig. 5. When the inlet temperature higher than 116K, the experimental results and theoretical prediction agreed quite well, however they diverged a little afterwards corresponding to the onset of condensation. In the range of 115K~112K, the theoretical model underestimates the efficiency which can be contributed to the phase state transiting process mentioned above. Both of the efficiencies under designed condition and experimental condition were around 70%, and dropped sharply afterwards. When the expander stepped into two phase, the relative density of liquid is larger than the gas density, which causes the collision of small droplets with wheel blades and a decrease of thermal efficiency.

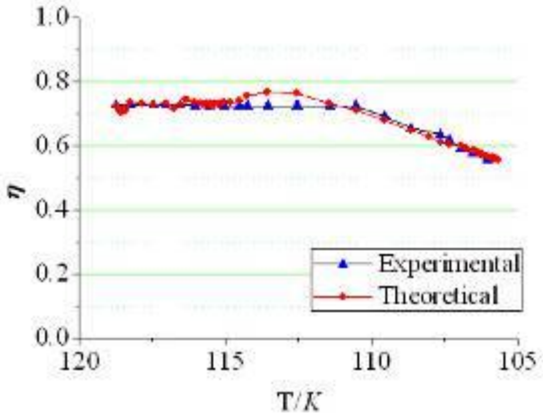

Figure 5 Efficiency VS. inlet temperatures

## 4. CONCLUSIONS

Cooling process of the air separation system for two phase turboexpander displayed a good agreement with theoretical predictions at single phase and small deviations in two phases requiring more accurate mathematical model.

1. The outlet temperature of turboexpander dropped with the decrease of inlet temperature at air cooling state. When the inlet temperature was lower than 106K, the outlet temperature tends towards stability which indicated that the turboexpander stepped into two-phase state;
2. There appeared a system hysteresis phenomena in the expander cooling process which caused by large heat inertia of the air separation plant;
3. The theoretical model predicts quite well the outlet pressure and efficiency at both single and two phase state, and misfit a bit in the transiting process from gas to gas-liquid.

## 5. AKNOWLEDGEMENT

This project was supported by National Nature Science Foundation of China (50976082) and the Specialized Research Fund for the Doctoral Program of Higher Education (20090201110006).

## 6. REFERENCES

US3495921 Variable nozzle turbine.

Ardashev VI, Plachendovskii DI. 1984, Examination of two-phase regimes of cryogenic turbine expansion engines. *Chemical and Petroleum Engineering*, 20(4): p. 182-185.

Kaypert KA. 2009, Design of two phase flow air separation turboexpanders (in Chinese).

Nag PK, Thermodynamic Engineering. 3rd Edition 2008, Tat McGraw-Hill Publishing Company Limited.

# POSTER SESSION
# - CRYOSURGERY

048

# Dreams and Reality of Cryogenic Technology in Surgery

**Butorina A.[*], Arkharov A.[**], Matveev V.[**]**

[*]The Russian National Research Medical University named after N.I. Pirogov, Moscow, Russia
[**]Moscow State Technical University named after N.E. Bauman, Moscow, Russia

## ABSTRACT

The physical mechanisms of cryogenic and MW impacts on the human organism tissues are disclosed, the tissues thermophysical properties are studied within a wide temperature range. On that ground, the effective technologies of abovementioned impacts application, are disclosed and for the first time approved for treatment of some complicated child's illnesses.

Today the notion "cryotherapy" includes combination of physical methods of treatment based on heat removing by means of liquid, solid and gaseous working bodies (from a humid cold rub-down to the impact using ultralow temperatures). A cooling effect may be applied to different areas of the body as well as to the all body of a man. In sportive medicine the temperature lowering of skin reduces the conduction of nerve impulses and at +5$^0$C the conduction of these impulses is completely blocked. We examined the rates of involution of pathological symptomatology of damages. We studied the data obtained after one week of treatment (analgesic freezing) of patients of an experimental group. During appraisal it was revealed that the sum time of rehabilitation of sportsmen using analgesic freezing decreased 2.5 times in comparison with the rehabilitation time of sportsmen which didn't use it. These technologies are included in the complex of rehabilitation actions with the sportsmen.

## 1. INTRODUCTION

Achievements of modern physics and engineering technologies allow to apply various physical medicinal manipulations – laser, ultrasonic, plasma, electromagnetic and cryogenic manipulations, on human living tissues and organs so as to suppress the pathology in their functioning or to destruct pathologic formations. First success of the cryogenic method in the 60th had allowed to take it as universal one, and that led to the overestimation of the method capabilities and to its unsubstantiated applications. Absence of indubitable methods to analyse and predict main parameters of cryogenic impact, as well as underrating of the necessity to use this process in combination with other physical manipulations had led to that the better part of cryosurgical operations earned their application for treatment of small pathologic formations of accessible localization. The situation was also aggravated by that the cryosurgical equipment design problems were considered without due regard for thermophysical properties of the impact object – biological tissue. Besides, it is experimentally stated that cryogenic impacts have got considerable restrictions in the freezing penetration depth and the destruction volume of large pathogenic formations. Even the use of powerful cryosurgical devices first constructed at the Bauman Moscow State Technical University in the 1970th for treatment of children's haemangioma, was not always successful. There were patients whose tumour after cryodestruction had the sphacelated tissue only on the surface but its deep part continued growing. Thus, the search of new methods to intensify cryodestruction in combination with other physical impacts in order to reach sufficient broadening of the cryogenic method application limits, is thus really actual. The methods intensifying cryodestruction and using the repeated cycles "freezing-thawing" as well as the ultrasound, did not provide a noticeable increase of the frozen tissue volume. To strengthen cryodestruction, it was crucial to find the impact type increasing the tissue sensibility to low temperature. Preliminary radiation of the freezing zone by microwave electromagnetic field (MW EMF) proved to be one of such impacts whose features had to be studied carefully.

## 2. KEY PART. RESEARCH AND APPLICATION

Biological tissue as the thermophysical object is multicomponent, capillary-porous, moisture-containing anisotropic body consisting of several layers with essentially different TPP: skin, hypodermic fatty tissue, muscles, bones, etc., where the pathologic inclusions can be formed. Heat evolution is in evidence in the *in vivo* biotissue due to the blood flow and metabolism. Biotissue is a very energetically saturated structure. Cryosurgical instruments, even cooled by means of powerful cryogenic system of a large refrigerating capacity, is just a point source of cold. So, for the first time an effective thermal conductivity of the *in vivo* biotissue reflecting the living tissue whole energetics, was taken into consideration.

The processes accompanying local impact on biotissue by cryosurgical appliance having flat probe can be illustrated schematically (Fig. 1). The cryosurgical probe tip contacts with the cryoimpact object – pathologic formation. Liquid nitrogen is fed into the probe at temperature 77 K. The temperature gradient originates, and it leads to that the heat starts to be transferred to the probe walls, and from them to liquid nitrogen boiling away partially or fully; the nitrogen is removed from the probe. The biotissue temperature around the probe tip starts to decrease.

When the biotissue temperature lowers below the cryoscopic one (~ -1°C), water contained in biotissue starts to pass to the solid state, and as a result a large quantity (~ 333 J/g) of the latent heat of ice formation is caused. This phase transition extends within some temperature interval, a large part of free water crystallizes at ~ -25°C. There is no heat release in the tissue zone with frozen water. Heat transfer by natural convection occurs on the boundary biotissue - environment.

The biotissue temperature in the area distant from the cryoimpact point is equal to initial temperature. If the cryoimpact object is not large, temperature on the borders distant from the probe tip can also decrease. At cryogenic impact, the necrosis zone in biotissue is smaller than the freezing zone. The modelling procedure reveals main regularities of the freezing zone formation on the basis of real TPP of *in vivo* and *in vitro* biological tissues.

The hemangiomas of a child aged six months having localization in the head and in the neck are growing very fast. It was found that the hemangiomas of a premature born child were growing 2-3 times fast than those of the normal newborn. Prematurity is not a contra-indication for the treatment. The child must be treated as soon as it is diagnosed (Kandel, 1974; Cherstvy and Kravtsov, 1991; Fedoreev, 1974).

Last time a cryogenic method of treatment was prevalent. The application of special apparatuses and cryogenic systems for local low temperature impact extends the possibilities of this method. Tanks to the almost painless treatment, cosmetic loyalty, absence of hemorrhage and general pronounced reaction of the organism a low temperature impact was named “surgery without scalpel”. The experience of treatment of 200,000 children with hemangiomas was accumulated.

For treatment an apparatus cryogenic method where liquid nitrogen is used as a refrigerant at – 196°C boiling temperature was applied. An out-patient treatment method didn’t need great expenses. Optimum time of cryogenic impact on hemangiomas placed on the skin is 20-25 seconds; optimum time of action on tumors placed on mucous membranes is 7-10 seconds. A total surface subject to cryogenic impact mustn’t exceed 10 square centimeters.

The success of treatment is 100%. The first important advantage of the treatment is good cosmetic and esthetic results (99,7%) thanks to particularities of skin regeneration after cryogenic intervention (organotypic regeneration).

Unfortunately this method was accepted as a panacea, and was applied in unfounded cases. Absence of reliable methods of calculations and prognostication led to the fact that cryosurgery was applied only to small formations easily accessible. In practice cryosurgery has limits to be applied when deep formations are to be destructed. Using modern cryogenic apparatuses is not always successful. If the hemangioma is large and deep the superficial part of the hemangioma is destroyed only but the deep one is continuing to grow.

It is an important problem of the cryosurgery of vast and complex formations to intensify cryodestruction. The MW-impact allows sufficient intensifying the destructive low-temperature effect on the biotissue. The known methods to strengthen cryodestruction such as repeated freezing – thawing cycles and ultrasound do

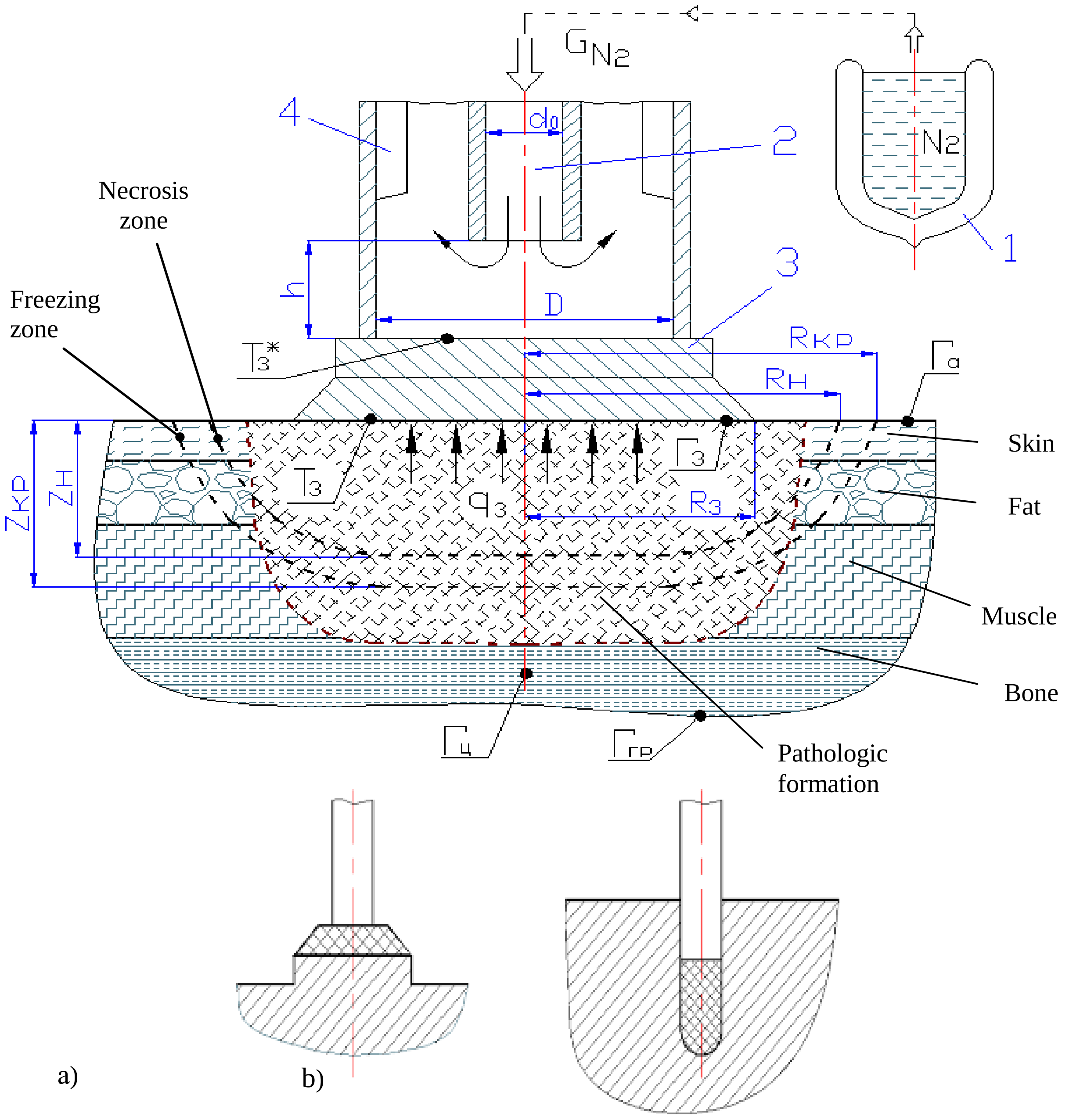

Figure1. Diagram of local cryogenic impact on biological tissue:
a) surface cryoimpact
б) penetration cryoimpact

$\Gamma_a$ – boundary with atmosphere; $\Gamma_s$ – axis of symmetry; $\Gamma_{bd}$ – analysis area boundary; $\Gamma_{pr}$ – cryogenic probe contact surface
1 – Dewar with liquid nitrogen; 2 – central pipe feeding the probe by liquid nitrogen; 3 – cryogenic probe; 4 – thermal insulation

not give evident increase in the necrosis volume.

In our judgement the physical factors increasing the tissue sensibility to low-temperature action form the methodological bases for solving the cryodestruction intensification problem. One of such factors is a microwave field, and its therapeutic possibilities were studied. The methods intensifying cryoimpact by means of preliminary microwave action on biotissue have tight restrictions on their application in medicine.

Absence of uniform understanding of mechanisms of the cryonecrosis amplification after preliminary MW-impact does not allow to build the process theoretical model and explains an empiric approach to the search of the combined impact optimal modes.

It is essential to remember that water as a basic component of biological tissues defines their TPP. The water crystallization temperature depends on its state. Three states of the water contained in biotissues can be singled out: free water, loosely coupled (immobilized), and tightly coupled (water of hydration). Water is accountable for the physical processes at freezing, and it freezes in biotissue not at 273.15 K but within the range from cryoscopic temperature (270.5...272.5 К) to eutectic (223...248 К) temperature. Freezing zone is as a rule larger than necrosis zone, and the ratio of these zones diameters reaches for the most tissues on the average 1.28.

Free water freezes at a temperature below zero. In the living organism, water of hydration is tightly coupled with albumens. The underlying physics of the freezing zone formation becomes evident owing to the research outcomes concerning the interdependence between the biotissue thermal conductivity, structure and freezing mode.

Microwaves are capable of interacting with aqueous lattice at “staggering” it. Free water content in biotissue increases at the MW EMF action and, consequently, the part of frozen water rises at cryoimpact that, in its turn, leads to the biotissue thermal conductivity growth. The relaxation processes arise in dipole molecules of water and liquid media, the resonance phenomena – in serous molecules of high dispersion. Alterations of the molecule hydration zone, as well as the breaks of intramolecular bonds can occur. Tissues with high water content absorb the fields 10…60 times stronger than adipose tissues. Increase in the biotissue thermal conductivity amplifies the cryodestruction effect after radiation by MW EMF.

The method to intensify cryodestruction by preliminary microwave impacting the area of forthcoming local freezing was developed by physicists and doctors. The method of physical modelling was used, the ratios of freezing and necrosis zone sizes were determined, and then the optimal parameters of cryoimpact modes as well as those of combined MW-cryo-impact modes verified by experiments, were proposed.

As long as the freezing zone formation in biotissue depends directly on its thermal conductivity, the MW influence on the *in vivo* and *in vitro* biotissue thermal conductivity was studied.

The MW-devices with frequency 915 MHz and power 0.1…20 W were used for electromagnetic impact on the biotissue. Cryogenic device had a flat probe tip of 7 mm diameter. Measurement and control of the probe and surrounding tissue temperatures were carried out by thermocouples. Research had been performed at -196°C with the use of gelatine gel of various moisture contents because gelatine gel is a substance adequate to biotissue in their thermophysical properties, and so it is capable of imitating such tissues. The dimensions of freezing and necrosis zones were measured with accuracy of ± 0.3 mm. Rabbits and dogs were put at the investigators’ disposal to study skin and muscle tissues.

Research of the influence of preliminary MW-impact on the sizes of freezing zone and necrosis zone of the animal’s skin-muscle tissue (Fig. 2) has shown that the optimal parameters of preliminary MW-impact are: power 10 W, frequency 915 MHz, radiation period - 3…5 min, with intervals 2 min. Freezing zone diameter in this case increases more than twice, and necrosis volume increases 5-6-fold as compared with simple freezing. Such combination of physical impacts, with maximal use of the resources of cryogenics operating with liquid nitrogen, gives the destruction mechanism for pathological formations with volume up to 12 $cm^3$.

The combined method of MW-cryo-impact allows to enlarge essentially both the necrosis zone and freezing zone, and their diameters ratio turned to be near to 1.1. It gives a possibility to subject to destruction large formations 4×4×4 $cm^3$ and larger by applying the same technical devices as for ordinary freezing, as well as to broaden sufficiently the domain of novel technologies application in medicine.

Performed analysis of the combined MW-cryoimpact application in cryosurgery has revealed optimal parameters of the MW-impact increasing the freezing and necrosis zones.

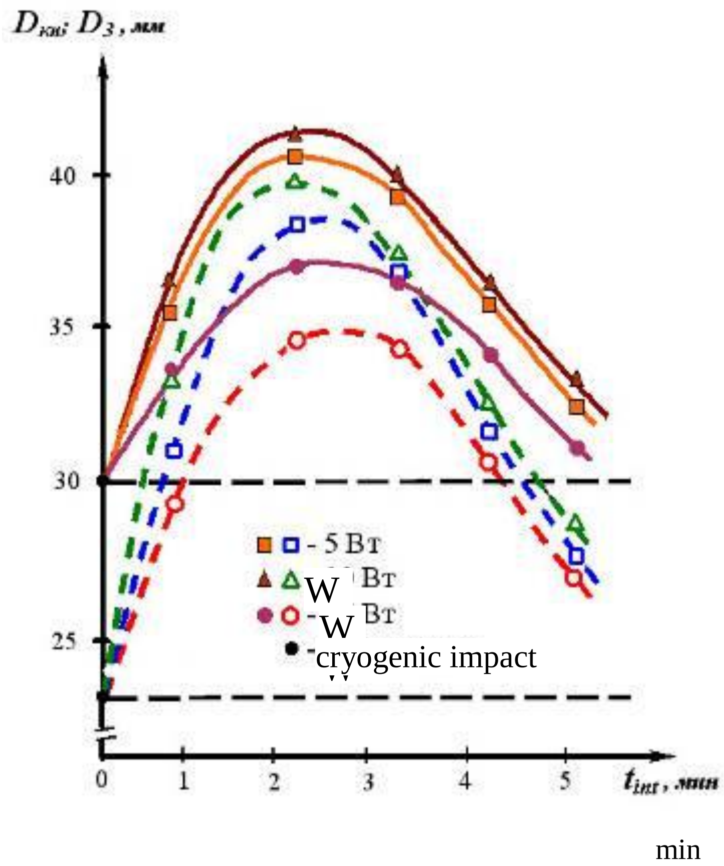

Figure 2. Relationships between the freezing zone diameter $D_{fr}$ and necrosis zone diameter $D_{nc}$ of skin-muscle tissue and time interval $t_{int}$ at various powers of preliminary MW-radiation.
MW-impact period – 3 min; frequency – 915 MHz; cryoimpact period – 15 min
——— freezing zone; – – – – necrosis zone.

The possibility appears to subject to the destruction large formations and to extend essentially the area of these technologies application in surgery, stomatology, genecology, dermatology, oncology, etc. The technique of complex MW-cryo-surgery has passed a wide clinical approbation.

Therefore searches of new methods of cryogenic impact intensification together with different physical factors were required. Well known methods of cryodestruction intensification like repeated cycles of freezing that are defrosting and ultrasound don’t kill pathological tissues completely. Theoretical bases for cryodestruction intensification are the factors, which increase the sensibility of tissues to low temperature impact. One of these factors is a super high frequency electromagnetic field (SHF EMF), remedial possibilities of which have been studied. Taking into account a possible mechanism of SHF EMF action on “water grille” of tissues it was surmised that a SHF field might intensify greatly destructive possibilities of a local cooling. Relaxation processes appear in dipole molecules of water and liquid mediums, resonance manifestations appear in high dispersed albumen molecules. Changes of a hydration zone of molecules are possible as well as a rupture of intermolecular liaisons. Tissues at high content of water absorb electromagnetic fields 10-60 times quicker than fat tissues.

The physicians together with scientists elaborated a method to intensify cryogenic destruction consisting in preliminary impact of SHF EMF on the region of local freezing. Preliminary heating of all volume of the vascular tumor with SHF EMF intensifies destructive possibilities of low temperatures 4-6 times with regard to depth of the tumor and 50 times with regard to its volume in comparison with simple cryodestruction. 1,200 children with cavernous and combined hemangiomas located under skin were treated by this method. The presented method is applied to deep hemangiomas located in the face (forehead, cheek, nose, parotic region).

The presented method gives the possibility to give up completely or in part complicated operational interventions particularly when little hemangiomas are placed in the face, in the neck, in the area of ear as well as to obtain good results (98%).

In practice we had a group of children with voluminous and deep hemangiomas placed in the face, parotic region, and the neck. Such hemangiomas are characterized by rapid growth, “clinical malignant” course, destruction of surrounding tissues, ulceration, and hemorrhage. After traditional surgical treatment the child with such hemangiomas becomes invalid because the tumor is taken out together with a facial nerve, and mimic musculature is paralyzed; during operation fatal hemorrhage might occur. Even ligation of the vessel feeding the tumor gives a short-term effect. Using prednisolone in big doses produce not always an effect. Also sclerotherapy is not effective. Local cryodestruction using powful automative cryogenic systems was pinned hopes on, but the success was temporary. 1-2 months later a recurrent tumor took place. This case gave a stimulus to carry out careful studies to define vitality of large, deep and complex hemangiomas. 1,500 children formed the group of patients with such hemangiomas.

Using roentgenangiography of hemangiomas at diagnosis showed that in all cases a big arterial trunk of abnormal texture came near the principal massif of the tumor; it fed the tumor and probably contributed to its fast growing. On the basis of the data obtained the method of reongenendovascular occlusion was elaborated; it consists in catheterization of feeding arterial trunk using the angiographic techniques and following occlusion of the distal arteries with embolization material (spherical and cylindrical gel from 0.4 to 0.6 mm). When arterial flow to the tumor is stopped heat loss of the hemangioma is stopped too; and so favorite conditions are created for further treatment (Fig.3). The conception of treatment of voluminous deep hemangiomas was elaborated that consisted in obligatory angiography, tumor embolization and further cryogenic or SHF cryogenic treatment (Polyaev et al.,1974).

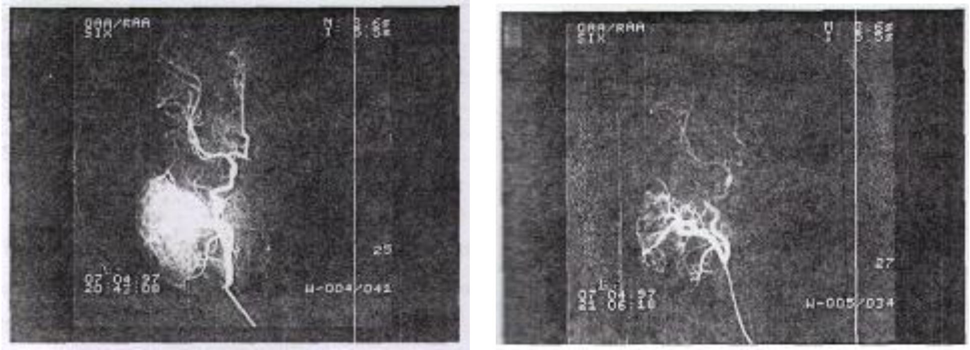

Figure 3. Roentgenangiography of haemangioma before and after the method of reongenendovascular occlusion

Taking into account that in general tumors are located in projection of the facial nerve it is better to use SHF cryogenic intervention because it guarantees to keep the facial nerve, mimic musculature and contours of the face intact. In 96% cases the treatment had positive results. (Fig. 4).

One must say that the problem of rehabilitation of a child appearance by elimination of innate defects has a great social importance. Every mother wants to have not only a valid but beautiful child. These technologies allow it.

Today the notion “cryotherapy” includes combination of physical methods of treatment based on heat removing by means of liquid, solid and gaseous working bodies (from a humid cold rub-down to the impact using ultralow temperatures).

An increasing traumatism presents an urgent problem in modern sports. The injury amount per thousand of athletes varies from 2 in track and field to 158 in rugby. Figure 1 shows relative incidences broken down by accident type and site: six of 10 sports injuries are dislocations, distortions, and/or torn ligaments (Kondratenko et al., 2010; Kondratenko and Nesterov, 2010; Butorina et al., 2009).

Figure 4.The child with parotic haemangioma before and after the microwave-cryogenic impact

A boiling gas mixture application at temperature T0 = 0 …-350 C is used to cool damaged tissue to achieve quick anesthetic effect. From the physical and biological point of view the reduction of skin temperature decreases the rate of nerve impulses transfer, and at skin temperature +50 C this process is blocked completely. This temperature is easily obtained when the cooling aerosol is used. Figure 5 shows the example of the temperature distribution in different time intervals after spraying of the cooling aerosol.

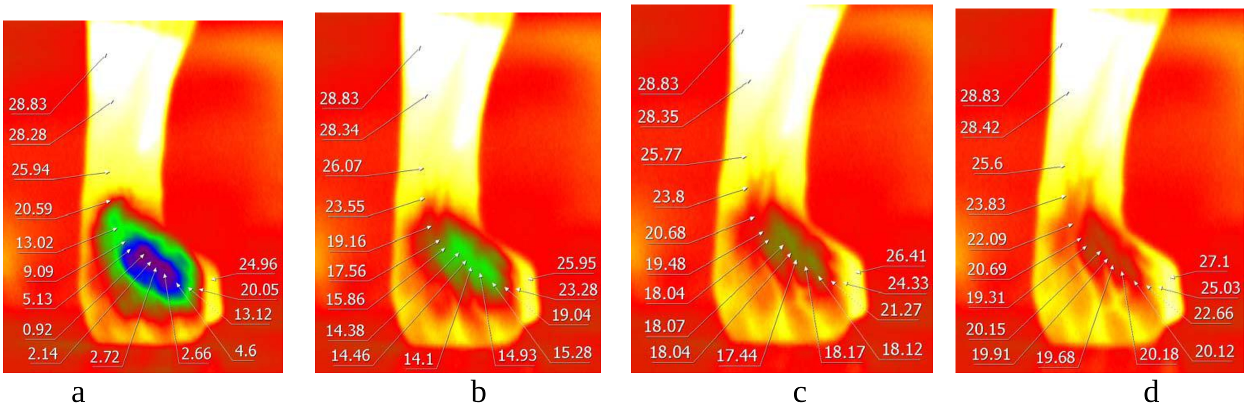

Figure 5. The temperature distribution on a human hand surface expressed in C at different time intervals after the cooling aerosol spraying (the temperature level -35.50 C) during 1 second from the distance of 20 cm.

a) immediately after cooling b) 20 seconds after cooling c) 40 seconds after cooling d) 60 seconds after cooling.

The picture is obtained using the thermograph “IRTIS- 2000 C”

The experimental data are obtained on the temperature distribution on the cooled surface at throttling from the nozzle (0.1; 0.5; 1 mm diameter) of the mixture (propane/butane/R123) to the temperature level T = -35,5; -25; -150 C used for sports medicine. The description of the pre-production model of the cooling spray “Ice wave” manufactured by the Vekshinski State Research Institute of Vacuum Technology is given. Approbation results on sportsmen are presented.

Experimental data are obtained on the gas jet temperature distribution in various volume points by refrigerating mixture throttling from the nozzle 0.1; 0.5; 1 mm diameter. The R123 mixture of propane\ butane is used for medical purposes. The study of the temperature field on the tissue surface is made by cooling gas mixtures dispersion to the temperature level -35.5; -25; -15 0C. Gas mixtures are propane-butane (40\60% mole); propane-butane\ R123 (12\18\70% mole); propane\butane\R123 (28\42\30% mole) coming from the nozzle with 0.1; 0.5; 1 mm in diameter from the distance of 5;50;100;200;250;300 mm.

A laboratory bench was developed to automate the work to investigate a gas jet thermodynamic parameters. The description of cooling spray for athletes “Ice wave” (preproduction models) is given. The pre-production models were made in the Vekshinski Institute. The method is suggested to use the aerosol with special gauze plasters which retain refrigerating medium after spraying. Thus the cooling effect is prolonged several times as much.

A cooling effect may be applied to different areas of the body as well as to the all body of a man. Today one of the pressing problems of modern sports is traumatism.

In sportive medicine the temperature lowering of skin reduces the conduction of nerve impulses and at $+5^0$C the conduction of these impulses is completely blocked. We examined the rates of involution of pathological symptomatology of damages. We studied the data obtained after one week of treatment (analgesic freezing) of patients of an experimental group. By the 7th day the linear velocity of the blood flow measured on the visible limit of a damage increased by 21.1% at the average. The volume velocity of the blood flow increased by 14.6%. The measurements in the undamaged areas far from the trauma of soft tissues also showed a positive dynamics: a linear velocity of a blood flow increased by 20.4%, the volume one by 16.5%. In the comparison group of patients the linear velocity of a blood flow increased only by 8.6%, and the volume one by 7.4%.

It has been found out that the “Ice wave” aerosol fully penetrates through the skin and produces a quick positive effect. During appraisal it was revealed that the sum time of rehabilitation of sportsmen using analgesic freezing decreased 2.5 times in comparison with the rehabilitation time of sportsmen which didn’t use it. These technologies are included in the complex of rehabilitation actions with the sportsmen.

## 3. CONCLUSIONS

1. Local cryodestruction using modern apparatuses where liquid nitrogen is used as a refrigerant (-196ºC), is the most successful method of treatment of simple hemangimas, thanks to this method a good oncological result is obtained (100%).
2. Method of preliminary radiation with SHF field of the region of freezing following cryodestruction gives the possibility to intensify destructives abilities of the low temperatures 4-6 times regarding to the depth of the hemangioma, and 50 times regarding to its volume if comparing with cryogenic destruction, but it keeps all useful properties of local low temperature destruction.
3. The method using obligatory angiography, embolization of the tumor helps to refuse severe traumatic operations with hemorrhage and injury of facial nerve branches.
4. During appraisal it was revealed that the sum time of rehabilitation of sportsmen using analgesic freezing decreased 2.5 times in comparison with the rehabilitation time of sportsmen which didn’t use it. These technologies are included in the complex of rehabilitation actions with the sportsmen.

## 4. REFERENCES

Kandel, E.I., 1974, *Cryosurgery,* Moscow, 303 p.

Polyaev Yu, Nikonorov A., Vodolazov Yu. Et al., 1994, *Vrach, Roentgenoendovascular Occlusion in Pediatric Surgery,* p. 21-23.

Cherstvy E.D., Kravtsov G.I., 1991, *Diseases of Fetus, Newborn, and Child, Vascular Tumors*, Minsk, p.111-113.

Fedoreev G.A., 1974, *Hemangiomas,* , Leningrad, 192 p.

Lectures on sports medicine, Educational textbook edited by B. Polyaev, 2008, Vol. 1,2,3,4. Moscow, Russian Association of Sports Medicine and sick people and invalid rehabilitation.

Kondratenko R, Nesterov S, Romanko V., 2010, Application of industrial gases as cooling agents for sports medicine and radio engineering. *Chemical oil and gas machine building*. 6: p.22-23.

Kondratenko R, Nesterov S. 2010, The study of the temperature field on different surfaces at cooling of the thin film of boiling gas mixture, *Vacuum technique and technology*. 20 (4): 264-267.

Butorina A, Kondratenko R, Polyaev B, Nesterov S, Romanko V, Vykhodets I, Trushanin I. 2009, The application of the anesthetic freezing aerosol at acute injures of musculoskeletal apparatus of sportsmen, *Journal of the Russian Association of Sports Medicine and sick people and invalids rehabilitation*. Poligraph Service, Moscow: 26-32.

# Author Index